# Thermodynamic Modelling of CaO-$Al_2O_3$-$SiO_2$-$H_2O$-Based Cements

Rupert Jacob Myers

Supervisors:

Prof. John L. Provis

Dr. Susan A. Bernal

Dr. Barbara Lothenbach

A thesis submitted in total fulfilment of the requirements for the degree of

Doctor of Philosophy


Department of Materials Science & Engineering

The University of Sheffield

May 2015

# Abstract

Most concrete is produced using calcium (alkali) aluminosilicate hydrate (C-(N-)A-S-H)-based cement. However, the chemistry of this phase in many cement-based materials is still not fully understood. This thesis presents a structural and thermodynamic investigation of C-(N-)A-S-H and C-(N-)A-S-H-based cements to provide insight into the chemistry of these materials.

A mixed cross-linked and non-cross-linked tobermorite-like structural model for C-(N)-A-S-H is developed (the CSTM), which more appropriately describes the spectroscopic information available for this phase. Application of the CSTM to a $Na_2SiO_3$-activated slag cement cured for 56 and 180 days indicates the presence of a poorly-crystalline zeolite-like phase. The role of Al in cross-linking of C-(N-)A-S-H is also studied, which provides a more advanced description of the chemistry and structure of C-(N-)A-S-H than previously reported.

A thermodynamic model for C-(N-)A-S-H (CNASH_ss) is derived, which greatly advances the utility of thermodynamic modelling of C-(N-)A-S-H-based cements by explicitly defining Al and alkali uptake in this phase. The chemistry of alkali-activated slag (AAS)-based cements is simulated using CNASH_ss and an ideal solid solution thermodynamic model for MgAl-OH-LDH that is also developed in the thesis. This analysis provides a good description of $Na_2SiO_3$-activated slag cement chemistry and accurately predicts chemical shrinkage in this material. Phase diagrams for NaOH, $Na_2SiO_3$, $Na_2Si_2O_5$ and $Na_2CO_3$-activated slag-based cements are also simulated. These results can be used to design the chemistry of AAS-based materials.

A detailed analysis of C-(N-)A-S-H solubility is presented, for Ca, Al, Si and alkali concentrations most relevant to C-(N-)A-S-H-based cements and at temperatures of 7-80°C. Solubility products for alkali-free C-(N-)A-S-H change slightly between 7°C and 80°C and as a function of Al/Si ratio. However, less soluble C-(N-)A-S-H is formed at higher Ca and alkali content. These results are important for understanding the stability of C-(N-)A-S-H in the majority of cement-based materials used worldwide.

# Table of Contents

# Preface

This thesis is mainly comprised of a collection of papers that have been published in or are currently in preparation for submission to peer-reviewed journals, which have been reformatted and revised for improved cohesion. Therefore, each results and discussion chapter (Chapters 4-9) contains a conclusions section, with an additional conclusions chapter (Chapter 10) and recommendations for future work (Chapter 11) provided to unify the thesis as a whole. The literature review includes additional discussion of thermodynamics, and structural and thermodynamic models that are not included in the publications from the thesis. Most of the experimental details are provided in the materials and methods chapter (Chapter 3), although some information is provided separately in the results and discussion chapters for improved clarity and flow, such as the thermodynamic data used to describe solid phases.

The work presented in the thesis was conducted at three different institutions. Chapters 4 and 5 were completed at the University of Melbourne and the University of Sheffield: scanning electron microscopy results were measured by Rackel San Nicolas, and X-ray diffraction and nuclear magnetic resonance data were obtained by Susan A. Bernal with assistance from John D. Gehman. Chapters 6 and 7 were completed at the University of Sheffield. Work on Chapters 8 and 9 was conducted at the Laboratory for Concrete and Construction Chemistry, EMPA, in collaboration with Barbara Lothenbach and Emilie L'Hôpital, with assistance from Salaheddine Alahrache and Daniel Rensch for the nuclear magnetic resonance experiments, Luigi Brunetti and Boris Ingold for assistance in the laboratory, X-ray diffraction and thermogravimetric analysis, and Ellina Bernard and Nikolajs Toropovs for additional

assistance with thermogravimetric analysis. The ion chromatography data was obtained by Emilie L'Hôpital with assistance from Luigi Brunetti.

# Declaration

This declaration certifies that:

1. The thesis comprises only my original work towards the PhD except where indicated otherwise in the Preface and/or at the start of each chapter; and

2. Due acknowledgement has been made in the text to all other material used.

Signed: 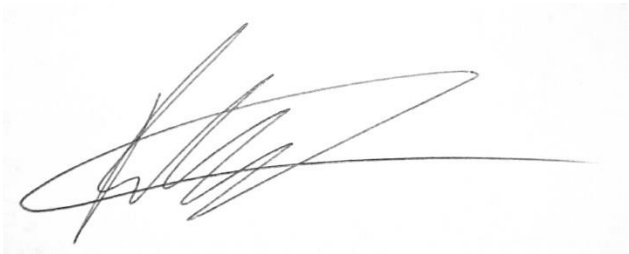

Date: 9 May 2015

# Acknowledgements

This thesis represents the culmination of an approximately three-year-long journey that has taken me from one side of the world to the other and has been influential in shaping my professional ambitions, which would not have been possible without the help of many people (in no particular order):

Jannie S. J. van Deventer, thank you for giving me the opportunity to work as a research assistant with the Geopolymer and Mineral Processing Group at the University of Melbourne as an undergraduate student years ago. Without your interest, I may have never pursued a career in materials science.

John L. Provis, thank you for also giving me that opportunity all those years ago, the option to live and work on my thesis in Sheffield, and for your continued support in my professional development. I have greatly enjoyed the independence that you have given me in my research activities, your encouragement in search of additional insight, and your desire for me to maximise my learning and scientific output in the years that we have worked together. Susan A. Bernal, it has also been a great pleasure to get to know and work with you in the last few years; the research culture that you and John foster is something that I will carry with me throughout my career. In particular, I come out of this PhD with an attitude to enshrine a generosity of spirit and a commitment to invest in and maximise the professional development and learning of others. Thank you.

My time spent working with Barbara Lothenbach and Emilie L'Hôpital at EMPA positively and profoundly impacted my approach to research. Thank you Barbara for bringing me into the EMPA family, showing me an alternative attitude to research,

teaching me some of the finer points of thermodynamics and geochemistry, and bestowing on me a similar generosity of spirit that my Sheffield and Melbourne research groups have done. Emilie, your guidance in teaching me the experimental side of materials science has been invaluable; I am a much improved researcher because of you. It has been a pleasure to work with you both.

Thanks are due to many others that I have met while working on this thesis. To the Sheffield group, in particular PGR3, it has been awesome to work alongside and/or live the daily international student life with you. This thesis would have been much more difficult and much less fun to complete without you. Walti Trindler, thank you for your amazing generosity in taking me into your Hegnau family. Your positive attitude is admirable. Nikolajs Toropovs, Switzerland would not have been the same without you. To everyone else at EMPA, thank you for showing me what is probably the best research environment that I have been a part of.

I would also like to thank Rackel San Nicolas at the University of Melbourne for instructing me in scanning electron microscopy, and the others in the Geopolymer and Mineral Processing Group for the great time that I spent there before moving to Sheffield.

Thank you to everyone else that I have worked with, met or learned from over these years, from those that I have seen present at scientific conferences to those that I have only learned from via their publications.

Finally, thank you to the Australian Government for providing financial support via the Australian Postgraduate Award during my time at the University of Melbourne, to John L. Provis and the University of Sheffield for financial support while based in Sheffield, and to the Laboratory for Concrete and Construction Chemistry at EMPA for the additional funding support to live and work in Switzerland.

# List of Tables and Figures

## List of Tables

## List of Figures

# Nomenclature

*Glossary of symbols*

| | |
|---|---|
| $a$ | Extent of substitution of trivalent cation *R* in bridging sites |
| $\dot{a}$ | Ion size parameter in the extended Debye-Hückel equation |
| $a'$, $b'$, ..., $e'$ | Stoichiometric coefficients in the additivity method |
| $A_\gamma$ | Temperature-dependent electrostatic parameter in the extended Debye-Hückel equation |
| *BCI* | Combined *BT*, *CB* and *IC* sites (*BCI* = *BT* + *CB* + *IC*) |
| $b^{sc}$ | Neutron scattering length |
| *BT* | Bridging tetrahedra |
| $B_\gamma$ | Pressure-dependent electrostatic parameter in the extended Debye-Hückel equation |
| $b_\gamma$ | Short-range interaction parameter in the extended Debye-Hückel equation |
| $c$ | Charge of the charge-balancing interlayer cation |
| [*C*] | Cross-linked |
| *CB* | Interlayer charge-balancing species for bridging tetrahedra |
| *CL* | Chain length of an end-member in the sublattice solid solution model |
| $Cp^o$ | Absolute isobaric heat capacity at standard state |
| $C_Q$ | Quadrupolar coupling parameter |
| *CU* | Interstitial 'solid solution' $Ca(OH)_2$ |
| $d_1$, $d_2$ | Coefficients for the *CB* sites |
| $e_1$, $e_2$ | Coefficients for the *IC* sites |
| $\Delta_f G^o$ | Standard Gibbs free energy of formation |
| $G_m$ | Gibbs free energy of mixing |
| $G_m^E$ | Excess Gibbs free energy of mixing |
| $h$ | The amount of water per dreierketten unit in a tobermorite-like structure |
| $\Delta_f H^o$ | Standard enthalpy of formation |
| $i$ | Species of the sublattice solid solution model |
| $I$ | Ionic strength of the aqueous electrolyte phase in the extended Debye-Hückel equation |
| I, II, III, IV, V, VI | Stoichiometric coefficients of the sublattice sites in the solid solution model |
| $i_1 i_2 i_3 ... i_s$ | End-member of the sublattice solid solution model written in terms of the species substituted in sublattice sites 1, 2, 3,…, *s* |
| *IAP* | Ion activity product |
| *IC* | Interlayer charge-balancing species for the *TU* sites |

*Glossary of symbols continued*

| | |
|---|---|
| *IW* | Interlayer water |
| *k* | End-member of the sublattice solid solution model |
| $K_s$ | Solubility product |
| $K_{so}$ | Solubility product at zero ionic strength |
| *l* | Charge-balancing interlayer cation |
| *m* | Interlayer water content |
| *MW* | Molecular weight |
| [*NC*] | Non-cross-linked |
| $N_A$ | Avogadro constant ($6.022 \times 10^{23}$ $mol^{-1}$) |
| $n_s$ | Sublattice sites |
| *R* | Trivalent cation in tetrahedral coordination |
| *R** | Universal gas constant ($8.3145$ $J \cdot mol^{-1} \cdot K^{-1}$) |
| *s* | Index of sublattice site *n* |
| $S^o$ | Absolute entropy at standard state |
| *SI** | Effective saturation index |
| *T* | Temperature |
| *TU* | Main chain site, $CaSiO_{3.5}^-$ |
| *u* | Interlayer $H^+$ content per dreierketten unit in C-(N-)A-S-H |
| *U* | Term containing the Gibbs free energies for the reciprocal reactions |
| $V^o$ | Standard molar volume |
| $x_{jw}$ | Molar quantity of water in the extended Debye-Hückel equation, mol |
| $X_w$ | Total molar amount of the aqueous phase in the extended Debye-Hückel equation |
| $y_i^{ns}$ | Site fraction of species *i* in the sublattice site $n_s$ |
| $z_j$ | Charge of aqueous species *j* |
| $\alpha_k$ | Activity of end-member *k* |
| $\gamma_j$ | Activity coefficient of aqueous species *j* |
| $\delta$ | Fraction of combined bridging site vacancies per cross-linked tobermorite unit |
| $\delta_{iso}$ | Isotropic chemical shift |
| $\delta_{obs}$ | Observed chemical shift |
| $\Delta_{rcp}{}^oG$ | Standard Gibbs free energy of a reciprocal reaction between end-members of the sublattice solid solution model |
| $\eta$ | Parameter describing the partitioning of $Q^1$ species into non-cross-linked and cross-linked C-(N-)A-S-H |
| $\lambda_k$ | Fictive activity coefficient of end-member *k* |
| $\mu$ | Chemical potential |
| $\nu$ | Fraction of bridging site vacancies per dreierketten unit |
| $\rho'$ | Density of an end-member of the sublattice solid solution model |
| $\rho^{sc}$ | Neutron scattering length density |
| $\varphi$ | Interlayer $Ca^{2+}$ content per dreierketten unit in C-(N-)A-S-H |
| $\Phi^o$ | Standard thermodynamic property estimated by the additivity method |

*Glossary of symbols continued*

| | |
|---|---|
| $\omega$ | Interlayer $Ca^{2+}$ content per cross-linked tobermorite unit in C-(N-)A-S-H |
| $\chi_k^{i,ns}$ | Effective mole fraction of end-member $k$ containing species $i$ in sublattice site $n_s$ |
| $\zeta$ | Stoichiometric coefficient of the $s^{th}$ sublattice site |

*Glossary of terms*

| | |
|---|---|
| AAS | Alkali-activated slag |
| AFm | Aluminoferrite-mono |
| AFt | Aluminoferrite-tri |
| C-S-H | Calcium silicate hydrate |
| C-A-S-H | Calcium aluminosilicate hydrate |
| C-(A-)S-H | Calcium (alumino)silicate hydrate |
| C-(N-)A-S-H | Calcium (alkali) aluminosilicate hydrate |
| CL | Chain length |
| CSTM | Cross-linked Substituted Tobermorite Model |
| FA | Fly ash |
| FWHH | Full width at half height |
| GBFS | Ground granulated blast furnace slag |
| LDH | Layered double hydroxide |
| MCL | Mean chain length |
| MK | Metakaolin |
| N-A-S(-H) | Alkali aluminosilicate (hydrate) |
| PC | Portland cement |
| SCM | Supplementary cementitious material |
| SF | Silica fume |
| SGM | Substituted General Model |
| TAH | Third aluminate hydrate |
| wPc | White Portland cement |

# 1

# Introduction

Concrete is by far the most widely used construction material. On a per volume basis, concrete is the second most used commodity after fresh water (Aïtcin, 2000). Concrete is comprised of at least three key ingredients: coarse and fine aggregates e.g. crushed rocks and sand; water; and cement. Cement, the integral component of concrete that gives the material its binding properties when hydrated, is also used in vast amounts: 4 Gt of cement were produced in 2013 (U.S. Geological Survey, 2014) (Figure 1.1), which is equivalent to ~1.5 kilograms/person/day at current world population levels. Cement production is projected to increase greatly over the forthcoming decades, due mostly to the continued industrialisation of developing countries e.g. India (Taylor et al., 2006).

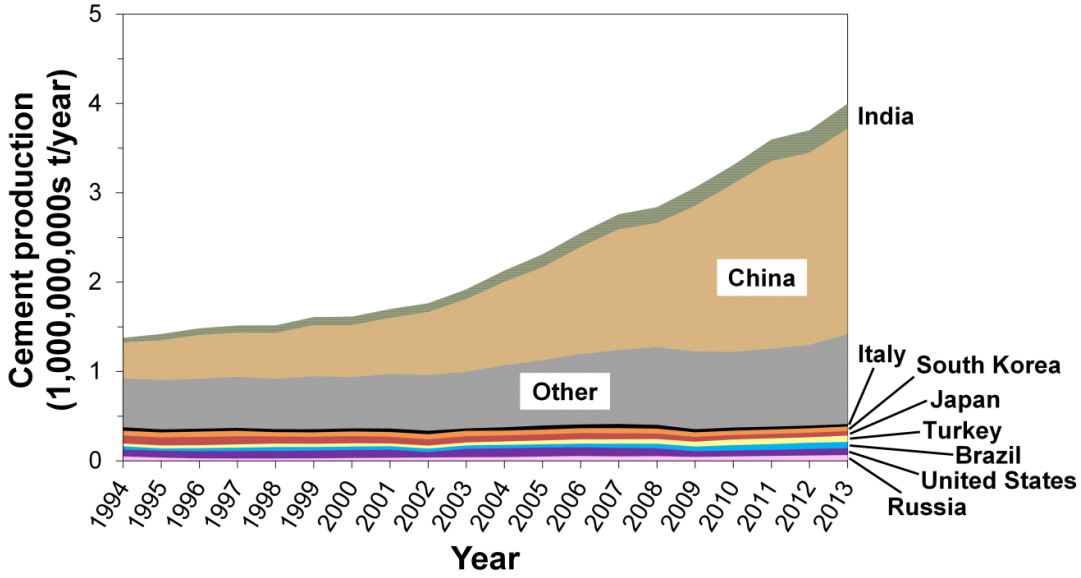


Figure 1.1. Global cement production from 1994 to 2013, showing the top nine cement producing countries and the rest of the world (other). Data from U.S. Geological Survey (2014).

The enormous quantities of cement and concrete used are reflected in the ubiquity and importance of the construction industry to the world economy, which accounts for approximately 5-10% of global employment and gross value added (Choy, 2011; Ng et al., 2009). The impact of the construction industry on the environment is also significant, with 5-8% of all anthropogenic $CO_2$ emissions attributable to the manufacture of cement alone (Olivier et al., 2012; Worrell et al., 2001). Improving the sustainability of the construction industry is a key driver in the development of modern construction materials.

Cement and concrete were developed approximately 2000 years ago by Romans, and these cements were principally produced using a mixture of volcanic ash, lime and water (Jackson et al., 2013). However, today, the great majority of cements used are Portland cement (PC)-based. PC is made by firing a mixture of limestone, clay and similar minerals to ~1450°C to produce clinker (Figure 1.2), which is then mixed with additives such as gypsum and finely ground to a powder (Taylor, 1997). Modern reinforced concrete structures made from PC-based materials have low embodied $CO_2$ content relative to other construction materials in heavy load applications (Purnell, 2012), despite the large $CO_2$-footprint of the global construction industry.

Approximately half of the $CO_2$ emissions from PC manufacture are produced from the calcination of limestone ($CaCO_3$) added as raw feed in the clinker production process (Figure 1.2). This $CO_2$ is intrinsic to the production of PC clinker; the embodied $CO_2$ content of modern PC-based materials varies between 0.73 and 0.99 t $CO_2$/t cement depending largely on the amount of PC clinker used in the cement formulation (Bernstein et al., 2007). The $CO_2$-footprint of the construction industry can therefore be reduced by replacing PC clinker with supplementary cementitious materials (SCMs) that contain lower embodied $CO_2$ content, do not require additional energy and $CO_2$-intensive processing, but have some cementitious value. These materials are called blended cements or blended PC-based materials.

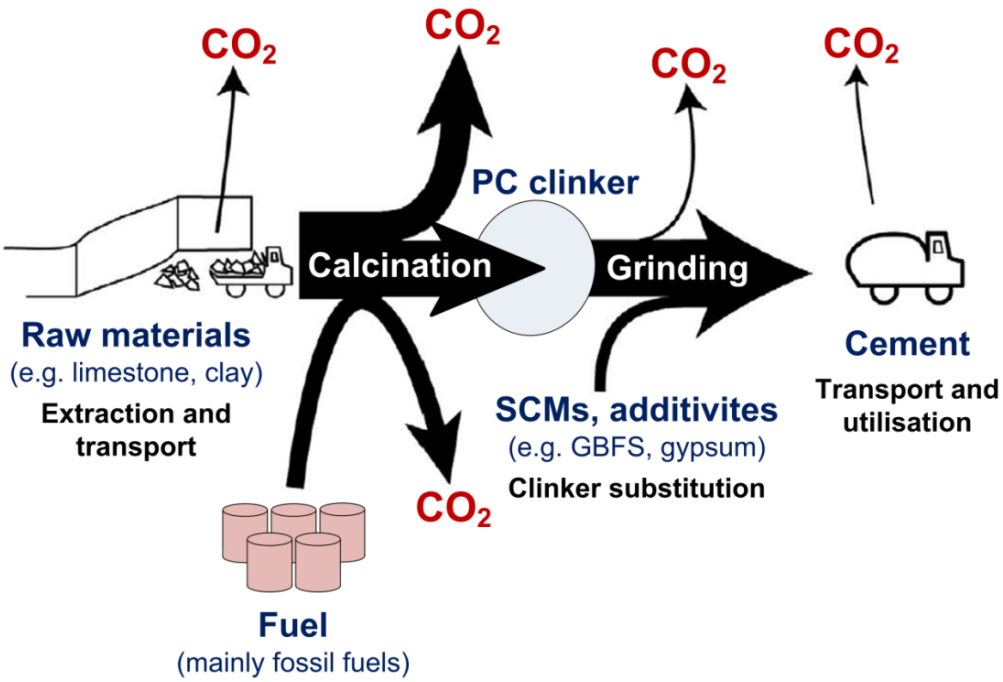


Figure 1.2. Schematic representation of the PC production process, adapted from (Habert et al., 2010). The thicknesses of the arrows correspond to the typical amount of material used. SCMs are supplementary cementitious materials and GBFS is ground granulated blast furnace slag (see text).

In 2011, the average PC clinker to cement ratio reported by the World Business Council for Sustainable Development (2012) was ~76% (representing ~20% of the global cement production capacity, although the data are mostly from Europe, North and Central America, and Brazil), reflecting the success of this strategy in the development of modern construction materials. The efficiency of the clinker manufacturing process is also important, but reducing the PC clinker to cement ratio is the most effective way to reduce the $CO_2$-footprint of the construction industry unless expensive and untried carbon capture and storage technology is adopted (Schneider et al., 2011).

An additional benefit of replacing PC clinker with SCMs is the utilisation of industrial by-products (Figure 1.2). Two of the most commonly used SCMs are ground granulated blast furnace slag (GBFS), which is a by-product from pig iron production, and fly ash, which is a by-product from coal-fired power generation. Metakaolin, which is a type of calcined clay, is another widely used SCM. The performance of hydrated PC-based materials can be improved substantially if the PC

clinker to cement ratio is designed correctly for the intended application, because SCMs are typically less reactive than PC clinker (Lothenbach et al., 2011). This reduced reactivity limits the extent to which SCMs can be used in high performance PC-based materials (Snellings et al., 2012), but can be overcome for some SCMs if an additional source of alkalinity is added. This additional alkaline source is called an activator. Activators can be present in solid or aqueous form, but water is essential to form a hardened solid binder.

Blended PC-based cements reacted with an activator (in addition to water) are called 'hybrid' alkali-activated cements (Figure 1.3). Alkali-activated cements are the class of cementitious materials formed from the reaction between an activator, water (if an anhydrous activator is used) and one or more solid precursors excluding PC, which are typically fly ash (FA), GBFS and metakaolin (MK) (Provis and Bernal, 2014), i.e. the same SCMs as used in blended PC-based materials. The increased alkalinity of these materials generally means that a greater variety of precursors can be used relative to the selection of SCMs available in hydrated PC-based materials, such as metallurgical slags with poorer hydraulic reactivity than GBFS (Shi and Qian, 2000). Alkali-activated cements can also offer substantial $CO_2$ savings relative to plain PC materials by avoiding the energy and $CO_2$-intensive PC clinkering process, but the savings depend greatly on the local availability of activators and precursor materials (McLellan et al., 2011). There are other important alternative cements with lower embodied $CO_2$ content relative to neat PC materials (Juenger et al., 2011), but these are not discussed further here.

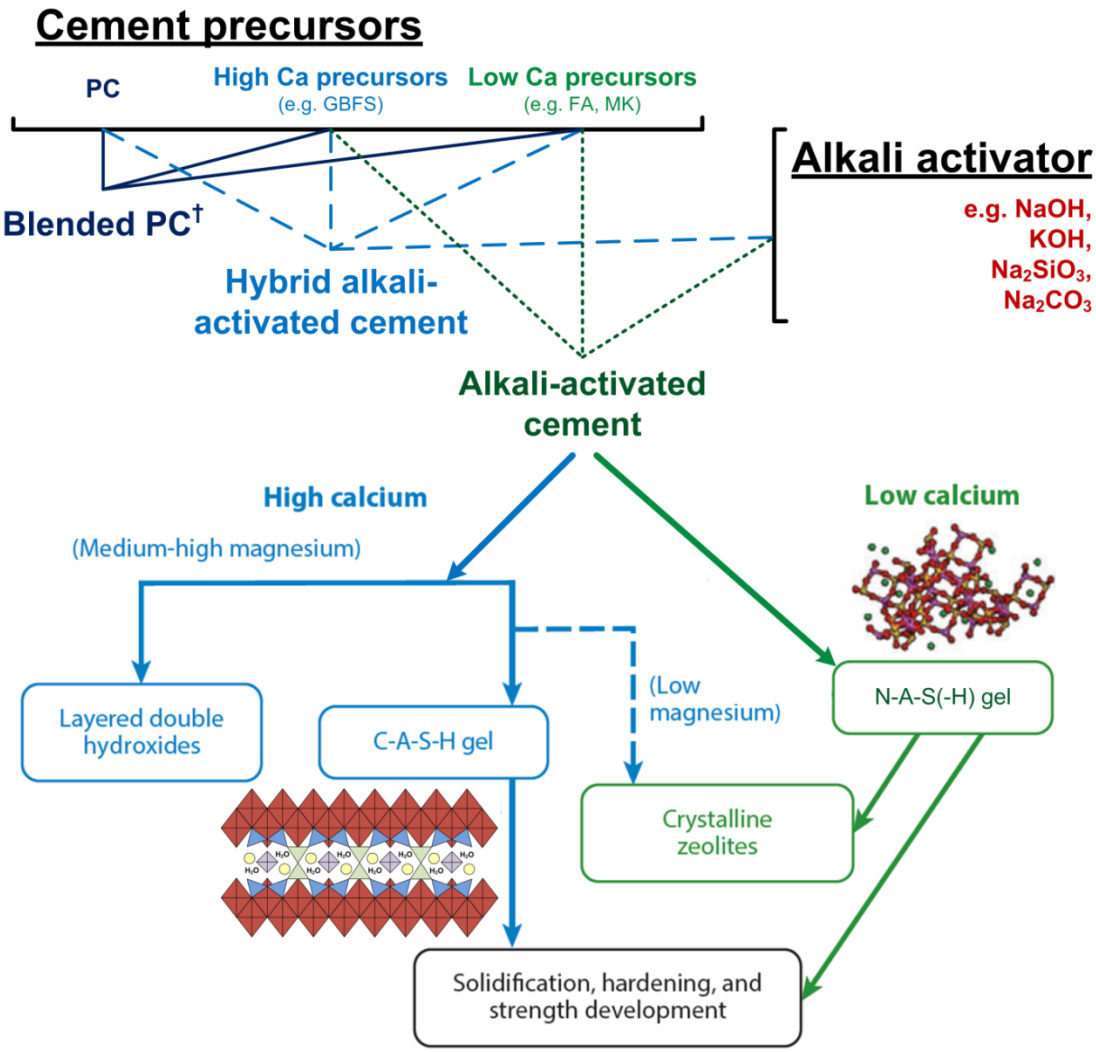


Figure 1.3. Flow diagram representing the materials used to produce blended PC, hybrid alkali-activated cements and alkali-activated cements, and reaction products in alkali-activated cements, adapted from (Provis and Bernal, 2014). † Blended PC typically contains SCMs not specifically mentioned here (e.g. gypsum).

The lower availability of SCMs and other precursors for alkali-activated cements, relative to the enormous quantities required by the construction industry, is a key limitation for their use. This limitation is apparent in the European context, as many European countries achieved 90-100% utilisation rates of fly ash more than two decades ago (Manz, 1997). Other countries have much lower fly ash utilisation rates (Bhattacharjee and Kandpal, 2002), although development of more $CO_2$ and energy-efficient industrial processes will likely further constrain the availability of the most commonly used SCMs in the future (Scrivener and Kirkpatrick, 2008). However, the widespread and continued use of SCMs in blended PC-based materials and the

development of alternative construction materials with lower embodied $CO_2$ content, such as alkali-activated cements, mean that the complexity and number of different cement formulations will continue to increase in the future. This demonstrates an essential and growing need to more fully understand the fundamental chemistry of cement-based materials, because their mechanical strength and durability properties can change greatly as a function of the cement formulation (Jennings and Bullard, 2011), and because cement chemistry is intrinsically linked to cement and concrete durability (van Deventer et al., 2012).

Therefore, this thesis aims to develop a deeper understanding of the chemistry of modern cementitious materials, with a particular focus on alkali-activated cements, although the work is also relevant to some hybrid alkali-activated cements and blended PC-based materials. This work is presented in three stages in addition to the literature review presented in Chapter 2. Chapters 4-5 discuss the nanostructure and chemical composition of calcium (alkali) aluminosilicate hydrate (C-(N-)A-S-H), which is the dominant reaction product in many modern cements, and is thus a key contributor to cement and concrete performance. This insight is used to develop and apply a thermodynamic model for C-(N-)A-S-H in Chapters 6-7, with the aim of advancing the utility of thermodynamic modelling in simulating the chemistry of modern cementitious materials. Chapters 8-9 provide additional analysis of C-(N-)A-S-H solubility, chemical composition and nanostructure, which is important for future development of thermodynamic models for this phase. The underlying thermodynamic principles used in the thesis provide a broadly-applicable theoretical framework from which the chemistry, and therefore durability, of modern cementitious materials can be better understood.

The literature review presented in Chapter 2 includes a detailed discussion of hydrated PC-based and alkali-activated slag (AAS)-based cement chemistry (i.e. alkali-activated cements derived from metallurgical slag precursors), with a particular focus on the C-(N-)A-S-H phase, although secondary and minor products are also discussed. A critical overview of the existing structural models for C-(N-)A-

S-H is presented, which is referred to later in the discussion of thermodynamic models for this phase. A discussion of some important thermodynamic concepts is provided to assist in the discussion of thermodynamic models for C-(N-)A-S-H and other cement phases, and thermodynamic databases.

Chapter 3 presents an overview of the materials and methods used in the thesis, including details of the thermodynamic modelling approach applied here. Detailed descriptions of the materials used in the thesis, GBFS and laboratory-synthesised C-S-H, C-(A-)S-H and C-(N-)A-S-H,[1] are presented. The experimental details and brief descriptions of the experimental techniques used in the thesis are also discussed.

A structural model for mixed cross-linked/non-cross-linked tobermorite-like C-(N-)A-S-H is proposed in Chapter 4; the 'Cross-linked Substituted Tobermorite Model' (CSTM). The CSTM is formulated to allow calculation of C-(N-)A-S-H structural parameters such as the mean chain length (MCL) and cross-linked phase fraction, and chemical composition information such as Al/Si and Ca/Si ratios, from $^{29}$Si magic angle spinning nuclear magnetic resonance (MAS NMR) spectral deconvolution results. This structural model is shown to greatly advance the detail in which C-(N-)A-S-H chemistry can be analysed by correct application of structural constraints to deconvolutions of $^{29}$Si MAS NMR spectra.

In Chapter 5, the role of Al in the nanostructural development of C-(N-)A-S-H in a $Na_2SiO_3$-activated slag cement is analysed by X-ray diffraction (XRD), and $^{27}$Al and

[1] The C-S-H, C-A-S-H, C-(A-)S-H and C-(N-)A-S-H notation describes calcium silicate hydrate type solid phases with similar nanostructure but with different overall chemical composition, in cement chemistry notation: C is CaO, S is $SiO_2$, H is $H_2O$, A is $Al_2O_3$ and N is $Na_2O$ (although N refers more generally to oxides of alkali elements, typically $Na_2O$ and $K_2O$, that are not intrinsic structural components of this solid phase, as identified by the parentheses). The hyphens indicate that the chemical compositions of these solid phases are variable and non-stoichiometric. This notation strictly implies that C-S-H contains only Ca, Si, H and O, and C-A-S-H contains these elements and additionally Al, but this distinction is not always needed because these phases form part of the same C-(N-)A-S-H solid solution. Therefore, the most general notation possible is used to describe C-S-H, C-A-S-H and C-(N-)A-S-H in the thesis unless the distinction between these phases is important.

$^{29}$Si MAS NMR up to 180 days of curing. Additional $^{27}$Al MAS NMR spectra for samples cured for 2 years are also analysed. Application of the CSTM to the $^{29}$Si MAS NMR spectral deconvolution results demonstrates the advanced structural description of C-(N-)A-S-H provided by the model.

A thermodynamic model for C-(N-)A-S-H, CNASH_ss, is developed in Chapter 6. The discussion of C-(N-)A-S-H nanostructure presented in Chapters 4-5 is used to guide development of the structural component of this thermodynamic model, which is formulated in terms of tobermorite-like phases. This structural definition is applicable to AAS cements and hybrid alkali-activated cements and blended PC-based materials with bulk Ca/Si $\leq$ 1.5. The thermodynamic model is validated against a large set of solubility data in the CaO-($Na_2O$,$Al_2O_3$)-$SiO_2$-$H_2O$ and AAS cement systems, chemical composition data for C-A-S-H, and the volumetric properties of C-(N-)A-S-H in AAS cements.

The CNASH_ss thermodynamic model is applied in Chapter 7 to simulate the chemistry and volumetric properties of AAS-based cements. An ideal solid solution model for MgAl-OH-LDH is also presented and applied. Thermodynamic modelling of the experimental $Na_2SiO_3$-activated slag cement studied in Chapters 4-5 is performed, and the results are compared to the experimentally-determined chemistry of this material. Additional thermodynamic modelling is performed for $Na_2SiO_3$-activated slag cements over a range of CaO, MgO and $Al_2O_3$ slag chemical compositions, and a $Na_2CO_3$-activated slag cement, and compared to the available information for these materials in the literature. Phase diagrams for the relevant range of CaO-$Al_2O_3$-MgO compositions in AAS-based cements are simulated, showing the composition envelope where zeolites and C-(N-)A-S-H are both stable. These results are important for the design of high-performance AAS-based materials.

Chapter 8 provides an analysis of the solubility, chemical composition and nanostructure of C-A-S-H as a function of temperature between 7 and 80°C, and Al content under equilibrium conditions. The results are important for further

development of thermodynamic models for this phase and for understanding the stability of C-A-S-H in cementitious materials.

C-(N-)A-S-H samples are synthesised similarly in Chapter 9, although the analysis of chemical composition nanostructure and solubility is performed at 50°C and in the presence of alkali. The results are compared with the solubility products for the end-members of the CNASH_ss thermodynamic model, and show important trends in the stability and nanostructure of C-(N-)A-S-H products as functions of Al, Ca and alkali concentrations.

The results from each Chapter 4-9 are then summarised in Chapter 10. Therefore, this chapter describes the improved utility of the thermodynamic modelling technique and the advanced chemical understanding of C-(N-)A-S-H-based cementitious materials, particularly AAS-based cements, resulting from the work undertaken in the thesis.

# 2

# Literature Review

## 2.1 Cement Chemistry

### 2.1.1 Portland Cement-Based Materials

Most cementitious binders used in the construction industry are produced from Portland cement (PC), which is a material that dates back nearly two hundred years (Moir, 2003). The main reaction product that results from the hydration of plain PC is a Ca-rich ($1.5 \leq Ca/Si \leq 2$) calcium silicate hydrate (C-S-H) (Taylor, 1997), which is thought to be comprised of non-cross-linked tobermorite-like structures with Ca-OH linkages (Chen et al., 2004; Grangeon et al., 2013; Richardson, 2008). Although the chemistry of hydrated plain PC materials is now relatively well established, most modern cements are comprised of PC blended with Al-containing supplementary cementitious materials (SCMs), which react to form binders containing calcium aluminosilicate hydrate (C-A-S-H) with significantly lower Ca content ($Ca/Si \leq 1.5$) as the dominant reaction product (Lothenbach et al., 2011; Richardson and Groves, 1992a). This phase plays an influential role in the performance of these materials (Jennings and Bullard, 2011) and contains relatively low Al content ($Al/Si < 0.1$ (Gallucci et al., 2013; Richardson and Groves, 1993a; Skibsted and Andersen, 2013)).

The most typical SCMs are ground granulated blast furnace slag (GBFS), metakaolin (MK), fly ash (FA) and silica fume (SF) (Lothenbach et al., 2011; Snellings et al., 2012). The solid phase assemblages in binders produced from blended cements vary greatly as a function of the SCMs used (Lothenbach et al., 2011), but the nature of the C-A-S-H products formed show a broad similarity to C-S-H in PC binders

(Richardson, 2004). The main secondary products formed in these materials are portlandite ($Ca(OH)_2$), 'aluminoferrite-mono' (AFm) type phases such as calcium monosulfoaluminate hydrate ($C_4A\bar{S}H_{12}$) and 'aluminoferrite-tri' (AFt) type phases such as ettringite ($C_6A\bar{S}_3H_{32}$) (Lothenbach et al., 2011), Figure 2.1.

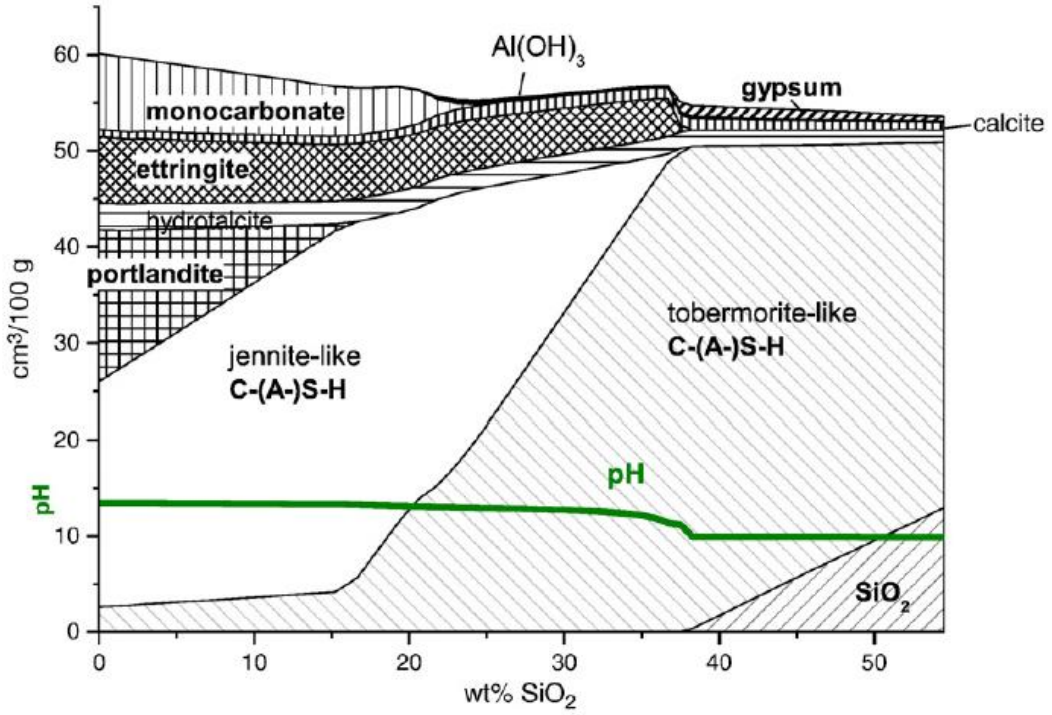


Figure 2.1. Modelled solid phase assemblage and pH of hydrated blended SF/PC pastes, assuming thermodynamic equilibrium and complete reaction of the PC, and representing C-(A-)S-H as a solid solution of jennite-like and tobermorite-like constituents. Reproduced from Lothenbach et al. (2011).

### 2.1.2 Alkali-Activated Slag (AAS) Cement

Most SCMs react slower than PC clinker phases during cement hydration (Lothenbach et al., 2011), but high-performance binders can be produced from the reaction between SCMs and a concentrated alkaline solution (called an alkali activator). GBFS is a SCM with 'latent hydraulicity', i.e. it reacts with water at a much slower rate than PC (Snellings et al., 2012), that can be used to produce high performance construction materials when reacted with an alkali activator; these materials are called alkali-activated slag (AAS). AAS has been developed and commercialised in many parts of the world as a high-performance alternative to PC

(Provis and Bernal, 2014), and durable concretes made using AAS binders have been used in structural applications for decades (Xu et al., 2008).

The level of Ca in alkali-activated slag cements is lower than in hydrated PC-based materials, which are formed through the reaction between GBFS and a highly alkaline solution, most commonly NaOH, KOH or $Na_2O{\cdot}mSiO_2{\cdot}xH_2O$. These materials are typically Na-based, although the products of activation with alternative alkalis such as K are generally similar (Provis and Bernal, 2014). The compositions of the C-A-S-H products formed in these materials (denoted C-(N-)A-S-H to reflect the increased alkali content in addition to the high levels of Al incorporated into this phase) vary depending on the activation conditions, but are typically poorer in Ca (Ca/Si ≈ 1 (Shi et al., 2006)) and richer in Al (Al/Si > 0.1 (Le Saoût et al., 2011; Myers et al., 2013; Richardson et al., 1994)) than the C-S-H products formed in PC-based binders (Taylor et al., 2010). C-(N-)A-S-H is the main strength-giving phase in AAS (Chen and Brouwers, 2007; Shi et al., 2006). AAS materials are a particularly relevant model system for the analysis of C-(N-)A-S-H chemistry in general because GBFS is a widely used replacement material in modern cements (Juenger et al., 2011), the chemical compositions of AAS cements sit within the compositional region which forms C-(N-)A-S-H (Lothenbach et al., 2011), and AAS chemistry is relatively well understood (Shi et al., 2006).

A detailed chemical-level understanding of AAS materials is a prerequisite for developing and increasing the commercial uptake of AAS technology in modern civil infrastructure, but this information has not yet been fully elucidated. This is due largely to the low crystallinity and complex chemistry of C-(N-)A-S-H, which varies in AAS according to:

i) the activator type and concentration (Ben Haha et al., 2011a; Schneider et al., 2001);
ii) the composition and reactivity of the GBFS precursor (Ben Haha et al., 2011b; 2012);

iii) the curing conditions to which the material is subjected (Schneider et al., 2001).

Secondary reaction products are intimately mixed with C-(N-)A-S-H in AAS cements, because the bulk composition of these materials generally falls outside the domain of stability of phase-pure C-(N-)A-S-H (García-Lodeiro et al., 2011; Lothenbach et al., 2011) (Figure 2.2). These products can include Mg-Al layered double hydroxide (LDH) phases (Richardson et al., 1994; Wang and Scrivener, 1995), AFm type phases including strätlingite ($C_2ASH_8$) (Ben Haha et al., 2012), and calcium monocarboaluminate hydrate ($C_4AcH_{11}$) in alkali carbonate-activated slag cement (Shi et al., 2006), katoite ($C_3AH_6$) (Bonk et al., 2003), which is an end-member of the hydrogarnet solid solution series ($Ca_3Al_2(SiO_4)_{3-y}(OH)_{4y}$; $0 \leq y \leq 3$) (Passaglia and Rinaldi, 1984), zeolites including gismondine and heulandite (Bernal et al., 2015; Bernal et al., 2011b), and the third aluminate hydrate (TAH) (Andersen et al., 2006), which is described as a poorly ordered $Al(OH)_3$ phase (Taylor et al., 2010).

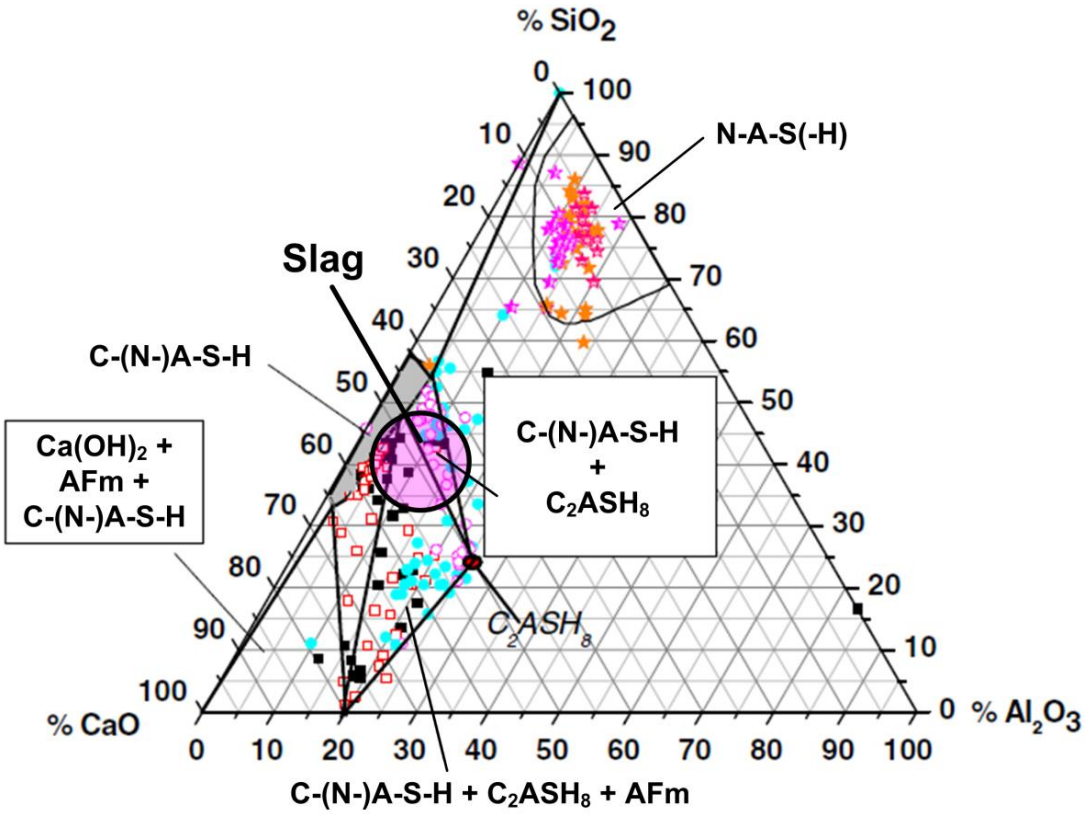


Figure 2.2. Projection of the chemical compositions of a typical slag (pink circle), proposed composition envelope of phase-pure C-(N-)A-S-H (grey shaded area), and synthetic samples and phase mixtures representing C-(N-)A-S-H and alkali aluminosilicate (hydrate) (N-A-S(-H))-based cements (small symbols and text) onto the $CaO$-$SiO_2$-$Al_2O_3$ ternary system. Adapted from García-Lodeiro et al. (2011).

### 2.1.3 Calcium (Alkali) Aluminosilicate Hydrate (C-(N-)A-S-H)

C-(N-)A-S-H chemistry has been studied for more than half a century (Kalousek, 1957), and the key solid product in this system is generally described as being similar in structure to the calcium silicate hydrate phase C-S-H(I) (Shi et al., 2006; Taylor, 1997). The structure of this phase is comprised of 'dreierketten' units, which are repeating sets of three silicate tetrahedra (Figure 2.3). C-S-H(I) is described to be a poorly ordered form of 14 Å tobermorite (Bonaccorsi et al., 2005). The tobermorite mineral group contains various structures differentiated by their basal spacing (14 Å, 11 Å or 9 Å) (McConnell, 1954), and 11 Å tobermorites can contain Si-O-Si cross-links between adjacent silicate chains while 14 Å and 9 Å tobermorites do not (Bonaccorsi et al., 2005; Merlino et al., 2000; 2001). Hydrated 14 Å tobermorite

(plombierite) has a bound water to Si ratio ($H_2O$/Si) of 7/6 and 0.5 atoms of interlayer Ca per dreierketten unit, giving an overall formula of $Ca_5Si_6O_{16}(OH)_2.7H_2O$ (Bonaccorsi et al., 2005), although small variations in chemical composition can exist (Taylor, 1997). There are two types of 11 Å tobermorite; those that shrink during dehydration and contain interlayer Ca are termed 'normal', while those that do not shrink during dehydration and contain no interlayer Ca are called 'anomalous' (Merlino et al., 2001). The bound water content also varies, with a reduction in bound water content associated with a decrease in the interlayer spacing (Merlino et al., 1999). Merlino et al. (2001) elucidated the structures of normal and anomalous 11 Å tobermorites, and found that anomalous 11 Å tobermorite has $H_2O$/Si = 5/6 and no interlayer Ca ($Ca_4Si_6O_{15}(OH)_2 \cdot 5H_2O$), whereas normal 11 Å tobermorite also has $H_2O$/Si = 5/6 but an interlayer Ca content of 0.25 atoms per dreierketten unit ($Ca_{4.5}Si_6O_{16}(OH) \cdot 5H_2O$). In an earlier study, Merlino et al. (2000) also analysed 9 Å tobermorite (riversideite), finding no bound water and an interlayer Ca content of 0.5 atoms per dreierketten unit, corresponding to a crystal chemical formula of $Ca_5Si_6O_{16}(OH)_2$.

A simplified representation of these tobermorites, shown in terms of sublattice sites, is provided in Figure 2.3, with complete descriptions provided in contributions by Merlino and co-workers (Bonaccorsi et al., 2005; Merlino et al., 1999; 2000; 2001). Representation of these structures in terms of 'sublattice sites' is clearer from a modelling perspective, and has been used throughout the thesis to construct structurally relevant formulae for these tobermorite phases, which can then be used to develop fully descriptive models for C-(N-)A-S-H chemistry.

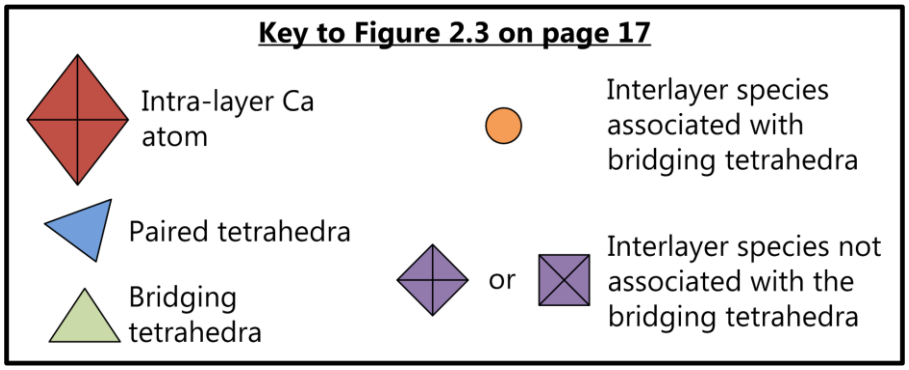

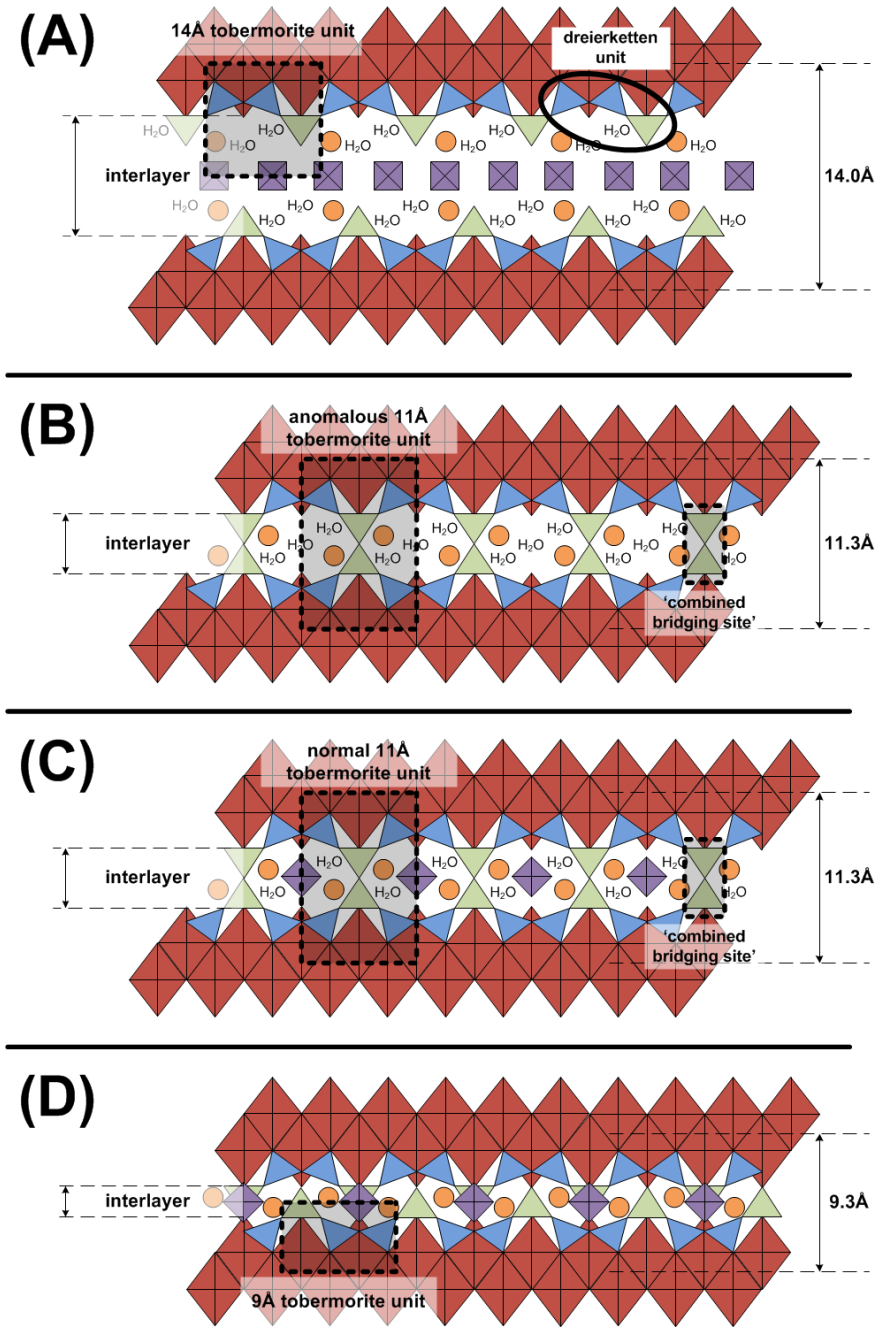


Figure 2.3. Schematic sublattice representations of A) 14 Å tobermorite; B) anomalous 11 Å tobermorite; C) normal 11 Å tobermorite; D) 9 Å tobermorite, all with 'infinite' chain length (no Si site vacancies). Paired and bridging tetrahedra are represented by blue and green triangles respectively, intra-layer Ca by the red oblongs, interlayer species associated with bridging tetrahedra by the orange circles, and interlayer species associated with the rest of the structure by purple squares. The specific size, location and number of these symbols are approximate; readers are referred to (Bonaccorsi et al., 2005; Merlino et al., 1999; 2000; 2001) for crystallographic structures. The combined bridging site is illustrated here to clarify its use in cross-linked C-(N-)A-S-H sublattice formulae. A dreierketten unit (three kinked repeating tetrahedra) is marked in A), and the interlayer spacing is also marked.

C-(N-)A-S-H contains finite chain length (alumino)silicate chains flanked on either side by an 'interlayer' comprised of $H_2O$ and aqueous species (e.g. $Ca^{2+}$, $H^+$, $Na^+$ and $K^+$), and a Ca-O sheet, analogous to the 'infinite' chain length tobermorites shown in Figure 2.3 but with the chains disrupted by vacancies. The chains are comprised of Al-substituted 'dreierketten' units with vacancies located in the bridging sites (Richardson et al., 1993). The C-(N-)A-S-H structure, in common with almost all tetrahedral aluminosilicate structures, is believed to exclude Al-O-Al bonding (Loewenstein, 1954). Al substitution is only significant in the bridging sites, not in the paired sites (Pegado et al., 2014). The mean chain length (MCL) is defined throughout the thesis as the number of silicate and aluminate tetrahedra per chain; the MCL and the Ca/Si ratio are known to have a significant effect on the mechanical properties of 14 Å tobermorite (Manzano et al., 2009a).

Studies analysing laboratory-synthesised C-(N-)A-S-H specimens have identified that phase-purity decreases as the Al/Si and Ca/(Al+Si) molar ratios of the solid phase increase, suggesting that a 'soft' upper bound on the Al content of C-(N-)A-S-H exists in the composition range relevant to hydrated cements of Al/Si $\approx$ 0.2 (L'Hôpital et al.; Pardal et al., 2009; Sun et al., 2006). Laboratory-synthesised solids containing approximately phase-pure C-(N-)A-S-H have typically shown chemical compositions of $0.5 < Ca/(Al+Si) \leq 1$ and $Al/Si \leq 0.20$ (Faucon et al., 1999a; Pardal et al., 2009; Sun et al., 2006), although the maximum theoretical Al/Si ratio of this phase is 0.5 (Richardson and Groves, 1993b).

Bound water is present in variable amounts in the interlayer spacing in C-(N-)A-S-H, with $H_2O$/Si ratios between 1.3-1.7 excluding adsorbed water (Jennings, 2008). MCL values for C-(N-)A-S-H in AAS cements produced using KOH or NaOH activators are typically between 4 and 8 (Bonk et al., 2003; Puertas et al., 2011; Richardson et al., 1993; Richardson et al., 1994) using a non-cross-linked tobermorite representation of this phase (Richardson and Groves, 1993b), compared with 8-10 for C-(N-)A-S-H derived from slag reacted with $Na_2SiO_3$ activators (Le Saoût et al., 2011). MCL values of C-(N-)A-S-H in hydrated blended cements depend on the

curing conditions and the type and amount of SCMs used, and can vary from ~2 in hydrated PC (Dai et al., 2014; Gallucci et al., 2013) to ~15 in hydrated blended cements with ≥50% replacement of PC with SCMs (Taylor et al., 2010).

C-(N-)A-S-H can incorporate large amounts of alkalis, up to 20% of the amount of Na or K added (Hong and Glasser, 1999), and alkali uptake increases as a direct function of the Ca/Si ratio (Hong and Glasser, 1999; 2002). A good understanding of C-(N-)A-S-H solubility currently exists up to bulk Na concentrations of 0.8 M NaOH (Hong and Glasser, 1999; Kalousek, 1944; L'Hôpital et al.; Lognot et al., 1998; Macphee et al., 1989; Way and Shayan, 1992), which represents the pH range relevant to most cement-based materials (pH ≤ 13.5), but fewer solubility data are available for this phase at bulk K concentrations up to 0.8 M KOH (Hong and Glasser, 1999; Macphee et al., 1989; Nieto and Zanni, 1997; Stade, 1989). These data are important for understanding the long-term stability of C-(N-)A-S-H and developing thermodynamic models for this phase, to simulate the chemistry of cement-based materials in service (Lothenbach et al., 2012a). The Ca-O sheets, interlayer regions and aluminosilicate chains in C-(N-)A-S-H are thought to stack together such that the chain structures form the external surfaces (Labbez et al., 2011) (Figure 2.4).

The variable molecular structure of C-(N-)A-S-H, as well as the nanoparticulate nature of the gel formed through agglomeration of structural units around several nanometres in size (Allen et al., 2007; Skinner et al., 2010), results in a structure with limited long-range ordering. Elucidation of the gel structure in AAS and hydrated blended SCM/PC materials is challenging when using conventional analytical techniques such as X-ray diffraction (XRD) because of this high level of structural disorder, and also because C-(N-)A-S-H almost always coexists with unreacted remnant precursor particles and secondary or minor reaction products.

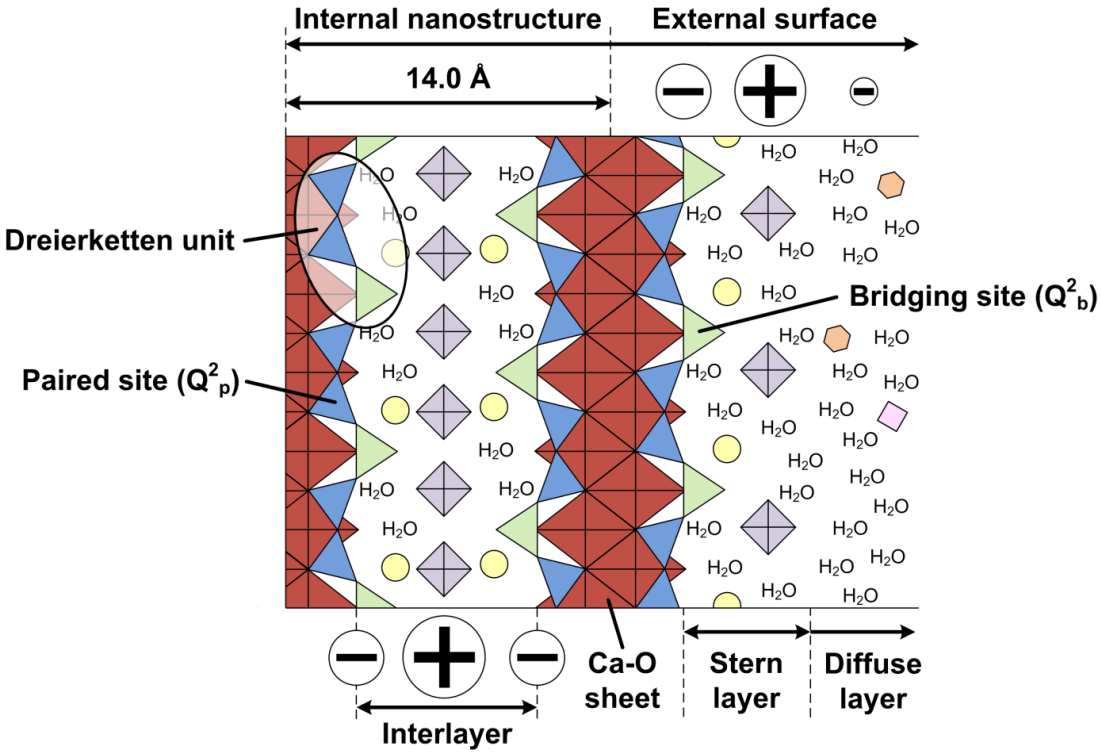


Figure 2.4. Schematic representation of infinite chain length non-cross-linked C-(N-)A-S-H as a structural analogue of 14 Å tobermorite (Bonaccorsi et al., 2005), with stacked layers to show alkali species adsorbed on the external surface and in the interlayer region of this phase. The red diamonds are Ca atoms in the Ca-O sheet, and the blue and green triangles are tetrahedral aluminate or silicate units in paired and bridging sites respectively, within the dreierketten chains. The yellow circles and purple squares represent positively-charged species that charge-neutralise the bridging sites and the rest of the layered structure respectively (typically $H^+$, $Ca^{2+}$ and/or alkali cations such as $K^+$ or $Na^+$). The orange hexagons are diffuse layer anions (e.g. $OH^-$ and $Cl^-$) that compensate the excess positive charge supplied by adsorbed cations (Labbez et al., 2011). The pink square is an additional diffuse layer cation (e.g. $Ca^{2+}$, $Na^+$). The positive and negative symbols represent the local distribution of charge in the structure. The size, number and location of the symbols are schematic rather than crystallographically exact, and different types of hydrated alkali complexes are not distinguished.

As a consequence of the complexity of this multi-phase system, elucidation of the structure of C-(N-)A-S-H has not yet been achieved. Important questions remain about its molecular chemistry, including:

i) the possibility of Al substitution into paired tetrahedra (Faucon et al., 1999a; Manzano et al., 2009b; Pardal et al., 2012; Pegado et al., 2014);

ii) the mechanism and selectivity of alkali uptake in C-(N-)A-S-H;

iii) the presence of cross-linked chains, for example in $Na_2SiO_3$-activated slag cements (Brough and Atkinson, 2002; Fernández-Jiménez et al., 2003; Le Saoût et al., 2011; Puertas et al., 2011); and

iv) the role and importance of five and six-coordinated Al (denoted Al[5] and Al[6]) (Andersen et al., 2006; Renaudin et al., 2009a; Sun et al., 2006).

Al substitution is widely considered to occur exclusively in bridging sites in C-(N-)A-S-H, consistent with the nearest-neighbour Al avoidance rule described by Loewenstein (Loewenstein, 1954), and the (3*n*-1) chain length rule (Richardson, 2004). Although some authors have proposed Al substitution in paired sites (Faucon et al., 1999a; Pardal et al., 2012), published $^{29}$Si magic angle spinning nuclear magnetic resonance (MAS NMR) spectra show little or no contribution from the $Q^1$(1Al), $Q^2$(2Al) and $Q^3$(2Al) units that would be expected in systems with Al substituted into paired tetrahedra (Richardson et al., 1993; Skibsted and Andersen, 2013; Sun et al., 2006; Taylor et al., 2010). Atomistic simulations of C-(N-)A-S-H have also shown that Al is bound in these chains in the bridging sites with great preference over the paired sites (Abdolhosseini Qomi et al., 2012; Manzano et al., 2009b; Pegado et al., 2014).

Incorporation of alkali species into the interlayer region and adsorption onto the external surfaces of C-(N-)A-S-H is thought to occur via a charge-compensation mechanism (Bach et al., 2013; Labbez et al., 2011; Renaudin et al., 2009a; Skibsted and Andersen, 2013; Viallis et al., 1999) (Figure 2.4), although no consensus exists regarding the exact mechanism of alkali uptake in this phase. This is corroborated by the large variation in existing results reported for Na and K uptake as a function of Al content in C-(N-)A-S-H: direct correlations (Hong and Glasser, 2002; Skibsted and Andersen, 2013), an inverse correlation (Stade, 1989), and the apparent absence of a direct relationship (Bach et al., 2013; Chappex and Scrivener, 2012) between the two parameters have been reported. There is also a lack of consensus on the selectivity of C-(N-)A-S-H for Na or K species, with existing publications reporting

no significant difference between uptake of these two alkali types (Hong and Glasser, 1999; 2002; Stade, 1989) or preferential selectivity for K over Na (Bach et al., 2013).

It is thought that the aluminosilicate chains in C-(N-)A-S-H products in low-Ca cements (bulk Ca/Si ≤ 1) can cross-link under ambient conditions to form disordered analogues of 'double chain' calcium silicate minerals, e.g. 11Å tobermorite (Merlino et al., 2001). Recent experimental results support a partially cross-linked structure for C-(N-)A-S-H formed in $Na_2SiO_3$ and $Na_2CO_3$-activated slag cements: $Q^3$ type species have been identified in deconvolutions of $^{29}$Si MAS NMR spectra of these materials (Fernández-Jiménez et al., 2003) and in laboratory-synthesised specimens (Pardal et al., 2012; Sun et al., 2006). A mixed cross-linked/non-cross-linked structural model was also needed to describe the mechanical properties of hydroxide and $Na_2SiO_3$-activated slag cements (Puertas et al., 2011). Schematic representations of cross-linked and non-cross-linked tobermorite-like C-(N-)A-S-H products are shown in Figure 2.5.

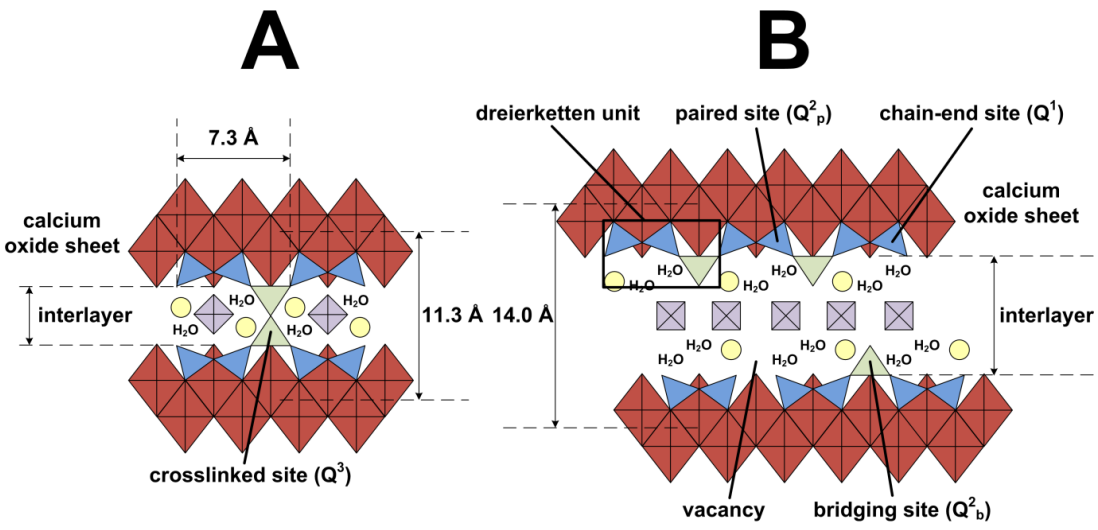


Figure 2.5. Schematic representation of finite chain length A) cross-linked and B) non-cross-linked C-(N-)A-S-H products as structural analogues of double chain 11 Å tobermorite (Merlino et al., 2001) and 14 Å tobermorite (Bonaccorsi et al., 2005) respectively. The grey diamonds are Ca atoms in the Ca-O sheet, and red and blue triangles are aluminosilicate units in paired and bridging sites respectively. The green circles and yellow squares represent sites which can be occupied by hydrated species that charge-neutralise the structure as a whole (typically $H^+$, $Ca^{2+}$ and/or alkali cations such as $K^+$ or $Na^+$).

It is thought that Al[5] can act as an interlayer charge-balancing species, although there is no consensus regarding the location of Al[6] uptake by C-(N-)A-S-H; it is not yet clear whether this can be located only on surfaces, or additionally in the interlayer (Andersen et al., 2006; Renaudin et al., 2009a; Sun et al., 2006).

### 2.1.4 Structural Models for C-(N-)A-S-H

The key value of a structural model is that the chemical composition and nanostructural parameters (e.g. MCL) of C-(N-)A-S-H can be directly calculated from experimental data such as $^{29}$Si MAS NMR spectral deconvolutions, and it can be validated by relating its predictions to independent experimental results.

*Bernal and coauthors*

The first tobermorite-like structural models for C-S-H were proposed by Bernal et al. (1952) based on powder XRD measurements that showed the same dreierketten-based structures in C-S-H and riversideite (9 Å tobermorite). Bernal et al. (1952) considered two types of dreierketten-based C-S-H phases: they described a solid solution between $CSH_x$ and $C_3S_2H_y$ as CSH(I), and $C_2SH_x$ as CSH(II), with both C-S-H types partly crystalline and closely structurally related.

*Stade and Wieker*

Stade and Wieker (1980) proposed a structural C-S-H model based on a dimeric tobermorite-like structure, with charge-balancing of silanol groups by interlayer $Ca^{2+}$ and $H^+$ species following the constraints: $0.4 \leq y \leq 2$ with $x > z$ for $y < 1$ and $x \leq 2$ for $y \geq 1$ in eq.(2.1):

$$Ca_{4+y}\left(OH\right)_z\left(H_{1+\frac{x}{2}}Si_2O_7\right)_2 \cdot nH_2O \qquad (2.1)$$

Glasser et al. (1987) used this model to develop a thermodynamic model for C-S-H, although additionally attributed no specific structural assignment to the $Ca(OH)_2$ component of the model.

*Taylor*

The C-S-H structural model proposed by Taylor (1986) represents this phase as a mixture of jennite-like and 14 Å tobermorite-like phases, with chain vacancies present in bridging sites only. The structural model also allows substitution of Al for Si in bridging sites only (Figure 2.4). Taylor's model precedes the 'General Model' (GM) (Richardson and Groves, 1992b) and the 'Substituted General Model' (SGM) (Richardson and Groves, 1993b); a detailed discussion of the similarities between these models is available in published comments by Richardson, Groves and Taylor (Richardson and Groves, 1993c; Taylor, 1993).

*Richardson and Groves: the 'Substituted General Model' (SGM)*

The SGM (Richardson and Groves, 1993b) is widely used in the cement chemistry literature (Skibsted and Andersen, 2013; Taylor et al., 2010), and describes a mixture of 14 Å tobermorite-like, jennite-like and $Ca(OH)_2$ structures (eq.(2.2)):

$$Ca_X H_{(6n-2X)} \left(Si_{(1-a_0)} R_{a_0}\right)_{(3n-1)} O_{(9n-2)} \cdot I^{c+}_{\frac{a_0}{c}(3n-1)} \cdot zCa(OH)_2 \cdot mH_2O \qquad (2.2)$$

Here, *R* is a trivalent cation in tetrahedral coordination in the bridging sites (usually $Al^{3+}$), *I* is a charge-balancing interlayer cation for the bridging sites (such as $Ca^{2+}$ or an alkali metal) with a positive charge of *c*, *m* defines the amount of bound interlayer water, *n* is the number of dreierketten units per 14 Å tobermorite chain, and $a_0$ is the extent of substitution of *I* into the structure (Figure 2.6).

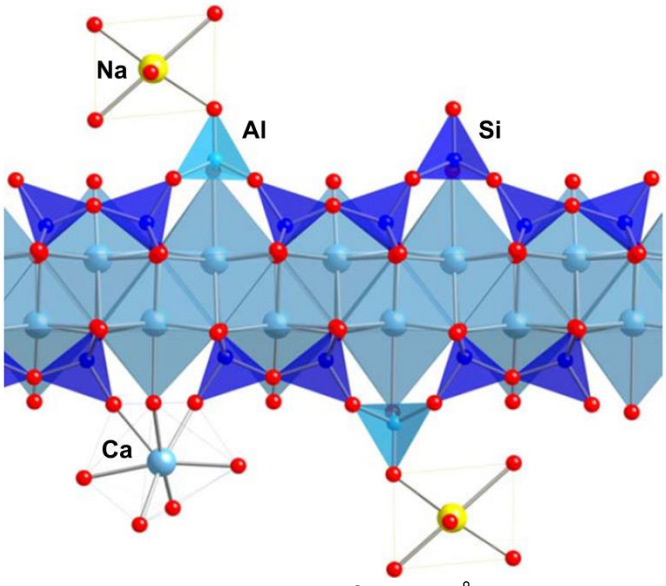


Figure 2.6. Schematic representation of the 14 Å tobermorite-like structures represented by the SGM. Yellow spheres are Na, light blue tetrahedra are Al and dark blue tetrahedra are Si. Adapted from Richardson (2004).

The parameters *X*, *z*, $a_0$ and *n* are defined in terms of *w* (the degree of protonation of the chain units) and *y* (the amount of $Ca(OH)_2$ in the model), according to eq.(2.3) (Richardson and Groves, 1993b):

$$\left.\begin{aligned} X &= 0.5(6n-w) \\ z &= 0.5\left[w+n(y-2)\right] \\ 0 \le a_0 &\le \frac{n-1}{(3n-1)} \end{aligned}\right\} \tag{2.3}$$

The MCL and Al/Si ratio can then be calculated, using the assumption that C-(N-)A-S-H and 14 Å tobermorite are structurally similar, and the Ca/Si ratio can be determined from eqs.(2.2-2.3), leading to eqs.(2.4-2.6) (Richardson et al., 1994):

$$MCL_{[NC]} = \frac{2\left[Q^1 + Q^2 + \left(\tfrac{3}{2}\right)Q^2(1Al)\right]}{Q^1} \tag{2.4}$$

$$\left(Al/Si\right)_{[NC]} = \frac{\left(\frac{1}{2}\right)Q^2(1Al)}{Q^1 + Q^2 + Q^2(1Al)} \quad (2.5)$$

$$\left(Ca/Si\right)_{[NC]} = \frac{4+y}{4+2\left(1-\nu\right)\left(1-a\right)} \quad (2.6)$$

where [*NC*] denotes non-cross-linked C-(N-)A-S-H structures.

The SGM is more generalised than the GM because it allows for structural incorporation of trivalent cations in bridging sites (e.g. $Al^{3+}$) and uptake of charge-balancing anions for these sites (e.g. $Na^{+}$), whereas the GM does not. The structural model of Taylor (1986) is less generalised than the GM and SGM: Taylor (1986) assumed that 'chain-end' Si-O groups (Figure 2.5) are protonated only, whereas the SGM allows bonding of 'chain-end' Si-O units to $H^{+}$ and $Ca^{2+}$ (Richardson and Groves, 1993b); and although Taylor's model and the SGM both represent C-(N-)A-S-H in terms of tobermorite-like/jennite-like structures, the SGM additionally describes mixtures of tobermorite-like/'solid solution $Ca(OH)_2$'.

The SGM has replicated experimental (electron microscopic) observations of C-(N-)A-S-H chemical compositions in hydroxide-activated AAS paste (Richardson, 1999) and hydrated blended PC (Taylor et al., 2010) using $^{29}$Si MAS NMR results. Many of the preexisting structural models are based on a mixture of non-cross-linked tobermorite-like, jennite-like and $Ca(OH)_2$ structures that can describe C-S-H chemical compositions and structure (described above and by Richardson (2008)), but none are as flexible as the SGM (Richardson, 2004; 2008). The key limitation of the SGM is that it does not describe cross-linked C-(N-)A-S-H structures; Richardson (2014) proposed an extension of the SGM that includes fully cross-linked or non-cross-linked tobermorite-like structures only, i.e. without considering the mixed cross-linked/non-cross-linked structures found in C-(N-)A-S-H and addressed in Chapters 4-6 and 8-9 of this thesis in the formulation and application of a more generalised structural C-(N-)A-S-H model. The SGM is also limited by the

lack of a specific structural description attributed to the 'solid solution $Ca(OH)_2$' component of the model, although this is only important for Ca/Si ratios > 1.5.

*Chen and coauthors*

Chen et al. (2004) formed their structural and compositional model from a comprehensive analysis of C-S-H solubility, and described C-S-H as a mixture of tobermorite-like and jennite-like structures, with different C-S-H solubility curves assigned to different structural configurations of Ca-OH bonds. This structural representation of C-S-H is equivalent to the GM (Richardson and Groves, 1992b).

*Sun and coauthors*

Sun et al. (2006) synthesised a series of C-(N-)A-S-H products with chemical compositions of $0.86 \leq$ bulk Ca/(Al+Si) $\leq 1.4$ and $0 \leq$ bulk Al/(Al+Si) $\leq 0.30$, characterised the samples using X-ray fluorescence (XRF), $^{29}$Si and $^{27}$Al MAS NMR, and XRD, and developed a structural model from the results. Their structural model describes C-(N-)A-S-H in terms of tobermorite-like structures over the range of bulk chemical compositions studied.

Structural incorporation of Al[4] was only allowed in bridging sites (Figure 2.5) in the model, with structural Al[5] and Al[6] assigned to cross-linked Al[4]-O-Al[5,6]-O-Al[4] sites. Sun et al. (2006) used these Al[4]-O-Al[5,6]-O-Al[4] sites to explain the much higher basal spacings found for their synthesised C-(N-)A-S-H products (up to 16.4 Å) relative to tobermorite (up to 14 Å, Figure 2.3). While Al-O-Al bonding is strongly energetically disfavoured in tetrahedral T-O-T (T = Si, Al) configurations in aluminosilicates (Loewenstein, 1954; Provis et al., 2005a), energetically favourable Al[4]-O-Al[6]-O-Al[4] configurations are observed in some minerals e.g. phlogopite (Langner et al., 2012), meaning that the assignment of cross-linked Al[4]-O-Al[5,6]-O-Al[4] sites in C-(N-)A-S-H may be possible. The structural model also includes Al[5] and Al[6] interlayer species without precluding incorporation of these units on C-(N-)A-S-H surfaces. Although $^{27}$Al MAS NMR

and transmission electron microscopy (TEM) with energy-dispersive X-ray spectroscopy (EDS) analysis (Andersen et al., 2006) and $^{27}Al\{^{1}H\}$ HETCOR NMR spectra (Rawal et al., 2010) of hydrated white Portland cement (wPc) pastes do not support Al[6] uptake in C-A-S-H interlayers, the same analysis has not been applied to lower Ca/Si C-(N-)A-S-H such as the tobermorite-like phases described by this structural model (Sun et al., 2006), meaning that the assignment of interlayer Al[6] is potentially plausible. $Na^{+}$ is also considered to be both loosely-bound on C-(N-)A-S-H surfaces and rigidly-bound in the interlayer, and $Ca^{2+}$ and $H^{+}$ are additionally described as being interlayer charge-balancing species. Many of these assignments are discussed further in this thesis, particularly in Chapters 8-9.

*Pellenq and coauthors*

The atomistic model of C-S-H by Pellenq et al. (2009) is based on extensive modifications of the 11 Å non-cross-linked tobermorite structure proposed by Hamid (1981), although later applications of the model also considered cross-linking and structural incorporation of Al (Abdolhosseini Qomi et al., 2012). The model describes finite chain length C-S-H at Ca/Si > 1, with structural Si monomers defined as intrinsic components of this phase at Ca/Si > 1.5 (and so the model does not follow the 3*n*-1 chain length rule in this chemical composition range). The limited Ca/Si ratio range described by the model (Ca/Si ≥ 1) precludes its application to many alkali-activated materials and other C-(N-)A-S-H-based cements with lower bulk Ca content. The combinatorial approach used in formulation of the model means that C-S-H structural parameters cannot be calculated from independent experimental input additional to the data used in model derivation, but does allow the prediction of important chemical-structural parameters e.g. Gibbs free energy and bulk modulus (Abdolhosseini Qomi et al., 2014).

The main criticism of the C-S-H model derived by Pellenq et al. (2009) is that the bonding environments of some of the atoms present are unrealistic when compared to calcium silicate hydrate phases such as tobermorite (Richardson, 2013a). For example, the model contains Ca atoms with Ca-O bond lengths <2 Å, which is much

shorter than the known Ca-O bond lengths of 2.26-2.74 Å in 14 Å tobermorite (Bonaccorsi et al., 2005), 2.31-3.19 Å in non-cross-linked 11 Å tobermorite (Hamid, 1981) and 2.24-2.89 Å in cross-linked 11 Å tobermorite (Merlino et al., 2001). There also are three, four, five and nine-coordinated Ca atoms in the model, whereas coordination states of six and seven are typical of calcium silicate hydrate minerals (Bonaccorsi et al., 2005; Bonaccorsi et al., 2004; Hamid, 1981; Merlino et al., 2001). Further criticism of the model is incurred by the cross-linked C-A-S-H structures assigned in later development of the model (Abdolhosseini Qomi et al., 2012): $Q^3$-type (alumino)silicate units are not experimentally observed in C-A-S-H with Ca/Si > 1 at ambient or slightly elevated temperatures (Chen et al., 2004; Cong and Kirkpatrick, 1996a; Gallucci et al., 2013; Taylor et al., 2010), which contradicts the inclusion of these structures in the model. In addition, hydrated Si monomers are not always identified in $^{29}$Si MAS NMR spectra of C-S-H (Chen et al., 2004) and hydrated wPc materials (Dai et al., 2014), which casts doubt on the inclusion of these units as intrinsic structural components of Ca/Si > 1.5 C-S-H.

*Puertas and coauthors*

Puertas et al. (2011) proposed a structural and compositional model for C-(N-)A-S-H in AAS cements, described as a mixture of jennite-like, and Al-containing 14 Å and 11 Å tobermorite-like phases with chain lengths ≤ 14. This model was validated against mechanical and compositional properties of AAS cement pastes determined by scanning electron microscopy (SEM)-EDS, $^{29}$Si MAS NMR and nanoindentation measurements, although no formulae for calculating MCLs and chemical compositions were provided. A key limitation of the Puertas et al. (2011) model is its lack of flexibility in describing C-(N-)A-S-H structure and chemical composition.

### 2.1.5 Secondary and Minor Cement Hydrate Phases

Some of the most common secondary and minor reaction products in hydrated PC-based materials and AAS cements are discussed in this section.

*Portlandite*

Portlandite contains layers of octahedrally-coordinated Ca bound to tetrahedrally-coordinated O atoms (Taylor, 1997), and has a trigonal crystal structure. The solubility of portlandite decreases with increasing pH (Duchesne and Reardon, 1995), and it is a typical reaction product in hydrated PC-based materials (Lothenbach and Winnefeld, 2006), as the Ca/Si ratio of PC clinker (Ca/Si > 2.5) is much higher than that which can be accommodated in C-S-H type phases.

*Mg-Al layered double hydroxide (LDH)*

Mg-Al LDH is a minor reaction product in hydrated PC (Lothenbach and Winnefeld, 2006) but is the main secondary product in AAS cements (Brough and Atkinson, 2002). The majority of Mg incorporated into the solid binder in AAS (Wang and Scrivener, 1995) and hydrated PC-based materials (Taylor et al., 2010) is bound in Mg-Al LDH phases, and the solubility of Mg is very low in these cements (Gruskovnjak et al., 2006; Lothenbach and Winnefeld, 2006; Puertas et al., 2004; Song and Jennings, 1999). The primary layer of this phase contains partially Al-substituted brucite-like sheets (brucite is structurally-similar to portlandite but has a chemical formula of $Mg(OH)_2$). These Al atoms are randomly substituted at low Al content (MacKenzie et al., 1993), but form an ordered distribution at high Al content (Taylor, 1997). The secondary layer contains $H_2O$ and dissolved anions (typically $CO_3^{2-}$ and $OH^-$ in cements, although a variety of other species are possible (Allada et al., 2005b)), that balance the positively-charged brucite-like layers.

*AFm/AFt*

AFm and AFt phases also contain LDH type structures, but the positively-charged main layers are derived from portlandite rather than brucite. These sheets are typically substituted by $Al^{3+}$ or $Fe^{3+}$ cations, and the excess positive charge is balanced by an interlayer containing negatively-charged dissolved species and $H_2O$. The typical negatively-charged species are $OH^-$ ($C_4AH_x$, where *x* depends on the relative humidity (Taylor, 1997) and occurs naturally as the mineral hydrocalumite

(Tilley et al., 1934)), $SO_4^{2-}$ ($C_4A\bar{S}H_{12}$ and ettringite), $CO_3^{2-}$ ($C_4AcH_{11}$ and $C_6Ac_3H_{32}$) and $AlSi(OH)_8^-$ (strätlingite). The aluminosilicate species in the interlayer of strätlingite can be represented by the more general formula $[(V,T)_4(OH,O)_8 \cdot 0.25H_2O]^-$, where V is a vacancy and T is Si or Al; around 45% of the T sites are vacant in strätlingite (Rinaldi et al., 1990). The type of AFm/AFt phases formed in hydrated cements depends greatly on the bulk chemical composition; for example, cements with high bulk $SO_3/Al_2O_3$ ratios tend to form AFt phases such as ettringite rather than AFm phases such as $C_4A\bar{S}H_{12}$ (Matschei et al., 2007a). Temperature also greatly affects the stability of AFm/AFt phases, for example $C_4AH_x$ decomposes to $C_3AH_6$ and portlandite at 25°C and 1 bar in systems with high $OH^-$ and low $SO_3$ and $CO_2$ content (Matschei et al., 2007a), but is thermodynamically stable below 8°C at high $OH^-$ content and low $SO_3$ and $CO_2$ concentrations (Matschei and Glasser, 2010) (Figure 2.7).

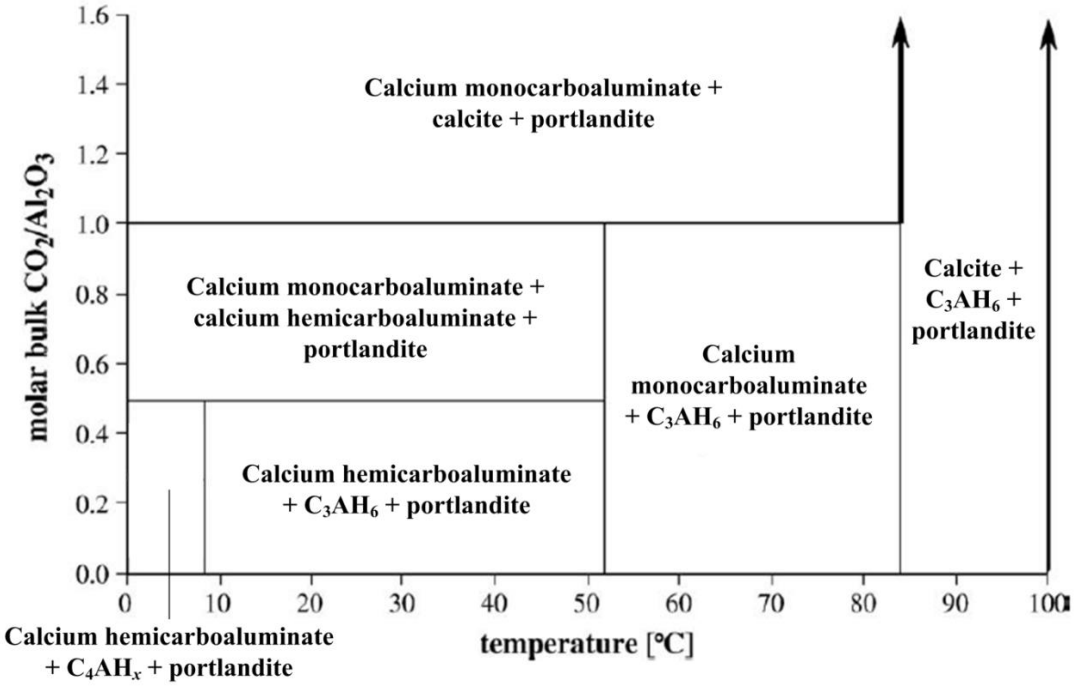


Figure 2.7. Stable phase assemblage in the $CaO\text{-}CO_2\text{-}Al_2O_3\text{-}H_2O$ system at portlandite saturation (1 bar pressure). Adapted from Matschei and Glasser (2010).

*Hydrogarnet*

The Al-Fe hydrogarnet solid solution series, $(Ca)_3(Al_xFe_{1-x})_2(SiO_4)_{3-y}(OH)_{4y}$ $0 \leq x \leq 1$ and $0 \leq y \leq 3$, contains the end-members grossular ($C_3AS_3$), andradite ($C_3FS_3$), katoite ($C_3AH_6$) and Fe-katoite ($C_3FH_6$). Fe-katoite is a stable phase in hydrated PC-based materials (Dilnesa et al., 2014) and katoite has been identified in AAS cement (Bonk et al., 2003), although these phases are only typically present in minor amounts. The anhydrous and hydrous garnets are structurally similar, containing eight (A), six (B), and fourfold coordinated (C) atoms, and an anionic species (D, typically $O^{2-}$), so may also be represented by the formula $(A)_3(B)_2(C)_3(D)_{12}$ (Locock, 2008). Substitution of $Si^{4+}$ for $4H^+$ and a fraction of site vacancies occurs in the C site (related to the *y* parameter in the chemical formula above), and causes expansion of the site and unit cell volume (Lager et al., 1987).

*Third aluminate hydrate (TAH)*

It was shown by Andersen et al. (2006) that an amorphous aluminium hydrate (the 'third aluminate hydrate', TAH) is observable in $^{27}$Al MAS NMR spectra of hydrated wPc pastes at $\delta_{iso}$ = 5.0 ppm. This phase decomposes upon heating to 70-90°C (Andersen et al., 2006). Andersen et al. (2006) described TAH as a separate precipitate, or a precipitate on C-(N-)A-S-H surfaces, because their NMR results could not be reconciled with chemical analysis from TEM-EDS measurements of C-(N-)A-S-H in hydrated PC. This phase is described as a poorly-ordered $Al(OH)_3$-type phase intimately mixed with other hydrate phases in hydrated PC/GBFS materials (Taylor et al., 2010), and has also been identified in AAS cement (Bernal et al., 2014b).

*Zeolites*

Zeolites (e.g. heulandite, $CAS_7H_{1.7}$) are formed in minor amounts at very high bulk Al content in laboratory-synthesised C-(N-)A-S-H samples (Sun et al., 2006), and can be identified in AAS cements in synchrotron-resolution XRD patterns (e.g. gismondine, $CAS_2H_4$) (Bernal et al., 2011b). Zeolites are more commonly produced

in hydrated cements with lower Ca content, such as alkali-activated metakaolin/GBFS cements (Bernal et al., 2011b), as these phases are structural analogues of the alkali aluminosilicate (hydrate) (N-A-S(-H)) gels formed through alkali-activation of low-Ca precursors such as metakaolin and fly ash (Provis et al., 2005b).

## 2.2 Thermodynamic Modelling

### 2.2.1 Applications in Cementitious Systems

The increasing complexity and number of modern cement formulations in development and use in the construction industry (Scrivener and Kirkpatrick, 2008), means that there is now, more than ever, an urgent need to develop general predictive methods for the durability of cement-based materials in service using design parameters such as the cement type and curing conditions. Thermodynamic modelling is a computationally inexpensive and theoretically rigorous technique that can be used to predict the chemistry, and thus important durability-related properties, of hydrated cement-based materials under the assumption of thermodynamic equilibrium. Metastable equilibrium constraints are normally employed to more realistically represent cement phases over the typical design life of engineered structures; for example, C-(N-)A-S-H is a poorly-crystalline material in cements cured under ambient conditions for years (Richardson et al., 1994) or even decades (Taylor et al., 2010), but has been observed to crystallise to Al-rich tobermorite in Roman concrete exposed to seawater for over 2000 years (Jackson et al., 2013), and so is normally described as a metastable phase in thermodynamic modelling of cement-based materials.

This approach has been validated for hydrated PC and some blended SCM/PC materials using the CEMDATA thermodynamic database (Kulik and Kersten, 2001; 2002; Lothenbach et al., 2008b; Lothenbach and Winnefeld, 2006; Matschei et al., 2007b; Möschner et al., 2008; Möschner et al., 2009; Schmidt et al., 2008), but has

been used to describe these materials with other thermodynamic databases for more than two decades (Atkins et al., 1992a). CEMDATA has also been applied to perform thermodynamic modelling of AAS cements (Lothenbach and Gruskovnjak, 2007), however the thermodynamic model (Kulik and Kersten, 2001) used to describe C-(N-)A-S-H in that study does not explicitly define the uptake of Al and Na into this phase. Explicit definition of Al chemistry in a thermodynamic model for AAS is essential because many of the reaction products formed in this material contain Al; this is also the case for many hydrated SCM/PC blends, and hybrid alkali-activated SCM/PC materials. The inclusion of alkalis as a key component in these models is important to correctly describe the solubility relationships of C-(N-)A-S-H under the pH conditions (>12) and alkali concentrations (tens to hundreds of mmol/L) relevant to the majority of cementitious materials. Therefore, the lack of a C-(N-)A-S-H thermodynamic model (formulated explicitly with Al uptake) that accurately represents this phase under pH > 12 conditions is the main limitation in applying thermodynamic modelling to describe the chemistry of a greater variety of hydrated cement types.

### 2.2.2 General Concepts

Thermodynamic modelling of cements is primarily concerned with the minimisation of free energy during hydration (or activation) of a cementitious precursor with water (or an activator) to form a hardened binder that typically contains several solid constituents (e.g. C-(N-)A-S-H). This is illustrated here by considering the chemical reaction shown in eq.(2.7):

$$aA + bB \rightleftharpoons cC + dD \tag{2.7}$$

where $A$ and $B$ are reactants, $C$ and $D$ are products, and $a$, $b$, $c$, $d$ are the respective stoichiometric coefficients. The equilibrium constant ($K$) for this reaction is shown in eq.(2.8):

$$K = \frac{\{C\}^c \{D\}^d}{\{A\}^a \{B\}^b} \tag{2.8}$$

where curly brackets denote activity and the value of $K$ indicates whether the forward reaction ($K > 1$) or backward reaction ($K < 1$) is energetically favoured. A system is defined to be at equilibrium when there are no internal driving forces for change, i.e. when the Gibbs free energy function ($G$) is minimal. Local and global minima for $G$ are denoted 'metastable' and 'stable' equilibrium states respectively (Figure 2.8).

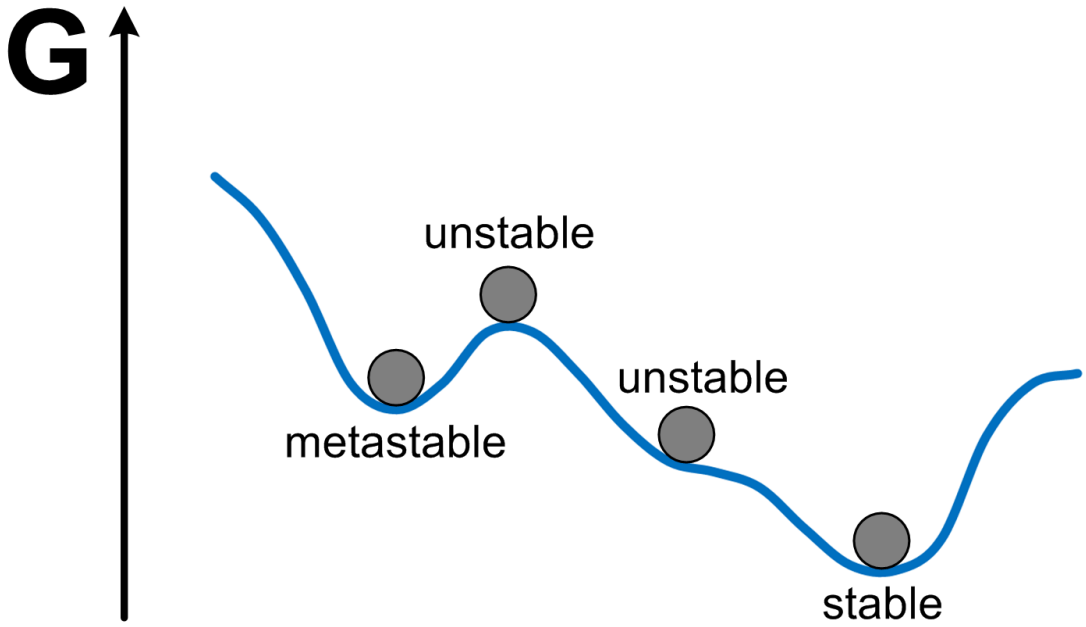


Figure 2.8. The different states of equilibrium represented by balls on a surface, where the height represents the Gibbs free energy function.

The equilibrium constant is related to the standard Gibbs free energy change of reaction ($\Delta_r G°$) by eq.(2.9):

$$\Delta_r G^o = \sum_j \left(\zeta_j \Delta_f G_j^o\right) = -RT \ln\left(K\right) \tag{2.9}$$

where $R$ is the universal gas constant (8.3145 J.mol$^{-1}$.K$^{-1}$), $T$ is temperature (K), and $\zeta_j$ and $\Delta_f G_j°$ are the stoichiometric coefficients (negative for reactants, positive for

products) and standard Gibbs free energies of formation for the $j^{th}$ species participating in the reaction, respectively. Eq.(2.9) is extremely useful because it allows equilibrium constants for many reactions to be calculated from a much smaller set of known $\Delta_f G_j°$ values, and thus allows the determination of standard thermodynamic functions: Gibbs free energy ($G°$); enthalpy ($H°$); and entropy ($S°$), from solubility experiments and known thermochemical data. The thermodynamic functions are related by eq.(2.10):

$$G = H - TS \tag{2.10}$$

where $H$ and S are enthalpy and entropy functions, respectively. The standard Gibbs free energy change of reaction for the reaction defined by eq.(2.7) can be written as shown in eq.(2.11) because $G$ is a state function, i.e. it depends only on the state of a system and is independent of the way in which a system changes from one state to another.

$$\Delta_r G^o_{eq.(2.7)} = (c\Delta_f G^o_C + d\Delta_f G^o_D) - (a\Delta_f G^o_A + b\Delta_f G^o_B) \tag{2.11}$$

In the special case when a reaction is written for the dissolution of a pure solid phase or a solid solution of constant composition the equilibrium constant is called the solubility product ($K_s$ or $K_{so}$). The subscript '$o$' indicates zero ionic strength. The solubility product is a particularly useful parameter in thermodynamic modelling of cement-based materials because it can be determined experimentally for individual solid phases and then used to provide information about the stability of these phases in different cement formulations. For example, the solubility product for portlandite ($Ca(OH)_2$) can be expressed by eq.(2.13), which corresponds to the reaction shown in eq.(2.12):

$$Ca(OH)_{2(s)} \rightleftharpoons Ca^{2+}{}_{(aq)} + 2OH^-{}_{(aq)} \tag{2.12}$$

$$K_{so,Ca(OH)_2} = \left\{Ca^{2+}\right\}\left\{OH^-\right\}^2 = IAP_{Ca(OH)_2} \quad (2.13)$$

where the activity of (pure) $Ca(OH)_{2(s)}$ is set equal to 1 by definition. The ion activity product (*IAP*) is defined similarly to the expression for $K_{so}$, but is also for disequilibrium (eq.(2.13)).

### 2.2.3 Solid Solutions

Several of the solid phases discussed in this thesis, including C-(N-)A-S-H, are described as (sublattice) solid solutions. The chemical formula of a solid solution phase with mixing on two sublattice sites can be represented in the form $Q^*[A,B]^1[C,D]^2$, which can have any of the following end-members: $Q^*[A]^1[C]^2$, $Q^*[A]^1[D]^2$, $Q^*[B]^1[C]^2$ or $Q^*[B]^1[D]^2$. Each of the two sublattice sites (identified by the square brackets) can accommodate two possible sublattice species; *A* or *B* can be present in the first site (denoted by the superscript *1*), and *C* or *D* in the second (superscript *2*). The sublattice species *A*, *B*, *C* and *D* partition into the sublattice sites, while component $Q^*$ represents the common component(s). Sublattice solid solutions are not limited to two sublattices or sublattice species, however the mathematical complexity of the related thermodynamic functions increases dramatically beyond such cases.

The Gibbs free energy of mixing ($G_m$) of a solid solution phase can be conceptualised in terms of three main contributions: mixing of simple components to the solid solution phase (analogous to Raoult's law); effects of atoms substituting in different configurations in the structure of the solid solution phase; and an (excess) non-ideal mixing component. These contributions are emphasised in the expression for $G_m$ shown by eq.(2.14) (Hillert and Staffansson, 1970):

$$G_m = G^{mech} - TS_m^{id} + G_m^E \quad (2.14)$$

where $G^{mech}$ is the Gibbs free energy of a compositionally-equivalent 'mechanical mixture' of simple components to the solid solution phase, $S_m^{id}$ is the difference in entropy between an ideal solid solution and its pure end-member components (i.e. the configurational entropy), and $G_m^E$ is the excess Gibbs free energy of the solid solution. 'Simple ideal mixing' or a 'mechanical mixture' is defined as $G_m = G^{mech}$, i.e. for solid solutions with $S_m^{id}$ and $G_m^E$ terms equal to 0. The configurational entropy term is expressed by $S_m^{id} = -R\Sigma_j[y_j \ln(y_j)]$, where $y_j$ is the site fraction of species $j$ if the species in each sublattice mix randomly. If each sublattice species is only allowed to enter into one sublattice site (i.e. 'simple random mixing') then the configurational entropy term can be expressed as $S_m^{id} = -R\Sigma_j[\chi_j \ln(\chi_j)]$, where $\chi_j$ is the mole fraction of species $j$. The $G_m^E$ term represents the deviation of the solid solution from ideality and is commonly expressed in the form of a 'Guggenheim expansion series' to describe mixing in solid solutions (Glynn and Reardon, 1990), which is shown in eq.(2.15) for a binary solution solution $Q^*[A,B]$:

$$G_m^E = \chi_{AQ^*}\chi_{BQ^*} \left[ A_0 + A_1\left(\chi_{AQ^*} - \chi_{BQ^*}\right) + \cdots \right] \tag{2.15}$$

where $A_0$ and $A_1$ are Guggenheim interaction parameters. The Redlich-Kister form of the Guggenheim expansion series is another commonly used expression for $G_m^E$ (Glynn, 1991), and is similar but contains dimensionless interaction parameters ($a_0$, $a_1$), eq.(2.16):

$$G_m^E = RT\chi_{AQ^*}\chi_{BQ^*} \left[ a_0 + a_1\left(\chi_{AQ^*} - \chi_{BQ^*}\right) + \cdots \right] \tag{2.16}$$

Real systems can generally be described quite closely by using the first two terms on the RHS of eqs.(2.15-2.16) only; this simplification makes these expressions functionally equivalent to the 'subregular' or 'two-parameter' asymmetric Margules equation. Therefore the interaction parameters $A_0$, $A_1$, $a_0$, and $a_1$ are related to

Margules parameters and may be conceptualised in terms of describing the interactions between atoms or components in the solid solution phase.

### 2.2.4 Thermodynamic Models for C-A-S-H

Only one C-A-S-H thermodynamic model had been published (Haas et al., 2011; 2012) prior to the commencement of this thesis.

*Haas and coauthors*

The thermodynamic model of Haas et al. is based on C-A-S-H solubility data at bulk Ca/Si ratios of 0.66, 0.8 and 0.95 at various bulk Al concentrations (Haas and Nonat, 2015; Haas et al., 2011; 2012; Pardal et al., 2009). It is presumed that the thermodynamic model is formulated as a mechanical mixture or set of independent C-(A-)S-H phases because Haas et al. provide no information about the mixing rules used in their model. Solubility product values are specified in this thermodynamic model by fitting equilibrium constants for a set of aluminosilicate chain condensation/surface reactions, and $Al(OH)^{2+}/Ca^{2+}$ complexation reactions and protonation reactions with internal and surface silanol groups, to C-(A-)S-H solubility data (Haas et al., 2011; 2012; Pardal et al., 2009). Optimised solubility products of the C-(N-)A-S-H phases described by the thermodynamic model were reported by (Haas and Nonat, 2015). The relatively low pH and Ca/Si ratios of the data set described by the model ($pH \leq 12.2$ and $0.66 \leq Ca/Si \leq 0.95$) suggests that it may not accurately represent the solubility of C-(N-)A-S-H in most hydrated PC-based materials and alkali-activated cements.

### 2.2.5 Thermodynamic Models for C-S-H

A substantial amount of research has been devoted to understanding the solubility of C-S-H (Atkins et al., 1992b; Atkinson et al., 1989; Chen et al., 2004; Cong and Kirkpatrick, 1996a; Flint and Wells, 1934; Fujii and Kondo, 1981; Glasser et al., 1999; Greenberg and Chang, 1965; Grutzeck et al., 1989; Harris et al., 2002;

Jennings, 1986; Roller and Ervin, 1940; Suzuki et al., 1985; Taylor, 1950; Walker et al., 2007), and development of solubility-based thermodynamic models for this phase has been ongoing over several decades (Atkins et al., 1992a; Berner, 1992; Flint and Wells, 1934; Gisby et al., 2007; Glasser et al., 1987; Greenberg and Chang, 1965; Kulik and Kersten, 2001; Reardon, 1990; Suzuki et al., 1985; Walker et al., 2007). The majority of published C-S-H solubility data have been identified to collapse onto several distinct solubility curves (Chen et al., 2004; Jennings, 1986), indicating that an important and complex structure-solubility relationship exists for this phase (Figure 2.9).

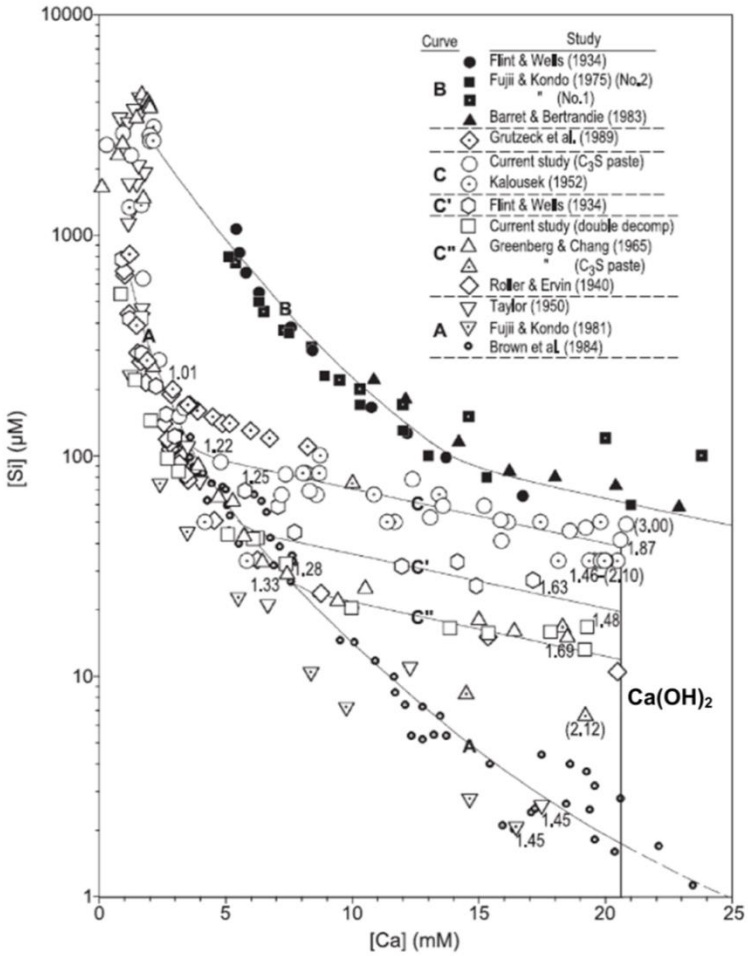


Figure 2.9. C-S-H solubility data compiled by Chen et al. (2004), with curves A, B, C, C' and C" representing C-S-H with different structural configurations of Ca-OH bonds. Numbers are Ca/Si ratios of the solids analysed. Numbers in parentheses indicate the Ca/Si ratios of solids containing $Ca(OH)_2$. Adapted from (Chen et al., 2004).

*Kulik, Lothenbach and coauthors*

The Kulik and Kersten (2001) C-S-H thermodynamic model contains two ideal solid solutions (i.e. the excess Gibbs free energy ($G^{EX}$) = 0) describing mechanical mixtures of i) tobermorite-like and jennite-like C-S-H structures of the type modelled by Taylor (1986) between 0.83 ≤ Ca/Si ≤ 1.67; and ii) a Ca/Si = 0.83 tobermorite-like phase and amorphous $SiO_2$ at lower Ca content. End-member solubility products were selected to fit the solubility data published by Greenberg and Chang (1965) in the original version of the thermodynamic model, but were later refitted to match a much more comprehensive set of C-S-H solubility data compiled by Lothenbach et al. (2008b). Lothenbach et al. (2008b) also adjusted the enthalpies of formation ($\Delta_f H^o$) and standard entropies ($S^o$) of the tobermorite-like and jennite-like end-members to fit published C-S-H solubility data between 20 and 80°C. This thermodynamic model has been applied extensively to accurately predict hydrated PC solid phase assemblages and pore solution compositions as functions of bulk solid binder chemical compositions (Lothenbach, 2010; Lothenbach and Winnefeld, 2006) (Figure 2.10).

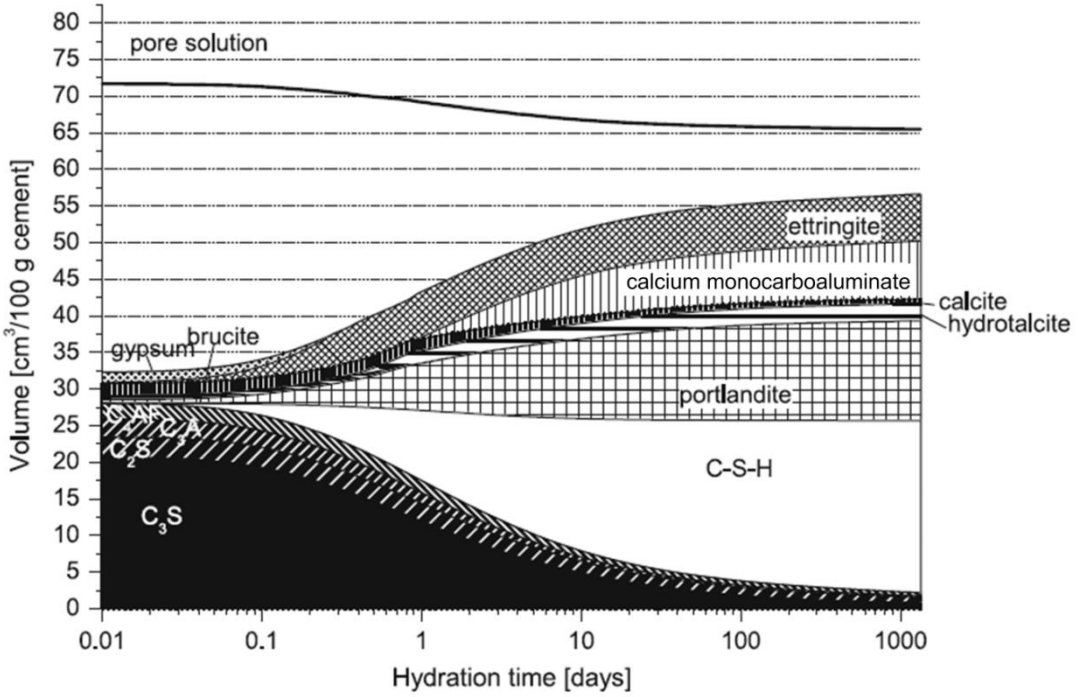


Figure 2.10. Predicted phase assemblage of hydrated PC as a function of the time of curing, assuming thermodynamic equilibrium. $C_4AF$, $C_3A$, $C_2S$ and $C_3S$ are PC clinker phases. Adapted from (Lothenbach, 2010).

More recently, Kulik (2011) developed two thermodynamic models for C-S-H based on the GM (Richardson and Groves, 1992b), which are therefore more structurally-consistent than the existing formulation of Kulik and Kersten (2001), using a much larger set of solubility data in the $CaO$-$SiO_2$-$H_2O$ system at ambient conditions (Figure 2.11): the downscaled CSHQ and CSH3T models. The downscaled CSH3T model is formulated as an ideal ($G^{EX}$ = 0) sublattice solution model with 'simple random mixing' to define the configurational entropy component, and describes a solid solution of tobermorite-like phases between 0.67 ≤ Ca/Si ≤ 1.5. The downscaled CSHQ model is defined in terms of an ideal ($G^{EX}$ = 0) mechanical mixture model describing a solid solution of mixed tobermorite-like/jennite-like phases between 0.67 ≤ Ca/Si ≤ 2.25. The downscaled CSHQ model has been used in a recent publication to describe the hydration and long-term chemistry of a PC/SF-based shotcrete cement (Lothenbach et al., 2014).

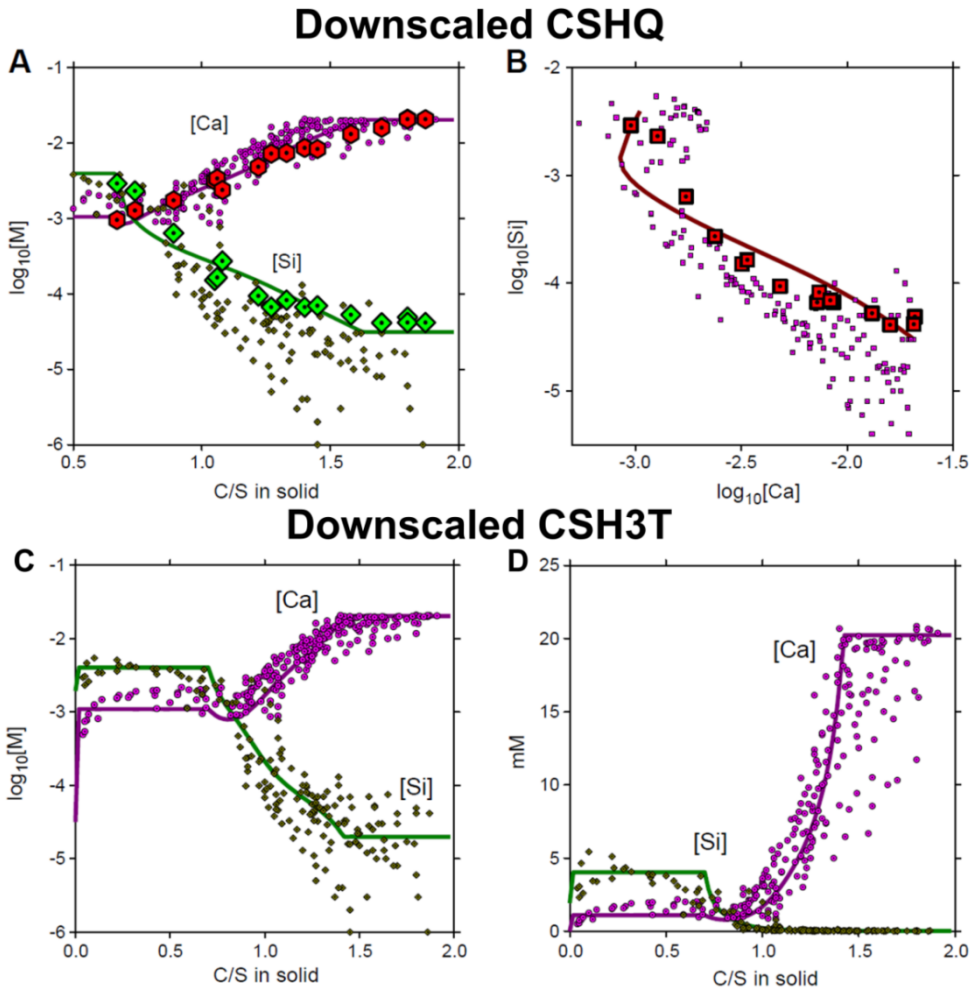


Figure 2.11. Predicted C-S-H solubility curves (traces) using the downscaled (A, B) CSHQ and (C, D) CSH3T thermodynamic models compared to reported solubility data for this phase (points). Data from Chen et al. (2004) are represented by large squares, diamonds and circles. Adapted from Kulik (2011).

*Walker and coauthors*

Walker et al. (2007) developed a C-S-H thermodynamic model to describe the total solubility of this phase for Ca/Si ratios ≥ 1. The thermodynamic model describes a non-ideal subregular binary solid solution, formulated using CSH and $Ca(OH)_2$ end-members, with activity coefficients calculated from Guggenheim interaction parameters used to describe the excess Gibbs free energy term. Thermodynamic modelling was performed to calculate 'stoichiometric saturation' (Glynn and Reardon, 1990) solubility products for CSH and $Ca(OH)_2$ using a comprehensive solubility dataset in the $CaO\text{-}SiO_2\text{-}H_2O$ system that was also determined by Walker

et al. (2007). The lower Ca boundary of the CSH-CH miscibility gap was determined from Fourier transform infrared spectroscopy (FTIR) and XRD results (Walker et al., 2007) to fall at Ca/Si = 1.64, and least squares fitting of the Guggenheim parameters was performed to best match the solubility data to obtain the upper Ca miscibility gap boundary (Ca/Si = 12.2).

*Atkins, Glasser and coauthors*

Thermodynamic models for C-S-H were developed by Atkins, Glasser and coauthors over a period of several years (Atkins et al., 1992a; Glasser et al., 1999), which were primarily utilised to predict the pore solution chemistry of hydrated blended PC-based cements in radioactive waste disposal applications (Atkins and Glasser, 1992; Glasser and Atkins, 1994). Two of the early models developed by Atkins, Glasser and coauthors were called the 'partial' and 'full' crystallisation models (Atkins et al., 1994), which were intended for use at temperatures <80°C and between 80 and 90°C respectively. Both models described C-S-H as a set of phase mixtures or single phases in discrete Ca/Si intervals between 0.8 and 1.5, with solubility products specified for each solid phase to best match the model to C-S-H solubility data obtained between 25 and 85°C. For example, the 'partial' crystallisation model contained:

i) $C_5S_6H_5$ (tobermorite) between Ca/Si = 0.8 and 0.85;
ii) $C_5S_6H_5$ and CSH between Ca/Si = 0.85 and 1;
iii) CSH and $C_3S_2H_3$ (afwillite) between Ca/Si = 1 and 1.5; and
iv) $C_3S_2H_3$ and $Ca(OH)_2$ for Ca/Si > 1.5.

Later development of the model expanded this composition range from Ca/Si = 0.85 to >2, increased the number of phase mixtures/single phases (Ca/Si intervals of 0.85-1, 1-1.2, 1.2-1.6, 1.6-2, >2), and adapted the solubility products for each phase to improve the fit of the model to a larger C-S-H solubility dataset.

*Davies, Gisby and coauthors*

The C-S-H solubility data at temperatures between 25 and 85°C used to parameterise the thermodynamic models of Atkins, Glasser and coauthors (Atkins et al., 1992a; Glasser et al., 1999) were used in the development of a non-ideal sublattice solid solution model by Davies, Gisby and coauthors (Davies et al., 2014; Gisby et al., 2007). This thermodynamic model describes C-S-H in terms of two solid solutions: a low Ca/Si ratio (≤1.11) solid solution for '$SiO_2$ gel' and a higher Ca/Si ratio ($0.78 \leq Ca/Si \leq 1.67$) solid solution for C-S-H. Mixing in the C-S-H solid solution model is specified using five sublattice sites and four C-S-H end-members, and is based on the compound energy model (Hillert, 1998). The Gibbs free energies of the C-S-H end-members were adjusted to fit a large set of solubility data for C-S-H at ~25°C. The thermodynamic model generally predicts lower Si concentrations than shown by the C-S-H solubility dataset used for model validation at Ca/Si ratios > 1.3 and does not match the concentrations of Ca measured in C-S-H solubility experiments performed by Glasser et al. (2005) at Ca/Si ratios > 1.5 and temperatures from 25-85°C. The thermodynamic model was extended to include mixing of $UO_3$, NaOH and KOH species in the C-S-H interlayer. No thermodynamic data for the 'C-S-H' or '$SiO_2$ gel' solid solution models were provided.

*Thomas and Jennings*

The thermodynamic model developed by Thomas and Jennings (1998) describes C-S-H as a solid solution with five sublattice sites: a paired site ($SiO_2$), a bridging site containing a vacancy represented by $2(OH^-)$ or $H_2SiO_4^{2-}$, a Ca-O layer site (CaO), a site for interlayer charge-balancing species ($Ca^{2+}$ or $2H^+$), and an interlayer $H_2O$ site, to describe an overall composition range of $0.78 \leq Ca/Si \leq 1.67$. Four end-members were selected from this definition (i.e. all possible combinations of species in the bridging site and the site for interlayer charge-balancing species were allowed), and the mixing rules for the sublattice solid solution model were defined as a mechanical mixture with a subregular Redlich-Kister (Guggenheim) type excess Gibbs free energy term (Glynn and Reardon, 1990), but without mention of the configurational entropy. The Gibbs free energies of the end-members and excess interaction

parameters were fitted to best match the C-S-H solubility data measured by Cong and Kirkpatrick (1996a).

*Berner*

The C-S-H thermodynamic model formulated by Berner (1992) describes a mixture of a $SiO_2$ end-member (Ca/Si = 0) with ideal ($G^{EX}$ = 0) solid solutions of $SiO_2$-$CaH_2SiO_4$ between 0 < C/S ≤ 1, $Ca(OH)_2$-$CaH_2SiO_4$ between 1 < C/S ≤ 2.5, and $CaH_2SiO_4$-$Ca(OH)_2$ for C/S > 2.5. The solid solutions are described as mechanical mixtures. Solubility products were specified for each of the end-members as constants or as functions of the Ca/Si ratio of the C-S-H phase. The thermodynamic model was applied to predict the pore solution chemical composition of hydrated PC, including a hydrated PC/(Ca-Si-)uranium oxide matrix, under thousands of groundwater exchange cycles, to simulate the long-term leaching behavior of these materials in a radioactive waste repository.

*Reardon*

Reardon (1990) developed a thermodynamic model for C-S-H using the Pitzer interaction model (Pitzer, 1991) to calculate ion activity coefficients in the aqueous phase. The model defined the C-S-H solubility product as an empirical function of the Ca/Si ratio of this phase, which was selected to match the low-Si solubility curve of Jennings (1986). Solid phase assemblages and aqueous phase chemical compostions were calculated to describe the reaction between sulfuric acid and a hypothetical mixture of C-S-H, $Ca(OH)_2$ and $C_4AH_{13}$ as a preliminary demonstration of the thermodynamic model.

### 2.2.6 Thermodynamic Data for Secondary and Minor Cement Phases

Thermodynamic models have also been developed for secondary and minor cement phases such as Fe-Al hydrogarnet (Dilnesa et al., 2014) and $C_4AcH_{11}$-$C_4A\bar{s}H_{12}$ (Matschei et al., 2007b). These models, thermodynamic models for C-(N-)A-S-H,

and thermodynamic data for pure secondary and minor cement phases are compiled in thermodynamic databases. Several thermodynamic databases for cement phases have been developed (Atkins et al., 1992a; Blanc et al., 2010a; 2010b; Lothenbach and Winnefeld, 2006; Savage et al., 2011), although the most widely used thermodynamic database in the cement chemistry literature is CEMDATA (Kulik and Kersten, 2001; 2002; Lothenbach et al., 2008b; Lothenbach and Winnefeld, 2006; Matschei et al., 2007b; Möschner et al., 2008; Möschner et al., 2009; Schmidt et al., 2008). Development of this database has been ongoing for nearly a decade. However, the thermodynamic model for C-(N-)A-S-H in CEMDATA is based on the C-S-H model of Kulik and Kersten (2001), so does not describe structural incorporation of Al in this phase. Consequently, the utility of CEMDATA is generally limited to relatively low-Al cement-based materials such as hydrated PC.

## 2.3 Conclusions

The main hydration product in hydrated PC-based materials and AAS is C-(N-)A-S-H. The chemistry of this phase has been studied for decades, although its exact structure is not fully understood. It is generally thought that C-(N-)A-S-H resembles a solid solution of poorly-crystalline tobermorite-like phases over a large range of Ca-Al-Si compositions: the theoretical composition envelope is $0.67 \leq Ca/(Al+Si) \leq 2.5$ and $Al/Si \leq 0.5$, although the Ca and Al-content of this phase is greatly limited by secondary and minor cement phases at high Ca and Al concentrations, so maximum Al/Si ratios of ~0.2 are typically obtained in phase-pure samples. Cross-linking of aluminosilicate chains in C-(N-)A-S-H is possible in low-Ca ($Ca/Si \leq 1$) materials such as $Na_2SiO_3$ and $Na_2CO_3$-activated slag cements. Al is generally thought to be structurally incorporated only in bridging sites in C-(N-)A-S-H, in accordance with the Al-O-Al avoidance principle of Loewenstein. Al may also be present as positively-charged aqueous species in the interlayer of C-(N-)A-S-H in five-fold coordination, although there is no consensus on the location of Al[6] incorporation into this phase. Other dissolved interlayer and surface complexes bound to C-(N-)A-

S-H include $Ca^{2+}$ and alkalis, although the exact mechanism of alkali uptake in this phase is not fully understood.

Many structural models have been developed for C-(N-)A-S-H, but none are as flexible for determining chemical compositions and structural parameters as the SGM. The major limitation of this structural model is that it does not contain a description of cross-linked C-(N-)A-S-H phases. The SGM is also limited by its non-specific structural description of 'solid solution $Ca(OH)_2$'.

The secondary and minor phases formed in hydrated cements depend greatly on the cement formulation and curing conditions; however, portlandite and AFm/AFt phases typically form in hydrated PC-based materials, and Mg-Al LDH and AFm phases are common precipitates in AAS cements. Thermodynamic modelling exploits this link between phase formation, cement formulation and curing conditions, which makes it a key technique in the development of a general framework to understand the durability of modern cement-based materials. Many thermodynamic models for C-S-H are available, although none have been developed for C-(N-)A-S-H that include structural incorporation of Al at pH conditions >12.5, which is the pH range of interest for most hydrated PC materials and AAS. This has limited the utility of the thermodynamic modelling technique to describe the chemistry of these materials in the past. Therefore, the development of a thermodynamic model for C-(N-)A-S-H, formulated with a description of Al structurally incorporated into this phase and parameterised to more accurately describe the solubility of cement-based materials at pH > 12.5, would represent a major step towards being able to predict the chemistry, and durability properties, of many more cement-based materials in service.

# 3
# Materials and Methods

## 3.1 Introduction

Chapter 3 describes the materials, experimental techniques and the thermodynamic modelling approach used in the thesis. The chemistry of AAS cements and the constituent solid reaction products formed in these materials are analysed using X-ray diffraction (XRD), scanning electron microscopy with energy-dispersive X-ray spectroscopy (SEM-EDS), and $^{27}$Al and $^{29}$Si magic angle spinning nuclear magnetic resonance (MAS NMR). Laboratory-synthesised C-S-H, C-A-S-H and C-(N-)A-S-H products are analysed by XRD with Rietveld analysis, $^{29}$Si MAS NMR, thermogravimetric analysis (TGA), ion chromatography (IC), pH analysis and thermodynamic modelling. The contributions of co-workers (i.e. other than Rupert J. Myers) to the thesis, in particular to the experimental program, are listed at the start of Chapters 4-9.

## 3.2 Materials

### 3.2.1 Alkali-Activated Slag (AAS) Cement

The AAS cement studied here was synthesised using GBFS supplied by Zeobond Pty Ltd. (Australia), with chemical composition given in Table 3.1 (measured by the Analytical X-ray Unit, Latrobe University, Australia). This GBFS has a specific gravity of 2800 kg/m$^3$, a Blaine fineness of 410 m$^2$/kg, a particle size range of 0.1-74 μm as determined through laser granulometry, and a $d_{50}$ of 15 μm.

Table 3.1. Chemical composition of the GBFS used in this work as determined by X-ray fluorescence. LOI is loss on ignition at 1000°C.

| Component | (mass % as oxide) |
|---|---|
| $SiO_2$ | 33.8 |
| $Al_2O_3$ | 13.7 |
| $Fe_2O_3$ | 0.4 |
| CaO | 42.6 |
| MgO | 5.3 |
| $Na_2O$ | 0.1 |
| $K_2O$ | 0.4 |
| Others | 1.9 |
| LOI | 1.8 |

The alkali activator was prepared by dissolution of solid NaOH pellets (Sigma-Aldrich, Australia) into D grade (PQ, Australia) sodium silicate, to reach a modulus ($SiO_2/Na_2O$ molar ratio) of 1.0. The AAS cements were activated using this solution, added at a ratio of 8g $Na_2SiO_3$/100g GBFS. Water was added to achieve a water/binder (w/b) ratio of 0.40, and the activator was allowed to cool to room temperature prior to preparation of the specimens. The AAS cements were cured in sealed bags at 23°C until testing, and were crushed by hand before analysis.

### 3.2.2 Laboratory-Synthesised C-(N-)A-S-H

C-(N-)A-S-H samples were prepared by mixing Milli-Q water (Merck Millipore), $SiO_2$ (Aerosil 200, Evonik), CaO (obtained by burning $CaCO_3$ (Merck Millipore) at 1000°C for 12 hours), $CaO{\cdot}Al_2O_3$ and 0 to 1 M solutions of NaOH and/or KOH (Merck Millipore) at a solution/solid ratio of 45 in an $N_2$-filled glovebox to obtain the bulk molar Al/Si ratios (Al/Si*) and bulk molar Ca/Si ratios (Ca/Si*) investigated in this thesis (Al/Si* $\leq$ 0.15 and 0.6 $\leq$ Ca/Si* $\leq$ 1.6). The $CaO{\cdot}Al_2O_3$ (99.1 wt.% determined by XRD with Rietveld analysis) was made from $CaCO_3$ and $Al_2O_3$ (Sigma Aldrich) by heating for 1 hour at 800°C, 4 hours at 1000°C and 8 hours at 1400°C in a Carbolite HTF 1700 furnace (the heating rate to 800°C and between each subsequent temperature was 300°C/hour), then cooled at 600°C/hour under

laboratory atmosphere and ground with a Retsch PM100 ball mill to a Blaine surface area of 3790 $cm^2/g$ (Lothenbach et al., 2012b).

Samples were equilibrated at 7°C, 20°C and 50°C in polyethylene vessels and at 80°C in teflon vessels. The 7°C, 50°C and 80°C samples were shaken twice per week and the 20°C samples were shaken continuously at 100 rpm. Once equilibrium was approached (1 year at 7°C, 182 days at 20°C, and 56 days at 50°C and 80°C), the samples were vacuum filtered with 0.45 µm nylon filters in a $N_2$-filled glovebox. Equilibration times were selected following the study of C-(A-)S-H kinetics at 20°C in (L'Hôpital et al.), which showed approximately constant supernatant compositions after 182 days; additional analysis generally showed small differences (< ±25%) in dissolved Si, Al and Ca concentrations between 91 days and 1 year for the 7°C samples and 56 and 91 days for the 50°C samples. The filtered solids were washed with a 50% v/v water-ethanol solution, followed by a >94 vol.% ethanol solution, and then freeze-dried for 7 days. The dried solids were stored in $N_2$-filled desiccators with humidity and $CO_2$ traps made from saturated $CaCl_2$ solutions (~30% relative humidity, RH) and solid NaOH pellets, until analysis.

## 3.3 Experimental Techniques

### 3.3.1 X-ray Diffraction (XRD) and Rietveld Analysis

XRD describes the phenomenon that occurs when an X-ray beam is diffracted by a surface. When the diffraction surface is approximately flat relative to the incident beam (e.g. ordered crystal planes), the diffracted X-rays that undergo constructive interference can be described by Bragg's law (eq.(3.1)):

$$n\lambda = 2d\sin(\theta) \tag{3.1}$$

where $n$ is an integer, $\lambda$ is the wavelength of the incident X-rays, $d$ is the depth between diffraction surfaces and $\theta$ is the scattering angle between the incident X-rays

and the diffraction surface. Constructive interference typically occurs at multiple scattering angles, rather than at a single value of $\theta$. The measured intensity of the diffracted X-rays, typically plotted as a function of $\theta$, yields a diffraction pattern. Identification of solid phases from diffraction patterns is possible because each crystalline phase has its own unique diffraction pattern; individual phases can be identified in materials containing more than one crystalline solid phase with XRD. XRD is a powerful characterisation tool for cements because the solid binders in these materials typically contain several (semi-)crystalline solid reaction products.

*AAS Cement*

Powder XRD analyses of AAS cement specimen were conducted using a Bruker D8 Advance instrument with Cu Kα radiation and a nickel filter. The tests were conducted with a step size of 0.020°, for a 2θ range of 5° to 70°. Solid phases were identified by comparison with reference cards in the Powder Diffraction File (PDF) as noted in Chapters 4-5.

*Laboratory-Synthesised C-(N-)A-S-H*

Powder XRD patterns of laboratory-synthesised C-(N-)A-S-H samples were recorded on a PANalytical X'Pert Pro MDF diffractometer equipped with a Ge(111) Johansson monochromator for Cu Kα radiation, and an X'Celerator detector, and a step size of 0.017° 2θ. An external $CaF_2$ standard was used for Rietveld analysis, enabling quantification of the amount of C-(N-)A-S-H in each sample (O'Connor and Raven, 1988). Average basal ($d_{(002)}$) spacings of the C-(N-)A-S-H products were determined by visual inspection. Rietveld analysis was performed in PANalytical HighScore Plus software. The PDF reference cards used to identify the solid phases present in the samples are provided in Chapters 8-9.

### 3.3.2 Scanning Electron Microscopy (SEM)

Energy-dispersive X-ray spectroscopy (EDS) is used to determine the (near-)surface elemental composition of a sample imaged by a scanning electron microscope (SEM). This technique is referred to as SEM-EDS. In a SEM, a high energy electron beam of specified energy and cross-sectional area is fired at the surface of a sample in a vacuum-sealed chamber. On impact with the sample, the electrons release energy in an impact volume in the vicinity of the impact spot (the typical impact volume for SEM-EDS analysis of cements is ~1 $\mu m^3$). Some electrons in the incident electron beam impact and eject inner-shell electrons residing in atoms within the impact volume, to create electron holes. These electron holes are filled with higher-energy outer-shell electrons, which generate characteristic X-rays that can be counted with a detector. Characteristic X-rays have energies that are equivalent in magnitude to the energetic differences between the inner and outer-shells of the excited atoms. The identity of the excited atoms can be determined because the energy levels of electron shells in each element are unique. For SEM-EDS analysis of materials containing multiple elements, characteristic X-rays can be classified according to their energy and counted to determine the relative amount of each element (chemical composition) in the impact volume.

*AAS Cement*

An FEI Quanta environmental SEM with a 15 kV accelerating voltage and a working distance of 10 mm was used to analyse AAS cement specimen. Polished, uncoated, samples were evaluated in low vacuum mode using a backscatter detector. A Link-Isis (Oxford Instruments) energy dispersive X-ray detector was used to determine chemical compositions. An average of approximately 30 data points were collected for elemental analysis at each time of curing studied.

### 3.3.3 $^{29}$Si Magic Angle Spinning Nuclear Magnetic Resonance (MAS NMR)

Nuclear magnetic resonance (NMR) spectrometers are used to probe the interactions between nuclei with intrinsic magnetic moments (non-zero spin) and applied magnetic fields to resolve the local chemical environment of nuclei such as $^{29}$Si. In an NMR experiment, relaxation of spinning nuclei back to thermal equilibrium in an applied static field ($B_0$), after perturbation by radiofrequency (*rf*) radiation, generates voltage in a coil surrounding the sample. The voltage response is time-dependent, is called the free induction decay (FID), and is recorded by the NMR spectrometer. Fourier transformation of a FID results in an NMR spectrum, which is a plot of the amount of resonating nuclei as a function of frequency, or more commonly chemical shift ($\delta$).

The FID generated by a NMR experiment is intrinsically linked to the total nuclear spin Hamiltonian, which represents the total energy of a non-zero spin atomic nucleus and consists of several components: the dipolar and chemical shift Hamiltonian components are important for resolving the total spin Hamiltonian of $^{29}$Si nuclei (spin = 1/2). The time-averaged value of the dipolar Hamiltonian is equal to 0 and chemical shift anisotropy is removed when a sample is spun rapidly at the magic angle spinning (MAS) condition, i.e. at an angle of $\cos^2(\theta_{MAS}) = 1/3$ ($\theta_{MAS} \approx 54.74°$) with respect to the static magnetic field ($B_0$). Therefore, local chemical environments for $^{29}$Si nuclei can be represented in terms of the isotropic chemical shift ($\delta_{iso}$, the average chemical shift) in MAS NMR spectra. Solid-state $^{29}$Si MAS NMR spectra are referenced to an external standard, typically tetramethylsilane (TMS), so that local chemical environments can be determined from known isotropic chemical shift assignments reported in the literature. NMR spectra for samples that are not spun sufficiently rapidly contain spinning sidebands, which are separated from each other and the central transition by the spinning frequency and can complicate this analysis. The $Q^n(m\text{Al})$ notation is used to describe $^{29}$Si site environments, as shown in Figure 3.1.

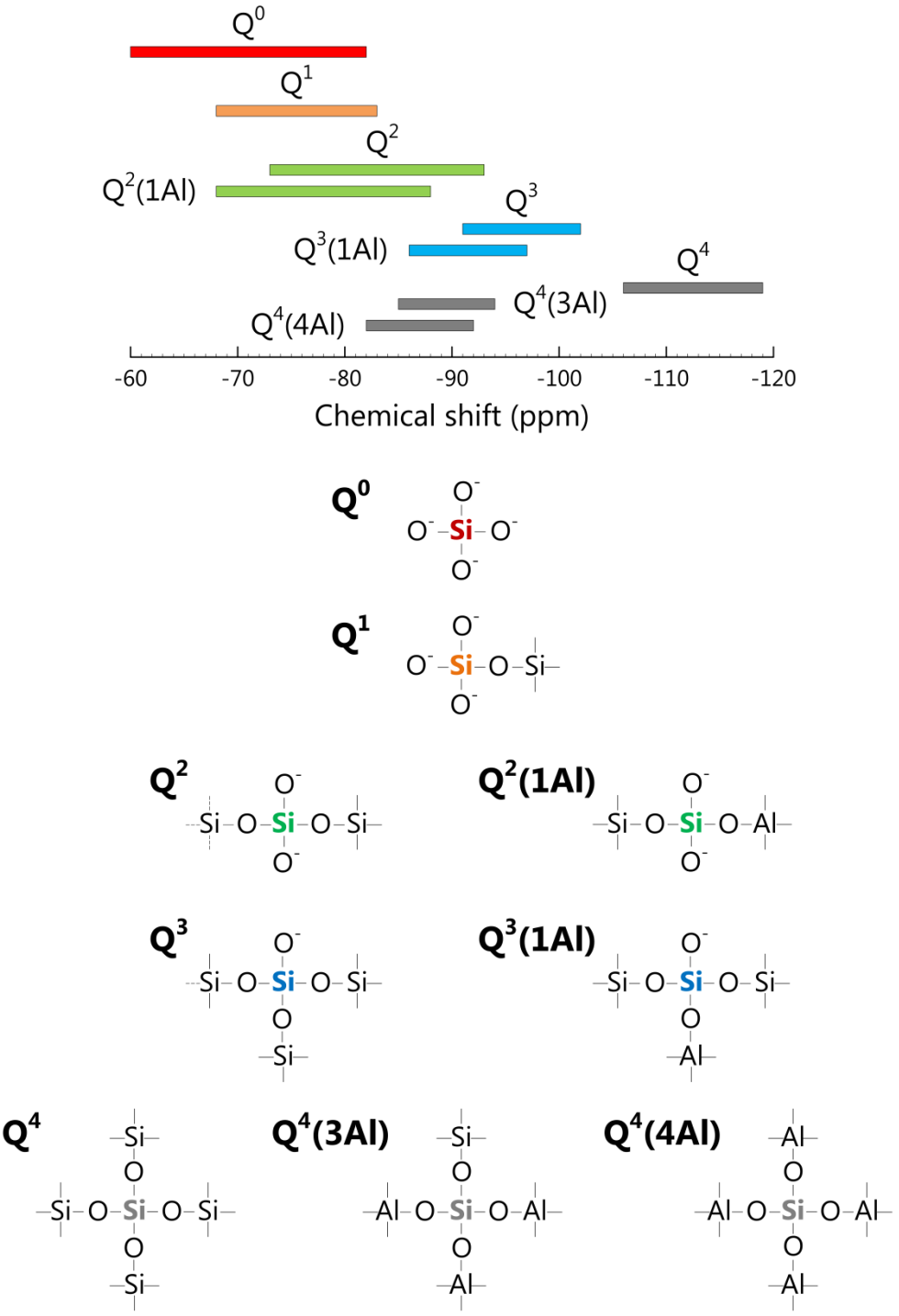


Figure 3.1. $Q^n(m\text{Al})$ notation and $^{29}$Si shift range for the $Q^n(m\text{Al})$ sites discussed in the thesis, adapted from (Engelhardt and Michel, 1987).

*AAS Cement*

Solid-state $^{29}$Si MAS NMR spectra for the AAS cement specimen were collected at 119.1 MHz on a Varian VNMRS-600 (14.1 T) spectrometer using a probe for 4 mm

o.d. zirconia (PSZ) rotors and a spinning speed ($\nu_R$) of 10.0 kHz. The $^{29}$Si MAS experiments employed a pulse width of 4 μs, a relaxation delay of 20 s, and 4096 scans. $^{29}$Si chemical shifts are referenced to external TMS.

Deconvolutions of the $^{29}$Si MAS NMR spectra for these samples are performed using the minimum number of component peaks needed to describe the spectra. These spectra were manually fitted with Gaussian functions, with the full width at half height (FWHH) of each component peak constrained to <10 ppm and assigned to connectivity states based on information available in the literature for cements (Richardson et al., 1993; Skibsted and Andersen, 2013), zeolites (Engelhardt and Michel, 1987), and silicate-activated slag cements (Bernal et al., 2013c). Peak positions and widths for each identified species were held constant throughout the deconvolution process. The component peaks assigned to the remnant anhydrous slag are rescaled vertically by a single factor in each spectrum, to provide the appropriate lineshape in the corresponding regions of the spectra and determine the slag reaction extent. A recent study (Le Saoût et al., 2011) showed that $^{29}$Si MAS NMR spectra of AAS cements can be appropriately quantified in this way.

Quantification of the $Q^4$(4Al) component in the $^{29}$Si MAS NMR spectral deconvolutions for the AAS cement specimens is performed using eq.(3.2) assuming that the only $Q^4$ units are $Q^4$(4Al) and $Q^4$(3Al), and that these sites are present in a separate Al-rich phase additional to the C-(N-)A-S-H gel:

$$I^{*}_{Q^4(4Al)} = I_{Q^4(3Al)}\left[\frac{\frac{3}{5}\left(Si/Al\right)^{*}-1}{1-\left(Si/Al\right)^{*}}\right] \qquad (3.2)$$

where $I_{Q^4(3Al)}$ is the relative intensity of the $Q^4$(3Al) component determined from deconvolution analysis of the experimental $^{29}$Si MAS NMR spectra, $I^{*}_{Q^4(4Al)}$ is the calculated relative intensity of $Q^4$(4Al) components and $(Si/Al)^{*}$ is the assumed Si/Al ratio of the $Q^4$-containing phase. An Si/Al ratio of 1.2 is used here, which is

consistent with the composition of N-A-S(-H) (geopolymer) gels determined from MAS NMR (Duxson et al., 2005) and statistical thermodynamic model predictions (Provis et al., 2005a).

*Laboratory-Synthesised C-(N-)A-S-H*

Solid-state $^{29}$Si MAS NMR spectra for the laboratory-synthesised C-(N-)A-S-H samples were collected at 79.49 MHz on a Bruker Avance 400 MHz NMR spectrometer with a 7 mm CP/MAS probe. The measurements were recorded using a 4500 Hz spinning rate, 9216 scans, $\pi/3$ pulses of 2.5 μs, and 20 s relaxation delays. $^{29}$Si chemical shifts were referenced to external TMS. Spectral deconvolutions are carried out using component peaks with a Lorentzian/Gaussian ratio of 0.5, full width at half height ≤ 3 ppm, constant chemical shifts for each peak, and constrained peak amplitudes. These constraints are for tobermorite-like nanostructures with nearest-neighbour Al-O-Al avoidance (Loewenstein, 1954) and are required for consistency with 'dreierketten-type' (3*n*-1) chain structures (Richardson, 2004). A ratio of $Q^2_p/Q^2_b = 2$ is specified for the non-cross-linked C-(N-)A-S-H products. The following additional constraints are specified for the cross-linked C-(N-)A-S-H products (Myers et al., 2013):

i) $Q^2(1Al) \geq 2Q^3(1Al)$;

ii) $Q^2 + Q^2(1Al) \geq 2(Q^3 + 2Q^3(1Al))$;

iii) $Q^2_p{*} \geq 0$;

iv) $Q^2(1Al){*} \geq 0$; and

v) $Q^2_p{*}/Q^2_b = 2$

where $Q^2_p{*} = Q^2_p - 2(Q^3 + Q^3(1Al))$ and $Q^2(1Al){*} = Q^2(1Al) - 2Q^3(1Al)$.

### 3.3.4 $^{27}$Al MAS NMR

The principles of $^{27}$Al and $^{29}$Si MAS NMR are similar, except the quadrupolar interaction Hamiltonian is non-zero for $^{27}$Al nuclei (spin = 5/2). High magnetic field strengths are used in NMR analysis of $^{27}$Al because this reduces second-order quadrupolar effects, which are inversely proportional to the magnetic field strength

(first-order quadrupolar effects can be removed by spinning at the magic angle). Chemical shifts for $^{27}$Al are typically referenced to an external standard such as $Al(H_2O)_6^{3+}{}_{(aq)}$. $^{27}$Al site environments are referenced using the $q^n$ notation, where this notation for Al sites is equivalent to the $Q^n$ notation for Si sites (Harris et al., 1997).

*AAS Cement*

Solid-state $^{27}$Al MAS NMR spectra were acquired at 156.3 MHz on a Varian VNMRS-600 (14.1 T) for AAS cement specimen cured for 1-180 days, with a pulse width of 0.5 μs, a relaxation delay of 2 s, and at least 1000 scans. All spectra were collected with a tip angle of 51°. Additional $^{27}$Al MAS NMR spectra were acquired at 104.2 MHz on a Varian VNMRS 400 (9.4 T) spectrometer for the anhydrous slag precursor and the sample cured for 2 years with $\nu_R$ = 14 kHz, a pulse duration of 1 μs, recycle delay of 0.2 s and 7000 repetitions. $^{27}$Al chemical shifts are referenced to external 1.0 M aqueous $Al(NO_3)_3$ via internal referencing using the hydrotalcite peak at $\delta_{iso}$ = 9.68 ppm, using the parameters $C_Q$ = 1.2 MHz and $\eta_Q$ = 0.8 as determined for a pure hydrotalcite sample (S.A. Walling and S.A. Bernal, unpublished data) and the calculation method reported in (Engelhardt and Koller, 1991).

$^{27}$Al MAS NMR spectra are deconvoluted manually using the Dmfit software (Massiot et al., 2002) and the (Czjzek) Gaussian Isotropic Model (Neuville et al., 2004) (exponent of the standard deviation of the Gaussian distribution for each component = 5) to model quadrupolar peak shapes. Secondary reaction products identified from the XRD data are quantified in the spectra using component peaks matched to coordination and connectivity states that are consistent with the literature (Andersen et al., 2006; Sideris et al., 2012). Quadrupolar coupling parameters ($C_Q$) used to define the peak shapes for these secondary products are taken from the literature, as shown in Chapters 4-5. The component peaks of the remnant anhydrous slag and the C-(N-)A-S-H gel are defined using quadrupolar coupling parameters that provided a good fit to the experimental spectra and are consistent with the established values for aluminosilicates such as zeolites (Klinowski, 1984). The first order spinning sidebands in the spectra for the samples cured up to 180 days ($\nu_R$ = 10

kHz) were fitted using symmetric quadrupolar lineshapes around the central transitions for the Al[4] and Al[6] components, and were taken into account in the quantification of deconvoluted spectra. It has been shown that the manifold of spinning sidebands in MAS NMR spectra of quadrupolar nuclei can be relatively accurately approximated by symmetric first-order contributions (Skibsted et al., 1991), which supports the methodology applied here.

The Al[4] component of the remnant anhydrous slag is rescaled by the same factors used in analysis of the $^{29}$Si MAS NMR spectra, assuming congruent dissolution of the slag and corrected to exclude silica supplied by the activator, so that the extent of reaction of the slag is identical in both sets of spectra at each time of curing. The Al[6] component of the anhydrous slag peak is excluded from the rescaling procedure because only <4% of the total spectral intensity remained in this region after subtracting contributions from the Al[4] spinning sidebands overlapping in the Al[6] region. The assumption of full incorporation of Si present in the activator into the solid binder leads to eq.(3.3):

$$R = \frac{(1-\frac{Y_1}{100})(X_1 + X_2) - X_2}{X_1} \tag{3.3}$$

where $R$ is the fraction of Si in the slag that has reacted, $Y_1$ is the percentage of the total Si added to the mix that has not reacted (i.e. the percentage of the 'anhydrous $Q^0$' peak in the deconvoluted $^{29}$Si MAS NMR spectra), $X_1$ is the number of moles of Si in the slag and $X_2$ is the number of moles of Si in the activator. The fraction of Al in the slag that has reacted is then defined as $R'$, thus the fraction of Al in the slag that has not reacted is 1 - $R'$. Hence, the congruent slag dissolution assumption can be applied to eq.(3.3) to yield eq.(3.4):

$$1 - R' = 1 - \frac{(1-\frac{Y_1}{100})(X_1 + X_2) - X_2}{X_1} \tag{3.4}$$

The lineshape of the Al[4] component of the anhydrous slag (determined through analysis of $^{27}$Al MAS NMR spectra for the anhydrous slag) is rescaled using eq.(3.4) in fitting of $^{27}$Al MAS NMR spectra to determine the fraction of Al in the slag remaining in the mix at each time of curing.

Component widths were unchanged and peak positions were held approximately constant (maximum variation of $\delta_{obs}$ ± 0.5 ppm) in the deconvolution process. Simulated line broadening of $L_B$ = 50 ppm is performed using Gaussian $L_B$ for the reaction products and Lorentzian $L_B$ for the anhydrous slag. Isotropic chemical shifts ($\delta_{iso}$) were calculated for the peaks in the deconvoluted spectra using the method described in (Andersen et al., 2006), using the observed chemical shift ($\delta_{obs}$) values determined here.

### 3.3.5 Thermogravimetric Analysis (TGA)

TGA is the study of how materials change in mass as a function of temperature. TGA of cements is typically performed up to ~1000°C to measure mass losses due to release of $H_2O$ and $CO_2$ from constituent phases in the solid binder. This technique is used for phase characterisation because the chemistry and mass loss temperatures of a solid phase are related. Phase characterisation is typically performed using the first derivatives of TGA traces, where the temperatures at which mass losses occur are more apparent.

*Laboratory-Synthesised C-(N-)A-S-H*

Thermogravimetric analysis (TGA) data were recorded on a Mettler Toledo TGA/SDTA851$^e$ at a heating rate of 20°C/min under an $N_2$ atmosphere. Mass losses between 30°C and 550°C were assigned to the combined dehydration and dehydroxylation effects of C-(N-)A-S-H, katoite, $Al(OH)_3$, strätlingite and portlandite products during heating; mass losses assigned to portlandite were measured between 400°C and 520°C.

### 3.3.6 Ion Chromatography (IC) and pH Analysis

An IC experiment separates aqueous species based on their affinity to bond to an ion exchange bed; those with greater affinity for the ion exchange bed are eluted slower than those with lower affinity. The eluted species are counted and classified in terms of residence time. Therefore, element concentrations in aqueous solutions can be determined using IC.

A pH meter measures the potential over a pH-sensitive glass membrane of a pH electrode that is referenced to an electrode with constant potential. Temperature probes are also commonly integrated into pH meters. Calibration of the pH electrode and conversion of measured potentials to pH values is performed via the Nernst equation (eq.(3.5)):

$$E = E_0 + \left( \frac{2.303RT}{nF} \right) pH \tag{3.5}$$

where $E$ is the potential difference, $E_0$ is the standard electrode potential, $R$ is the universal gas constant (8.3145 $J.mol^{-1}.K^{-1}$), $T$ is temperature (K), $n$ is the stoichiometric amount of electrons transferred in the electrochemical reaction (mol), $F$ is the Faraday constant (96485.34 C/mol) and $pH$ is defined by eq.(3.6):

$$pH = -\log_{10} \left\{ H^+ \right\} \tag{3.6}$$

where the curly brackets denote activity.

*Laboratory-Synthesised C-(N-)A-S-H*

A Dionex DP ICS-3000 ion chromatograph was used to determine Ca, Si and Al concentrations in the filtrates (relative measurement error ±10% in the concentration range of interest and detection limit of 0.1 ppm). Si was detected using a sodium carbonate/bicarbonate eluent and a postcolumn reagent of sodium molybdate/sodium lauryl sulphate in metasulfonic acid. Al was measured using a HCl eluent and a Tiron/ammonium acetate postcolumn reagent. Aqueous hydroxide concentrations were determined at ~23°C with a Knick pH meter (pH-Meter 766) equipped with a Knick SE100 electrode that was calibrated against KOH solutions of known concentrations.

## 3.4 Thermodynamic Modelling

### 3.4.1 Modelling Method

Thermodynamic modelling is performed in GEM Selektor v.3 software (http://gems.web.psi.ch/) (Kulik et al., 2013; Wagner et al., 2012) using the

PSI/Nagra 12/07 thermodynamic database (Thoenen et al., 2013), which is updated from (Hummel et al., 2002) via the inclusion of two additional aqueous (alumino)silicate species, and the CEMDATA07 thermodynamic database (Kulik and Kersten, 2001; 2002; Lothenbach et al., 2008b; Lothenbach and Winnefeld, 2006; Matschei et al., 2007b; Möschner et al., 2008; Möschner et al., 2009; Schmidt et al., 2008) updated to include recently published data for $Al(OH)_3$ and hydrogarnet phases (Dilnesa et al., 2014; Lothenbach et al., 2012b), and C-(N-)A-S-H, MgAl-OH-LDH, zeolites and alkali carbonate minerals as described in Chapters 6-9 of this thesis. The thermodynamic properties of the gases and aqueous species used in these calculations are shown in Tables 3.2-3.3, with full details of the solid phases used described in each thermodynamic modelling chapter (Chapters 6-9).

The ideal gas equation of state is used to describe the gases and the Truesdell-Jones form of the extended Debye-Hückel equation, eq.(3.7) (Helgeson et al., 1981), is used to describe the aqueous species.

$$\log_{10}\gamma_j = \frac{-A_\gamma z_j^2\sqrt{I}}{1+\dot{a}B_\gamma\sqrt{I}} + b_\gamma I + \log_{10}\frac{x_{jw}}{X_w} \qquad (3.7)$$

Here, $\gamma_j$ and $z_j$ are the activity coefficient and charge of the $j^{th}$ aqueous species respectively, $A_\gamma$ and $B_\gamma$ are temperature and pressure-dependent electrostatic parameters, $I$ is the ionic strength of the aqueous electrolyte phase, $\dot{a}$ is the ion size parameter, $b_\gamma$ is a parameter that describes short-range interactions between charged aqueous species in an electrolyte solution (representing the predominant electrolyte in the system), $x_{jw}$ is the molar quantity of water, and $X_w$ is the total molar amount of the aqueous phase. Constant values of $\dot{a}$ (3.31 Å) and $b_\gamma$ (0.098 kg/mol) are taken to represent the average ion size and common short-range interactions of charged aqueous species in a NaOH-dominated solution (Helgeson et al., 1981) in Chapters 6-7. Ion size and extended term parameters for KOH ($\dot{a}$ = 3.67 Å and $b_\gamma$ = 0.123 kg/mol) (Helgeson et al., 1981) are used in Chapters 8-9. The water activity is calculated from the osmotic coefficient (Helgeson et al., 1981).

Table 3.2. Thermodynamic properties of the gases used in the thermodynamic modelling simulations. The reference state is 298.15 K and 1 bar.

| Gas | $V°$ ($cm^3$/mol) | $\Delta_f H°$ (kJ/mol) | $\Delta_f G°$ (kJ/mol) | $S°$ (J/(mol.K)) | $Cp°$ (J/(mol.K)) | Reference |
|---|---|---|---|---|---|---|
| $N_2$ | 24790 | 0 | 0 | 191.6 | 29.1 | (Wagman et al., 1982) |
| $O_2$ | 24790 | 0 | 0 | 205.1 | 29.3 | (Wagman et al., 1982) |
| $H_2$ | 24790 | 0 | 0 | 130.7 | 28.8 | (Wagman et al., 1982) |

Table 3.3. Thermodynamic properties of the aqueous species used in the thermodynamic modelling simulations. The reference state is unit activity in a hypothetical one molal solution referenced to infinite dilution at any temperature and pressure for aqueous species (Helgeson et al., 1981).

| Species | $V°$ ($cm^3$/mol) | $\Delta_f H°$ (kJ/mol) | $\Delta_f G°$ (kJ/mol) | $S°$ (J/(mol.K)) | $Cp°$ (J/(mol.K)) | Reference |
|---|---|---|---|---|---|---|
| $Al^{3+}$ | -45.2 | -530.6 | -483.7 | -325.1 | -128.7 | (Shock et al., 1997) |
| $AlO^+$ (+ $H_2O$ = $Al(OH)_2^+$) | 0.3 | -713.6 | -660.4 | -113 | -125.1 | (Shock et al., 1997) |
| $AlO_2^-$ (+ $2H_2O$ = $Al(OH)_4^-$) | 9.5 | -925.6 | -827.5 | -30.2 | -49 | (Shock et al., 1997) |
| $AlOOH^o$ (+ $2H_2O$ = $Al(OH)_3^o$) | 13 | -947.1 | -864.3 | 20.9 | -209.2 | (Shock et al., 1997) |
| $AlOH^{2+}$ | -2.7 | -767.3 | -692.6 | -184.9 | 56 | (Shock et al., 1997) |
| $AlHSiO_3^{2+}$ (+ $H_2O$ = $AlSiO(OH)_3^{2+}$) | -40.7 | -1718 | -1541 | -304.2 | -215.9 | (Matschei et al., 2007b) |
| $AlSiO_4^-$ (+ $3H_2O$ = $AlSiO(OH)_6^-$) | 25.5 | -1834 | -1681 | 11.1 | -4.6 | (Matschei et al., 2007b) |
| $AlSO_4^+$ | -6.0 | -1423 | -1250 | -172.4 | -204.0 | (Matschei et al., 2007b) |
| $Al(SO_4)_2^-$ | 31.1 | -2338 | -2006 | -135.5 | -268.4 | (Matschei et al., 2007b) |
| $Ca^{2+}$ | -18.4 | -543.1 | -552.8 | -56.5 | -30.9 | (Shock et al., 1997) |
| $CaOH^+$ | 5.8 | -751.6 | -717 | 28 | 6 | (Shock et al., 1997) |
| $Ca(HSiO_3)^+$ (+ $H_2O$ = $CaSiO(OH)_3^+$) | -6.7 | -1687 | -1574 | -8.3 | 137.8 | (Sverjensky et al., 1997) |

Table 3.3. Continued.

| Species | $V°$ ($cm^3$/mol) | $\Delta_f H°$ (kJ/mol) | $\Delta_f G°$ (kJ/mol) | $S°$ (J/(mol.K)) | $Cp°$ (J/(mol.K)) | Reference |
|---|---|---|---|---|---|---|
| $CaSiO_3^o$ (+ $H_2O$ = $CaSiO_2(OH)_2^o$) | 15.7 | -1668 | -1518 | -136.7 | 88.9 | (Matschei et al., 2007b) |
| $CaSO_4^o$ | 4.7 | -1448 | -1310 | 20.9 | -104.6 | (Sverjensky et al., 1997) |
| $K^+$ | 9.0 | -252.1 | -282.5 | 101 | 8.4 | (Shock et al., 1997) |
| $KOH^o$ | 15 | -474.1 | -437.1 | 108.4 | -85 | (Shock et al., 1997) |
| $KSO_4^-$ | 27.5 | -1159 | -1032 | 146.4 | -45.1 | (Sverjensky et al., 1997) |
| $Na^+$ | -1.2 | -240.3 | -261.9 | 58.4 | 38.1 | (Shock et al., 1997) |
| $NaOH^o$ | 3.5 | -470.1 | -418.1 | 44.8 | -13.4 | (Shock et al., 1997) |
| $NaSO_4^-$ | 18.6 | -1147 | -1010 | 101.8 | -30.1 | (Matschei et al., 2007b) |
| $HSiO_3^-$ (+ $H_2O$ = $SiO(OH)_3^-$) | 4.5 | -1145 | -1014 | 20.9 | -87.2 | (Sverjensky et al., 1997) |
| $SiO_2^o$ | 16.1 | -887.9 | -833.4 | 41.3 | 44.5 | (Kulik and Kersten, 2001; Shock et al., 1989) |
| $SiO_3^{2-}$ (+ $H_2O$ = $SiO_2(OH)_2^{2-}$) | 34.1 | -1099 | -938.5 | -80.2 | 119.8 | (Matschei et al., 2007b) |
| $S_2O_3^{2-}$ | 27.6 | -649.9 | -520.0 | 66.9 | -238.5 | (Shock et al., 1997) |
| $HSO_3^-$ | 33.0 | -627.7 | -529.1 | 139.7 | -5.4 | (Shock et al., 1997) |
| $SO_3^{2-}$ | -4.1 | -636.9 | -487.9 | -29.3 | -281.0 | (Shock et al., 1997) |
| $HSO_4^-$ | 34.8 | -889.2 | -755.8 | 125.5 | 22.7 | (Shock et al., 1997) |
| $SO_4^{2-}$ | 12.9 | -909.7 | -744.5 | 18.8 | -266.1 | (Shock et al., 1997) |
| $H_2S^o$ | 35.0 | -39.0 | -27.9 | 125.5 | 179.2 | (Shock et al., 1989) |
| $HS^-$ | 20.2 | -16.2 | 12.0 | 68.2 | -93.9 | (Shock et al., 1997) |
| $S^{2-}$ | 20.2 | 92.2 | 120.4 | 68.2 | -93.9 | (Hummel et al., 2002) |
| $Mg^{2+}$ | -22.0 | -465.9 | -454.0 | -138.1 | -21.7 | (Shock et al., 1997) |
| $MgOH^+$ | 1.6 | -690.0 | -625.9 | -79.9 | 129.2 | (Shock et al., 1997) |
| $MgHSiO_3^+$ (+ $H_2O$ = $MgSiO(OH)_3^+$) | -10.9 | -1614 | -1477 | -99.5 | 158.6 | (Shock et al., 1997) |
| $MgSO_4^o$ | 1.8 | -1369 | -1212 | -50.9 | -90.3 | (Hummel et al., 2002; Shock et al., 1997) |

Table 3.3. Continued.

| Species | $V°$ ($cm^3$/mol) | $\Delta_f H°$ (kJ/mol) | $\Delta_f G°$ (kJ/mol) | $S°$ (J/(mol.K)) | $Cp°$ (J/(mol.K)) | Reference |
|---|---|---|---|---|---|---|
| $MgSiO_3^o$ (+ $H_2O$ = $MgSiO_2(OH)_2^o$) | 12.1 | -1597 | -1425 | -218.3 | 98.2 | (Hummel et al., 2002) |
| $OH^-$ | -4.7 | -230 | -157.3 | -10.7 | -136.3 | (Shock et al., 1997) |
| $H^+$ | 0 | 0 | 0 | 0 | 0 | (Shock et al., 1997) |
| $H_2O^o$ | 18.1 | -285.9 | -237.2 | 69.9 | 75.4 | (Johnson et al., 1992) |
| $N_2^o$ | 33.4 | -10.4 | 18.2 | 95.8 | 234.2 | (Shock et al., 1989) |
| $O_2^o$ | 30.5 | -12.2 | 16.4 | 109 | 234.1 | (Shock et al., 1989) |

The extended Debye-Hückel equation is accurate to moderate ionic strengths (up to ~ 1 molal) (Helgeson et al., 1981), so is appropriate for the laboratory-synthesised C-(N-)A-S-H products (Chapters 8-9), but this limit is lower than the ionic strength in AAS pore solutions (~1-3 mol/kg in sodium silicate activated slag cements, e.g. (Gruskovnjak et al., 2006)). This equation is chosen for thermodynamic modelling of AAS cements (Chapters 6-7) because it is directly encoded in GEM-Selektor and this thesis presents the first step in the development of a thermodynamic model for C-(N-)A-S-H in these materials.

*Laboratory-Synthesised C-(N-)A-S-H*

Solubility products for laboratory-synthesised C-(N-)A-S-H products are calculated from experimental data obtained in the thesis using the reaction represented by eq.(3.8):

$$\begin{aligned}(CaO)_a\left(SiO_2\right)_b\left(Al_2O_3\right)_c\left(Na_2O\right)_d\left(K_2O\right)_e\left(H_2O\right)_f &\xrightleftharpoons{K_s} \\ aCa^{2+}{}_{(aq)} + bSiO_3^{2-}{}_{(aq)} + 2cAlO_2^{-}{}_{(aq)} + 2dNa^{+}{}_{(aq)} + 2eK^{+}{}_{(aq)} & \\ +2\left(a-b-c+d+e\right)OH^{-}{}_{(aq)} + \left(b+c+f-a-d-e\right)H_2O_{(l)} &\end{aligned} \quad (3.8)$$

where *a*, *b*, *c* , *d*, *e* and *f* are the respective stoichiometric coefficients for CaO, $SiO_2$, $Al_2O_3$, $Na_2O$, $K_2O$ and $H_2O$ in C-(N-)A-S-H. This reaction implies the following relationships for $K_s$ (eq.(3.9)):

$$\begin{aligned}K_s = &\left\{Ca^{2+}{}_{(aq)}\right\}^a \cdot \left\{SiO_3^{2-}{}_{(aq)}\right\}^b \cdot \left\{AlO_2^{-}{}_{(aq)}\right\}^{2c} \\ &\cdot \left\{Na^{+}{}_{(aq)}\right\}^{2d} \cdot \left\{K^{+}{}_{(aq)}\right\}^{2e} \cdot \left\{OH^{-}{}_{(aq)}\right\}^{2(a-b-c+d+e)} \cdot \left\{H_2O_{(l)}\right\}^{(b+c+f-a-d-e)}\end{aligned} \quad (3.9)$$

Activities of $Ca^{2+}{}_{(aq)}$, $SiO_3^{2-}{}_{(aq)}$, $AlO_2^{-}{}_{(aq)}$, $Na^{+}{}_{(aq)}$, $K^{+}{}_{(aq)}$, $OH^{-}{}_{(aq)}$ and $H_2O_{(l)}$ species were determined in GEM-Selektor v.3 (Kulik et al., 2013; Wagner et al., 2012). The $OH^-$ concentration is matched to the measured pH values in these calculations in

Chapter 8, and the measured concentrations of Ca, Si, Al, Na, K and $OH^-$ in the supernatants were used in Chapter 9.

Effective saturation indices (*SI**) are calculated from solubility and ion activity products using eq.(3.10), which indicates whether a solid phase is likely to precipitate from an aqueous solution at equilibrium:

$$SI_i^* = \frac{1}{n_i} \log_{10} \left( \frac{IAP_i}{K_{so,i}} \right) \tag{3.10}$$

where $IAP_i$ and $K_{so,i}$ refer to the dissolution reaction defined for solid *i* and $n_i$ is the total number of species in the $i^{th}$ dissolution reaction. These calculations define effective supersaturation ($SI_i^* > 0$, precipitation), saturation ($SI_i^* = 0$) and undersaturation ($SI_i^* < 0$, dissolution) states with respect to solid *i* at equilibrium. At equilibrium, solid phases may form from supersaturated or saturated aqueous solutions but not from undersaturated aqueous solutions.

# 4

# Cross-Linked Substituted Tobermorite Model (CSTM)

This chapter is based on the paper 'Generalized Structural Description of Calcium-Sodium Aluminosilicate Hydrate Gels: The Cross-Linked Substituted Tobermorite Model', published in *Langmuir* **2013**, *29*, 5294-5306. AAS cement samples were prepared by Susan A. Bernal and Rackel San Nicolas. The SEM-EDS measurements were carried out by Rackel San Nicolas with assistance from Roger Curtain (Bio21 Institute, University of Melbourne). The $^{27}$Al and $^{29}$Si MAS NMR experiments were performed by Susan A. Bernal with assistance from John Gehman (Bio21 Institute, School of Chemistry, University of Melbourne).

## 4.1 Introduction

While the Substituted General Model (SGM) developed by Richardson and Groves (1993b) (section 2.1.4) provides good descriptions of the nanostructure and chemical composition of C-(N-)A-S-H in alkali hydroxide-activated slag cements and PC-based materials (Richardson, 2004; Taylor et al., 2010), and some sodium silicate-activated slag cements (Le Saoût et al., 2011), recent experimental results for sodium silicate-activated slag cements have supported alternative C-(N-)A-S-H nanostructures not described by that structural model. The SGM represents C-(N-)A-S-H as a mixture of non-cross-linked tobermorite-like nanostructures if the 'solid solution' $Ca(OH)_2$ component of the model is deactivated (Richardson, 2004), which corresponds to the chemical composition of C-(N-)A-S-H in cementitious materials with bulk Ca/Si $\leq$ 1.5, such as alkali-activated cements.

Evidence supporting alternative C-(N-)A-S-H nanostructures in Ca/Si compositions ≤1.5 is found in high resolution $^{29}$Si MAS NMR results of sodium silicate-activated slag cements (Bernal et al., 2013c; Brough and Atkinson, 2002; Puertas et al., 2011), sodium carbonate-activated slag cements (Fernández-Jiménez et al., 2003), and laboratory-synthesised C-A-S-H products (Pardal et al., 2012), where the formation of cross-linked Si sites ($Q^3$ and/or $Q^3$(1Al)) has been identified. $Q^3$ type silica bonding environments can only be explained in tobermorite-like structural models by cross-linking between bridging sites in the silicate chains (e.g. as displayed in Figure 2.5 for cross-linking in the *c* direction). Therefore, the small but non-zero concentration of $Q^3$ units found in C-(N-)A-S-H supports the description of this phase as a mixture of cross-linked and non-cross-linked tobermorite-like structures.

It was also shown by Oh et al. (2012) that the model structure of 14Å tobermorite could only describe the mechanical properties of C-S-H(I) in the *a-b* plane (parallel to the Ca-O sheets); the response to compression in the *c* direction (perpendicular to the Ca-O sheets) was significantly different. This result indicates that the species present in the interlayer spacing between the silicate chains of 14Å tobermorite and C-S-H(I) are significantly different, meaning that alternative C-(N-)A-S-H structural models to those based on 14Å tobermorite-like nanostructures are needed to describe the observed mechanical properties. A structural model that can describe C-(N-)A-S-H using a flexible definition of nanostructure and chemical composition would enable a greater understanding of the mechanical behaviour of modern cement-based materials. Therefore, it is both appropriate and necessary to conceptualise and model C-(N-)A-S-H nanostructures in an alternative way, generalising from the SGM of Richardson and Groves (1993b).

The aim of this investigation is to derive a structural model formulated in terms of 9Å, 11Å and 14Å tobermorite-like structures, and develop rigorous analytical methods using this model for the calculation of structural and chemical parameters such as Ca/Si, Al/Si and mean chain length (MCL). The structural model is validated

by comparison with experimental SEM-EDS, and $^{27}$Al and $^{29}$Si MAS NMR data for an $Na_2SiO_3$-activated slag cement cured for 7, 28 and 56 days.

## 4.2 Derivation of a Generalised Structural Model for C-(N-)A-S-H

### 4.2.2 Non-Cross-Linked Tobermorite-Like Structural Model

The structural model for non-cross-linked tobermorite-like C-(N-)A-S-H is derived from eq.(2.2) (section 2.1.4) but rewritten in terms of sublattice sites. This is shown in eq.(4.1) by limiting substitution in the chain structures to bridging sites, and selection of Al as the tetrahedrally coordinated trivalent cation (*R*) and Na as the charge-balancing interlayer cation (*I*):

$$\left[\left(Ca(OH)_2\right)_{\left(\frac{u+y-2}{4}\right)}\right]_2\cdot\left[\left(CaSiO_{3.5}\right)_2^-\right]\cdot\left[\left(Si_{(1-a)}Al_aO_2\right)_{(1-v)}\cdot\left(Na^+_{a(1-v)}\right)\cdot\left(Ca_{\left(1-\frac{u}{2}\right)}H_u\right)^{2+}\right]\cdot mH_2O \quad (4.1)$$

where *a* is the extent of substitution in bridging sites; $v = 1/n$ ($0 \le v \le 1$), the ratio of chains to dreierketten units (a measure of chain site vacancies); and $u = w/n$, the amount of hydroxyl water (or equivalently the number of protons) per dreierketten unit. All other symbols have the same definitions as provided for eq.(2.2).

9Å tobermorite consists of non-cross-linked silicate chains, which means that its structure can be represented according to the same formulation (eqs.(2.2-2.6, 4.1)) used to describe 14Å tobermorite in the SGM (Richardson et al., 1994). The extent of protonation (*u*) is specified to maintain charge balance in eq.(4.1). Further derivation of the non-cross-linked structural model replaces the *u* parameter with a measure of the concentration of Ca cations in the interlayer region, $\varphi$, with $\varphi = 1 - u/2$ ($0 \le \varphi \le 1$). This is more consistent with the important role that the interlayer Ca content has on the way that the layer spacing of tobermorite minerals change as a

function of temperature (Merlino et al., 2000). It must also be noted that this substitution is possible because tobermorite contains no 'solid solution' $Ca(OH)_2$, i.e. $u + y = 2$ (Richardson, 2004; Richardson and Groves, 1993b), thus $u$ is not an independent parameter in eq.(4.1) for tobermorite-like structures. This relationship ($u + y = 2$) is also now specified for consistency with tobermorite-like structures.

The MCL and Al/Si relationships are the same for C-(N-)A-S-H with non-cross-linked 9Å or 14Å tobermorite-like nanostructures (eqs.(2.4-2.5). Eq.(4.1) is reformulated with these changes and also written in terms of one dreierketten unit, leading to eqs.(4.2-4.3):

$$\left[\left(CaSiO_{3.5}\right)_2^-\right]\cdot\left[\left(\left[Si_{(1-a)}Al_aO_2\right]\cdot\left[Na_a^+\right]\right)_{(1-\nu)}\cdot\left(Ca_\varphi H_{2(1-\varphi)}\right)^{2+}\right]\cdot mH_2O \qquad (4.2)$$

$$\left(Ca/Si\right)_{[NC]} = \frac{2+\varphi}{2+\left(1-\nu\right)\left(1-a\right)} \qquad (4.3)$$

where [*NC*] denotes non-cross-linked C-(N-)A-S-H. The Ca/(Si+Al) ratio is then:

$$Ca/(Si+Al)_{[NC]} = \frac{2+\varphi}{2+\left(1-\nu\right)} \qquad (4.4)$$

Eq.(4.2) reduces to the chemical formula for non-substituted infinite chain length 9Å tobermorite, $Ca_5Si_6O_{16}(OH)_2$ (Merlino et al., 2000), when $\varphi$, $a$, $\nu$ and $H_2O/Si$ are 0.5, 0, 0, and 0 respectively. The formula for non-substituted infinite chain length 14Å tobermorite, $Ca_5Si_6O_{16}(OH)_2{\cdot}7H_2O$ (Bonaccorsi et al., 2005), is similarly recovered from eq.(4.2) when $\varphi$, $a$, $\nu$ and $H_2O/Si$ are 0.5, 0, 0, and 7/6 respectively.

The parameters $\nu$ and $a$ can be determined from eqs.(4.5-4.6) using the relationships for the Al/Si ratio and MCL of non-cross-linked tobermorite (eqs.(2.4-2.5)):

$$\nu = \frac{3}{MCL_{[NC]} + 1} \tag{4.5}$$

$$a = \frac{\left[2+(1-\nu)\right] \times (Al/Si)_{[NC]}}{(1-\nu) \times \left[(Al/Si)_{[NC]} + 1\right]} \tag{4.6}$$

### 4.2.1 Cross-Linked Tobermorite-Like Structural Model

The derivation of a cross-linked tobermorite-like structural model begins by defining a cross-linked tobermorite unit (including 2 bridging and 4 paired aluminosilicate tetrahedra), as shown for anomalous and normal 11Å tobermorite in Figure 2.3. This structural model excludes Al-O-Al bonding in bridging sites for consistency with the Al-avoidance principle of Loewenstein (1954), and leads to the relationships shown in eq.(4.7-4.8) for the Al/Si ratio and MCL of cross-linked C-(N-)A-S-H. These relationships can be solved directly using $^{29}$Si MAS NMR spectral deconvolution results.

$$MCL_{[C]} = \frac{4\left(Q^1 + Q^2 + Q^2\left(1Al\right) + Q^3 + 2Q^3\left(1Al\right)\right)}{Q^1} \tag{4.7}$$

$$\left(Al/Si\right)_{[C]} = \frac{Q^3(1Al)}{Q^1 + Q^2 + Q^2\left(1Al\right) + Q^3 + Q^3\left(1Al\right)} \tag{4.8}$$

where [*C*] denotes cross-linked C-(N-)A-S-H.

The Ca content of cross-linked tobermorite-like C-(N-)A-S-H is defined in the structural model by grouping the cross-linked bridging tetrahedra together to form a ‘combined bridging site’ (Figure 2.3) and using Na as the alkali charge-balancing species (*I* in eq.(2.2)). The chemical formula for a cross-linked C-(N-)A-S-H, shown

in terms of one cross-linked tobermorite unit, can be expressed according to eq.(4.9) (equivalent to eq.(4.2) for the non-cross-linked case):

$$\left[\left(Ca(OH)_2\right)_{\left(\frac{u+y-2}{4}\right)}\right]_4\cdot\left[\left(CaSiO_{3.5}\right)^-\right]_4\cdot \left[\left(\left[SiO_{1.5}^+\right]\cdot\left[Si_{(1-\alpha)}Al_\alpha O_{1.5}^{(1-\alpha)+}\right]\cdot\left[Na_\alpha^{\alpha+}\right]\right)_{(1-\delta)}\cdot\left(Ca_\omega H_{2(1+\delta-\omega)}\right)^{2(1+\delta)+}\right]_1\cdot mH_2O \tag{4.9}$$

where $\alpha$ is the fraction of Al substitution in cross-linked C-(N-)A-S-H gel, $\delta = 1/(\sigma + 1)$ is the fraction of combined bridging site vacancies per cross-linked tobermorite unit, $\sigma$ is the number of cross-linked tobermorite units per C-(N-)A-S-H chain, $\omega = 1 - u/2$ ($0 \le \omega \le 1 + \delta$) is the interlayer Ca content per cross-linked tobermorite unit, and all other parameters have the same definitions as in eqs.(4.1).

Eq.(4.9) is now rewritten using $u + y = 2$ for consistency with tobermorite-like structures, leading to eq.(4.10) as a charge-balanced formula in terms of one dreierketten unit:

$$\left[\left(CaSiO_{3.5}\right)^-\right]_2\cdot \left[\left(\left[SiO_{1.5}^+\right]\cdot\left[Si_{(1-\alpha)}Al_\alpha O_{1.5}^{(1-\alpha)+}\right]\cdot\left[Na_\alpha^{\alpha+}\right]\right)_{(1-\delta)}\cdot\left(Ca_\omega H_{2(1+\delta-\omega)}\right)^{2(1+\delta)+}\right]_{0.5}\cdot mH_2O \tag{4.10}$$

Giving:

$$\left(Ca/Si\right)_{[C]} = \frac{4+\omega}{4+\left(1-\delta\right)(2-\alpha)} \tag{4.11}$$

$$Ca/(Al+Si)_{[C]} = \frac{4+\omega}{2(3-\delta)} \tag{4.12}$$

Eq.(4.10) reduces to the chemical formula for non-substituted infinite chain length normal 11Å tobermorite, $Ca_{4.5}Si_6O_{16}(OH)\cdot 5H_2O$ (Merlino et al., 2001), when $\omega$, $\alpha$, $\delta$ and $H_2O/Si$ are 0.5, 0, 0, and 5/6 respectively. The formula for non-substituted infinite chain length anomalous 11Å tobermorite, $Ca_4Si_6O_{15}(OH)_2\cdot 5H_2O$ (Merlino et al., 2001), is similarly obtained from eq.(4.10) when $\omega$, $\alpha$, $\delta$ and $H_2O/Si$ are 0, 0, 0, and 5/6 respectively.

While non-substituted normal 11Å tobermorite was identified by Merlino et al. (2001) to contain 0.25 interlayer Ca atoms per dreierketten unit, it is reasonable to suggest that the interlayer Ca content is non-constant in C-(N-)A-S-H. The $\delta$ parameter has therefore been left variable in eq.(4.10). The parameters $\delta$ and $\alpha$ can then be determined from eqs.(4.13-4.14) using the relationships for the Al/Si ratio and MCL for cross-linked C-(N-)A-S-H (eqs.(4.7-4.8)):

$$\delta = \frac{6}{MCL_{[C]} + 2} \tag{4.13}$$

$$\alpha = \frac{(Al/Si)_{[C]} \times \left[4+2(1-\delta)\right]}{\left[(Al/Si)_{[C]}+1\right] \times (1-\delta)} \tag{4.14}$$

These formulae, eqs.(2.3-2.4, 4.2-4.14), are suitable for structural modelling of mixed cross-linked/non-cross-linked C-(N-)A-S-H, and can be solved using structural parameters obtained from $^{29}$Si MAS NMR spectral deconvolutions, as will be demonstrated in detail in section 4.3.

### 4.2.3 'Cross-Linked Substituted Tobermorite Model' (CSTM)

It is reasonable to expect that C-(N-)A-S-H in AAS cements can be represented as a mixture of 14Å, 11Å and 9Å tobermorite-like components, as discussed in sections 2.1.3 and 4.1 (Bernal et al., 2013b; Brough and Atkinson, 2002; Fernández-Jiménez et al., 2003; Oh et al., 2012; Pardal et al., 2012; Puertas et al., 2011). Here a simple and flexible structural model is proposed, the 'Cross-linked Substituted Tobermorite Model' (CSTM), which can be used to determine the relative contributions of non-cross-linked and cross-linked tobermorite-like components, and the chemical compositions and MCL of a particular C-(N-)A-S-H gel. The CSTM only allows for Al substitution in bridging sites (Richardson et al., 1993), and does not include Al-O-Al bonding (Loewenstein, 1954), single tetrahedron vacancies in the combined bridging site, or incorporation of $Q^0$ or $Q^1$(1Al) species into C-(N-)A-S-H (Richardson et al., 1993).

Single vacancies in the combined bridging site are not allowed in the CSTM to circumvent an explicit description of the two-coordinated bridging Si ($Q^2_B$) sites, and is possible because the aluminosilicate chains in C-(N-)A-S-H can be represented as a mixture of non-cross-linked and cross-linked structures. This is illustrated in Figure 4.1, which shows that a realistic section of C-(N-)A-S-H with cross-linked structure containing a single bridging site vacancy is conceptually equivalent to a mixture of non-cross-linked and cross-linked tobermorite-like components in the CSTM formulation.

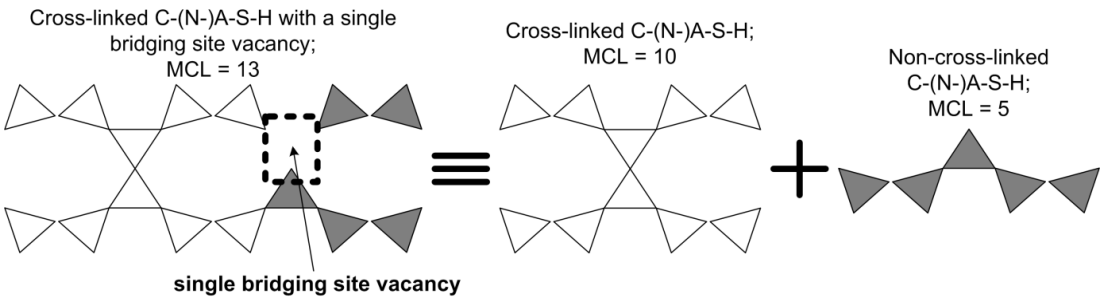


Figure 4.1. An illustration of how the CSTM represents single bridging site vacancies in C-(N-)A-S-H.

The CSTM is derived using the following structural constraints: i) there are twice as many ($Q^2$+$Q^2$(1Al)) silicate species as there are ($Q^3$+$Q^3$(1Al)+Al[4]) silicate species in cross-linked tobermorite; ii) the fraction of Al substitution into $Q^3$ type sites is equivalent to the ratio of $Q^2$(1Al) to $Q^2$ sites in cross-linked tobermorite, because Al is only substituted into bridging sites; and iii) the substitution of one Al[4] species into cross-linked tobermorite introduces one $Q^3$(1Al) and two $Q^2$(1Al) Si species. These assumptions and structural constraints are shown in Figure 4.2.

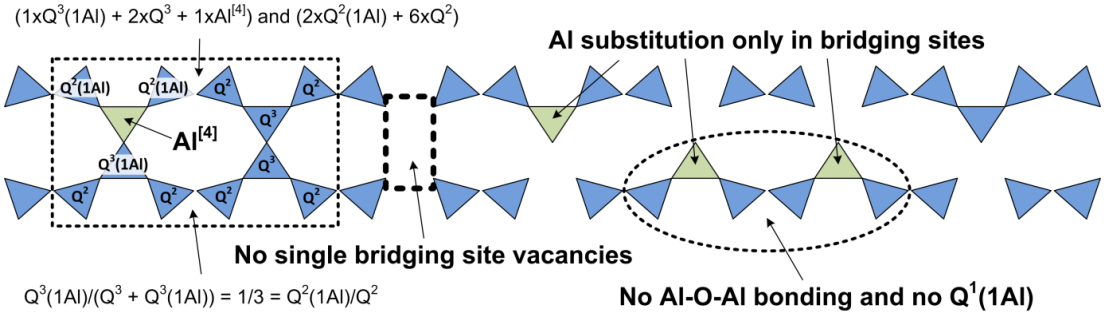


Figure 4.2. An illustration of the structural constraints and assumptions included in the CSTM.

These structural constraints lead to eqs.(4.15-4.17):

$$2\left(Q^3_{[C]} + Q^3\left(1Al\right)_{[C]} + Al[4]_{[C]}\right) = \left(Q^2_{[C]} + Q^2\left(1Al\right)_{[C]}\right) \tag{4.15}$$

$$\frac{Q^3\left(1Al\right)_{[C]}}{Q^3_{[C]} + Q^3\left(1Al\right)_{[C]}} = \frac{Q^2\left(1Al\right)_{[C]}}{Q^2_{[C]}} \tag{4.16}$$

$$Al[4]_{[C]} = Q^3\left(1Al\right)_{[C]} \tag{4.17}$$

where [$C$] denotes that the coordinated aluminate or silicate species are present in cross-linked C-(N-)A-S-H gel. Eqs.(4.15-4.17) are solved to obtain eq.(4.18):

$$Q^2\left(1Al\right)_{[C]} = 2Q^3\left(1Al\right)_{[C]} \tag{4.18}$$

Eq.(4.18) is then used together with eqs.(4.19-4.22) to calculate the MCL and Al/Si molar ratios for non-cross-linked and cross-linked C-(N-)A-S-H (eqs.(4.25-4.26)):

$$Q^3_{[C]} = Q^3_{total} \tag{4.19}$$

$$Q^3(1Al)_{[C]} = Q^3\left(1Al\right)_{total} \tag{4.20}$$

$$Q^1{}_{[C]} = \eta Q^1{}_{total} \tag{4.21}$$

$$Q^i_{[NC]} = Q^i_{total} - Q^i_{[C]} \tag{4.22}$$

where [*NC*] denotes that the silicate species is present in non-cross-linked C-(N-)A-S-H gel, $\eta$ ($0 < \eta < 1$) is a parameter describing the partitioning of $Q^1$ species into non-cross-linked and cross-linked C-(N-)A-S-H, adjusted to satisfy the structural constraints of this phase for the calculated Al-substitution extents (eqs.(4.6, 4.14)) and match experimentally observed chemical compositions, and $i$ ($0 \leq i \leq 4$) denotes the connectedness of silicate tetrahedra in C-(N-)A-S-H. The Al/Si and MCL values for non-cross-linked and cross-linked tobermorites can be calculated from eqs.(2.4-2.5) and eqs.(4.7-4.8) respectively, leading to eqs.(4.23-4.26), the relationships that describe the total amount of Al and Si present, and average Al/Si and MCL values for the entire C-(N-)A-S-H phase:

$$(Al+Si)_{[NC]} = Q^1{}_{[NC]} + \left(\tfrac{3}{2}\right)Q^2(1Al)_{[NC]} + Q^2{}_{[NC]} \tag{4.23}$$

$$(Al+Si)_{[C]} = Q^1{}_{[C]} + Q^2(1Al)_{[C]} + Q^2{}_{[C]} + 2Q^3(1Al)_{[C]} + Q^3{}_{[C]} \qquad (4.24)$$

$$(Al/Si)_{C-(N-)A-S-H} = \frac{\left[\frac{(Al/Si)_{[NC]}}{\left(1+(Al/Si)_{[NC]}\right)}\right](Al+Si)_{[NC]} + \left[\frac{(Al/Si)_{[C]}}{\left(1+(Al/Si)_{[C]}\right)}\right](Al+Si)_{[C]}}{\left[\frac{1}{\left(1+(Al/Si)_{[NC]}\right)}\right](Al+Si)_{[NC]} + \left[\frac{1}{\left(1+(Al/Si)_{[C]}\right)}\right](Al+Si)_{[C]}} \qquad (4.25)$$

$$MCL_{C-(N-)A-S-H} = \frac{MCL_{[NC]}MCL_{[C]}\left[(Al+Si)_{[NC]} + (Al+Si)_{[C]}\right]}{MCL_{[C]}(Al+Si)_{[NC]} + MCL_{[NC]}(Al+Si)_{[C]}} \qquad (4.26)$$

Eqs.(4.25-4.26) are derived from the fractional concentrations of Si and Al in 9Å, 11Å and 14Å tobermorite chains, i.e. Al/Si = (1 - Si)/Si. The Ca/Si and Ca/(Al+Si) ratios are calculated similarly, but vary depending on the level of interlayer Ca and the extent of protonation of the C-(N-)A-S-H chains:

$$(Ca/Si)_{C-(N-)A-S-H} = \frac{\left[\frac{(Ca/Si)_{[NC]}}{\left(1+(Al/Si)_{[NC]}\right)}\right](Al+Si)_{[NC]} + \left[\frac{(Ca/Si)_{[C]}}{\left(1+(Al/Si)_{[C]}\right)}\right](Al+Si)_{[C]}}{\left[\frac{1}{\left(1+(Al/Si)_{[NC]}\right)}\right](Al+Si)_{[NC]} + \left[\frac{1}{\left(1+(Al/Si)_{[C]}\right)}\right](Al+Si)_{[C]}} \qquad (4.27)$$

$$Ca/(Al+Si)_{C-(N-)A-S-H} = \frac{\left[\frac{(Ca/Si)_{[NC]}}{\left(1+(Al/Si)_{[NC]}\right)}\right](Al+Si)_{[NC]} + \left[\frac{(Ca/Si)_{[C]}}{\left(1+(Al/Si)_{[C]}\right)}\right](Al+Si)_{[C]}}{(Al+Si)_{[NC]} + (Al+Si)_{[C]}} \qquad (4.28)$$

where $(Ca/Si)_{[NC]}$ is given by eq.(4.3) and $(Ca/Si)_{[C]}$ can be calculated from eq.(4.11). Eqs.(4.27-4.28) give the overall Ca/Si and Al/Si ratios for the C-(N-)A-S-H phase as calculated by the structural model. The CSTM also describes the more general case where the chemical compositions can be specified separately for 9Å, anomalous

11Å, normal 11Å and 14Å tobermorites, but the corresponding Ca/Si and Ca/(Al+Si) relationships are considerably more complicated than eqs.(4.27-4.28) (Myers et al., 2013).

The following sections of the chapter present the application of the CSTM to a series of $Na_2SiO_3$-activated slag cements, as well as a discussion of the implications of the model results.

## 4.3 Application of the CSTM

### 4.3.1 Characterisation of an Alkali-Activated Slag (AAS) Cement

A complete description of the experimental details for this investigation is given in Chapter 3. Figures 4.3-4.4 show the SEM-EDS results, and the $^{29}$Si MAS NMR spectra and associated deconvolution results are shown in Figure 4.5 and Table 4.1 respectively. The $^{27}$Al MAS NMR spectra are shown in Figure 4.6 with corresponding spectral deconvolutions presented in Table 4.2.

The solid binder chemical composition data in Figures 4.3-4.4 show that C-(N-)A-S-H coexists with at least one additional solid phase. Hydrotalcite has been identified through XRD in $Na_2SiO_3$-activated slag cements produced using similar raw materials to those used here (Bernal et al., 2013c), consistent with Figures 4.3-4.4. However, the existence of additional Ca, Al and/or Si-containing solid phases cannot be discounted purely on the basis of a good correlation between the observed chemistry of the AAS cement and a mixture of C-(N-)A-S-H and hydrotalcite, as phases such as hydrogarnet and AFm are sometimes observable by XRD in aged AAS cements (Bernal et al., 2012a).

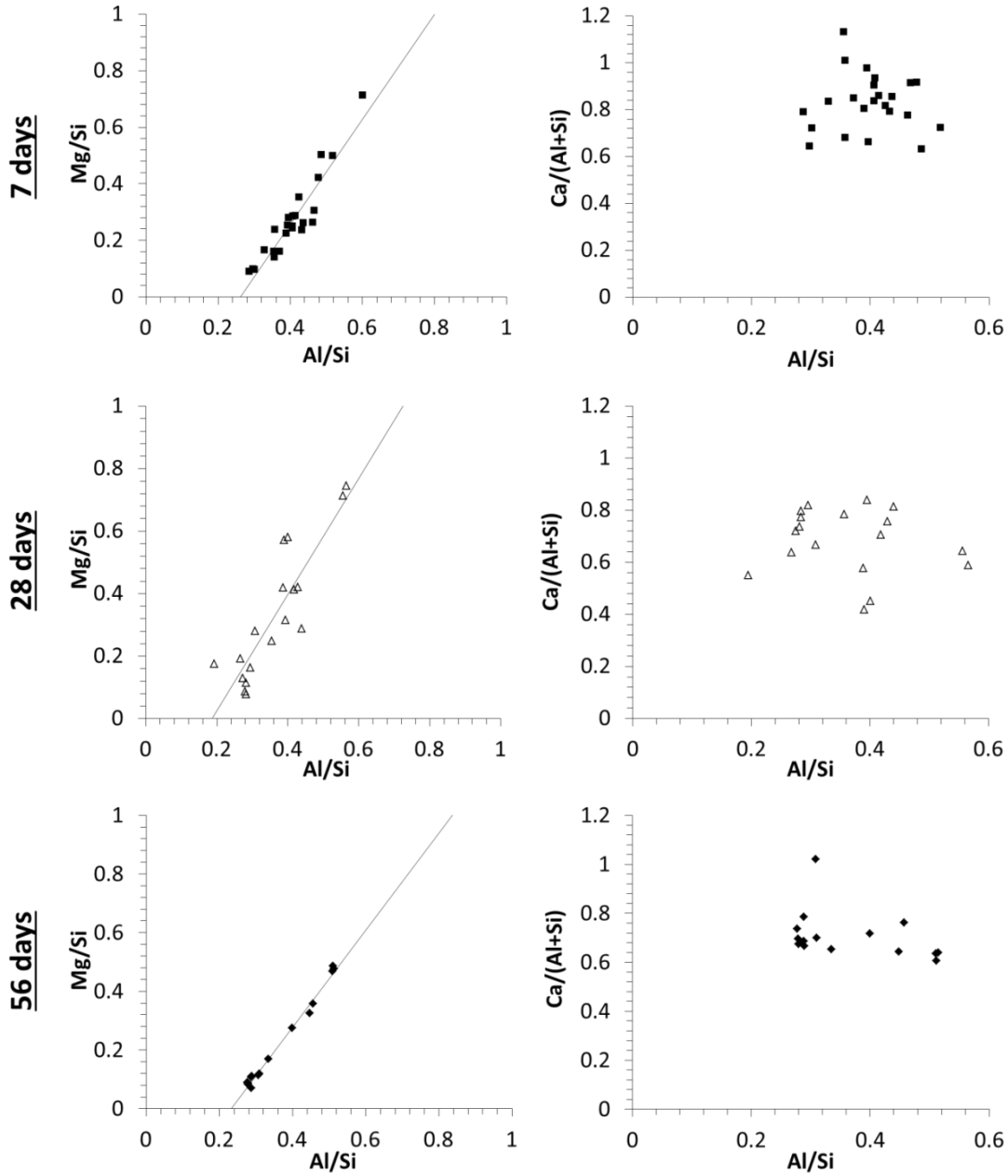


Figure 4.3. Molar ratios of the solid binder in the $Na_2SiO_3$-activated slag cement measured through SEM-EDS, as a function of curing time. Lines in the figures plotting Mg/Si vs Al/Si are provided as eye guides only.

The Al/Si molar ratios of the C-(N-)A-S-H gel, which can be viewed as the trendline x-axis intercepts in Figure 4.3 for the AAS cements studied here because the amounts of Mg-free secondary products are low (2% of the total Al intensity for each sample), are in the range $0.19 \leq Al/Si \leq 0.26$; Ca/Si molar ratios vary from approximately $0.8 \leq Ca/Si \leq 1.2$ with the exception of the 7 day sample where Ca/Si ratios up to 1.4 are observed. The trendlines drawn in Figure 4.3 do not preclude very

low levels of Mg-Ca substitution in the C-(N-)A-S-H gel. These measured chemical compositions correlate well with existing AAS studies where chemical compositions of 0.20 < Al/Si < 0.25 and 0.8 < Ca/Si < 1.2 are consistently reported for AAS cements produced from GBFS with moderate Al (12-14 wt.%) and Mg (7-9 wt.%) content (Ben Haha et al., 2011a; Ben Haha et al., 2011b; 2012; Brough and Atkinson, 2002; Pardal et al., 2009; Richardson et al., 1994; Wang and Scrivener, 1995).

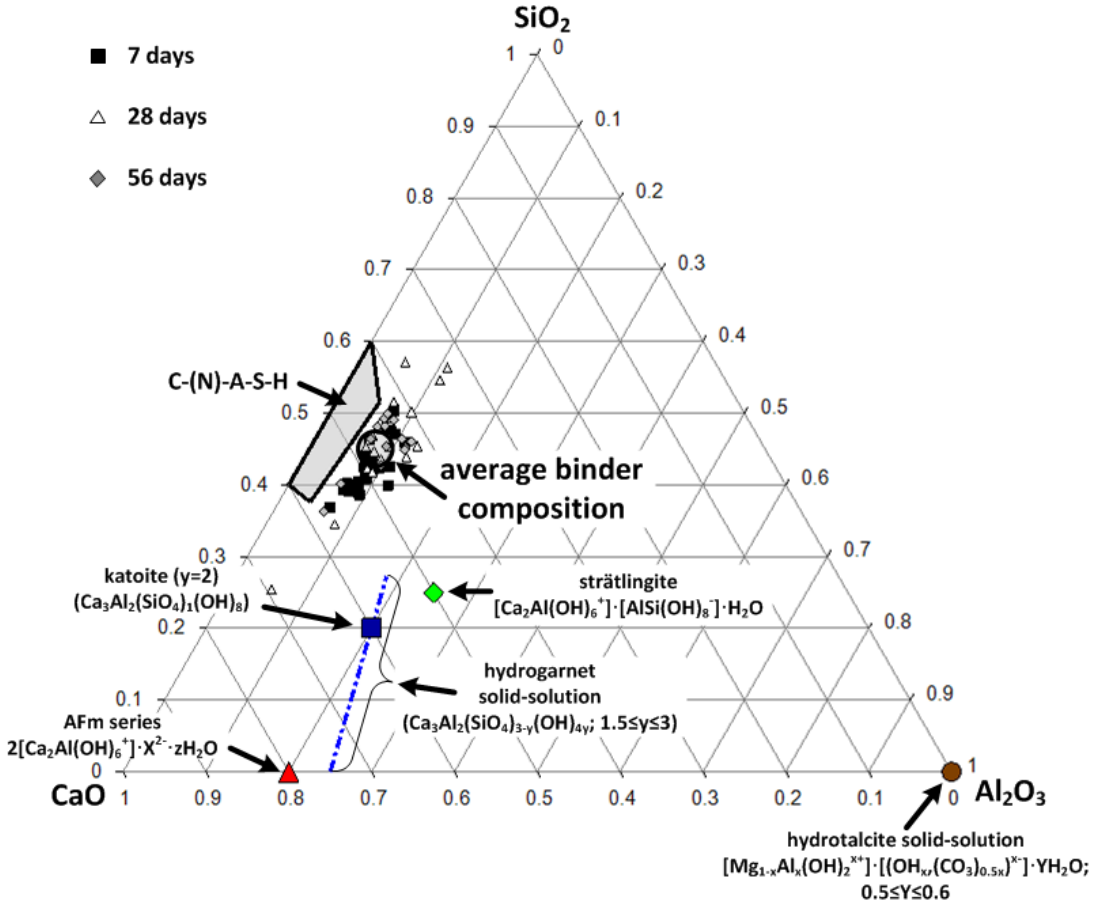


Figure 4.4. Projection of AAS chemistry onto the ternary $CaO$-$SiO_2$-$Al_2O_3$ system, showing elemental compositions of the $Na_2SiO_3$-activated slag cements measured by SEM-EDS at different times of curing, along with the compositions of some model phases. The average solid binder chemical composition is marked, assuming congruent slag dissolution, complete incorporation of the silica supplied by the activator into the solid binder, and without distinction between product phases.

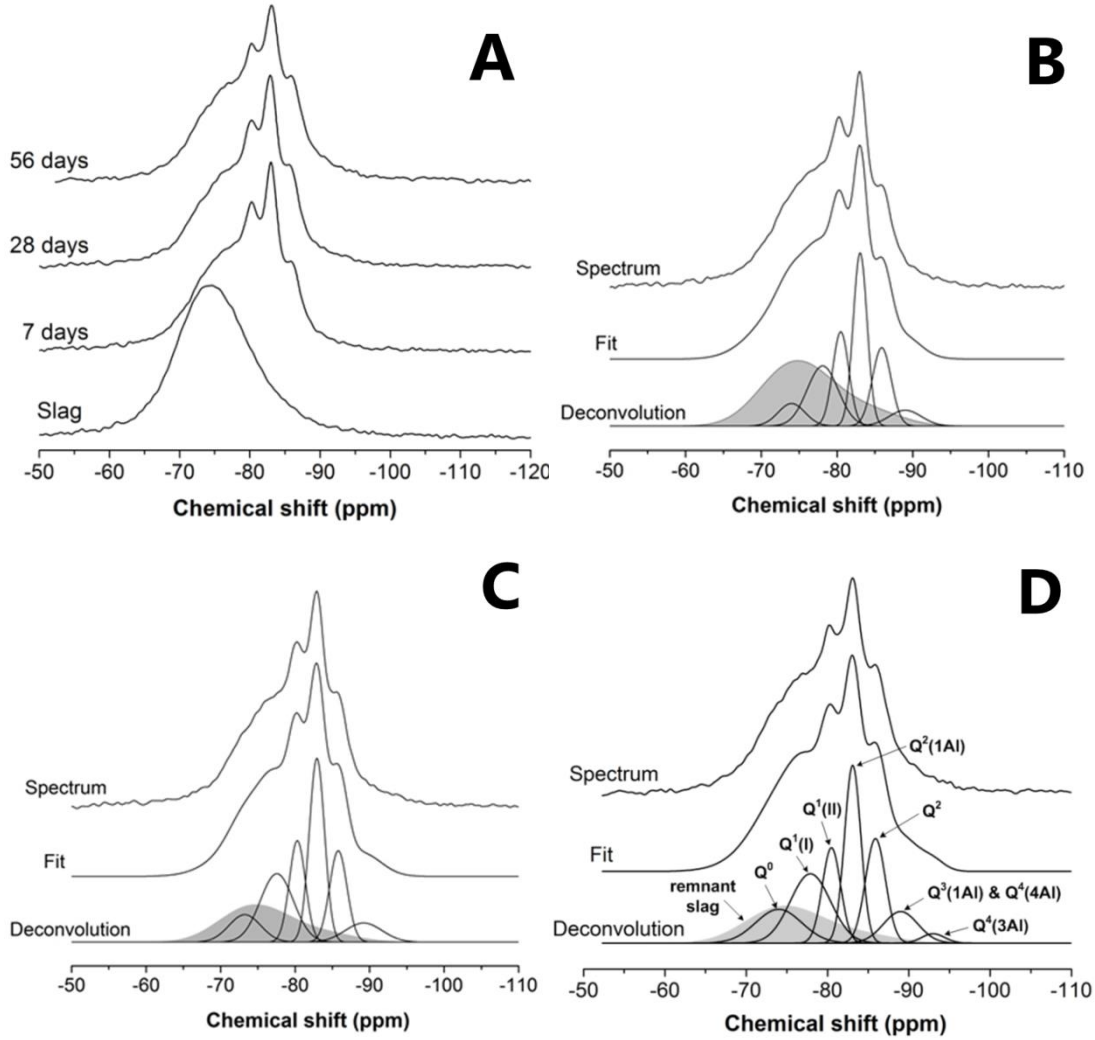


Figure 4.5. $^{29}$Si MAS NMR spectra (14.1 T, $\nu_R$ = 10 kHz) of the $Na_2SiO_3$-activated slag cement and the anhydrous slag: A) as a function of curing time; and deconvoluted spectra for the B) 7 days, C) 28 days and D) 56 day cured samples, with $Q^n(m\text{Al})$ sites shown in D). The dark grey band represents the contribution of the remnant anhydrous slag.

The $^{27}$Al MAS NMR spectra in Figure 4.6 corroborate the formation of secondary phases in addition to C-(N-)A-S-H gel in the AAS cement, as there are significant contributions from six-coordinated Al (Al[6]). The presence of Al[6] in the interlayer and structural incorporation of these species into C-(N-)A-S-H has been hypothesised by some authors (Abdolhosseini Qomi et al., 2012; Faucon et al., 1999a; Rawal et al., 2010; Stade and Müller, 1987), but Al[6] is not considered in the CSTM. In a recent study (Rawal et al., 2010), associations in solid-state 2D $^{27}$Al{$^1$H} HETCOR NMR spectra were only observed for bands of narrow line width (which were assigned to AFt/AFm type products and TAH) in the Al[6] region of

$^{27}$Al MAS NMR spectra. From these data, and from the discussion presented by Andersen et al. (2006), it can be tentatively concluded that not much Al[6] substitutes for Ca in the interlayer of C-(N-)A-S-H.

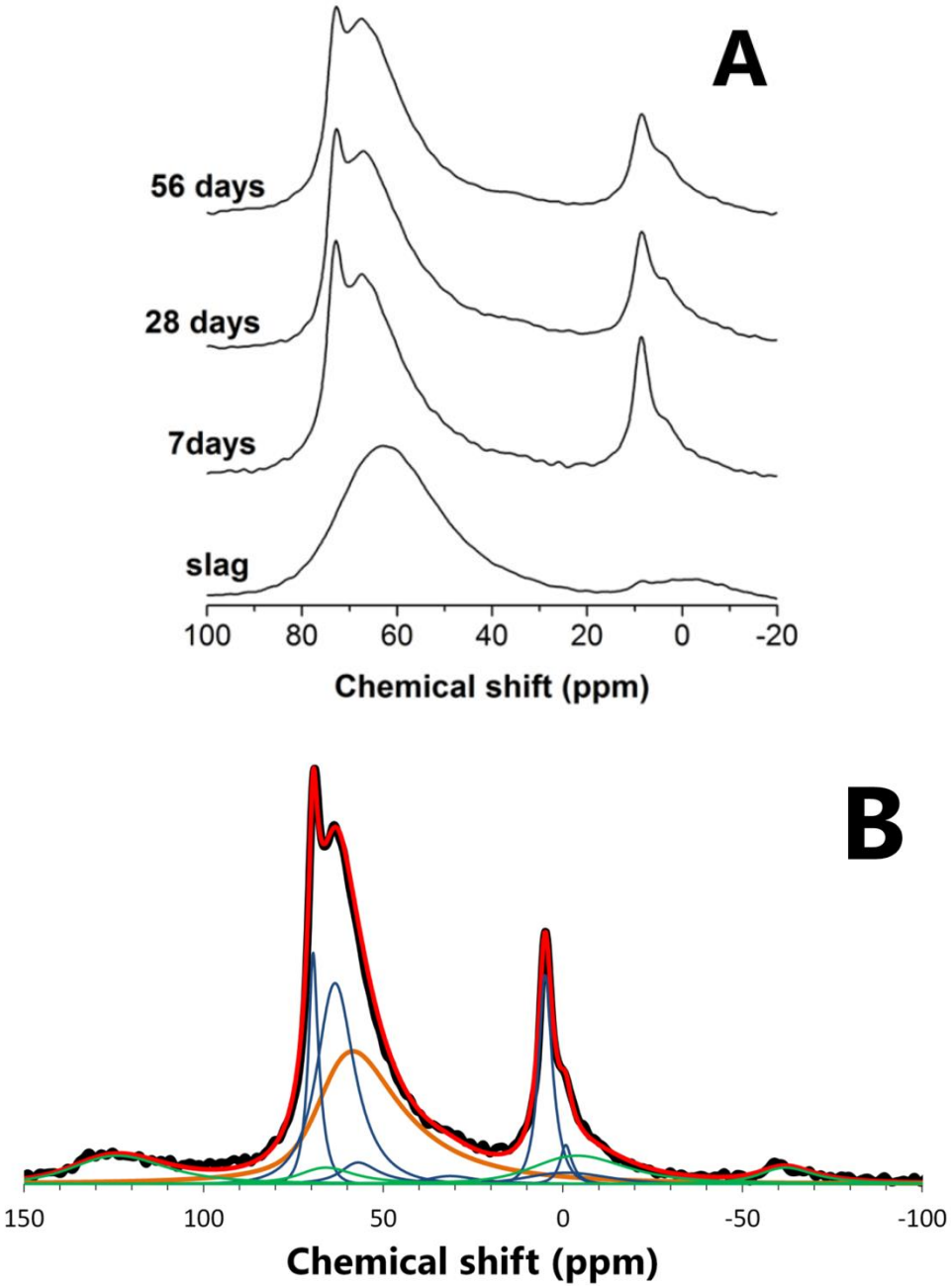


Figure 4.6. $^{27}$Al MAS NMR spectra (14.1 T, $\nu_R$ = 10 kHz) of the $Na_2SiO_3$-activated slag cement and anhydrous slag: A) as a function of curing time; and deconvoluted spectra for the B) 7 days, C) 28 days and D) 56 day cured samples, with $q^n$ sites shown in D). In D), the green sub-peaks are spinning sidebands, the blue traces are the deconvoluted sub-peaks, and the red line is the sum of the deconvoluted components of the spectrum.

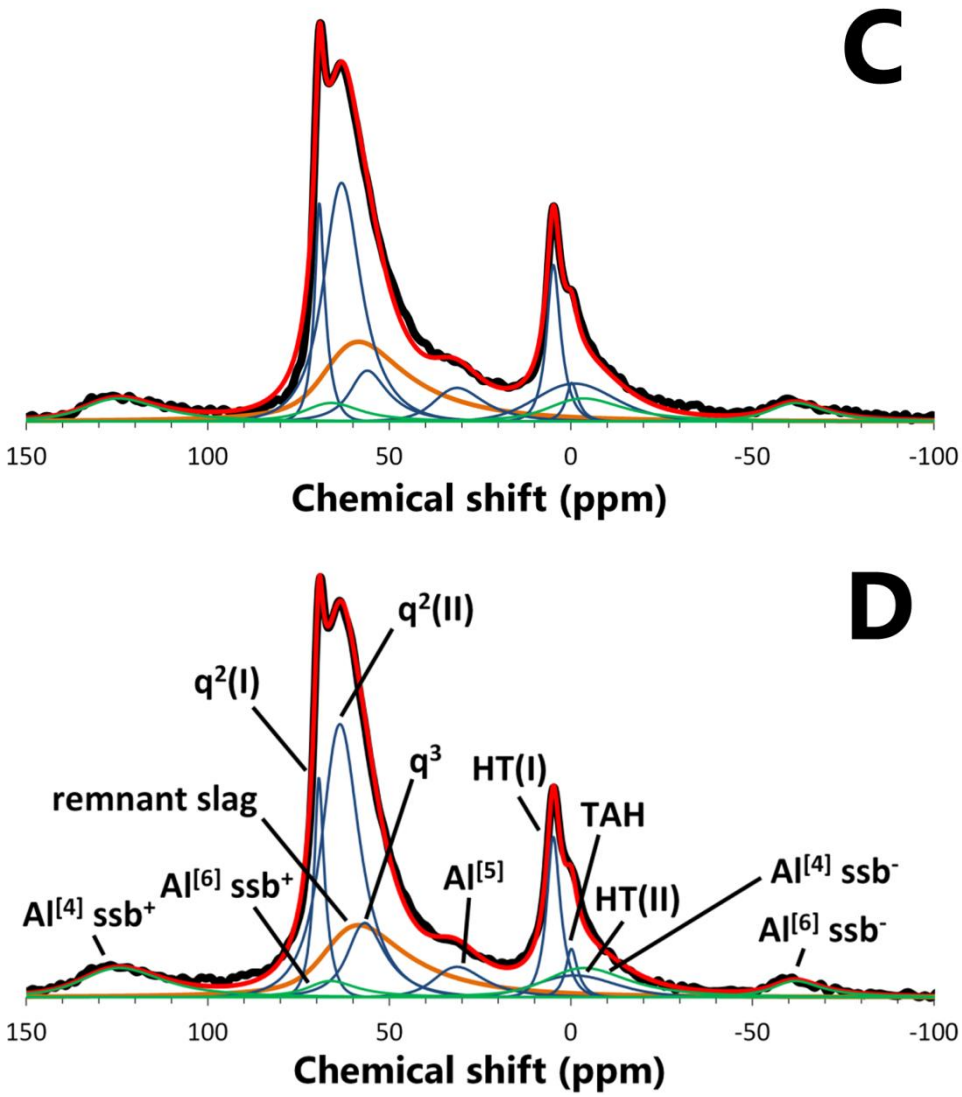


Figure 4.6. Continued.

Table 4.1. Summary of $Q^n$ environments identified in $^{29}Si$ MAS NMR spectra of the $Na_2SiO_3$-activated slag cement as a function of curing time. Estimated uncertainty in site percentages is ±2%, based on the influence of the signal/noise ratio of the spectra on the deconvolution procedures.

| Age | Unreacted slag | **Reaction products** | | | | | | | |
|---|---|---|---|---|---|---|---|---|---|
| | | $Q^0$ | $Q^1$(I) | $Q^1$(II) | $Q^2$(1Al) | $Q^2$ | $Q^3$(1Al) | $Q^4$(4Al) | $Q^4$(3Al) |
| | | -74 ppm | -78 ppm | -80 ppm | -83 ppm | -86 ppm | -89 ppm [a] | -89 ppm [a] | -93 ppm |
| Unreacted | 100 | - | - | - | - | - | - | - | - |
| 7 days | 39 | 4 | 14 | 11 | 18 | 11 | 4 | - | - |
| 28 days | 24 | 7 | 18 | 13 | 22 | 12 | 5 | - | - |
| 56 days | 21 | 10 | 18 | 11 | 19 | 13 | 5 | 2 | 1 |

[a] A single peak at -89 ppm is used to describe both $Q^3$(1Al) and $Q^4$(4Al) components as discussed in the text

Table 4.2. Summary of Al coordination environments identified in $^{27}$Al MAS NMR spectra of the $Na_2SiO_3$-activated slag cement as a function of curing time. Estimated uncertainty in site percentages is ±3%, based on the influence of the signal/noise ratio of the spectra on the deconvolution procedures. HT represents hydrotalcite.

| **Assignment** | **Al[4] in unreacted slag** | **$q^2$(I)** | **$q^2$(II)** | **$q^3$** [a] | **Al[5]** | **HT(I)** | **HT(II)** | **TAH** |
|---|---|---|---|---|---|---|---|---|
| **Isotropic chemical shift, $\delta_{iso}$ (ppm)** [f] | **65** | **75** | **68** | **62** | **38** | **9.68** [b] | **9.1** | **4.6** |
| **$C_Q$ (MHz) and reference** | 6.7 [c] | 1.1 [c] | 2.0 [c] | 3.0 [c] | 4.0 [c] | 1.2 [b] | 3.55 [d] | 1.13 [e] |
| **Age** | | | | | | | | |
| Unreacted | 100 | - | - | - | - | - | - | - |
| 7 days | 44 | 9 | 27 | 3 | 1 | 11 | 3 | 2 |
| 28 days | 26 | 9 | 32 | 7 | 6 | 8 | 10 | 2 |
| 56 days | 23 | 9 | 37 | 10 | 5 | 8 | 5 | 2 |

[a] It is likely that the $q^3$ site contains contributions from $q^4$ aluminate species, but attempts to resolve this site into two separate sub-peaks led to an underconstrained deconvolution process.
[b] Values determined through analysis of a pure hydrotalcite sample; S.A. Walling and S.A. Bernal, unpublished data.
[c] (Klinowski, 1984)
[d] (Sideris et al., 2012)
[e] (Andersen et al., 2006)
[f] Isotropic chemical shifts were calculated using an additional $^{27}$Al MAS NMR spectra acquired at 104.2MHz, $\nu_R$ = 14 kHz, for the $Na_2SiO_3$-activated slag cement cured for 2 years.

The secondary products containing Al[6] are hydrotalcite (Bernal et al., 2013c; Schilling et al., 1994b; Wang and Scrivener, 1995) and TAH (Andersen et al., 2006). The spectral deconvolutions (Table 4.2) also show significant contributions from $q^3$ Al (where the $q^n$ notation for Al sites is equivalent to the $Q^n$ notation for Si sites (Harris et al., 1997)), suggesting a high degree of cross-linking. Broad contributions from $q^2$ units indicate significant local disorder in these sites, as Al in C-(N-)A-S-H can coordinate with various positively-charged species in the interlayer region.

The $^{29}$Si MAS NMR spectra (Figure 4.5) show small but distinct contributions from $Q^3$(1Al) sites, in addition to $Q^1$, $Q^2$ and $Q^2$(1Al) silicate species, indicating high levels of Al substitution in C-(N-)A-S-H. The band at -74 ppm is tentatively assigned to $Q^0$ sites, without precluding some intensity in this peak also from $Q^1$(1Al) or $Q^1$ species (due to the various charge-balancing cations present in the system). This peak has previously been identified in deconvoluted $^{29}$Si MAS NMR spectra of sodium silicate-activated slag cements (Le Saoût et al., 2011), but no definitive assignment for this band has been established to date. Although the absolute concentrations of $Q^3$(1Al) sites are low, the structural constraints of cross-linked tobermorite (Figure 4.2 and eqs.(4.15-4.18)) lead to the calculation of highly cross-linked C-(N-)A-S-H, as will be discussed in detail below. The $^{29}$Si MAS NMR spectra also show non-zero levels of intensity at chemical shifts of approximately -93 ppm, indicating the presence of $Q^4$(3Al) units in the solid binder. This assignment necessitates contributions from at least one additional four-connected silicate unit ($Q^4$ type) in the experimental spectra (Provis et al., 2005a). Therefore, it is assumed that $Q^4$(4Al) sites are present the $^{29}$Si MAS NMR spectra, which is consistent with the significant levels of intensity in the low-ppm range (52-62 ppm) for four-coordinated Al species as observed by $^{27}$Al MAS NMR, statistical thermodynamic model predictions (Provis et al., 2005a) and experimental NMR data (Duxson et al., 2005) for Al-rich metakaolin-based geopolymers.

Assignment of the peak located at a chemical shift of -93 ppm to $Q^4$(3Al) species is justified because this is the only plausible assignment consistent with a mixed cross-

linked/non-cross-linked tobermorite-like C-(N-)A-S-H gel for the spectral deconvolution results found in this work. The only possible alternative silicate coordination environment that is located at approximately -93 ppm and is consistent with the established nature of AAS cements are $Q^3$ units (Engelhardt and Michel, 1987). Hypothetical deconvolution of the $^{29}$Si MAS NMR spectra to exclusively assign the peak at -93 ppm to $Q^3$ units yields the results shown in Table 4.3.

It is readily observed in Table 4.3 that the hypothetical spectral deconvolution for the 56 days sample is inconsistent with the structural definition of mixed cross-linked/non-cross-linked C-(N-)A-S-H gels, as described by the structural constraints of the CSTM (Figure 4.2). This is because there are not enough $Q^2$ units to account for the amount of $Q^3$(1Al) and $Q^3$ units identified in the hypothetical deconvolution for the 56 days sample, i.e. $2(Q^3(1Al)+Q^3) > Q^2$. Therefore, the only remaining possibility is to attribute the peak located at -93 ppm to $Q^4$(3Al) species.

### 4.3.2 An Additional Aluminosilicate Reaction Product?

The CSTM, when applied to the $^{29}$Si MAS NMR spectral deconvolution data presented in Table 4.1, yields the results shown in Table 4.4.

Table 4.3. Summary of hypothetical $Q^n$ environments in $^{29}Si$ MAS NMR spectra of the $Na_2SiO_3$-activated slag cement as a function of curing time, given that the assignment of the peak located at a chemical shift of -93 ppm corresponds exclusively to $Q^3$ units.

| Age | Unreacted slag | **Reaction products** | | | | | | |
|---|---|---|---|---|---|---|---|---|
| | | $Q^0$ | $Q^1$(I) | $Q^1$(II) | $Q^2$(1Al) | $Q^2$ | $Q^3$(1Al) | $Q^3$ |
| | | -74 ppm | -78 ppm | -80 ppm | -83 ppm | -86 ppm | -89 ppm | -93 ppm |
| Unreacted | 100 | - | - | - | - | - | - | - |
| 7 days | 39 | 4 | 14 | 11 | 18 | 11 | 4 | - |
| 28 days | 24 | 7 | 18 | 13 | 22 | 12 | 5 | - |
| 56 days | 21 | 10 | 18 | 11 | 19 | 13 | 7 | 1 |

Table 4.4. The calculated output of the CSTM from the $^{29}$Si MAS NMR spectral deconvonlution results in Table 4.1. A constant interlayer Ca content of $\varphi = \omega = 0.25$ and maximum partitioning of $Q^1$ sites into the cross-linked C-(N-)A-S-H component (i.e. maximising $\eta$) is specified.

| Curing time | Component | $Q^1$ | $Q^2$(1Al) | $Q^2$ | $Q^3$(1Al) | MCL | Al/Si | Ca/Si | Ca/(Al+Si) |
|---|---|---|---|---|---|---|---|---|---|
| 7 days | non-cross-linked | 0.098 | 0.1 | 0.033 | 0 | 5.8 | 0.22 | 1.1 | 0.88 |
| | cross-linked | 0.15 | 0.074 | 0.074 | 0.037 | 10 | 0.11 | 0.94 | 0.85 |
| 28 days | non-cross-linked | 0.085 | 0.11 | 0.016 | 0 | 6.2 | 0.26 | 1.1 | 0.87 |
| | cross-linked | 0.22 | 0.11 | 0.11 | 0.054 | 10 | 0.11 | 0.94 | 0.85 |
| 56 days | non-cross-linked | 0.092 | 0.086 | 0.035 | 0 | 5.6 | 0.2 | 1.1 | 0.88 |
| | cross-linked | 0.2 | 0.099 | 0.099 | 0.049 | 10 | 0.11 | 0.94 | 0.85 |

**Bulk C-(N-)A-S-H gel properties**

| Curing time | $\eta$ | MCL | Al/Si | Ca/Si | Ca/(Al+Si) |
|---|---|---|---|---|---|
| 7 days | 0.6 | 7.6 | 0.15 | 1 | 0.86 |
| 28 days | 0.72 | 8.3 | 0.16 | 0.99 | 0.86 |
| 56 days | 0.68 | 7.9 | 0.14 | 0.98 | 0.86 |

The calculated chemical compositions of the C-(N-)A-S-H gel (Table 4.4) agree well with the chemistry of laboratory-synthesised C-(N-)A-S-H products, where the molar Al/Si ratio of phase-pure C-(N-)A-S-H has generally been found to be less than or equal to 0.20 for relevant Ca/(Al+Si) molar ratios in AAS cements ($0.7 \leq Ca/(Al+Si) \leq 1.3$) (Faucon et al., 1999a; Pardal et al., 2012; Pardal et al., 2009; Sun et al., 2006). The formation of strätlingite (an AFm phase) is typically observed in AAS cements if the Al/Si molar ratio is higher than this (Sun et al., 2006). This must then be contrasted with the results presented in Table 4.4, which show that the CSTM can reproduce the experimentally observed Ca/Si ratios, but does not agree with the Al/Si molar ratios for the Mg-free C-(N-)A-S-H gels and the experimental AAS cements as identified by SEM-EDS (Figure 4.3). In all cases the Al content of the C-(N-)A-S-H gel is significantly underestimated by the assumption that all of the tetrahedral Al is contained within tobermorite-type phases.

This disagreement is also corroborated by the average chemical compositions of the solid binders calculated using the experimentally determined GBFS reaction extents in these samples (as determined from the $^{29}$Si MAS NMR spectral deconvolutions, Table 4.1), of overall Al/Si molar ratios of 0.396, 0.413 and 0.415 for the solid binders in the 7, 28 and 56 day samples respectively (Figure 4.4). These calculations are performed using the elemental compositions of the mix formulations assuming congruent slag dissolution and full incorporation of the silica supplied by the activator into the binder, but without distinction between Al in C-(N-)A-S-H or secondary phases.

However, secondary phases are evident in the $^{27}$Al MAS NMR spectra (Figure 4.6), which show that Al present in secondary products corresponds to 15-20% of the total Al in the AAS cements. The $^{27}$Al MAS NMR spectral deconvolutions also show that hydrotalcite is always the dominant secondary phase in these systems, contributing ≥87% of the Al[6] present in the samples (Table 4.2). Hydrotalcite can therefore be expected to account for up to 18-24% of the Al in the solid binder (i.e. excluding contributions from remnant GBFS particles). Using this information to correct the

Al/Si molar ratios predicted by the CSTM to account for the presence of hydrotalcite gives Al/Si molar ratios of 0.21, 0.21 and 0.18 for the sum of the C-(N-)A-S-H and hydrotalcite components of the solid binder after 7, 28 and 56 days respectively. Incorporation of five-coordinated Al (Al[5]) and Al in the TAH phase (assuming that the TAH phase is not Si-bearing), which are minor (≤8% of total Al intensity for each sample), would give a slight further increase in the calculated Al/Si molar ratios, but the variable or unknown chemistry of each of these phases prevents their use in direct calculations at this time.

In any case, it is unlikely that inclusion of these phases in the calculations would be sufficient to increase the Al/Si molar ratio of the solid binder, compared to the predictions based on combinations of C-(N-)A-S-H and hydrotalcite phases, to a large enough extent to reconcile the difference between the average chemical composition of the solid binder as determined by SEM-EDS and the calculated chemical composition from the CSTM (Figure 4.3 and Table 4.4). Possible explanations for this discrepancy, given that recent developments in the literature strongly support the presence of cross-linked C-(N-)A-S-H gels in AAS cements (Bernal et al., 2013c; Brough and Atkinson, 2002; Fernández-Jiménez et al., 2003; Puertas et al., 2011), include:

i.) significant, non-zero amounts of four-coordinated Al (Al[4]) species substituting into paired sites in C-(N-)A-S-H gel;

ii.) the interlayer region containing significant amounts of Al; or

iii.) the presence of an Al-rich gel that is more cross-linked than C-(N-)A-S-H, but is poorly ordered and is present in sufficiently low quantities so as to be not readily identifiable through XRD, SEM-EDS, $^{27}$Al MAS NMR or $^{29}$Si MAS NMR experiments.

The possibility that Al[4] can substitute into paired sites in C-(N-)A-S-H has been previously explored in the literature (Manzano et al., 2008; Pegado et al., 2014); inclusion of these species in the CSTM would lead to an increase in the calculated Al/Si molar ratio of the C-(N-)A-S-H gel because cross-linked structures that include

Al substitution in paired sites can accommodate much higher concentrations of Al. However, the presence of Al[4] in paired sites is believed to be strongly disfavored in C-(N-)A-S-H chains (Pegado et al., 2014; Richardson et al., 1993). Using atomistic simulations, Manzano et al. (2008) concluded that Al[4] substitution in paired sites in C-(N-)A-S-H was possible, depending on the Al content of this phase, but only reaching significant concentrations at Al contents notably higher than those which are generally observed in C-(N-)A-S-H in experimental studies. Other atomistic simulations of Al substitution into silicate chains have identified a thermodynamic preference for the bridging site over the paired site in isolated pentameric chains (Manzano et al., 2009b), in pentameric chains confined within an environment representative of 14Å tobermorite (Abdolhosseini Qomi et al., 2012), and in a single sheet (on the *a*-*b* plane, i.e. one Ca-O layer) of tobermorite (Pegado et al., 2014), indicating that it is unlikely that Al in paired sites will be a major contributor to the chemistry of AAS cements. Substitution of a small amount of Al into a fraction of the paired sites cannot be entirely discounted, but it is unlikely that these species could solely account for the significant differences between calculated and experimental Al/Si ratios found here.

The possibility that Al can act as a charge-balancing species in the interlayer region of C-(N-)A-S-H has been discussed in the literature (Andersen et al., 2006; Faucon et al., 1999a; Sun et al., 2006), but is not included in the CSTM. Interlayer Al has been hypothesised to exist as Al[5] (Andersen et al., 2006; Sun et al., 2006) because Al[4] is anionic and thus cannot act as a charge-balancer for anionic chain sites. Al[6] has been proposed to be present in the interlayer (Abdolhosseini Qomi et al., 2012; Rawal et al., 2010) but is not considered in the CSTM, as discussed above. The potential contributions of these species to the chemical composition of the solid binder can thus be determined from the $^{27}$Al MAS NMR spectral deconvolutions, particularly in the Al[5] region of the spectra. However, it is evident that inclusion of interlayer Al species will not resolve the significant discrepancies between the modelled and experimentally measured chemical compositions of the AAS cement, as this difference is founded in the Al[4] concentrations alone.

Having eliminated the other possible Al-containing phases from consideration, it is therefore proposed that an additional Al-containing activation product must be present. This phase must be long-range disordered, and probably has a characteristic size on the order of nanometers so as to not be observable by SEM-EDS or XRD. This product is also not readily detectable in $^{27}$Al or $^{29}$Si MAS NMR spectra, most likely due to its presence at a low concentration with peaks overlapping those assigned to the established silicate and aluminate species in C-(N-)A-S-H. The most likely answer is that some part of the intensity in the $^{29}$Si bands at -89 ppm and -93 ppm is actually representing $Q^4$(4Al) or $Q^4$(3Al) silicate species in this additional phase, and that a fraction of the $^{27}$Al peak assigned to the $q^3$ aluminate species is also related to this product. An obvious candidate for such an assignment would be a disordered nanoparticulate zeolite-like product with Si/Al ratio close to 1, similar to the conceptual structural model which has been proposed for gels formed through alkali-activation of low-Ca aluminosilicate precursors (Provis et al., 2005b). Such an assignment would be consistent with the fact that crystalline zeolites are sometimes observed in AAS cements, particularly in systems where there is insufficient Mg to form hydrotalcite (Bernal et al., 2011b; Talling and Krivenko, 1997). This strongly supports the inclusion of $Q^4$(3Al) and $Q^4$(4Al) species in the deconvolution results for the 56 days sample (Table 4.1).

However, the assignment of some of the $Q^3$(1Al) (or $Q^3$) intensity in the $^{29}$Si MAS NMR spectra to a phase other than C-(N-)A-S-H would indicate that cross-linking between aluminosilicate chains in the C-(N-)A-S-H gel may occur to a lower extent than would be predicted based on complete assignment of $Q^3$, $Q^3$(1Al) and $q^3$ silicate and aluminate species to this phase. This is actually to some extent consistent with the observations of low or zero concentrations of $Q^3$ and $Q^3$(1Al) silicate species in some hydroxide-activated slag cements (Richardson et al., 1993), because the chemistry of these cements can be well explained by existing non-cross-linked tobermorite structural models (Richardson and Groves, 1993b). Contributions assigned to $q^3$, $Q^3$ and $Q^3$(1Al) species are typically observed in $^{27}$Al MAS NMR and

$^{29}$Si MAS NMR spectra of AAS cements activated by alkali silicate solutions (Bernal et al., 2013c; Brough and Atkinson, 2002; Fernández-Jiménez et al., 2003; Puertas et al., 2011), but non-zero intensities for silicate and aluminate species in cross-linked sites have also been observed in laboratory-synthesised and hydroxide-activated slag pastes (Palacios and Puertas, 2006; Pardal et al., 2012; Renaudin et al., 2009a; Sun et al., 2006). The increased intensity of the bands in the regions traditionally assigned to cross-linked C-(N-)A-S-H suggest that this additional Al-rich, potentially zeolite-like phase will be more prevalent in silicate-activated AAS cements.

Therefore, the application of the CSTM to the analysis of experimental NMR data does provide a strong indication of the presence of an Al-rich phase distinct from the C-(N-)A-S-H gel in silicate-activated slag cements, because the structure of cross-linked tobermorite-like chains is unable to accommodate as much Al as is supplied by the slag precursor in this system. This means that the model predictions of the degree of cross-linking between chains in AAS should be viewed as an upper bound, rather than as an exact value. However, it is clear that a mixture of cross-linked and non-cross-linked tobermorite-like structures provides a more readily generalised view of C-(N-)A-S-H chemistry than the previous models based solely on the non-cross-linked silicate chain structure. This is likely to be useful in application to some blended PC-based materials in addition to the alkali-activated slag cement systems discussed here.

## 4.4 Conclusions

This chapter has presented a generalised structural model for tobermorite-like C-(N-)A-S-H, incorporating the possibility of cross-linking between tobermorite chains to better describe the chemistry of high-Al cements. The model is named the ‘Cross-linked Substituted Tobermorite Model’, CSTM. The structures modeled in the CSTM are consistent with Loewenstein’s rule of Al-O-Al avoidance, and exclude Al substitution into paired tetrahedra. The partitioning of Al into secondary phases such

as hydrotalcite is considered through the use of $^{27}$Al MAS NMR spectra to identify the concentrations of Al in different coordination states.

The CSTM differs from previous structural models for the C-(N-)A-S-H phase, which are primarily based on non-cross-linked tobermorite-like structures, and so is more consistent with recent developments regarding the density and nanostructure of C-(N-)A-S-H in AAS cements. The CSTM is the first structural model that enables mixed non-cross-linked/cross-linked C-(N-)A-S-H to be studied over the full range of chemical compositions observed in AAS cements. The CSTM supports aluminosilicate chain cross-linking in C-(N-)A-S-H formed in AAS cements, but also indicates the presence of an additional Al-containing activation product in $Na_2SiO_3$-activated slag cements. Therefore, this study provides a profoundly deeper and more detailed description of sodium silicate-activated slag cement chemistry when compared with the existing literature in this area, and is more readily reconciled with the recent developments in the literature.

# 5

# Nanostructural Analysis of $Na_2SiO_3$-Activated Slag Cement

This chapter is based on the paper 'The Role of Al in Cross-Linking of Alkali-Activated Slag Cements', published in *Journal of the American Ceramic Society*, 2015, DOI: 10.1111/jace.13360. AAS cement samples were prepared, and XRD, and $^{27}Al$ and $^{29}Si$ MAS NMR experiments, were performed by Susan A. Bernal. The $^{27}Al$ MAS NMR data for the pure hydrotalcite sample were obtained by Sam A. Walling and Susan A. Bernal (University of Sheffield).

## 5.1 Introduction

AAS cements are particularly relevant systems for studying the chemistry of C-(N-)A-S-H because they are produced by the reaction between an alkali source and GBFS, which is one of the most common replacement materials used in modern cements. These materials have also been studied for over half a century (Juenger et al., 2011; Provis and Bernal, 2014; Purdon, 1940; Roy, 1999) with a view toward the production of concretes with high mechanical performance, low life cycle $CO_2$ emissions relative to PC, and good durability (Bernal and Provis, 2014; Juenger et al., 2011). Understanding the durability of modern concretes remains the primary scientific challenge in the development of this technology, because durability is closely related to the chemistry and the pore network geometry of the binding phase in these systems (Provis et al., 2012). Therefore, elucidation of the chemistry of the cement binder, and in particular the C-(N-)A-S-H gel which is the key space-filling and strength-giving component, is essential. Work in this area has been ongoing for

more than two decades (Richardson and Groves, 1992a; Roy, 1999), but the chemistry and structural details of the binding phases in these systems are not yet fully understood.

Various studies applying $^{29}$Si MAS NMR and $^{27}$Al MAS NMR spectroscopy to silicate-activated slag cements have been published (Bonk et al., 2003; Puertas et al., 2011; Wang and Scrivener, 2003), but where deconvolution of the spectra has been undertaken, the contribution of unreacted slag is not always distinguished and quadrupolar lineshapes are not always used in deconvolutions of $^{27}$Al MAS NMR spectra, which greatly affects the calculated contributions of the different identifiable site environments.

Therefore, this study presents $^{29}$Si and $^{27}$Al MAS NMR analysis of a sodium silicate-activated slag cement as a function of the time of curing, to clarify the complex relationship that exists between the chemical composition and nanostructure of C-(N-)A-S-H, and the solid phase assemblage in these materials. The spectra are deconvoluted with consideration of remnant unreacted slag particles and quadrupolar coupling effects, enabling quantification of the chemistry of the reaction products, with secondary phases identified by XRD. Application of a model that represents C-(N-)A-S-H as a mixture of non-cross-linked/cross-linked tobermorite-like structures (Myers et al., 2013) to the $^{29}$Si MAS NMR deconvolution results provides information regarding the structure and chemical composition of this phase.

## 5.2 Experimental

The AAS sample studied was synthesised in sealed bags at 23°C using a $Na_2SiO_3$ activator at a dose of 8 g $Na_2SiO_3$/100g slag and a w/b = 0.40. Tests were conducted at room temperature on the unreacted GBFS and on the AAS paste at 1, 3 7, 28, 56, 90 and 180 days using XRD, and $^{27}$Al and $^{29}$Si MAS NMR. A complete description of the experimental details for this investigation is given in Chapter 3.

## 5.3 Results and Discussion

### 5.3.1 X-ray Diffraction

The XRD results are presented in Figure 5.1. There is a small quantity of åkermanite ($Ca_2MgSi_2O_7$, PDF#00-035-0592) in the remnant slag (Bernal et al., 2013c). Peaks corresponding to a poorly crystalline tobermorite-like C-S-H type gel are observed (similar to $Ca_5(Si_6O_{16})(OH_2)$, PDF#01-089-6458), consistent with the literature for sodium silicate-activated slag cements (Bernal et al., 2013c; Fernández-Jiménez and Puertas, 2003; Wang and Scrivener, 1995). Hydrotalcite ($Mg_6Al_2(CO_3)(OH)_{16}{\cdot}4H_2O$, PDF#00-041-1428) is also identified as a reaction product, which is consistent with other studies of AAS with significant magnesium content (Ben Haha et al., 2011b; Bernal et al., 2013c; Bernal et al., 2014b; Fernández-Jiménez et al., 2003; Richardson et al., 1994; Wang and Scrivener, 1995). The increase in intensity of the main hydrotalcite peak (11.4° 2θ) with increasing time of curing, and similarly the peak of the C-S-H type gel at 29.5° 2θ, are consistent with the activation reaction continuing with age.

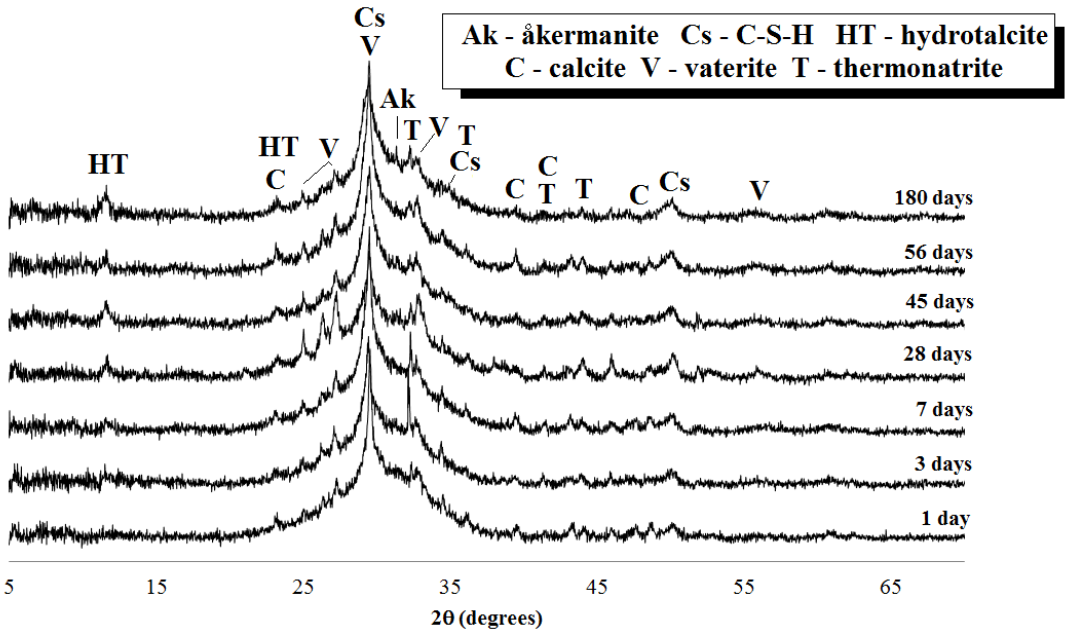


Figure 5.1. Cu Kα diffractograms of the $Na_2SiO_3$-activated slag cement as a function of curing time.

Minor traces of calcite (PDF#01-083-0577) and vaterite (PDF#01-074-1867), along with thermonatrite ($Na_2CO_3 \cdot H_2O$, PDF#01-072-0578), are associated with slight atmospheric carbonation of the specimens during sample preparation and analysis.

### 5.3.2 $^{29}$Si MAS NMR

The $^{29}$Si MAS NMR spectrum of the unreacted slag (Figure 5.2) is in good agreement with results for a melilite-type glass (Kirkpatrick, 1988), consistent with the identification of åkermanite by XRD in the slag used in this study. The activation of the slag precursor results in the formation of at least three intense bands at -80 ppm, -83 ppm and -86 ppm in the $^{29}$Si MAS NMR spectra (Figure 5.2), which are assigned to $Q^1$, $Q^2$(1Al) and $Q^2$ sites respectively in C-(N-)A-S-H (Bernal et al., 2013c; Brough and Atkinson, 2002; Richardson et al., 1993; Schneider et al., 2001; Wang and Scrivener, 2003).

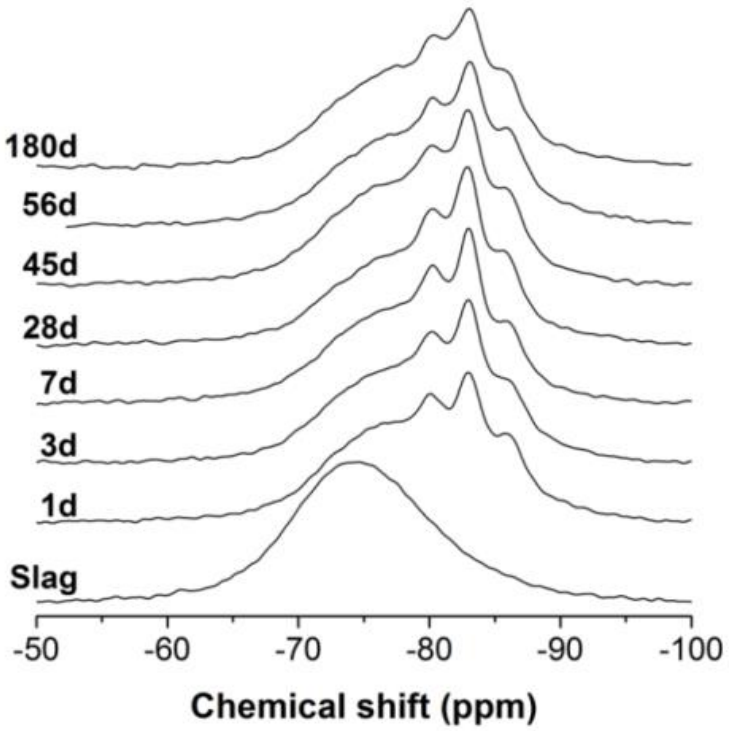


Figure 5.2. $^{29}$Si MAS NMR spectra of the $Na_2SiO_3$-activated slag cement as a function of curing time.

A reduction in the intensity of the band corresponding to the remnant slag is observed, which is attributed to the progress of the activation reaction. A $Q^0$ site at -74 ppm and an additional $Q^1$ site at -78 ppm (Figure 5.3), distinct from the site at -80 ppm, were assigned because the lineshapes of the experimental spectra in the less negative chemical shift region (> -80 ppm) could not all be matched using a single peak attributed to the remnant slag, or to any two out of the three aforementioned components, under the deconvolution constraints applied here.

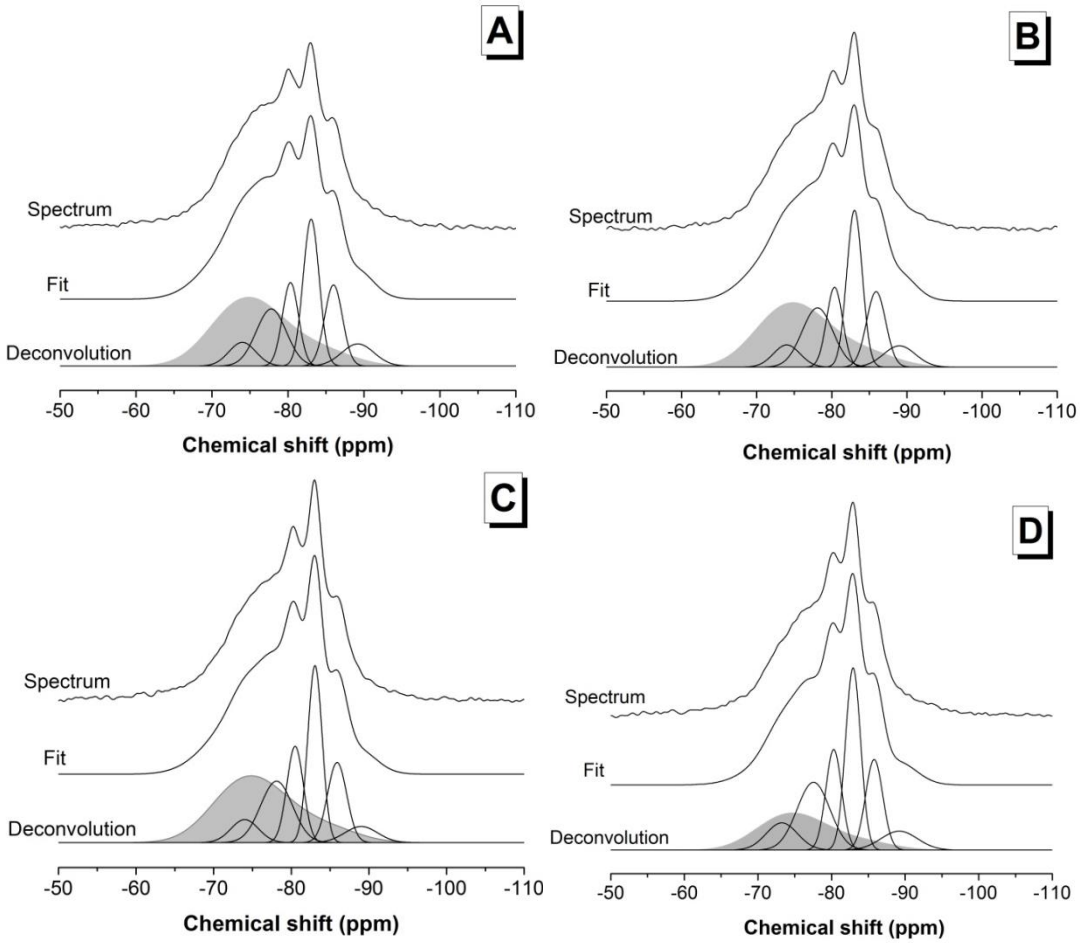


Figure 5.3. Deconvoluted $^{29}Si$ MAS NMR spectra (14.1 T, $\nu_R$ = 10 kHz) of $Na_2SiO_3$-activated slag cement cured for A) 1 day, B) 3 days, C) 7 days, D) 28 days, E) 45 days, F) 56 days and G) 180 days, with $Q^n(m\text{Al})$ sites shown in G). The dark grey band represents the contribution of the remnant slag, which is directly scaled from the spectrum collected for the unreacted slag.

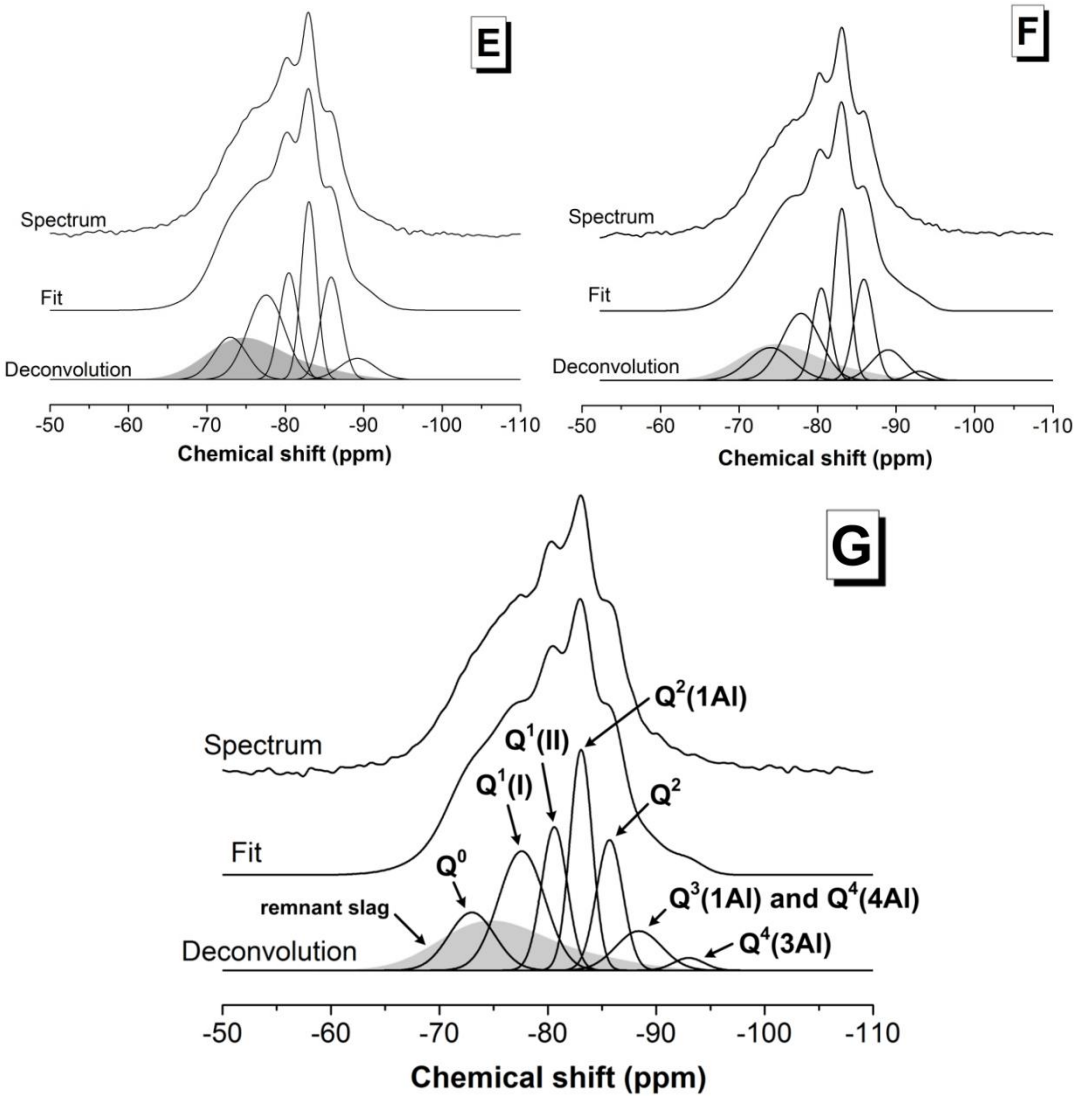


Figure 5.3. Continued.

The identification of two non-equivalent $Q^1$ environments in the binder is consistent with molecular dynamics studies of non-isolated C-S-H gels, which identified significant differences between the shielding behavior (and hence chemical shifts) of $Q^1$ sites charge-balanced by $Ca^{2+}$ or $H^+$ (Figure 5.4) (Rejmak et al., 2012). Charge-balancing by $Na^+$ is also likely in the systems studied here. There are many possible combinations of potential charge-balancing species for $Q^1$ sites; these are represented in the deconvolutions by two Gaussian peaks as this is the smallest number of peaks which can adequately represent this region of the spectra, while acknowledging that there are in fact many more chemically distinct sites than this within the material. For the purposes of the analysis, these peaks are labelled $Q^1$(I) and $Q^1$(II), where it is

likely that $Q^1$(I) at -78 ppm corresponds generally to sites connected to charge-balancing atoms (e.g. $H^+$, $Na^+$) with less strong positive charges than those associated with $Q^1$(II) at -80 ppm (e.g. $Ca^{2+}$). It is also noted that the differences in calculated chemical shift values for $Q^2$ units as a function of charge-balancing species are much less pronounced (Rejmak et al., 2012), supporting the assignment of a single site for structurally-similar $Q^2$ species in the deconvolutions. The site environments marked in Figure 5.3 are shown in Figure 5.5.

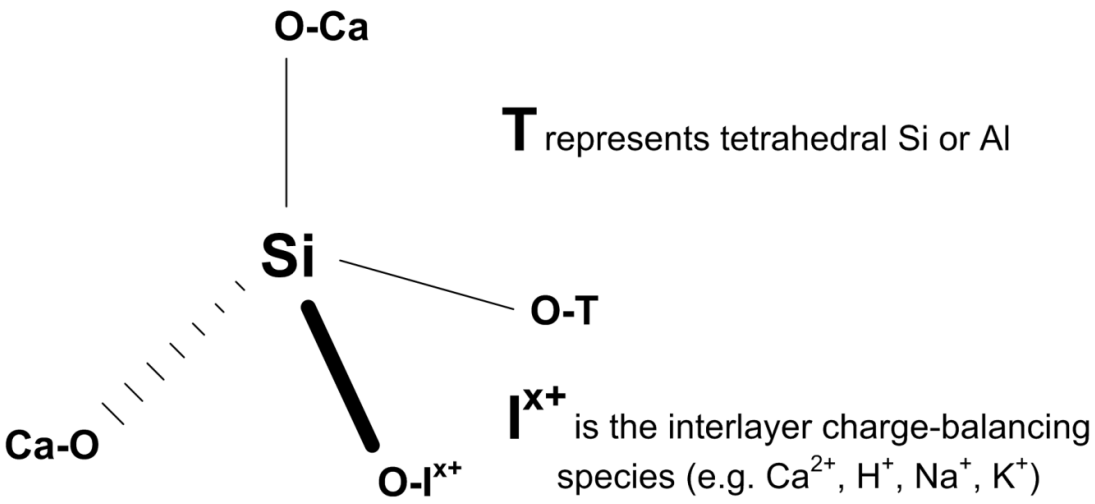


Figure 5.4. Illustration of the variety of charge-balancing species which can bind to a $Q^1$ site in C-(N-)A-S-H, leading to multiple peaks in the spectra. The Ca species are located in the Ca-O sheets.

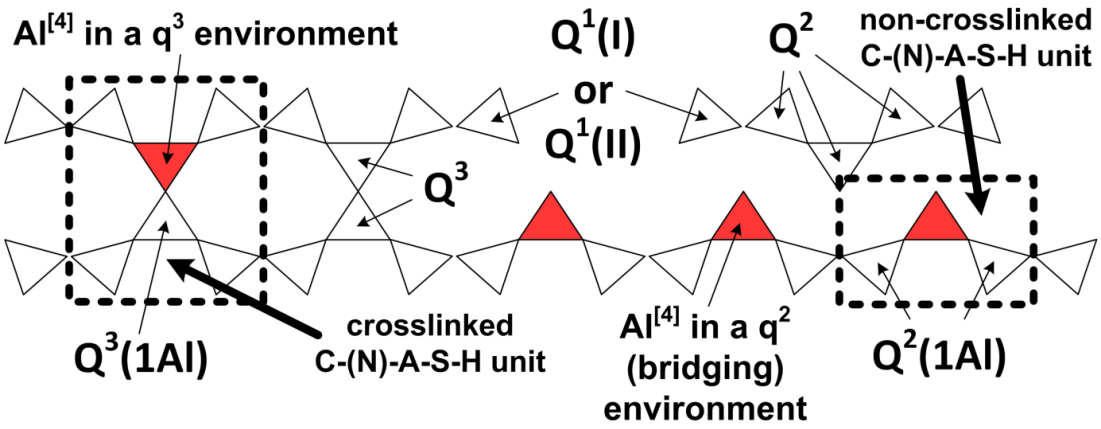


Figure 5.5. Schematic representation of cross-linked and non-cross-linked chain structures which represent the generalised structure of C-(N-)A-S-H. The red and white tetrahedra are aluminate and silicate species respectively.

Significant non-zero intensity at approximately -91 ppm becomes apparent at 56 and 180 days of curing (Figure 5.3). This signal is assigned in part to $Q^4$(3Al) and $Q^4$(4Al) in a disordered aluminosilicate product, tentatively proposed here to resemble an alkali aluminosilicate (hydrate) (N-A-S(-H)) gel, and in part to $Q^3$(1Al) units in C-(N-)A-S-H. In the deconvolutions here, a combined band for $Q^4$(4Al)/$Q^3$(1Al) and a peak for $Q^4$(3Al) are positioned at -89 ppm and -93 ppm respectively, consistent with a recent structural model and interpretation of $^{29}$Si MAS NMR results (Myers et al., 2013), without precluding the presence of a small concentration of $Q^3$ units that could also be present at approximately -93 ppm in AAS cements (Pardal et al., 2012; Puertas et al., 2011). These assignments are also chosen because this is the minimum number of peaks that can satisfactorily fit the lineshape of the spectra in this chemical shift range.

In Chapter 4 (Myers et al., 2013), a generalised model for Al-substituted, alkali charge-balanced cross-linked and non-cross-linked tobermorite-like structures, the 'Cross-linked Substituted Tobermorite Model' (CSTM), was developed and applied to describe C-(N-)A-S-H in AAS cements. It was found that a mixture of cross-linked and non-cross-linked tobermorite-like C-(N-)A-S-H and established secondary product phases could not fully explain the chemistry of the sodium-silicate activated slag binder alone, due to the inherent structural constraints of C-(N-)A-S-H gels, suggesting the presence of an additional Al-containing activation product. If this product contains aluminosilicate species contributing to the intensity of the -89 ppm and -93 ppm bands in $^{29}$Si MAS NMR spectra, these are most likely $Q^4$(4Al) and $Q^4$(3Al) units respectively and the additional product is probably a N-A-S(-H) gel with Si/Al $\leq$ 1.2 (Provis et al., 2005a). Therefore, the assignment of the -93 ppm peak to $Q^4$(3Al) in a N-A-S(-H) gel, rather than $Q^3$ in C-(N-)A-S-H, is necessary to satisfy the structural constraints of mixed non-cross-linked/cross-linked tobermorite-like C-(N-)A-S-H gels (Myers et al., 2013).

The small band at -89 ppm (Figure 5.3) increases slightly in intensity with curing time. This peak is attributed to cross-linked $Q^3$(1Al) silicate sites in C-(N-)A-S-H, as

well as $Q^4$(4Al) in N-A-S(-H) gel, which is again consistent with the structural model and interpretation of $^{29}$Si MAS NMR results recently proposed by Myers et al. (2013) and with previous studies on sodium silicate-activated and sodium carbonate-activated slag cements (Bernal et al., 2013c; Brough and Atkinson, 2002; Fernández-Jiménez et al., 2003; Palacios and Puertas, 2006). It is necessary here to attribute part of this band to $Q^4$(4Al), because the inclusion of $Q^4$(3Al) sites into the $^{29}$Si MAS NMR spectral deconvolution results requires the presence of additional $Q^4$ type units; there is no aluminosilicate gel which consists solely of $Q^4$(3Al) sites (Provis et al., 2005a). It was previously shown (Provis et al., 2005a) that Al-rich (Si/Al $\leq$ 1.2) geopolymers contain almost exclusively $Q^4$(3Al) and $Q^4$(4Al) units. This strongly supports the inclusion of $Q^4$(3Al) and $Q^4$(4Al) into the $^{29}$Si MAS NMR spectral deconvolutions here, and indicates that AAS cements may contain disordered nanoparticulate, possibly zeolite-like, products similar to the N-A-S(-H) gels formed through activation of low-calcium aluminosilicate precursors (Bell et al., 2008; Provis et al., 2005b). This assignment is also consistent with the observation of zeolites in some AAS cements after extended curing periods (Bernal et al., 2011a; Bernal et al., 2013a; Provis and Bernal, 2014). The assigned $Q^4$(3Al) and $Q^4$(4Al) peaks may alternatively be attributed to $Q^4$(*m*Al)-containing aluminosilicate gels formed through degradation of C-(N-)A-S-H during superficial carbonation of the specimen (Bernal et al., 2013c), however the XRD results (Figure 5.1) do not show the systematic increase in carbonation with curing time needed for full consistency with this assignment ($Q^4$(*m*Al) sites are only apparent at 56 and 180 days here).

Quantification of $^{29}$Si sites, determined through deconvolution of the $^{29}$Si MAS NMR spectra as a function of curing duration, is reported in Table 5.1. As much as 54% of the slag is seen to have reacted within the first day of curing, and 77% after 56 days, assuming congruent dissolution of the slag and complete uptake of the silica supplied by the activator into the solid binder The reaction extent of the slag identified by this method is greater than was determined by SEM image analysis for slag particles (of unspecified fineness) reacted with a $Na_2SiO_3 \cdot 5H_2O$ activator (~3 g $Na_2O$ equivalent/100 g slag) at w/b = 0.40 and 23°C (Le Saoût et al., 2011), which

gave hydration degrees of approximately 40% at 1 day and 55% at 56 days. Similar or lower extents of reaction have been observed for AAS cements activated at 20°C using sodium silicate and NaOH solutions (~3 g $Na_2O$ equivalent/100 g slag) (Ben Haha et al., 2011a), and in water-activated blended slag/PC materials (Kocaba et al., 2012), suggesting that the slag precursor used here is more reactive under alkaline activation conditions compared to the slags used in those studies.

Table 5.1. Results of deconvolution of $^{29}$Si MAS NMR spectra of the $Na_2SiO_3$-activated slag pastes as a function of curing time. The estimated uncertainty in absolute site percentages is ± 2%.

| **Age** | **Total unreacted slag (%)** | **Reaction products** | | | | | | | |
|---|---|---|---|---|---|---|---|---|---|
| | | $Q^0$ | $Q^1$(I) | $Q^1$(II) | $Q^2$(1Al) | $Q^2$ | $Q^3$(1Al) | $Q^4$(4Al) | $Q^4$(3Al) |
| | | -74 ppm | -78 ppm | -80 ppm | -83 ppm | -86 ppm | -89 ppm* | -89 ppm* | -93 ppm |
| Unreacted | 100 | - | - | - | - | - | - | - | - |
| 1 day | 41 | 5 | 12 | 10 | 17 | 10 | 5 | 0 | 0 |
| 3 days | 39 | 4 | 14 | 9 | 18 | 11 | 5 | 0 | 0 |
| 7 days | 39 | 4 | 14 | 11 | 18 | 11 | 4 | 0 | 0 |
| 28 days | 24 | 7 | 18 | 13 | 22 | 12 | 5 | 0 | 0 |
| 45 days | 23 | 9 | 20 | 13 | 18 | 13 | 5 | 0 | 0 |
| 56 days | 21 | 10 | 18 | 11 | 19 | 13 | 5 | 2 | 1 |
| 180 days | 21 | 10 | 19 | 13 | 17 | 12 | 4 | 2 | 1 |

* A single peak at -89 ppm is used to describe both $Q^3$(1Al) and $Q^4$(4Al) components, and distributed among these two site types based on the concentration of the $Q^4$(3Al) site, as discussed in the text.

A single band was fitted for $Q^2$ sites despite the known ~2 ppm difference between Si present in paired ($Q^2_p$) environments relative to bridging ($Q^2_b$) sites within C-S-H gels (Pardal et al., 2012), because assigning peaks for both $Q^2_b$ and $Q^2_p$ sites would lead to an unconstrained deconvolution procedure.

Significant amounts of $Q^2$(1Al) are present, indicating high levels of Al substitution in the C-(N-)A-S-H gel. The presence of $Q^3$(1Al) units also shows that the C-(N-)A-S-H gel is significantly cross-linked. Constant non-zero quantities of $Q^4$(3Al) and $Q^4$(4Al) sites are resolved at 56 and 180 days of curing. Quantification of the $Q^4$(4Al) site was performed assuming that the additional N-A-S(-H) gel only contains $Q^4$(3Al) and $Q^4$(4Al) units at an Si/Al ratio of 1.2, and the remainder of the intensity of the peak at -89 ppm was assigned to $Q^3$(1Al). This Si/Al ratio was selected as it is at the upper end of the range in which an aluminosilicate gel would be comprised almost entirely of $Q^4$(3Al) and $Q^4$(4Al) units (Duxson et al., 2005; Provis et al., 2005a); a higher Si/Al ratio would also require the presence of $Q^4$(2Al) sites, and these are not evident in the spectra here.

The evolving structure of the C-(N-)A-S-H gel is represented in Figure 5.6, by normalising the contributions of reaction products to sum to 100%.

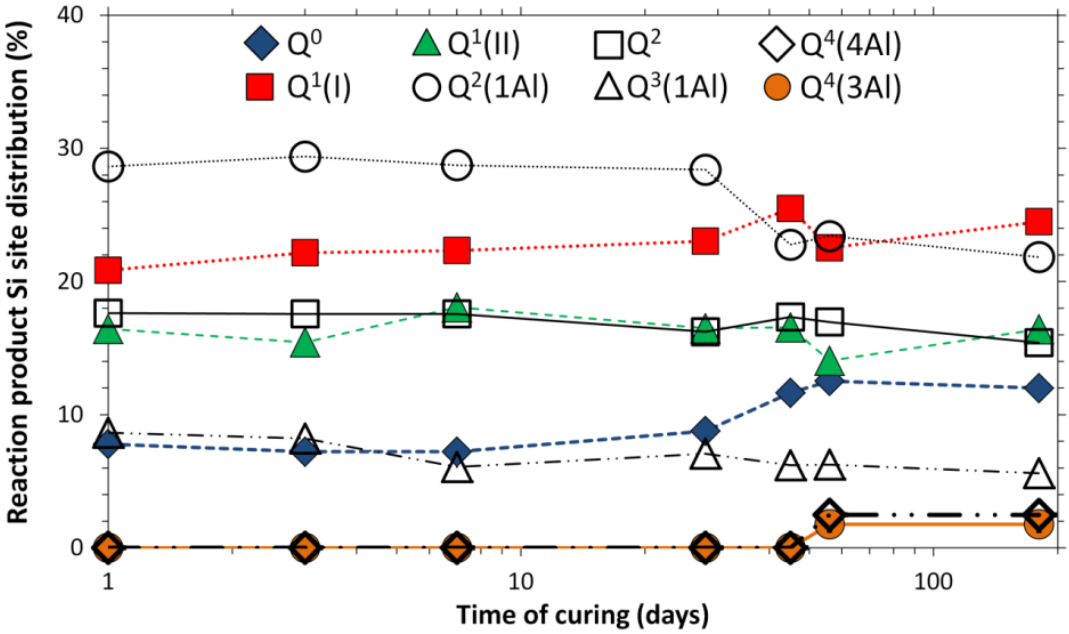


Figure 5.6. Deconvolution results of the $^{29}$Si MAS NMR spectra, normalised to the total intensity of the reaction products.

The normalised $^{29}$Si MAS NMR spectral deconvolutions (Figure 5.6) show that the relative concentrations of the $Q^1$(II) and $Q^2$ sites do not vary greatly from 1 to 180 days of curing. An increasing trend in the relative concentrations of $Q^0$ and $Q^1$(I) sites, and a decreasing trend in the relative concentrations of $Q^2$(1Al) and $Q^3$(1Al) sites, are observed over the entire range of curing ages studied. The increasing prevalence of $Q^1$(I) sites, and the corresponding reduction in the concentrations of $Q^2$(1Al) and $Q^3$(1Al) units, are associated with the gradual transformation of the C-(N-)A-S-H gel to structures with lower mean chain length (MCL; see section 5.3.4) and increasing secondary product formation (Figure 5.1 and section 5.3.3) as the time of curing increases. This reduction in MCL can also potentially be reconciled with the relative increase in percentage of the bands at -74 ppm (tentatively assigned to $Q^0$ here) if these peaks represent surface-bound $Q^0$ units, as increasing the relative surface area of C-(N-)A-S-H gel can be consistent with a reduction in MCL. The decreasing trend in the concentration of $Q^3$(1Al) sites (in cross-linked C-(N-)A-S-H) is also consistent with the observed decreasing relative percentage of $Q^2$(1Al) sites, because a reduction in $Q^3$(1Al) necessitates a lower concentration of $Q^2$(1Al) (Figure 5.5). Therefore, these results indicate that the degree of cross-linking of the C-(N-)A-

S-H gel decreases over time, which is to some extent a counterintuitive result, and which will be explored in more detail in section 5.3.4 below.

The $Q^0$ site at -74 ppm is assigned to partially hydrated silicate monomers or $Q^0$ components of the remnant slag that have not reacted congruently without precluding the possibility that $Q^1$(1Al) species contribute to a small fraction of this peak. The presence of $Q^1$(1Al) in the $^{29}$Si MAS NMR spectra would imply Al substitution in paired tetrahedral sites in C-(N-)A-S-H, given that tetrahedral site vacancies only occur in the bridging position (as described by 3*n*-1 chain length models for C-(N-)A-S-H (Richardson, 2004)). Al substitution into paired sites is not expected because atomistic simulations of Al-substituted pentameric chains in environments representative of 14 Å tobermorite (Abdolhosseini Qomi et al., 2012), in sheets representing 14 Å tobermorite (Pegado et al., 2014), and in isolated chains (Manzano et al., 2009b), have shown significant energetic preferences for Al substitution in bridging sites instead. Deconvolutions of the $^{29}$Si MAS NMR spectra have also been performed without including $Q^n$ components related to Al substitution into paired sites, because $Q^1$(1Al) units are not often observed in published $^{29}$Si MAS NMR spectra of calcium silicate hydrate-based gels (Brough and Atkinson, 2002; Richardson et al., 1993; Schilling et al., 1994a; Sun et al., 2006; Wang and Scrivener, 2003), and also because inclusion of these additional $Q^n$ components ($Q^1$(1Al), $Q^2$(2Al) and $Q^3$(2Al) species) would lead to an underconstrained deconvolution procedure. This band at -74 ppm has been observed previously in sodium silicate-activated slag cements (Le Saoût et al., 2011), where (similar to the conclusion reached here) it was assigned to $Q^0$ units, but no strongly established assignment for this peak to a specific site environment within the AAS cement phase assemblage currently exists.

### 5.3.3 $^{27}$Al MAS NMR

Three distinct Al environments (Al[4], Al[5] and Al[6]) are observed in the $^{27}$Al MAS NMR spectra (Figure 5.7), at $\delta_{obs}$ = 52-80 ppm (i.e. the observed chemical

shift), 30-40 ppm and 0-20 ppm, respectively (Engelhardt and Michel, 1987). The profiles of the experimental spectra remain similar as the duration of curing increases, but some variation in all three environments is observed between 1-180 days, including:

i) formation of two distinct Al[4] sites at $\delta_{obs}$ = 74 ppm and 68 ppm, which is consistent with the dissolution of the slag and the formation of aluminosilicate reaction products;

ii) an increase in the concentration of Al[5] sites, and a sharpening of the peaks corresponding to Al[5] with increasing curing time; and

iii) the increased sharpness and intensity of the Al[6] peak at $\delta_{obs}$ = 4 ppm.

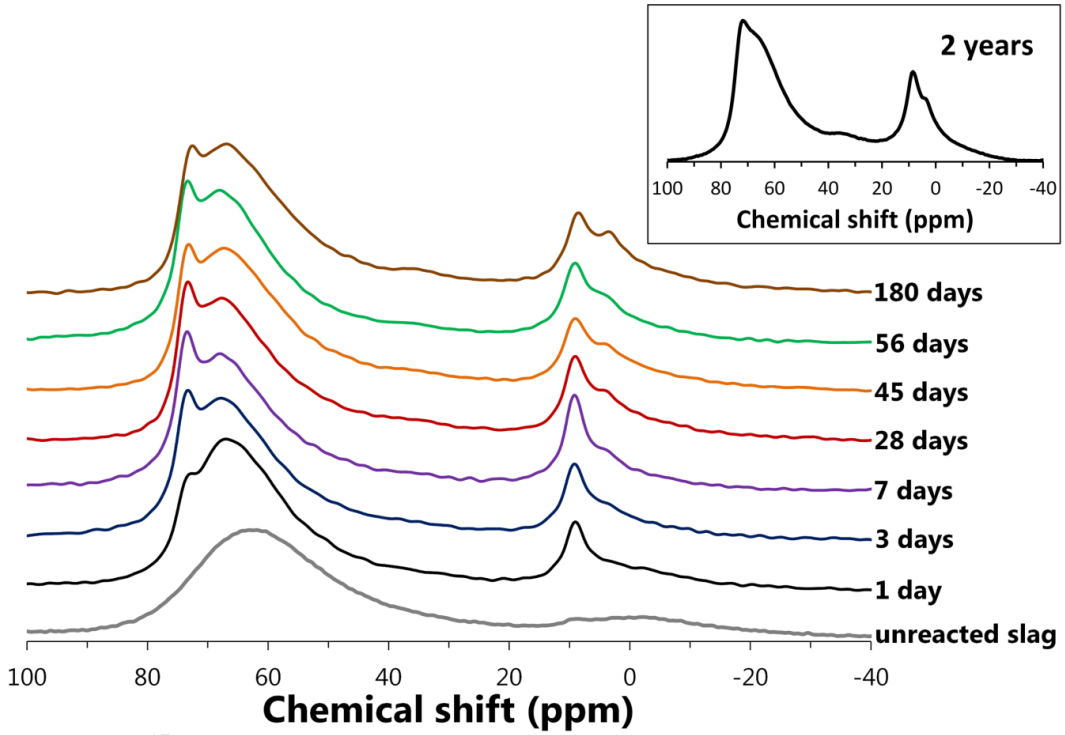


Figure 5.7. $^{27}$Al MAS NMR spectra of the $Na_2SiO_3$-activated slag paste up to 180 days of curing (14.1 T, $\nu_R$=10 kHz) and the spectrum for the sample cured for 2 years (9.4 T, $\nu_R$=14 kHz).

The four-coordinated Al environments are assigned to the remnant slag particles in the AAS cement, according to the spectrum of the unreacted slag, and also to C-(N-)A-S-H. Three distinct Al sites in C-(N-)A-S-H are identified at $\delta_{obs}$ = 74 ppm, 68 ppm and 62 ppm ($\delta_{iso}$ = 75 ppm, 68 ppm and 62 ppm respectively), in agreement

with the literature (Faucon et al., 1999a; Pardal et al., 2012; Sun et al., 2006). The peaks present in the Al[6] region are assigned to hydrotalcite at $\delta_{obs}$ = 9.3 ppm and 5.9 ppm ($\delta_{iso}$ = 9.68 ppm and 9.1 ppm respectively) (Sideris et al., 2012; Vyalikh et al., 2009), which is consistent with the observation of this phase in the XRD results (Figure 5.1), as well as the third aluminate hydrate (TAH) at $\delta_{obs}$ = 3.9 ppm ($\delta_{iso}$ = 4.6 ppm). Contributions from TAH are evident because the sharp lineshape of the $\delta_{obs} \approx 4$ ppm peak cannot be described as hydrotalcite alone.

The quadrupolar coupling parameters used to describe the component peak shapes for the reaction products in the $^{27}$Al MAS NMR deconvoluted spectra and the quantified site fractions for these phases are illustrated in Figures 5.8-5.9 and reported in Table 5.2. Accurate descriptions of the quadrupolar coupling effects (d'Espinose de Lacaillerie et al., 2008) in these phases are typically absent in the alkali-activated cement chemistry literature (where Gaussian/Lorentzian peak shapes are often assumed, even for quadrupolar nuclei), despite the importance of the quadrupolar coupling parameter in determining the component peak shapes and hence intensities, although quadrupolar effects have been accounted for in analysis of $^{27}$Al MAS NMR spectra for hydrated PC-based materials (Bach et al., 2012; d'Espinose de Lacaillerie et al., 2008) and laboratory synthesised C-A-S-H (Pardal et al., 2012). It is therefore noteworthy that the $^{27}$Al MAS NMR spectral deconvolutions presented here provide a greatly enhanced description of the experimental spectra. The proposed peak assignments (where the $q^n$ notation for Al sites is equivalent to the $Q^n$ notation for Si sites (Harris et al., 1997)) are also consistent with the phases identified through XRD (Figure 5.1).

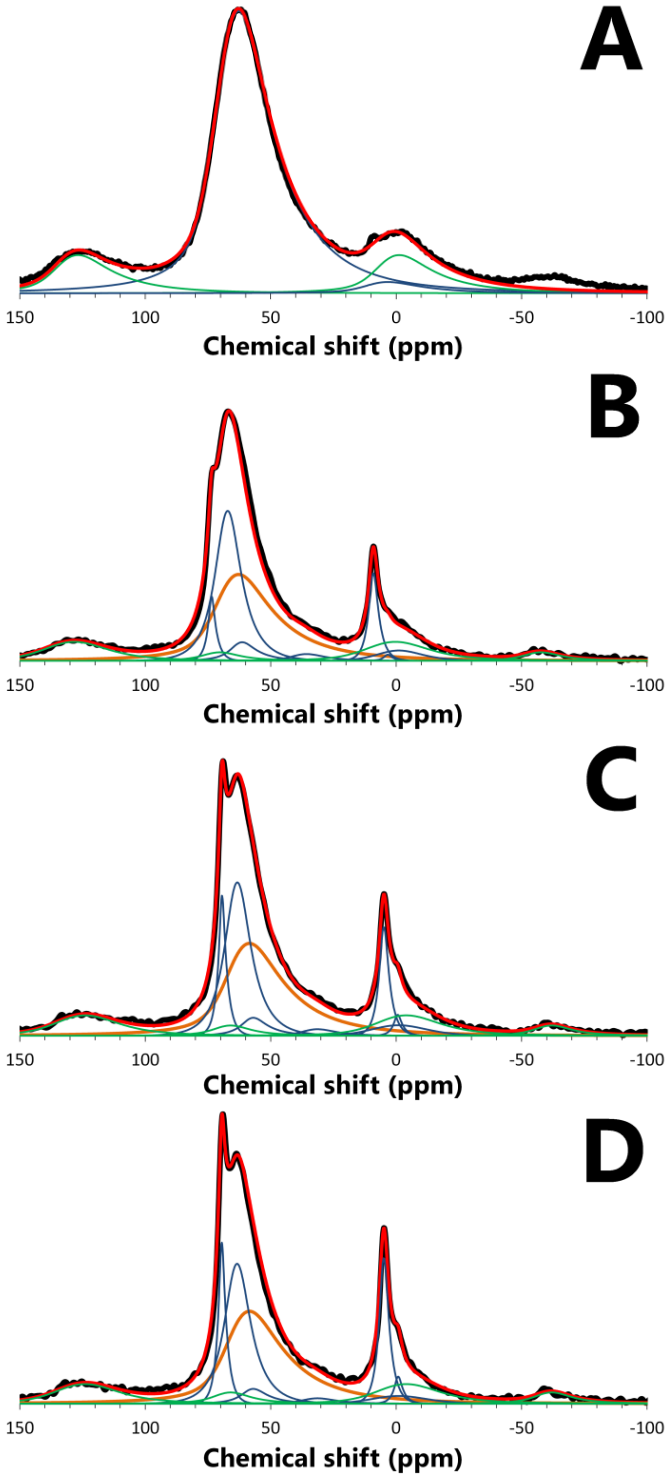


Figure 5.8. Deconvoluted $^{27}$Al MAS NMR spectra (14.1 T, $\nu_R$=10 kHz) of the A) anhydrous slag and sodium silicate-activated slag cured for B) 1 day, C) 3 days, D) 7 days, E) 28 days, F) 45 days, G) 56 days and H) 180 days, with $q^n$ sites shown in H). The contribution of the remnant slag is directly scaled according to the extent of reaction defined from the $^{29}$Si MAS NMR spectra. The bold orange traces represent the contribution of the remnant anhydrous slag, the green sub-peaks are spinning sidebands, the blue traces represent product phase and the red line is the sum of the deconvoluted components of the spectrum.

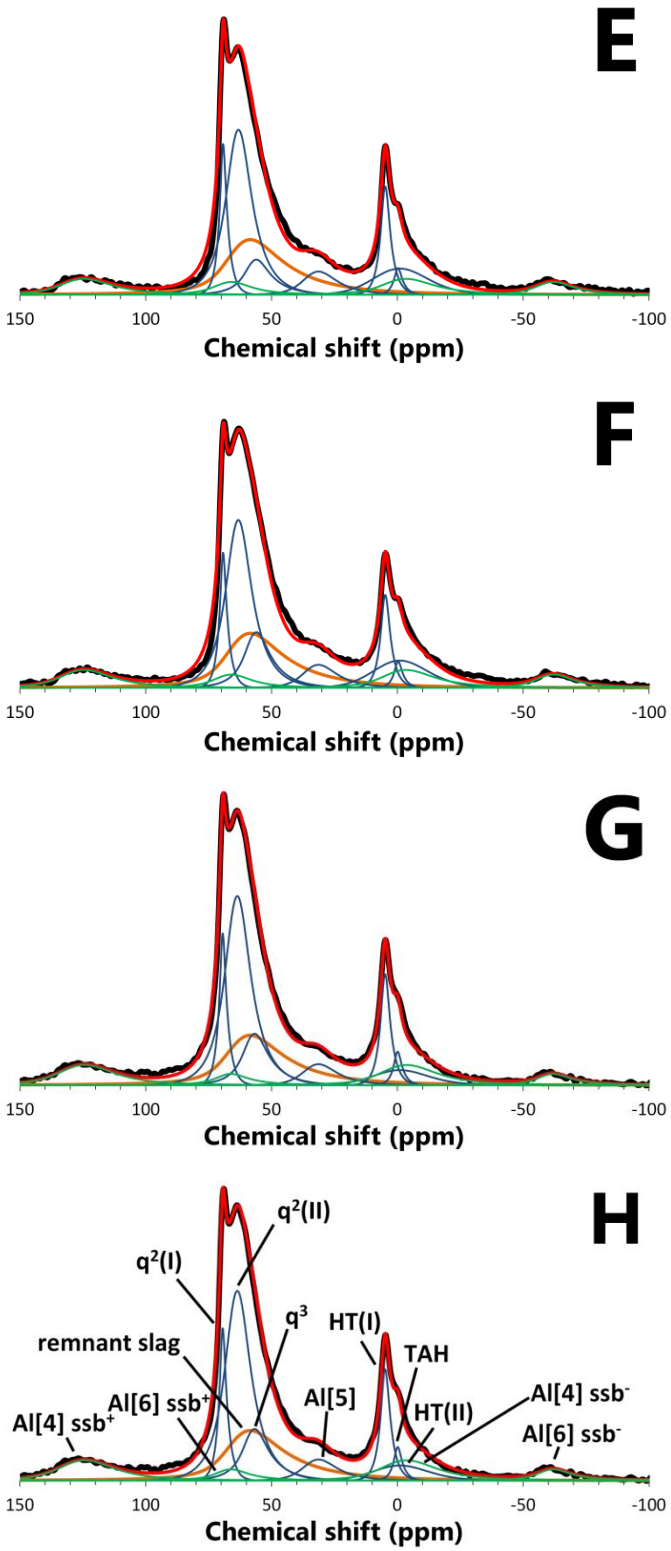


Figure 5.8. Continued.

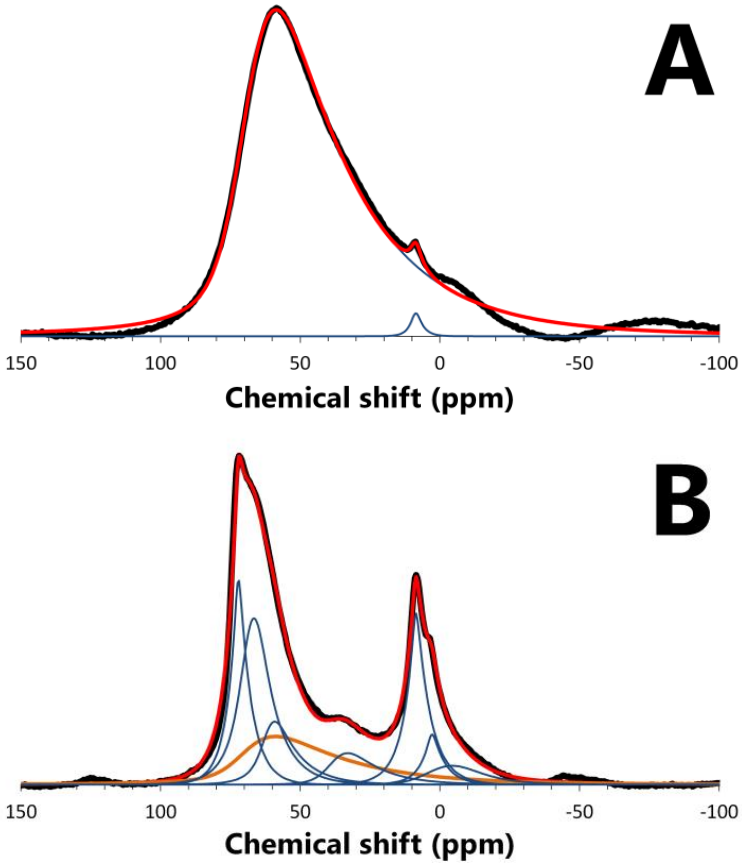


Figure 5.9. Deconvoluted $^{27}$Al MAS NMR spectra (9.4 T, $\nu_R$=14 kHz) of the A) anhydrous slag and B) sodium silicate-activated slag cured for 2 years, with $q^n$ sites shown in Figure 5.8H. The bold orange trace represents the contribution of the remnant anhydrous slag in B). The blue and red traces represent product phases and the sum of the deconvoluted peaks respectively.

Table 5.2. Deconvolution results of the $^{27}$Al MAS NMR spectra for the $Na_2SiO_3$-activated slag pastes as a function of curing time. The estimated uncertainty in absolute site percentages is ± 3%. Samples aged for 1-180 days were measured at 14.1 T, $\nu_R$=10 kHz, and the sample cured for 2 years was measured at 9.4 T, $\nu_R$=14 kHz.

| **Assignment** | **Al[4] in unreacted slag** | **$q^2$(I)** | **$q^2$(II)** | **$q^3$†** | **Al[5]** | **HT(I)** | **HT(II)** | **TAH** |
|---|---|---|---|---|---|---|---|---|
| **Isotropic chemical shift, $\delta_{iso}$ (ppm)** | 65 | 75 | 68 | 62 | 38 | 9.68* | 9.1 | 4.6 |
| **$C_Q$ (MHz) and reference** | 6.7 (Klinowski, 1984) | 1.1 (Klinowski, 1984) | 2.0 (Klinowski, 1984) | 3.0 (Klinowski, 1984) | 4.0 (Klinowski, 1984) | 1.2* | 3.55 (Sideris et al., 2012) | 1.13 (Andersen et al., 2006) |
| **Age** | | | | | | | | |
| Unreacted | 100 | - | - | - | - | - | - | - |
| 1 day | 46 | 4 | 32 | 4 | 2 | 7 | 4 | 0 |
| 3 days | 44 | 8 | 30 | 4 | 2 | 8 | 4 | 1 |
| 7 days | 44 | 9 | 27 | 3 | 1 | 11 | 3 | 2 |
| 28 days | 26 | 9 | 32 | 7 | 6 | 8 | 10 | 2 |
| 45 days | 25 | 8 | 32 | 11 | 6 | 7 | 10 | 2 |
| 56 days | 23 | 9 | 37 | 10 | 5 | 8 | 5 | 2 |
| 180 days | 23 | 6 | 31 | 13 | 6 | 7 | 11 | 3 |
| 2 years | 22 | 16 | 23 | 9 | 6 | 15 | 6 | 4 |

***** Values determined through analysis of a pure hydrotalcite sample; S.A. Walling and S.A. Bernal, unpublished data.

† It is likely that the $q^3$ site contains contributions from $q^4$ aluminate species, but attempts to resolve this site into two separate sub-peaks led to an underconstrained deconvolution process.

The $^{27}$Al MAS NMR deconvolution results (Table 5.2) show that hydrotalcite is the dominant Al[6]-containing phase at all ages, which is consistent with the prominent reflections for this phase in the XRD results (Figure 5.1). Contributions from hydrotalcite are represented by two asymmetric peaks here (marked as HT(I) and HT(II) in Figure 5.8H and Table 5.2), to match the known spectrum of this phase (Sideris et al., 2012; Vyalikh et al., 2009). Here, the HT(II) site ($\delta_{iso}$ = 9.1 ppm) is assigned specifically to octahedral Al in hydrotalcite that are coordinated to $CO_3^{2-}$ as the interlayer charge-compensating anion (Sideris et al., 2012), whereas the HT(I) site ($\delta_{iso}$ = 9.68 ppm) is assigned to contain contributions from octahedral Al bonded to $OH^-$ in addition to $CO_3^{2-}$. Despite careful handling and preparation to minimise carbonation of the paste specimen, the XRD results (Figure 5.1) do show that the samples were slightly carbonated, and recent results by Bernal et al. (2014b), which suggest that carbonation of hydrotalcite occurs preferentially to the other reaction products in AAS cements, indicates that the hydrotalcite phases formed here may contain carbonate species. The deconvolution results show that the intensity of the HT(II) band is generally greater relative to the HT(I) peak at advanced ages of curing, which is also consistent with the assignment made here because it is reasonable to expect that the specimens are slightly more carbonated at later times of curing. However, the isotropic chemical shift of the reference HT(I) peak and the HT(II) band are 2-3 ppm lower than the reported values of $\delta_{iso}$ = 11.8 ppm (Sideris et al., 2012) and $\delta_{iso}$ = 11 ppm (Vyalikh et al., 2009), meaning that this assignment cannot be made unequivocally.

The $q^2$ aluminate species at $\delta_{obs}$ = 74 and 68 ppm are assigned to two different local environments, $q^2$(I) and $q^2$(II) respectively, with lower electron density in the $q^2$(I) site. The $q^2$(I) peaks are significantly narrower (Figures 5.8-5.9), suggesting more ordered environments in these sites. Earlier studies have assigned this site to Al substituted into paired tetrahedra in C-A-S-H (Pardal et al., 2012); however, this site has been left to the more general $q^2$(I) assignment here, analogously to the $Q^1$(I) and $Q^1$(II) silicate sites discussed above. The peak widths of the specific site types are also likely to be affected by the disorder of the aluminosilicate chains in C-(N-)A-S-

H gel (Taylor, 1997). The $q^2$(II) site is assigned to Al[4] in bridging sites of the aluminosilicate chains in C-(N-)A-S-H (Figure 5.5) (Houston et al., 2009; Pardal et al., 2012) .

The deconvolutions show significant intensity at chemical shifts corresponding to $q^3$ (and possibly $q^4$) coordinated Al ($\delta_{iso}$ = 62 ppm), suggesting high levels of cross-linking in the C-(N-)A-S-H gel. This is consistent with the literature for silicate-activated slag cements (Fernández-Jiménez et al., 2003; Palacios and Puertas, 2006). It is expected that this site contains overlapping contributions from $q^3$ units with different charge-balancing environments, similar to the situation discussed above for the $q^2$(I), $q^2$(II), $Q^1$(I) and $Q^1$(II) sites, and potentially also from $q^4$ sites. These are expected given the assignment of $Q^4$(3Al) and $Q^4$(4Al) silicate units in the $^{29}$Si MAS NMR spectral deconvolutions. However, quantification of $q^4$ sites in the deconvoluted $^{27}$Al MAS NMR spectra has not been performed here because the deconvolution becomes underconstrained with the inclusion of an additional $q^4$ peak.

The evolving nature of the Al environments in the AAS cement can be illustrated by normalising the reaction product intensities to 100% and removing the contributions attributed to the remnant slag component (Figure 5.10), comparable to Figure 5.6 describing Si environments. The relative intensities assigned to the $q^3$ (and possibly $q^4$) and $q^2$ sites, and the HT(I) and HT(II) sites, have also been combined in Figure 5.10 because these site environments are not yet well defined in AAS cements.

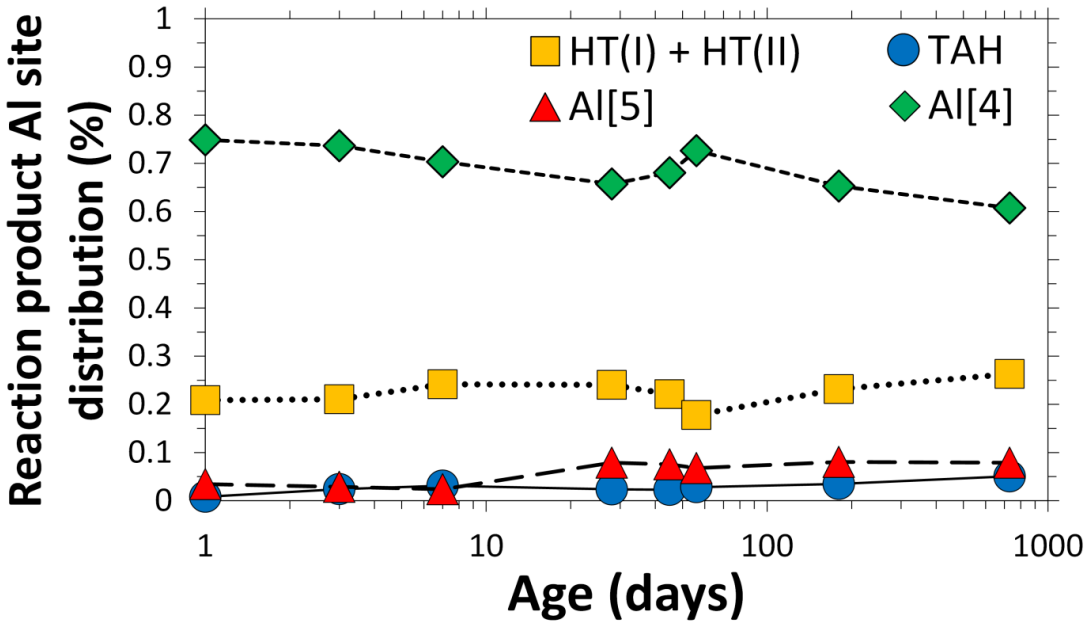


Figure 5.10. Deconvolution results for the $^{27}$Al MAS NMR spectra normalised to the total intensity of the reaction products as a function of the time of curing. Samples aged for 1-180 days were measured at 14.1 T, $\nu_R$=10 kHz, and the sample cured for 2 years was measured at 9.4 T, $\nu_R$=14 kHz.

In general, the normalised $^{27}$Al MAS NMR spectral deconvolution results (Figure 5.10) show that as curing time increases, the relative percentage of Al[4] environments in the solid binder decreases and the combined relative intensity of the HT peaks remain approximately constant. The intensity of the TAH and Al[5] peaks increase as a function of curing time. Here, Al[5] is tentatively assigned to interlayer species in C-(N-)A-S-H that charge-balance the aluminosilicate chains present in this phase (Andersen et al., 2006; Love et al., 2007; Sun et al., 2006). The increased amount of this component at 28 days and later in the $^{27}$Al MAS NMR spectra is consistent with experimental $^{27}$Al MAS NMR spectra of AAS cements (Bonk et al., 2003; Richardson et al., 1994), laboratory-synthesised C-(N-)A-S-H (Faucon et al., 1999a; Sun et al., 2006), and PC-based materials (Andersen et al., 2006; Love et al., 2007; Taylor et al., 2010).

No clear contributions from AFm or hydrogarnet are observed in the $^{27}$Al MAS NMR spectra, which is consistent with the absence of prominent reflections corresponding to these phases in the XRD results (Figure 5.1). These results indicate

that the solid phase assemblage varies only slightly between 1 day and 2 years of curing (noting again that the effect of the extent of reaction has been removed from these data), with the exception of the appearance of a small amount of N-A-S(-H) gel at 56 days and later, as discussed in section 5.3.2.

### 5.3.4 Characterisation of the C-(N-)A-S-H Gel

The deconvoluted $^{29}$Si MAS NMR spectra (Table 5.1) are interpreted using the CSTM structural description of cross-linking in tobermorite-like gels (Myers et al., 2013), to characterise the chemistry and structure of the C-(N-)A-S-H gel formed here (Table 5.3).

Table 5.3. The structure and chemistry of the C-(N-)A-S-H gel formed here as calculated by the CSTM structural description (Myers et al., 2013). A constant interlayer calcium content of $\omega = \phi = 0.25$, maximal partitioning of $Q^1$ sites into the cross-linked component of the gel ($\eta$), Si/Al = 1.2 for the additional disordered activation product, and complete assignment of the band at -93 ppm to $Q^4$(3Al) units are specified for all pastes. Uncertainty in the deconvoluted Si site percentages gives a relative error of ~±10% in all model outputs.

| Age | C-(N-)A-S-H gel | | | | | Cross-linked (C) and non-cross-linked (NC) phases | | | |
|---|---|---|---|---|---|---|---|---|---|
| | **Cross-linked phase fraction** | **% of Al in cross-linked phase** | **Partitioning of $Q^1$ into the cross-linked phase ($\eta$)** | **MCL** | **Al/Si** | **type** | **MCL** | **Al/Si** | **Fraction of bridging sites substituted by Al †** |
| 1 day | 0.81 | 60 | 0.92 | 11 | 0.16 | NC | 14 | 0.39 | 0.98 |
| | | | | | | C | 10 | 0.11 | 1 |
| 3 days | 0.77 | 56 | 0.88 | 10 | 0.16 | NC | 11 | 0.35 | 0.94 |
| | | | | | | C | 10 | 0.11 | 1 |
| 7 days | 0.57 | 42 | 0.60 | 7.6 | 0.15 | NC | 5.8 | 0.22 | 0.82 |
| | | | | | | C | 10 | 0.11 | 1 |
| 28 days | 0.67 | 50 | 0.72 | 8.3 | 0.16 | NC | 6.2 | 0.26 | 0.91 |
| | | | | | | C | 10 | 0.11 | 1 |
| 45 days | 0.62 | 55 | 0.60 | 6.7 | 0.13 | NC | 4.4 | 0.16 | 0.76 |
| | | | | | | C | 10 | 0.11 | 1 |
| 56 days | 0.66 | 53 | 0.68 | 7.9 | 0.14 | NC | 5.6 | 0.20 | 0.79 |
| | | | | | | C | 10 | 0.11 | 1 |
| 180 days | 0.59 | 51 | 0.55 | 6.4 | 0.13 | NC | 4.2 | 0.16 | 0.79 |
| | | | | | | C | 10 | 0.11 | 1 |

† with Al-O-Al avoidance maintained, i.e. only one Al is allowed in each cross-linked C-(N-)A-S-H unit (Figure 5.5).

Fixed values of interlayer calcium content ($\omega = \phi = 0.25$) were used in the model to match the average binder composition (Ca/Si and Ca/(Al+Si)) of this AAS cement measured by environmental scanning electron microscopy with energy-dispersive X-ray spectroscopy (ESEM-EDS) as a function of curing time (Myers et al., 2013). The structure of the C-(N-)A-S-H gel is mostly cross-linked between 1-180 days, despite the low apparent intensity of the $Q^3$(1Al) component in the deconvoluted $^{29}$Si MAS NMR spectra (Table 5.1). The Al/Si ratio of the C-(N-)A-S-H gel decreases slightly as curing time increases, reflecting the reduction in the relative $Q^2$(1Al), $Q^3$(1Al) and Al[4] site percentages (Figures 5.6 and 5.10). The decreasing fraction of the cross-linked component of the gel at later ages is a consequence of the relative reduction in $Q^3$(1Al) sites and the formation of the additional disordered ($Q^4$ and possibly $q^4$ containing) activation product at extended ages. A similar decreasing trend in MCL is found with increasing curing time, indicating that the cross-linked phase fraction – so also the intensities of the $Q^3$(1Al) sites and the formation of the additional $Q^4$-containing product – are the key parameters influencing the extent of polymerisation of the partially cross-linked C-(N-)A-S-H gels characterised here. The Ca/Si ratio of the binder was not found to increase from 7 to 56 days by ESEM-EDS (Myers et al., 2013), in support of this analysis. The percentage of Al in the cross-linked component of the gel is between 40-60 % at all curing times, which suggests that Al substitutes into both cross-linked and non-cross-linked components of C-(N-)A-S-H without a clear preference for either structural type.

The percentages of Al in the cross-linked gel components are calculated according to eq.(5.1):

$$\%Al_{[C]} = 100\frac{\left(Al/Si\right)_{[C]}\left[Q^1 + Q^2(1Al) + Q^2 + Q^3(1Al) + Q^3\right]_{[C]}}{\sum_k\left(\left(Al/Si\right)_k\left[Q^1 + Q^2(1Al) + Q^2 + Q^3(1Al) + Q^3\right]_k\right)} \qquad (5.1)$$

where the subscripts [*C*] and [*NC*] represent the cross-linked and non-cross-linked components of the C-(N-)A-S-H gel respectively, $k \in \{[C],[NC]\}$ , the $Q^n$ site

fractions are taken from the $^{29}$Si MAS NMR spectral deconvolution results (Table 5.1), and $(Al/Si)_{[C]}$ and $(Al/Si)_{[NC]}$ are defined by eqs.(5.2-5.3):

$$\left(Al/Si\right)_{[C]} = \frac{Q^3(1Al)}{Q^1 + Q^2 + Q^2\left(1Al\right) + Q^3 + Q^3\left(1Al\right)} \tag{5.2}$$

$$\left(Al/Si\right)_{[NC]} = \frac{\left(\frac{1}{2}\right)Q^2(1Al)}{Q^1 + Q^2 + Q^2(1Al)} \tag{5.3}$$

The maximum partitioning of $Q^1$ units into the cross-linked C-(N-)A-S-H component ($\eta \rightarrow \eta_{max}$) was specified because the MCL and Al/Si ratio of this phase are similar (MCL ≈ 10 and Al/Si ≈ 0.11) at all values of $\eta$ that satisfy the structural constraints of the gel (Myers et al., 2013), for the C-(N-)A-S-H gel formed here. Partitioning of $Q^1$ sites can be defined differently (e.g. specifying the minimum value of $\eta$ that satisfies the structural constraints of the gel), but as long as the method used is consistent, the structural trends obtained from the CSTM are the same. Hence the trends related to the structure of the C-(N-)A-S-H gel, rather than the absolute values, are the key targets for analysis. The choice of $\eta$ does not affect the calculated overall Al/Si ratio of the C-(N-)A-S-H gel or the concentration of Al in the cross-linked component of the gel.

A strong link between the Al content and MCL of the C-(N-)A-S-H gel is found by distinguishing the cross-linked and non-cross-linked components (Table 5.3). This is a consequence of the low capacity of cross-linked C-(N-)A-S-H structures to incorporate Al, as illustrated by Figure 5.5: only one in each six tetrahedral sites in cross-linked C-(N-)A-S-H units can accommodate Al, compared to one in three tetrahedral sites in non-cross-linked C-(N-)A-S-H units. The data in Table 5.3 indicate that if the average Al/Si ratio of the C-(N-)A-S-H gel is significantly greater than 0.11 (the Al/Si ratio of Al-saturated, MCL = 10 cross-linked tobermorite), then the non-cross-linked chain structures are significantly more polymerised and Al-rich than the C-(N-)A-S-H gel as a whole, because these structures must incorporate all of

the remaining Al. Therefore, small variations in the overall Al/Si ratio of the C-(N-)A-S-H gel can lead to major structural and chemical changes in the non-cross-linked component of C-(N-)A-S-H gels, meaning that significant variations in the structure and chemistry of the C-(N-)A-S-H gel can be expected in AAS cements of superficially similar composition.

### 5.3.5 Perspectives

This new understanding of C-(N-)A-S-H further highlights the importance of a fundamental scientific approach to the design and formulation of modern cement materials. The relationship between structure and Al content in C-(N-)A-S-H may be important in determining the mechanical and thermodynamic properties of blended PC/Al-containing SCM materials and alkali-activated cements. The results presented here indicate strongly that single-phase structural representations of C-(N-)A-S-H are insufficient to accurately characterise the chemical composition and structure of this phase; multi-phase or solid solution models for C-(N-)A-S-H gels (Kulik, 2011; Puertas et al., 2011) should be used to describe these materials.

However, because the CSTM does not embody a description of the $Q^4$-containing disordered aluminosilicate phase, separate quantification is needed. Here, this phase is discussed as resembling an intimately-mixed zeolite-like phase similar to the N-A-S(-H) gels formed through the alkali-activation of low-calcium aluminosilicate precursors (Provis et al., 2005b), which was quantified from the $^{29}$Si MAS NMR spectral deconvolutions, enabling use of the CSTM to fully characterise the structure and chemistry of the C-(N-)A-S-H gel formed here. It may also possibly be described as a degradation product of carbonated C-(N-)A-S-H gel, although the application of multinuclear NMR techniques to better distinguish the $Q^n(m\text{Al})$ environments in the solid binder seems to be essential in further refining the understanding in this area. The identification of this disordered aluminosilicate phase also indicates a need to understand the influence of this phase on the chemical stability of the solid binder,

because the chemical stability of calcium-deficient sodium-aluminosilicate gels and C-(N-)A-S-H are known to differ significantly (van Deventer et al., 2012).

## 5.4 Conclusions

Spectroscopic and diffractometric analysis of the nanostructural development of a sodium silicate-activated slag cement up to 180 days of curing shows the presence of a dominant C-(N-)A-S-H gel, with hydrotalcite and TAH secondary products. Five-coordinated Al, tentatively assigned to interlayer charge-balancing species in the C-(N-)A-S-H gel, was also observed at all ages.

Application of the 'Cross-linked Substituted Tobermorite Model', describing mixed cross-linked/non-cross-linked tobermorite-like structures, showed decreasing trends in the MCL, extent of cross-linking and Al/Si ratio of the C-(N-)A-S-H gel over time. The C-(N-)A-S-H gel was highly cross-linked despite the low relative intensity of $Q^3$(1Al) sites, and an additional highly-polymerised aluminosilicate phase, containing $Q^4$(3Al) and $Q^4$(4Al) sites and proposed here to potentially resemble the nanocrystalline products found in calcium-deficient sodium-aluminosilicate hydrate ('geopolymer') gels, was required for consistency with the spectra collected at later ages. This has important implications for understanding the durability of AAS cement-based materials, as the phase stabilities of geopolymer gels and C-(N-)A-S-H are known to differ significantly. The chemical and structural nature of the C-(N-)A-S-H gel varied significantly across a relatively narrow range of chemical compositions. A complex relationship exists between the Al content and the extent of polymerisation of the C-(N-)A-S-H gels, due to the lower relative capacity of cross-linked C-(N-)A-S-H to structurally incorporate Al. Increasing the Al content of cross-linked C-(N-)A-S-H gels may not necessarily induce increased polymerisation.

These results, and the methods for analysis of $^{29}$Si and $^{27}$Al MAS NMR spectra developed here, will have significant implications for the ways in which AAS

cements and blended PC/Al-containing SCM materials are described, understood and modelled.

# 6

# Thermodynamic Model for C-(N-)A-S-H: Derivation and Validation

This chapter is based on the paper 'A Thermodynamic Model for C-(N-)A-S-H Gel: CNASH_ss. Derivation and Validation', published in *Cement Concrete Research* **2014**, *66*, 27-47.

## 6.1 Introduction

A key factor governing the long-term performance of any cement or concrete is the stability of the reaction products constituting the solid binder. The chemistry of the reaction products in hydrated neat PC materials is relatively well established (Taylor, 1997), and these cements can be accurately modelled at equilibrium (Lothenbach et al., 2008b; Lothenbach and Winnefeld, 2006) using existing thermodynamic models for C-S-H gel (Kulik, 2011; Kulik and Kersten, 2001).

However, the existing descriptions of PC/SCM blended cements (Atkins et al., 1994; Lothenbach et al., 2011) and AAS cements (Ben Haha et al., 2012) at equilibrium are not as accurate. This is partly because empirical descriptions of Al substitution in C-(N-)A-S-H gels (e.g. by attributing amounts of Al to these gels to match experimentally measured Al/Si values of the solid binders in the materials), or no description of Al uptake into this phase, have been utilised in the modelling performed. These methods have been used because existing C-S-H thermodynamic

model formulations do not contain explicit definitions of Al (Atkins et al., 1992a; Berner, 1992; Kulik, 2011; Kulik and Kersten, 2001; Walker et al., 2007). The ability to formally account for the extent of Al incorporation into these models is important because it offers scope to significantly improve the level of detail and confidence in predictions of the solid phases formed in the $CaO$-$Al_2O_3$-$SiO_2$-$H_2O$ system as simulated by thermodynamic modelling. Hence, the development of thermodynamic models with explicit descriptions of Al in C-(N-)A-S-H signifies an important advancement in how cementitious materials are modelled and understood.

Here, a thermodynamic model is proposed to account explicitly for the tetrahedral Al and Na species bound in C-(N-)A-S-H gel, and applied to simulate the chemistry of AAS cements as an initial example. This model may also be applicable to high-volume blended PC/SCM materials (e.g. CEM III blast furnace cements specified under the EN 197-1 standard) because the structurally-bound Al and alkali species are specified independently in the model formulation, and because the C-(N-)A-S-H gels formed in these materials and in AAS cements are similar in nanostructure and chemical composition (Lothenbach et al., 2011).

## 6.2 Sublattice Solid Solution Model for C-(N-)A-S-H

### 6.2.1 Sublattice Solid Solution Definition

There exist several structural models that can describe C-S-H gels, as reviewed in detail by Richardson (Richardson, 2004; 2008). However, only the 'Substituted General Model' (SGM) (Richardson and Groves, 1993b) and the 'Cross-linked Substituted Tobermorite Model' (CSTM) (Chapter 4) (Myers et al., 2013), can explicitly account for Al-substituted, alkali charge-balanced structures such as C-(N-)A-S-H using a fully flexible formulation of the gel chemistry. For $Ca/Si \leq 1.5$ the treatments of non-cross-linked C-(N-)A-S-H gel components in the SGM and the CSTM are identical, with structural incorporation of Al and charge-balancing by positively-charged interlayer species such as $Na^+$. These structural models can be

used to constrain thermodynamic models because they provide a structurally-consistent basis from which chemical compositions of C-(N-)A-S-H end-members can be determined.

Cross-linked and non-cross-linked C-(N-)A-S-H structures cannot always be distinguished from one another by bulk chemical composition alone, which complicates the ability to differentiate between these two structural types in thermodynamic models for this phase. Therefore, the SGM has been used as a basis from which to derive the chemical composition of the C-(N-)A-S-H gel here explicitly in terms of non-cross-linked structures, without precluding the possibility that the thermodynamic model may also implicitly represent the bulk chemistry of cross-linked C-(N-)A-S-H. It is also important to note that the C-S-H gel models derived by Kulik (2011) used the 'General Model' (GM) developed by Richardson and Groves (1992b), which is a simpler model related to the SGM. The notation used by Kulik (2011) and Richardson and Groves (1993b) has been conserved where possible for clarity.

Derivation of the C-(N-)A-S-H thermodynamic model begins by rearranging the SGM (eq.(2.2), (Richardson and Groves, 1993b)) into an alternative structural form, by normalising eq.(2.2) to a basis of one dreierketten unit by dividing by *n*, expressed in terms of *w* and *n* for *X* and *z*, and then simplified to obtain eq.(6.1):

$$Ca_{\left(3-\frac{w}{2n}\right)}H_{\left(\frac{w}{n}\right)}O_{\left(9-\frac{2}{n}\right)}\cdot\left(Si_{(1-a_0)}R_{a_0}\right)_{\left(3-\left(\frac{1}{n}\right)\right)}\cdot l^{c+}_{\frac{a_0}{c}\left(3-\frac{1}{n}\right)}\cdot\left(\frac{w}{2n}-\frac{y}{2}-1\right)Ca(OH)_2\cdot\left(\frac{m}{n}\right)H_2O \quad (6.1)$$

The following notation is now introduced into eq.(6.1): $v = 1/n$ ($0 \leq v \leq 1$), defines the ratio of chains per dreierketten unit, which is a measure of the number of vacant bridging tetrahedra; $u = w/n$, the content of chemically incorporated (hydroxyl) water per dreierketten unit; and $h = m/n$, the bound water content. The introduction of this notation results in eq.(6.2):

$$Ca_{\left(3-\frac{u}{2}\right)}H_uO_{(9-2\nu)}\cdot\left(Si_{(1-a_0)}R_{a_0}\right)_{(3-\nu)}\cdot l^{c+}_{\frac{a_0}{c}(3-\nu)}\cdot\left(\frac{u}{2}-\frac{y}{2}-1\right)Ca(OH)_2\cdot hH_2O \qquad (6.2)$$

Eq.(6.2) is then re-written to isolate two distinct sublattice sites within the chain structure, being a 'main chain dreierketten unit' (*TU*) and a 'bridging tetrahedral unit' (*BT*). This leads to a subtle change in the substitution parameter, $a_0$, which is now written as $a$, the extent of substitution in bridging sites. The resulting equation is:

$$\left[Ca(OH)_2\right]_{\left(\frac{u+y-2}{2}\right)}\cdot\left[\left(CaSiO_{3.5}\right)_2^-\right]\cdot \left[\left(Si_{(1-a)}R_aO_2\right)_{(1-\nu)}\right]^{a(1-\nu)-}\cdot\left[\left(l^{c+}_{\frac{a}{c}(1-\nu)}\right)\right]^{a(1-\nu)+}\cdot\left[Ca_{\left(1-\frac{u}{2}\right)}H_u\right]^{2+}\cdot hH_2O \qquad (6.3)$$

Eq.(6.3) is then represented in terms of one dreierketten unit in eq.(6.4):

$$\left[\mathrm{Ca(OH)_2}\right]_{\left(\frac{u+y-2}{2}\right)}\cdot\left[\left(\mathrm{CaSiO_{3.5}}\right)_2^-\right]\cdot \left[\left(\mathrm{Si}_{(1-a)}R_a\mathrm{O}_2\right)_{(1-\nu)}\right]^{a(1-\nu)-}\cdot\left[\left(l^{c+}_{\frac{a}{c}(1-\nu)}\right)\right]^{a(1-\nu)+}\cdot\left[\mathrm{Ca}_{\left(1-\frac{u}{2}\right)}\mathrm{H}_u\right]^{2+}\cdot h\mathrm{H_2O} \qquad (6.4)$$

where $R$ is a trivalent cation in tetrahedral coordination (e.g. $Al^{3+}$), $l$ is a charge-balancing interlayer cation (such as $Na^+$, $Ca^{2+}$ and/or $H^+$) with a positive charge of $c$, $a$ is the extent of $R$ substitution in bridging sites (Figure 6.1), $\nu$ is the fraction of bridging site vacancies per dreierketten unit, $u$ is the interlayer $H^+$ content per dreierketten unit for the main chain sites (*TU*, $CaSiO_{3.5}^-$), and $h$ defines the amount of water per dreierketten unit. The SGM explicitly defines Al substitution in bridging sites only, and excludes Al-O-Al bonding, consistent with Loewenstein's rule (Loewenstein, 1954).

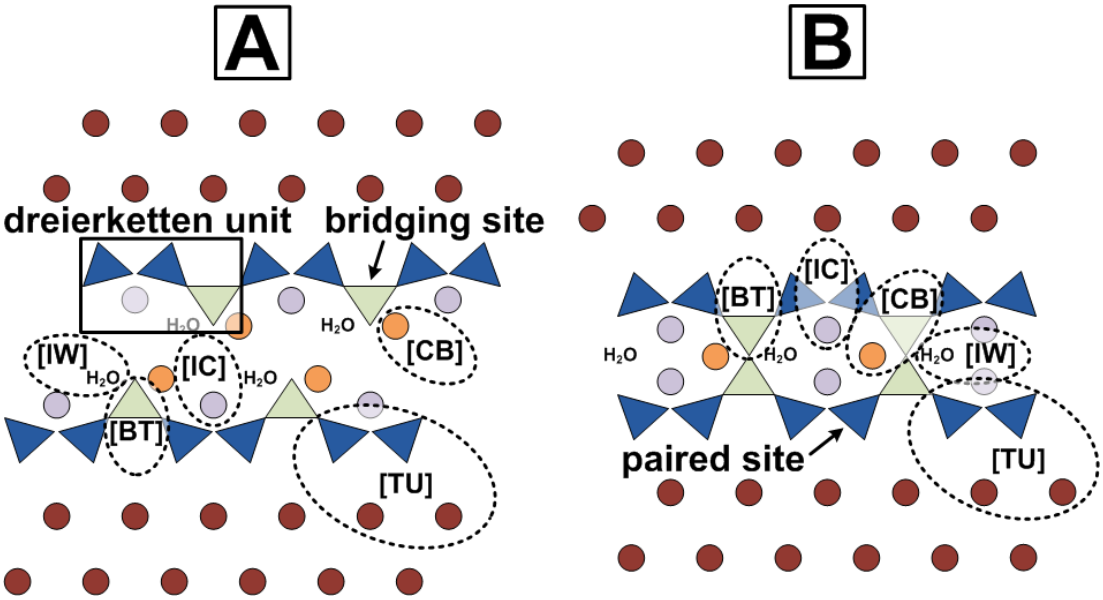


Figure 6.1. Schematic representations of infinite chain length non-cross-linked A) and crosslinked B) C-(N-)A-S-H structures, with sublattice sites labelled: *TU*; *BT*; *CB*; *IC*; *IW*, as defined in the text (eqs.(6.5,6.7)). Light green and dark blue triangles are paired and bridging tetrahedral sites respectively, dark red circles represent Ca sites in the Ca-O sheets, and the orange and purple circles are positively charged species (typically $Ca^{2+}$, $H^{+}$, $Na^{+}$ and/or $K^{+}$) that charge-balance the aluminosilicate tetrahedra in the BT and TU sites respectively.

Eq.(6.4) can be equivalently written in sublattice notation as eq.(6.5):

$$\left[CU\right]_2 \cdot \left[TU^{-}\right]_2 \cdot \left[BT^{a(1-\nu)-}\right]_1 \cdot \left[CB^{a(1-\nu)+}\right]_1 \cdot \left[IC^{2+}\right]_1 \cdot \left[IW\right]_h \qquad (6.5)$$

where *CU* represents interstitial 'solid solution' $Ca(OH)_2$ (Richardson and Groves, 1992b), *BT* are the bridging tetrahedra ($Si_{(1-a)}R_aO_{2(1-\nu)}^{\ a(1-\nu)-}$), *CB* are the interlayer charge-balancing species for the bridging tetrahedra ($l_{a(1-\nu)/c}^{\ a(1-\nu)+}$), *IC* are the interlayer charge-balancing species for the *TU* sites ($Ca_{(1-u/2)}H_u^{\ 2+}$), and *IW* represents interlayer water ($H_2O$). The *CU* sites in tobermorite are vacant (there is no interstitial 'solid solution' $Ca(OH)_2$), and are therefore eliminated from the structural definition in eqs.(6.4-6.5). This limits the chemical composition of the sublattice solid solution model to $0.67 \leq Ca/Si \leq 1.5$ and leads to eqs.(6.6-6.7):

$$\left[\left(\mathrm{CaSiO_{3.5}}\right)_2^-\right]\cdot\left[\left(\mathrm{Si}_{(1-a)}R_a\mathrm{O}_2\right)_{(1-\nu)}\right]^{a(1-\nu)-}\cdot\left[\left(l^{c+}_{\frac{u}{c}(1-\nu)}\right)\right]^{a(1-\nu)+}\cdot\left[\mathrm{Ca}_{\left(1-\frac{u}{2}\right)}\mathrm{H}_u\right]^{2+}\cdot h\mathrm{H_2O} \quad (6.6)$$

$$\left[TU^-\right]_2\cdot\left[BT^{a(1-\nu)-}\right]_1\cdot\left[CB^{a(1-\nu)+}\right]_1\cdot\left[IC^{2+}\right]_1\cdot\left[IW\right]_h \quad (6.7)$$

This elimination of $Ca(OH)_2$ therefore provides the major limitation on the domain of applicability of the model described here; it is not able to be used for Ca/Si ratios > 1.5, but is valuable for alkali-activated cements and blended PC/SCM materials in which the composition of the C-(N-)A-S-H gel formed falls below this ratio. The sublattice sites shown in eq.(6.7) are illustrated in Figure 6.1.

The *IC* sites are now modified to enable the *TU* sites to be charge-balanced by $Na^+$ species in addition to the *BT* sites. The possible interlayer charge-balancing species in C-(N-)A-S-H gel are not limited to $Ca^{2+}$, $H^+$ and $Na^+$, but these are the only species for which sufficient data have been published to enable validation of the thermodynamic model developed here. Na-based solutions are also the most relevant alkaline activators for commercial use because they are relatively inexpensive and widely available (Shi et al., 2006). The *BT* sites in C-(N-)A-S-H are mostly filled by vacancies, Si and/or Al species, meaning that *R* = Al can also be specified. Eq.(6.6) is re-written with the modified *IC* sites and with similarly modified *CB* sites, and with Al-substitution in the *BT* sites, which results in eq.(6.8):

$$\left[\left(\mathrm{CaSiO_{3.5}}\right)_2^-\right]\cdot \left[\left(\mathrm{Si}_{(1-a)}\mathrm{Al}_a\mathrm{O}_2\right)_{(1-\nu)}\right]^{a(1-\nu)-}\cdot\left[\left(\mathrm{Ca}_{\left(\frac{1-d_1-d_2}{2}\right)}\mathrm{H}_{d_1}\mathrm{Na}_{d_2}\right)_{a(1-\nu)}\right]^{a(1-\nu)+}\cdot\left[\mathrm{Ca}_{\left(\frac{2-e_1-e_2}{2}\right)}\mathrm{H}_{e_1}\mathrm{Na}_{e_2}\right]^{2+}\cdot h\mathrm{H_2O} \quad (6.8)$$

where $d_1 + d_2 \leq 1$ and $e_1 + e_2 \leq 2$.

While eqs.(6.7-6.8) are satisfactory for thermodynamic modelling, it is desirable to obtain a thermodynamic model which is consistent with existing validated

formulations such as the downscaled CSH3T model (Kulik, 2011). In that model, the *BT*, *CB* and *IC* sites are combined into two potentially-equivalent *BCI* sites that could have different substitutions via the choice of two sublattice species, and the sublattice formula was 'downscaled' to 0.5 dreierketten units. The use of two such sites, rather than a single *BCI* site, is beneficial because it increases the number of unique chemical compositions that can be represented by the sublattice solid solution and can greatly improve the fit of the thermodynamic model output to the validation data (e.g. solubility measurements) for the same set of mixing rules used (e.g. simple random ideal mixing). However, this means that end-member stoichiometries, and sublattice species and formulae are more likely to be represented in terms of fractional quantities rather than integer amounts. Fractional expressions obviously cannot directly correspond to atomistic-level structures, which means that thermodynamic models developed in this way can only describe the chemistry of solid solutions on the bulk scale rather than at the atomistic scale. Therefore, downscaling is useful in the development of thermodynamic models to describe complex phases such as C-(N-)A-S-H with atomistic structures that have not yet been fully resolved. Here, downscaling is essential to improve the number of unique chemical compositions and the volume of experimental data described by the sublattice solid solution model while keeping its formulation relatively simple, particularly because this model is required to describe C-(N-)A-S-H chemistry in the complex AAS cement system. The downscaled chemical and sublattice formulae (to 0.5 dreierketten units), written in terms of potentially-equivalent *BCI* sites (*BCI = BT + CB + IC*) and thus consistent with the downscaled CSH3T model (Kulik, 2011), are shown in eqs.(6.9-6.10) respectively:

$$\left[\mathrm{CaSiO_{3.5}}\right]^{-} \cdot \left[\left\{\left(\mathrm{Si}_{(1-a)}\mathrm{Al}_{a}\mathrm{O}_{2}\right)_{\frac{(1-\nu)}{2}} \cdot \left(\mathrm{Ca}_{\left(\frac{1-d_1-d_2}{2}\right)}\mathrm{H}_{d_1}\mathrm{Na}_{d_2}\right)_{\frac{a(1-\nu)}{2}} \cdot \left(\mathrm{Ca}_{\left(\frac{2-e_1-e_2}{2}\right)}\mathrm{H}_{e_1}\mathrm{Na}_{e_2}\right)_{\frac{1}{2}}\right\}_{\frac{1}{2}}^{0.5+}\right]_2 \cdot \left[\left(\frac{h}{2}\right)\mathrm{H_2O}\right] \tag{6.9}$$

$$\left[TU^{-}\right]_1 \cdot \left[BCI^{0.5+}\right]_1 \cdot \left[BCI^{0.5+}\right]_1 \cdot \left[IW\right]_{\frac{h}{2}} \tag{6.10}$$

Here, at least one additional (Al,Na)-containing sublattice species is necessary to represent C-(N-)A-S-H chemistry, compared to previous thermodynamic models for the $CaO$-$SiO_2$-$H_2O$ system. Increasing the number of sublattice species and sites allows the description of a greater diversity of bulk C-(N-)A-S-H gel chemical compositions, and facilitates independent incorporation of Na and Al in C-S-H type structures. Additionally, as the quantities of bound water in C-(N-)A-S-H and C-S-H gels are significantly different (Allen et al., 2007; Thomas et al., 2012), it is also necessary to allow for variation in the *IW* site. Here, C-(N-)A-S-H is assumed to contain one mole of $H_2O$ in the *IW* site per 0.5 dreierketten units ($h = 2$), because this is approximately equal to the chemistry of 11 Å and 14 Å tobermorites (Bonaccorsi et al., 2005; Merlino et al., 2001) and the C-(N-)A-S-H gels formed in AAS cements ($H_2O/Si \approx 1$) (Thomas et al., 2012).

These factors thus require the use of a sixth-order sublattice solid solution for the C-(N-)A-S-H thermodynamic model developed here. This solid solution contains five *BCI* sites, with each carrying a positive charge of 0.125 and grouped as shown in eqs.(6.11-6.12), and one variable *IW* site:

$$\left[CaSiO_{3.5}\right]^{-}\cdot\left[H_2O\right]\cdot \left[\left\{\left(Si_{(1-a)}Al_aO_2\right)_{\frac{(1-v)}{2}}\cdot\left(Ca_{\left(\frac{1-d_1-d_2}{2}\right)}H_{d_1}Na_{d_2}\right)_{\frac{a(1-v)}{2}}\cdot\left(Ca_{\left(\frac{2-e_1-e_2}{2}\right)}H_{e_1}Na_{e_2}\right)_{\frac{1}{2}}\right\}^{0.125+}_{\frac{1}{8}}\right]_8\cdot\left[\left(\frac{h}{2}-1\right)H_2O\right] \tag{6.11}$$

$$\left[TU^{-}\right]_1\cdot\left[IW^{*}\right]_1\cdot \left[BCI^{0.125+}\right]_2\cdot\left[BCI^{0.125+}\right]_2\cdot\left[BCI^{0.125+}\right]_2\cdot\left[BCI^{0.125+}\right]_1\cdot\left[BCI^{0.125+}\right]_1\cdot\left[IW\right]_1 \tag{6.12}$$

where $IW^{*}$ represents a fixed interlayer water site (with full occupancy of $H_2O$ but otherwise identical to the *IW* site depicted in Figure 6.1). Eqs.(6.11-6.12) are the fundamental formulae that represent the C-(N-)A-S-H thermodynamic model developed here.

### 6.2.2 End-Member Selection

As discussed in section 6.1, a goal of this study is to develop a sublattice solid solution model that can describe the solubility and chemical composition of C-(N-)A-S-H in AAS cements. Based on the sublattice solid solution definition established in eqs.(6.11-6.12), it is now necessary to select a set of end-members, sublattice sites and species that can represent the chemistry of C-(N-)A-S-H gel.

Six species that can substitute into the five *BCI* sites given in eq.(6.12), and which are compatible with the chemical formula for these sites (eq.(6.11)) and the chemistry of C-(N-)A-S-H in AAS cements, were selected to represent a sublattice solid solution of the form shown in eq.(6.13):

$$Q^{*}\left[A,B,C,D,E\right]_{\mathrm{I}}^{n_1}\left[F,G,H,I,J\right]_{\mathrm{II}}^{n_2}\left[K,L,M\right]_{\mathrm{III}}^{n_3}\left[N,O,P,Q,R,S\right]_{\mathrm{IV}}^{n_4}\left[T,U,V,W\right]_{\mathrm{V}}^{n_5}\left[X,Y\right]_{\mathrm{VI}}^{n_6} \tag{6.13}$$

Here, species *A,F,K,N,T* are $Ca_{0.0625}O_{0.0625}H_{0.125}^{0.125+}$, *B,G,L,O,U* are $Si_{0.0625}O_{0.125}H_{0.125}^{0.125+}$ and *D,I,M,Q,V* are $Si_{0.0625}O_{0.125}Na_{0.125}^{0.125+}$, which can be present in five different *BCI* sites, the species *C,H,P* are $Al_{0.0625}O_{0.125}H_{0.1875}^{0.125+}$ and *E,J,R* are $Al_{0.0625}Na_{0.0625}O_{0.125}H_{0.125}^{0.125+}$, which can fill four of the *BCI* sites, the species *S,W* are $Ca_{0.0625}O_{0.0625}Na_{0.125}^{0.125+}$, which can fill two of the *BCI* sites, *X* is $H_2O$, *Y* is a vacancy ($V_{IW}$), and $Q^{*}$ is $CaSiO_{3.5}^{-}\cdot H_2O$. This combination of sublattice sites and species was chosen as it comprises the least complex formulation of the sublattice solid solution that can represent the chemistry of C-(N-)A-S-H in AAS cements. In this work the coefficients I=2, II=2, III=2, IV=1, V=1 and VI=1 define the stoichiometry of the sublattice sites, and the superscripts $n_1$, $n_2$, $n_3$, $n_4$, $n_5$ and $n_6$ correspond to the five *BCI* sites and single *IW* site in eq.(6.12). Vacancies in *BCI* sites are included in the thermodynamic model via the *v* parameter in eq.(6.11).

A minimal set of eight end-members was chosen within this sublattice solid solution model to define the C-(N-)A-S-H gel in this work, as shown in Table 6.1. This is the smallest number of end-members that can resemble the chemistry of C-(N-)A-S-H gels (section 2.1.3) and describe the available solubility data for AAS cement and the $CaO$-($Na_2O$,$Al_2O_3$)-$SiO_2$-$H_2O$ systems (section 6.4). The solid solution contains three C-S-H end-members, one C-(N-)S-H end-member, two C-A-S-H end-members and two C-(N-)A-S-H end-members. The C-S-H end-members have the same chemical compositions as the T2C, T5C and TobH end-members of the downscaled CSH3T model (T2C*, T5C* and TobH* respectively) (Kulik, 2011), which contain the *TU* site, $h = 4$, and two *BCI* sublattice species, $Si_{0.25}O_{0.5}H_{0.5}^{+}$ and $Ca_{0.25}O_{0.25}H_{0.5}^{+}$, for $a = 0$, to cover the range $0.67 \leq Ca/Si \leq 1.5$ in the $CaO$-$SiO_2$-$H_2O$ system. One $H_2O$ molecule is also added per vacancy in the bridging tetrahedra for each of the eight end-members (determined by the value of $v$).

Table 6.1. Chemical compositions of the eight end-members of the C-(N-)A-S-H thermodynamic model, and parameters chosen for use in eq.(6.11). One $H_2O$ molecule is added to the *BCI* site per bridging site vacancy for consistency with the C-S-H thermodynamic model developed by Kulik (2011).

| **End- member** | ***v*** | ***a*** | $i_1$ | $i_2$ | $u_1$ | $u_2$ | ***M*** | **Chemical formula** |
|---|---|---|---|---|---|---|---|---|
| 5CA | 0.5 | 1 | 1 | 0 | 1 | 0 | 2 | $(CaO)_{1.25}(Al_2O_3)_{0.125}(SiO_2)_1(H_2O)_{1.625}$ |
| INFCA | 0 | 0.625 | 1 | 0 | 2 | 0 | 2 | $(CaO)_1(Al_2O_3)_{0.15625}(SiO_2)_{1.1875}(H_2O)_{1.65625}$ |
| 5CNA | 0.5 | 1 | 0 | 1 | 0.5 | 0.5 | 2 | $(CaO)_{1.25}(Na_2O)_{0.25}(Al_2O_3)_{0.125}(SiO_2)_1(H_2O)_{1.375}$ |
| INFCNA | 0 | 0.625 | 0 | 1 | 1.25 | 0.75 | 2 | $(CaO)_1(Na_2O)_{0.34375}(Al_2O_3)_{0.15625}(SiO_2)_{1.1875}(H_2O)_{1.3125}$ |
| INFCN | 0 | 0 | 1 | 0 | 0.75 | 1.25 | 2 | $(CaO)_1(Na_2O)_{0.3125}(SiO_2)_{1.5}(H_2O)_{1.1875}$ |
| T2C* [a] | 1 | 0 | 0 | 0 | 0 | 0 | 4 | $(CaO)_{1.5}(SiO_2)_1(H_2O)_{2.5}$ |
| T5C* [a] | 0.5 | 0 | 0 | 0 | 1 | 0 | 4 | $(CaO)_{1.25}(SiO_2)_{1.25}(H_2O)_{2.5}$ |
| TobH* [a] | 0 | 0 | 0 | 0 | 2 | 0 | 4 | $(CaO)_1(SiO_2)_{1.5}(H_2O)_{2.5}$ |

[a] The asterisks for the T2C*, T5C* and TobH* end-members indicate that these components have the same bulk chemistry but slightly modified thermodynamic properties relative to the T2C, T5C and TobH end-members of the downscaled CSH3T model (Kulik, 2011).

Table 6.1. Continued.

| End- member | Sublattice formula [b] |
|---|---|
| 5CA | $[(CaSiO_{3.5})^{-}]_1 \cdot [H_2O]_1 \cdot [Al_{0.0625}O_{0.125}H_{0.1875}^{0.125+}]_2 \cdot [Al_{0.0625}O_{0.125}H_{0.1875}^{0.125+}]_2 \cdot [Ca_{0.0625}O_{0.0625}H_{0.125}^{0.125+}]_2 \cdot [Ca_{0.0625}O_{0.0625}H_{0.125}^{0.125+}]_1 \cdot [Ca_{0.0625}O_{0.0625}H_{0.125}^{0.125+}]_1 \cdot [V_{H2O}]_1$ |
| INFCA | $[(CaSiO_{3.5})^{-}]_1 \cdot [H_2O]_1 \cdot [Al_{0.0625}O_{0.125}H_{0.1875}^{0.125+}]_2 \cdot [Al_{0.0625}O_{0.125}H_{0.1875}^{0.125+}]_2 \cdot [Si_{0.0625}O_{0.125}H_{0.125}^{0.125+}]_2 \cdot [Al_{0.0625}O_{0.125}H_{0.1875}^{0.125+}]_1 \cdot [Si_{0.0625}O_{0.125}H_{0.125}^{0.125+}]_1 \cdot [V_{H2O}]_1$ |
| 5CNA | $[(CaSiO_{3.5})^{-}]_1 \cdot [H_2O]_1 \cdot [Al_{0.0625}Na_{0.0625}O_{0.125}H_{0.125}^{0.125+}]_2 \cdot [Al_{0.0625}Na_{0.0625}O_{0.125}H_{0.125}^{0.125+}]_2 \cdot [Ca_{0.0625}O_{0.0625}H_{0.125}^{0.125+}]_2 \cdot [Ca_{0.0625}O_{0.0625}Na_{0.125}^{0.125+}]_1 \cdot [Ca_{0.0625}O_{0.0625}Na_{0.125}^{0.125+}]_1 \cdot [V_{H2O}]_1$ |
| INFCNA | $[(CaSiO_{3.5})^{-}]_1 \cdot [H_2O]_1 \cdot [Al_{0.0625}Na_{0.0625}O_{0.125}H_{0.125}^{0.125+}]_2 \cdot [Al_{0.0625}Na_{0.0625}O_{0.125}H_{0.125}^{0.125+}]_2 \cdot [Si_{0.0625}O_{0.125}Na_{0.125}^{0.125+}]_2 \cdot [Al_{0.0625}Na_{0.0625}O_{0.125}H_{0.125}^{0.125+}]_1 \cdot [Si_{0.0625}O_{0.125}Na_{0.125}^{0.125+}]_1 \cdot [V_{H2O}]_1$ |
| INFCN | $[(CaSiO_{3.5})^{-}]_1 \cdot [H_2O]_1 \cdot [Si_{0.0625}O_{0.125}Na_{0.125}^{0.125+}]_2 \cdot [Si_{0.0625}O_{0.125}Na_{0.125}^{0.125+}]_2 \cdot [Si_{0.0625}O_{0.125}H_{0.125}^{0.125+}]_2 \cdot [Si_{0.0625}O_{0.125}Na_{0.125}^{0.125+}]_1 \cdot [Si_{0.0625}O_{0.125}H_{0.125}^{0.125+}]_1 \cdot [V_{H2O}]_1$ |
| T2C* [a] | $[(CaSiO_{3.5})^{-}]_1 \cdot [H_2O]_1 \cdot [Ca_{0.0625}O_{0.0625}H_{0.125}^{0.125+}]_2 \cdot [Ca_{0.0625}O_{0.0625}H_{0.125}^{0.125+}]_2 \cdot [Ca_{0.0625}O_{0.0625}H_{0.125}^{0.125+}]_2 \cdot [Ca_{0.0625}O_{0.0625}H_{0.125}^{0.125+}]_1 \cdot [Ca_{0.0625}O_{0.0625}H_{0.125}^{0.125+}]_1 \cdot [H_2O]_1$ |
| T5C* [a] | $[(CaSiO_{3.5})^{-}]_1 \cdot [H_2O]_1 \cdot [Si_{0.0625}O_{0.125}H_{0.125}^{0.125+}]_2 \cdot [Si_{0.0625}O_{0.125}H_{0.125}^{0.125+}]_2 \cdot [Ca_{0.0625}O_{0.0625}H_{0.125}^{0.125+}]_2 \cdot [Ca_{0.0625}O_{0.0625}H_{0.125}^{0.125+}]_1 \cdot [Ca_{0.0625}O_{0.0625}H_{0.125}^{0.125+}]_1 \cdot [H_2O]_1$ |
| TobH* [a] | $[(CaSiO_{3.5})^{-}]_1 \cdot [H_2O]_1 \cdot [Si_{0.0625}O_{0.125}H_{0.125}^{0.125+}]_2 \cdot [Si_{0.0625}O_{0.125}H_{0.125}^{0.125+}]_2 \cdot [Si_{0.0625}O_{0.125}H_{0.125}^{0.125+}]_2 \cdot [Si_{0.0625}O_{0.125}H_{0.125}^{0.125+}]_1 \cdot [Si_{0.0625}O_{0.125}H_{0.125}^{0.125+}]_1 \cdot [H_2O]_1$ |

[b] $V_{H2O}$ is a vacancy in the *IW* sublattice site.

As each species (*A* to *Y*) is defined to only substitute into one site (i.e., species with the same chemistry but occupying different sites are treated as being distinct), the site fraction of a species $i$ in a given site $n_s$, $y_i^{n_s}$, is defined as $y_i^{n_s} = \sum\left(\chi_k^{i,n_s}\right)$ for $\sum\left(y_i^{n_s}\right) = 1$. Here $n_s \in \{n_1, n_2, n_3, n_4, n_5, n_6\}$ is the sublattice site, $\chi_k^{i,n_s}$ is the effective mole fraction of end-member $k$ containing the species $i$ in the sublattice site $n_s$, with $\sum_k(\chi_k) = 1$. In defining an end-member of the sublattice solid solution model, the species present in the $s^{th}$ sublattice site may be identified by the same subscript number i.e. $i_1$ is the species present in the sublattice site $n_1$, and $i_1 \in \{A, B, C, D, E\}$. Thus an end-member can be equivalently written in terms of its substituting species, i.e. $k = i_1 i_2 i_3 \cdots i_s$.

The chain length (*CL*) for each of the end-members, and the MCL of the C-(N-)A-S-H gel as a whole, can then be calculated from eq.(6.14).

$$CL = \frac{3}{\sum_k(\chi_k \nu_k)} - 1 \tag{6.14}$$

The fraction of bridging site vacancies per dreierketten unit, $v$, is shown in Table 6.1 for each end-member of the C-(N-)A-S-H thermodynamic model. This equation represents the minimum chain length possible for the end-members, and thus the minimum MCL of the C-(N-)A-S-H gel, because eq.(6.14) implies that the end-members are strictly non-cross-linked. The chain lengths of cross-linked C-(N-)A-S-H end-members would be calculated in the same way, but with a factor of two included (i.e. $CL_{cross\text{-}linked} = 2CL$) to reflect the double chain structures in these phases. Here, these cross-linked and non-cross-linked structures were not explicitly differentiated in defining the end-members (eqs.(6.11-6.12)), meaning that eq.(6.14) provides a lower bound on the MCLs of partially (or fully) cross-linked C-(N-)A-S-H gels.

### 6.2.3 Thermodynamic Basis of the Sublattice Solid Solution Model

The chemical potential (partial molal Gibbs free energy), $\mu_{i_1 i_2 i_3 \cdots i_s}$, of end-member $i_1 i_2 i_3 \cdots i_s$ in a multi-component solid solution can be represented by eq.(6.15) (Hillert, 1998):

$$\mu_{i_1 i_2 i_3 \cdots i_s} = G_m + \left[ \frac{\partial G_m}{\partial y_{i_1}^{n_1}} + \frac{\partial G_m}{\partial y_{i_2}^{n_2}} + \frac{\partial G_m}{\partial y_{i_3}^{n_3}} + \cdots + \frac{\partial G_m}{\partial y_{i_s}^{n_s}} \right] - \left[ \sum_i \left( y_i \frac{\partial G_m}{\partial y_i} \right) \right] \quad (6.15)$$

where $G_m$ is the Gibbs free energy of mixing using the notation previously introduced, and can be expressed by eq.(2.15) (section 2.2.2).

Here, the 'compound energy formalism' is used to define the surface of reference for the Gibbs free energy of mixing as a weighted average of the Gibbs free energy of each of the (pure) end-members in the C-(N-)A-S-H solid solution (Hillert, 1998). This is formally expressed by eq.(6.16) for a multi-site, multi-component sublattice solid solution, assuming random mixing within each sublattice (Andersson et al., 1986):

$$\begin{aligned} G_m = & \left[ \sum_{n_1} \sum_{n_2} \sum_{n_3} \cdots \sum_{n_s} \left( y_{i_1}^{n_1} y_{i_2}^{n_2} y_{i_3}^{n_3} \cdots y_{i_s}^{n_s} \right) \cdot {}^{o}G_{i_1 i_2 i_3 \cdots i_s} \right] + \\ & RT \left[ \mathrm{I} \sum_{i_1} \left( y_{i_1} \ln\left( y_{i_1} \right) \right) + \mathrm{II} \sum_{i_2} \left( y_{i_2} \ln\left( y_{i_2} \right) \right) + \mathrm{III} \sum_{i_3} \left( y_{i_3} \ln\left( y_{i_3} \right) \right) + \cdots + \zeta \sum_{i_s} \left( y_{i_s} \ln\left( y_{i_s} \right) \right) \right] + G_m^E \end{aligned} \quad (6.16)$$

where ${}^{o}G_{i_1 i_2 i_3 \cdots i_s}$ is the standard Gibbs free energy of end-member $i_1 i_2 i_3 \cdots i_s$, $R$ is the universal gas constant, $T$ is temperature and $\zeta$ is the stoichiometric coefficient of the $s^{\text{th}}$ sublattice site. The random mixing assumption is appropriate here because it greatly simplifies the expression for the configurational entropy and because the solid solution definition (eqs.(6.11-6.12)) does not represent atomic-scale structures; assigning hypothetical weightings to non-physical mixing combinations would not

make physical sense. This choice is reasonable given that this is the first attempt to develop a sublattice solid solution model for C-(N-)A-S-H gel, and will be validated in section 6.4 through the ability of the model to accurately describe chemical composition and solubility data for this phase.

Eq.(6.16) can be expanded explicitly for the sublattice solid solution defined by the eight end-members shown in Table 6.1. Substituting this expanded version of eq.(6.16) into eq.(6.15), defining a generalised end-member with species *A, F, K, N, T, X* in sublattice sites $n_1$, $n_2$, $n_3$, $n_4$, $n_5$, $n_6$ and then simplifying, results in eq.(6.17):

$$\mu_{AFKNTX} = {}^{o}G_{AFKNTX} + RT\left[2\ln\left(y_A\right)+2\ln\left(y_F\right)+2\ln\left(y_K\right)+\ln\left(y_N\right)+\ln\left(y_T\right)+\ln\left(y_X\right)\right]+G_m^E+U \quad (6.17)$$

Equivalent relationships for $\mu_{AFKNTX}$ can be written for all other combinations of sublattice site occupancies. The *U* term contains the Gibbs free energies for the reciprocal reactions ($\Delta_{rcp}{}^{o}G$), which denotes the difference in Gibbs free energy between combinations of end-members in the sublattice solid solution (which must by definition contain equal numbers of reactant and product terms). For example, the reciprocal reaction (eq.(6.18)) has a corresponding Gibbs free energy of reaction given by eq.(6.19):

$$AFKOTX + AFLNTX \leftrightarrow AFKNTX + AFLOTX \quad (6.18)$$

$$\Delta_{rcp}{}^{o}G_{LO} = {}^{o}G_{AFKOTX} + {}^{o}G_{AFLNTX} - {}^{o}G_{AFKNTX} - {}^{o}G_{AFLOTX} \quad (6.19)$$

It is possible to make two key simplifications here. The first is setting $G_m{}^E = 0$, i.e. interactions between atoms in the same sublattice sites are neglected, meaning that the sublattice solid solution model is ideal. The second is that the Gibbs free energies of the reciprocal reactions in the solid solution are numerically approximated to zero

($U$ = 0). The reciprocal reaction terms describe the nearest-neighbour interactions in the solid solution, so are likely to influence end-member chemical potentials more than the next-nearest-neighbour interactions described by the excess Gibbs free energy terms. These terms are likely to be non-zero in C-(N-)A-S-H gels, because it is known that thermodynamic energetic differences arise from nearest-neighbour Si-Al substitution in aluminosilicate systems (Provis et al., 2005a), but this approach can be validated by the good fit of the thermodynamic model to the published solubility and chemical composition data in the CaO-($Na_2O$,$Al_2O_3$)-$SiO_2$-$H_2O$ systems (section 6.4). In defining the mixing rules in this way, the accuracy of the thermodynamic model is determined semi-empirically through the use of end-members with carefully selected chemical compositions and Gibbs free energies that internalise the nearest and next-nearest neighbour interactions in C-(N-)A-S-H gels, rather than through the explicit definition of these interactions. However, quantification of these interactions in terms of chemical potentials for hypothetical C-(N-)A-S-H end-members, and a better understanding of the solubility of C-(N-)A-S-H gels, will be important future steps in the model development.

Application of these assumptions to eq.(6.17) leads to the final, simplified formula for the chemical potential of an end-member in the C-(N-)A-S-H sublattice solid solution model (eq.(6.20)):

$$\mu_{AFKNTX} = {}^{o}G_{AFKNTX} + RT\left[2\ln\left(y_A\right)+2\ln\left(y_F\right)+2\ln\left(y_K\right)+\ln\left(y_N\right)+\ln\left(y_T\right)+\ln\left(y_X\right)\right] \quad (6.20)$$

The C-(N-)A-S-H thermodynamic model developed here is implemented in the GEM-Selektor v3 thermodynamic modelling software (http://gems.web.psi.ch/) (Kulik et al., 2013; Wagner et al., 2012). Sublattice solid solution models can be specified in GEM-Selektor by modifying the activities of the chosen end-members (Table 6.1) through the introduction of a 'fictive activity coefficient' $\lambda$, which internalises the thermodynamic mixing relationships within the solid solution. This

method was used in the C-S-H thermodynamic model developed by Kulik (2011). The fictive activity coefficient is defined by eq.(6.21):

$$\lambda_k = \frac{\alpha_k}{\chi_k} \tag{6.21}$$

where $\alpha_k$ is the activity of the $k^{th}$ end-member, eq.(6.22):

$$\mu_k = \mu_k^o + RT\ln\left(\alpha_k\right) \tag{6.22}$$

The fictive activity coefficient is defined by eliminating $\mu_k$ and the ${}^oG_{AFKNTX}$ term (equivalent to $\mu_k{}^o$ as defined here) from eqs.(6.20,6.22), then substituting eq.(6.21) into the resulting equation and simplifying to obtain eq.(6.23):

$$\ln\left(\lambda_{AFKNTX}\right) = \left[2\ln\left(y_A\right) + 2\ln\left(y_F\right) + 2\ln\left(y_K\right) + \ln\left(y_N\right) + \ln\left(y_T\right) + \ln\left(y_X\right)\right] - \ln\left(\chi_{AFKNTX}\right) \tag{6.23}$$

Relationships equivalent to eq.(6.23) can thus be obtained for all eight end-members (Table 6.1). The relationships for the fictive activity coefficients for the end-members of the C-(N-)A-S-H sublattice solid solution model are defined here in terms of the following notation (eqs.(6.24-6.31)): 5CA = 0, INFCA = 1, 5CNA = 2, INFCNA = 3, INFCN = 4, T2C* = 5, T5C* = 6, TobH* = 7.

$$\ln\left(\lambda_0\right) = 2\ln(\chi_0+\chi_1) + 2\ln(\chi_0+\chi_1) + 2\ln(\chi_0+\chi_2+\chi_5+\chi_6) + \ln(\chi_0+\chi_5+\chi_6) + \ln(\chi_0+\chi_5+\chi_6) + \ln(\chi_0+\chi_1+\chi_2+\chi_3+\chi_4) - \ln(\chi_0) \tag{6.24}$$

$$\ln\left(\lambda_1\right) = 2\ln(\chi_0+\chi_1) + 2\ln(\chi_0+\chi_1) + 2\ln(\chi_1+\chi_4+\chi_7) + \ln(\chi_1) + \ln(\chi_1+\chi_4+\chi_7) + \ln(\chi_0+\chi_1+\chi_2+\chi_3+\chi_4) - \ln(\chi_1) \tag{6.25}$$

$$\ln(\lambda_2) = 2\ln(\chi_2+\chi_3)+2\ln(\chi_2+\chi_3)+2\ln(\chi_0+\chi_2+\chi_5+\chi_6)+ \ln(\chi_2)+\ln(\chi_2)+\ln(\chi_0+\chi_1+\chi_2+\chi_3+\chi_4)-\ln(\chi_2) \quad (6.26)$$

$$\ln(\lambda_3) = 2\ln(\chi_2+\chi_3)+2\ln(\chi_2+\chi_3)+2\ln(\chi_3)+ \ln(\chi_3)+\ln(\chi_3)+\ln(\chi_0+\chi_1+\chi_2+\chi_3+\chi_4)-\ln(\chi_3) \quad (6.27)$$

$$\ln(\lambda_4) = 2\ln(\chi_4)+2\ln(\chi_4)+2\ln(\chi_1+\chi_4+\chi_7)+ \ln(\chi_4)+\ln(\chi_1+\chi_4+\chi_7)+\ln(\chi_0+\chi_1+\chi_2+\chi_3+\chi_4)-\ln(\chi_4) \quad (6.28)$$

$$\ln(\lambda_5) = 2\ln(\chi_5)+2\ln(\chi_5)+2\ln(\chi_0+\chi_2+\chi_5+\chi_6)+ \ln(\chi_0+\chi_5+\chi_6)+\ln(\chi_0+\chi_5+\chi_6)+\ln(\chi_5+\chi_6+\chi_7)-\ln(\chi_5) \quad (6.29)$$

$$\ln(\lambda_6) = 2\ln(\chi_6+\chi_7)+2\ln(\chi_6+\chi_7)+2\ln(\chi_0+\chi_2+\chi_5+\chi_6)+ \ln(\chi_0+\chi_5+\chi_6)+\ln(\chi_0+\chi_5+\chi_6)+\ln(\chi_5+\chi_6+\chi_7)-\ln(\chi_6) \quad (6.30)$$

$$\ln(\lambda_7) = 2\ln(\chi_6+\chi_7)+2\ln(\chi_6+\chi_7)+2\ln(\chi_1+\chi_4+\chi_7)+ \ln(\chi_7)+\ln(\chi_1+\chi_4+\chi_7)+\ln(\chi_5+\chi_6+\chi_7)-\ln(\chi_7) \quad (6.31)$$

## 6.3 Modelling Method

### 6.3.1 Modelling System Definition

The kernel Nagra/PSI (Hummel et al., 2002), which is the default thermodynamic database for GEM-Selektor v3 (http://gems.web.psi.ch/) (Kulik et al., 2013; Wagner et al., 2012), and the CEMDATA07 thermodynamic database (Kulik and Kersten, 2001; 2002; Lothenbach et al., 2008b; Lothenbach and Winnefeld, 2006; Matschei et al., 2007b; Möschner et al., 2008; Möschner et al., 2009; Schmidt et al., 2008), which contains data for various compounds commonly found in cement systems, were used during simulations. Thermodynamic data for the gases and aqueous species are shown in Tables 3.2 and 3.3 respectively (section 3.4.1). The solid phases used in the thermodynamic modelling simulations in this chapter are shown in Table 6.2.

Table 6.2. Thermodynamic properties of the solid phases used in the thermodynamic modelling simulations. The reference state is 298.15 K and 1 bar.

| Phase | $V°$ ($cm^3$/mol) | $\Delta_f H°$ (kJ/mol) | $\Delta_f G°$ (kJ/mol) | $S°$ (J/(mol.K)) | $Cp°$ (J/(mol.K)) | Reference |
|---|---|---|---|---|---|---|
| $Al(OH)_3$ (microcrystalline) | 32.0 | -1265 | -1148 | 140 | 93.1 | (Lothenbach et al., 2012b) |
| Portlandite, $Ca(OH)_2$ | 33.1 | -984.7 | -897 | 83.4 | 87.5 | (Robie and Hemingway, 1995) |
| Amorphous $SiO_2$ | 29.0 | -903.3 | -849 | 41.3 | 44.5 | (Helgeson et al., 1978; Kulik and Kersten, 2001) |
| $C_2AH_8$ | 90.1 | -5278 | -4696 | 450 | 521 | (Lothenbach et al., 2012b) |
| $C_3AH_6$ | 150 | -5537 | -5008 | 422 | 446 | (Lothenbach et al., 2012b) |
| $C_4AH_{13}$ | 27.4 | -8302 | -7327 | 700 | 930 | (Lothenbach et al., 2008b) |
| $C_4AH_{19}$ | 382 | -1002 | -8750 | 1120 | 1382 | (Lothenbach et al., 2012b) |
| $C_4AH_{10}$ | 194 | -5388 | -4623 | 610 | 668 | (Lothenbach et al., 2012b) |
| Monosulfate, $C_4AsH_{12}$ | 309 | -8750 | -7779 | 821 | 942 | (Matschei et al., 2007b) |
| Stratlingite, $C_2ASH_8$ | 21.6 | -6360 | -5705 | 546 | 603 | (Matschei et al., 2007b) |
| Ettringite, $C_6As_3H_{32}$ | 707 | -17535 | -15206 | 1900 | 2174 | (Lothenbach et al., 2008b) |
| Hydrotalcite, $M_4AH_{10}$ | 220 | -7196 | -6395 | 549 | 649 | (Lothenbach et al., 2008b) |
| Brucite, $Mg(OH)_2$ | 24.6 | -923 | -832 | 63.1 | 77.3 | (Helgeson et al., 1978) |
| **The 'downscaled CSH3T' model** [a] | | | | | | |
| TobH, $(CaO)_1(SiO_2)_{1.5}(H_2O)_{2.5}$ | 85.0 | -2833 | -2562 | 153 | 231 | (Kulik, 2011) |
| T5C, $(CaO)_{1.25}(SiO_2)_{1.25}(H_2O)_{2.5}$ | 79.3 | -2782 | -2519 | 160 | 234 | (Kulik, 2011) |
| T2C, $(CaO)_{1.5}(SiO_2)_1(H_2O)_{2.5}$ | 80.6 | -2722 | -2467 | 167 | 237 | (Kulik, 2011) |

[a] The mixing rules used to describe the downscaled CSH3T model and the thermodynamic properties that define the TobH, T5C and T2C end-members in GEM-Selektor are the same as those described in (Kulik, 2011) for this model. The Gibbs free energies (and thus the enthalpies) of these components are modified slightly to the corresponding values used to define the TobH*, T5C* and T2C* end-members of the CNASH_ss model (Table 6.4).

Aqueous phase activity coefficients were calculated using the Truesdell-Jones form of the extended Debye-Hückel equation, as described in section 3.4.1.

### 6.3.2 Thermodynamic Property Estimation

The standard absolute isobaric heat capacity ($Cp^o$) and absolute entropy at standard state ($S^o$) of the five (Al,Na)-containing C-(N-)A-S-H end-members were estimated using the additivity method and eq.(6.32), defined in terms of structurally-relevant constituents: T2C (the Ca-rich end-member of the downscaled CSH3T model (Kulik, 2011), $(CaO)_{1.5}(SiO_2)_1(H_2O)_{2.5}$), portlandite ($Ca(OH)_2$), amorphous $SiO_2$, gibbsite ($Al(OH)_3$) and NaOH $_{(s)}$.

$$\begin{aligned}\Phi^o_{(CaO)_{a'}(SiO_2)_{b'}(Al_2O_3)_{c'}(Na_2O)_{d'}(H_2O)_{e'}} &= \frac{1}{2}(5a'-3e'+9c'+3d')\Phi^o_{Ca(OH)_2} \\ &+(b'-e'+a'+3c'+d')\Phi^o_{SiO_2}+2c'\Phi^o_{Al(OH)_3}+2d'\Phi^o_{NaOH} \\ &+(e'-a'-3c'-d')\Phi^o_{(CaO)_{1.5}(SiO_2)_1(H_2O)_{2.5}}\end{aligned} \quad (6.32)$$

Here $\Phi^o$ denotes the standard thermodynamic property undergoing estimation ($Cp^o$ or $S^o$), *a', b', c', d', e'* are the stoichiometric coefficients for the respective oxide components CaO, $SiO_2$, $Al_2O_3$, $Na_2O$ and $H_2O$, and the numerical coefficients for these terms are the values that result from solving the elemental balance for eq.(6.32). The thermodynamic properties of the constituent phases, shown in Table 6.3, are consistent with the Nagra/PSI (Hummel et al., 2002) and CEMDATA07 thermodynamic databases (Kulik and Kersten, 2001; 2002; Lothenbach et al., 2008b; Lothenbach and Winnefeld, 2006; Matschei et al., 2007b; Möschner et al., 2008; Möschner et al., 2009; Schmidt et al., 2008).

Table 6.3. Thermodynamic properties of the solid constituents used to estimate $Cp^o$ and $S^o$ for the C-(N-)A-S-H end-members. The reference state is 298.15 K and 1 bar.

| **Phase** | ***V*°** **($cm^3$/mol)** | **$\Delta_f H$°** **(kJ/mol)** | **$\Delta_f G$°** **(kJ/mol)** | ***S*°** **(J/(mol.K))** | ***Cp*°** **(J/(mol.K))** | **Reference** |
|---|---|---|---|---|---|---|
| Portlandite, $Ca(OH)_2$ | 33.1 | -984.7 | -897.0 | 83.4 | 87.5 | (Robie and Hemingway, 1995) |
| Amorphous $SiO_2$ | 29.0 | -903.3 | -848.9 | 41.3 | 44.5 | (Helgeson et al., 1978; Kulik and Kersten, 2001) |
| Gibbsite, $Al(OH)_3$ | 32.0 | -1289 | -1151 | 70.1 | 93.1 | (Helgeson et al., 1978) |
| $NaOH_{(s)}$ | 18.8 | -425.8 | -379.6 | 64.4 | 59.5 | (Chase, 1998; Robie and Hemingway, 1995) |
| T2C, $(CaO)_{1.5}(SiO_2)_1(H_2O)_{2.5}$ | 80.6 | -2722 | -2467 | 167 | 237 | (Kulik, 2011) |

The additivity method is expected to yield relatively small errors in estimated values for $Cp^o$ and $S^o$ if suitable constituents are chosen (Anderson and Crerar, 1993). The changes in $S^o$ and $Cp^o$, and the solubility product ($K_{so}$) of the (Al,Na)-containing C-(N-)A-S-H end-members for the dissociation reaction represented by eq.(6.33), were determined to enable thermodynamic property calculations in GEM-Selektor:

$$\begin{aligned}(CaO)_{a'}(SiO_2)_{b'}(Al_2O_3)_{c'}(Na_2O)_{d'}(H_2O)_{e'(s)} &\overset{K_{so}}{\rightleftharpoons} a'Ca^{2+}{}_{(aq)} \\ &+ b'SiO_3^{2-}{}_{(aq)} + 2c'AlO_2^{-}{}_{(aq)} + 2d'Na^{+}{}_{(aq)} + 2(a'-b'-c'+d')OH^{-}{}_{(aq)} \\ &+ (b'+c'+e'-a'-d')H_2O_{(l)}\end{aligned} \qquad (6.33)$$

The ReacDC module in GEM-Selektor was used to determine the standard partial molal Gibbs free energies ($\Delta_f G^o$) and enthalpies of formation ($\Delta_f H^o$) for the proposed C-(N-)A-S-H end-members by specifying 'optimised' solubility products for the reaction shown in eq.(6.33), the value of $S^o$ determined via the additivity method (using the components listed previously), and the change in $S^o$ of the dissociation reaction (eq.(6.33)). The Gibbs free energies (and thus the enthalpies) of the T2C*, T5C* and TobH* end-members were modified slightly from the values reported in the downscaled CSH3T model (Kulik, 2011), and solubility products of the (Al,Na)-containing C-(N-)A-S-H end-members were selected, to obtain the optimised fit of the thermodynamic model to the solubility and solid phase chemistry data in the CaO-($Na_2O$,$Al_2O_3$)-$SiO_2$-$H_2O$ (Atkins et al., 1992b; Atkinson et al., 1989; Chen et al., 2004; Cong and Kirkpatrick, 1996a; Faucon et al., 1999a; Flint and Wells, 1934; Fujii and Kondo, 1981; Glasser et al., 1999; Greenberg and Chang, 1965; Grutzeck et al., 1989; Harris et al., 2002; Hong and Glasser, 1999; Kalousek, 1944; Lognot et al., 1998; Macphee et al., 1989; Pardal et al., 2012; Renaudin et al., 2009a; Renaudin et al., 2009b; Roller and Ervin, 1940; Sun et al., 2006; Suzuki et al., 1985; Taylor, 1950; Walker et al., 2007; Way and Shayan, 1992) and AAS cement systems (Gruskovnjak et al., 2006; Lloyd et al., 2010; Puertas et al., 2004; Song and Jennings, 1999) used in model validation (section 6.4). All other thermodynamic

parameters of the T2C*, T5C* and TobH* end-members were adopted directly from the downscaled CSH3T model.

Standard molar volumes ($V^o$) of the (Al,Na)-containing C-(N-)A-S-H end-members were determined from density calculations using the method proposed by Thomas et al. (2012), but extended to include Na via eq.(6.34):

$$\rho^{sc}{}_{CNASH} = N_A \rho'_{CNASH} \left[ \frac{\left(\frac{CaO}{SiO_2}\right) b^{sc}{}_{CaO} + b^{sc}{}_{SiO_2} + \left(\frac{Al_2O_3}{SiO_2}\right) b^{sc}{}_{Al_2O_3} + \left(\frac{Na_2O}{SiO_2}\right) b^{sc}{}_{Na_2O} + \left(\frac{H_2O}{SiO_2}\right) b^{sc}{}_{H_2O}}{MW_{CNASH}} \right] \quad (6.34)$$

where the $b^{sc}$ parameters are the established neutron scattering lengths for CaO, $SiO_2$, $Al_2O_3$, $Na_2O$ and $H_2O$, $\rho^{sc}$ is the scattering length density taken from the literature (Thomas et al., 2012), $\rho'_{CNASH}$ is the predicted density of a C-(N-)A-S-H end-member, $N_A$ is Avogadro's number, $MW_{CNASH}$ is the molecular weight of a C-(N-)A-S-H end-member, and the ratios $CaO/SiO_2$, $Al_2O_3/SiO_2$, $Na_2O/SiO_2$, and $H_2O/SiO_2$ are molar composition ratios of a C-(N-)A-S-H end-member. The optimised thermodynamic properties for the C-(N-)A-S-H end-members are summarised in Table 6.4.

Table 6.4. Thermodynamic properties, densities and the change in thermodynamic properties for the dissociation reaction (eq.(6.33)) for the end-members of the C-(N-)A-S-H solid solution (25°C, 1 bar).

| **Standard thermodynamic properties and density** | | | | | | |
|---|---|---|---|---|---|---|
| End-member | $V°$ ($cm^3$/mol) | $\Delta_f H°$ (kJ/mol) | $\Delta_f G°$ (kJ/mol) | $S°$ (J/(mol.K)) | $Cp°$ (J/(mol.K)) | $\rho'_{CNASH}$ ($g/cm^3$) |
| 5CA | 57.3 | -2491 | -2293 | 163 | 177 | 3.01 |
| INFCA | 59.3 | -2551 | -2343 | 154 | 181 | 2.92 |
| 5CNA | 64.5 | -2569 | -2382 | 195 | 176 | 2.84 |
| INFCNA | 69.3 | -2667 | -2474 | 198 | 180 | 2.72 |
| INFCN | 71.1 | -2642 | -2452 | 186 | 184 | 2.63 |
| T2C* [a] | 80.6 | -2721 | -2465 | 167 | 237 | 2.35 |
| T5C* [a] | 79.3 | -2780 | -2517 | 160 | 234 | 2.40 |
| TobH* [a] | 85.0 | -2831 | -2560 | 153 | 231 | 2.25 |
| **Change in thermodynamic properties for the dissociation reaction (eq.(6.33))** | | | | | | |
| End-member | $\Delta_r V°$ ($cm^3$/mol) | $\Delta_r H°$ (kJ/mol) | $\Delta_r G°$ (kJ/mol) | $\Delta_r S°$ (J/(mol.K)) | $\Delta_r Cp°$ (J/(mol.K)) | $\log_{10}(K_{so})$ |
| 5CA | -17.9 | -4.0 | 61.4 | -219 | -29.3 | -10.75 |
| INFCA | 5.1 | 0.58 | 50.8 | -168 | 160 | -8.90 |
| 5CNA | -37.1 | -18.8 | 59.4 | -262 | -115 | -10.4 |
| INFCNA | -21.3 | -10.8 | 57.1 | -228 | 41.5 | -10.0 |
| INFCN | -12.5 | -6.2 | 61.1 | -226 | 144 | -10.7 |

**[a]** The $\log_{10}(K_{so})$ values for the T2C*, T5C* and TobH* end-members, for the dissociation reaction eq.(6.33), are -11.6, -10.5 and -7.9 respectively.

## 6.4 Application of the C-(N-)A-S-H Thermodynamic Model

### 6.4.1 Approach

The success of a thermodynamic model is measured in terms of its ability to describe the available thermochemical data in the target system(s) - here, for Ca-rich alkali-activated cements such as AAS cements and hybrid alkali-activated/PC materials - and its ability to predict the chemistry of simulated systems where experimental data are either not available or are difficult to obtain. Hence, thermodynamic models for cements must be developed using existing experimental results such as solubility measurements (Chen et al., 2004; Pardal et al., 2009), solid product assemblages (Bonk et al., 2003; Richardson et al., 1994; Wang and Scrivener, 1995), and/or C-(N-)A-S-H chemistry (Sun et al., 2006). An extensive set of experimental solubility data in the $CaO$-$SiO_2$-$H_2O$ system is available for the development of thermodynamic

models for C-S-H gels (Atkins et al., 1992b; Atkinson et al., 1989; Chen et al., 2004; Cong and Kirkpatrick, 1996a; Flint and Wells, 1934; Fujii and Kondo, 1981; Glasser et al., 1999; Greenberg and Chang, 1965; Grutzeck et al., 1989; Harris et al., 2002; Roller and Ervin, 1940; Suzuki et al., 1985; Taylor, 1950; Walker et al., 2007), but the use of such information to develop models for C-(N-)A-S-H is significantly more complicated. Solubility measurements in the $CaO$-$Na_2O$-$Al_2O_3$-$SiO_2$-$H_2O$ system are not available in sufficient detail to enable development of thermodynamic models using this information alone, meaning that validation against other data is necessary. In this light, AAS cements provide an opportunity to validate the thermodynamic model; these materials are described mostly in terms of the more complex $CaO$-$Na_2O$-$Al_2O_3$-$SiO_2$-$H_2O$-$MgO$ system, but are relatively well characterised. Hence, the thermodynamic model here is validated for the less complex $CaO$-($Na_2O$,$Al_2O_3$)-$SiO_2$-$H_2O$ systems, and also AAS cements. The ability of the thermodynamic model to predict solid phase assemblages in these systems will be discussed in a subsequent publication.

GEM-Selektor simulations for the $CaO$-$SiO_2$-$H_2O$ and $CaO$-($Na_2O$,$Al_2O_3$)-$SiO_2$-$H_2O$ systems were performed at a constant temperature and pressure of 25°C and 1 bar, using 1 g of each of the gases $O_{2\,(g)}$ and $N_{2\,(g)}$. Simulations were performed by adding $H_2O$, NaOH, CaO, $Al(OH)_3$ and $SiO_2$ at a fixed liquid/solid ratio = 50 using a basis of 1000 g $H_2O$. The C-(N-)A-S-H thermodynamic model developed here (CNASH_ss) was used in all simulations.

### 6.4.2 Model Validation in the $CaO$-$SiO_2$-$H_2O$ System

An extensive body of solubility data for the $CaO$-$SiO_2$-$H_2O$ system is available (Atkins et al., 1992b; Atkinson et al., 1989; Chen et al., 2004; Cong and Kirkpatrick, 1996a; Flint and Wells, 1934; Fujii and Kondo, 1981; Glasser et al., 1999; Greenberg and Chang, 1965; Grutzeck et al., 1989; Harris et al., 2002; Roller and Ervin, 1940; Suzuki et al., 1985; Taylor, 1950; Walker et al., 2007), which has been used to develop thermodynamic models for C-S-H gels in the past (Berner, 1992; Gisby et

al., 2007; Kulik, 2011; Kulik and Kersten, 2001; Walker et al., 2007). The fit of the new model to these data (Figure 6.2) is very good regarding description of the available data for pH, for concentrations of [Ca] < 2 mmol/L and [Si] > 0.1 mmol/L, and for Ca and Si solubilities up to a molar Ca/Si ratio in the solid ≈ 1.3. The thermodynamic model is less consistent with the full body of available data at higher dissolved Ca concentrations, lower aqueous Si concentrations, and higher Ca/Si ratios in the solid, but matches more closely with the more recently published data, particularly the measurements reported in (Chen et al., 2004). The poorer fit of the thermodynamic model to these data indicate that it is partly limited by the assumption of no additional solid solution $Ca(OH)_2$; the simulated C-S-H gels are in equilibrium with portlandite for Ca/Si > 1.4 and amorphous $SiO_2$ is simulated at Ca/Si ratios in the solid ≤ 0.67 (Figure 6.2). It has previously been proposed (Chen et al., 2004) that C-S-H solubility varies as a function of the nanostructure of this phase, which is much more pronounced for Ca/Si > 1 when many nanostructural configurations and potential bonding environments for Ca are possible (for example, Ca can be accommodated in the *CB* and *IC* sites here). This would mean that C-S-H thermodynamic models with a single curve for the solubility-structure relationships in these gels are inherently unable to describe the full range of available solubility data for this phase. However, the compositional region that is described accurately by the thermodynamic model is the region of principal importance for cementitious materials with compositions in the $CaO$-$Na_2O$-$Al_2O_3$-$SiO_2$-$H_2O$ system, which typically contain C-(N-)A-S-H with Ca/Si ≤ 1.2 (as discussed in section 2.1.2).

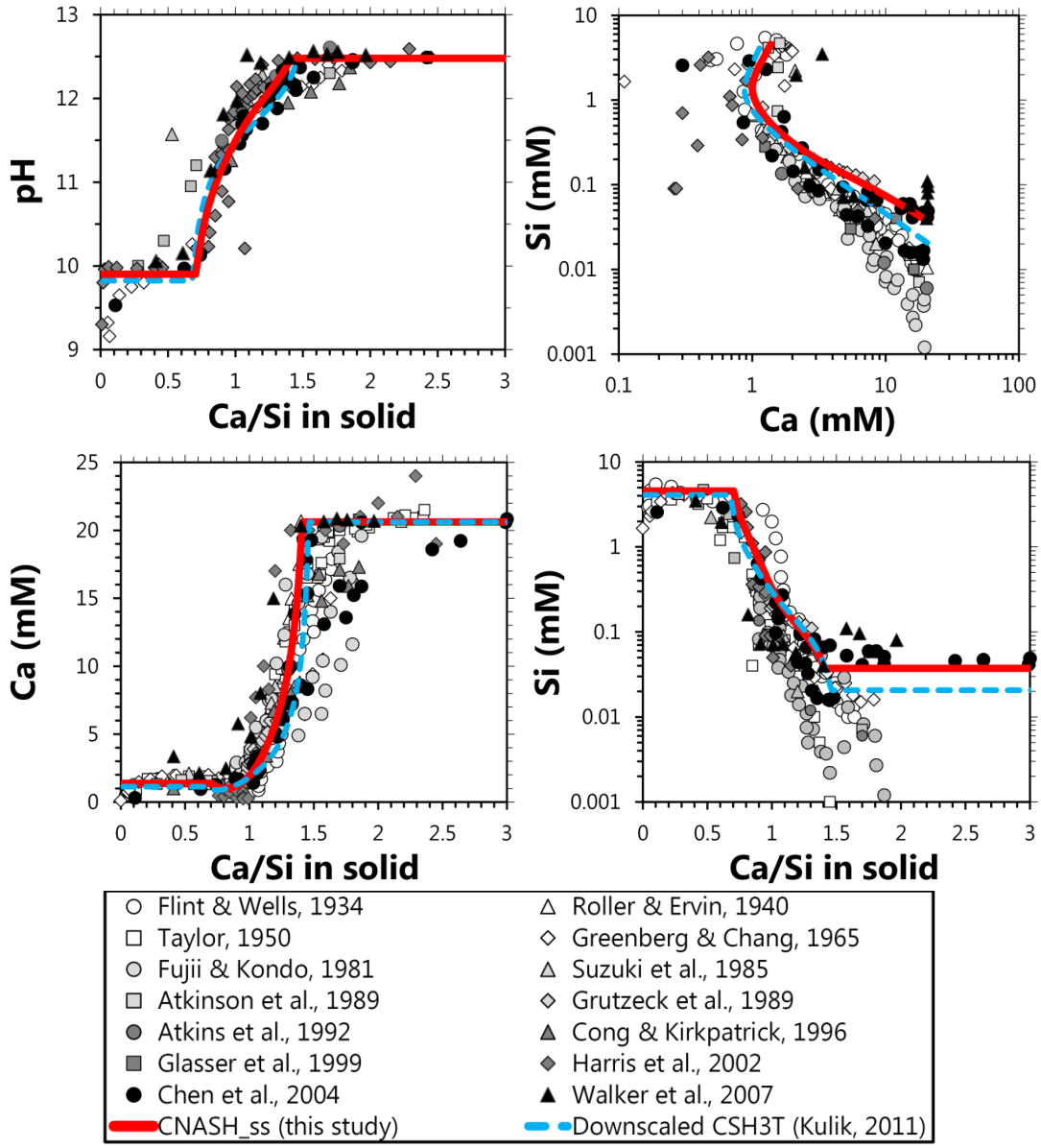


Figure 6.2. Comparison of the simulation results (25°C, 1 bar, water/solids mass ratio = 50) using the thermodynamic model developed here (CNASH_ss, bold red traces) to the downscaled CSH3T model (dashed blue traces) (Kulik, 2011) and published solubility data in the $CaO$-$SiO_2$-$H_2O$ system (Atkins et al., 1992b; Atkinson et al., 1989; Chen et al., 2004; Cong and Kirkpatrick, 1996a; Flint and Wells, 1934; Fujii and Kondo, 1981; Glasser et al., 1999; Greenberg and Chang, 1965; Grutzeck et al., 1989; Harris et al., 2002; Roller and Ervin, 1940; Suzuki et al., 1985; Taylor, 1950; Walker et al., 2007). mM = mmol/L.

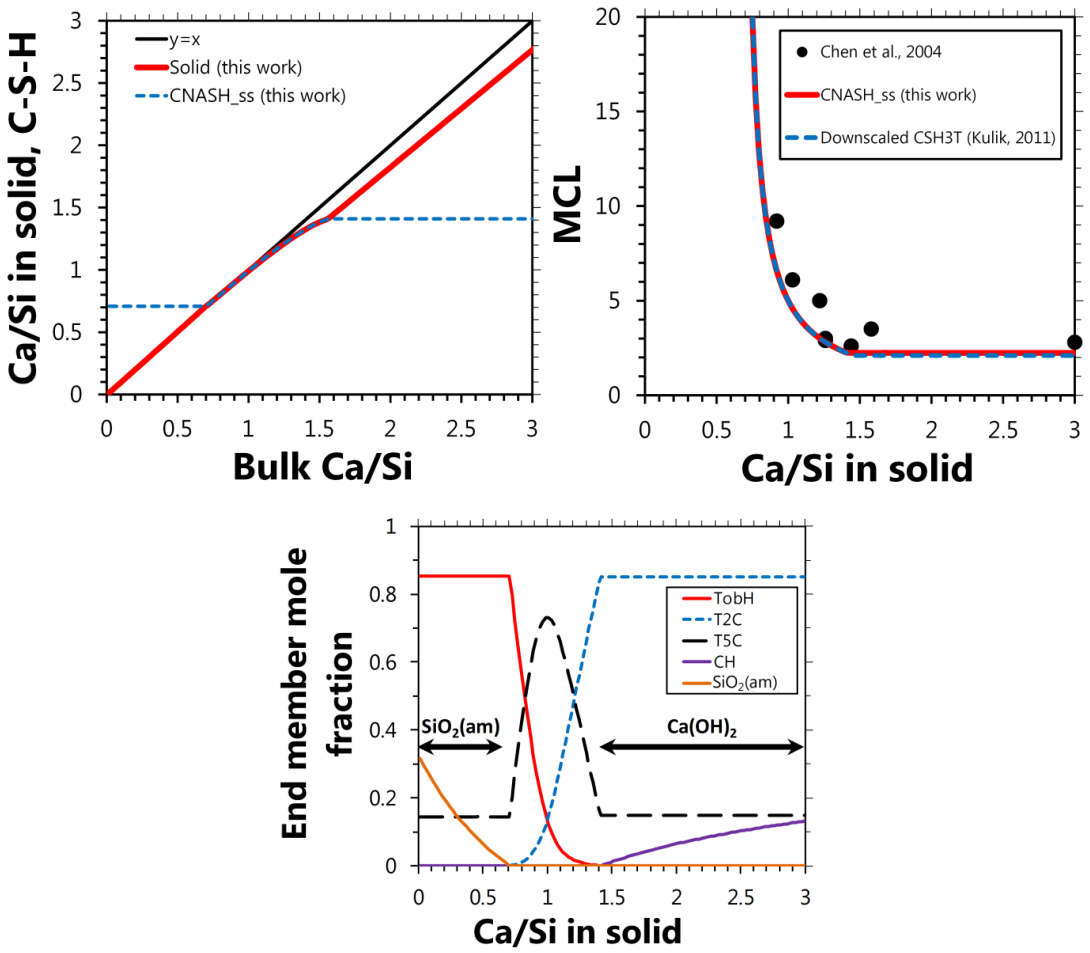


Figure 6.2. Continued.

### 6.4.3 Model Validation in the CaO-$Na_2O$-$SiO_2$-$H_2O$ System

Significantly fewer thermochemical data are available for cements in the more complex CaO-$Na_2O$-$SiO_2$-$H_2O$ system than in the CaO-$SiO_2$-$H_2O$ system. Simulations for the CaO-$Na_2O$-$SiO_2$-$H_2O$ system (Figures 6.3-6.6) were performed at bulk NaOH concentrations of 0.25, 0.5, 1 and 3 mol/L, and compared to published results in the respective ranges of [NaOH] = 0.1 – 0.3 M, 0.3 – 0.8 M, 0.8 – 1 M, 1 – 5 M. This grouping was chosen to constrain the range of NaOH concentrations in the experimental studies relatively tightly to the bulk alkali concentrations used in the simulations, while maintaining enough data points in each group to enable reliable validation of the thermodynamic model.

The maximum Ca content of equilibrated (sodium) calcium silicate hydrate (C-(N-)S-H) products and the bulk system alkalinity are inversely related (Lognot et al., 1998); C-(N-)S-H with solid Ca concentrations above this maximum value are more soluble than portlandite at equilibrium (a maximum value of Ca/Si ≈ 1 has been reported for C-(N-)S-H equilibrated (Lognot et al., 1998) at bulk NaOH concentrations ≈ 1 mol/kg). The thermodynamic modelling simulations performed here show this same trend (Figures 6.3-6.6), which indicate that the C-(N-)S-H gels modelled at a bulk NaOH concentration of 3 M are in equilibrium with portlandite at all Ca/Si ratios ≥ 1, rather than the much higher Ca/Si ratios at which this is observed in the $CaO\text{-}SiO_2\text{-}H_2O$ system (Ca/Si ≥ 1.4, Figure 6.2).

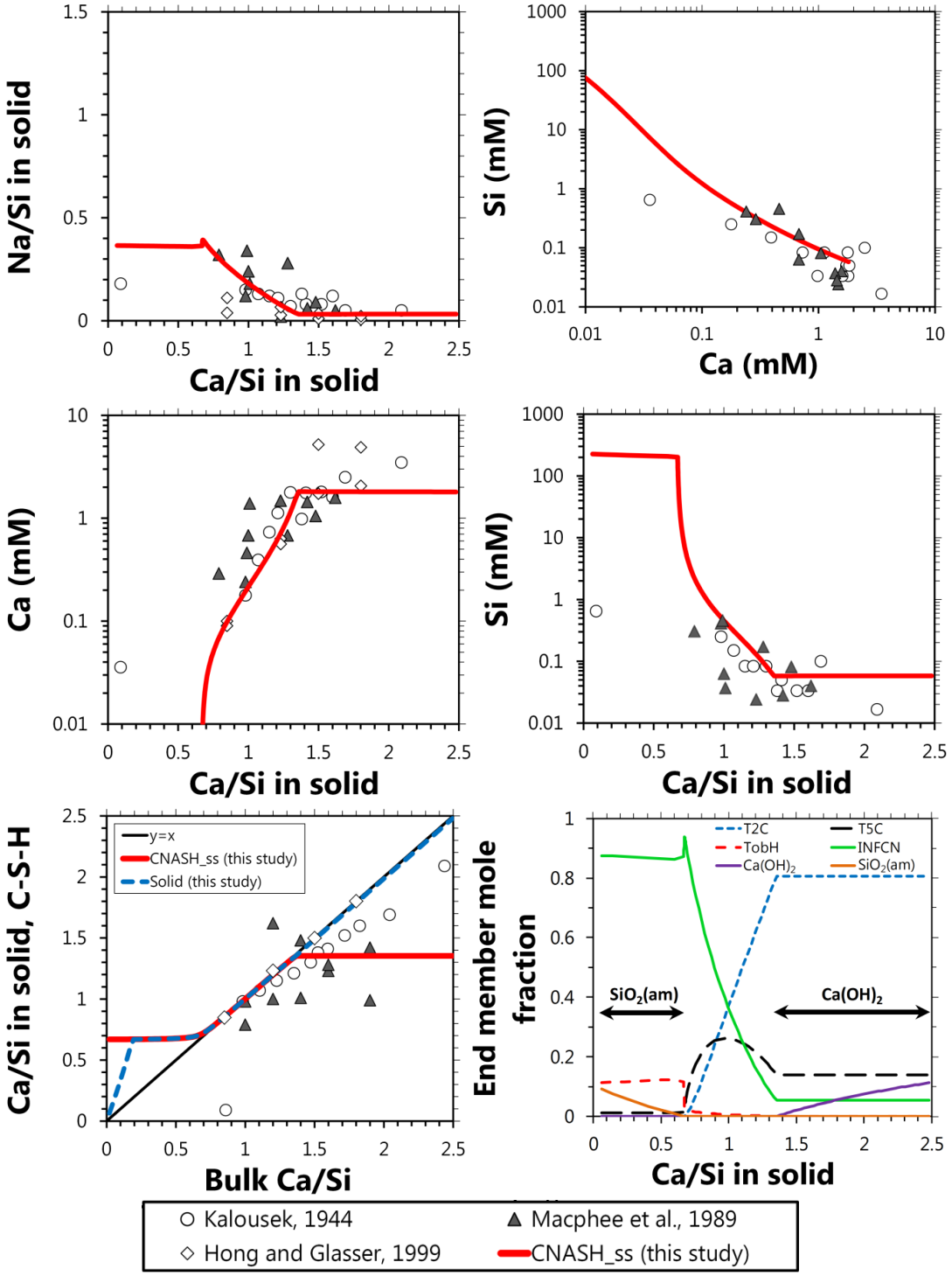


Figure 6.3. Comparison of the simulation results (25°C, 1 bar, 0.25 M NaOH/solids mass ratio = 50) using the thermodynamic model developed here (CNASH_ss, bold red traces) to published solubility data in the $CaO$-$Na_2O$-$SiO_2$-$H_2O$ system at alkali concentrations 0.1 M ≤ [NaOH] ≤ 0.3 M (Hong and Glasser, 1999; Kalousek, 1944; Macphee et al., 1989). mM = mmol/L.

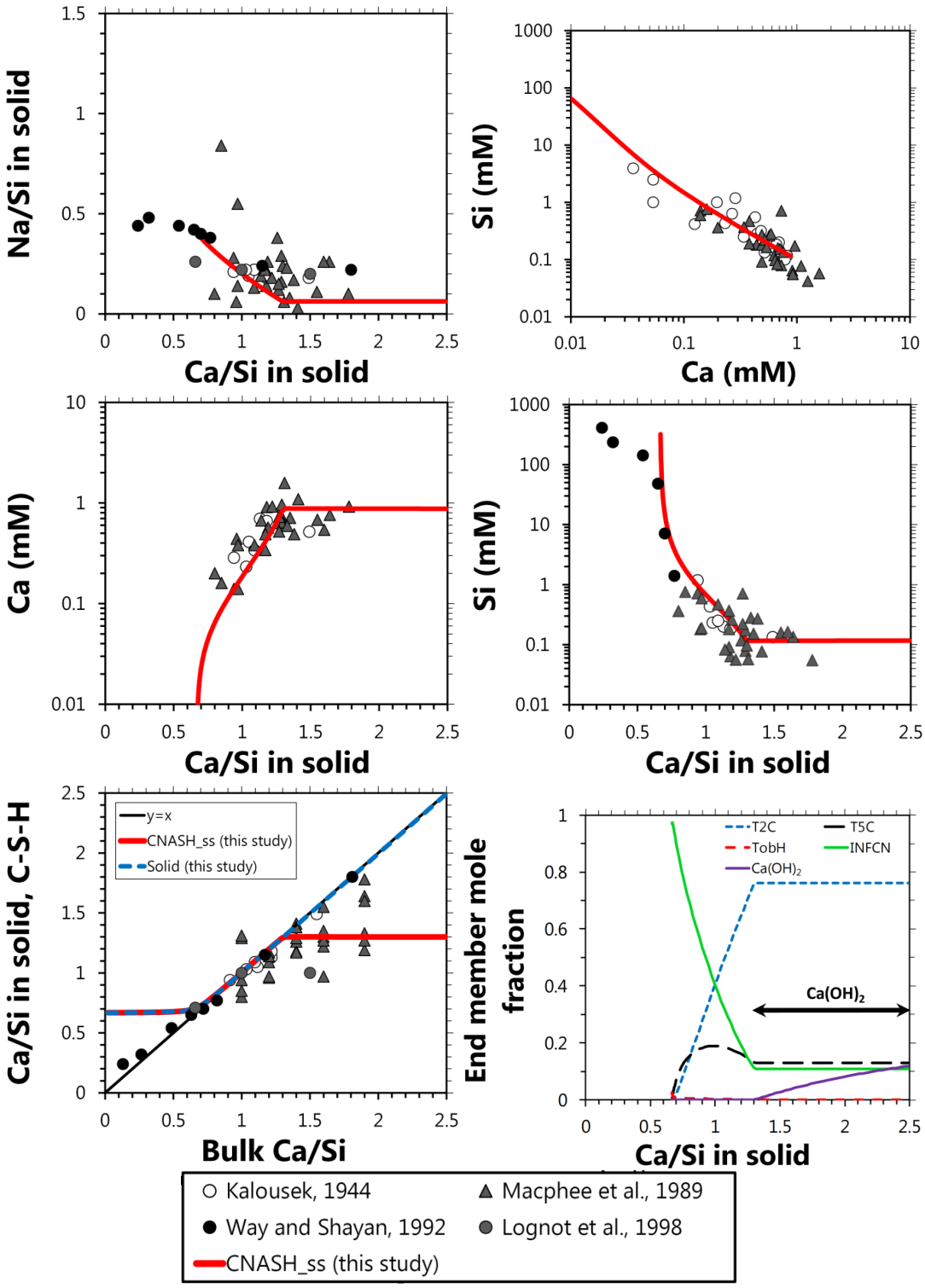


Figure 6.4. Comparison of the simulation results (25°C, 1 bar, 0.5 M NaOH/solids mass ratio = 50) using the thermodynamic model developed here (CNASH_ss, bold red traces) to published solubility data in the CaO-$Na_2O$-$SiO_2$-$H_2O$ system at alkali concentrations 0.3 M ≤ [NaOH] ≤ 0.8 M (Hong and Glasser, 1999; Kalousek, 1944; Macphee et al., 1989; Way and Shayan, 1992). The simulated C-S-H gels are in equilibrium with portlandite at molar ratios of Ca/Si in the solid ≥ 1.3. mM = mmol/L.

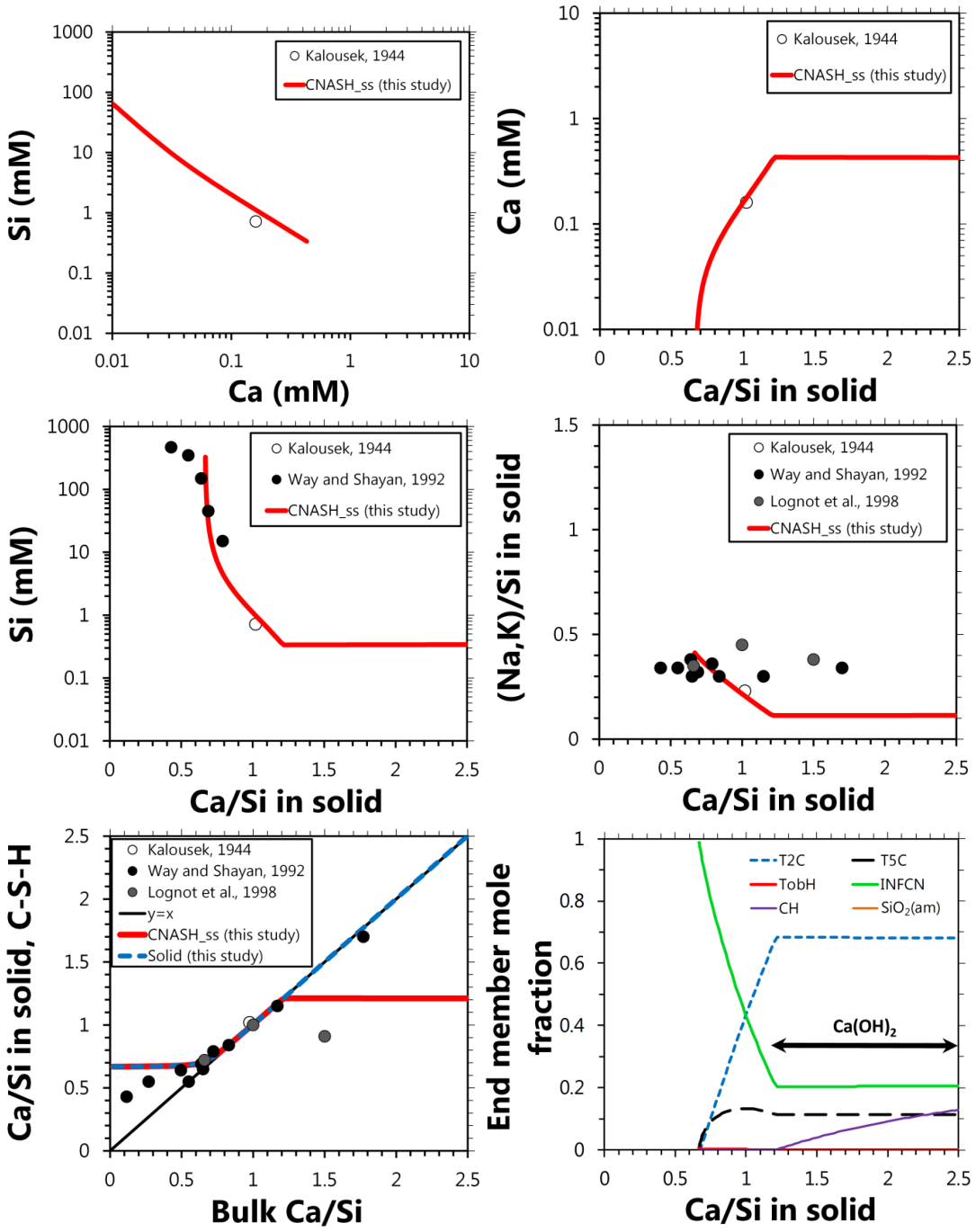


Figure 6.5. Comparison of the simulation results (25°C, 1 bar, 1 M NaOH/solids mass ratio = 50) using the thermodynamic model developed here (CNASH_ss, bold red traces) to solubility and solid phase chemistry data in the $CaO$-$Na_2O$-$SiO_2$-$H_2O$ system at alkali concentrations 0.8 M ≤ [NaOH] ≤ 1 M (Kalousek, 1944; Lognot et al., 1998; Way and Shayan, 1992). The corresponding end member mole fraction results are also shown. mM = mmol/L.

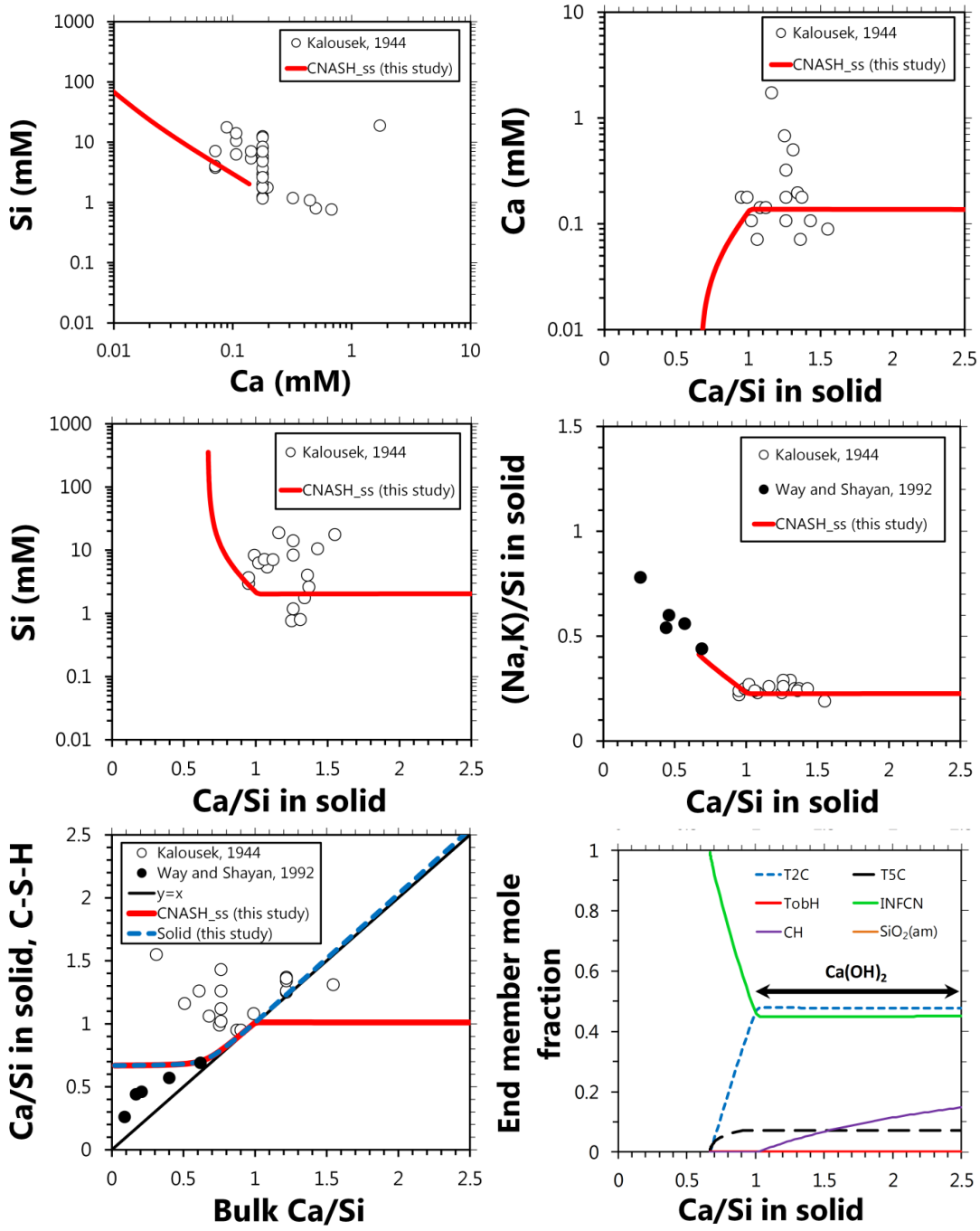


Figure 6.6. Comparison of the simulation results (25°C, 1 bar, 3 M NaOH/solids mass ratio = 50) using the thermodynamic model developed here (CNASH_ss, bold red traces) to solubility and solid phase chemistry data in the $CaO$-$Na_2O$-$SiO_2$-$H_2O$ system at alkali concentrations 1 M ≤ [NaOH] ≤ 5 M (Kalousek, 1944; Way and Shayan, 1992). The corresponding end member mole fraction results are also shown. mM = mmol/L.

The good agreement between the measured solubility data for NaOH concentrations of 0.3 M-0.8 M and the simulations at [NaOH] = 0.25 and 0.5 M are evident in

Figures 6.3-6.4. The composition of the simulated C-(N-)S-H gel also captures the relatively higher Na content measured in this phase at lower Ca/Si ratios (Way and Shayan, 1992). The comparisons between the simulated and reported solubility data in the other alkali concentration ranges studied are generally also good, with the exception of some of the data reported at NaOH concentrations > 1 M by Kalousek (1944). This may be explained by the presence of additional sodium calcium silicate hydrate gels in those highly alkaline systems that are not described in the thermodynamic databases used here (e.g. phases with similarities to the kanemite group of minerals (Kirkpatrick et al., 2005), which are thought to be similar to alkali-aggregate reaction products). This would mean that the aqueous composition data for [NaOH] concentrations > 1 M reported by Kalousek (1944) may not be solely determined by the solubility of C-(N-)S-H phases.

### 6.4.4 Model Validation in the $CaO$-$Al_2O_3$-$SiO_2$-$H_2O$ System

Analysis of C-A-S-H solubility from published solubility data for this phase (Faucon et al., 1999b; Pardal et al., 2012) is complicated by the coexistence of secondary phases such as strätlingite and/or superficial carbonation products (e.g. calcium hemicarboaluminate hydrate, $C_4Ac_{0.5}H_{12}$) in the solids analysed. Here, the thermodynamic model is validated against the solubility dataset published by Pardal et al. (2012) (Figure 6.7) over the bulk composition range most relevant for AAS cements, $0.66 \leq Ca/(Al+Si) \leq 1$ and $0 \leq Al/Si \leq 0.33$. The simulation results and the measured solubility data are comparable, to within an order of magnitude. These data show a similar inverse relationship between [Si] and [Ca] to that described by the solubility data for these elements in the $CaO$-$SiO_2$-$H_2O$ system (Figure 6.2).

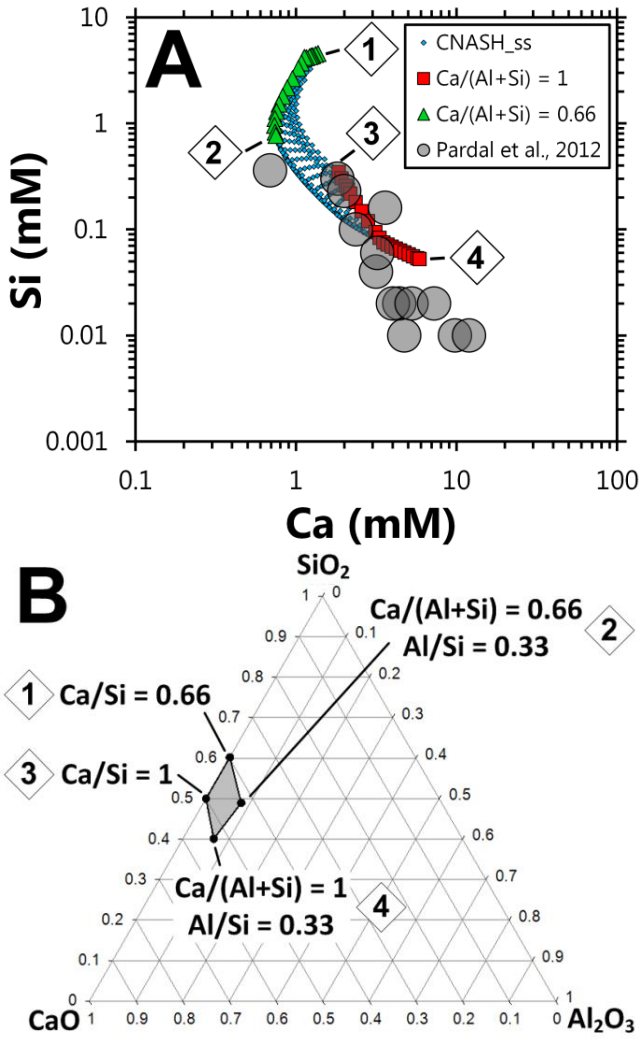


Figure 6.7. A) Comparison of the simulation results (25°C, 1 bar, water/solids mass ratio = 50) using the thermodynamic model developed here (CNASH_ss, small blue diamonds, red squares and green triangles) to published solubility data for C-A-S-H gels in the $CaO$-$Al_2O_3$-$SiO_2$-$H_2O$ system (large grey circles (Pardal et al., 2012)). The corresponding range of bulk compositions simulated, projected onto the $CaO$-$SiO_2$-$Al_2O_3$ ternary system, is shown in B). mM = mmol/L.

Chemical composition data for C-A-S-H are also used for model validation (Faucon et al., 1999a; Renaudin et al., 2009a; Renaudin et al., 2009b; Sun et al., 2006); most of these data exist at three bulk Al/Si compositions: Al/Si ≈ 0.1, 0.2 and 0.33. Comparison of the modelling results against these data (Figures 6.8A-6.8C), for the relevant composition range in AAS cements (0.65 ≤ bulk Ca/(Al+Si) ≤ 1), shows that the simulations accurately describe all of the reported chemical composition data for this phase.

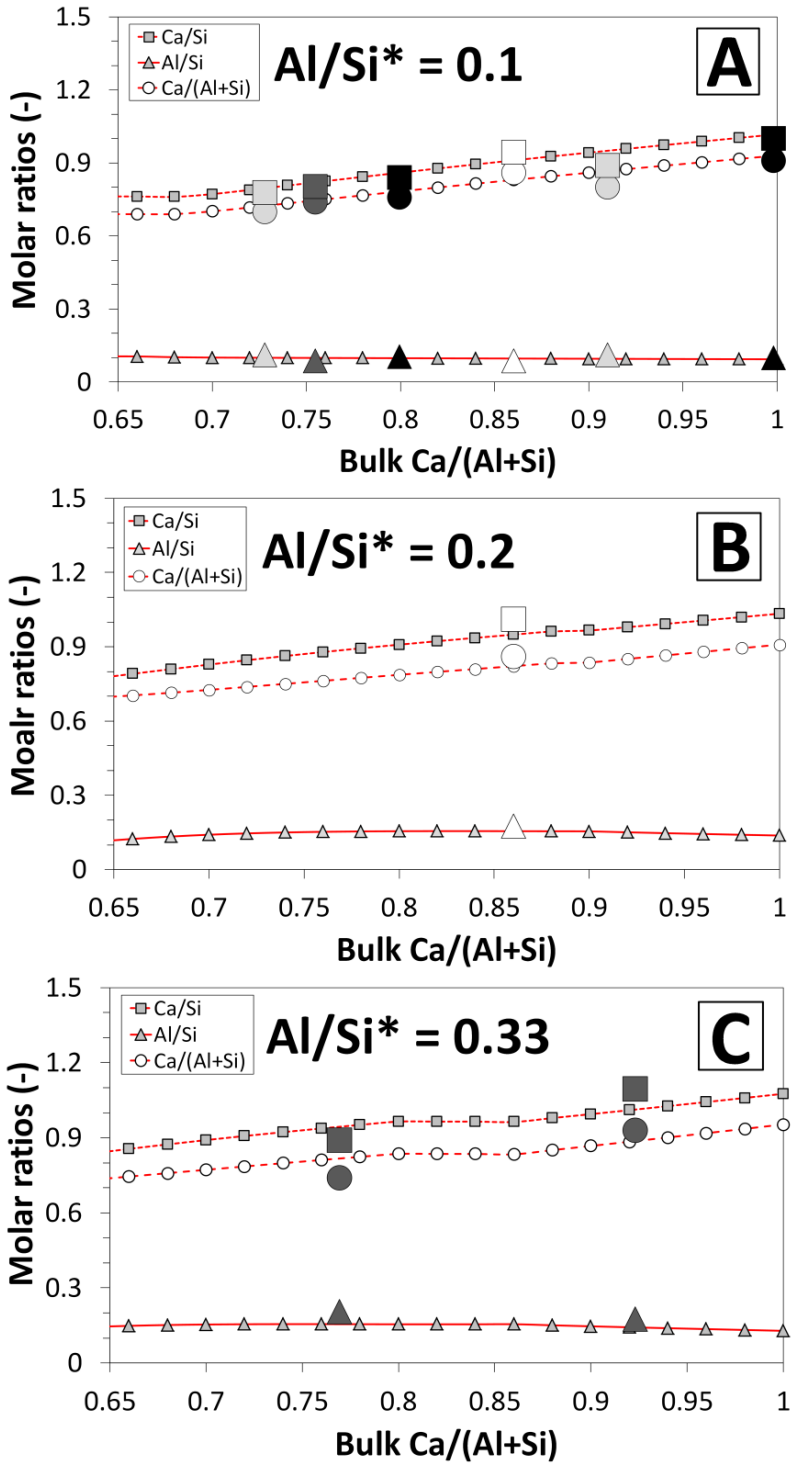


Figure 6.8. Comparison of the simulation results (25°C, 1 bar, water/solids mass ratio = 50) using the thermodynamic model developed here (CNASH_ss, small symbols and red lines) to the published chemical composition data for C-A-S-H gels (large symbols represent data from the literature: white (Sun et al., 2006); light grey (Renaudin et al., 2009b); dark grey (Faucon et al., 1999a); black (Renaudin et al., 2009a)). Al/Si* = bulk Al/Si.

End-member mole fractions for the simulations plotted in Figure 6.8 are shown in Figure 6.9.

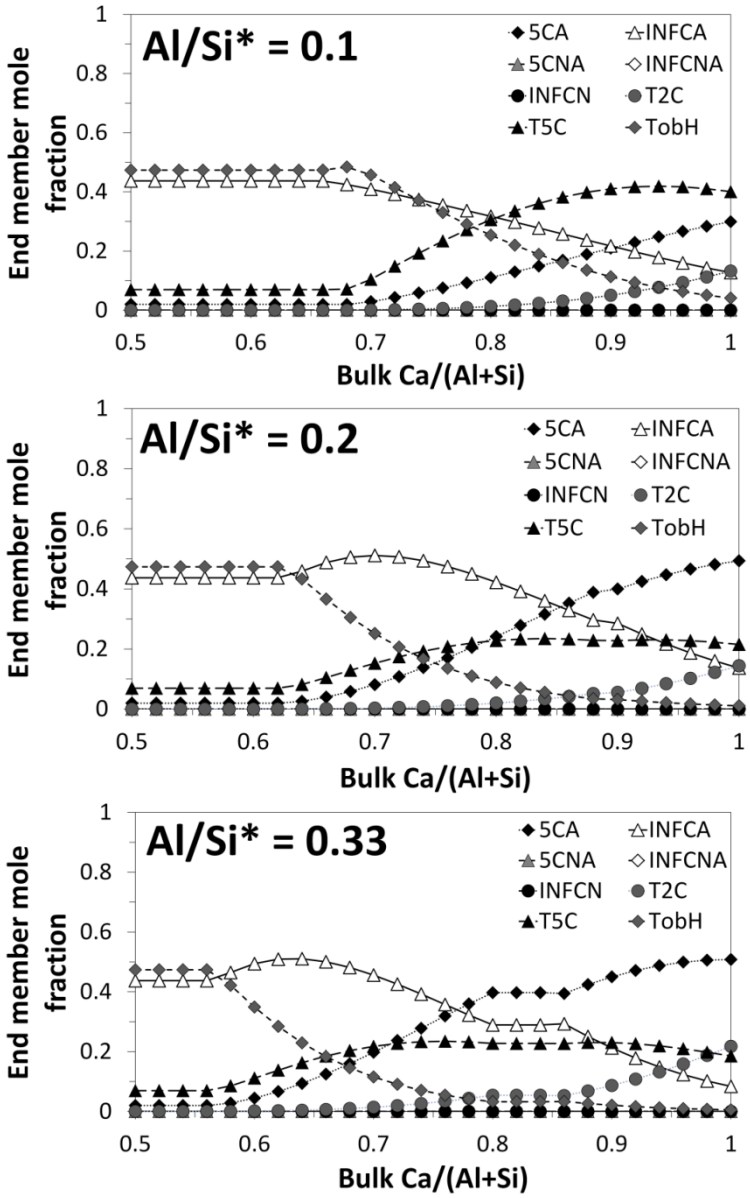


Figure 6.9. End member mole fractions corresponding to the simulation results shown in Figure 6.8 (25°C, 1 bar, water/solids mass ratio = 50). Al/Si* = bulk Al/Si.

### 6.4.5 Model Validation in Alkali-Activated Slag Cement Systems

Simulations for calculating the solubility of AAS cements were performed in an $N_2$ atmosphere (1 g of $N_{2\ (g)}$, to avoid oxidation of the system) at 25°C, 1 bar and at water/binder ratios specified as reported in the literature, shown here in Table 6.5.

Table 6.5. Slag reaction extents, curing times and activating conditions used to simulate the pore solution chemistry of AAS cements.

| System (corresponding to the legend labels in Figure 6.6) | Curing time (days) | Activator | Water/binder | Slag reaction extent used in simulations (%) | Reference |
|---|---|---|---|---|---|
| Gruskovnjak et al., 2006 | 1 | $Na_2SiO_3.5H_2O$ | 0.3 [a] | 32 | (Gruskovnjak et al., 2006) |
| Gruskovnjak et al., 2006 | 7 | $Na_2SiO_3.5H_2O$ | 0.3 [a] | 36 | (Gruskovnjak et al., 2006; Lothenbach and Gruskovnjak, 2007) |
| Gruskovnjak et al., 2006 | 28 | $Na_2SiO_3.5H_2O$ | 0.3 [a] | 38 | (Gruskovnjak et al., 2006; Lothenbach and Gruskovnjak, 2007) |
| Gruskovnjak et al., 2006 | 180 | $Na_2SiO_3.5H_2O$ | 0.3 [a] | 42 | (Gruskovnjak et al., 2006; Lothenbach and Gruskovnjak, 2007) |
| Puertas et al., 2004 | 7 | $Na_2O{\cdot}1.5SiO_2{\cdot}xH_2O$ | 0.5 [b] | 36 | (Puertas et al., 2004) |
| Puertas et al., 2004 | 7 | NaOH | 0.5 [b] | 36 | (Puertas et al., 2004) |
| Lloyd et al., 2010 | 90 | $Na_2O{\cdot}mSiO_2{\cdot}xH_2O$ | 0.35 | 40 | (Lloyd et al., 2010) |
| Song and Jennings, 1999 | 28 | 1 M NaOH | 0.45 [c] | 36 | (Song and Jennings, 1999) |
| Song and Jennings, 1999 | 28 | 0.5 M NaOH | 0.45 [c] | 31 | (Song and Jennings, 1999) |
| Song and Jennings, 1999 | 28 | 0.1 M NaOH | 0.45 [c] | 26 | (Song and Jennings, 1999) |
| Song and Jennings, 1999 | 41 | $H_2O$ | 0.45 [c] | 21 | (Song and Jennings, 1999) |
| Song and Jennings, 1999 | 44 | 1 M NaOH | 0.45 [c] | 39 | (Song and Jennings, 1999) |
| Song and Jennings, 1999 | 44 | 0.5 M NaOH | 0.45 [c] | 34 | (Song and Jennings, 1999) |
| Song and Jennings, 1999 | 44 | 0.1 M NaOH | 0.45 [c] | 29 | (Song and Jennings, 1999) |

[a] water/cement.
[b] (water + activator)/slag.
[c] liquid/slag.

Congruent slag dissolution was assumed, with the slag reaction extents and bulk chemical compositions simulated by proportional additions of $SiO_2$, CaO, MgO, $Al_2O_3$, $Na_2O$, $K_2O$, and $H_2SO_4$ or dissociated $H_2S_{(aq)}$ (matching the $SO_4^{2-}$ and $S^{2-}$ content in the slag where reported, otherwise all sulfur is assumed to be present as $S^{2-}$), to match the bulk slag chemical compositions and reaction extents reported in the literature (e.g. (Bernal et al., 2014b; Le Saoût et al., 2011; Lothenbach and Gruskovnjak, 2007)). All other components of the slag were excluded, as the concentrations of other elements in the slags studied are minor and the reactivity of Fe entrained in slag appears to be very low (Bernal et al., 2014a). For the cases where the degree of reaction of the slag is needed but not available, the extent of reaction of the slag was set so that the bulk chemistry of the simulations matched the bulk chemistry of the binder assumed in the original work (Thomas et al., 2012), or estimated where no further information was available (using the reaction extents provided in (Lothenbach and Gruskovnjak, 2007) as reference values, then modifying based on the bulk alkalinity and curing time).

The simulated solubility results (Figure 6.10) match the experimentally-measured solubility data to approximately ±1 order of magnitude, with the poorest agreement found for the aqueous Si species in $Na_2O{\cdot}mSiO_2{\cdot}xH_2O$-activated cements, which are under-predicted by the thermodynamic model. However, the uncertainty associated with each experimental data point is expected to be large, possibly also up to one order of magnitude, because slag reaction extents are not quantified in the experimental studies referenced here (with the exception of the estimations in (Lothenbach and Gruskovnjak, 2007) for the data in (Gruskovnjak et al., 2006)) and the data correspond to systems that are quite far from equilibrium in some cases (e.g. samples were cured for 7 days in (Puertas et al., 2004)). Similar slag reaction degrees to those estimated here (~40% at 100 days of curing) have been observed in sodium silicate and NaOH-activated slag pastes (35%-45% at 100 days of curing (Ben Haha et al., 2011a)), which does indicate that the estimates used here are reasonable, but does not fully resolve the uncertainty attributed to this factor. With this in mind, the accuracy of the fit between the simulation and experimental results is similar to the

level of uncertainty that can be expected for modelling dissolved elemental concentrations in AAS cements.

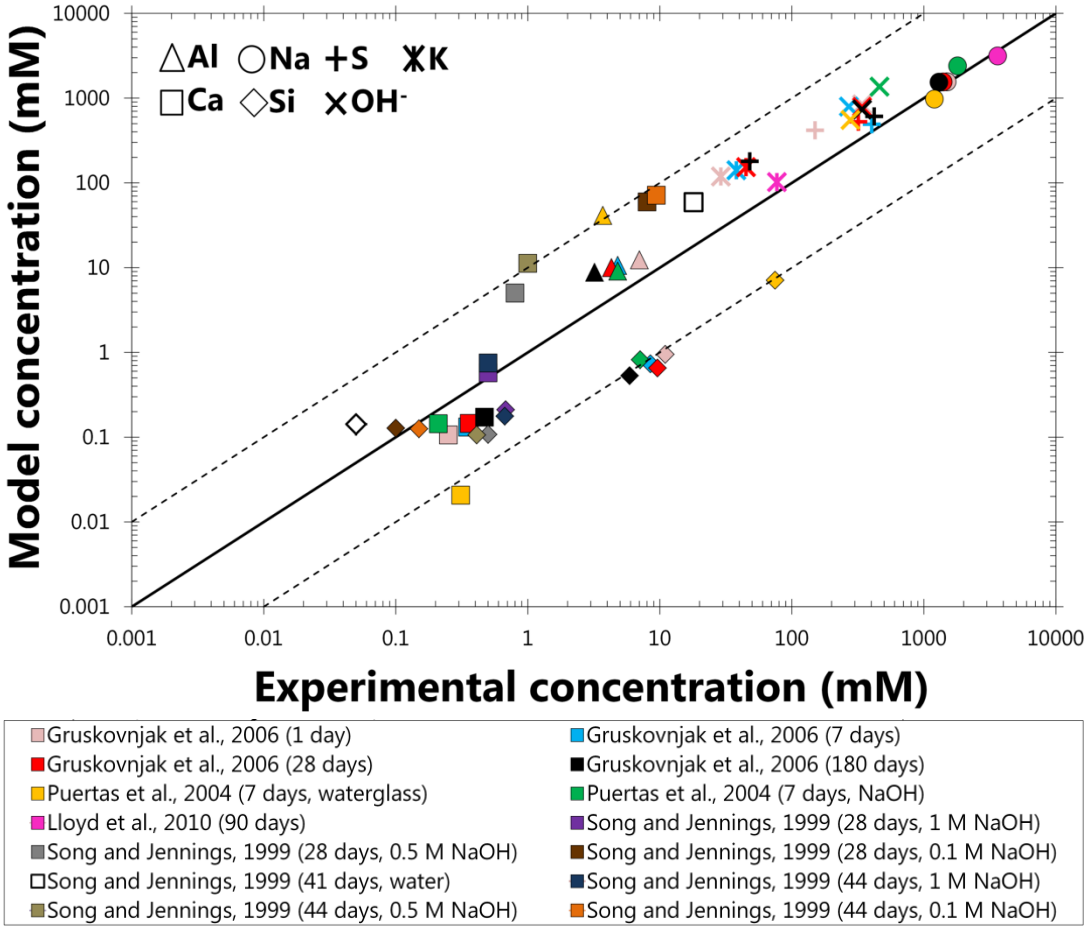


Figure 6.10. Simulated elemental concentrations in the aqueous phase compared to experimental pore solution composition data for AAS cements (Gruskovnjak et al., 2006; Lloyd et al., 2010; Puertas et al., 2004; Song and Jennings, 1999). The dotted lines show ±1 order of magnitude deviation from the solid y = x line. The slag reaction extents used in these simulations are shown in Table 6.5. mM = mmol/L.

Comparisons between thermodynamic modelling results and experimental measurements of C-(N-)A-S-H gel chemical compositions in AAS cements are not straightforward because secondary products are often intimately intermixed with C-(N-)A-S-H gel in these materials (Richardson and Groves, 1992a) and because the nanostructure and chemical composition of this phase can vary considerably at extended ages (Myers et al., 2013). In this sense, thermodynamic modelling can play an important role in understanding how the solid phase assemblage and chemical

composition of C-(N-)A-S-H gel may change over time, with simulation results representing the predicted nature of the solid binder at equilibrium.

It is also important to assess how accurately the thermodynamic model represents the bulk volumetric properties of C-(N-)A-S-H gels, because this is a central aspect of the application of thermodynamic modelling to cement-based materials (Lothenbach et al., 2008a). The C-(N-)A-S-H gels formed in AAS cements are significantly denser than the C-S-H gels formed in neat PC materials (Thomas et al., 2012), which is a result that should be embodied in thermodynamic models for this phase. Hence simulations using the thermodynamic model developed here are compared to the available volumetric data for C-(N-)A-S-H gels in AAS cements (Table 6.6).

Table 6.6. Simulated C-(N-)A-S-H gel properties in AAS cements (Bernal et al., 2014b; Le Saoût et al., 2011; Thomas et al., 2012) compared to the results reported in (Thomas et al., 2012), using the bulk chemistry described in that study.

| **Activator** | **Curing time (days)** | **Density (g/cm$^3$)** | **Molar volume (cm$^3$/mol Si in C-(N-)A-S-H)** | **Reference** |
|---|---|---|---|---|
| | | **Experimental values** | | |
| $Na_2O{\cdot}1.82SiO_2{\cdot}xH_2O$ | 90 | 2.73 | 50.8 | (Thomas et al., 2012) |
| | | **Simulated values** | | |
| $Na_2O{\cdot}1.82SiO_2{\cdot}xH_2O$ | 90 | 2.6 | 58 | (Thomas et al., 2012) |
| $Na_2SiO_3$ | 180 | 2.7 | 53 | COL-GBFS, (Bernal et al., 2014b) |
| $Na_2SiO_3$ | 180 | 2.7 | 54 | AUS-GBFS, (Bernal et al., 2014b) |
| $Na_2SiO_3$ | 180 | 2.7 | 53 | SP-GBFS, (Bernal et al., 2014b) |
| NaOH | 100 | 2.6 | 57 | (Le Saoût et al., 2011) |
| $Na_2SiO_3{\cdot}5H_2O$ | 100 | 2.5 | 56 | (Le Saoût et al., 2011) |

The C-(N-)A-S-H bulk densities and molar volumes simulated by thermodynamic modelling are similar to the reported volumetric properties of this phase (Table 6.6) (Thomas et al., 2012). This result is consistent with a much more tightly packed atomic structure for the C-(N-)A-S-H gels formed in AAS cements than for the C-S-H gels formed in neat PC materials ($(CaO)_{1.7}(SiO_2)_1(H_2O)_{1.8}$, molar volume = 72.1 cm$^3$/mol (Allen and Thomas, 2007)). This is also consistent with the discussion presented in (Thomas et al., 2012), where it was argued that the reported density and

molar volume of the C-(N-)A-S-H gels formed in AAS cements are only weakly related to the bulk composition of these materials. Therefore, it can be expected that the thermodynamic model developed here is able to closely represent the bulk volumetric properties of C-(N-)A-S-H gels in AAS cements.

### 6.4.6 Perspectives

This paper represents the first step towards developing a structurally-consistent thermodynamic model for C-(N-)A-S-H gel that contains explicit descriptions of Al and alkali components, which provides a relatively simple basis for further development and utilisation. Therefore, there are a number of aspects that would improve the thermodynamic model, and some are listed here to guide future development:

- The thermodynamic model has been designed for C-(N-)A-S-H with significant Al and alkali incorporation, particularly those formed in AAS cement. This model may also be relevant to high volume blended PC/SCM materials reacted with either water or an alkali source (e.g. CEM III blast furnace cements as specified in EN 197-1), as the bulk chemical compositions of these materials and AAS cements can be similar (Ca/(Al+Si) ≈ 1) (Taylor et al., 2010). Its suitability for use in simulating the chemistry of these materials needs to be assessed further.
- Improvement can be found by removing the assumptions used to simplify the mixing relationships for the sublattice solid solution model, which approximated the Gibbs free energies of the reciprocal reactions and the excess Gibbs free energies to zero. This will become possible as more information is obtained about the energetic differences arising between hypothetical end-members (i.e. energetic information regarding Si-for-Al substitution in chain sites, and ($Ca^{2+}$,$2Na^{+}$,$2H^{+}$) substitution in interlayer sites) and the solubility of C-(N-)A-S-H.
- The utility of the pore solution composition data used to parameterise the thermodynamic model in AAS cements would be significantly improved if

such data were published alongside quantification of the reaction extent of the slag. This information, along with more solubility data for AAS cements and synthetic $CaO$-$Na_2O$-$Al_2O_3$-$SiO_2$-$H_2O$ systems, will be needed to enable further development of thermodynamic models for C-(N-)A-S-H.

## 6.5 Conclusions

This paper has presented a thermodynamic model for the C-(N-)A-S-H gel in AAS cements, which for the first time accounts explicitly for the structurally-incorporated Al and Na species in this phase. This model represents C-(N-)A-S-H as an ideal solid solution of tobermorite-like end-members with independent substitution of tetrahedral Al and Na species allowed in its formulation, meaning that it may also be applicable to cement-based materials that are less alkali- and/or Al-rich than AAS cements. The model was implemented in GEM-Selektor using thermodynamic properties for the C-(N-)A-S-H end-members that were parameterised to match a comprehensive set of solubility data in the $CaO$-($Na_2O$,$Al_2O_3$)-$SiO_2$-$H_2O$ and AAS cement systems, and published chemical compositions of C-A-S-H.

A good fit was found between the full set of data used in the parameterisation procedure and the simulation results, which were within ±1 order of magnitude in simulations of aqueous phase chemical compositions in AAS cements, indicating that the model is suitable for thermodynamic modelling of these materials. The molar volume and density of the C-(N-)A-S-H gels simulated by the model were also in close agreement with the available data for this phase in AAS cements, meaning that the model can describe chemical shrinkage in these systems. Therefore, the thermodynamic model developed here greatly improves the scope of thermodynamic modelling applications to Ca-rich alkali-activated cements and hybrid alkali-activated/PC materials, which is important for understanding the durability of these materials under sealed, ambient and aggressive environmental conditions.

# 7

# Thermodynamic Modelling of Alkali-Activated Slag-Based Cements

This chapter is based on the manuscript 'Thermodynamic modelling of alkali-activated slag-based cements', by Myers, R. J., Lothenbach B., Bernal, S. A. and Provis, J. L., currently in preparation.

## 7.1 Introduction

Development of alternative, high performance and low $CO_2$ cements is an important advancement that is urgently needed to reduce the $CO_2$-footprint of the construction industry. Alkali-activated cements are formed through the reaction of an activator (an alkaline source), water and aluminosilicate precursors, which are often sourced as industrial by-products (Provis, 2014), and these cements can provide substantial $CO_2$ savings relative to Portland cement (PC) materials (McLellan et al., 2011). Understanding the durability of alkali-activated materials, which is intimately linked to the chemistry of these materials (van Deventer et al., 2012) and differs from conventional PC for important physicochemical reasons (Provis and Bernal, 2014), is a key scientific challenge for their utilisation (Juenger et al., 2011). Alkali-activated slag (AAS) cements are an important type of high-Ca alkali-activated materials (Provis and Bernal, 2014) that are produced using metallurgical slags (Shi and Qian, 2000), typically ground granulated blast furnace slag (GBFS), as precursors.

Evidence for the formation of a highly-connected and poorly-ordered aluminosilicate activation product in sodium silicate-activated slag was presented earlier in this

thesis (Myers et al., 2015a; Myers et al., 2013); this phase is considered to be similar to the alkali aluminosilicate (hydrate) (N-A-S(-H)) 'geopolymer' gels formed through alkali-activation of low-Ca precursor materials (Provis et al., 2005b). These gels are known to show good resistance to elevated temperatures and in the presence of aggressive chemicals, such as in carbonate-rich environments (Bernal et al., 2013c). Accelerated carbonation depths of $Na_2SiO_3$-activated slag cements have been shown to be inversely proportional to the MgO content of the slag precursor used (Bernal et al., 2014b), indicating the important role of Mg in determining the carbonation performance of these materials. (Shi et al., 2006). These results highlight the important role of alkali-activated cement chemistry on the durability of these materials.

The CNASH_ss thermodynamic model (Myers et al., 2014) derived in Chapter 6 was developed to formally account for tetrahedral Al and Na species incorporated in C-(N-)A-S-H with Ca/Si ratios < 1.3. Here, this thermodynamic model is used to simulate the chemistry of AAS cements activated by NaOH, $Na_2O{\cdot}nSiO_2$ ($n$ = 1 and 2) and $Na_2CO_3$. The thermodynamic model is assessed here in terms of predicting solid phase assemblages and the Al content of C-(N-)A-S-H over the bulk slag chemical composition range relevant to AAS cements. These simulations are performed using an expanded thermodynamic database for cementitious materials, based on the CEMDATA07 database with the addition of an updated definition of Mg-Al layered double hydroxide (LDH) phase intercalated with $OH^-$ (MgAl-OH-LDH), and thermodynamic data for some zeolites and alkali carbonates. The results are also discussed in terms of implications for the design of high performance alkali-activated slag-based materials.

## 7.2 Methods

### 7.2.1 Thermodynamic Model for C-(N-)A-S-H

The CNASH_ss thermodynamic model (Myers et al., 2014) developed in Chapter 6 is formulated as an ideal sublattice solid solution comprising three C-S-H end-members, one calcium (alkali) silicate hydrate (C-(N-)S-H) end-member, two C-A-S-H end-members and two C-(N-)A-S-H end-members (Table 7.1). End-member chemical compositions are defined in this model by extension of the 'Substituted General Model' (SGM) (Richardson and Groves, 1993b) for consistency with tobermorite-like nanostructures containing no 'solid solution $Ca(OH)_2$' (Richardson, 2004), which limits the applicability of the model to bulk Ca/Si compositions <1.3.

Table 7.1. The eight end-members of the ideal sublattice solid solution defined in the CNASH_ss thermodynamic model (Myers et al., 2014). Thermodynamic data for these end-members are shown in Table 6.4.

| End-member | Chemical formula |
|---|---|
| 5CA | $(CaO)_{1.25}(SiO_2)_1(Al_2O_3)_{0.125}(H_2O)_{1.625}$ |
| INFCA | $(CaO)_1(SiO_2)_{1.1875}(Al_2O_3)_{0.15625}(H_2O)_{1.65625}$ |
| 5CNA | $(CaO)_{1.25}(SiO_2)_1(Al_2O_3)_{0.125}(Na_2O)_{0.25}(H_2O)_{1.375}$ |
| INFCNA | $(CaO)_1(SiO_2)_{1.1875}(Al_2O_3)_{0.15625}(Na_2O)_{0.34375}(H_2O)_{1.3125}$ |
| INFCN | $(CaO)_1(SiO_2)_{1.5}(Na_2O)_{0.3125}(H_2O)_{1.1875}$ |
| T2C* [a] | $(CaO)_{1.5}(SiO_2)_1(H_2O)_{2.5}$ |
| T5C* [a] | $(CaO)_{1.25}(SiO_2)_{1.25}(H_2O)_{2.5}$ |
| TobH* [a] | $(CaO)_1(SiO_2)_{1.5}(H_2O)_{2.5}$ |

[a] The asterisks for the T2C*, T5C* and TobH* end-members indicate that these components have slightly modified thermodynamic properties but the same chemical compositions relative to the T2C, T5C and TobH end-members of the downscaled CSH3T model (Kulik, 2011).

C-(N-)A-S-H is formally described in terms of non-cross-linked chain structures in the CNASH_ss thermodynamic model, but without precluding representation of cross-linked tobermorite-like chain structures, because these structural types cannot be differentiated by bulk chemical composition alone. Thermodynamic calculations using CNASH_ss are therefore also consistent with cross-linked C-(N-)A-S-H structural models such as those described by the 'Cross-linked Substituted

Tobermorite Model' (CSTM) (Myers et al., 2013). Full details of the development and implementation of the CNASH_ss model are given in Chapter 6 (Myers et al., 2014).

### 7.2.2 Speciation of Iron and Sulfur

Thermodynamic modelling of AAS cements requires consideration of additional constituent elements outside the $CaO$-$Na_2O$-$Al_2O_3$-$SiO_2$-$H_2O$ system, most notably Mg, Fe and sulfur, as well as carbonates. While the speciation of Mg in AAS is generally well explained by its incorporation into Mg-Al LDH phases (Ben Haha et al., 2011b; Richardson et al., 1994; Wang and Scrivener, 1995), there is less consensus regarding the speciation of Fe and sulfur.

It has been reported that Fe is largely present in GBFS as entrained unreactive submicron metallic ($Fe^0$) particles rather than being distributed through the glassy phase of the slag (Bernal et al., 2014a), as the composition of blast furnace slag is specifically designed to reduce Fe solubility in the melt phase, but droplets of metallic iron can become entrained in the slag through splashing in the blast furnace. While minor amounts of $Fe^{2+}$ can also exist in these particles (Taylor, 1997), no distinct Fe-rich secondary products have yet been identified in AAS cements. It is possible that any available $Fe^{2+}$ or $Fe^{3+}$ may be incorporated into solid phases such as C-(N-)A-S-H or AFm/LDH-type products in these materials (Richardson et al., 1994), as is the case in PC-based systems where it is supplied in reactive form by the $C_4AF$ clinker phase. However, the very low content of available Fe in GBFS (i.e. Fe present in the glassy phases rather than as discrete metallic particles) means that the influence of this element on phase formation in AAS is expected to be small. Fe was therefore excluded from the thermodynamic simulations here, to represent the passivated state of this element in GBFS.

Sulfide or polysulfide-containing reaction products have been identified to form in AAS cements (Roy, 2009); the initial hardened product is green in colour

(Lothenbach and Gruskovnjak, 2007) prior to atmospheric oxidation of the sulfur, which is mostly present as sulfide in GBFS (Taylor, 1997). Sulfur is mostly present as sulfide in the pore solution (Gruskovnjak et al., 2006), although the specific chemistry of the sulfide-bearing solid phases is not yet well understood. 'Aluminoferrite-tri' (AFt) products are typically not observed in AAS cements derived from GBFS unless significant additional sulfates are provided by the activator (Rashad et al., 2013), which is consistent with the low sulfur/Al ratio (<< 1) that prevails in these materials (Matschei et al., 2007a). Sulfur was therefore represented in the calculation basis here as $S^{2-}$ supplied by the simulated slag precursors; its oxidation was limited by using a $N_{2\ (g)}$ atmosphere in the thermodynamic modelling calculations.

### 7.2.3 MgAl-OH-LDH

Thermodynamic data for MgAl-OH-LDH were reformulated into an ideal solid solution model containing three end-members with Mg/Al ratios of 2, 3 and 4, to match the known chemical composition range of this solid solution ($Mg_{(1-x)}Al_x(OH)_{(2+x)}\cdot mH_2O$, $0.2 \leq x \leq 0.33$ (Richardson, 2013b)).

Recalculation of recently published solubility data for Mg/Al = 2 MgAl-OH-LDH ($M_4AH_{10}$) (Gao and Li, 2012) and existing solubility data for this phase (Bennett et al., 1992) was performed in GEM-Selektor v.3 (http://gems.web.psi.ch/) (Kulik et al., 2013; Wagner et al., 2012) using the dissolution reaction eq.(7.1):

$$Mg_4Al_2(OH)_{14}\cdot 3H_2O \overset{K_{so}}{\rightleftharpoons} 4Mg^{2+} + 2AlO_2^- + 6(OH)^- + 7H_2O \qquad (7.1)$$

where $K_{so}$ is the solubility product. Solubility data for this phase were also calculated using the additivity method (Anderson and Crerar, 1993) with brucite ($Mg(OH)_{2\ (s)}$), magnesite ($MgCO_{3\ (s)}$) and hydrotalcite ($Mg_{0.74}Al_{0.26}(OH)_2(CO_3)_{0.13}\cdot 0.39H_2O_{\ (s)}$) (Allada et al., 2005a) constituents (Table 7.2).

Table 7.2. Constituents used in the additivity method for MgAl-OH-LDH (298.15 K, 1 bar).

| **Solids** | **V°** **($cm^3$/mol)** | **$\Delta_f H°$** **(kJ/mol)** | **$\Delta_f G°$** **(kJ/mol)** | **S°** **(J/(mol.K))** | **Cp°** **(J/(mol.K))** | **Reference** |
|---|---|---|---|---|---|---|
| Brucite, $Mg(OH)_2$ | 24.6 | -923.3 | -832.2 | 63.1 | 77.3 | (Hummel et al., 2002; Thoenen et al., 2013) |
| Magnesite, $MgCO_3$ | 28.0 | -1113 | -1029 | 65.7 | 75.8 | (Helgeson et al., 1978; Hummel et al., 2002; Thoenen et al., 2013) |
| Hydrotalcite, $Mg_{0.74}Al_{0.26}(OH)_2(CO_3)_{0.13}\cdot 0.39H_2O$ | - [a] | -1166 | -1043 | 85.6 | 101 | (Allada et al., 2005a) |

[a] Not provided

The recalculation results indicate that the solubility product used previously to describe this phase ($\log_{10}(K_{so})$ = -56.02 at 25°C and 1 bar (Lothenbach and Winnefeld, 2006), for the calculated low-solubility data from (Bennett et al., 1992)) is not consistent with the full set of available solubility data for this phase (Figure 7.1). Here, a solubility product of $\log_{10}(K_{so})$ = -49.70 at 25°C and 1 bar is selected for improved consistency with these data. The standard heat capacity and entropy of this phase are adapted from the thermodynamic data reported in (Allada et al., 2005a) for $Mg_{0.74}Al_{0.26}(OH)_2(CO_3)_{0.13}.0.39H_2O$ using the additivity method with $Mg(OH)_{2\ (s)}$ and $MgCO_{3\ (s)}$ constituents (Table 7.2), i.e. the standard heat capacity for $M_4AH_{10}$ is calculated by eq.(7.2):

$$Cp^{o}_{M_4AH_{10}} = 2\left(\frac{1}{0.26}Cp^{o}_{Mg_{0.74}Al_{0.26}(OH)_2(CO_3)_{0.13}\cdot 0.39H_2O} - 0.5Cp^{o}_{MgCO_3} - 0.346Cp^{o}_{Mg(OH)_2}\right) \quad (7.2)$$

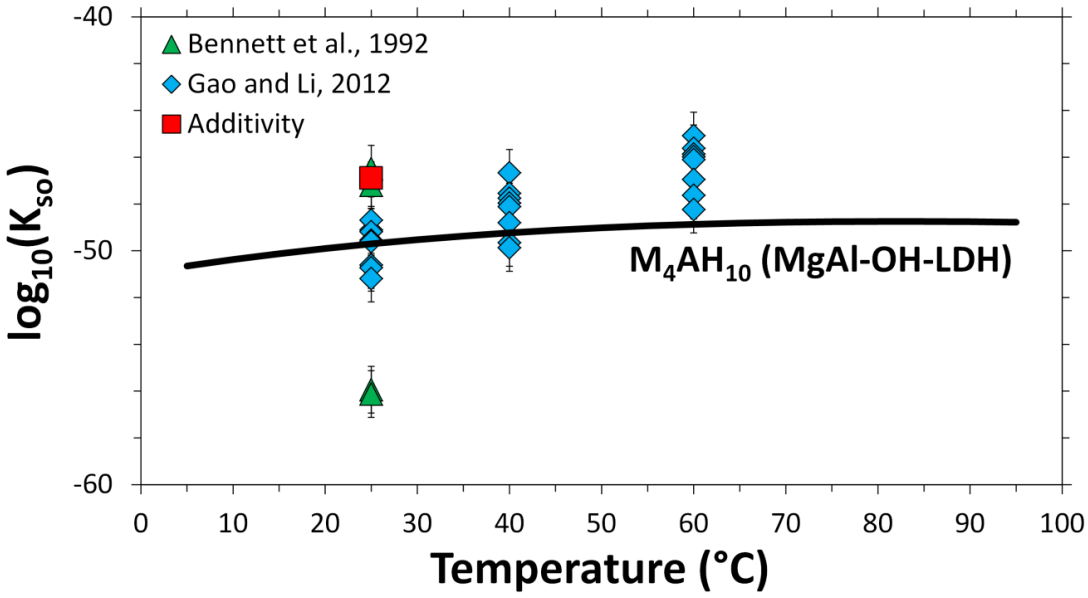


Figure 7.1: Comparison between the recalculated solubility data (Bennett et al., 1992; Gao and Li, 2012), results using the additivity method, and calculated solubility of the $M_4AH_{10}$ end-member of the MgAl-OH-LDH solid solution used in this work, MgAl-OH-LDH_ss (P = 1 bar). The green triangles at $\log_{10}(K_{so})$ = -56.02 (25°C and 1 bar), represents the solubility product used previously to describe this phase in discussions of cement chemistry. Error bars represent the typical maximum uncertainty in solubility products for cement phases (±1 $\log_{10}$ unit).

Standard entropies and heat capacities for Mg/Al = 3 MgAl-OH-LDH ($M_6AH_{12}$) and Mg/Al = 4 MgAl-OH-LDH ($M_8AH_{14}$) were determined in the same manner (using solid constituents and a reaction analogous to eq.(7.2)), using the thermodynamic data reported in (Allada et al., 2005a). A difference of -22.32 $\log_{10}$ units was specified between the solubility products of $M_4AH_{10}$ ($\log_{10}(K_{so})$ = -49.70) and $M_6AH_{12}$ ($\log_{10}(K_{so})$ = -72.02), and between $M_6AH_{12}$ and $M_8AH_{14}$ ($\log_{10}(K_{so})$ = -94.34) at 25°C and 1 bar, which is the difference between the solubility products of these phases when determined using the additivity method described here. A similar difference is found between reported thermodynamic data for MgAl-$CO_3$-LDH ($Mg_4Al_2(OH)_{12}(CO_3).4H_2O$, $\log_{10}(K_{so})$ = -44.19 (Rozov et al., 2011) and $Mg_6Al_2(OH)_{16}(CO_3).5H_2O$, $\log_{10}(K_{so})$ = -66.58 (Rozov, 2010)), which suggests that the additivity approach is appropriate for the structurally-similar Mg-Al-LDH phases. These three MgAl-OH-LDH phases ($M_4AH_{10}$, $M_6AH_{12}$ and $M_8AH_{14}$) were specified as end-members of the simple ideal solid solution 'MgAl-OH-LDH_ss'. This is justified because it has been shown that the assumption of simple ideal mixing is appropriate for modelling the total solubility of the structurally-similar hydrotalcite-pyroaurite solid solution series (Rozov et al., 2011). This MgAl-OH-LDH solid solution is used in the thermodynamic modelling performed in this work.

### 7.2.4 Other Solid Phases

Thermodynamic data for cement-related solid phases other than C-(N-)A-S-H and MgAl-OH-LDH were taken from the PSI/Nagra 12/07 thermodynamic database (Thoenen et al., 2013), which is updated from (Hummel et al., 2002) via the inclusion of two additional dissolved (alumino)silicate species, and the CEMDATA07 thermodynamic database (Kulik and Kersten, 2001; 2002; Lothenbach et al., 2008b; Lothenbach and Winnefeld, 2006; Matschei et al., 2007b; Möschner et al., 2008; Möschner et al., 2009; Schmidt et al., 2008) updated to include recently published data for $Al(OH)_3$ and hydrogarnet phases (Dilnesa et al., 2014; Lothenbach et al., 2012b) (Table 7.3).

Table 7.3. Thermodynamic properties of the secondary and minor solid phases simulated. The reference state is 298.15 K and 1 bar.

| **Phases** [d] | **V°** **($cm^3$/mol)** | **$\Delta_f H°$** **(kJ/mol)** | **$\Delta_f G°$** **(kJ/mol)** | **S°** **(J/(mol.K))** | **Cp°** **(J/(mol.K))** | **Reference** |
|---|---|---|---|---|---|---|
| $Al(OH)_3$ (microcrystalline) | 32.0 | -1265 | -1148 | 140 | 93.1 | (Lothenbach et al., 2012b) |
| Portlandite, CH | 33.1 | -985 | -897 | 83.4 | 87.5 | (Robie and Hemingway, 1995) |
| $SiO_2$ (amorphous) | 29.0 | -903 | -849 | 41.3 | 44.5 | (Helgeson et al., 1978; Kulik and Kersten, 2001) |
| $C_2AH_8$ | 90.1 | -5278 | -4696 | 450 | 521 | (Lothenbach et al., 2012b) |
| Katoite, ($C_3AH_6$) | 150 | -5537 | -5008 | 422 | 446 | (Lothenbach et al., 2012b) |
| $C_4AH_{19}$ | 382 | -1002 | -8750 | 1120 | 1382 | (Lothenbach et al., 2012b) |
| $CAH_{10}$ | 194 | -5288 | -4623 | 610 | 668 | (Lothenbach et al., 2012b) |
| Strätlingite, $C_2ASH_8$ | 216 | -6360 | -5705 | 546 | 603 | (Matschei et al., 2007b) |
| Calcium monocarboaluminate, $C_4AcH_{11}$ | 262 | -8250 | -7337 | 657 | 881 | (Matschei et al., 2007b) |
| Calcium hemicarboaluminate, $C_4Ac_{0.5}H_{12}$ | 285 | -8270 | -7336 | 713 | 906 | (Matschei et al., 2007b) |
| Calcium tricarboaluminate, $C_6Ac_3H_{32}$ | 650 | -16792 | -14566 | 1858 | 2121 | (Matschei et al., 2007b) |
| Ettringite, $C_6A\overline{S}_3H_{32}$ | 707 | -17535 | -15206 | 1900 | 2174 | (Lothenbach et al., 2008b) |
| Gypsum, $C\overline{S}H_2$ | 74.7 | -2023 | -1798 | 194 | 186 | (Hummel et al., 2002; Thoenen et al., 2013) |
| Anhydrite, $C\overline{S}$ | 45.9 | -1435 | -1322 | 107 | 99.6 | (Hummel et al., 2002; Thoenen et al., 2013) |
| CaO | 16.8 | -635 | -604 | 39.7 | 42.8 | (Helgeson et al., 1978) |
| Brucite, MH | 24.6 | -923 | -832 | 63.1 | 77.3 | (Helgeson et al., 1978; Hummel et al., 2002; Thoenen et al., 2013) |
| MgAl-$CO_3$-LDH, $M_4AcH_9$ | 220 | -7374 | -6580 | 551 | 647 | (Lothenbach et al., 2008b) |

Table 7.3. Continued.

| | | | | | | |
|---|---|---|---|---|---|---|
| **Calcium monosulfoaluminate-hydroxoaluminate non-ideal solid solution (Matschei et al., 2007b)** | | | | | | |
| Calcium monosulfoaluminate, $C_4A\bar{S}H_{12}$ | 309 | -8750 | -7779 | 821 | 942 | (Matschei et al., 2007b) |
| $C_4AH_{13}$ | 274 | -8300 | -7324 | 700 | 930 | (Lothenbach et al., 2012b) |
| **Carbonates** | | | | | | |
| Aragonite, $CaCO_3$ | 34.2 | -1207 | -1128 | 90.2 | 81.3 | (Hummel et al., 2002; Thoenen et al., 2013) |
| Calcite, $CaCO_3$ | 36.9 | -1207 | -1129 | 92.7 | 81.9 | (Hummel et al., 2002; Thoenen et al., 2013) |
| Dolomite (disordered), $CMc_2$ | 64.4 | -2317 | -2157 | 167 | 158 | (Hummel et al., 2002; Thoenen et al., 2013) |
| Natron, $NcH_{10}$ | 197 | -4079 | -3428 | 563 | 550 | (Königsberger et al., 1999; Taga, 1969) |
| Gaylussite, $NCc_2H_5$ | 149 | -3834 | -3372 | 387 | - [a] | (Dickens and Brown, 1969; Königsberger et al., 1999) |
| Pirssonite, $NCc_2H_2$ | 104 | -2956 | -2658 | 239 | 329 | (Dickens and Brown, 1969; Königsberger et al., 1999) |
| Magnesite, Mc | 28.0 | -1113 | -1029 | 65.7 | 75.8 | (Hummel et al., 2002; Thoenen et al., 2013) |
| Huntite, $CM_3c_4$ | 123 | -4533 | -4206 | 300 | 310 | (Graf and Bradley, 1962; Hemingway and Robie, 1972; Königsberger et al., 1999) |
| Artinite, $M_2cH_4$ | 96.2 | -2921 | -2568 | 233 | 248 | (de Wolff, 1952; Hemingway and Robie, 1972; Königsberger et al., 1999) |
| Lansfordite, $McH_5$ | 103 | -2574 | -2198 | 250 | 386 | (Hill et al., 1982; Königsberger et al., 1999) |
| **MgAl-OH-LDH ideal solid solution end-members, 'MgAl-OH-LDH_ss'** | | | | | | |
| $M_4AH_{10}$ | 219 | -7160 | -6358 | 549 | 648 | (Allada et al., 2005a; Richardson, 2013b) |
| $M_6AH_{12}$ | 305 | -9007 | -8023 | 675 | 803 | This study [b] |
| $M_8AH_{14}$ | 392 | -10853 | -9687 | 801 | 958 | This study [b] |

Table 7.3. Continued.

| | | | | | | |
|---|---|---|---|---|---|---|
| **Zeolites** | | | | | | |
| Na-analcime, $\|Na_{0.32}\|.[Al_{0.32}Si_{0.68}O_2].0.333H_2O$ | 32.5 [c] | -1099 | -1026 | 75.6 | 70.5 | (Johnson et al., 1982) |
| Natrolite, $\|Na_{0.4}\|.[Al_{0.4}Si_{0.6}O_2].0.4H_2O$ | 33.8 [c] | -1144 | -1063 | 71.9 | 60.4 | (Johnson et al., 1983) |
| Ca-heulandite, $\|Ca_{0.111}\|.[Al_{0.222}Si_{0.778}O_2].0.667H_2O$ | 35.2 [c] | -1179 | -1090 | 87.1 | 82.9 | (Kiseleva et al., 2001) |
| (Ca,Na)-heulandite, $\|Ca_{0.111}Na_{0.028}\|.[Al_{0.25}Si_{0.75}O_2].0.667H_2O$ | 35.2 [c] | -1185 | -1094 | 84.0 | 82.9 | (Kiseleva et al., 2001) |
| Basic sodalite, $\|Na_{0.65}(OH)_{0.15}\|.[Al_{0.5}Si_{0.5}O_2].0.27H_2O$ | 35.0 [c] | -1190 | -1106 | 67.8 [e] | 66.7 [e] | (Moloy et al., 2006) |

[a] Not available

[b] Thermodynamic properties based on the thermochemical data in (Allada et al., 2005a) and solubility data in (Bennett et al., 1992; Gao and Li, 2012), with molar volumes calculated from (Richardson, 2013b).

[c] Molar volumes calculated from framework densities, lattice types and lattice cell parameters for each zeolite framework type (Baerlocher et al., 2007).

[d] Cement chemistry notation is used: C = CaO; S = $SiO_2$; A = $Al_2O_3$; H = $H_2O$; N = $Na_2O$; M = MgO; c = $CO_2$; $\bar{S}$ = $SO_3$.

[e] Standard entropy and heat capacity estimated using the additivity method (Anderson and Crerar, 1993) based on $H_2O_{(l)}$ (Table 3.3, section 3.4.1), gibbsite (Helgeson et al., 1978; Hummel et al., 2002), $NaOH_{(s)}$ (Robie and Hemingway, 1995) and amorphous $SiO_2$ (Table 7.3).

Thermodynamic data for some zeolites and alkali carbonate minerals were used to provide a preliminary assessment of the stability of these phases in AAS cements. The thermodynamic data used to describe these phases here (Table 7.3) should be treated as provisional only, because the thermodynamic data were not recompiled for full internal consistency with the Nagra-PSI and CEMDATA07 thermodynamic databases. Reliable thermodynamic data for other potentially important Na-carbonates which can form in AAS cements (i.e. natrite ($Na_2CO_3$), thermonatrite ($Na_2CO_3 \cdot H_2O$), nahcolite ($NaHCO_3$) and trona ($Na_2CO_3 \cdot NaHCO_3 \cdot 2H_2O$)) are not available (Königsberger et al., 1999; Monnin and Schott, 1984); therefore they were excluded from the simulations.

The formation of siliceous hydrogarnet was suppressed in the simulations because this phase is kinetically hindered at ambient temperature and pressure (Lothenbach et al., 2008b). No additional restrictions related to the formation of any other solid reaction products were specified.

### 7.2.5 Approach

Thermodynamic modelling was performed using the Gibbs energy minimisation software GEM-Selektor v.3 (http://gems.web.psi.ch/) (Kulik et al., 2013; Wagner et al., 2012), with thermodynamic data for the solid phases discussed in sections 7.2.1-7.2.4, and thermodynamic data for aqueous species and gases shown in Tables 3.2-3.3 in section 3.4.1. The Truesdell-Jones form of the extended Debye-Hückel equation (eq.(3.7)) (Helgeson et al., 1981) and the ideal gas equation of state were used for the aqueous and gaseous phase models respectively; the activity coefficient models used in this thesis are described in section 3.4.1.

Chemical equilibrium between the solid, aqueous and gaseous phases was assumed, and the slag was specified to dissolve congruently. The assumption of congruent dissolution is valid for calcium aluminosilicate glasses of similar bulk chemical compositions to GBFS in highly under-saturated conditions at pH = 13 (Snellings,

2013). This condition is likely to be approximated in AAS cements when the solution pH is sufficiently high (Bernal et al., 2015), although it is clear that this assumption will need to be revisited in some systems, particularly for AAS cements cured for long times or synthesised with less basic activators such as $Na_2CO_3$ (Bernal et al., 2015).

A basis of 100 g slag (including the unreacted and reacted slag components), additions of $H_2O$, NaOH or $Na_2O$, $SiO_2$ and $Na_2CO_3$ to achieve fixed water to binder (w/b) ratios of 0.4 and activator concentrations of 4 g $Na_2O$ equivalent/100 g slag (the activators used are NaOH, $Na_2SiO_3$, $Na_2Si_2O_5$ and $Na_2CO_3$), a nitrogen atmosphere (10 mol $N_{2\ (g)}$ per 100 g slag), and temperature/pressure conditions of 298.15 K and 1 bar were specified. A specific gravity of 2.8 g/cm$^3$ was selected for the unreacted slag component (Bernal et al., 2015). This simulation setup directly represents the AAS cements studied in (Bernal et al., 2015; Bernal et al., 2014b; Myers et al., 2015a; Myers et al., 2013), and is also similar to the AAS cement formulations reported in (Ben Haha et al., 2011b; 2012; Le Saoût et al., 2011) (which had ~3 wt.% $Na_2O$ equivalent and w/b = 0.4). With the exception of the phase diagram simulations (section 7.3.4), the simulated slag compositions are based on the GBFS composition shown in Table 3.1 (section 3.2.1).

In section 7.3.1, the utility of the thermodynamic database (Table 7.3 for secondary phases, Table 6.4 for C-(N-)A-S-H, and Tables 3.2-3.3 in section 3.4.1 for aqueous species and gases) is assessed by assigning a reactive slag component comprised of $SiO_2$, CaO, MgO, $Al_2O_3$, $Na_2O$, $K_2O$, and $H_2S$ (corresponding to the "$SO_3$" content of the slag in Table 3.1) and an unreactive slag component; the masses of both reactive and unreactive slag components sum to 100 g at 100% slag reaction extent. The mass of each reactive oxide component added to the simulation is specified using the slag composition given in Table 3.1 (i.e. 33.8 g $SiO_2$ is specified for 100 g slag), except for the variable reactive oxide component ($Al_2O_3$, MgO or CaO), which was specified according to the simulation conducted: the $Al_2O_3$, MgO or CaO content in the slag was varied from 6-20 wt.%, 0-18 wt.% or 30-50 wt.%

respectively. The reactive slag component was rescaled to 60 g for each simulation step, to simulate a slag reaction extent of 60%, which represents a typical degree of reaction quantified for GBFS in sodium silicate-activated slag cements (~48% at 180 days in (Ben Haha et al., 2011a), 54 ±3% at 100 days in (Le Saoût et al., 2011), 58-61% at 180 days in (Bernal et al., 2014b) and >70% after 1 month in (Myers et al., 2015a)).

Specific details pertaining to the different descriptions of the slag-based precursors used here, for each other aspect of the study, are shown near the beginning of each of sections 7.3.2-7.3.4.

## 7.3 Results and Discussion

### 7.3.1 Utility of CNASH_ss and MgAl-OH-LDH_ss

Figure 7.2A shows that the calculated phase assemblage in $Na_2SiO_3$-activated slag cement changes greatly as a function of $Al_2O_3$ content in the slag. The secondary products (forming in addition to C-(N-)A-S-H) are dominated by MgAl-OH-LDH between 6 and 9 wt.% $Al_2O_3$, and strätlingite, which forms alongside this phase between 9 and 20 wt.% $Al_2O_3$. Small amounts of katoite are predicted for slags with 7-11 wt.% $Al_2O_3$, and natrolite between 17 and 20 wt.% $Al_2O_3$. The prediction of katoite here is relatively consistent with the observation of small amounts of this phase in sodium silicate-activated slag cements produced from slags with ~13 wt.% $Al_2O_3$ (Bernal et al., 2014b; Schneider et al., 2001). MgAl-OH-LDH phases are widely identified in sodium silicate-activated slag cements derived from slags with ≥5 wt.% MgO (Bernal et al., 2014b), in good agreement with these results; LDH formation is reassessed in detail below. Very small quantities of brucite are predicted for slags with 6 wt.% $Al_2O_3$. The simulated volume of the MgAl-OH-LDH phase does not change greatly here because its formation is limited by the amount of Mg supplied by the slag, which is constant at a fixed slag reaction extent.

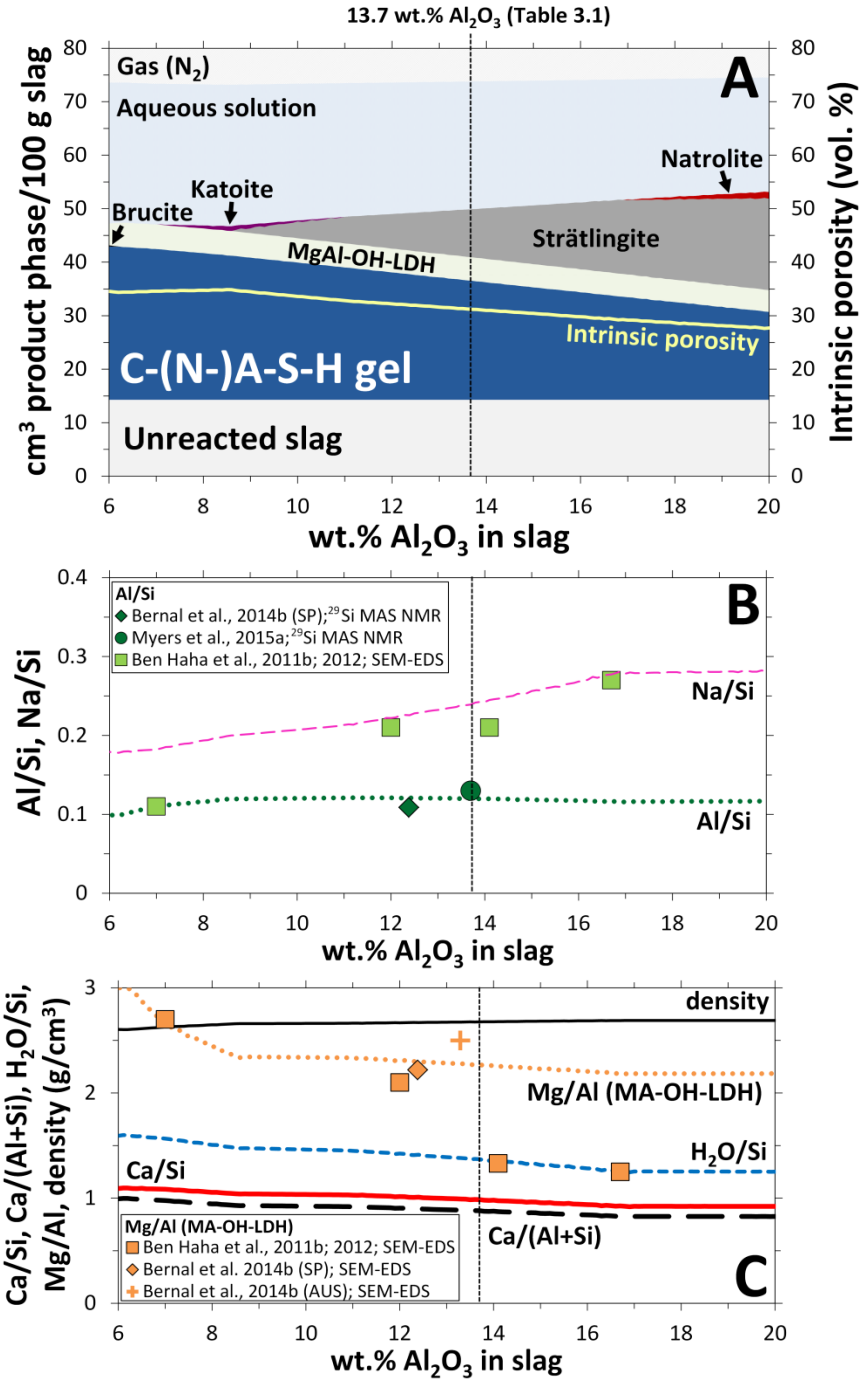


Figure 7.2. Simulated A) solid phase assemblages, B) Al/Si ratios in C-(N-)A-S-H gel, and C) Mg/Al ratios in MgAl-OH-LDH in $Na_2SiO_3$-activated slag cements with bulk slag chemical compositions rescaled from Table 3.1 except for the $Al_2O_3$ content, which is varied here. Changes in B) Na/Si, C) $H_2O$/Si, Ca/Si and Ca/(Al+Si) ratios in C-(N-)A-S-H gel, and C) C-(N-)A-S-H gel density (g/cm$^3$) are shown for visual reference. The symbols in B) and C) are experimental results for sodium silicate-activated slag cements cured for 180 days and derived from slag precursors with similar MgO and equivalent or slightly lower CaO content (5.2 < wt.% MgO < 7.7, 35 < wt.% CaO ≤ 42.6) to the slag represented by Table 3.1.

The Mg/Al ratio of the MgAl-OH-LDH solid solution is between 2 and 3 over the full range of simulated slag $Al_2O_3$ compositions (Figure 7.2C), in excellent agreement with experimentally determined Mg/Al ratios for this phase by scanning electron microscopy (SEM) with energy-dispersive X-ray spectroscopy (EDS) analysis in sodium silicate-activated slag cements for slags containing $7 \leq$ wt.% $Al_2O_3 \leq 13.3$ (Ben Haha et al., 2012; Bernal et al., 2014b). However, the experimental SEM-EDS data suggest a systematic reduction in the Mg/Al ratio of this phase to below 2 as a function of increasing slag $Al_2O_3$ content (Ben Haha et al., 2012; Bernal et al., 2014b), that is not able to be captured by the modelling performed here, as the model only describes solid solutions in the range $2 \leq Mg/Al \leq 4$. Regions with Mg/Al ratios < 2 identified in transmission electron microscopy (TEM)-EDS analysis of hydrated PC/GBFS pastes (Taylor et al., 2010) are discussed in terms of intimate mixtures of Mg-Al-LDH and $Al(OH)_3$-type phases because the chemical composition of Mg-Al-LDH is theoretically limited to the range modelled here, $2 \leq Mg/Al \leq 4$ (Richardson, 2013b); the experimental Mg/Al ratios < 2 shown in Figure 7.2C can thus be described similarly, which would explain the difference between the modelled and experimentally measured data. This analysis suggests a need for additional thermodynamic data describing Al-rich and Mg-poor solid phases that are not currently included in the thermodynamic database (e.g. TAH (Andersen et al., 2006)) rather than a deficiency in the MgAl-OH-LDH thermodynamic model (section 7.2.3).

The amount of C-(N-)A-S-H formed in the simulated $Na_2SiO_3$-activated slag cements decreases with increasing $Al_2O_3$ content of the slag (Figure 7.2A), while more strätlingite is formed. An Al/Si ratio ≈ 0.12 is calculated for C-(N-)A-S-H in $Na_2SiO_3$-activated slag cements derived from slags with >8 wt.% $Al_2O_3$ (Figure 7.2B), which corresponds closely to the Al/Si ratios determined for this phase by analysis of deconvoluted $^{29}$Si MAS NMR spectra for these materials at 180 days of age (Bernal et al., 2014b; Myers et al., 2015a). However, the experimental Al/Si ratios determined from $^{29}$Si MAS NMR shown here exclude the potential uptake of $Al^{[5]}$ (Andersen et al., 2006) and $Al^{[6]}$ (Sun et al., 2006) in C-(N-)A-S-H, so are

expected to be slightly lower than the 'true' Al/Si ratio in this phase. Slightly increased experimental Al/Si ratios would provide better agreement with the SEM-EDS datum at a slag $Al_2O_3$ content of 12 wt.% but would be less consistent with the modelling results. This discrepancy is discussed further in section 7.3.2. The much higher Al/Si ratios shown by the other SEM-EDS data, with Mg/Al < 2, could indicate mixtures of C-(N-)A-S-H with Mg-free and Al-containing phases in the interaction volumes analysed, similar to the analysis above for the MgAl-OH-LDH phase, so are not necessarily inconsistent with the thermodynamic modelling results.

The total binder volume (solid + aqueous phases) is calculated to be approximately constant over the full range of slag $Al_2O_3$ compositions studied (Figure 7.2A), suggesting that the bulk Al content of the slag in $Na_2SiO_3$-activated slag cements should not greatly affect the chemical shrinkage properties of these materials. The results indicate a 20% change in intrinsic porosity (i.e., excluding gases and thus corresponding only to the solid binder and free water) for slag compositions between ~8 and 20 wt.% $Al_2O_3$. This interpretation is facilitated by the simulated C-(N-)A-S-H density of 2.5-2.7 g/cm$^3$ and $H_2O$/Si ratios between 1.3 and 1.7 (corresponding to RH ≈ 25% (Muller et al., 2013b)), as shown in Figure 7.2C; therefore this phase is conceptually equivalent to C-(N-)A-S-H with interlayer and some adsorbed water but no 'gel' or 'free' water (Jennings, 2008). It is important to note that this phase contains less bound water in AAS than in hydrated PC (Thomas et al., 2012). However, the reduced intrinsic porosity found here at higher bulk slag $Al_2O_3$ content does not explain the weak dependency of sodium silicate-activated slag cement compressive strengths on bulk slag $Al_2O_3$ content (Ben Haha et al., 2012), where an increase would be expected at lower porosity. This discrepancy is attributed to the higher amount of strätlingite simulated here compared to the amount of this phase which is identified in AAS cements; this issue is revisited in section 7.3.2.

Simulations of $Na_2SiO_3$-activated slag cements derived from slags with 0-18 wt.% MgO (Figure 7.3) show little change in intrinsic porosity and total binder volume as a function of MgO content. This result differs from previous thermodynamic

modelling that showed a significant increase in intrinsic porosity (total solid volume) over this same MgO composition range (Ben Haha et al., 2011b). This difference is partly founded in the high amounts of strätlingite predicted, but also relates to the use of the CNASH_ss thermodynamic model here, rather than the less complex thermodynamic model used to describe C-(N-)A-S-H in that previous study (density ≈ 2.2-2.4 g/cm$^3$ (Lothenbach et al., 2008b)), as the current work formally defines the uptake of Al in C-(N-)A-S-H and much more closely describes the volumetric properties of this phase in sodium silicate-activated slag cements (density = 2.6-2.7 g/cm$^3$, Figure 7.3C) and in underwater-cured cement paste (density = 2.68 g/cm$^3$ (Muller et al., 2013b)).

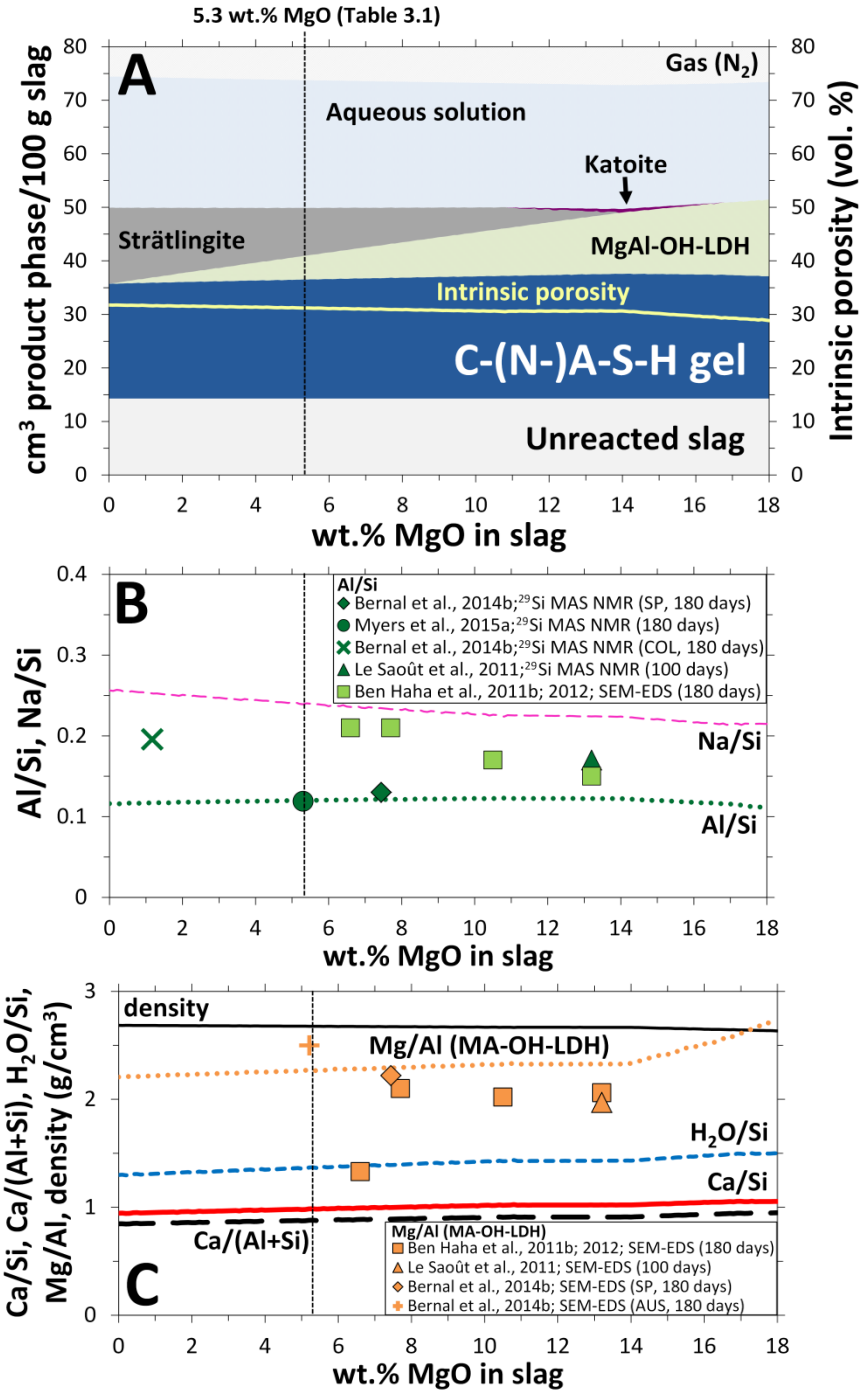


Figure 7.3. Simulated A) solid phase assemblages, B) Al/Si ratios in C-(N-)A-S-H gel, and C) Mg/Al ratios in MgAl-OH-LDH in NS-AS cements with bulk slag chemical compositions rescaled from Table 3.1 except for the Mg content, which is varied here. Changes in B) Na/Si, C) $H_2O$/Si, Ca/Si and Ca/(Al+Si) ratios in C-(N-)A-S-H gel, and C) C-(N-)A-S-H gel density (g/cm$^3$) are shown for visual reference. The symbols in B) and C) represent experimentally measured data for sodium silicate-activated slag cements (curing times are indicated in parentheses) derived from slag precursors with similar $Al_2O_3$ and equivalent or slightly lower CaO content (11.3 < wt.% $Al_2O_3$ < 14.1, 33.4 < wt.% CaO ≤ 42.6) to the slag represented by Table 3.1.

The secondary product assemblage changes markedly as a function of the MgO content of the slag (Figure 7.3A), but little change in C-(N-)A-S-H volume is simulated between 0 and 18 wt.% MgO. The only Mg-bearing secondary product predicted is MgAl-OH-LDH, which increases in volume as a function of the slag MgO content. The simulated and experimentally measured Mg/Al ratios of this phase in sodium silicate-activated slag cements are in relatively good agreement (simulated Mg/Al ≈ 2.3, Figure 7.3C) (Ben Haha et al., 2011b; Bernal et al., 2014b; Le Saoût et al., 2011), with the exception of the samples containing significant intermixing of additional products (with Mg/Al << 2). This result further supports the thermodynamic description of MgAl-OH-LDH used here. The only predicted minor phase is katoite at 11-17 wt.% MgO. Brucite is not predicted here, in good agreement with experimentally observed solid phase assemblages in AAS cements (Ben Haha et al., 2011b; Myers et al., 2015a; Richardson et al., 1994; Schneider et al., 2001; Wang and Scrivener, 1995).

The Al/Si ratio of the simulated C-(N-)A-S-H product (Al/Si ≈ 0.12) is similar to the experimentally determined Al content of this phase in sodium silicate-activated slag cements derived from slags with wt.% MgO ≤ 13.2 (Bernal et al., 2014b; Le Saoût et al., 2011) (Figure 7.3B), except for the SEM-EDS datum at ~7.8 wt.% MgO (Ben Haha et al., 2012) and the $^{29}$Si MAS NMR datum at 1.2 wt.% MgO (Al/Si ≈ 0.2) (Bernal et al., 2014b). This discrepancy can be partly attributed to the incomplete description of secondary phases in the thermodynamic database, which would be particularly relevant for the datum at 1.2 wt.% MgO, as gismondine and/or N-A-S(-H) gel (which is thought to be a poorly-ordered zeolite-type phase (Provis et al., 2005b)) were identified as reaction products in that binder (Bernal et al., 2014b); these phases contain $Q^4(n\text{Al})$ Si sites that resonate in NMR experiments at the same chemical shift as $Q^3$(1Al) sites in C-(N-)A-S-H (Klinowski, 1984; Myers et al., 2013). Simulations of $Na_2SiO_3$-activated slag cements show that zeolites are predicted for slags with ≤41 wt.% CaO (Figure 7.4), in good agreement with this analysis and the identification of zeolites in these materials (Bernal et al., 2011b; Bernal et al., 2014b). The bulk CaO concentration is therefore a key parameter

controlling the formation of zeolite-type phases in AAS-based cements. However, it is important to note that Ca-rich zeolites such as gismondine, which are expected to have relatively high stability in AAS-based materials, are not described in the thermodynamic database used here due to the absence of appropriate thermodynamic data for these phases.

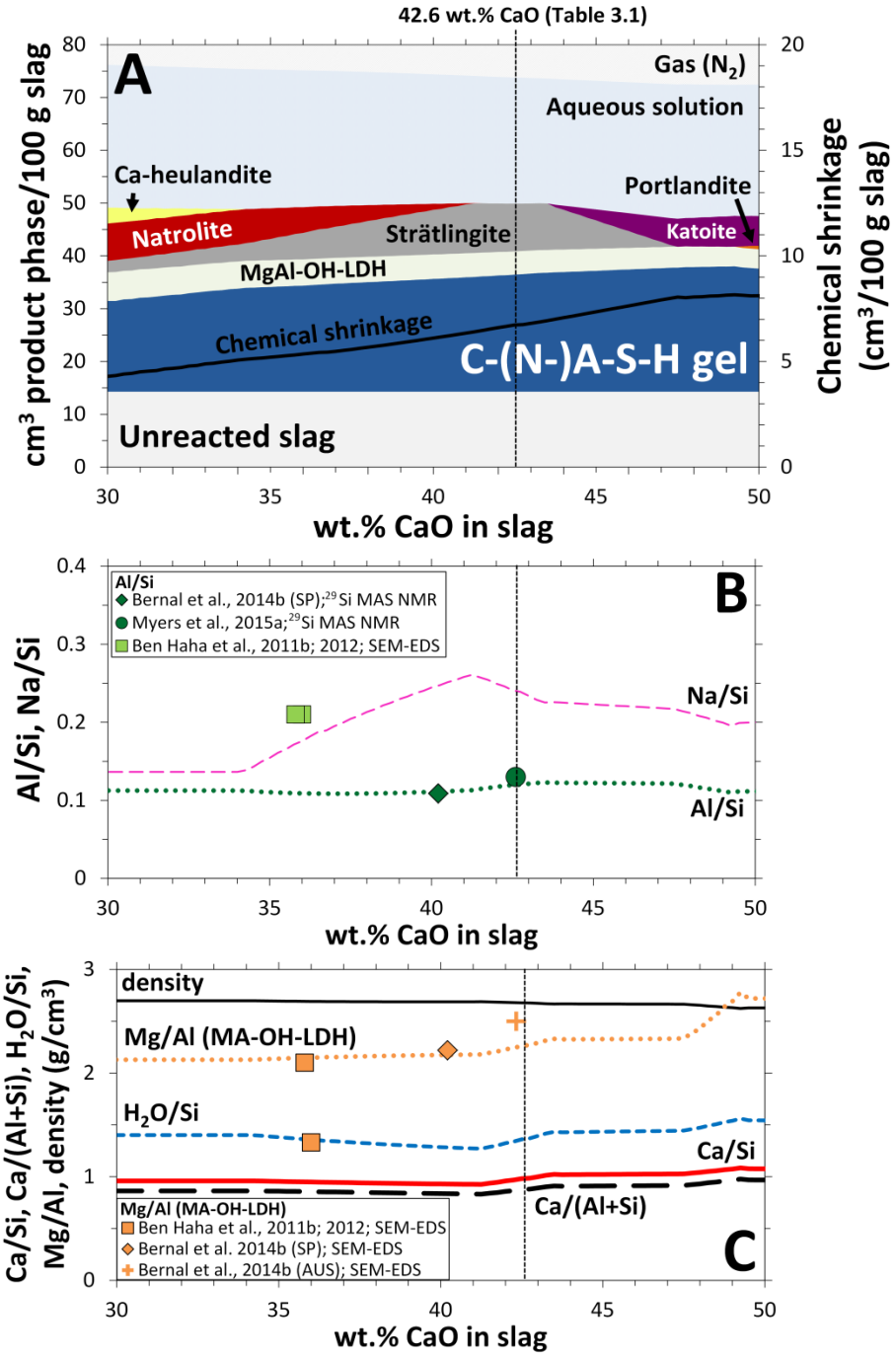


Figure 7.4. Simulated A) solid phase assemblages, B) Al/Si ratios in C-(N-)A-S-H gel, and C) Mg/Al ratios in MgAl-OH-LDH in NS-AS cements with bulk slag chemical compositions rescaled from Table 3.1 except for the Ca content, which is varied here (traces). Changes in B) Na/Si, C) $H_2O$/Si, Ca/Si and Ca/(Al+Si) ratios in C-(N-)A-S-H gel, and C) C-(N-)A-S-H gel density (g/cm$^3$) are shown for visual reference. The symbols in B) and C) represent experimentally measured data for sodium silicate-activated slag cements derived from slag precursors with similar $Al_2O_3$ and MgO content (12 < wt.% $Al_2O_3$ < 14.1, 5.2 < wt.% MgO < 7.7) to the slag represented by Table 3.1. The difference in intrinsic porosity within the full range of modelled CaO compositions is 3%.

It is also notable that the total binder volume changes markedly as a function of the CaO content in the slag, which suggests that the bulk CaO concentration is also a key parameter for the chemical shrinkage properties of these materials; a difference of 3.8 $cm^3$/100 g slag ($\Delta CS$ = 47%) is identified over the range 30 ≤ CaO ≤ 49 wt.% (Figure 7.4A). Simulated Mg/Al ratios of the MgAl-OH-LDH phase and Al/Si ratios of C-(N-)A-S-H are in close agreement with the experimental data, with the exception of the SEM-EDS data at a slag CaO content of ~36 wt.% which likely contains some intermixed low-Mg high-Al phases (Taylor et al., 2010).

Therefore, the wide range of slag compositions where the modelling results generally describe the experimental data shown here (7 ≤ wt.% $Al_2O_3$ ≤ 13.7, Figure 7.2, 5.2 ≤ wt.% MgO ≤ 13.2, Figure 7.3, and 35.8 ≤ wt.% CaO ≤ 42.3, Figure 7.4), means that the CNASH_ss and MgAl-OH_LDH_ss thermodynamic models can be used with some confidence to describe the chemistry of $Na_2SiO_3$-activated slag cements over the most common ranges of slag compositions and activator doses used in these materials. Within this range, the model predictions are within ~0.04 units in the Al/Si ratios of the C-(N-)A-S-H and ~0.3 units in the Mg/Al ratios of the MgAl-OH-LDH phase.

### 7.3.2 Simulated Reaction of a $Na_2SiO_3$-Activated Slag Cement

Additional thermodynamic modelling analysis of $Na_2SiO_3$-activated slag cements is performed by varying the slag reaction extent from 0-100%, in the presence of $Na_2SiO_3$ (8 g $Na_2SiO_3$/100 g slag), while holding the slag chemical composition constant (Table 3.1, section 3.2.1).

The predicted solid phase assemblage consists of C-(N-)A-S-H as the primary reaction product, and MgAl-OH-LDH (Mg/Al ≈ 2), strätlingite, Ca-heulandite, brucite, natrolite and katoite as secondary or minor products (Figure 7.5A). Zeolites are only predicted for slag reaction extents <40% (i.e. effectively at low bulk CaO concentrations, consistent with Figure 7.4), which is less than the experimentally-

determined slag reaction extent for AAS cement after 1 day of curing (Myers et al., 2015a), and is relatively consistent with the experimental observation of only minor amounts of these phases in AAS cements (Bernal et al., 2011b; Bernal et al., 2014b).

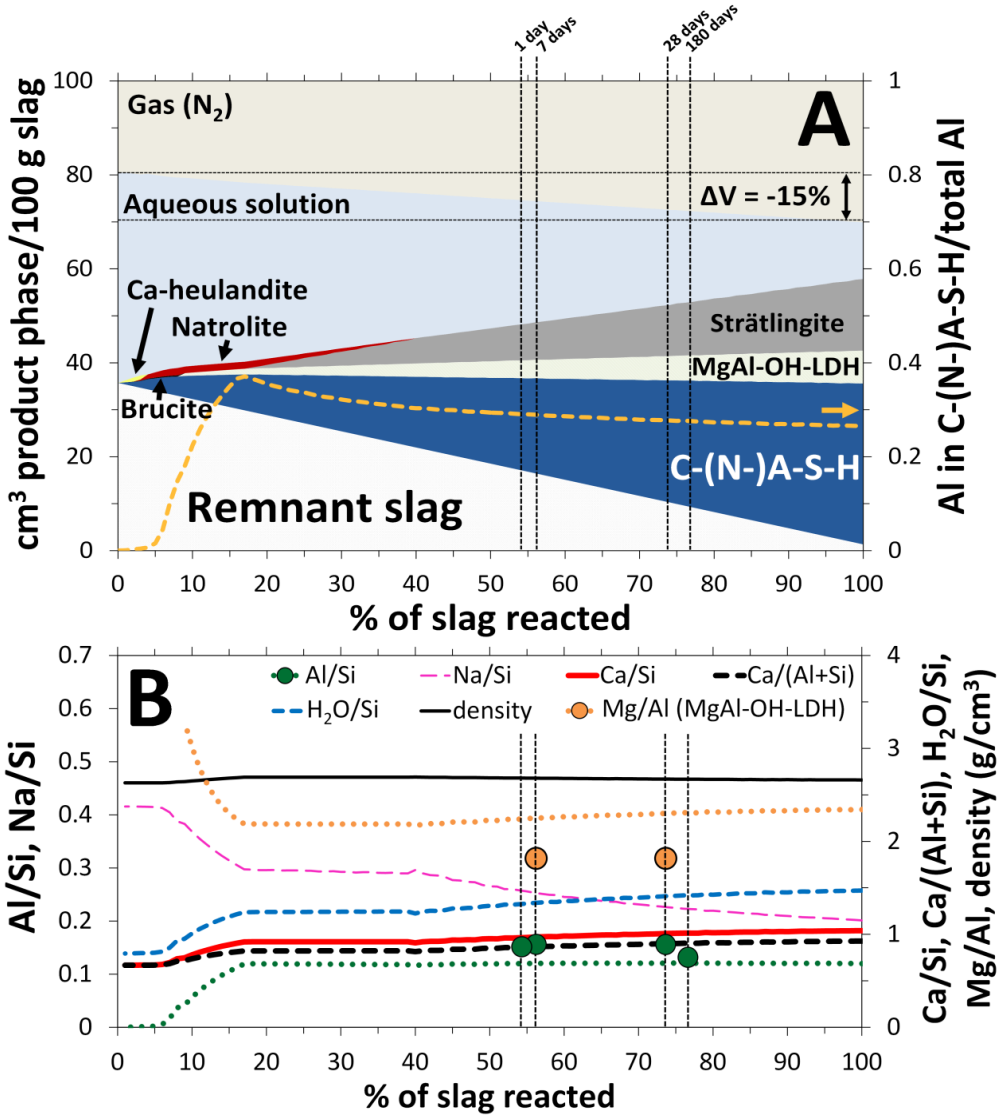


Figure 7.5. Simulated A) solid phase assemblages and B) C-(N-)A-S-H chemical compositions and densities (g/cm$^3$), and Mg/Al ratios of the MgAl-OH-LDH phase in an $Na_2SiO_3$-activated slag cement (traces). The slag chemical composition is shown in Table 3.1. The dashed vertical lines correspond to slag reaction extents determined experimentally at each time of curing (Myers et al., 2015a). In B), the dark green circles are experimental Al/Si ratios in C-(N-)A-S-H determined by deconvolutions of $^{29}$Si MAS NMR spectra (Myers et al., 2015a), and the white circles are experimental Mg/Al ratios in the MgAl-OH-LDH phase determined by SEM-EDS (Myers et al., 2013). Horizontal dashed lines in A) represent the predicted chemical shrinkage at complete reaction of the slag (11 cm$^3$/100 g slag). The dashed orange trace in A) represents the fraction of Al bound in C-(N-)A-S-H relative to the total amount of Al in the solid reaction products.

The prediction of MgAl-OH-LDH and strätlingite is in relatively good agreement with experimentally-determined solid phase assemblages in $Na_2SiO_3$-activated slag cements (Ben Haha et al., 2012; Brough and Atkinson, 2002; Burciaga-Díaz and Escalante-García, 2013; Myers et al., 2015a; Wang and Scrivener, 1995), where Mg-Al LDH phases are often identified and the formation of AFm-type phases are likely, although the calculations here do markedly over-predict the amount of strätlingite formed compared to the experimental observations. Approximately constant proportions of the main hydrate phases (strätlingite, MgAl-OH-LDH and C-(N-)A-S-H) are predicted relative to the total reaction product volume at slag reaction extents exceeding 40%. The influence of the additional Si supplied by the activator is diluted as more slag reacts, i.e. the slag chemical composition controls the stable product phase assemblage at higher extents of reaction. The chemical shrinkage in this system is predicted to be 11 $cm^3$/100 g slag at complete reaction of the slag (an overall volume reduction of 15%, Figure 7.5A), which matches the chemical shrinkage quantified experimentally by Thomas et al. (Thomas et al., 2012) for a sodium silicate-activated slag cement (12.2 ± 1.5 $cm^3$/100 g slag) and is close to the values modelled by Chen and Brouwers (Chen and Brouwers, 2007) (11.5-13.9 $cm^3$/100 g slag) at 100% degree of reaction of the slag.

The increased Ca content and decreased Na/Si ratio of the C-(N-)A-S-H product at higher slag reaction extents (Figure 7.5B) are reflected in the reduced bulk Si and Na concentrations and the relative decrease in the fraction of Na-containing end-members simulated as the alkali activation reaction progresses (Figure 7.6). A ~50% reduction in the concentration of Na in the pore solution is predicted from 0 to 100% slag reaction extent, although a constant pH of ~14 is maintained and >10 times more Na is always predicted to be present in the aqueous phase relative to C-(N-)A-S-H. The simulated amounts of $H_2O$ and Ca in C-(N-)A-S-H are directly linked via the end-member chemical compositions defined in the CNASH_ss thermodynamic model (Myers et al., 2014): the Ca-rich T2C* end-member (Ca/Si = 1.5) has a higher $H_2O$/Si ratio (= 2.5) compared to the Al and Na-containing end-members ($H_2O$/Si < 2, Table 7.1), and relatively more of this end-member is simulated at higher bulk slag

reaction extents (Figure 7.6B). The simulated trends in pore solution element concentrations at >40% slag reaction extent (Figure 7.6A) closely resemble those reported for $Na_2SiO_3$-activated slag cement cured for 1-180 days (Gruskovnjak et al., 2006). More solubility data for $Na_2SiO_3$-activated slag cement are needed to further assess the accuracy of the simulated pore solution compositions.

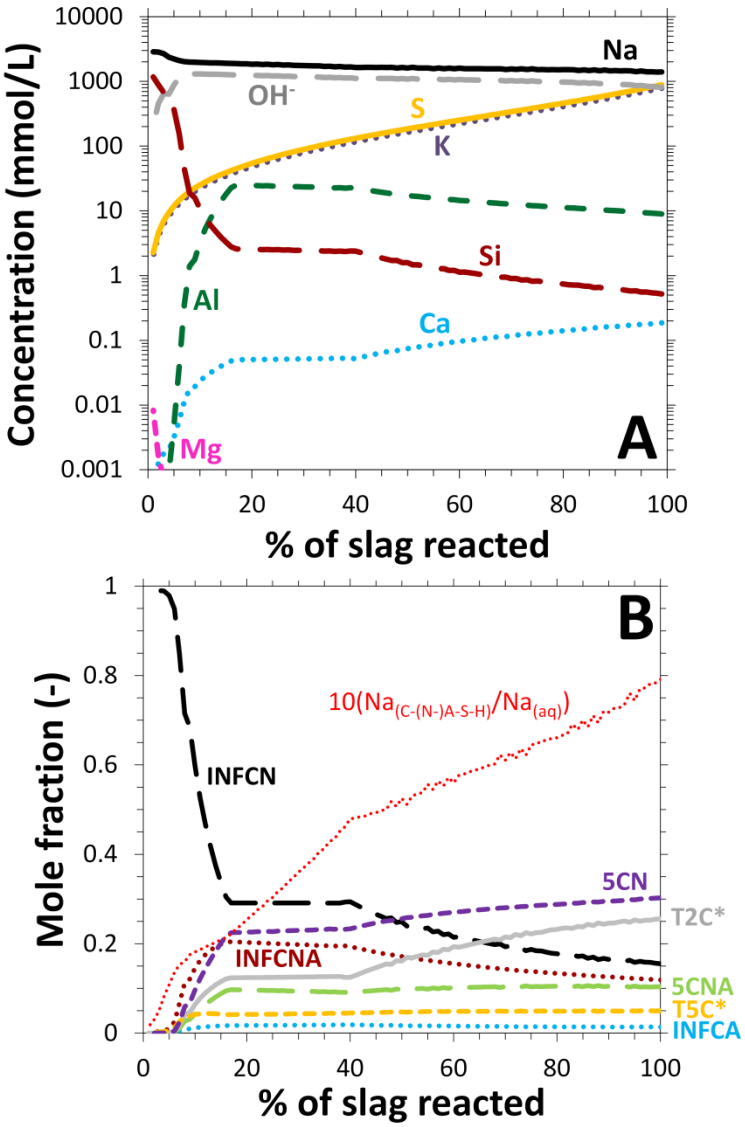


Figure 7.6. Simulated A) pore solution chemical compositions and B) end-member mole fractions and ratio of Na in C-(N-)A-S-H relative to Na in the aqueous phase (aq). The mole fraction of the TobH* end-member is close to 0 over the full range of simulated slag reaction extents (not shown in Figure 7.6B).

The simulated fraction of Al in MgAl-OH-LDH relative to the total amount of Al in the reaction products ($Al_{MgAl\text{-}LDH}/Al_{products}$) is ~0.22, which is consistent with

deconvolution analysis of $^{27}$Al MAS NMR spectra for the analogous experimental $Na_2SiO_3$-activated slag cement between 1-180 days of curing ($Al_{MgAl\text{-}LDH}/Al_{products}$ = 18-26%) (Myers et al., 2015a), but the predicted Mg/Al ratios are greater than those measured by SEM-EDS analysis for this material (Figure 7.5B). This result provides further support for explaining Mg/Al ratios < 2 in terms of intimately intermixed low-Mg high-Al phases with Mg-Al-LDH products, e.g. TAH or N-A-S(-H). However, the simulations predict that the fraction of Al in C-(N-)A-S-H relative to the total amount of Al in the reaction products ($Al_{CNASH}/Al_{products}$) is ~28% for slag reaction extents >50% (Figure 7.5A), which is much less than the relative amount of four-coordinated Al (Al[4]) assigned to the reaction products ($Al[4]/Al_{products}$) in $^{27}$Al MAS NMR spectral deconvolution analysis of this $Na_2SiO_3$-activated slag cement ($Al[4]/Al_{products}$ = 60-75%) (Myers et al., 2015a). Recent solubility results for C-(N-)A-S-H (Myers et al.) do not support any further increase in the stability of the Al-containing end-members in the CNASH_ss thermodynamic model, meaning that this discrepancy in the distribution of Al[4] is probably due to other factors: incomplete description of Al[4]-containing secondary products in the thermodynamic database used here; or that the discrepancy is founded in the experimental $^{29}$Si and $^{27}$Al MAS NMR analysis. Both options are now discussed.

More strätlingite is predicted by thermodynamic modelling (Figures 7.2-7.5) than the amount of this phase observed experimentally in $Na_2SiO_3$-activated slag cements. The solubility product used to describe this phase (Table 7.3) has an estimated uncertainty interval of ±1 log unit derived directly from the scatter in the available solubility data for this phase (see (Matschei et al., 2007b) and references therein), and so an error in this value is unlikely to contribute significantly to the over-prediction of this phase. It is unlikely that prolonged curing of experimental sodium silicate-activated slag pastes would lead to the formation of significantly more strätlingite, because this phase is not clearly distinguished in X-ray diffractograms of sodium silicate-activated slag cements cured for 180 days (bulk slag $Al_2O_3$ content ≤ 14.1 wt.%) (Ben Haha et al., 2012), 15 months (bulk slag $Al_2O_3$ content = 12.6 wt.%) (Wang and Scrivener, 1995) or 720 days (bulk slag $Al_2O_3$ content = 11.3

wt.%) (Burciaga-Díaz and Escalante-García, 2013), or in $Na_2SiO_3$-activated slag/4 wt.% PC blends cured for 3 years (Bernal et al., 2012b). Therefore, it is likely that additional solid phase(s) are missing from the thermodynamic database used here (Table 7.3), which would be predicted to form in preference to strätlingite if they were present in the simulation. These may be zeolites such as gismondine and thomsonite (Bernal et al., 2011b; Bernal et al., 2014b), or poorly ordered $Q^4$-type N-A-S(-H) ('geopolymer') gels (Myers et al., 2013), each of which will accommodate Al in tetrahedral form and could account for the difference between the high tetrahedral fraction determined experimentally, and the notably lower tetrahedral fraction predicted in the current simulations. Thermodynamic data are available for a large number of zeolites (see the compilation in (Arthur et al., 2011) for example), but the large variety of possible chemical compositions and the availability of only a few data for each zeolite framework type (often only one datum), mean that more thermochemical or solubility data are needed to define these phases in thermodynamic databases with confidence.

However, the maximum possible amount of Al[4] attributable to zeolites or N-A-S(-H) gel is limited by the lineshapes of the $^{27}$Al MAS NMR spectra of this $Na_2SiO_3$-activated slag cement (Myers et al., 2015a) at ~60 ppm relative to $Al(H_2O)_6^{3+}$, which is the typical observed chemical shift at which Al[4] resonates in these phases (Davidovits, 1991; Duxson et al., 2007; Fyfe et al., 1982). The limited amount of zeolites and N-A-S(-H) gels formed in these materials means that it is unlikely that the large discrepancy between the modelled amount of Al[4] in C-(N-)A-S-H (~28%, Figure 7.5A) and the experimentally observed amount of Al[4] assigned to reaction products (60-75% (Myers et al., 2015a)) can be explained by these phases alone. Further explanation for this discrepancy can be found in the assumption of congruent slag dissolution applied in the analysis of $^{29}$Si and $^{27}$Al MAS NMR spectra used as experimental data here (Bernal et al., 2014b; Myers et al., 2015a), which may not be fully attained in slag-based binders, and could significantly alter the deconvolution analysis presented (Dyson et al., 2007). Development of this understanding will be

essential to further enhance the accuracy of the characterisation and simulation of the complex phase assemblages which are formed in AAS-based cements.

### 7.3.3 Simulated Reaction of a $Na_2CO_3$-Activated Slag Cement

$Na_2CO_3$-activated slag cements utilise an activator with relatively low initial alkalinity (pH ≈ 11, although this increases during the reaction process) and are capable of developing comparable compressive strengths to PC-based materials (Shi and Qian, 2000) after extended curing, which makes these materials particularly useful in some applications, for example nuclear waste disposal (Bai et al., 2011). Durable concretes made from these materials have been used in structural applications for decades (Hu et al., 2008), although a more detailed chemical understanding of $Na_2CO_3$-activated slag cements is needed to improve the mechanical and durability properties of these materials (Bernal et al., 2015). Here, the reaction of a $Na_2CO_3$-activated slag cement is simulated in a manner identical to the simulation of $Na_2SiO_3$-activated slag cement discussed in section 7.3.2 (with the exception of the simulated $Na_2CO_3$ activator used here).

The simulated solid phase assemblage contains C-(N-)A-S-H as the primary reaction product (Figure 7.7A). The secondary products are $C_4AcH_{11}$, MgAl-OH-LDH, calcite and natrolite. The prediction of calcite is consistent with the observation of $CaCO_3$ polymorphs in $Na_2CO_3$-activated slag cements cured for 20 months (Sakulich et al., 2010) and 180 days (Bernal et al., 2015). Simulation of natrolite and Ca-heulandite is also in good agreement with the identification of heulandite and zeolite-A in $Na_2CO_3$-activated slag cement (Bernal et al., 2015). The modelling results presented here are consistent with the identification of more prominent peaks for zeolites in X-ray diffraction patterns for $Na_2CO_3$-activated (Bernal et al., 2015), compared to $Na_2SiO_3$-activated, slag cements (Bernal et al., 2014b). $C_4AcH_{11}$ has been identified in X-ray diffractograms of $Na_2CO_3$-activated slag pastes cured for 1 day and for 540 days (Shi et al., 2006), although this phase is not always observable (Bernal et al., 2015; Sakulich et al., 2010) due to its tendency to be present as intermixed

(Richardson et al., 1994) and/or poorly crystalline structures (Wang and Scrivener, 1995). The simulated chemical shrinkage extents for $Na_2CO_3$-activated (Figure 7.7) and $Na_2SiO_3$-activated slag cements (Figure 7.5) at 100% slag reaction extent are comparable, at 11 $cm^3$/100 g slag.

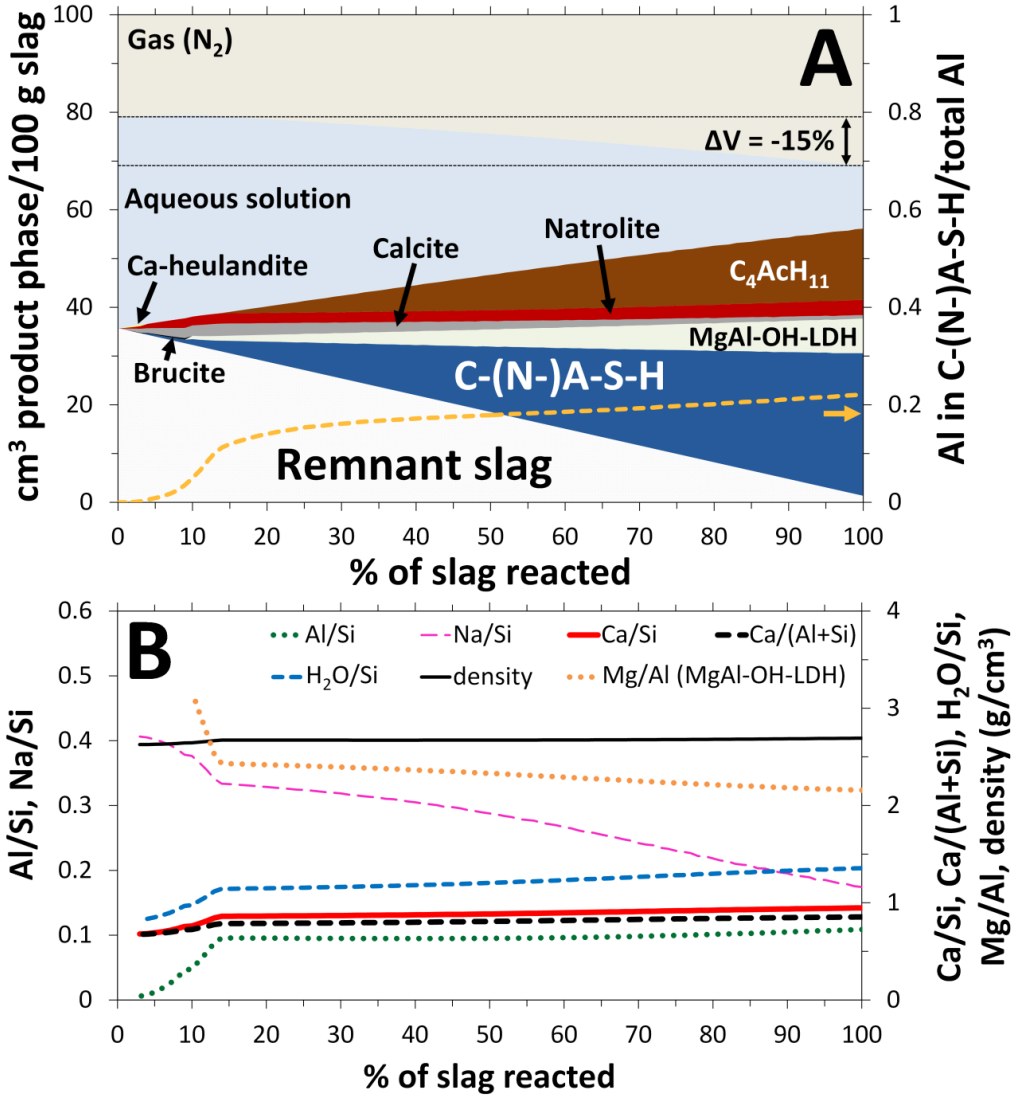


Figure 7.7. Simulated A) solid phase assemblages and B) C-(N-)A-S-H chemical compositions and densities ($g/cm^3$), and Mg/Al ratios of the MgAl-OH-LDH phase in an $Na_2CO_3$-activated slag cement (traces). The bulk slag chemical composition is shown in Table 3.1. A volume decrease of 15% is shown by the horizontal dashed lines in A), which represents the chemical shrinkage in this system at complete reaction of the slag (11 $cm^3$/100 g slag). The dashed orange curve in A) represents the fraction of Al bound in C-(N-)A-S-H relative to the total amount of Al in the solid reaction products.

Mg-Al LDH phases are experimentally observed in $Na_2CO_3$-activated slag cements after 180 days (Bernal et al., 2015) and 55 days (Sakulich et al., 2009) of curing, in good agreement with the predicted phase assemblage (Figure 7.7A). Here, MgAl-$CO_3$-LDH is not predicted despite the high availability of $CO_2$, demonstrating the very high stability of MgAl-OH-LDH under the pH ≥ 13 conditions in a hardened $Na_2CO_3$-activated slag cement (in common with many other hydrated cementitious materials). Further clarification of this result is needed because recent $^{27}$Al MAS NMR results for superficially carbonated $Na_2SiO_3$-activated slag cements (Myers et al., 2015a), and carbonation depth analysis of these materials after exposure to air for 16 months (Bernal et al., 2014b) can be interpreted in support of the formation of Mg-Al LDH phases intercalated with $CO_3^{2-}$. Detailed assessment of solubility and thermochemical data for Mg-Al LDH phases intercalated with $OH^-$ and $CO_3^{2-}$ (Bennett et al., 1992; Gao and Li, 2012; Johnson and Glasser, 2003; Morimoto et al., 2012; Rozov et al., 2011) indicates that the solubility product used to describe the Mg/Al = 2 MgAl-OH-LDH end-member here may be in error by as much as several log units (section 7.2.3), but this uncertainty alone is not enough to explain the increased stability of MgAl-OH-LDH over MgAl-$CO_3$-LDH. This clearly demonstrates a need for further studies on the characteristics and description of Mg-Al LDH phases in thermodynamic modelling of cementitious materials, as well as the possibility of kinetic effects being significant to some extent in this process.

Gaylussite has been observed in $Na_2CO_3$-activated slag cement at early age (Bernal et al., 2015) but is not present in the solid phase assemblage simulated here (Figure 7.7); this phase is slightly undersaturated at low slag reaction extents at ~25°C (Bury and Redd, 1933; Königsberger et al., 1999). This difference indicates that kinetic factors enable the formation of gaylussite in $Na_2CO_3$-activated slag cement cured at room temperature, and this is consistent with its observed consumption as the reaction proceeds (Bernal et al., 2015).

### 7.3.4 Phase Diagrams for Alkali-Activated Slag-Based Cements

The good overall agreement between the thermodynamic modelling simulations and the experimental data strongly supports the equilibrium approach used here, and increases the confidence with which thermodynamic modelling can be applied to describe the chemistry of AAS-based cements. The prediction of several secondary and minor reaction products in the simulated AAS cements is consistent with the bulk chemical composition of the mixes, which generally lie outside the composition envelope of phase-pure C-(N-)A-S-H (Figure 7.8).

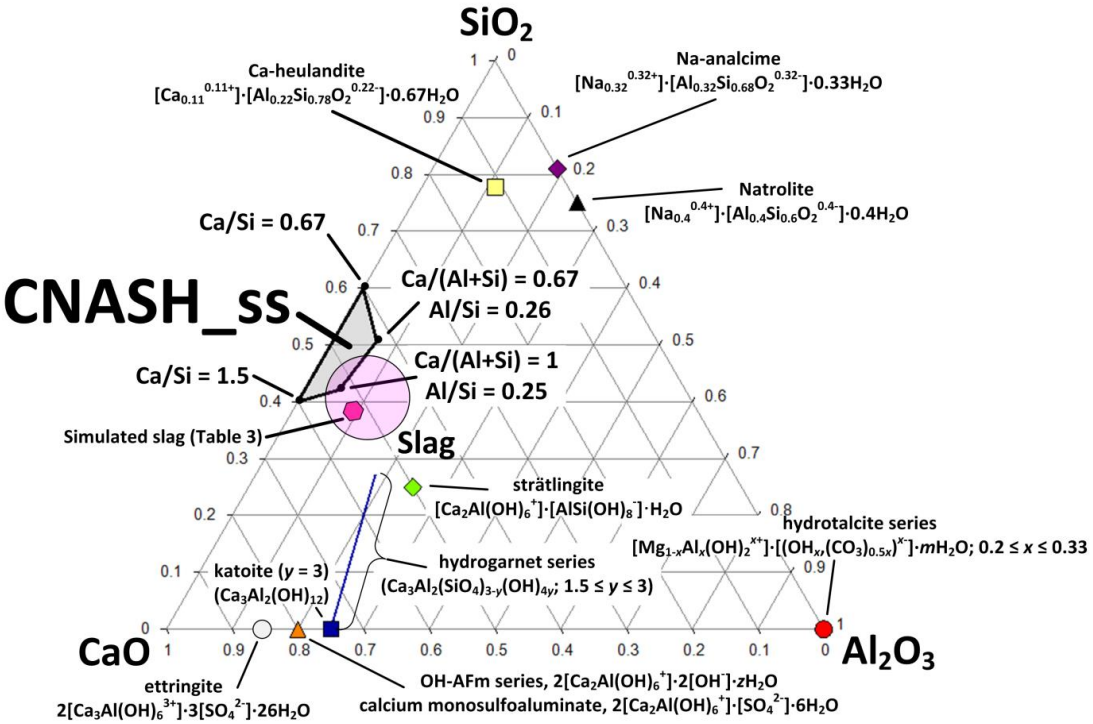


Figure 7.8. Projection of the chemical composition of some reaction products in AAS-based cements onto the $CaO$-$SiO_2$-$Al_2O_3$ ternary system. The grey and pink shaded regions are the composition range described by the CNASH_ss thermodynamic model for C-(N-)A-S-H gel (Myers et al., 2014), and the typical bulk chemical composition range of slag, respectively. The simulated slag described in Table 3.1 is represented by the pink hexagon.

Further analysis of AAS cement chemistry is performed by simulating phase diagrams at a fixed slag reaction extent of 60%, a constant amount of $H_2S$

(equivalent in S content to a slag composition of 2 wt.% $SO_3$, which is taken as a representative value of sulfur content in slags studied in the literature (Ben Haha et al., 2011a; Bernal et al., 2014b; Gruskovnjak et al., 2006; Puertas et al., 2011; Richardson et al., 1994; Shi et al., 2006)) and slag compositions of either 30 or 40 wt.% $SiO_2$, with the remaining chemical composition specified in terms of CaO, $Al_2O_3$ and MgO only. The CaO-$Al_2O_3$-MgO composition range selected here was chosen to represent the bulk chemical composition range relevant to AAS-based cements.

Zeolites are predicted in every phase diagram for the AAS-based cements simulated (shown for $Na_2SiO_3$-activated slag cements only in Figure 7.9), and are more prominent at higher Si (i.e. lower Ca) and Al concentrations, but only Ca-heulandite and natrolite are simulated. The CaO-$Al_2O_3$-MgO composition region where C-(N-)A-S-H and zeolites are both simulated indicates where C-(N-)A-S-H and N-A-S(-H) are likely to coexist in alkali-activated materials, due to the fundamental similarities of zeolites and N-A-S(-H) ('geopolymer') gels (Provis et al., 2005b). Inclusion of thermodynamic data for N-A-S(-H) and more data for zeolites in the thermodynamic database will be an important development in thermodynamic modelling of alkali-activated cements, to clarify the chemical compositional envelope in which these gels can coexist.

The prediction of zeolites here, in both the higher pH (NaOH-activated) and lower pH systems ($Na_2CO_3$-activated), indicates that pH is not a key parameter influencing the stability of these phases and the corresponding N-A-S(-H) gels, as was proposed previously by García-Lodeiro et al. (García-Lodeiro et al., 2011). The increased stability of zeolites at lower CaO content (Figure 7.4), or alternatively higher Si and Al concentrations (Figure 7.9) – i.e. decreasing CaO/($Al_2O_3$ + $SiO_2$) – demonstrates that careful control of Ca-Al-Si compositions is needed to form alkali-activated materials with mixed C-(N-)A-S-H and N-A-S(-H) gels (Ismail et al., 2014). Figure 7.9 shows that mixtures of C-(N-)A-S-H and zeolites are expected to be stable in $Na_2SiO_3$-activated 75 wt.% GBFS/25 wt.% fly ash (FA) or metakaolin (MK)

cements, but not in a hybrid system of $Na_2SiO_3$-activated 75 wt.% GBFS/25 wt.% PC (based on a PC chemical composition of 19.7 wt.% $SiO_2$, 63.2 wt.% CaO, 1.85 wt.% MgO, 4.7 wt.% $Al_2O_3$, 3.35 wt.% $SO_3$ (Lothenbach and Winnefeld, 2006)). Figure 7.9 also shows that the stability of zeolites, and therefore of N-A-S(-H) gels, in $Na_2SiO_3$-activated slag cement depends greatly on the slag $SiO_2$ content.

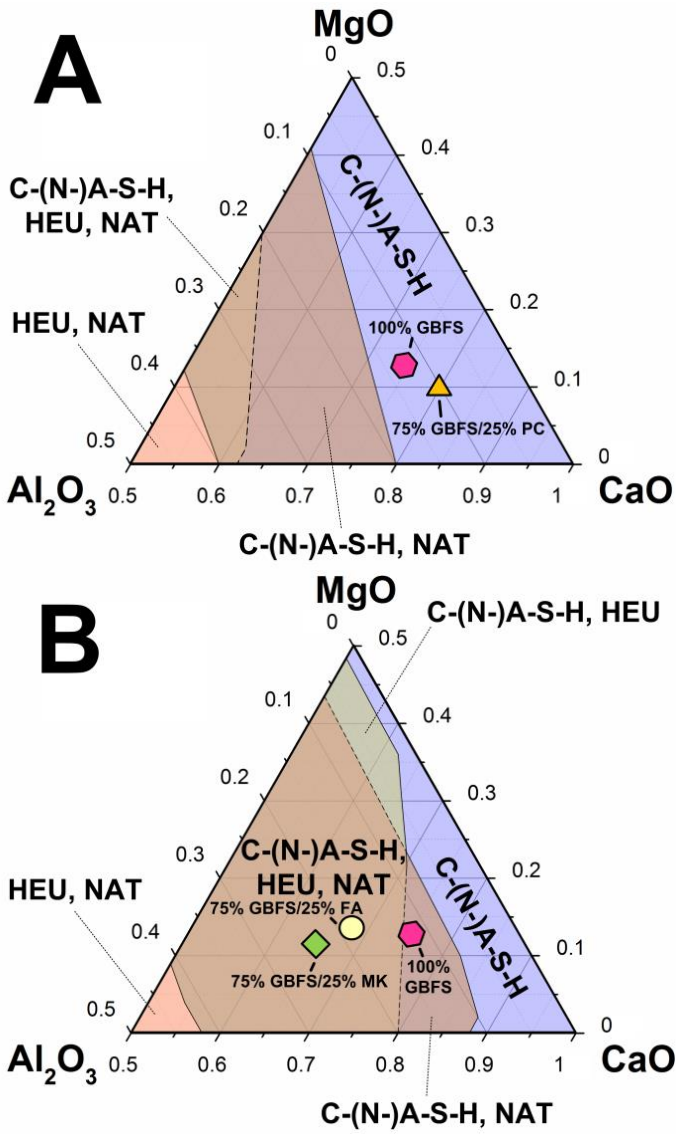


Figure 7.9. Phase diagrams for $Na_2SiO_3$-activated slag-based cement systems with overall precursor chemical compositions of 2 mass% $SO_3$ equivalent and A) 30 mass% $SiO_2$ and B) 40 mass% $SiO_2$, with only the regions of stability for C-(N-)A-S-H gel and zeolites shown (Mg-containing phases are also typical reaction products: MgAl-OH-LDH at moderate and high $Al_2O_3$ content ($Al_2O_3/(CaO+Al_2O_3+MgO) > 0.1$); and brucite at moderate and low $Al_2O_3$ concentrations ($Al_2O_3/(CaO+Al_2O_3+MgO) < 0.25$)). See text for the GBFS, FA, MK and PC chemical compositions used. The w/b ratio is 0.4, the overall precursor reaction extent is 60% and the units are in mole fraction.

Simulated phase diagrams for AAS-based cements produced using NaOH, $Na_2SiO_3$, $Na_2Si_2O_5$, and $Na_2CO_3$ activators are shown in Figure 7.10. Legends for the symbols (solid phase assemblages) shown in Figure 7.10 are presented in Tables 7.4-7.5.

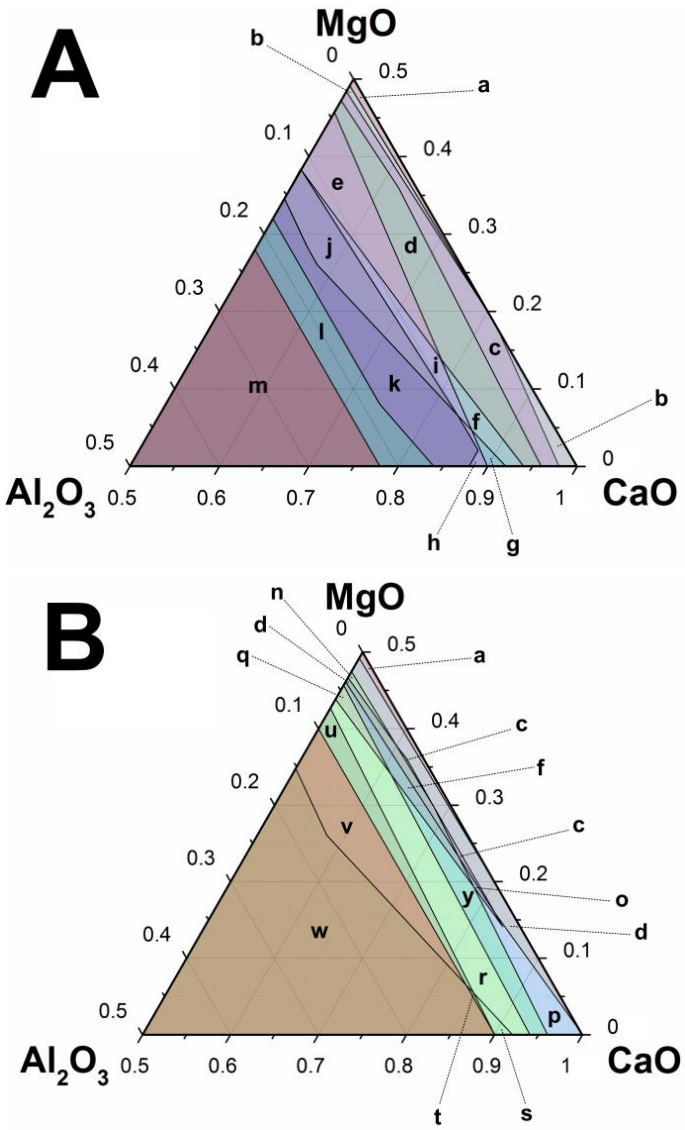


Figure 7.10. Phase diagrams in the relevant bulk CaO-$Al_2O_3$-MgO composition range for NaOH-activated slag cements derived from slag with A) 30 wt.% $SiO_2$ and B) 40 wt.% $SiO_2$, $Na_2SiO_3$-activated slag cements derived from slag with C) 30 wt.% $SiO_2$ and D) 40 wt.% $SiO_2$, $Na_2Si_2O_5$-activated slag cements derived from slag with E) 30 wt.% $SiO_2$ and F) 40 wt.% $SiO_2$, and $Na_2CO_3$-activated slag cements derived from slag with G) 30 wt.% $SiO_2$ and H) 40 wt.% $SiO_2$, with all slags containing 2 wt.% $SO_3$ equivalent. The w/b ratio is 0.4, the slag reaction extent is 60% and the units are in mol fraction. Listings of the phases present in each of the regions on each diagram are provided in Tables 7.4-7.5.

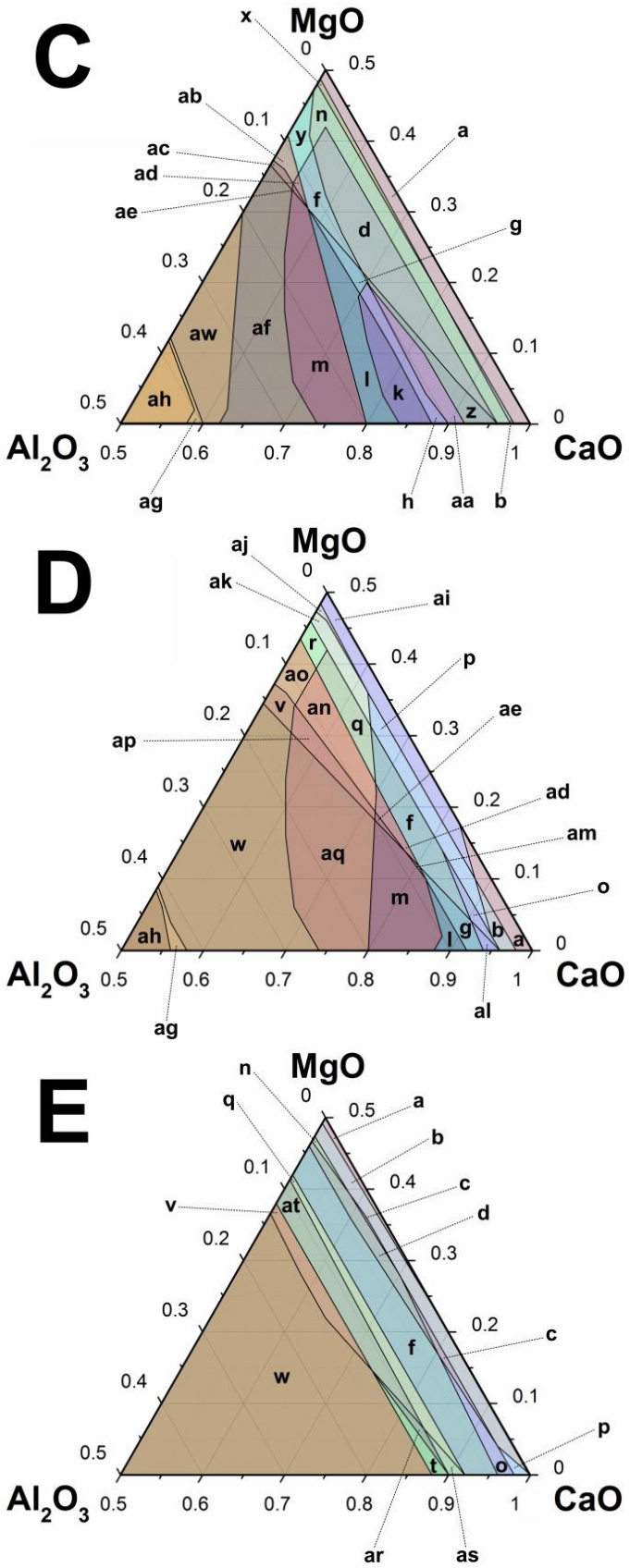


Figure 7.10. Continued.

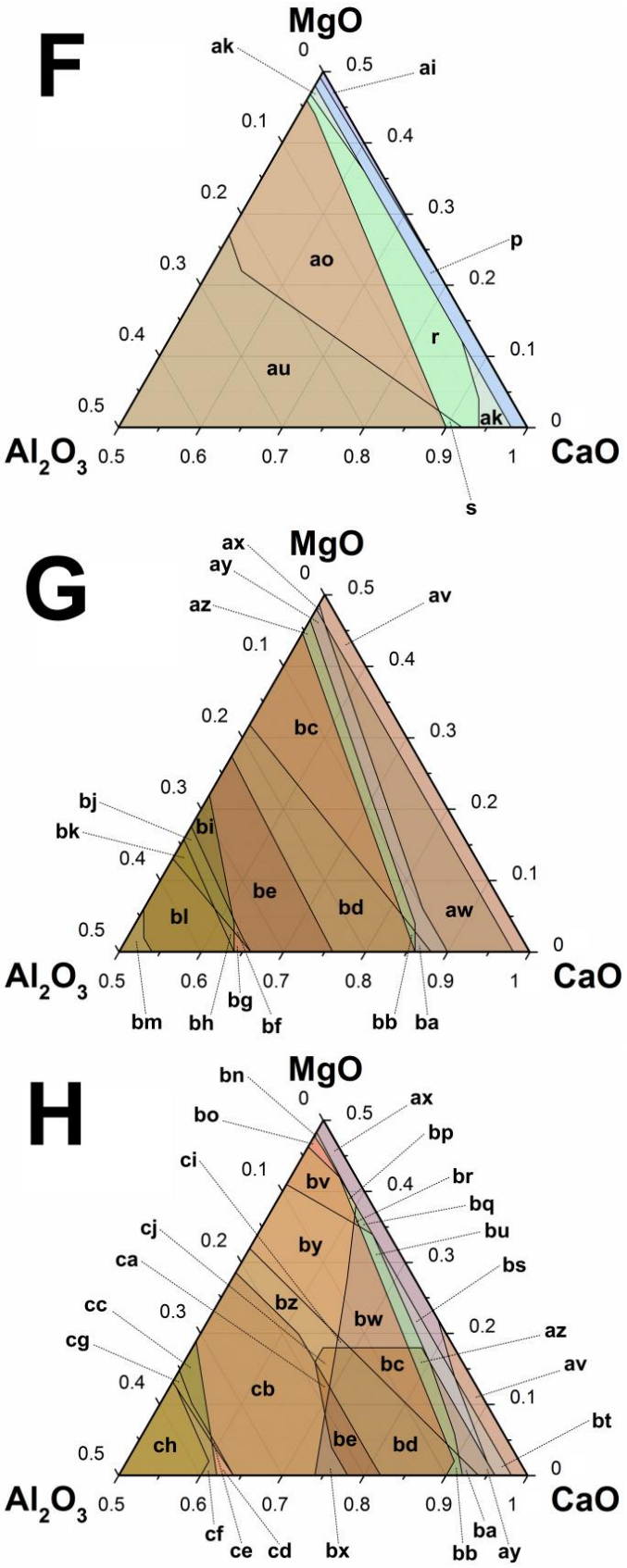


Figure 7.10. Continued.

Table 7.4. Legend for the $CO_2$-free phase diagrams (Figures 7.10A-7.10F).

| **Symbol** | **Simulated solid phase assemblage** | - | - | - | - | - | - | - | - | - | - |
|---|---|---|---|---|---|---|---|---|---|---|---|
| a | C-(N-)A-S-H | - | - | - | - | - | - | - | portlandite | brucite | - |
| b | C-(N-)A-S-H | - | - | - | ettringite | - | - | - | portlandite | brucite | - |
| c | C-(N-)A-S-H | - | - | - | ettringite | $C_4A\overline{S}H_{12}$ | - | - | portlandite | brucite | - |
| d | C-(N-)A-S-H | MgAl-OH-LDH | - | - | ettringite | $C_4A\overline{S}H_{12}$ | - | - | portlandite | brucite | - |
| e | C-(N-)A-S-H | MgAl-OH-LDH | - | $C_3AH_6$ | ettringite | $C_4A\overline{S}H_{12}$ | - | - | portlandite | brucite | - |
| f | C-(N-)A-S-H | MgAl-OH-LDH | - | - | ettringite | $C_4A\overline{S}H_{12}$ | - | - | - | brucite | - |
| g | C-(N-)A-S-H | MgAl-OH-LDH | - | - | ettringite | $C_4A\overline{S}H_{12}$ | - | - | - | - | - |
| h | C-(N-)A-S-H | MgAl-OH-LDH | - | $C_3AH_6$ | ettringite | $C_4A\overline{S}H_{12}$ | - | - | - | - | - |
| i | C-(N-)A-S-H | MgAl-OH-LDH | - | $C_3AH_6$ | ettringite | $C_4A\overline{S}H_{12}$ | - | - | - | brucite | - |
| j | C-(N-)A-S-H | MgAl-OH-LDH | strätlingite | $C_3AH_6$ | ettringite | $C_4A\overline{S}H_{12}$ | - | - | - | brucite | - |
| k | C-(N-)A-S-H | MgAl-OH-LDH | strätlingite | $C_3AH_6$ | ettringite | $C_4A\overline{S}H_{12}$ | - | - | - | - | - |
| l | C-(N-)A-S-H | MgAl-OH-LDH | strätlingite | - | ettringite | $C_4A\overline{S}H_{12}$ | - | - | - | - | - |
| m | C-(N-)A-S-H | MgAl-OH-LDH | strätlingite | - | ettringite | $C_4A\overline{S}H_{12}$ | natrolite | - | - | - | - |
| n | C-(N-)A-S-H | MgAl-OH-LDH | - | - | ettringite | - | - | - | portlandite | brucite | - |
| o | C-(N-)A-S-H | - | - | - | ettringite | $C_4A\overline{S}H_{12}$ | - | - | - | brucite | - |
| p | C-(N-)A-S-H | - | - | - | ettringite | - | - | - | - | brucite | - |
| q | C-(N-)A-S-H | MgAl-OH-LDH | - | - | ettringite | $C_4A\overline{S}H_{12}$ | - | Ca-heulandite | - | brucite | - |
| r | C-(N-)A-S-H | MgAl-OH-LDH | - | - | ettringite | - | - | Ca-heulandite | - | brucite | - |
| s | C-(N-)A-S-H | MgAl-OH-LDH | - | - | ettringite | - | - | Ca-heulandite | - | - | - |
| t | C-(N-)A-S-H | MgAl-OH-LDH | strätlingite | - | ettringite | - | - | Ca-heulandite | - | - | - |
| u | C-(N-)A-S-H | MgAl-OH-LDH | strätlingite | - | ettringite | - | - | Ca-heulandite | - | brucite | - |

Table 7.4. Continued.

| | | | | | | | | | | | |
|---|---|---|---|---|---|---|---|---|---|---|---|
| v | C-(N-)A-S-H | MgAl-OH-LDH | strätlingite | - | ettringite | - | natrolite | Ca-heulandite | - | brucite | - |
| w | C-(N-)A-S-H | MgAl-OH-LDH | strätlingite | - | ettringite | - | natrolite | Ca-heulandite | - | - | - |
| x | C-(N-)A-S-H | MgAl-OH-LDH | - | - | - | - | - | - | portlandite | brucite | - |
| y | C-(N-)A-S-H | MgAl-OH-LDH | - | - | ettringite | - | - | - | - | brucite | - |
| z | C-(N-)A-S-H | MgAl-OH-LDH | - | - | ettringite | $C_4A\overline{S}H_{12}$ | - | - | portlandite | - | - |
| aa | C-(N-)A-S-H | MgAl-OH-LDH | - | $C_3AH_6$ | ettringite | $C_4A\overline{S}H_{12}$ | - | - | portlandite | - | - |
| ab | C-(N-)A-S-H | MgAl-OH-LDH | - | - | ettringite | - | natrolite | - | - | brucite | - |
| ac | C-(N-)A-S-H | MgAl-OH-LDH | strätlingite | - | ettringite | - | natrolite | - | - | brucite | - |
| ad | C-(N-)A-S-H | MgAl-OH-LDH | - | - | ettringite | $C_4A\overline{S}H_{12}$ | natrolite | - | - | brucite | - |
| ae | C-(N-)A-S-H | MgAl-OH-LDH | strätlingite | - | ettringite | $C_4A\overline{S}H_{12}$ | natrolite | - | - | brucite | - |
| af | C-(N-)A-S-H | MgAl-OH-LDH | strätlingite | - | ettringite | - | natrolite | - | - | - | - |
| ag | - | MgAl-OH-LDH | strätlingite | - | ettringite | - | natrolite | Ca-heulandite | - | - | - |
| ah | - | MgAl-OH-LDH | strätlingite | - | ettringite | - | natrolite | Ca-heulandite | - | - | $Al(OH)_{3\ (mc)}$ |
| ai | C-(N-)A-S-H | - | - | - | - | - | - | - | - | brucite | - |
| aj | C-(N-)A-S-H | - | - | - | - | - | - | Ca-heulandite | - | brucite | - |
| ak | C-(N-)A-S-H | - | - | - | ettringite | - | - | Ca-heulandite | - | brucite | - |
| al | C-(N-)A-S-H | - | - | - | ettringite | $C_4A\overline{S}H_{12}$ | - | - | - | - | - |
| am | C-(N-)A-S-H | MgAl-OH-LDH | - | - | ettringite | $C_4A\overline{S}H_{12}$ | natrolite | - | - | - | - |
| an | C-(N-)A-S-H | MgAl-OH-LDH | - | - | ettringite | $C_4A\overline{S}H_{12}$ | natrolite | Ca-heulandite | - | brucite | - |
| ao | C-(N-)A-S-H | MgAl-OH-LDH | - | - | ettringite | - | natrolite | Ca-heulandite | - | brucite | - |
| ap | C-(N-)A-S-H | MgAl-OH-LDH | strätlingite | - | ettringite | $C_4A\overline{S}H_{12}$ | natrolite | Ca-heulandite | - | brucite | - |
| aq | C-(N-)A-S-H | MgAl-OH-LDH | strätlingite | - | ettringite | $C_4A\overline{S}H_{12}$ | natrolite | Ca-heulandite | - | - | - |
| ar | C-(N-)A-S-H | MgAl-OH-LDH | strätlingite | - | ettringite | $C_4A\overline{S}H_{12}$ | - | Ca-heulandite | - | - | - |
| as | C-(N-)A-S-H | MgAl-OH-LDH | - | - | ettringite | $C_4A\overline{S}H_{12}$ | - | Ca-heulandite | - | - | - |
| at | C-(N-)A-S-H | MgAl-OH-LDH | strätlingite | - | ettringite | $C_4A\overline{S}H_{12}$ | - | Ca-heulandite | - | brucite | - |
| au | C-(N-)A-S-H | MgAl-OH-LDH | - | - | ettringite | - | natrolite | Ca-heulandite | - | - | - |

Table 7.5. Legend for the $CO_2$-containing phase diagrams (Figures 7.10G-7.10H). Calcite is present in all simulated solid phase assemblages.

| **Symbol** | **Simulated solid phase assemblage** | - | - | - | - | - | - | - | - | - | - |
|---|---|---|---|---|---|---|---|---|---|---|---|
| av | C-(N-)A-S-H | - | - | - | - | - | portlandite | brucite | - | - | - |
| aw | C-(N-)A-S-H | - | - | ettringite | - | - | portlandite | brucite | - | $C_4AcH_{11}$ | - |
| ax | C-(N-)A-S-H | - | - | - | - | - | - | brucite | - | - | - |
| ay | C-(N-)A-S-H | - | - | ettringite | - | - | - | brucite | - | $C_4AcH_{11}$ | - |
| az | C-(N-)A-S-H | MgAl-OH-LDH | - | ettringite | - | - | - | brucite | - | $C_4AcH_{11}$ | - |
| ba | C-(N-)A-S-H | - | - | ettringite | - | - | - | - | - | $C_4AcH_{11}$ | - |
| bb | C-(N-)A-S-H | MgAl-OH-LDH | - | ettringite | - | - | - | - | - | $C_4AcH_{11}$ | - |
| bc | C-(N-)A-S-H | MgAl-OH-LDH | - | ettringite | natrolite | - | - | brucite | - | $C_4AcH_{11}$ | - |
| bd | C-(N-)A-S-H | MgAl-OH-LDH | - | ettringite | natrolite | - | - | - | - | $C_4AcH_{11}$ | - |
| be | C-(N-)A-S-H | MgAl-OH-LDH | strätlingite | ettringite | natrolite | - | - | - | - | $C_4AcH_{11}$ | - |
| bf | - | MgAl-OH-LDH | strätlingite | ettringite | natrolite | - | - | - | - | $C_4AcH_{11}$ | - |
| bg | - | - | strätlingite | ettringite | natrolite | - | - | - | - | $C_4AcH_{11}$ | - |
| bh | - | - | strätlingite | ettringite | natrolite | - | - | - | - | $C_4AcH_{11}$ | $MgAl\text{-}CO_3\text{-}LDH$ |
| bi | C-(N-)A-S-H | MgAl-OH-LDH | strätlingite | ettringite | natrolite | - | - | - | - | $C_4AcH_{11}$ | $MgAl\text{-}CO_3\text{-}LDH$ |
| bj | - | MgAl-OH-LDH | strätlingite | ettringite | natrolite | - | - | - | - | $C_4AcH_{11}$ | $MgAl\text{-}CO_3\text{-}LDH$ |
| bk | - | MgAl-OH-LDH | strätlingite | ettringite | natrolite | - | - | - | $Al(OH)_{3\,(mc)}$ | $C_4AcH_{11}$ | $MgAl\text{-}CO_3\text{-}LDH$ |
| bl | - | - | strätlingite | ettringite | natrolite | - | - | - | $Al(OH)_{3\,(mc)}$ | $C_4AcH_{11}$ | $MgAl\text{-}CO_3\text{-}LDH$ |
| bm | - | - | strätlingite | ettringite | natrolite | - | - | - | $Al(OH)_{3\,(mc)}$ | - | $MgAl\text{-}CO_3\text{-}LDH$ |
| bn | C-(N-)A-S-H | - | - | - | - | Ca-heulandite | - | brucite | - | - | - |
| bo | C-(N-)A-S-H | - | - | - | natrolite | Ca-heulandite | - | brucite | - | - | - |
| bp | C-(N-)A-S-H | MgAl-OH-LDH | - | - | - | Ca-heulandite | - | brucite | - | - | - |
| bq | C-(N-)A-S-H | MgAl-OH-LDH | - | - | - | - | - | brucite | - | - | - |
| br | C-(N-)A-S-H | MgAl-OH-LDH | - | - | natrolite | - | - | brucite | - | - | - |
| bs | C-(N-)A-S-H | - | - | ettringite | - | - | - | brucite | - | - | - |
| bt | C-(N-)A-S-H | - | - | ettringite | - | - | portlandite | brucite | - | - | - |
| bu | C-(N-)A-S-H | MgAl-OH-LDH | - | ettringite | - | - | - | brucite | - | - | - |
| bv | C-(N-)A-S-H | MgAl-OH-LDH | - | - | natrolite | Ca-heulandite | - | brucite | - | - | - |
| bw | C-(N-)A-S-H | MgAl-OH-LDH | - | ettringite | natrolite | - | - | brucite | - | - | - |

Table 7.5. Continued.

| | | | | | | | | | | | |
|---|---|---|---|---|---|---|---|---|---|---|---|
| bx | C-(N-)A-S-H | MgAl-OH-LDH | strätlingite | ettringite | natrolite | - | - | - | - | - | |
| by | C-(N-)A-S-H | MgAl-OH-LDH | - | ettringite | natrolite | Ca-heulandite | - | brucite | - | - | |
| bz | C-(N-)A-S-H | MgAl-OH-LDH | - | ettringite | natrolite | Ca-heulandite | - | - | - | - | |
| ca | C-(N-)A-S-H | MgAl-OH-LDH | strätlingite | ettringite | natrolite | Ca-heulandite | - | - | - | $C_4AcH_{11}$ | |
| cb | C-(N-)A-S-H | MgAl-OH-LDH | strätlingite | ettringite | natrolite | Ca-heulandite | - | - | - | - | |
| cc | C-(N-)A-S-H | MgAl-OH-LDH | strätlingite | ettringite | natrolite | Ca-heulandite | - | - | - | - | MgAl-$CO_3$-LDH |
| cd | - | - | strätlingite | ettringite | natrolite | Ca-heulandite | - | - | - | - | |
| ce | - | MgAl-OH-LDH | strätlingite | ettringite | natrolite | Ca-heulandite | - | - | - | - | |
| cf | - | - | strätlingite | ettringite | natrolite | Ca-heulandite | - | - | - | - | MgAl-$CO_3$-LDH |
| cg | - | MgAl-OH-LDH | strätlingite | ettringite | natrolite | Ca-heulandite | - | - | - | - | MgAl-$CO_3$-LDH |
| ch | - | - | strätlingite | ettringite | natrolite | Ca-heulandite | - | - | $Al(OH)_{3\ (mc)}$ | - | MgAl-$CO_3$-LDH |
| ci | C-(N-)A-S-H | MgAl-OH-LDH | - | ettringite | natrolite | - | - | - | - | - | |
| cj | C-(N-)A-S-H | MgAl-OH-LDH | - | ettringite | natrolite | Ca-heulandite | - | - | - | $C_4AcH_{11}$ | |

The dominant solids in the simulated phase diagrams (Figure 7.10) are C-(N-)A-S-H, MgAl-OH-LDH and additionally calcite in the $CO_2$-containing systems (which is predicted for the full range of simulated CaO-$Al_2O_3$-MgO compositions). C-(N-)A-S-H is predicted everywhere except at $Al_2O_3/(CaO+Al_2O_3+MgO) > 0.3$, and MgAl-OH-LDH is generally formed in the same composition region except at very low $Al_2O_3$ content ($Al_2O_3/(CaO+Al_2O_3+MgO) < 0.1$). The high stability of calcite in the $Na_2CO_3$-activated slag systems indicates that aragonite and/or vaterite can also be expected to form in these materials, as is experimentally observed (Bernal et al., 2015; Sakulich et al., 2010), because the stabilities of these phases are similar (Table 7.3), and their interrelationships tend to be controlled by kinetics and minor dissolved species.

Ettringite is predicted over a much larger range of CaO-$Al_2O_3$-MgO compositions than calcium monosulfoaluminate hydrate ($C_4A\bar{S}H_{12}$), and is present in most solid phase assemblages. These phases are predicted to form here but not in sections 7.3.1-7.3.3 – for slag containing 0.8 wt.% equivalent $SO_3$ (Table 3.1) – because more sulfur is specified in the slag simulated here (2 wt.% $SO_3$ equivalent). Katoite is only present in the phase diagrams for slags with 30 wt.% $SiO_2$ and activated with NaOH (Figure 7.10A) and $Na_2SiO_3$ (Figure 7.10C). Portlandite is most prominent in the 30 wt.% $SiO_2$ NaOH-activated slag system (Figure 7.10A), but is only formed at relatively low $Al_2O_3$ content ($Al_2O_3/(CaO+Al_2O_3+MgO) \leq 0.12$). Brucite is predicted in each of the simulated phase diagrams, but not at high $Al_2O_3$ concentrations ($Al_2O_3/(CaO+Al_2O_3+MgO) > 0.25$). Strätlingite is not predicted in the 40 wt.% $SiO_2$ $Na_2Si_2O_5$-activated slag system, but is typically formed for $Al_2O_3/(CaO+Al_2O_3+MgO) > 0.1$ in the less Si-rich systems, indicating that this phase is stable at intermediate Ca-Si-Al compositions. $C_4AcH_{11}$ and MgAl-$CO_3$-LDH are additionally predicted in the phase diagrams for $Na_2CO_3$-activated slag cements; $C_4AcH_{11}$ is stable over a large range of CaO-$Al_2O_3$-MgO compositions but MgAl-$CO_3$-LDH is only formed at very high $Al_2O_3$ content ($Al_2O_3/(CaO+Al_2O_3+MgO) \geq 0.28$).

The phase diagrams present here should therefore be viewed as being an important tool in understanding the chemistry of AAS-based materials. This work represents a highly substantial advance in the ability to design high-performance AAS-based materials, by providing a framework for understanding the chemistry, and thus the closely linked durability properties (van Deventer et al., 2012), of these construction materials.

## 7.4 Conclusions

This paper has presented a thermodynamic modelling analysis of AAS-based cements. The thermodynamic database used contains the CNASH_ss thermodynamic model for C-(N-)A-S-H, which explicitly describes tetrahedral Al and Na species incorporated into this phase, an ideal solid solution model for MgAl-OH-LDH, and thermodynamic data for some alkali carbonate and zeolite phases.

Thermodynamic modelling of $Na_2SiO_3$-activated slag cements generally showed that the CNASH_ss thermodynamic model described the Al/Si ratios of the C-(N-)A-S-H products formed in the most relevant composition range/alkali content for the majority of AAS cements. The Mg/Al ratios of the simulated MgAl-OH-LDH phase was generally in good agreement with experimental results for this phase in AAS cements, although additional thermodynamic data for MgAl-OH-LDH are needed to clarify the stability of this phase in carbonated and $Na_2CO_3$-activated cement materials. Additional thermodynamic data for other reaction products such as TAH, zeolites and N-A-S(-H) gels are also needed for better consistency with the experimental data. Simulated solid phase assemblages for $Na_2SiO_3$-activated slag cements compared closely to reaction product assemblages identified experimentally in these materials, and the simulations accurately predicted the experimentally measured chemical shrinkage in sodium silicate-activated slag cement.

Phase diagrams for NaOH, $Na_2SiO_3$, $Na_2Si_2O_5$ and $Na_2CO_3$-activated slag-based cements were simulated, which showed that C-(N-)A-S-H and MgAl-OH-LDH are

formed over the majority of chemical compositions relevant to these materials, and that calcite is stable in $Na_2CO_3$-activated slag-based cements. Natrolite and Ca-heulandite featured more prominently in the phase diagrams at lower CaO concentration, and higher $SiO_2$ and $Al_2O_3$ content, indicating that the bulk $CaO/(SiO_2 + Al_2O_3)$ ratio plays a significant role in stabilising zeolites, and therefore N-A-S(-H) gels, in $Na_2SiO_3$-activated slag-based cements. Zeolites were predicted to be stable in $Na_2SiO_3$-activated 75 wt.% GBFS/25 wt.% FA and MK cements but not in hybrid $Na_2SiO_3$-activated 75 wt.% GBFS/25 wt.% PC. Therefore, these phase diagrams provide a useful reference tool for the development of high-performance alkali-activated materials, by enabling the solid reaction products – and thus potentially the durability properties of these materials – to be manipulated based on bulk chemical composition alone.

# 8

# Effect of Temperature on C-(A-)S-H Chemistry Under Equilibrium Conditions

This chapter is based on the paper 'Effect of temperature and aluminium on calcium (alumino)silicate hydrate chemistry under equilibrium conditions', published in *Cement and Concrete Research*, **2015**, *68*, 83-93. C-(A-)S-H synthesis, and XRD and TGA measurements were performed by Emilie L'Hôpital for samples equilibrated at 7 and 20°C and Rupert J. Myers for samples equilibrated at 50°C and 80°C with assistance from Boris Ingold (Laboratory for Concrete/Construction Chemistry, EMPA) and Luigi Brunetti (Laboratory for Concrete/Construction Chemistry, EMPA). The IC measurements were performed by Emilie L'Hôpital with assistance from Luigi Brunetti. The $^{29}$Si MAS NMR experiments were performed by Salaheddine Alahrache (Laboratory for Concrete/Construction Chemistry, EMPA) with assistance from Daniel Rentsch (Laboratory for Functional Polymers, EMPA).

## 8.1 Introduction

Temperatures experienced by cement and concrete based construction materials in service can vary greatly, due to heat evolution from cement hydration, variable ambient environmental conditions, steam curing, and other factors. The effects of temperature on hydrated blended and neat Portland cement (PC) material properties are important, and can include: increased reaction rate and density of calcium silicate hydrate (C-S-H) (Lothenbach et al., 2007), coarsening of paste microstructures

(Gallucci et al., 2013), and decreasing compressive strengths (Escalante-García and Sharp, 1998) with increasing temperature.

Despite the wealth of engineering information available in this area, only a few studies are available in the literature regarding the equilibrium phase assemblages and aqueous chemistry of PC systems as a function of temperature (Atkins et al., 1994; Lothenbach et al., 2007; Thomas et al., 2003). However, a good understanding of the nature of C-S-H and other constituent phases in these systems at equilibrium (Barbarulo, 2003; Courault, 2000; Glasser et al., 2005; Matschei et al., 2007b) has meant that hydrated neat PC materials can be accurately described by thermodynamic modelling at temperatures from 5°C to above 80°C (Lothenbach et al., 2008b). Extending this analysis to the $CaO$-$Al_2O_3$-$SiO_2$-$H_2O$ system represents a major step toward applying this technique to hydrated PC blends with high replacement levels of supplementary cementitious materials, which are not fully described by existing thermodynamic models (Kulik, 2011). This will enable a much deeper understanding of the chemistry and phase composition, and hence durability, of these materials in service.

Considering the aqueous phases in equilibrium with C-(A-)S-H at different temperatures, it has been observed that the dissolved concentrations of Ca and Si are inversely related (L'Hôpital et al.; Pardal et al., 2009), similar to the solubility of these elements in C-S-H systems (Chen et al., 2004; Walker et al., 2007). The dissolved Al content is closely linked to the amount of Al incorporated into C-(A-)S-H, and the nature and quantity of secondary phases formed. However, more experimental work is needed to provide data covering the full range of compositions and temperatures relevant to modern cementitious materials. Therefore, this chapter aims to clarify the effects of temperature and Al on the chemistry, structure and solubility of equilibrated C-(A-)S-H systems at 7°C, 50°C and 80°C, which are not yet well-described in the literature, and also utilises a recently published data set collected at 20°C (L'Hôpital et al.) to complete the temperature series.

## 8.2 Experimental

C-(A-)S-H samples were synthesised under an $N_2$-atmosphere at a bulk molar Ca/Si ratio (Ca/Si*) = 1 and bulk molar Al/Si ratios (Al/Si*) = 0, 0.05, 0.1 and 0.15 at a water/solid ratio = 45. Samples were equilibrated for 1 year at 7°C, 182 days at 20°C, and 56 days at 50°C and 80°C. The specimens were studied by IC and pH analysis, XRD with Rietveld analysis, TGA, $^{29}$Si MAS NMR and thermodynamic modelling. Thermodynamic modelling was performed in GEM Selektor v.3 software (http://gems.web.psi.ch/) (Kulik et al., 2013; Wagner et al., 2012) using the thermodynamic properties of the gases and aqueous species shown in Chapter 3 (Tables 3.2-3.3); thermodynamic properties of the solid phases used in this investigation are shown in Tables 8.1-8.2. Solubility products ($K_{so}$) for C-(A-)S-H, and effective saturation indices ($SI$*) for relevant solid phases, were calculated from experimental data obtained here. A complete description of the experimental details for this investigation is given in Chapter 3.

Table 8.1. Standard partial molar thermodynamic properties of the solid phases used in the thermodynamic modelling calculations. The reference state is 298.15 K and 1 bar.

| Phase | V ° ($cm^3$/mol) | $\Delta_f H°$ (kJ/mol) | $\Delta_f G°$ (kJ/mol) | S° (J/(mol.K)) | Cp° (J/(mol.K)) | Reference |
|---|---|---|---|---|---|---|
| $Al(OH)_3$ (microcrystalline) | 32.0 | -1265.3 | -1148.4 | 140.0 | 93.1 | (Lothenbach et al., 2012b) |
| Gibbsite | 32.0 | -1288.7 | -1151.0 | 70.1 | 93.1 | (Helgeson et al., 1978) |
| Portlandite | 33.1 | -984.7 | -897.0 | 83.4 | 87.5 | (Robie and Hemingway, 1995) |
| $SiO_2$ (amorphous) | 29.0 | -903.3 | -848.9 | 41.3 | 44.5 | (Kulik, 2011) |
| Katoite, $C_3AH_6$ | 149.7 | -5537.3 | -5008.2 | 421.7 | 445.6 | (Lothenbach et al., 2012b) |
| Si-hydrogarnet, $C_3AS_{0.84}H_{4.32}$ | 142.5 | -5847.5 | -5365.2 | 375.2 | 412.6 | (Dilnesa et al., 2014) |
| Strätlingite, $C_2ASH_8$ | 216.1 | -6360.0 | -5705.1 | 546.2 | 602.7 | (Matschei et al., 2007b) |
| **C-S-H solid solution, the 'downscaled CSH3T' model** | | | | | | |
| TobH - $(CaO)_1(SiO_2)_{1.5}(H_2O)_{2.5}$ | 85.0 | -2833.0 | -2562.0 | 152.8 | 231.2 | (Kulik, 2011) |
| T5C - $(CaO)_{1.25}(SiO_2)_{1.25}(H_2O)_{2.5}$ | 79.3 | -2782.0 | -2519.0 | 159.9 | 234.1 | (Kulik, 2011) |
| T2C - $(CaO)_{1.5}(SiO_2)_1(H_2O)_{2.5}$ | 80.6 | -2722.0 | -2467.0 | 167.0 | 237.0 | (Kulik, 2011) |

Table 8.2. Dissociation constant reactions for the solid phases used in the thermodynamic modelling calculations.

| Phase | Reaction | $\log_{10}(K_{so})$ | Reference |
|---|---|---|---|
| $Al(OH)_3$ (microcrystalline) | $Al(OH)_3 + OH^- \rightleftharpoons AlO_2^- + 2H_2O$ | -0.67 | (Lothenbach et al., 2012b) |
| Gibbsite | $Al(OH)_3 + OH^- \rightleftharpoons AlO_2^- + 2H_2O$ | -1.12 | (Hummel et al., 2002; Thoenen et al., 2013) |
| Portlandite | $Ca(OH)_2 \rightleftharpoons Ca^{2+} + 2OH^-$ | -5.20 | (Hummel et al., 2002; Thoenen et al., 2013) |
| $SiO_2$ (amorphous) | $SiO_2$ (am) $\rightleftharpoons SiO(OH)_3^- - OH^- - H_2O$ | 1.476 | (Lothenbach and Winnefeld, 2006) |
| Katoite, $C_3AH_6$ | $(CaO)_3(Al_2O_3)(H_2O)_6 \rightleftharpoons 3Ca^{2+} + 2AlO_2^- + 4H_2O + 4OH^-$ | -20.50 | (Lothenbach et al., 2012b) |
| Si-hydrogarnet, $C_3AS_{0.84}H_{4.32}$ | $(CaO)_3(Al_2O_3)(SiO_2)_{0.84}(H_2O)_{4.32} \rightleftharpoons 3Ca^{2+} + 2AlO_2^- + 2.32H_2O + 3.16OH^- + 0.84HSiO_3^-$ | -26.70 | (Dilnesa et al., 2014) |
| Strätlingite, $C_2ASH_8$ | $(CaO)_2(Al_2O_3)(SiO_2)(H_2O)_8 \rightleftharpoons 2Ca^{2+} + 2AlO_2^- + HSiO_3^- + 7H_2O + OH^-$ | -19.70 | (Matschei et al., 2007b) |
| C-S-H, $(CaO)_{1.25}(SiO_2)_{1.25}(H_2O)_{2.5}$ | $(CaO)_{1.25}(SiO_2)_{1.25}(H_2O)_{2.5} \rightleftharpoons 1.25SiO(OH)_3^- + 1.25Ca^{2+} + 1.25OH^-$ | -11.625 | (Kulik, 2011) |

## 8.3 Results and Discussion

### 8.3.1 XRD and Rietveld Analysis

The XRD results show that C-(A-)S-H phases are the dominant reaction products in each sample (Figure 8.1). Katoite ($C_3AH_6$, PDF# 00-024-0217) and strätlingite ($C_2ASH_8$, PDF# 00-029-0285) are also observed in some systems. Siliceous hydrogarnet ($C_3AS_yH_{6-2y}$, $0 < y \leq 3$) is not identified in any of the samples. Katoite and strätlingite are more commonly found as secondary products in the systems with higher bulk Al/Si ratios and lower equilibration temperatures: strätlingite and katoite are observed in every Al-containing system at 7°C, but these phases are only observed in the Al/Si* ≥ 0.1 samples at 20°C, and only katoite is identified in the Al/Si* ≥ 0.1 samples at 50°C. Small amounts of katoite are also found in the Al/Si* = 0.15, 80°C sample. Calcite ($CaCO_3$, PDF# 00-005-0586) is identified in some samples, which is attributed to minor carbonation during sample preparation, storage and/or analysis.

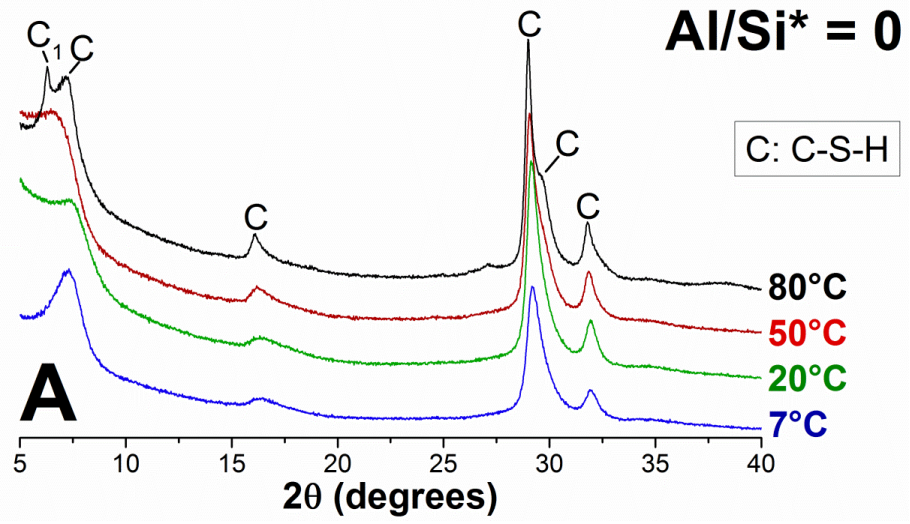


Figure 8.1. Cu Kα diffractograms of the A) C-S-H, and B) Al/Si* = 0.05, C) Al/Si* = 0.1 and D) Al/Si* = 0.15 C-A-S-H systems. Data at 20°C are reproduced from (L'Hôpital et al.). The peaks marked by $C_1$ and $C_2$ represent C-(A-)S-H products with average basal spacings similar to 14 Å tobermorite and 11 Å tobermorite respectively, and C represents C-(A-)S-H products with similarities to both tobermorite types. There is an additional unassigned minor peak at ~43° 2θ in the trace for the Al/Si = 0.1, 7°C sample (not shown). Al/Si* = bulk Al/Si.

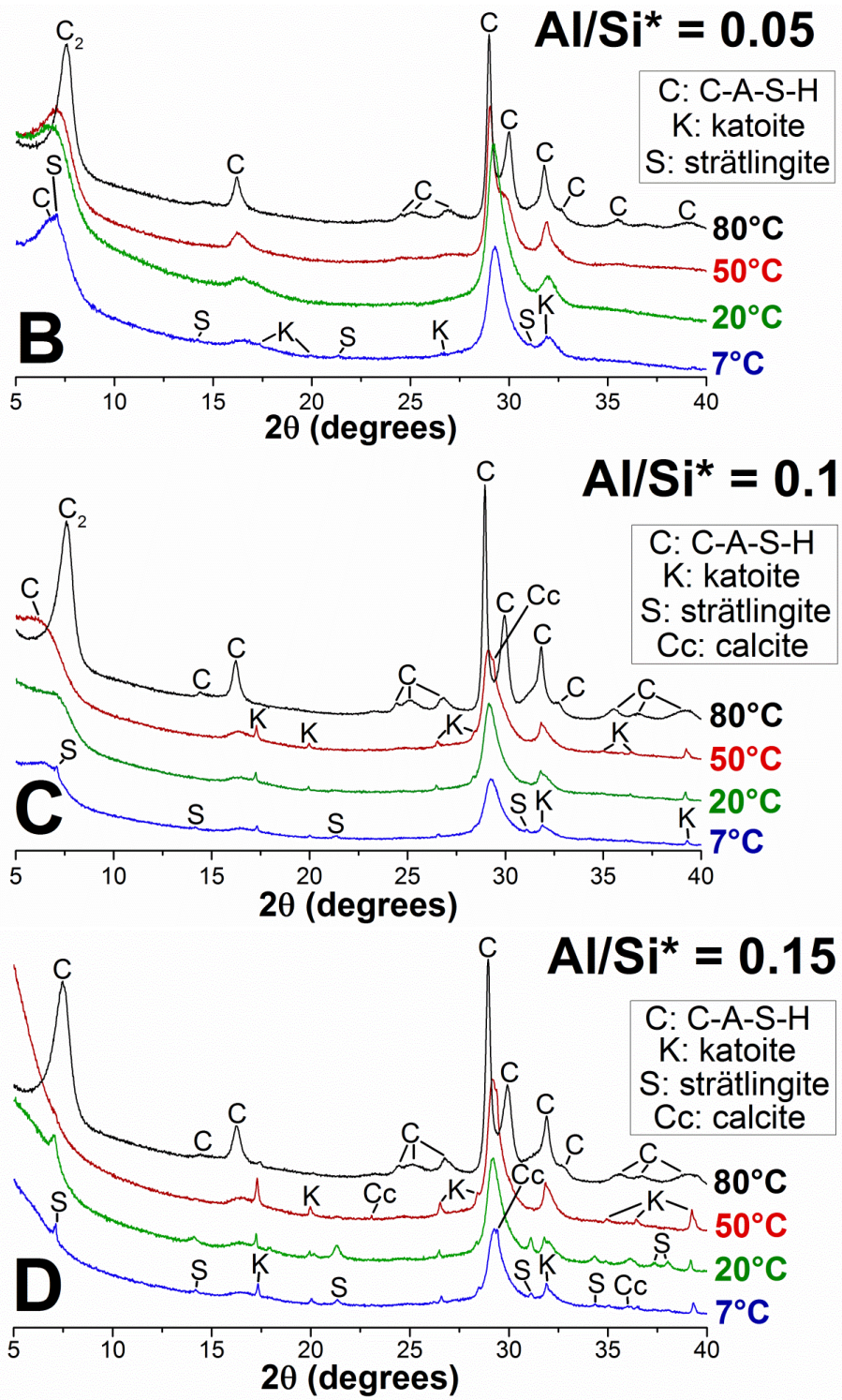


Figure 8.1. Continued.

The long-range order of the C-(A-)S-H products formed, as identified particularly by the intensity and sharpness of the reflections below 8° 2θ and at ~16° 2θ (Figure 8.1), increases as a monotonic function of temperature and Al content, to a maximum at Al/Si* = 0.1 or 0.15, and a temperature of 80°C. The peaks for the C-(A-)S-H products correspond to poorly-ordered structural analogues of 14 Å tobermorite ($5CaO{\cdot}6SiO_2{\cdot}9H_2O$, PDF# 00-029-0331), and 11 Å tobermorite ($4.5CaO{\cdot}6SiO_2{\cdot}5.5H_2O$, PDF# 01-074-2784) (Merlino et al., 2001). These phases can be differentiated in the diffractograms by their different basal spacings; peaks marked $C_1$ and $C_2$ in Figure 8.1 correspond to C-(A-)S-H products with basal spacings that match closely to the (002) reflections for the 14 Å and 11 Å reference tobermorite patterns used here, respectively. The peaks simply marked C indicate reflections of C-(A-)S-H phases with structural similarities to both 14 Å and 11 Å reference tobermorite types. These assignments are consistent with the analysis in (Grangeon et al., 2013), where mixtures of 11 Å and 14 Å tobermorite-like structures could best explain the observed shifts of the (002) reflections in the diffractograms of C-S-H systems over the composition range 0.6 < Ca/Si < 1.8. The average (002) spacings that correspond to the positions of the reflections in the XRD results here do not vary systematically with equilibration temperature or Al/Si ratio, and are between 11 Å and 14 Å for each system studied (Table 8.3).

Rietveld analysis of the diffractograms indicates that at most only small amounts of secondary products were formed in the systems studied (all samples contained ≥ 93 wt.% C-(A-)S-H, Table 8.3). Phase purity increased with increasing temperature and decreasing Al content; phase-pure C-S-H was formed in the Al-free systems, and ≥ 99.7 wt.% C-A-S-H was found in the Al-containing samples that were equilibrated at 80°C.

Table 8.3. Average ($d_{(002)}$) basal spacings and solid phase assemblages of the C-(A-)S-H systems, determined from Rietveld analysis. Data at 20°C are reproduced from (L'Hôpital et al.). The estimated absolute error is ±2 wt.% for the secondary products. Al/Si* = bulk Al/Si.

| **Temperature (°C)** | **Average basal spacing, $d_{(002)}$ (Å)** | **C-(A-)S-H (wt. %)** | **Katoite (wt. %)** | **Strätlingite (wt. %)** | **Calcite (wt. %)** |
|---|---|---|---|---|---|
| **Al/Si * = 0** | | | | | |
| 7 | 12.1 | 100 | 0 | 0 | 0 |
| 20 | 11.9 | 100 | 0 | 0 | 0 |
| 50 | 12.9 | 100 | 0 | 0 | 0 |
| 80 | 12.1, 14.0 [a] | 100 | 0 | 0 | 0 |
| **Al/Si* = 0.05** | | | | | |
| 7 | 12.6 | 99 | 0.4 | 0.6 | 0 |
| 20 | 12.8 | 100 | 0 | 0 | 0 |
| 50 | 12.3 | 100 | 0 | 0 | 0 |
| 80 | 11.6 | 100 | 0 | 0 | 0 |
| **Al/Si* = 0.1** | | | | | |
| 7 | 13.1 | 98.8 | 0.8 | 0.4 | 0 |
| 20 | 12.4 | 97.2 | 2.8 | 0 | 0 |
| 50 | 13.6 | 97.6 | 1.9 | 0 | 0.5 |
| 80 | 11.6 | 100 | 0 | 0 | 0 |
| **Al/Si* = 0.15** | | | | | |
| 7 | - | 96.1 | 2.1 | 1.4 | 0.4 |
| 20 | - | 93.4 | 2.2 | 4.5 | 0 |
| 50 | - | 98.5 | 1.3 | 0 | 0.2 |
| 80 | 11.8 | 99.7 | 0.3 | 0 | 0 |

[a] Two distinct $d_{(002)}$ reflections were distinguished in the diffractogram of this sample.

### 8.3.2 Thermogravimetric Analysis

The solid phase assemblages identified in the TGA results (Figure 8.2) are similar to those identified by XRD (section 8.3.1); the peaks centred at 80-150°C in the TGA results indicate that >77% of the total mass lost in each sample is from interlayer and structurally bound water in C-(A-)S-H (noting that samples were freeze-dried and equilibrated to ~30% RH to remove the capillary and gel water (Muller et al., 2013b)). The central positions of these mass loss peaks, and the total mass losses in

each temperature range, do not vary systematically across the sample synthesis temperature range of 7-80°C, which suggests that the equilibration temperature is not the primary factor controlling the interlayer and structural water content of the C-(A-)S-H products formed here. The relationship between temperature and bound water content in tobermorite (Gmira et al., 2002) and hydrated PC pastes (Gallucci et al., 2013) is different; these materials dehydrate progressively with increasing temperature over this temperature range.

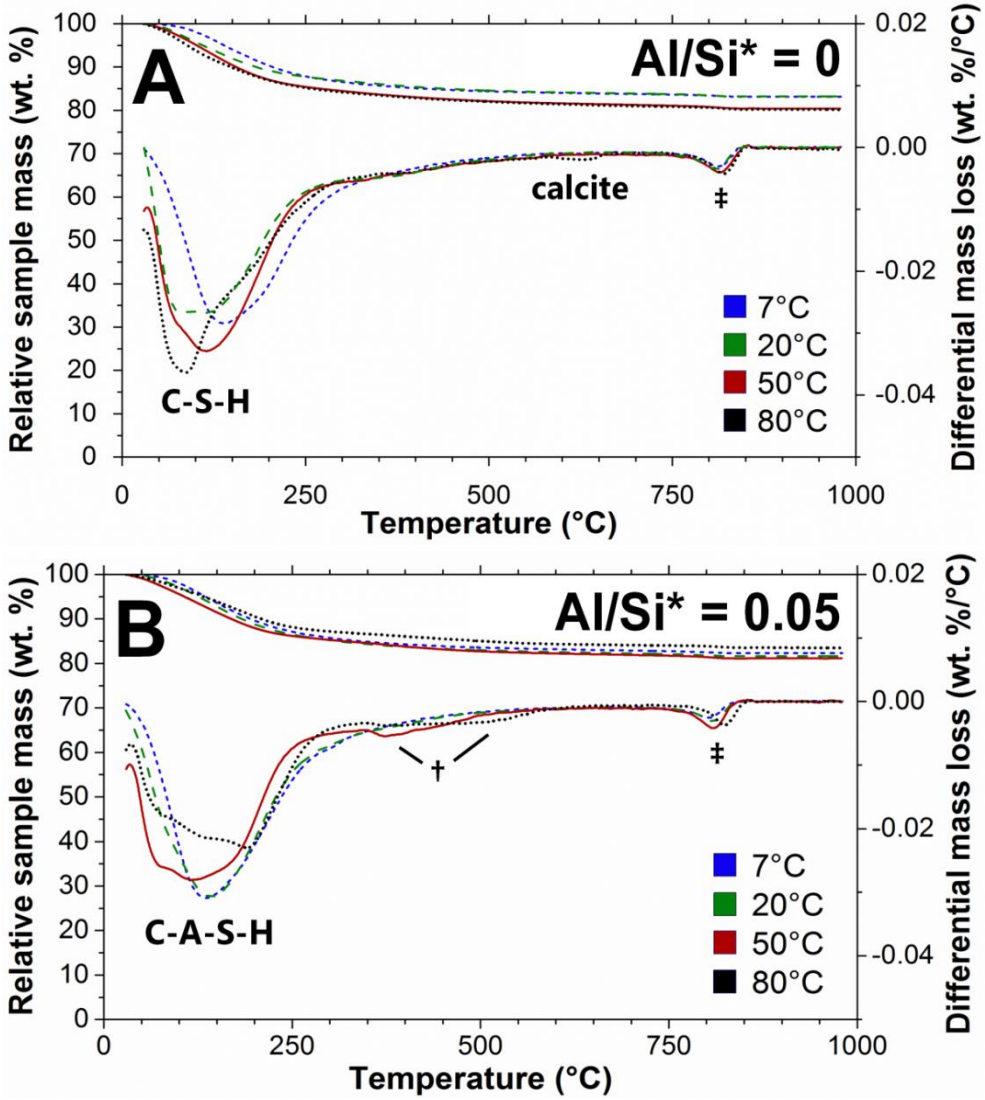


Figure 8.2. TGA results for the A) C-S-H, and B) Al/Si* = 0.05, C) Al/Si* = 0.1 and D) Al/Si* = 0.15 C-A-S-H systems. Data at 20°C are reproduced from (L'Hôpital et al.). The data are represented by short-dashed traces at 7°C, long-dashed traces at 20°C, solid traces at 50°C and dotted traces at 80°C. The peaks labelled † and ‡ are assigned to C-(A-)S-H and the decomposition of C-(A-)S-H to wollastonite ($CaSiO_3$), respectively (Appendix A). Al/Si* = bulk Al/Si.

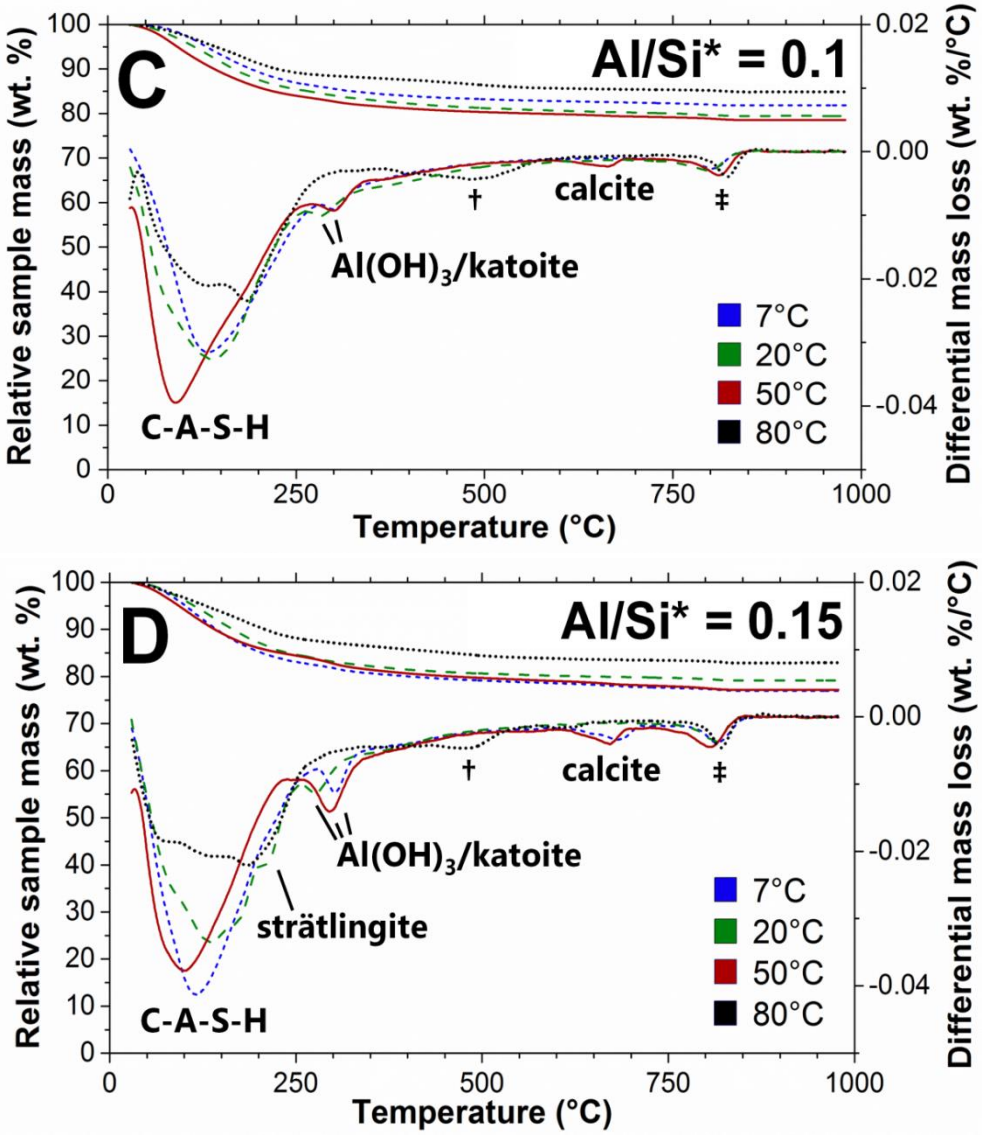


Figure 8.2. Continued.

A distinct shoulder at ~200°C is observed in the differential mass loss trace for the Al/Si* = 0.15 sample equilibrated at 20°C (Figure 8.2D), which is assigned to strätlingite (Kuzel, 1976). Small peaks at ~300°C are observed in the differential mass loss traces for the Al/Si* = 0.1 and Al/Si* = 0.15 samples at 7°C and 50°C (Figures 8.2C-8.2D), and at ~275°C in the trace for the Al/Si* = 0.1 and Al/Si* = 0.15, 20°C systems. These peaks are assigned to $Al(OH)_3$ at ~275°C and katoite at ~300°C (Lothenbach et al., 2012b). Minor carbonation during sample preparation, storage and/or analysis is also identified in some samples, by peaks centred at ~650°C.

The derivative mass loss traces for the Al/Si* = 0.05, 50°C sample and the Al/Si* ≥ 0.05, 80°C samples contain wide and shallow peaks at ~380°C and ~500°C (marked by † in Figures 8.2B-8.2D). These features are principally affected by equilibration temperature because they are only apparent in the 50°C and 80°C samples, but also appear to be related to Al content because the band at ~500°C is largest in the Al/Si* = 0.1, 80°C sample compared to the other samples equilibrated at this temperature. These peaks are assigned to thermal decomposition of C-(A-)S-H because none of the additional phases identified by TGA or XRD (section 8.3.1) can explain the mass losses associated with these bands. The peaks at ~810°C are present in all of the samples studied here (marked by ‡ in Figure 8.2) and are assigned to the decomposition of C-(A-)S-H to wollastonite ($CaSiO_3$) (Trojer, 1968); wollastonite is known to crystallise from C-S-H (Kalousek, 1952) and tobermorite (Mitsuda and Taylor, 1978) at this temperature. Decomposition of C-A-S-H in the temperature range 600-950°C also forms mayenite ($C_{12}A_7$), although distinct differential mass loss peaks for this process are not apparent in Figure 8.2. Additional XRD data supporting these assignments are shown in Appendix A.

### 8.3.3 Aqueous Phase Chemistry and C-S-H Chemical Composition

Figure 8.3A shows that the concentrations of Si and $OH^-$ in the supernatant solutions generally increase slightly with increasing temperature in the C-S-H systems. However, there is not a clear dependence of the measured Ca concentrations on temperature. This result is consistent with published solubility data for C-S-H systems (Atkins et al., 1994; Barbarulo, 2003; Chen et al., 2004; Courault, 2000; Fujii and Kondo, 1981; Greenberg and Chang, 1965; Grutzeck et al., 1989; Roller and Ervin, 1940; Taylor, 1950; Walker et al., 2007). In both the C-S-H (Figure 8.3A) and C-A-S-H (Figure 8.3B) samples, the concentrations of Ca, Si and $OH^-$ species in the filtrates change by less than an order of magnitude between 7°C and 80°C.

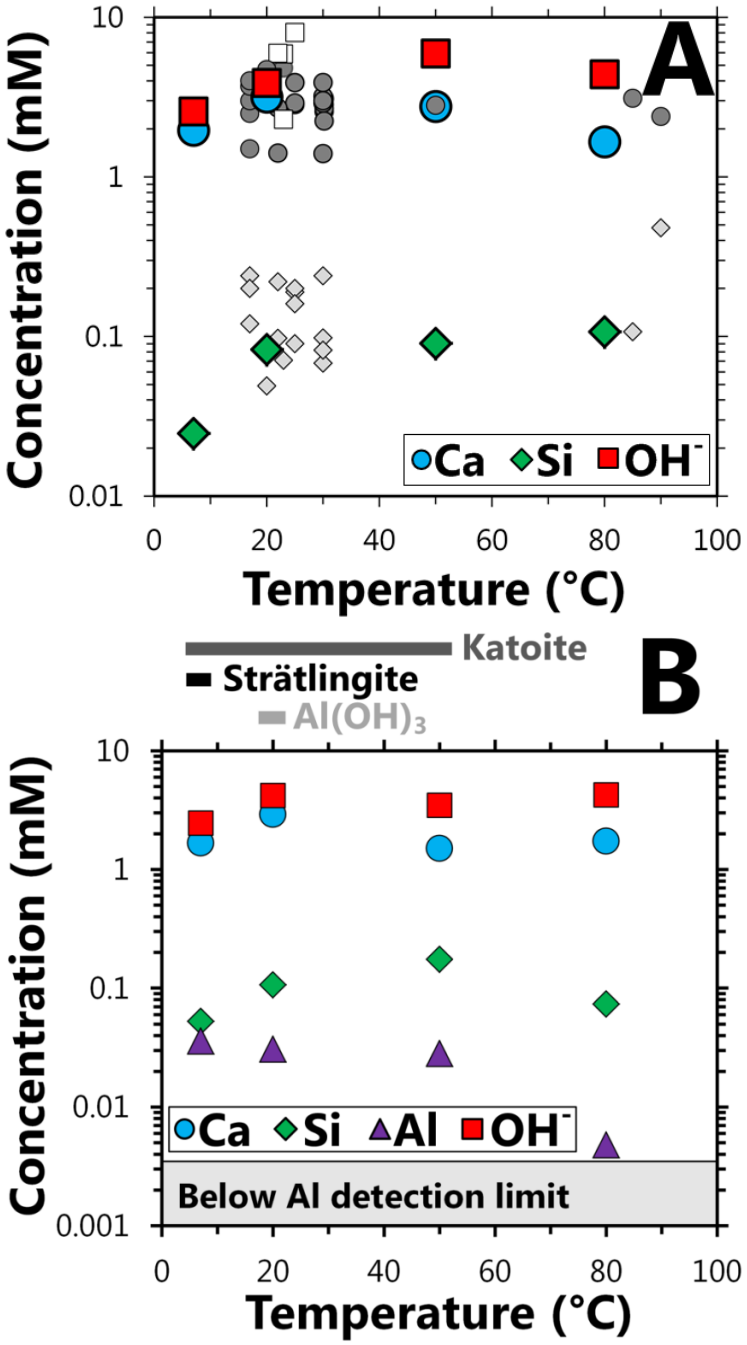


Figure 8.3. Concentrations of Si, Ca, Al and $OH^-$ species in the filtrates of A) C-S-H and B) C-A-S-H (Al/Si* = 0.1) systems. Data at 20°C are reproduced from (L'Hôpital et al.). Previously published C-S-H solubility data for systems with solid-phase Ca/Si ratios = 1 ±0.1 (Atkins et al., 1994; Barbarulo, 2003; Chen et al., 2004; Courault, 2000; Fujii and Kondo, 1981; Greenberg and Chang, 1965; Grutzeck et al., 1989; Roller and Ervin, 1940; Taylor, 1950; Walker et al., 2007) are shown as small white and grey symbols in A), with shapes corresponding to the coloured points for the new data. The data measured here (relative error = ±10%) are tabulated in Appendix B. Minor amounts of additional solid products were identified by XRD and TGA in some systems, as marked by horizontal black and grey bars in B). mM = mmol/L.

The C-A-S-H systems, Figure 8.3B and Appendix B, show weak increasing trends in the concentrations of dissolved Si and $OH^-$ species as a function of temperature and little variation of aqueous Ca content, which is a similar result to that found for the C-S-H systems (Figure 8.3A). In general, the concentration of dissolved Al is lower at higher temperatures. An increase in bulk Al/Si ratio generally leads to a higher concentration of dissolved Si and Al, and less Ca and $OH^-$ (Figure 8.3 and Appendix B). The variation in chemical composition of the C-(A-)S-H products is the main factor contributing to the trends in dissolved Ca, Si, Al and $OH^-$ concentrations, and will be addressed in detail below. This result is consistent with the published solubility data for C-S-H, which show the same trends in Ca, Si and $OH^-$ concentrations as functions of Ca/Si in the solid phase (Chen et al., 2004; Walker et al., 2007). Small amounts of secondary products precipitated in the Al-containing systems (sections 8.3.1-8.3.2), and also contribute slightly to the measured solubilities of Ca, Si, Al and $OH^-$ species.

Analysis of C-(A-)S-H solubility from these results is complex because the aqueous Si, Ca, Al and $OH^-$ concentrations do not follow monotonically increasing or decreasing trends, and because the samples with Al/Si $\geq$ 0.1, and the Al/Si = 0.05, 7°C system, contain additional strätlingite, katoite and/or $Al(OH)_3$ products (see sections 8.3.1-8.3.2), meaning that the results do not represent the solubility of C-(A-)S-H alone. Therefore, the measured aqueous phase compositions were used to calculate effective saturation index (*SI**) values for each precipitated phase and for some common solid products in the $CaO\text{-}SiO_2\text{-}Al_2O_3\text{-}H_2O$ system using eq.(3.7) (section 3.4.1) to clarify the relative solubilities of the solids formed here (Table 8.4).

The total stoichiometric amount of ions in the dissociation reactions for the solid phases (Table 8.2), are 3.75 for C-S-H ($C_{1.25}S_{1.25}H_{2.5}$), 3 for CH, 2 for $SiO_{2\ (am)}$, 2 for $Al(OH)_3$, 9 for katoite, 9 for Si-hydrogarnet, and 6 for strätlingite.

Table 8.4. Effective saturation indices for the relevant reaction products in the C-(A-)S-H systems, calculated from the solution compositions in Figure 8.3 and Appendix B. Effective saturation indices marked in bold represent solid phases that are observed in the TGA and/or XRD results of the respective experimental systems. A 'near saturated' condition of $-0.4 \leq SI_i^* < 0$ is assumed, as discussed in the text.

| Temperature (°C) | C-S-H [a] | CH | $SiO_{2\ (am)}$ [b] | $Al(OH)_3$ [c] | Katoite | Si-hydrogarnet | Strätlingite |
|---|---|---|---|---|---|---|---|
| **Al/Si* = 0** | | | | | | | |
| 7 | **-0.4** | -1.4 | -1.6 | n/a [d] | n/a [d] | n/a [d] | n/a [d] |
| 20 | **-0.1** | -0.9 | -1.7 | n/a [d] | n/a [d] | n/a [d] | n/a [d] |
| 50 | **-0.1** | -0.6 | -1.7 | n/a [d] | n/a [d] | n/a [d] | n/a [d] |
| 80 | **-0.2** | -0.6 | -1.4 | n/a [d] | n/a [d] | n/a [d] | n/a [d] |
| **Al/Si* = 0.05** | | | | | | | |
| 7 | **-0.3** | -1.4 | -1.5 | -0.5 | **-1.1** | -0.6 | **-0.4** |
| 20 | **0.0** | -0.9 | -1.6 | -0.8 | -0.8 | -0.3 | -0.3 |
| 50 | **-0.1** | -0.7 | -1.6 | -1.3 | -0.9 | -0.4 | -0.7 |
| 80 | **-0.2** | -0.6 | -1.5 | b.d.l. [e] | b.d.l. [e] | b.d.l. [e] | b.d.l. [e] |
| **Al/Si* = 0.1** | | | | | | | |
| 7 | **-0.3** | -1.5 | -1.4 | -0.3 | **-1.1** | -0.5 | **-0.4** |
| 20 | **-0.1** | -0.9 | -1.7 | **-0.7** | **-0.8** | -0.3 | -0.3 |
| 50 | **-0.1** | -0.8 | -1.4 | -0.7 | **-0.8** | -0.3 | -0.4 |
| 80 | **-0.3** | -0.6 | -1.5 | -1.2 | -0.9 | -0.4 | -0.8 |
| **Al/Si* = 0.15** | | | | | | | |
| 7 | **-0.4** | -1.6 | -1.3 | -0.2 | **-1.2** | -0.6 | **-0.4** |
| 20 | **0.0** | -1.1 | -1.3 | **-0.7** | **-1.0** | -0.4 | **-0.3** |
| 50 | **-0.1** | -1.0 | -1.1 | -0.5 | **-0.9** | -0.3 | -0.3 |
| 80 | **-0.3** | -0.8 | -1.4 | -0.6 | **-0.8** | -0.3 | -0.5 |

[a] C-S-H is represented here by the MCL = 5 end-member of the 'downscaled CSH3T model' (Ca/Si = 1, Al/Si = 0) (Kulik, 2011); [b] Amorphous $SiO_2$; [c] Microcrystalline $Al(OH)_3$ at 7°C, 20°C and 50°C, and gibbsite at 80°C (Lothenbach et al., 2012b); [d] n/a = not applicable (systems contain no Al); and [e] Dissolved Al concentration is below the detection limit (b.d.l.).

The effective saturation indices (Table 8.4) show that the supernatant solutions are near saturated ($-0.4 \leq SI_i^* < 0$) with respect to C-S-H, and undersaturated with respect to $Ca(OH)_2$ and $SiO_2$, which is consistent with the solid phase assemblages observed experimentally in these systems (sections 8.3.1-8.3.2). The 'near-saturation' range of $SI_i^*$ values chosen here represents the uncertainty associated with both concentration determinations and solubility calculations.

The effective saturation indices (Table 8.4) indicate that C-S-H is the solid phase most likely to precipitate in each of the Al-free systems. The filtrates in the Al-containing systems are near saturated with respect to C-S-H in each of the systems studied, with respect to $Al(OH)_3$ at 7°C and higher Al concentrations, with respect to strätlingite ($C_2ASH_8$) at temperatures ≤ 50°C and bulk Al/Si ratios ≥ 0.05, and with respect to Si-hydrogarnet ($C_3AS_{0.84}H_{4.32}$) at temperatures ≥ 20°C and bulk Al/Si ≥ 0.05, which suggests that the systems are close to equilibrium. Katoite ($C_3AH_6$) was calculated to be undersaturated in each simulated system, although small amounts of this phase were identified in some of the Al-containing systems (sections 8.3.1-8.3.2), which indicates that katoite forms initially from $CaO{\cdot}Al_2O_3$, CaO and $H_2O$ and that the dissolution of this phase is kinetically hindered. Similar observations have been reported for laboratory-synthesised C-(A-)S-H samples aged for more than 1 year at 20°C (L'Hôpital et al.). These results suggest that the solid phase assemblages in the $CaO\text{-}Al_2O_3\text{-}SiO_2\text{-}H_2O$ systems studied here are likely to contain several Al-containing solid products at equilibrium. However, the solid phase assemblages found in the experimental samples are dominated by C-(A-)S-H (sections 8.3.1-8.3.2), which suggests that this phase outcompetes the other near-saturated phases to form in these systems.

A mass balance was performed using these results, the XRD and Rietveld refinement results and the TGA data, to determine chemical compositions for the C-(A-)S-H products formed in each sample (Table 8.5). This analysis excluded contributions from $Al(OH)_3$ because no diffraction lines for this phase are present in the XRD results: small mass losses (≤1 wt.%) were associated with $Al(OH)_3$ in the differential

mass loss traces for the Al/Si* = 0.1 and Al/Si* = 0.15, 20°C samples only (section 8.3.2), meaning that any error introduced in the reported C-(A-)S-H compositions by neglecting Al incorporated into this phase, is minor.

Table 8.5. Chemical compositions of the C-(A-)S-H products, determined from the aqueous phase concentrations, TGA results and Rietveld analysis. Data at 20°C are reproduced from (L'Hôpital et al.). The estimated absolute errors are ±0.04 units in the Ca/Si ratios, ±0.2 units in the $H_2O$/Si ratios, and ±0.04 units at 7°C, ±0.03 units at 20°C, ±0.02 units at 50 and 80°C in the Al/Si ratios of the C-(A-)S-H products. Al/Si* = bulk Al/Si.

| Temperature (°C) | C-S-H chemical composition |
|---|---|
| **Al/Si * = 0** | |
| 7 | $(CaO)_{0.99}(SiO_2)_1(H_2O)_{1.2}$ |
| 20 | $(CaO)_{0.98}(SiO_2)_1(H_2O)_{1.5}$ |
| 50 | $(CaO)_{0.99}(SiO_2)_1(H_2O)_{1.4}$ |
| 80 | $(CaO)_{0.99}(SiO_2)_1(H_2O)_{1.4}$ |
| **Al/Si* = 0.05** | |
| 7 | $(CaO)_{0.98}(Al_2O_3)_{0.022}(SiO_2)_1(H_2O)_{1.3}$ |
| 20 | $(CaO)_{0.99}(Al_2O_3)_{0.025}(SiO_2)_1(H_2O)_{1.4}$ |
| 50 | $(CaO)_{0.99}(Al_2O_3)_{0.025}(SiO_2)_1(H_2O)_{1.4}$ |
| 80 | $(CaO)_{0.99}(Al_2O_3)_{0.025}(SiO_2)_1(H_2O)_{1.2}$ |
| **Al/Si* = 0.1** | |
| 7 | $(CaO)_{0.98}(Al_2O_3)_{0.045}(SiO_2)_1(H_2O)_{1.3}$ |
| 20 | $(CaO)_{0.95}(Al_2O_3)_{0.039}(SiO_2)_1(H_2O)_{1.4}$ |
| 50 | $(CaO)_{0.96}(Al_2O_3)_{0.043}(SiO_2)_1(H_2O)_{1.6}$ |
| 80 | $(CaO)_{0.99}(Al_2O_3)_{0.050}(SiO_2)_1(H_2O)_{1.1}$ |
| **Al/Si* = 0.15** | |
| 7 | $(CaO)_{0.95}(Al_2O_3)_{0.061}(SiO_2)_1(H_2O)_{1.7}$ |
| 20 | $(CaO)_{0.94}(Al_2O_3)_{0.051}(SiO_2)_1(H_2O)_{1.5}$ |
| 50 | $(CaO)_{0.97}(Al_2O_3)_{0.070}(SiO_2)_1(H_2O)_{1.7}$ |
| 80 | $(CaO)_{0.98}(Al_2O_3)_{0.074}(SiO_2)_1(H_2O)_{1.3}$ |

The calculated Ca/Si and Al/Si ratios of the C-(A-)S-H products are generally more similar to the bulk conditions used (Ca/Si = 1 and $0 \leq$ Al/Si $\leq 0.15$) in the systems with lower Al content and higher temperatures, because these samples typically contain lower amounts of secondary phases. The Al content of the C-(A-)S-H products and the concentrations of Al dissolved in the supernatant solutions are

directly related (Figure 8.4), and both typically increase with increasing bulk Al/Si ratio. In general, the concentration of dissolved Al decreases and the Al/Si ratio of the C-(A-)S-H phase increases as a function of the equilibration temperature.

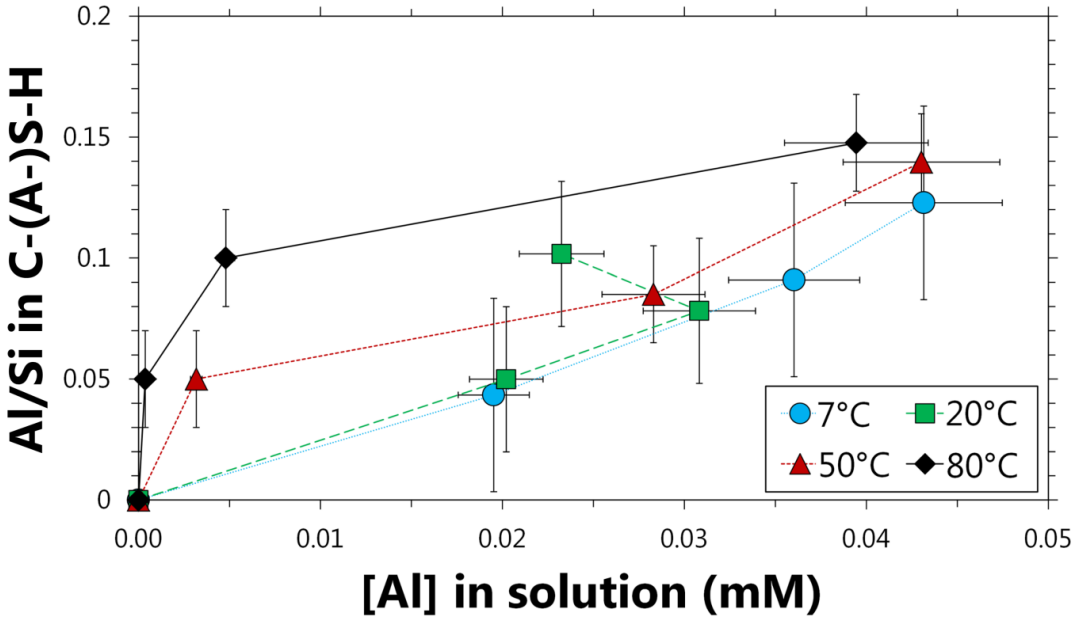


Figure 8.4. Al/Si ratios of the C-(A-)S-H products as a function of the concentration of Al in the supernatant. Data at 20°C are reproduced from (L'Hôpital et al.). The uncertainties of the Al/Si ratios calculated for the C-(A-)S-H phases are ±0.04 units at 7°C, ±0.03 units at 20°C, and ±0.02 units at 50 and 80°C. A relative measurement error of ±10% is specified for the aqueous concentrations. Lines are for eye-guides only. mM = mmol/L.

The low water contents determined for the C-(A-)S-H products formed here ($1.1 \leq H_2O/Si \leq 1.7$) compare closely to the proposed values for C-S-H with no adsorbed water ($1.3 \leq H_2O/Si \leq 1.8$ (Jennings, 2008; Muller et al., 2013a)), which suggests that only interlayer and structural water remains after the drying procedure used here (dried to RH ≈ 30% (Muller et al., 2013b)). The use of a more severe drying procedure here than in a recent study of temperature effects on PC pastes (Gallucci et al., 2013) explains why the $H_2O/Si$ ratios of the low-Al C-(A-)S-H in that study were found to vary as a function of temperature and were significantly higher ($2.28 \leq H_2O/Si \leq 3.31$) than those determined here.

### 8.3.4 $^{29}$Si MAS NMR

The $^{29}$Si MAS NMR spectra are dominated by intense bands at -79.4 ppm, -83.5 ppm and -85.3 ppm (Figure 8.5), which are characteristic of silicate species in chain-end ($Q^1$), bridging ($Q^2_b$) and paired ($Q^2_p$) sites respectively (Figure 2.5) (Skibsted and Andersen, 2013). An additional peak is apparent between the $Q^1$ and $Q^2_p$ sites in the Al/Si* = 0.1 spectra compared to the Al-free samples, which indicates that $Q^2$(1Al) sites are present in the C-A-S-H systems. These species lead to bands centred at -81.9 ppm in the deconvoluted spectra (Richardson et al., 1993). Cross-linked $Q^3$(1Al) and $Q^3$ sites are also evident at -91.9 ppm and -96.6 ppm respectively in the spectrum of the Al/Si* = 0.1, 80°C sample, which is the only spectrum that contains clearly visible resonance signals for these sites. $Q^3$-type sites have also been identified in $^{29}$Si MAS NMR spectra of hydrated 60% PC/40% silica fume cements (Ca/Si ≈ 0.83 and Al/Si ≈ 0.035), which were found to increase greatly in intensity at 80°C relative to 20°C and 50°C (Bach et al., 2012), although these sites are not observed in more Ca-rich materials in this temperature range (e.g. hydrated PC and $C_3S$ (Masse et al., 1993)). Strätlingite is not explicitly taken into account in deconvolutions of the $^{29}$Si MAS NMR spectra; this phase is thought to contain aluminosilicate species with $^{29}$Si isotropic chemical shifts of -80 to -90 ppm (Kwan et al., 1995), but is not expected to greatly affect the deconvolution analysis because it was seen to be a minor component via Rietveld analysis for the Al/Si* = 0.1 samples (≤ 0.4 wt.%, Table 8.3).

The deconvoluted spectra and quantified site environments for each of the C-S-H and C(A-)S-H samples are shown in Figures 8.6 and 8.7 respectively, with the results tabulated in Table 8.6.

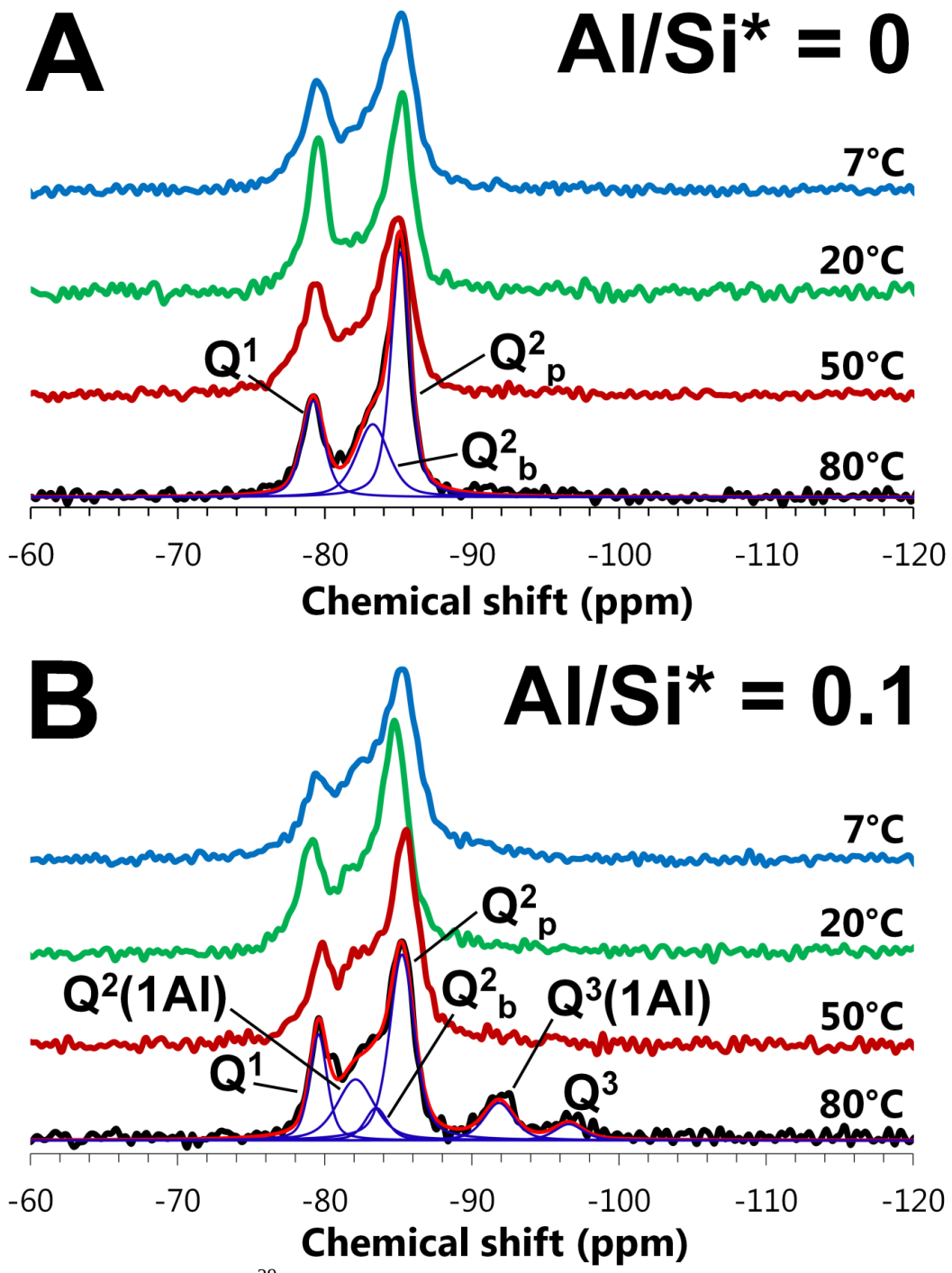


Figure 8.5. Solid-state $^{29}$Si MAS NMR spectra of the A) C-S-H and B) Al/Si* = 0.1 C-A-S-H systems. The fits and deconvoluted peaks for the spectra of the 80°C samples are shown as bright red and blue lines respectively. The chemical shift range corresponding to aluminosilicate sites in strätlingite is approximately -80 to -90 ppm (Kwan et al., 1995). Data at 20°C are reproduced from (L'Hôpital et al.). Al/Si* = bulk Al/Si.

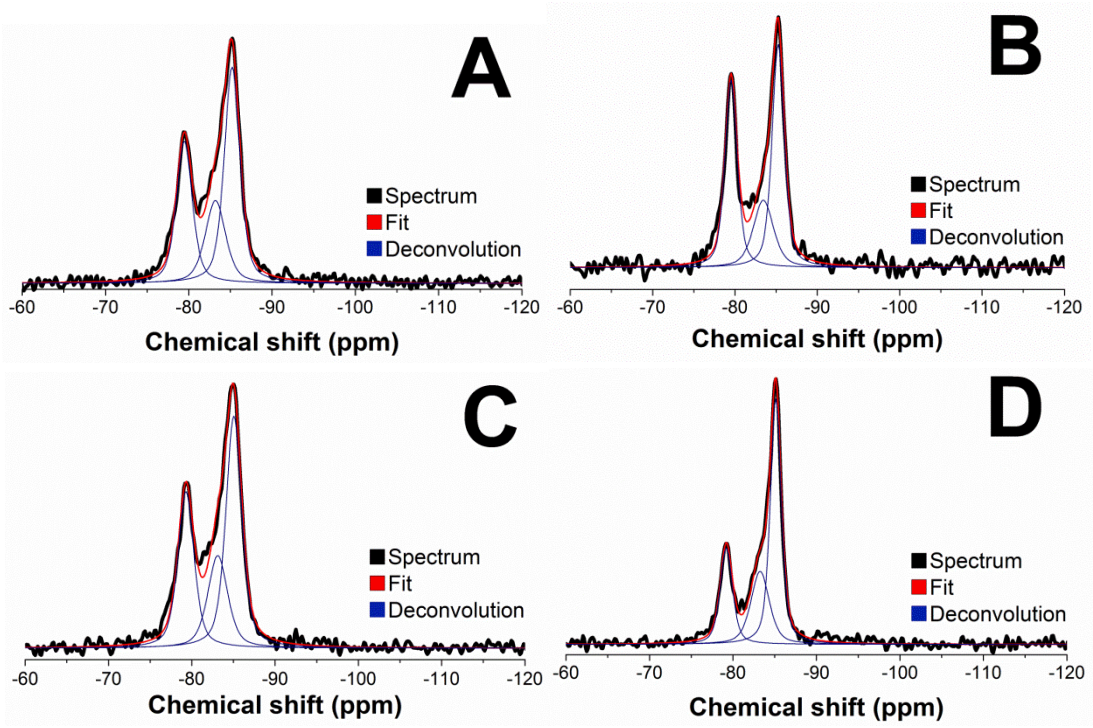


Figure 8.6. Solid-state $^{29}$Si MAS NMR spectra of the C-S-H systems (Al/Si* = 0) equilibrated at A) 7°C, B) 20°C, C) 50°C, D) 80°C.

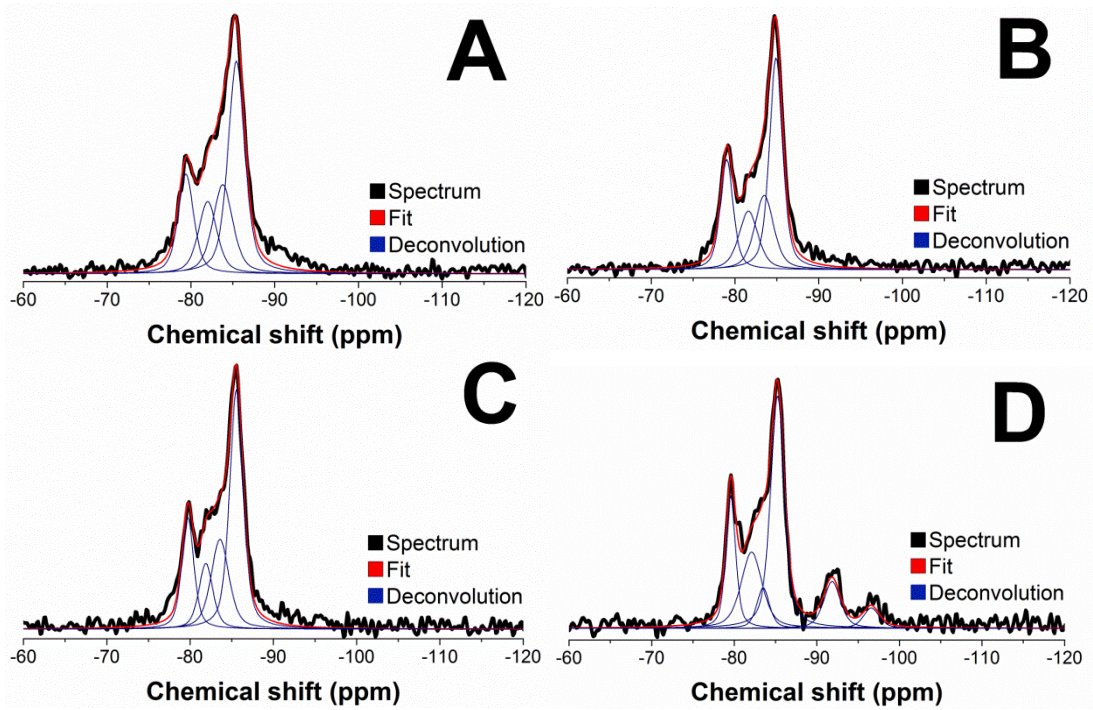


Figure 8.7. Solid-state $^{29}$Si MAS NMR spectra of the C-A-S-H systems (Al/Si* = 0.1) equilibrated at A) 7°C, B) 20°C, C) 50°C, D) 80°C.

Table 8.6. Deconvolution results for the $^{29}$Si MAS NMR spectra. The estimated error in absolute site percentages is ±0.03. Al/Si* = bulk Al/Si.

| Al/Si* | Temperature (°C) | $Q^1$ -79.4 ±0.3 ppm | $Q^2$(1Al) -81.9 ±0.2 ppm | $Q^2_b$ -83.5 ±0.3 ppm | $Q^2_p$ -85.3 ±0.3 ppm | $Q^3$(1Al) -91.9 ppm | $Q^3$ -96.6 ppm | Al/Si | MCL |
|---|---|---|---|---|---|---|---|---|---|
| 0 | 7 | 0.31 | 0 | 0.23 | 0.46 | 0 | 0 | 0 | 6.5 |
| 0 | 20 | 0.36 | 0 | 0.21 | 0.43 | 0 | 0 | 0 | 5.6 |
| 0 | 50 | 0.32 | 0 | 0.23 | 0.46 | 0 | 0 | 0 | 6.4 |
| 0 | 80 | 0.23 | 0 | 0.26 | 0.51 | 0 | 0 | 0 | 8.8 |
| 0.1 | 7 | 0.19 | 0.16 | 0.22 | 0.43 | 0 | 0 | 0.081 | 11.4 |
| 0.1 | 20 | 0.21 | 0.17 | 0.21 | 0.42 | 0 | 0 | 0.084 | 10.4 |
| 0.1 | 50 | 0.20 | 0.16 | 0.21 | 0.43 | 0 | 0 | 0.082 | 11.0 |
| 0.1 | 80 | 0.17 | 0.21 | 0.07 | 0.42 | 0.1 | 0.04 | 0.10 | 19.8 |

The lineshapes of the spectra for the samples equilibrated at ≤ 50°C and the same bulk Al/Si ratio are similar, which indicates that the C-(A-)S-H products formed in these samples have similar degrees of polymerisation, as shown in Figure 8.8, calculated using eq.(2.4) for non-cross-linked C-(A-)S-H (subscript *NC*) (Richardson and Groves, 1993b). Al/Si ratios for non-cross-linked C-(A-)S-H are calculated by eq.(2.5) (Richardson and Groves, 1993b). The MCL and Al/Si values for mixed cross-linked (subscript *C*)/non-cross-linked C-(A-)S-H structures (i.e. a C-(A-)S-H product containing $Q^3$ and/or $Q^3$(1Al) sites) are calculated using the CSTM (Myers et al., 2013), which is described in full in Chapter 4 of this thesis.

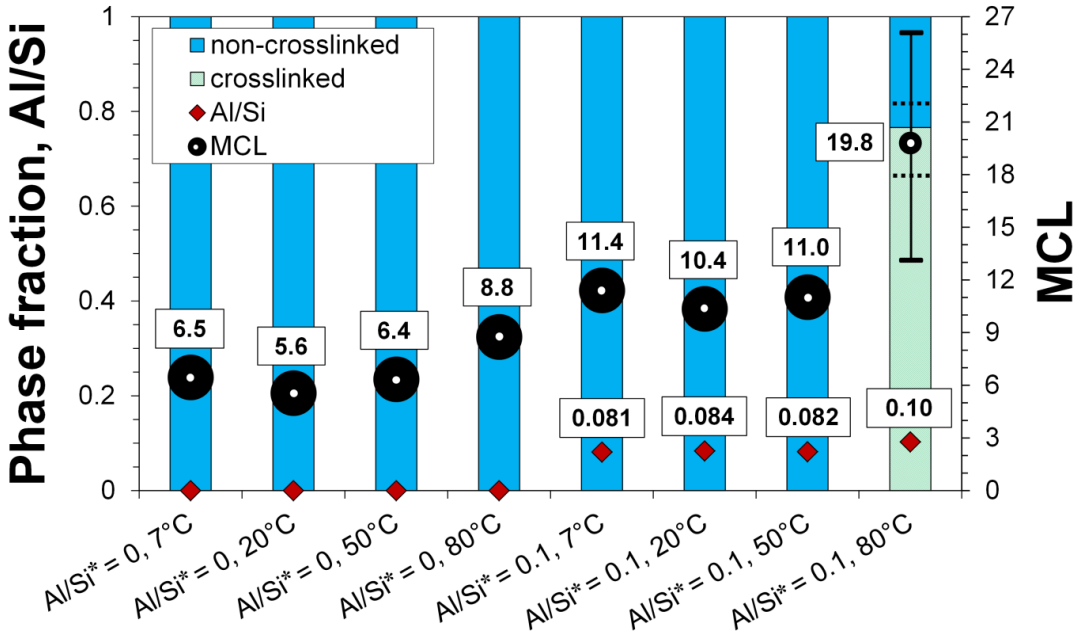


Figure 8.8. C-(A-)S-H structural parameters calculated from deconvolution analysis of the $^{29}$Si MAS NMR spectra, determined using the SGM (Richardson and Groves, 1993b) for the non-cross-linked phases and the CSTM (Myers et al., 2013) for the mixed cross-linked/non-cross-linked phases. The sizes of the symbols represent the expected error bounds of the deconvolution results, except for the Al/Si* = 0.1, 80°C sample, where the uncertainty of the MCL calculation is represented by error bars. The cross-linked phase fraction for the C-A-S-H product in this sample has an error bound of +0.05 and -0.1, as marked by the dotted black lines. Al/Si* = bulk Al/Si.

The C-(A-)S-H products formed in the samples equilibrated at 80°C are significantly more polymerised than those produced at lower temperatures; the same trend has been reported for C-(A-)S-H products formed in hydrated 60% PC/40% silica fume

cements (Bach et al., 2012). MCL values of 8.8 and 19.8 ± 6 were calculated for the C-(A-)S-H products in the Al/Si* = 0 and Al/Si* = 0.1 systems at 80°C, respectively. This increase in chain length is associated with a significant increase in the long-range order of the C-(A-)S-H products at 80°C relative to the C-(A-)S-H phases formed at lower temperatures (section 8.3.1), which is particularly pronounced for the Al-containing samples. The increase in chain polymerisation from 50°C to 80°C is much smaller in the Al-free system relative to the Al/Si* = 0.1 system, and this is consistent with the observation of cross-linked chain structures only in the Al/Si* = 0.1 sample. Therefore, these results indicate that the formation of highly polymerised and cross-linked C-(A-)S-H products is promoted substantially by the presence of Al.

Figure 8.9 shows that the Al/Si ratios determined from analysis of the $^{29}$Si MAS NMR spectral deconvolution results (Figures 8.5-8.7) match closely with the chemical compositions of the C-(A-)S-H products determined independently by the TGA results, measured filtrate compositions and Rietveld analysis (Table 8.5). The formation of a highly cross-linked C-A-S-H product in the Al/Si* = 0.1, 80°C sample is also consistent with the low average basal spacing for the C-A-S-H phase in this system (11.6 Å, Table 8.3), which is similar to the layer spacing of double chain 11 Å tobermorite (11.3 Å).

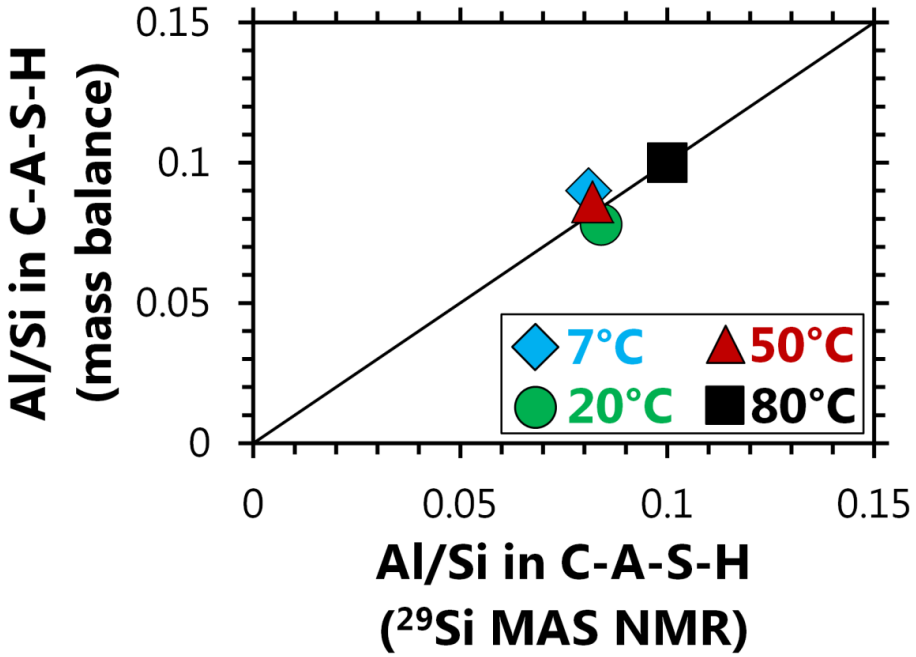


Figure 8.9. Comparison between the chemical compositions of the C-A-S-H products in the Al/Si* = 0.1 samples, as determined by mass balance (TGA, XRD, aqueous phase compositions – Table 8.5) and deconvolutions of $^{29}$Si MAS NMR spectra (Table 8.6). The sizes of the symbols represent the expected uncertainty in the spectral deconvolution results. The solid y = x line is intended as an eye-guide only.

### 8.3.5 C-(A-)S-H Solubility

Solubility products ($K_{so}$) were calculated for hypothetical C-(A-)S-H end-members with chemical compositions corresponding to the bulk chemistry of the systems studied (Al/Si = 0, 0.05, 0.1, 0.15) but normalised to Ca/(Al+Si) = 1 and $H_2O$/Si = 1.2, using eqs.(3.8-3.9). These calculations are described in full in section 3.4.1.

The results of these calculations, for the hypothetical C-(A-)S-H end-members, are shown in Figure 8.10. Solubility products were calculated in the same way for the experimental C-(A-)S-H products with chemical compositions determined from the measured supernatant concentrations, TGA data and XRD results (Table 8.5), which are shown in Appendix B.

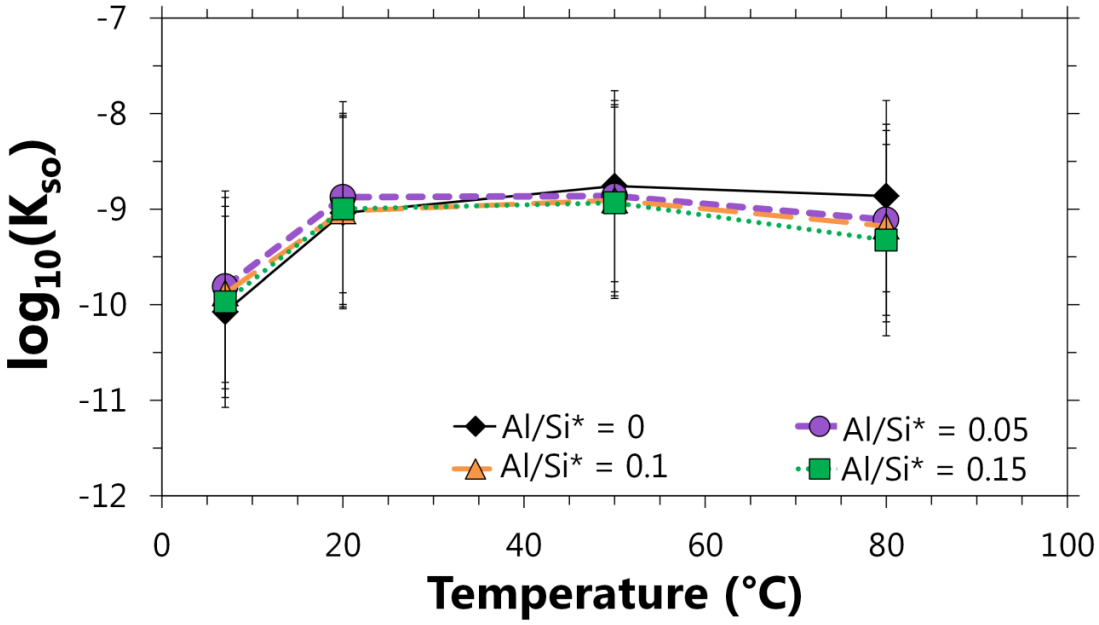


Figure 8.10. Calculated $\log_{10}(K_{so})$ values for hypothetical C-(A-)S-H end-members with chemical compositions of Ca/(Al+Si) = 1, Al/Si = 0, 0.05, 0.1 and 0.15, and $H_2O$/Si = 1.2, and normalised to 1 mol $SiO_2$. The approximate uncertainty in the $\log_{10}(K_{so})$ values are ±1 $\log_{10}$ unit. The solubility product for the C-A-S-H product formed in the Al/Si* = 0.05 sample equilibrated at 80°C was calculated with [Al] = 0.001 mmol/L because the measured Al concentration was below the detection limit. Al/Si* = bulk Al/Si.

The solubility products of the hypothetical C-(A-)S-H end-members change slightly between 7°C and 80°C, and very slightly as a function of Al/Si ratio, but remain within the error bound of ±1 log unit (Figure 8.10). These solubility products ($-9 < \log_{10}(K_{so}) < -10$) are comparable to those recalculated from reported Ca, Si and $OH^-$ solubilities in laboratory-synthesised Ca/Si = 0.83 tobermorite specimens using eq.(8.6) (-8.1 ±0.3 at 25°C, -9.3 ±0.6 at 55°C and -9.6 ±0.2 at 85°C (Dickson et al., 2004)), as expected for these structurally and compositionally-similar phases. Despite the large uncertainty relative to the variation in the calculated solubility products, the 80°C data do show a small systematic reduction in C-(A-)S-H solubility as the Al/Si ratio of this phase increases, which could indicate that these phases are slightly stabilised by the incorporation of Al at high temperature, but further experimental solubility data are necessary to clarify this point. The precipitation of small amounts of katoite, strätlingite and calcite (Table 8.3) is not expected to significantly affect the trends in C-(A-)S-H solubility reported here, although the results depend slightly on this factor.

Nonetheless, the weak dependency of C-(A-)S-H solubility on temperature, clearly shown by these data, is an important result which will influence the development of thermodynamic models for cementitious materials across the temperature range of interest for the majority of service conditions worldwide.

## 8.4 Conclusions

This paper has analysed the structure and solubility of calcium (alumino)silicate hydrates, with and without the inclusion of Al, as a function of temperature. The long-range order and degree of polymerisation of the C-(A-)S-H products, and the type and quantity of secondary phases formed in the equilibrated $CaO$-$Al_2O_3$-$SiO_2$-$H_2O$ systems studied here, were significantly influenced by the synthesis temperature. The supernatants in these systems were close to saturation with respect to strätlingite and $Al(OH)_3$ products at lower temperatures and higher Al/Si ratios, and equilibrium was attained more rapidly at high temperatures, meaning that the Al-

free and 80°C systems contained the most phase-pure C-(A-)S-H products. The C-(A-)S-H phases formed at 80°C were much more polymerised and long-range ordered than those produced at 7, 20 and 50°C, and the C-A-S-H product in the 80°C, Al/Si = 0.1 system was also highly cross-linked. However, no $Q^3$-type sites were evident in the $^{29}$Si MAS NMR spectra for the C-S-H formed in the Al-free system at this temperature, indicating that cross-linking in C-(A-)S-H products is promoted by the presence of Al. Solubility products for the C-(A-)S-H phases formed here did not vary beyond the experimental error bounds as a function of temperature or Al/Si ratio, but a small systematic reduction in C-(A-)S-H solubility at 80°C as the bulk Al/Si ratio was increased could indicate that these phases are slightly stabilised by Al at this temperature. Therefore, this study is an important step towards the development of thermodynamic models for C-A-S-H and advances the application of thermodynamic modelling to C-(A-)S-H based cements across the temperature range 7-80°C, which will provide new insight into the performance of these materials in service.

# 9

# Composition-Solubility-Structure Relationships in C-(N-)A-S-H

This chapter is based on the manuscript 'Composition-solubility-structure relationships in calcium (alkali) aluminosilicate hydrate (C-(N-)A-S-H)', by Myers, R. J., L'Hôpital, E., Provis, J. L. and Lothenbach B., currently in preparation. C-(N-)A-S-H samples were synthesised by Rupert J. Myers with assistance from Emilie L'Hôpital. The XRD and TGA measurements were performed by Rupert J. Myers and Boris Ingold (Laboratory for Concrete/Construction Chemistry, EMPA) with assistance from Ellina Bernard and Nikolajs Toropovs. The IC measurements were performed by Emilie L'Hôpital with assistance from Luigi Brunetti. The $^{29}$Si MAS NMR experiments were performed by Salaheddine Alahrache (Laboratory for Concrete/Construction Chemistry, EMPA) with assistance from Daniel Rentsch (Laboratory for Functional Polymers, EMPA).

## 9.1 Introduction

The alkalinity of cement-based materials varies greatly as a function of the cement formulation and type: Portland cement (PC) typically contains up to 1 wt.% alkali (mainly K) oxide equivalent (Taylor, 1997); fly ash, a common supplementary cementitious material (SCM), generally contains >1 wt.% alkali (Na + K) oxide equivalent (Fernández-Jiménez and Palomo, 2003); and alkali-activated materials are typically derived from highly concentrated Na-based solutions (up to or exceeding 5 M) (Provis and Bernal, 2014). The elevated pH environment that prevails in most hydrated cement-based materials (pH > 13) provides the crucial function of steel

passivation in reinforced concrete applications. Alkalinity is an important design parameter in other applications, such as for safe geological storage of radioactive waste, where 'low-pH' cements (pH ≈ 11) are desired (Bai et al., 2011; Lothenbach et al., 2012a). The alkalinity of cement-based materials also plays an important role in the dissolution of cementitious precursors (Bernal et al., 2015; Snellings, 2013), deterioration of concrete due to alkali silica reaction (Chappex and Scrivener, 2012; Leemann et al., 2011), and the chemical composition, structure and solubility of reaction products formed during hydration (activation in the case of alkali-activated cements) (Bach et al., 2013; Duchesne and Reardon, 1995; L'Hôpital et al.; Lognot et al., 1998).

The solubility of C-(N-)A-S-H is poorly understood relative to C-(N-)S-H, although recent results (L'Hôpital et al.) indicate that the solubility of these phases are significantly different. The availability of a comprehensive set of solubility data for C-(N-)A-S-H is necessary for the development of more accurate thermodynamic models for this phase (Myers et al., 2014), which would advance the utility of thermodynamic modelling to cement-based materials. The lack of consensus for the exact mechanism and selectivity of alkali uptake in C-(N-)A-S-H (Bach et al., 2013; Chappex and Scrivener, 2012; Hong and Glasser, 1999; 2002; Skibsted and Andersen, 2013; Stade, 1989) clearly demonstrates a need for additional studies to clarify the relationships between the uptake of Na, K and Al in C-(N-)A-S-H. Therefore, this paper aims to clarify the effect of Na, K and Al on the chemical composition, structure, and solubility of C-(N-)A-S-H products at bulk Ca/Si ratios of 0.6, 1 and 1.4 under equilibrium conditions at 50°C, which are not currently well-described in the literature.

## 9.2 Experimental

C-(N-)A-S-H samples were synthesised at bulk molar Al/Si ratios (Al/Si*) of 0-0.1 and bulk molar Ca/Si ratios (Ca/Si*) of 0.6-1.6 using Milli-Q water (Merck Millipore) and 0-1 M solutions of NaOH and/or KOH (Merck Millipore), at a

solution/solid ratio of 45 in a $N_2$-filled glovebox by the method described in section 3.2.2 (L'Hôpital et al.; Myers et al., 2015b). Samples were equilibrated at 50°C for 56 days. The specimens were studied by IC and pH analysis, XRD with Rietveld analysis, TGA, $^{29}$Si MAS NMR and thermodynamic modelling. Thermodynamic modelling was performed in GEM Selektor v.3 software (http://gems.web.psi.ch/) (Kulik et al., 2013; Wagner et al., 2012) using the thermodynamic properties of the gases and aqueous species shown in Chapter 3 (Tables 3.2-3.3); thermodynamic properties of the solid phases used are shown in Tables 9.1-9.2. A complete description of the experimental details for this investigation is given in Chapter 3.

Table 9.1. Standard partial molar thermodynamic properties of the solid phases used in the thermodynamic modelling calculations. The reference state is 298.15 K and 1 bar.

| Phase | V° ($cm^3$/mol) | $\Delta_f H°$ (kJ/mol) | $\Delta_f G°$ (kJ/mol) | S° (J/(mol.K)) | Cp° (J/(mol.K)) | Reference |
|---|---|---|---|---|---|---|
| $Al(OH)_3$ (microcrystalline), ½$AH_3$ | 32.0 | -1265.3 | -1148.4 | 140.0 | 93.1 | (Lothenbach et al., 2012b) |
| Gibbsite, ½$AH_3$ | 32.0 | -1288.7 | -1151.0 | 70.1 | 93.1 | (Helgeson et al., 1978) |
| Portlandite, CH | 33.1 | -984.7 | -897.0 | 83.4 | 87.5 | (Robie and Hemingway, 1995) |
| $SiO_2$ (amorphous) | 29.0 | -903.3 | -848.9 | 41.3 | 44.5 | (Kulik, 2011) |
| Katoite, $C_3AH_6$ | 149.7 | -5537.3 | -5008.2 | 421.7 | 445.6 | (Lothenbach et al., 2012b) |
| Si-hydrogarnet, $C_3AS_{0.84}H_{4.32}$ | 142.5 | -5847.5 | -5365.2 | 375.2 | 412.6 | (Dilnesa et al., 2014) |
| Strätlingite, $C_2ASH_8$ | 216.1 | -6360.0 | -5705.1 | 546.2 | 602.7 | (Matschei et al., 2007b) |
| **C-(N-)A-S-H solid solution, CNASH_ss** | | | | | | |
| 5CA, $C_{1.25}A_{0.125}SH_{1.625}$ | 57.3 | −2491 | −2293 | 163 | 177 | (Myers et al., 2014) |
| INFCA, $CA_{0.15625}S_{1.1875}H_{1.65625}$ | 59.3 | −2551 | −2343 | 154 | 181 | (Myers et al., 2014) |
| 5CNA, $C_{1.25}N_{0.25}A_{0.125}SH_{1.375}$ | 64.5 | −2569 | −2382 | 195 | 176 | (Myers et al., 2014) |
| INFCNA, $CN_{0.34375}A_{0.15625}S_{1.1875}H_{1.3125}$ | 69.3 | −2667 | −2474 | 198 | 180 | (Myers et al., 2014) |
| INFCN, $CN_{0.3125}S_{1.5}H_{1.1875}$ | 71.1 | −2642 | −2452 | 186 | 184 | (Myers et al., 2014) |
| T2C*, $C_{1.5}SH_{2.5}$ | 80.6 | −2721 | −2465 | 167 | 237 | (Myers et al., 2014) |
| T5C*, $C_{1.25}S_{1.25}H_{2.5}$ | 79.3 | −2780 | −2517 | 160 | 234 | (Myers et al., 2014) |
| TobH*, $CS_{1.5}H_{2.5}$ | 85.0 | −2831 | −2560 | 153 | 231 | (Myers et al., 2014) |

Table 9.2. Dissolution reactions for the solid phases used in the thermodynamic modelling calculations (298.15 K, 1 bar).

| Phase | Reaction | $\log_{10}(K_s)$ | Reference |
|---|---|---|---|
| $Al(OH)_3$ (microcrystalline), $\frac{1}{2}AH_3$ | $Al(OH)_3 + OH^- \rightleftharpoons AlO_2^- + 2H_2O$ | -0.67 | (Lothenbach et al., 2012b) |
| Gibbsite, $\frac{1}{2}AH_3$ | $Al(OH)_3 + OH^- \rightleftharpoons AlO_2^- + 2H_2O$ | -1.12 | (Hummel et al., 2002; Thoenen et al., 2013) |
| Portlandite, CH | $Ca(OH)_2 \rightleftharpoons Ca^{2+} + 2OH^-$ | -5.20 | (Hummel et al., 2002; Thoenen et al., 2013) |
| $SiO_2$ (amorphous) | $SiO_2$ (am) $\rightleftharpoons SiO(OH)_3^- - OH^- - H_2O$ | 1.476 | (Lothenbach and Winnefeld, 2006) |
| Katoite, $C_3AH_6$ | $(CaO)_3(Al_2O_3)(H_2O)_6 \rightleftharpoons 3Ca^{2+} + 2AlO_2^- + 4H_2O + 4OH^-$ | -20.50 | (Lothenbach et al., 2012b) |
| Si-hydrogarnet, $C_3AS_{0.84}H_{4.32}$ | $(CaO)_3(Al_2O_3)(SiO_2)_{0.84}(H_2O)_{4.32} \rightleftharpoons 3Ca^{2+} + 2AlO_2^- + 2.32H_2O + 3.16OH^- + 0.84HSiO_3^-$ | -26.70 | (Dilnesa et al., 2014) |
| Strätlingite, $C_2ASH_8$ | $(CaO)_2(Al_2O_3)(SiO_2)(H_2O)_8 \rightleftharpoons 2Ca^{2+} + 2AlO_2^- + HSiO_3^- + 7H_2O + OH^-$ | -19.70 | (Matschei et al., 2007b) |

Table 9.2. Continued.

| Phase | Reaction | $\log_{10}(K_s)$ | Reference |
|---|---|---|---|
| 5CA, $C_{1.25}A_{0.125}SH_{1.625}$ | $(CaO)_{1.25}(Al_2O_3)_{0.125}(SiO_2)_1(H_2O)_{1.625} \rightleftharpoons SiO_3^{2-} + 1.25Ca^{2+} + 0.25AlO_2^- + 0.25OH^- + 1.5H_2O$ | -10.75 | (Myers et al., 2014) |
| INFCA, $CA_{0.15625}S_{1.1875}H_{1.65625}$ | $(CaO)_1(Al_2O_3)_{0.15625}(SiO_2)_{1.1875}(H_2O)_{1.65625} + 0.6875OH^- \rightleftharpoons 1.1875SiO_3^{2-} + Ca^{2+} + 0.3125AlO_2^- + 2H_2O$ | -8.90 | (Myers et al., 2014) |
| 5CNA, $C_{1.25}N_{0.25}A_{0.125}SH_{1.375}$ | $(CaO)_{1.25}(Na_2O)_{0.25}(Al_2O_3)_{0.125}(SiO_2)_1(H_2O)_{1.375} \rightleftharpoons SiO_3^{2-} + 1.25Ca^{2+} + 0.25AlO_2^- + 0.5Na^+ + 0.75OH^- + H_2O$ | -10.4 | (Myers et al., 2014) |
| INFCNA, $CN_{0.34375}A_{0.15625}S_{1.1875}H_{1.3125}$ | $(CaO)_1(Na_2O)_{0.34375}(Al_2O_3)_{0.15625}(SiO_2)_{1.1875}(H_2O)_{1.3125} \rightleftharpoons 1.1875SiO_3^{2-} + Ca^{2+} + 0.3125AlO_2^- + 0.6875Na^+ + 1.3125H_2O$ | -10.0 | (Myers et al., 2014) |
| INFCN, $CN_{0.3125}S_{1.5}H_{1.1875}$ | $(CaO)_1(Na_2O)_{0.3125}(SiO_2)_{1.5}(H_2O)_{1.1875} + 0.375OH^- \rightleftharpoons 1.5SiO_3^{2-} + Ca^{2+} + 0.625Na^+ + 1.375H_2O$ | -10.7 | (Myers et al., 2014) |
| T2C*, $C_{1.5}SH_{2.5}$ | $(CaO)_{1.5}(SiO_2)_1(H_2O)_{2.5} \rightleftharpoons SiO_3^{2-} + 1.5Ca^{2+} + OH^- + 2H_2O$ | -11.57 | (Myers et al., 2014) |
| T5C*, $C_{1.25}S_{1.25}H_{2.5}$ | $(CaO)_{1.25}(SiO_2)_{1.25}(H_2O)_{2.5} \rightleftharpoons 1.25SiO_3^{2-} + 1.25Ca^{2+} + 2.5H_2O$ | -10.48 | (Myers et al., 2014) |
| TobH*, $CS_{1.5}H_{2.5}$ | $(CaO)_1(SiO_2)_{1.5}(H_2O)_{2.5} + OH^- \rightleftharpoons 1.5SiO_3^{2-} + Ca^{2+} + 3H_2O$ | -7.91 | (Myers et al., 2014) |

## 9.3 Results and Discussion

### 9.3.1 XRD and Rietveld Analysis

The XRD results (Figure 9.1) show that the main solid phase formed in each of the Al-free samples is C-(N-)S-H. This is the only reaction product identified in the samples synthesised with Ca/Si* ratios of 0.6 and 1 by XRD; reflections assigned to portlandite ($Ca(OH)_2$, Powder Diffraction File (PDF)# 00-044-1481) are only present in the Al-free sample synthesised with 0.5 M NaOH/0.5 M KOH at a Ca/Si* ratio of 1.4, although this phase is also identified in some other Al-free samples synthesised with alkali hydroxide solutions and Ca/Si* ratios = 1.4. Portlandite has been observed in C-(N-)S-H samples cured for 3 weeks or longer at 25°C with Ca/Si* ratios > 1 and [NaOH] ≥ 1 M (Kalousek, 1944; Lognot et al., 1998), in good agreement with these results. Calcite ($CaCO_3$, PDF# 00-005-0586), aragonite ($CaCO_3$, PDF# 00-041-1475), natrite ($Na_2CO_3$, PDF# 01-075-6816), thermonatrite ($Na_2CO_3 \cdot H_2O$, PDF# 00-005-0586) and trona ($Na_3H(CO_3)_2 \cdot 2H_2O$, PDF# 01-078-1064) are present in some of the samples, formed by superficial carbonation during preparation and/or analysis.

The solid reaction products identified in the C-(N-)A-S-H samples with Al/Si* = 0.05 are similar to those identified in their Al-free counterparts: the main reaction product in each specimen is C-(N-)A-S-H, and portlandite is only identified in samples synthesised with 0.1 M and 1 M alkali hydroxide solutions at a Ca/Si* ratio of 1.4 by XRD (Figure 9.1). Katoite ($(CaO)_3(Al_2O_3)(H_2O)_6$, PDF# 00-024-0217) is additionally present in some samples, although only in minor amounts (≤2 wt.% of the total sample mass). The superficial carbonation products calcite, aragonite, vaterite ($CaCO_3$, PDF# 04-015-9018), natrite and thermonatrite are identified in some of the Al-containing samples. These phase assemblages are close to those identified by XRD in C-(N-)A-S-H samples synthesised using the same method and bulk chemical compositions but at 20°C (L'Hôpital et al.). The small peaks at 12.6° 2θ and 11.3° 2θ in the diffractograms of the Ca/Si* = 0.6 and Ca/Si* = 1 samples

synthesised with 0.5 M NaOH/0.5 M KOH are tentatively assigned to K-natrolite (PDF# 01-080-0519) (Lee et al., 2010) and carbonated calcium hemicarboaluminate (Runčevski et al., 2012), respectively.

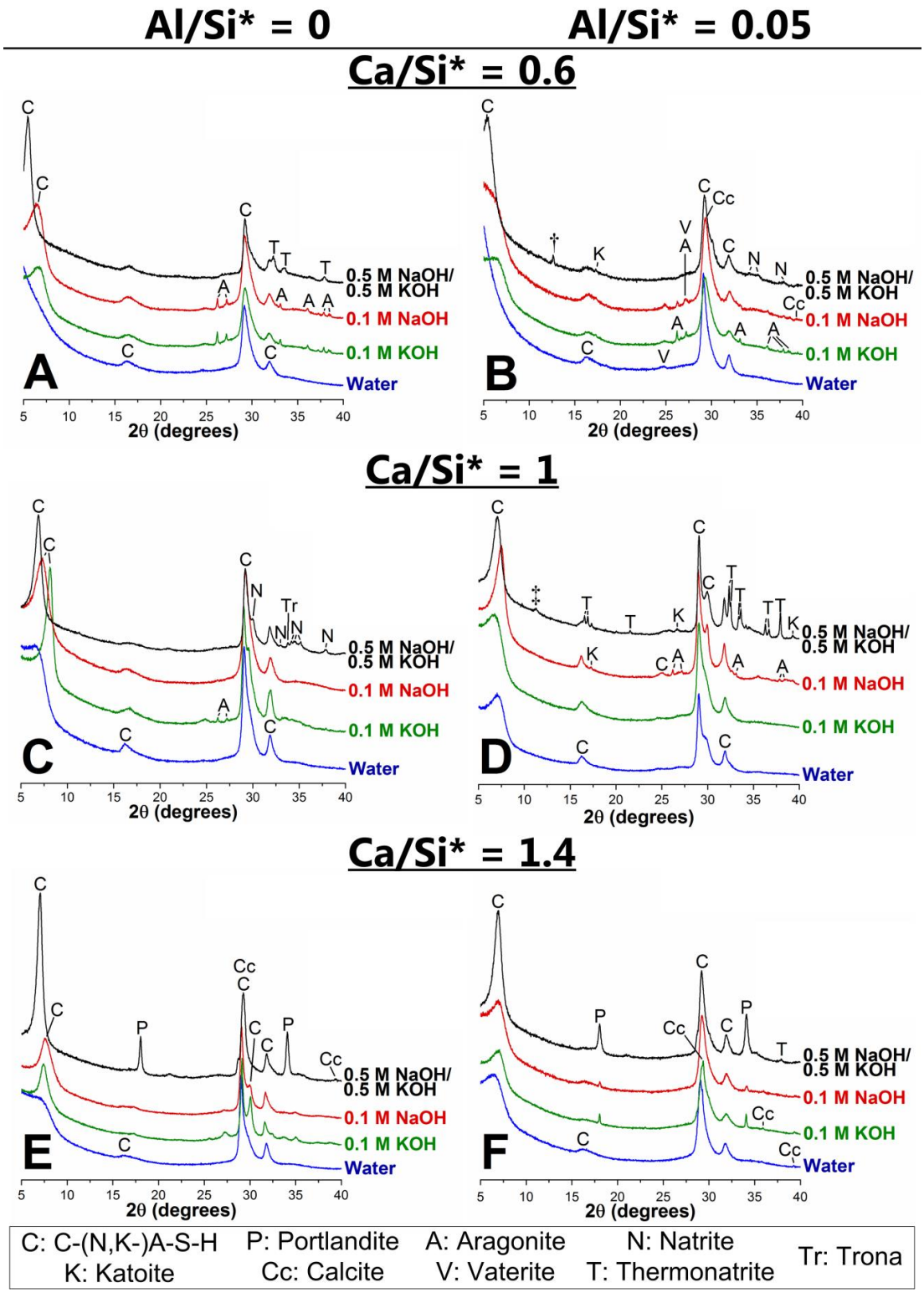


Figure 9.1. Cu Kα diffractograms of C-(N-)A-S-H samples equilibrated at 50°C: A) Ca/Si* = 0.6 and Al/Si* = 0; B) Ca/Si* = 0.6 and Al/Si* = 0.05; C) Ca/Si* = 1 and Al/Si* = 0; D) Ca/Si* = 1 and Al/Si* = 0.05; E) Ca/Si* = 1.4 and Al/Si* = 0; and F) Ca/Si* = 1.4 and Al/Si* = 0.05. The peaks marked by † and ‡ are tentatively assigned to K-natrolite and carbonated calcium hemicarboaluminate. Ca/Si* = bulk Ca/Si. Al/Si* = bulk Al/Si.

The C-(N-)A-S-H products in the alkali-containing samples are much more crystalline than the specimen prepared from water only, as identified by the much clearer and sharper (002) reflections between 5 and 10° 2θ in the presence of Na and/or K (Figure 9.1). The positions of these reflections correspond to average basal spacings of 10.8-16 Å for the C-(N-)S-H products, as shown in Figure 9.2A for Al/Si* = 0, and average basal spacings of 11.7-16.1 Å for the C-(N-)A-S-H products (Al/Si* = 0.05, Figure 9.2B). This variation is explained by the assignment of the C-(N-)A-S-H products formed as corresponding to poorly-ordered structural analogues of orthorhombic 14 Å tobermorite (PDF# 00-029-0331), 11 Å tobermorite (PDF# 04-017-1028), 9 Å tobermorite (PDF# 04-012-1761), a mixture of these minerals (Grangeon et al., 2013), or monoclinic clinotobermorite (PDF# 01-088-1328) (Richardson, 2014), with further expansion of the basal spacing beyond 14 Å assigned to additional differences in the interlayer chemistry, as discussed below.

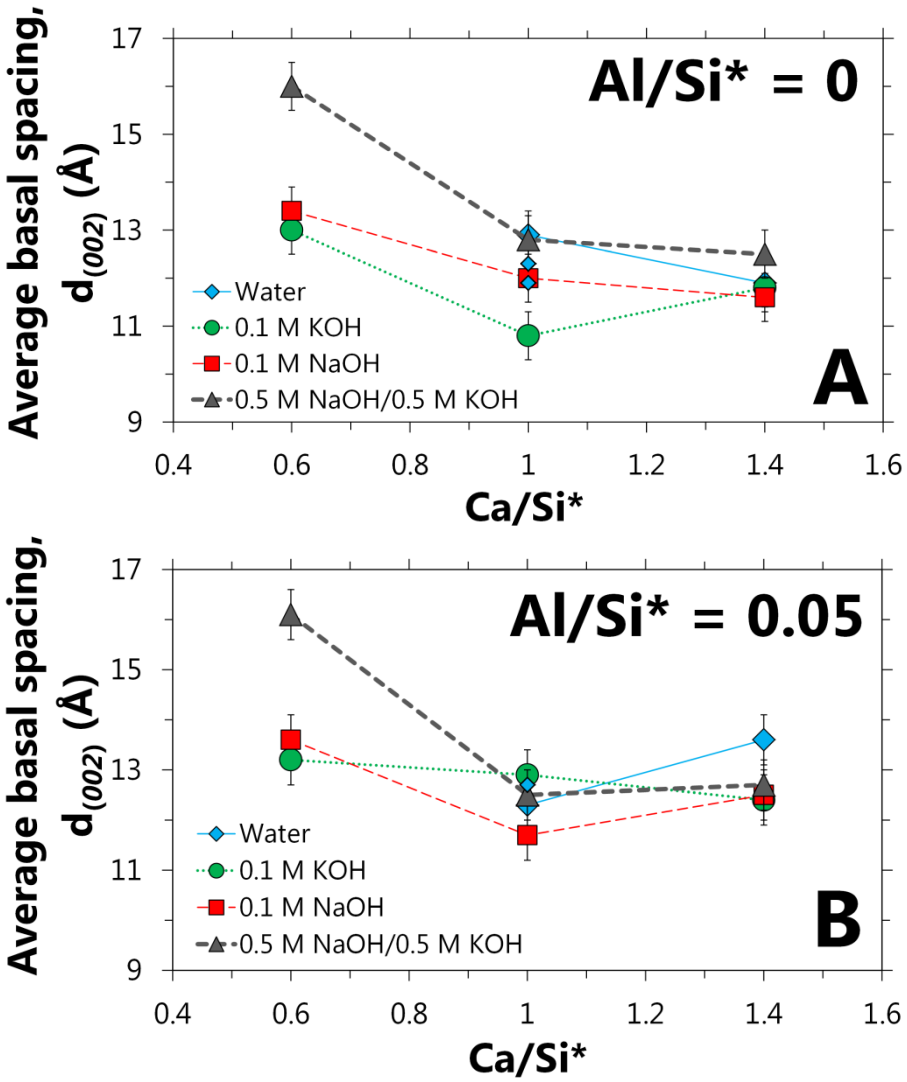


Figure 9.2. Average ($d_{(002)}$) basal spacings (estimated uncertainty = ±0.5 Å) of the C-(N-)A-S-H products synthesised with A) Al/Si* = 0 and B) Al/Si* = 0.05 (large symbols). Small symbols are data from samples equilibrated at 20°C in (L'Hôpital et al.). Al/Si* = bulk Al/Si.

The C-(N-)S-H (Al/Si* = 0) basal spacings generally decrease with increasing Ca/Si* ratio at fixed alkali concentration (Figure 9.2A), in agreement with the published data for alkali-free calcium silicate hydrate (Grangeon et al., 2013), and increase as a direct function of the bulk alkali content in the Na and/or K-containing samples. However, larger basal spacings are apparent in the water-synthesised specimen than in some of the alkali-containing specimens; Bach et al. (Bach et al., 2013) reported the same trend for C-(N-)S-H synthesised at bulk [NaOH] < 0.03 M. Here, the XRD results suggest that Na and K species are incorporated in C-(N-)S-H interlayers at alkali concentrations ≥ 0.1 M: increased basal spacings can be attributed to the

incorporation of more aqueous alkali species into interlayer spaces at higher alkali content. The reduced basal spacings generally found for the samples synthesised with 0.1 M alkali hydroxide solutions relative to the water synthesised specimens can partly be attributed to some exchange of interlayer $Ca^{2+}$ with $K^{+}$ and/or $Na^{+}$ (hydrated ionic radii of $Ca^{2+}$ = 4.12 Å, $K^{+}$ = 3.31 Å and $Na^{+}$ = 3.58 Å (Conway, 1981)), although the comparatively large differences in average basal spacings between these samples indicate that other factors – such as variations in the adsorbed interlayer water content, layer stacking configuration and chain lengths of the C-(N-)A-S-H phases formed (Richardson, 2014) – are likely to be important.

The measured C-(N-)A-S-H basal spacings at Al/Si* = 0 and Al/Si* = 0.05 are similar; no clear relationship between $d_{(002)}$ and Al content is observed in Figure 9.2. In common with the Al-free samples, a reduction in $d_{(002)}$ values is identified for the alkali-containing samples between Ca/Si* = 0.6 and Ca/Si* = 1, which indicates that the Ca/Si ratio in C-(N-)A-S-H is a key factor influencing the basal spacing of this phase over this Ca composition range. A much lower basal spacing was also measured for the alkali-free Ca/Si = 0.9 calcium aluminosilicate hydrate (C-A-S-H) (14.5 Å) compared to the C-A-S-H with Ca/Si = 0.8 (~16.8 Å) formed in (Renaudin et al., 2009b), in support of this analysis. A clear trend in $d_{(002)}$ as a function of the bulk alkali concentration is only identifiable at Ca/Si* = 0.6 for the Al-containing samples; the largest C-(N-)A-S-H basal spacing is identified for the sample synthesised with 0.5 M NaOH/0.5 M KOH ($d_{(002)}$ = 16.1 Å). This increase is basal spacing is again explained by higher concentrations of alkali species in C-(N-)A-S-H interlayers at higher alkali content.

### 9.3.2 Thermogravimetric Analysis

The results of analysis of the solid samples by TGA (Figures 9.3-9.8) are consistent with the XRD data in Figure 9.1. C-(N-)A-S-H is the dominant solid phase in each sample, as identified by the main mass loss peaks centred between 80°C and 200°C in the DTG traces. Portlandite is identifiable by mass loss peaks at ~450°C; these

peaks are generally much larger in the samples synthesised with 0.5 M NaOH/0.5 M KOH and at higher Ca/Si* ratios. Superficial carbonation products are identified between 600°C and 700°C in some samples but are most prominent at Ca/Si* = 0.6 and 1.2, which is also consistent with the XRD results. The peaks located between 800°C and 900°C are assigned to decomposition of C-(N-)A-S-H to wollastonite (Beaudoin et al., 1990; Kalousek, 1952; Myers et al., 2015b). Additional peaks marked by #, † and ‡, and centred at 150-250°C, ~350°C and ~400°C in some of the differential mass loss traces in Figures 9.3-9.8, are tentatively assigned to thermal decomposition of C-(N-)A-S-H (Myers et al., 2015b).

Katoite is identified in the TGA results for the Al-containing C-(N-)A-S-H samples synthesised with Ca/Si* = 0.6, 1 and 1.2, and 0.5 M NaOH/0.5 M KOH (Figures 9.3-9.8). This phase is identified via the mass loss peaks at ~300°C (Lothenbach et al., 2012b); this assignment does not preclude the additional presence of small amounts of poorly-crystalline $Al(OH)_3$, which has a characteristic mass loss peak at ~275°C (Lothenbach et al., 2012b).

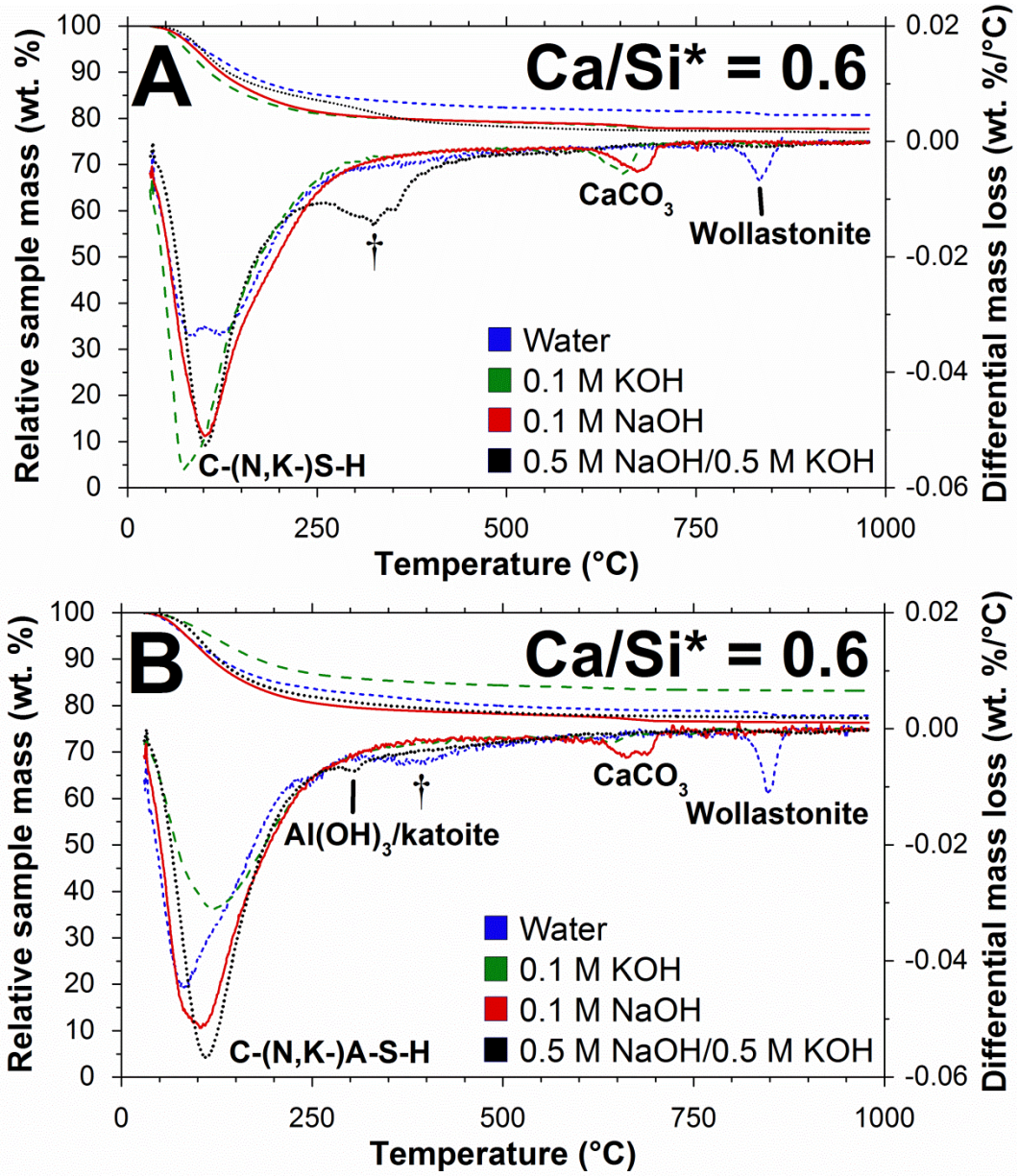


Figure 9.3. TGA results for C-(N-)A-S-H samples synthesised with Ca/Si* = 0.6 and A) Al/Si* = 0 or B) Al/Si* = 0.05. The peaks marked by † are tentatively assigned to dehydration of C-(N-)A-S-H. Ca/Si* = bulk Ca/Si. Al/Si* = bulk Al/Si.

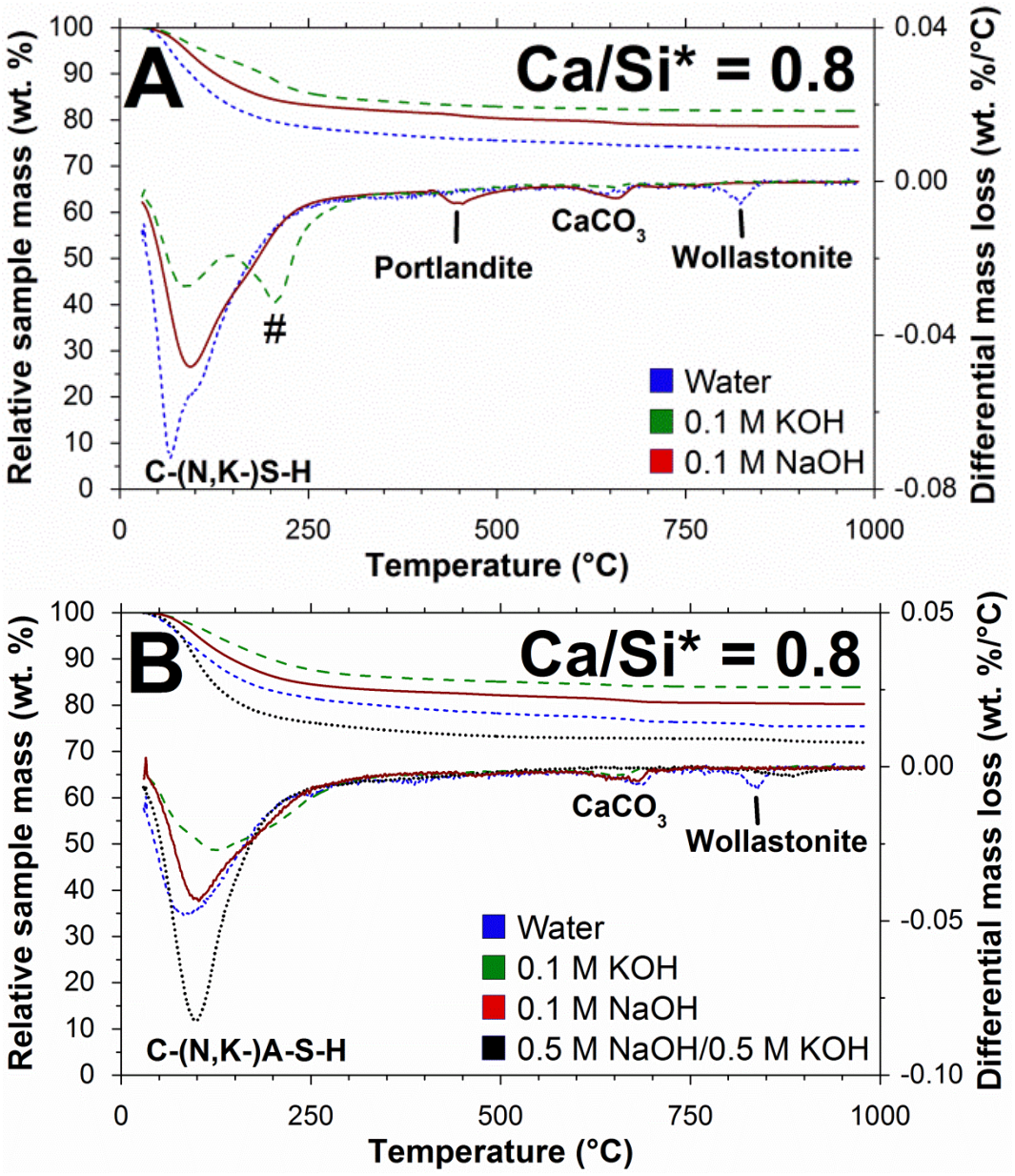


Figure 9.4. TGA results for C-(N-)A-S-H samples synthesised with Ca/Si* = 0.8 and A) Al/Si* = 0 or B) Al/Si* = 0.05. The peak marked by # is tentatively assigned to dehydration of C-(N-)A-S-H. Ca/Si* = bulk Ca/Si. Al/Si* = bulk Al/Si.

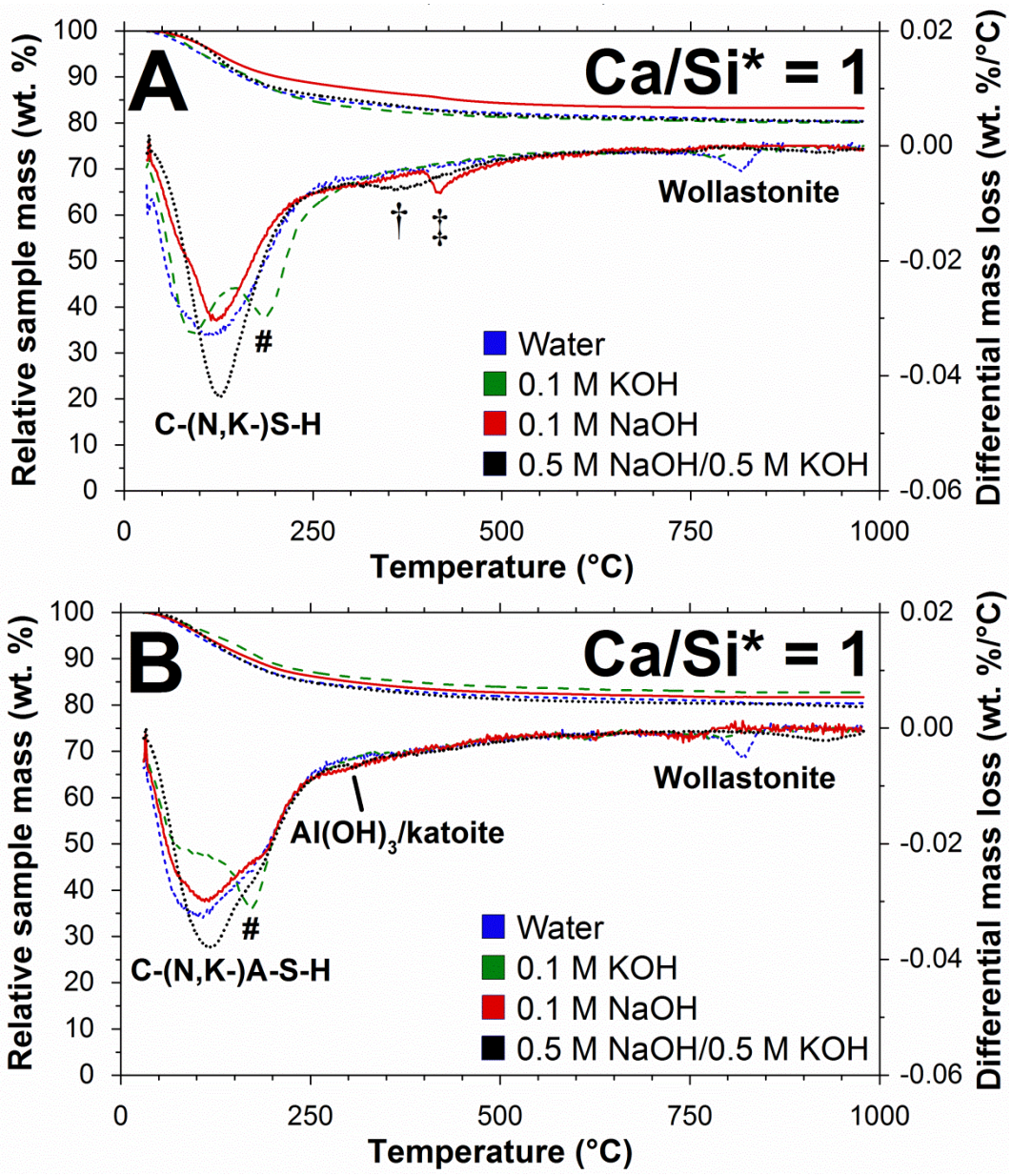


Figure 9.5. TGA results for C-(N-)A-S-H samples synthesised with Ca/Si* = 1 and A) Al/Si* = 0 or B) Al/Si* = 0.05. The peaks marked by #, † and ‡ are tentatively assigned to decomposition of C-(N-)A-S-H. Ca/Si* = bulk Ca/Si. Al/Si* = bulk Al/Si.

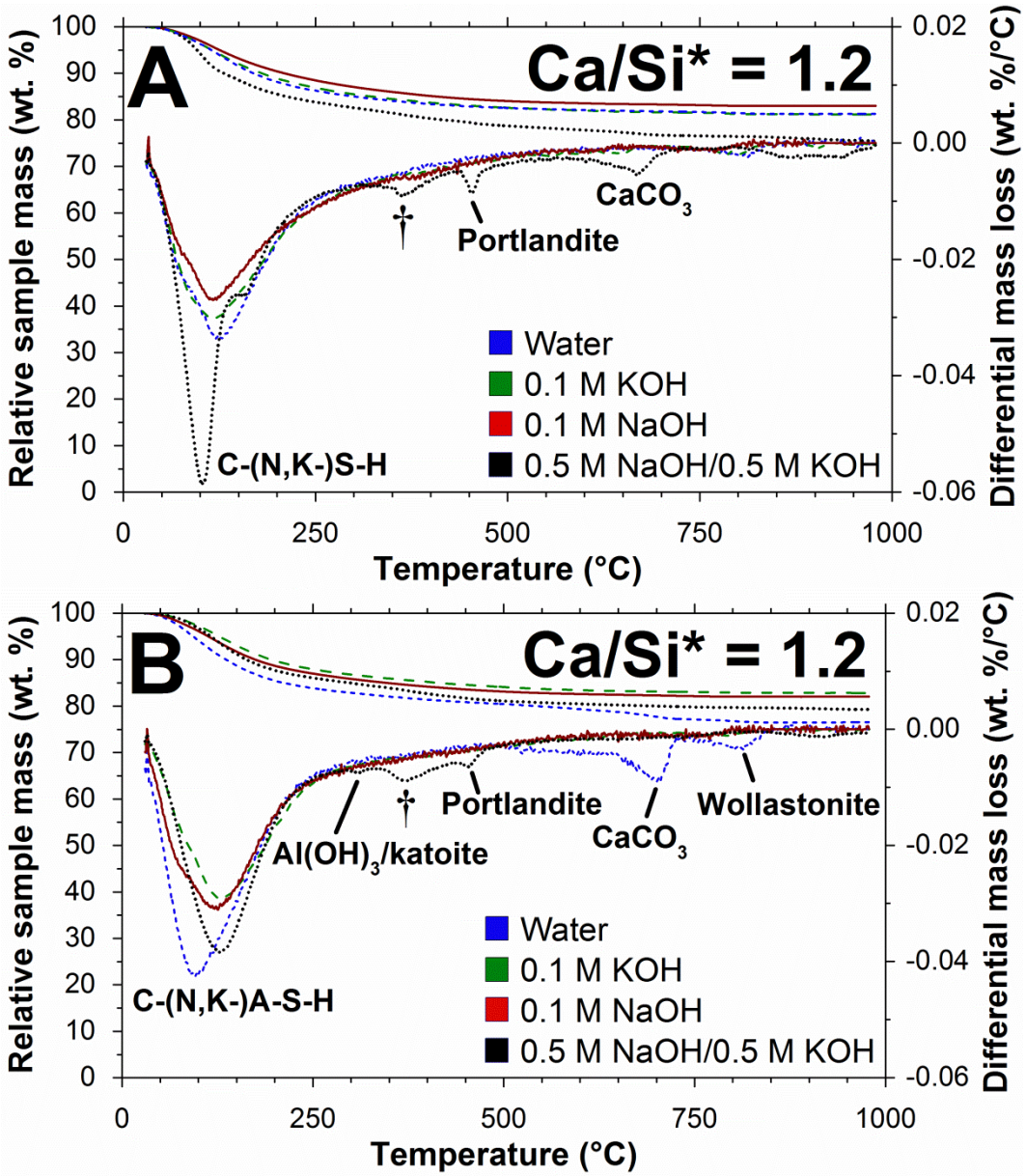


Figure 9.6. TGA results for C-(N-)A-S-H samples synthesised with Ca/Si* = 1.2 and A) Al/Si* = 0 or B) Al/Si* = 0.05. The peaks marked by † are tentatively assigned to decomposition of C-(N-)A-S-H. Ca/Si* = bulk Ca/Si. Al/Si* = bulk Al/Si.

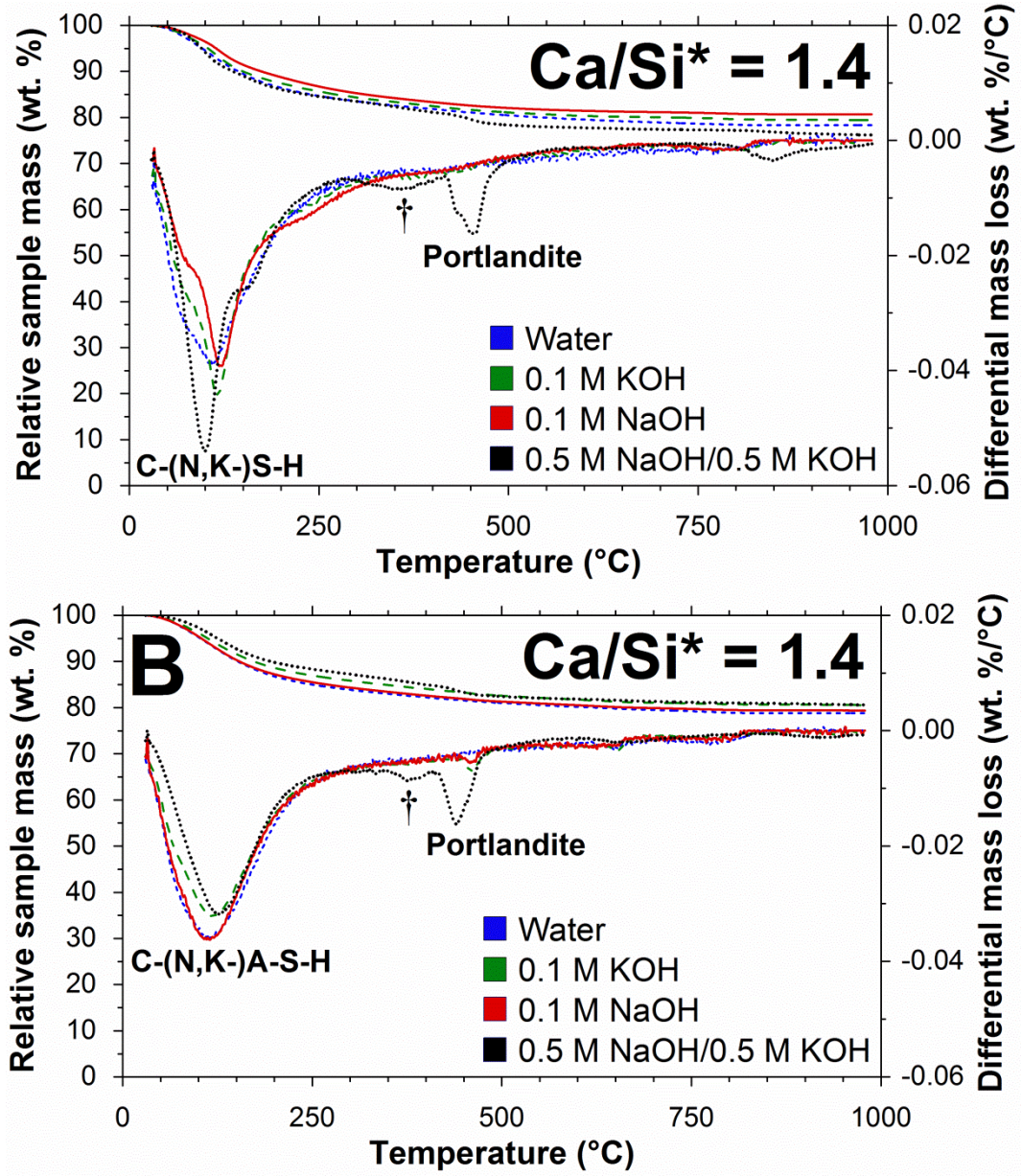


Figure 9.7. TGA results for the C-(N-)A-S-H samples synthesised with Ca/Si* = 1.4 and A) Al/Si* = 0 or B) Al/Si* = 0.05. The peaks marked by † are tentatively assigned to decomposition of C-(N-)A-S-H. Ca/Si* = bulk Ca/Si. Al/Si* = bulk Al/Si.

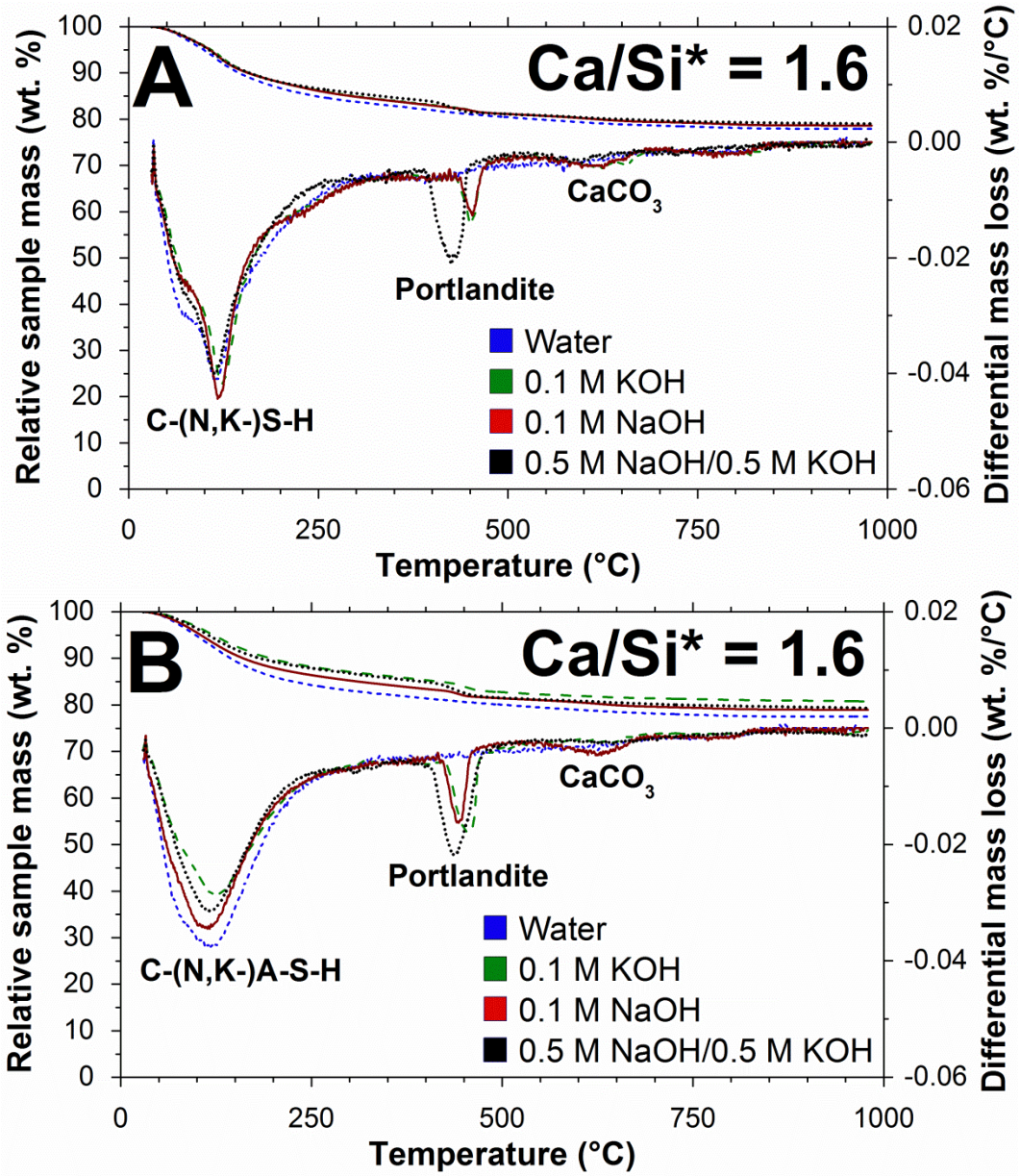


Figure 9.8. TGA results for the C-(N-)A-S-H samples synthesised with Ca/Si* = 1.6 and A) Al/Si* = 0 or B) Al/Si* = 0.05. Ca/Si* = bulk Ca/Si. Al/Si* = bulk Al/Si.

The TGA data show that between 15.1% and 24.7% of the total mass in each sample is lost due to dehydration and dehydroxylation of reaction products. The central positions of the differential mass loss peaks assigned to C-(N-)A-S-H, and the total mass lost from room temperature to 980°C, do not vary systematically as a function of the Ca/Si* ratio or alkali concentration, because the water content of the samples are much more strongly influenced by the drying method used. The same observation has been made for C-(N-)A-S-H samples prepared at 20°C (L'Hôpital, 2014). Here,

the measured mass losses reflect the removal of bulk water (freeze-dried for 7 days and equilibrated at ~30% RH), partial dehydration of adsorbed water, and little or no removal of structurally-bound water from the C-(N-)A-S-H products (Muller et al., 2013b; Myers et al., 2015b) by the drying protocol used prior to analysis.

The results of phase quantification by XRD, Rietveld analysis and TGA are shown in Tables 9.3-9.4.

Table 9.3. Solid phase assemblages of the C-(N-)S-H samples (Al/Si* = 0) synthesised at 50°C, as determined by TGA (italic font), and XRD and Rietveld analysis (normal font). The estimated absolute error is ±2 wt.% in the values determined by Rietveld analysis for the secondary products and ±4 wt.% in the values determined for portlandite by TGA.

| **Synthesis solution** | **C-(N-)S-H (wt.%)** | **CH (wt.%)** | **$C_3AH_6$ (wt.%)** | **Calcite (wt.%)** | **Aragonite (wt.%)** | **Vaterite (wt.%)** | **Natrite (wt.%)** | **Thermonatrite (wt.%)** | **Trona (wt.%)** |
|---|---|---|---|---|---|---|---|---|---|
| **Ca/Si* = 0.6** | | | | | | | | | |
| Water | 100 | 0 | n/a [a,b] | 0 | 0 | 0 | n/a [a,c] | n/a [a,c] | n/a [a,c] |
| 0.1 M NaOH | 97.5 | 0 | n/a [a,b] | 0 | 2.5 | 0 | 0 | 0 | 0 |
| 0.1 M KOH | 97.7 | 0 | n/a [a,b] | 0 | 2.3 | 0 | n/a [a,c] | n/a [a,c] | n/a [a,c] |
| 0.5 M NaOH/ 0.5 M KOH | 96.3 | 0 | n/a [a,b] | 0 | 0 | 0 | 0 | 3.7 | 0 |
| **Ca/Si* = 0.8** | | | | | | | | | |
| Water | *100* | *0* | *n/a [a,b]* | *0* | *0* | *0* | *n/a [a,c]* | *n/a [a,c]* | *n/a [a,c]* |
| 0.1 M NaOH | *≥96* | *≤ 2 [d]* | *n/a [a,b]* | *≤ 2 [e]* | *≤ 2 [e]* | *≤ 2 [e]* | *0* | *0* | *0* |
| 0.1 M KOH | *100* | *0* | *n/a [a,b]* | *0* | *0* | *0* | *n/a [a,c]* | *n/a [a,c]* | *n/a [a,c]* |
| 0.5 M NaOH/ 0.5 M KOH | *-[f]* | *-[f]* | *-[f]* | *-[f]* | *-[f]* | *-[f]* | *-[f]* | *-[f]* | *-[f]* |
| **Ca/Si* = 1** | | | | | | | | | |
| Water | 100 | 0 | n/a [a,b] | 0 | 0 | 0 | n/a [a,c] | n/a [a,c] | n/a [a,c] |
| 0.1 M NaOH | 100 | 0 | n/a [a,b] | 0 | 0 | 0 | 0 | 0 | 0 |
| 0.1 M KOH | 99.2 | 0 | n/a [a,b] | 0 | 0.8 | 0 | n/a [a,c] | n/a [a,c] | n/a [a,c] |
| 0.5 M NaOH/ 0.5 M KOH | 96.4 | 0 | n/a [a,b] | 0 | 0 | 0 | 3.2 | 0 | 0.3 |

Table 9.3. Continued.

| Synthesis solution | C-(N-)S-H (wt.%) | CH (wt.%) | $C_3AH_6$ (wt.%) | Calcite (wt.%) | Aragonite (wt.%) | Vaterite (wt.%) | Natrite (wt.%) | Thermonatrite (wt.%) | Trona (wt.%) |
|---|---|---|---|---|---|---|---|---|---|
| **Ca/Si* = 1.2** | | | | | | | | | |
| Water | *100* | *0* | *n/a* [a,b] | *0* | *0* | *0* | *n/a* [a,c] | *n/a* [a,c] | *n/a* [a,c] |
| 0.1 M NaOH | *100* | *0* | *n/a* [a,b] | *0* | *0* | *0* | *0* | *0* | *0* |
| 0.1 M KOH | *100* | *0* | *n/a* [a,b] | *0* | *0* | *0* | *n/a* [a,c] | *n/a* [a,c] | *n/a* [a,c] |
| 0.5 M NaOH/ 0.5 M KOH | *≥91* | *7* | *n/a* [a,b] | *≤ 2* [e] | *≤ 2* [e] | *≤ 2* [e] | *0* | *0* | *0* |
| **Ca/Si* = 1.4** | | | | | | | | | |
| Water | 100 | 0 | n/a [a,b] | 0 | 0 | 0 | n/a [a,c] | n/a [a,c] | n/a [a,c] |
| 0.1 M NaOH | 100 | 0 | n/a [a,b] | 0 | 0 | 0 | 0 | 0 | 0 |
| 0.1 M KOH | 100 | 0 | n/a [a,b] | 0 | 0 | 0 | n/a [a,c] | n/a [a,c] | n/a [a,c] |
| 0.5 M NaOH/ 0.5 M KOH | 85.3 | 12.6 | n/a [a,b] | 2.2 | 0 | 0 | 0 | 0 | 0 |
| **Ca/Si* = 1.6** | | | | | | | | | |
| Water | *100* | *0* | *n/a* [a,b] | *0* | *0* | *0* | *n/a* [a,c] | *n/a* [a,c] | *n/a* [a,c] |
| 0.1 M NaOH | *≥90* | *8* | *n/a* [a,b] | *≤ 2* [e] | *≤ 2* [e] | *≤ 2* [e] | *0* | *0* | *0* |
| 0.1 M KOH | *≥89* | *9* | *n/a* [a,b] | *≤ 2* [e] | *≤ 2* [e] | *≤ 2* [e] | *n/a* [a,c] | *n/a* [a,c] | *n/a* [a,c] |
| 0.5 M NaOH/ 0.5 M KOH | *82* | *18* | *n/a* [a,b] | *0* | *0* | *0* | *0* | *0* | *0* |

[a] n/a = not applicable; no [b] Al or [c] Na was added during synthesis (<0.6 mmol/L Na is present as an impurity in the 0.1 M KOH synthesis solution).

[d] a small amount of $Ca(OH)_2$ was detected in this sample by TGA (phase mass estimated to be ≤ 2 wt.% of the sample).

[e] a small amount of $CaCO_3$ was detected in this sample by TGA (total $CaCO_3$ mass estimated to be ≤ 2 wt.% of the sample).

[f] Solid phase assemblage not measured

Table 9.4. Solid phase assemblages of the C-(N-)A-S-H samples (Al/Si* = 0.05) synthesised at 50°C, as determined by TGA (italic font), and XRD and Rietveld analysis (normal font). The estimated absolute error is ±2 wt.% in the values determined by Rietveld analysis for the secondary products and ±4 wt.% in the values determined for portlandite by TGA.

| Synthesis solution | C-(N-)A-S-H (wt.%) | CH (wt.%) | $C_3AH_6$ (wt.%) | Calcite (wt.%) | Aragonite (wt.%) | Vaterite (wt.%) | Natrite (wt.%) | Thermonatrite (wt.%) | Trona (wt.%) |
|---|---|---|---|---|---|---|---|---|---|
| **Ca/Si* = 0.6** | | | | | | | | | |
| Water | 99.8 | 0 | 0 | 0 | 0 | 0.2 | n/a [a] | n/a [a] | n/a [a] |
| 0.1 M NaOH | 100 | 0 | 0 | 0 | 0 | 0 | 0 | 0 | 0 |
| 0.1 M KOH | 98.5 | 0 | 0 | 0 | 1.5 | 0 | n/a [a] | n/a [a] | n/a [a] |
| 0.5 M NaOH/ 0.5 M KOH [b] | 98.0 | 0 | 0.3 | 0 | 0 | 0 | 1.7 | 0 | 0 |
| **Ca/Si* = 0.8** | | | | | | | | | |
| Water | *100* | *0* | *0* | *0* | *0* | *0* | *n/a* [a] | *n/a* [a] | *n/a* [a] |
| 0.1 M NaOH | *≥98* | *0* | *0* | *≤ 2* [d] | *≤ 2* [d] | *≤ 2* [d] | *0* | *0* | *0* |
| 0.1 M KOH | *100* | *0* | *0* | *0* | *0* | *0* | *n/a* [a] | *n/a* [a] | *n/a* [a] |
| 0.5 M NaOH/ 0.5 M KOH | *100* | *0* | *0* | *0* | *0* | *0* | *0* | *0* | *0* |
| **Ca/Si* = 1** | | | | | | | | | |
| Water | 100 | 0 | 0 | 0 | 0 | 0 | n/a [a] | n/a [a] | n/a [a] |
| 0.1 M NaOH | 98.1 | 0 | 0.6 | 0 | 1.2 | 0 | 0 | 0 | 0 |
| 0.1 M KOH | 100 | 0 | 0 | 0 | 0 | 0 | n/a [a] | n/a [a] | n/a [a] |
| 0.5 M NaOH/ 0.5 M KOH [c] | 89.8 | 0 | 0.6 | 0 | 0 | 0 | 0 | 9.6 | 0 |

Table 9.4. Continued.

| Synthesis solution | C-(N-)A-S-H (wt.%) | CH (wt.%) | $C_3AH_6$ (wt.%) | Calcite (wt.%) | Aragonite (wt.%) | Vaterite (wt.%) | Natrite (wt.%) | Thermonatrite (wt.%) | Trona (wt.%) |
|---|---|---|---|---|---|---|---|---|---|
| **Ca/Si* = 1.2** | | | | | | | | | |
| Water | *100* | *0* | *0* | *0* | *0* | *0* | *n/a* [a] | *n/a* [a] | *n/a* [a] |
| 0.1 M NaOH | *100* | *0* | *0* | *0* | *0* | *0* | *0* | *0* | *0* |
| 0.1 M KOH | *100* | *0* | *0* | *0* | *0* | *0* | *n/a* [a] | *n/a* [a] | *n/a* [a] |
| 0.5 M NaOH/ 0.5 M KOH | *≥92* | *6* | *≤ 2* [e] | *0* | *0* | *0* | *0* | *0* | *0* |
| **Ca/Si* = 1.4** | | | | | | | | | |
| Water | 99.5 | 0 | 0 | 0.5 | 0 | 0 | n/a [a] | n/a [a] | n/a [a] |
| 0.1 M NaOH | 99.3 | 0.7 | 0 | 0 | 0 | 0 | 0 | 0 | 0 |
| 0.1 M KOH | 97.8 | 1.1 | 0 | 1.1 | 0 | 0 | n/a [a] | n/a [a] | n/a [a] |
| 0.5 M NaOH/ 0.5 M KOH | 91.6 | 7.3 | 0 | 0 | 0 | 0 | 0 | 1.1 | 0 |
| **Ca/Si* = 1.6** | | | | | | | | | |
| Water | *100* | *0* | *0* | *0* | *0* | *0* | *n/a* [a] | *n/a* [a] | *n/a* [a] |
| 0.1 M NaOH | *≥89* | *9* | *0* | *≤ 2* [d] | *≤ 2* [d] | *≤ 2* [d] | *0* | *0* | *0* |
| 0.1 M KOH | *88* | *12* | *0* | *0* | *0* | *0* | *n/a* [a] | *n/a* [a] | *n/a* [a] |
| 0.5 M NaOH/ 0.5 M KOH | *87* | *13* | *0* | *0* | *0* | *0* | *0* | *0* | *0* |

[a] n/a = not applicable; no Na was added during synthesis (<0.6 mmol/L Na is present as an impurity in the 0.1 M KOH synthesis solution).
[b] peaks tentatively assigned to K-natrolite in the diffractogram of this sample were excluded from Rietveld analysis.
[c] peaks tentatively assigned to carbonated calcium hemicarboaluminate in the diffractogram of this sample were excluded from Rietveld analysis.
[d] a small amount of $CaCO_3$ was detected in this sample by TGA (total $CaCO_3$ mass estimated to be ≤ 2 wt.% of the sample).
[e] a small amount of $C_3AH_6$/$Al(OH)_3$ was detected in this sample by TGA (phase mass estimated to be ≤ 2 wt.% of the sample), which is assigned here to $C_3AH_6$.

### 9.3.3 Aqueous Phase Analysis

The measured concentrations of Si, Ca and $OH^-$ in the supernatants of the C-(N-)A-S-H samples do not change greatly as a function of the bulk Al concentration (Figure 9.9). In general, the measured aqueous Si and $OH^-$ concentrations are higher and the dissolved Ca concentrations are lower in samples synthesised with solutions containing more alkalis. The aqueous Si concentrations typically decrease and the dissolved Ca concentrations generally increase as functions of the Ca/Si* ratio. The $OH^-$ concentrations are generally greater and less dependent on chemical composition at higher bulk Ca content. These results are consistent with existing solubility measurements in the CaO-($Na_2O$,$K_2O$-)$Al_2O_3$-$SiO_2$-$H_2O$ systems at ~25°C (Faucon et al., 1999b; Hong and Glasser, 1999; Kalousek, 1944; L'Hôpital et al.; Macphee et al., 1989; Pardal et al., 2009; Way and Shayan, 1992), which show the same trends in dissolved Si, Ca and $OH^-$ concentrations with respect to the bulk alkali content and Ca/Si ratio. Here, dissolved Al concentrations were generally found to be lower at higher Ca/Si* ratios, and higher in samples more highly concentrated in alkalis.

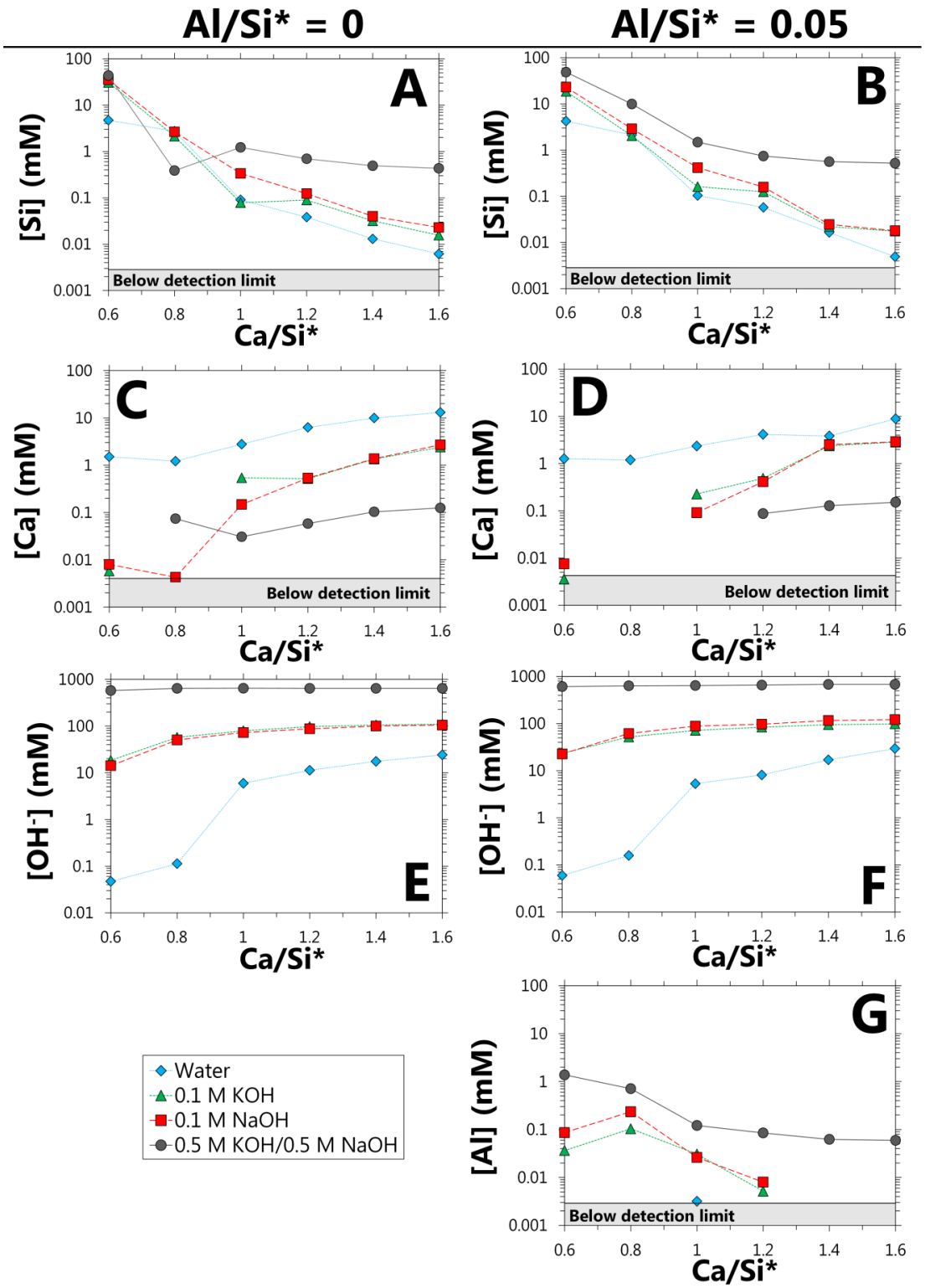


Figure 9.9. Concentrations of dissolved Si, Ca, $OH^-$ and Al in the supernatants of the C-(N-)A-S-H samples: A) [Si], Al/Si* = 0; B) [Si], Al/Si* = 0.05; C) [Ca], Al/Si* = 0; D) [Ca], Al/Si* = 0.05; E) [$OH^-$], Al/Si* = 0; F) [$OH^-$], Al/Si* = 0.05; G) [Al], Al/Si* = 0.05. $OH^-$ concentrations are calculated from pH measurements at ~24°C. The estimated relative uncertainty of the IC measurements is ±10%. Ca/Si* = bulk Ca/Si. Al/Si* = bulk Al/Si. Lines are for eye-guides only. mM = mmol/L.

Dissolved Si, Ca and $OH^-$ concentrations in the sample sets synthesised with 0.1 M KOH and with 0.1 M NaOH are equal for Ca/Si* ≥ 1.2, and are also similar for most samples with lower Ca content (Figure 9.9). This result suggests that C-(N-)A-S-H solubility does not vary greatly as a function of the nature of the alkali cation (Na or K) present. However, the large changes in dissolved Si, Ca, $OH^-$ and Al concentrations as functions of the bulk alkali concentration and the Ca/Si ratio indicate that C-(N-)A-S-H solubility may change significantly with respect to these parameters, as will be discussed further in section 9.3.5.

Effective saturation indices (*SI**) were calculated from the measured dissolved Si, Ca, $OH^-$ and Al concentrations, using eq.(3.10), to assess the proximity of the samples to equilibrium (Tables 9.5-9.6).

Table 9.5. Effective saturation indices (*SI**) for relevant solid phases in the C-(N-)S-H samples (Al/Si* = 0), calculated from the filtrate chemical compositions in Figure 9.9 and Appendix C. Bold text indicates solid phases that are observed in the TGA and/or XRD results of the respective samples (C-(N-)A-S-H is represented by end-members of the CNASH_ss thermodynamic model (Myers et al., 2014)). A 'near-saturation' condition of $-0.5 \leq SI^* < 0$ is assumed, as discussed in the text.

| Synthesis solution | $CN_{0.3125}S_{1.5}H_{1.1875}$ [a] | $C_{1.5}SH_{2.5}$ [a] | $CS_{1.5}H_{2.5}$ [a] | CH | $SiO_2$ [b] |
|---|---|---|---|---|---|
| **Ca/Si* = 0.6** | | | | | |
| Water | n/a [d] | **-0.7** | **0** | -1.6 | -0.1 |
| 0.1 M NaOH | **-0.1** | **-0.9** | **-0.4** | -1.6 | -0.5 |
| 0.1 M KOH | n/a [d] | **-0.9** | **-0.4** | -1.7 | -0.5 |
| 0.5 M NaOH/0.5 M KOH | **≤-0.1** [c] | **≤-0.6** [c] | **≤-0.8** [c] | ≤-0.8 [c] | -1.8 |
| **Ca/Si* = 0.8** | | | | | |
| Water | n/a [d] | **-0.6** | **-0.1** | -1.5 | -0.3 |
| 0.1 M NaOH | **-0.3** | **-0.8** | **-0.8** | **-1.2** | -1.4 |
| 0.1 M KOH | n/a [d] | **≤-1.0** [c] | **≤-0.9** [c] | ≤-1.3 [c] | -1.4 |
| 0.5 M NaOH/0.5 M KOH | -0.1 [e] | -0.6 [e] | -0.8 [e] | -0.8 [e] | -1.8 [e] |
| **Ca/Si* = 1** | | | | | |
| Water | n/a [d] | **-0.3** | **-0.5** | -0.7 | -1.6 |
| 0.1 M NaOH | **-0.2** | **-0.3** | **-0.7** | -0.5 | -1.9 |
| 0.1 M KOH | n/a [d] | **-0.2** | **-0.8** | -0.3 | -2.3 |
| 0.5 M NaOH/0.5 M KOH | **-0.4** | **-0.5** | **-1.1** | -0.4 | -2.6 |
| **Ca/Si* = 1.2** | | | | | |
| Water | n/a [d] | **-0.2** | **-0.7** | -0.3 | -2.1 |
| 0.1 M NaOH | **-0.3** | **-0.2** | **-0.7** | -0.3 | -2.2 |
| 0.1 M KOH | n/a [d] | **-0.2** | **-0.8** | -0.3 | -2.3 |
| 0.5 M NaOH/0.5 M KOH | **-0.4** | **-0.4** | **-1.1** | **-0.3** | -2.7 |

Table 9.5. Continued.

| Synthesis solution | $CN_{0.3125}S_{1.5}H_{1.1875}$ [a] | $C_{1.5}SH_{2.5}$ [a] | $CS_{1.5}H_{2.5}$ [a] | CH | $SiO_2$ [b] |
|---|---|---|---|---|---|
| **Ca/Si* = 1.4** | | | | | |
| Water | n/a [d] | **-0.2** | **-0.9** | -0.2 | -2.6 |
| 0.1 M NaOH | **-0.4** | **-0.2** | **-0.9** | -0.1 | -2.6 |
| 0.1 M KOH | n/a [d] | **-0.2** | **-0.9** | -0.1 | -2.6 |
| 0.5 M NaOH/0.5 M KOH | **-0.4** | **-0.3** | **-1.1** | **-0.2** | -2.8 |
| **Ca/Si* = 1.6** | | | | | |
| Water | n/a [d] | **-0.3** | **-1.1** | -0.1 | -2.8 |
| 0.1 M NaOH | **-0.5** | **-0.1** | **-0.9** | **0** | -2.8 |
| 0.1 M KOH | n/a [d] | **-0.2** | **-1.0** | **0** | -2.8 |
| 0.5 M NaOH/0.5 M KOH | **-0.4** | **-0.3** | **-1.2** | **-0.1** | -2.9 |

[a] $CN_{0.3125}S_{1.5}H_{1.1875}$, $C_{1.5}SH_{2.5}$ and $CS_{1.5}H_{2.5}$ are the INFCN, T2C* and TobH* end-members of the CNASH_ss thermodynamic model (Myers et al., 2014), respectively

[b] Amorphous $SiO_2$

[c] The values shown are calculated at the detection limit for Ca (~0.004 mmol/L) because dissolved Ca concentrations were below the detection limit

[d] n/a = not applicable: no Na was added to the system (<0.6 mmol/L Na is present as an impurity in the 0.1 M KOH synthesis solution)

[e] Solid phase assemblage not measured

Table 9.6. Effective saturation indices (*SI**) for relevant solid phases in the C-(N-)A-S-H samples (Al/Si* = 0.05), calculated from the filtrate chemical compositions in Figure 9.9 and Appendix C. Bold text indicates solid phases that are observed in the TGA and/or XRD results of the respective samples (C-(N-)A-S-H is represented by end-members of the CNASH_ss thermodynamic model (Myers et al., 2014)). A 'near-saturation' condition of $-0.5 \leq SI^* < 0$ is assumed, as discussed in the text.

| **Synthesis solution** | **$C_{1.25}A_{0.125}SH_{1.625}$** [a] | **$CA_{0.15625}S_{1.1875}H_{1.65625}$** [a] | **$CN_{0.3125}S_{1.5}H_{1.1875}$** [a] | **$C_{1.5}SH_{2.5}$** [a] | **$CS_{1.5}H_{2.5}$** [a] | **$\frac{1}{2}AH_3$** [b] | **$C_3AH_6$** | **CH** | **$SiO_2$** [c] |
|---|---|---|---|---|---|---|---|---|---|
| **Ca/Si* = 0.6** | | | | | | | | | |
| Water | **≤-0.5** [e] | **≤-0.1** [e] | n/a [f] | **-0.8** | **-0.1** | ≤-0.8 [e] | ≤-1.7 [e] | -1.7 | -0.1 |
| 0.1 M NaOH | **-0.6** | **-0.4** | **-0.1** | **-0.8** | **-0.4** | -0.8 | -1.6 | -1.5 | -0.7 |
| 0.1 M KOH | **-0.8** | **-0.5** | n/a [f] | **-0.9** | **-0.5** | -1.1 | -1.7 | -1.6 | -0.8 |
| 0.5 M NaOH/ 0.5 M KOH | **≤-0.6** [d] | **≤-0.7** [d] | **≤-0.1** [d] | **≤-0.6** [d] | **≤-0.8** [d] | **-1.2** | **≤-1.1** [d] | ≤-0.9 [d] | -1.8 |
| **Ca/Si* = 0.8** | | | | | | | | | |
| Water | **≤-0.4** [e] | **≤-0.3** [e] | n/a [f] | **-0.5** | **-0.1** | ≤-1.7 [e] | ≤-1.8 [e] | -1.4 | -0.4 |
| 0.1 M NaOH | **≤-0.7** [d] | **≤-0.6** [d] | **≤-0.4** [d] | **≤-0.8** [d] | **≤-0.7** [d] | -0.8 | ≤-1.3 [d] | ≤-1.2 [d] | -1.3 |
| 0.1 M KOH | **≤-0.8** [d] | **≤-0.7** [d] | n/a [f] | **≤-0.8** [d] | **≤-0.8** [d] | -1.0 | ≤-1.3 [d] | ≤-1.2 [d] | -1.5 |
| 0.5 M NaOH/ 0.5 M KOH | **≤-0.7** [d] | **≤-0.8** [d] | **≤-0.3** [d] | **≤-0.7** [d] | **≤-1.0** [d] | -1.2 | ≤-0.9 [d] | ≤-0.7 [d] | -2.1 |
| **Ca/Si* = 1** | | | | | | | | | |
| Water | **-0.2** | **-0.3** | n/a [f] | **-0.4** | **-0.4** | -1.0 | -0.9 | -0.8 | -1.4 |
| 0.1 M NaOH | **-0.4** | **-0.5** | **-0.2** | **-0.4** | **-0.7** | **-1.4** | **-0.9** | -0.6 | -1.9 |
| 0.1 M KOH | **-0.3** | **-0.6** | n/a [f] | **-0.3** | **-0.7** | -1.4 | -0.7 | -0.4 | -2.1 |
| 0.5 M NaOH/ 0.5 M KOH | **≤-1.0** [d] | **≤-1.1** [d] | **≤-0.5** [d] | **≤-0.8** [d] | **≤-1.3** [d] | **-1.7** | **≤-1.1** [d] | ≤-0.7 [d] | -2.5 |

Table 9.6. Continued.

| Synthesis solution | $C_{1.25}A_{0.125}SH_{1.625}$ [a] | $CA_{0.15625}S_{1.1875}H_{1.65625}$ [a] | $CN_{0.3125}S_{1.5}H_{1.1875}$ [a] | $C_{1.5}SH_{2.5}$ [a] | $CS_{1.5}H_{2.5}$ [a] | ½$AH_3$ [b] | $C_3AH_6$ | CH | $SiO_2$ [c] |
|---|---|---|---|---|---|---|---|---|---|
| **Ca/Si* = 1.2** | | | | | | | | | |
| Water | **≤-0.2** [e] | **≤-0.4** [e] | n/a [f] | **-0.2** | **-0.6** | ≤-1.4 [e] | ≤-0.8 [e] | -0.5 | -1.9 |
| 0.1 M NaOH | **-0.3** | **-0.5** | **-0.2** | **-0.2** | **-0.7** | -1.7 | -0.8 | -0.3 | -2.2 |
| 0.1 M KOH | **-0.3** | **-0.6** | n/a [f] | **-0.2** | **-0.7** | **-1.8** | **-0.8** | **-0.3** | -2.2 |
| 0.5 M NaOH/ 0.5 M KOH | **-0.5** | **-0.8** | **-0.3** | **-0.3** | **-1.0** | -1.7 | -0.6 | **-0.2** | -2.7 |
| **Ca/Si* = 1.4** | | | | | | | | | |
| Water | **≤-0.4** [e] | **≤-0.6** [e] | n/a [f] | **-0.4** | **-0.8** | ≤-1.4 [e] | ≤-0.8 [e] | -0.5 | -2.1 |
| 0.1 M NaOH | **≤-0.3** [e] | **≤-0.7** [e] | **-0.5** | **-0.1** | **-0.9** | ≤-1.9 [e] | ≤-0.6 [e] | **-0.1** | -2.7 |
| 0.1 M KOH | **≤-0.3** [e] | **≤-0.8** [e] | n/a [f] | **-0.1** | **-0.9** | ≤-1.9 [e] | ≤-0.6 [e] | **0** | -2.8 |
| 0.5 M NaOH/ 0.5 M KOH | **-0.5** | **-0.8** | **-0.3** | **-0.3** | **-1.0** | -1.7 | -0.6 | **-0.1** | -2.8 |
| **Ca/Si* = 1.6** | | | | | | | | | |
| Water | **≤-0.5** [e] | **≤-0.8** [e] | n/a [f] | **-0.4** | **-1.1** | ≤-1.5 [e] | ≤-0.6 [e] | -0.2 | -2.7 |
| 0.1 M NaOH | **≤-0.4** [e] | **≤-0.8** [e] | **-0.5** | **-0.2** | **-1.0** | ≤-1.9 [e] | ≤-0.6 [e] | **0** | -2.8 |
| 0.1 M KOH | **≤-0.4** [e] | **≤-0.8** [e] | n/a [f] | **-0.2** | **-1.0** | ≤-1.9 [e] | ≤-0.5 [e] | **0** | -2.8 |
| 0.5 M NaOH/ 0.5 M KOH | **-0.4** | **-0.8** | **-0.3** | **-0.3** | **-1.0** | -1.7 | -0.6 | **-0.1** | -2.8 |

[a] $C_{1.25}A_{0.125}SH_{1.625}$, $CA_{0.15625}S_{1.1875}H_{1.65625}$, $CN_{0.3125}S_{1.5}H_{1.1875}$, $C_{1.5}SH_{2.5}$ and $CA_{1.5}H_{2.5}$ are the 5CA, INFCA, INFCN, T2C* and TobH* end-members of the CNASH_ss thermodynamic model (Myers et al., 2014), respectively

[b] Microcrystalline $Al(OH)_3$

[c] Amorphous $SiO_2$

[d] The values shown are calculated at the detection limit for Ca (~0.004 mmol/L) because dissolved Ca concentration was below the detection limit

[e] The values shown are calculated at the detection limit for Al (~0.003 mmol/L) because dissolved Al concentration was below the detection limit

[f] n/a = not applicable: no Na was added to the system (<0.6 mmol/L Na is present as an impurity in the 0.1 M KOH synthesis solution)

A near-saturation condition of $-0.5 \leq SI^* < 0$ is assumed, which accounts for the uncertainty in the modelling calculations and experimental measurements, indicating that solid phases with *SI** values within this range can potentially precipitate at equilibrium, even though the calculated saturation index is slightly negative. This interpretation means that C-(N-)A-S-H is expected to form in every sample, while portlandite could precipitate in the alkali-containing samples at Ca/Si* = 1 without Al, in the Al-containing sample synthesised with 0.1 M KOH at a Ca/Si* = 1, and in all Ca/Si* ≥ 1.2 samples (Tables 9.5-9.6). Portlandite is generally only identified in samples with Ca/Si* ratios ≥ 1 (Figures 9.1 and 9.3-9.8), and C-(N-)A-S-H is formed in all of the specimens, in good agreement with the expected equilibrium phase assemblages and this interpretation of near-saturated *SI** values. Amorphous $SiO_2$ is only predicted to be near saturated in the Ca/Si* ≤ 0.8 C-(N-)A-S-H samples synthesised with water. A small amount of partially dissolved amorphous $SiO_2$ has been observed in samples synthesised at 20°C and Ca/Si* = 0.6 using the same protocols that were applied here (L'Hôpital, 2014), which indicates that precipitation of C-(N-)A-S-H is strongly preferred at Ca/Si* ≤ 0.8.

Small amounts of katoite are identified in some of the Al-containing samples by XRD and TGA (Figures 9.1 and 9.3-9.8), but this phase is predicted to be undersaturated at equilibrium in every sample that this phase was observed (Table 9.6), which indicates that not all samples have yet reached equilibrium. The calculated *SI** values predict that strätlingite is undersaturated in all samples, in good agreement with the XRD and TGA results, where this phase is not identified. Si-hydrogarnet is predicted to be near-saturated in the Al-containing samples at Ca/Si* ratios ≥ 1 except the sample synthesised with 0.5 M NaOH/0.5 M KOH at Ca/Si* = 1, but this phase is not identified in the XRD or TGA results, which suggests that it is kinetically hindered from forming under the synthesis conditions used here. This result is consistent with the higher temperatures (110°C) needed experimentally to form Si-hydrogarnet in the $CaO$-$Al_2O_3$-$SiO_2$-$H_2O$ system within a laboratory timeframe (Dilnesa et al., 2014).

### 9.3.4 C-(N-)A-S-H Chemical Composition

Chemical compositions of the C-(N-)A-S-H products are shown in Tables 9.7 and 9.8. Most C-(N-)A-S-H products at $0.6 \leq Ca/Si^* \leq 1.4$ have Ca/Si and Al/Si ratios similar to the bulk synthesis conditions used in the samples synthesised with water and 0.1 M alkali solutions, due to the relatively low levels of secondary or superficial carbonation products formed in these specimen (yield from experiments is ≥91 wt.% C-(N-)A-S-H in these samples, Tables 9.3-9.4). Samples synthesised with Ca/Si* ratios = 1.6 and alkali hydroxide solutions contain more portlandite due to the decreased solubility of this phase at higher Ca and alkali content. Portlandite is the only secondary product that was used in mass balance calculations to determine C-(N-)A-S-H chemical compositions for the Ca/Si* = 0.8, 1.2 and 1.6 samples (with solid phase assemblages determined by TGA), as all the other secondary phases are present in small quantities in these specimen (≤2 wt.%), see Tables 9.3-9.4.

Table 9.7. Chemical compositions of the C-(N-)S-H products (Al/Si* = 0), determined from Rietveld analysis and IC, TGA, XRD and pH measurements (normal font), and from IC, TGA and pH measurements considering C-(N-)S-H and portlandite only (italic font). The estimated absolute errors are ±0.05 units in the Ca/(Al+Si) ratios, ±0.2 units in the $H_2O$/(Al+Si) ratios, and ±0.08 units for the 0.1 M alkali samples and ±0.7 for the 1 M alkali samples in the (Na+K)/(Al+Si) ratios of the C-(N-)S-H products. Ca/Si* = bulk Ca/Si.

| Synthesis solution | C-(N-)S-H chemical formula | Ca/Si | Na/Si | K/Si | $H_2O$/Si |
|---|---|---|---|---|---|
| | **Ca/Si* = 0.6** | | | | |
| Water | $(CaO)_{0.61}(SiO_2)_1(H_2O)_{1.1}$ | 0.61 | n/a [a] | n/a [b] | 1.1 |
| 0.1 M NaOH | $(CaO)_{0.70}(Na_2O)_{0.11}(SiO_2)_1(H_2O)_{1.6}$ | 0.70 | 0.23 | n/a [b] | 1.6 |
| 0.1 M KOH | $(CaO)_{0.69}(K_2O)_{0.13}(SiO_2)_1(H_2O)_{1.6}$ | 0.69 | n/a [a] | 0.27 | 1.6 |
| 0.5 M NaOH/0.5 M KOH | $(CaO)_{0.73}(Na_2O)_{0.04}(K_2O)_{0.08}(SiO_2)_1(H_2O)_{1.7}$ | 0.73 | 0.08 | 0.16 | 1.7 |
| | **Ca/Si* = 0.8** | | | | |
| Water | *$(CaO)_{0.80}(SiO_2)_1(H_2O)_{1.9}$* | *0.80* | *n/a [a]* | *n/a [b]* | *1.9* |
| 0.1 M NaOH | *$(CaO)_{0.81}(Na_2O)_{0.09}(SiO_2)_1(H_2O)_{1.5}$* | *0.81* | *0.18* | *n/a [b]* | *1.5* |
| 0.1 M KOH | *$(CaO)_{0.81}(K_2O)_{0.10}(SiO_2)_1(H_2O)_{1.3}$* | *0.81* | *n/a [a]* | *0.21* | *1.3* |
| 0.5 M NaOH/0.5 M KOH | - [c] | - [c] | - [c] | - [c] | - [c] |
| | **Ca/Si* = 1** | | | | |
| Water | $(CaO)_{1.0}(SiO_2)_1(H_2O)_{1.4}$ | 1.0 | n/a [a] | n/a [b] | 1.4 |
| 0.1 M NaOH | $(CaO)_{1.0}(Na_2O)_{0.06}(SiO_2)_1(H_2O)_{1.3}$ | 1.0 | 0.12 | n/a [b] | 1.3 |
| 0.1 M KOH | $(CaO)_{1.0}(K_2O)_{0.07}(SiO_2)_1(H_2O)_{1.6}$ | 1.0 | n/a [a] | 0.13 | 1.6 |
| 0.5 M NaOH/0.5 M KOH | $(CaO)_{1.0}(Na_2O)_{0.07}(K_2O)_{0.08}(SiO_2)_1(H_2O)_{1.7}$ | 1.0 | 0.15 | 0.17 | 1.7 |
| | **Ca/Si* = 1.2** | | | | |
| Water | *$(CaO)_{1.2}(SiO_2)_1(H_2O)_{1.5}$* | *1.2* | *n/a [a]* | *n/a [b]* | *1.5* |
| 0.1 M NaOH | *$(CaO)_{1.2}(Na_2O)_{0.02}(SiO_2)_1(H_2O)_{1.4}$* | *1.2* | *0.05* | *n/a [b]* | *1.4* |
| 0.1 M KOH | *$(CaO)_{1.2}(K_2O)_{0.03}(SiO_2)_1(H_2O)_{1.6}$* | *1.2* | *n/a [a]* | *0.06* | *1.6* |
| 0.5 M NaOH/0.5 M KOH | *$(CaO)_{1.0}(Na_2O)_{0.09}(K_2O)_{0.08}(SiO_2)_1(H_2O)_{2.0}$* | *1.0* | *0.19* | *0.16* | *2.0* |

Table 9.7. Continued.

| Synthesis solution | C-(N-)S-H chemical formula | Ca/Si | Na/Si | K/Si | $H_2O$/Si |
|---|---|---|---|---|---|
| **Ca/Si* = 1.4** | | | | | |
| Water | $(CaO)_{1.3}(SiO_2)_1(H_2O)_{1.9}$ | 1.3 | n/a [a] | n/a [b] | 1.9 |
| 0.1 M NaOH | $(CaO)_{1.4}(SiO_2)_1(H_2O)_{1.7}$ | 1.4 | 0 | n/a [b] | 1.7 |
| 0.1 M KOH | $(CaO)_{1.4}(K_2O)_{0.02}(SiO_2)_1(H_2O)_{1.9}$ | 1.4 | n/a [a] | 0.03 | 1.9 |
| 0.5 M NaOH/0.5 M KOH | $(CaO)_{1.4}(Na_2O)_{0.09}(K_2O)_{0.08}(SiO_2)_1(H_2O)_{2.1}$ | 1.4 | 0.18 | 0.16 | 2.1 |
| **Ca/Si* = 1.6** | | | | | |
| Water | $(CaO)_{1.5}(SiO_2)_1(H_2O)_{2.0}$ | *1.5* | *n/a* [a] | *n/a* [b] | *2.0* |
| 0.1 M NaOH | $(CaO)_{1.4}(SiO_2)_1(H_2O)_{1.8}$ | *1.4* | *0* | *n/a* [b] | *1.8* |
| 0.1 M KOH | $(CaO)_{1.4}(K_2O)_{0.01}(SiO_2)_1(H_2O)_{1.7}$ | *1.4* | *n/a* [a] | *0.02* | *1.7* |
| 0.5 M NaOH/0.5 M KOH | $(CaO)_{1.3}(SiO_2)_1(H_2O)_{1.1}$ | *1.3* | *0* | *0* | *1.1* |

[a] n/a = not applicable: no Na was added during synthesis (<0.6 mmol/L Na is present as an impurity in the 0.1 M KOH synthesis solution).
[b] n/a = not applicable: no K was added during synthesis.
[c] Solid phase assemblage not measured

Table 9.8. Chemical compositions of the C-(N-)A-S-H products (Al/Si* = 0.05), determined from Rietveld analysis and IC, TGA, XRD and pH measurements (normal font), and from IC, TGA and pH measurements considering C-(N-)S-H and portlandite only (italic font). The estimated absolute errors are ±0.05 units in the Ca/(Al+Si) ratios, ±0.2 units in the $H_2O$/(Al+Si) ratios, ±0.02 units in the Al/Si ratios, and ±0.08 units for the 0.1 M alkali samples and ±0.7 for the 1 M alkali samples in the (Na+K)/(Al+Si) ratios of the C-(N-)A-S-H products. Ca/Si* = bulk Ca/Si.

| Synthesis solution | C-(N-)A-S-H chemical formula | Ca/(Al+Si) | Al/Si | Na/(Al+Si) | K/(Al+Si) | $H_2O$/(Al+Si) |
|---|---|---|---|---|---|---|
| **Ca/Si* = 0.6** | | | | | | |
| Water | $(CaO)_{0.60}(Al_2O_3)_{0.026}(SiO_2)_1(H_2O)_{1.4}$ | 0.57 | 0.051 | n/a [a] | n/a [b] | 1.3 |
| 0.1 M NaOH | $(CaO)_{0.66}(Al_2O_3)_{0.28}(Na_2O)_{0.13}(SiO_2)_1(H_2O)_{1.7}$ | 0.63 | 0.055 | 0.25 | n/a [b] | 1.6 |
| 0.1 M KOH | $(CaO)_{0.65}(Al_2O_3)_{0.027}(K_2O)_{0.13}(SiO_2)_1(H_2O)_{1.2}$ | 0.62 | 0.054 | n/a [a] | 0.24 | 1.1 |
| 0.5 M NaOH/ 0.5 M KOH | $(CaO)_{0.76}(Al_2O_3)_{0.028}(Na_2O)_{0.13}(K_2O)_{0.13}(SiO_2)_1(H_2O)_{1.9}$ | 0.72 | 0.056 | 0.24 | 0.24 | 1.8 |
| **Ca/Si* = 0.8** | | | | | | |
| Water | $\mathit{(CaO)_{0.80}(Al_2O_3)_{0.025}(SiO_2)_1(H_2O)_{1.7}}$ | *0.76* | *0.051* | *n/a* [a] | *n/a* [b] | *1.6* |
| 0.1 M NaOH | $\mathit{(CaO)_{0.81}(Al_2O_3)_{0.25}(Na_2O)_{0.11}(SiO_2)_1(H_2O)_{1.4}}$ | *0.77* | *0.050* | *0.21* | *n/a* [b] | *1.3* |
| 0.1 M KOH | $\mathit{(CaO)_{0.81}(Al_2O_3)_{0.025}(K_2O)_{0.10}(SiO_2)_1(H_2O)_{1.2}}$ | *0.77* | *0.050* | *n/a* [a] | *0.19* | *1.1* |
| 0.5 M NaOH/ 0.5 M KOH | $\mathit{(CaO)_{0.84}(Al_2O_3)_{0.024}(Na_2O)_{0.18}(K_2O)_{0.17}(SiO_2)_1(H_2O)_{2.8}}$ | *0.80* | *0.049* | *0.35* | *0.33* | *2.7* |
| **Ca/Si* = 1** | | | | | | |
| Water | $(CaO)_{0.99}(Al_2O_3)_{0.025}(SiO_2)_1(H_2O)_{1.5}$ | 0.94 | 0.050 | n/a [a] | n/a [b] | 1.4 |
| 0.1 M NaOH | $(CaO)_{1.0}(Al_2O_3)_{0.023}(Na_2O)_{0.06}(SiO_2)_1(H_2O)_{1.3}$ | 1.00 | 0.045 | 0.12 | n/a [b] | 1.3 |
| 0.1 M KOH | $(CaO)_{1.0}(Al_2O_3)_{0.025}(K_2O)_{0.06}(SiO_2)_1(H_2O)_{1.3}$ | 0.95 | 0.050 | n/a [a] | 0.11 | 1.3 |
| 0.5 M NaOH/ 0.5 M KOH | $(CaO)_{1.0}(Al_2O_3)_{0.025}(Na_2O)_{0.13}(K_2O)_{0.10}(SiO_2)_1(H_2O)_{1.8}$ | 0.96 | 0.050 | 0.25 | 0.20 | 1.7 |

Table 9.8. Continued.

| Synthesis solution | C-(N-)A-S-H chemical formula | Ca/(Al+Si) | Al/Si | Na/(Al+Si) | K/(Al+Si) | $H_2O$/(Al+Si) |
|---|---|---|---|---|---|---|
| **Ca/Si* = 1.2** | | | | | | |
| Water | *$(CaO)_{1.2}(Al_2O_3)_{0.025}(SiO_2)_1(H_2O)_{1.8}$* | *1.12* | *0.050* | *n/a [a]* | *n/a [b]* | *1.7* |
| 0.1 M NaOH | *$(CaO)_{1.2}(Al_2O_3)_{0.025}(Na_2O)_{0.04}(SiO_2)_1(H_2O)_{1.5}$* | *1.14* | *0.050* | *0.08* | *n/a [b]* | *1.4* |
| 0.1 M KOH | *$(CaO)_{1.2}(Al_2O_3)_{0.025}(K_2O)_{0.02}(SiO_2)_1(H_2O)_{1.4}$* | *1.14* | *0.050* | *n/a [a]* | *0.04* | *1.4* |
| 0.5 M NaOH/ 0.5 M KOH | *$(CaO)_{1.0}(Al_2O_3)_{0.025}(Na_2O)_{0.14}(K_2O)_{0.10}(SiO_2)_1(H_2O)_{1.8}$* | *0.99* | *0.050* | *0.26* | *0.20* | *1.7* |
| **Ca/Si* = 1.4** | | | | | | |
| Water | $(CaO)_{1.4}(Al_2O_3)_{0.025}(SiO_2)_1(H_2O)_{1.9}$ | 1.3 | 0.050 | n/a [a] | n/a [b] | 1.8 |
| 0.1 M NaOH | $(CaO)_{1.4}(Al_2O_3)_{0.025}(Na_2O)_{0.02}(SiO_2)_1(H_2O)_{1.8}$ | 1.3 | 0.050 | 0.05 | n/a [b] | 1.8 |
| 0.1 M KOH | $(CaO)_{1.4}(Al_2O_3)_{0.025}(SiO_2)_1(H_2O)_{1.5}$ | 1.3 | 0.050 | n/a [a] | 0 | 1.4 |
| 0.5 M NaOH/ 0.5 M KOH | $(CaO)_{1.2}(Al_2O_3)_{0.025}(Na_2O)_{0.12}(K_2O)_{0.10}(SiO_2)_1(H_2O)_{1.7}$ | 1.2 | 0.050 | 0.23 | 0.19 | 1.6 |
| **Ca/Si* = 1.6** | | | | | | |
| Water | *$(CaO)_{1.5}(Al_2O_3)_{0.025}(SiO_2)_1(H_2O)_{2.1}$* | *1.5* | *0.050* | *n/a [a]* | *n/a [b]* | *2.0* |
| 0.1 M NaOH | *$(CaO)_{1.3}(Al_2O_3)_{0.025}(Na_2O)_{0.02}(SiO_2)_1(H_2O)_{1.7}$* | *1.3* | *0.050* | *0.03* | *n/a [b]* | *1.7* |
| 0.1 M KOH | *$(CaO)_{1.3}(Al_2O_3)_{0.025}(SiO_2)_1(H_2O)_{1.5}$* | *1.2* | *0.050* | *n/a [a]* | *0* | *1.4* |
| 0.5 M NaOH/ 0.5 M KOH | *$(CaO)_{1.2}(Al_2O_3)_{0.025}(Na_2O)_{0.15}(K_2O)_{0.12}(SiO_2)_1(H_2O)_{1.8}$* | *1.2* | *0.050* | *0.29* | *0.23* | *1.7* |

[a] n/a = not applicable: no Na was added during synthesis (<0.6 mmol/L Na is present as an impurity in the 0.1 M KOH synthesis solution).
[b] n/a = not applicable: no K was added during synthesis.

The C-(N-)A-S-H products typically contain $H_2O$/(Al+Si) ratios between 1 and 2 (Figure 9.10): the $H_2O$ content in C-(N-)A-S-H was determined by assigning the mass losses between 30°C and 550°C to the decomposition of C-(N-)A-S-H, portlandite, katoite and $Al(OH)_3$ during heating by TGA. Portlandite was the only secondary product quantified by TGA and used in C-(N-)A-S-H chemical composition calculations in the absence of XRD data; the formation of only very small quantities of other secondary products here (≤ 2 wt.% of the total mass of each sample) means that any errors introduced into the reported C-(N-)A-S-H chemical compositions due to use of this method, are minor.

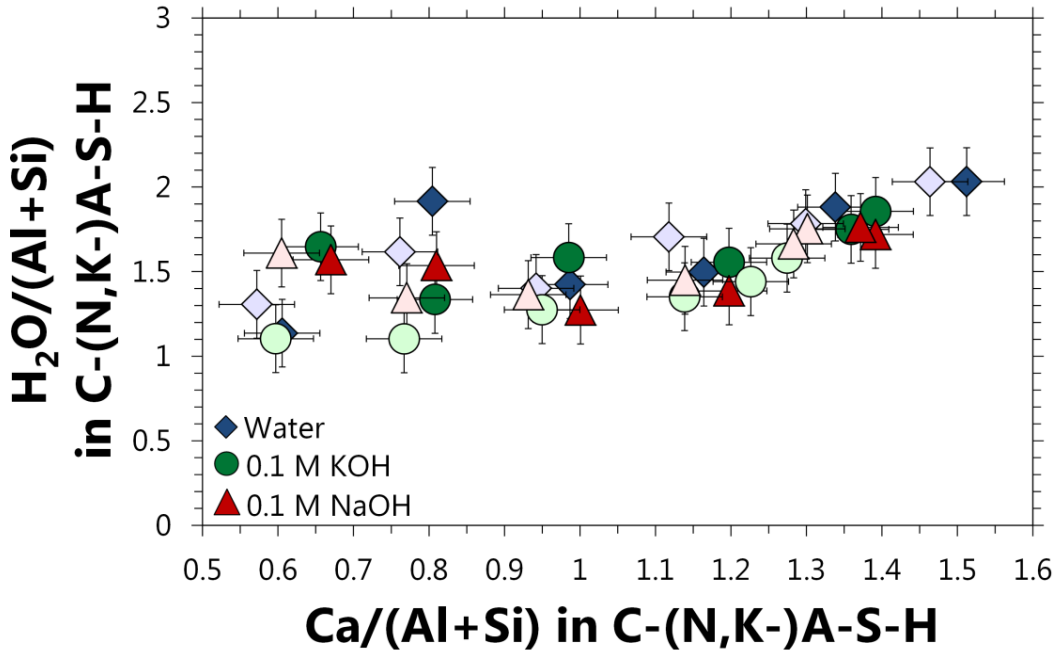


Figure 9.10. $H_2O$/(Al+Si) ratios of the C-(N-)S-H (dark symbols) and Al/Si* = 0.05 C-(N-)A-S-H (light symbols) as functions of the Ca/(Al+Si) ratio, for samples synthesised with ≤0.1 M alkali hydroxide solutions and equilibrated at 50°C. The estimated absolute errors are ±0.05 units in the Ca/(Al+Si) ratios and ±0.2 in the $H_2O$/(Al+Si) ratios of the C-(N-)A-S-H products.

The reported $H_2O$/(Al+Si) ratios (Figure 9.10) are in relatively good agreement with the expected result for C-(N-)A-S-H equilibrated at ~30% RH, where no 'free' water is present and some adsorbed water is removed (Jennings, 2008; Muller et al., 2013b), and with the $H_2O$ content of C-(N-)A-S-H synthesised at 20°C (L'Hôpital et al.). In general, the $H_2O$/(Al+Si) ratios increase slightly as a direct function of the

Ca/(Al+Si) ratios of the C-(N-)A-S-H products formed, but no significant correlations are found between the $H_2O$/(Al+Si) ratio and the alkali or Al content in this phase. A strong direct relationship between the $H_2O$/(Al+Si) and Ca/(Al+Si) ratios is reported for laboratory-synthesised C-S-H (Richardson, 2014), but is not as evident here from the data presented in Figure 9.10. Chemical compositions of the C-(N-)A-S-H products synthesised using 0.5 M NaOH/0.5 KOH solutions are omitted from Figure 9.10 due to the relatively higher quantities of secondary products formed in these samples.

The amount of alkali incorporated in the C-(N-)A-S-H products decreases with the Ca/(Al+Si) ratio of this phase (Figure 9.11), from (Na+K)/(Al+Si) = 0.25 at Ca/(Al+Si) = 0.6 to zero alkali incorporated at Ca/(Al+Si) = 1.6. This trend, and the quantified (Na+K)/(Al+Si) ratios, are consistent with those reported in earlier studies of alkali uptake in laboratory-synthesised C-(N-)A-S-H at room temperature (Hong and Glasser, 1999; 2002; L'Hôpital, 2014; Stade, 1989). The (Na+K)/(Al+Si) ratios of the C-(N-)A-S-H products are independent of the alkali element (Na or K). The high level of uncertainty in the quantification of bound alkali in the C-(N-)A-S-H samples synthesised with 1 M alkali hydroxide solutions prevents their inclusion in Figure 9.11 (reflecting the error associated with the IC measurements).

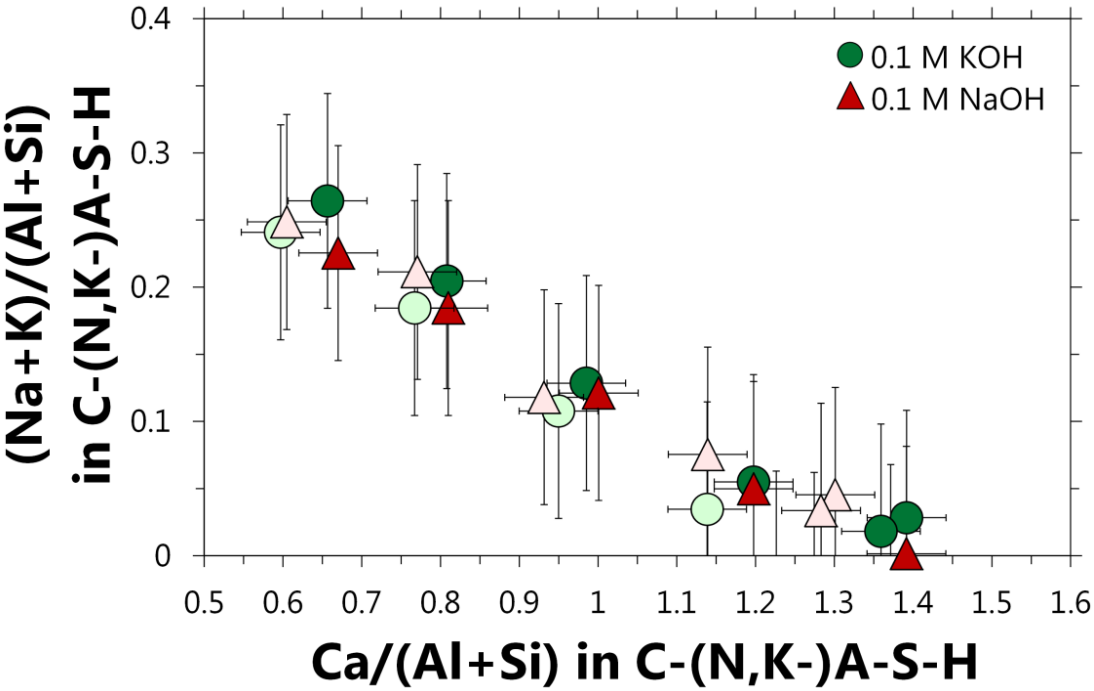


Figure 9.11. Na and/or K uptake in the C-(N-)S-H (Al/Si* = 0, dark symbols) and Al/Si* = 0.05 C-(N-)A-S-H (light symbols) as functions of the Ca/(Al+Si) ratio, for samples synthesised with 0.1 M alkali hydroxide solutions at 50°C. The estimated absolute errors are ±0.05 units in the Ca/(Al+Si) ratios and ±0.08 units in the (Na+K)/(Al+Si) ratios of the C-(N-)A-S-H products.

The alkali and Al content of the C-(N-)A-S-H products formed (Figure 9.11) are independent at the relatively low amounts of Al added to each sample (Al/Si* = 0 or 0.05). At Al/Si* ratios ≤ 0.05, all of the Al added is generally incorporated into C-(N-)A-S-H products synthesised with water (Table 9.8) (Myers et al., 2015b). However, the amount of Al which can be incorporated into C-(N-)A-S-H is limited by the dissolved concentration of this element at higher bulk Al content: increasing the bulk alkali metal (Na or K here) concentration increases the amount of dissolved Al (Figure 9.9) and consequently the amount of Al which can be incorporated into C-(N-)A-S-H (L'Hôpital et al.). This description is consistent with $^{29}$Si MAS NMR analysis of hydrated white Portland cement with different alkali contents (Skibsted and Andersen, 2013), which showed the formation of C-(N-)A-S-H products with increased Al/Si ratios at higher bulk alkali concentration. This description is also in agreement with the lack of a direct relationship found in (Bach et al., 2013) between alkali and Al content in laboratory-synthesised C-(N-)S-H, and in C-(N-)A-S-H with Al/Si = 0.04 in hydrated blends of PC and silica fume.

### 9.3.5 C-(N-)A-S-H Solubility

Solubility products are calculated using eqs.(3.8,3.9) for C-(N-)A-S-H with hypothetical chemical compositions of Ca/(Al+Si) = 0.6, 0.8, 1, 1.2, 1.4 and 1.6, Al/Si = 0 and 0.05, Na/(Al+Si) = 0.2 for samples containing Na, K/(Al+Si) = 0.2 for samples containing K, $H_2O$/Si = 1.2, and 1 mol (Al+Si). These Na/(Al+Si) and K/(Al+Si) ratios were chosen to approximately match the alkali contents of the experimental C-(N-)A-S-H products (Tables 9.7 and 9.8). The solubility products for these hypothetical C-(N-)A-S-H phases are shown in Figure 9.12. Solubility products for C-(N-)A-S-H with chemical compositions determined by mass balances from the XRD (Figure 9.1), IC and pH measurements (Figure 9.9), and TGA and Rietveld analysis (Tables 9.3-9.4), are shown in Appendix C.

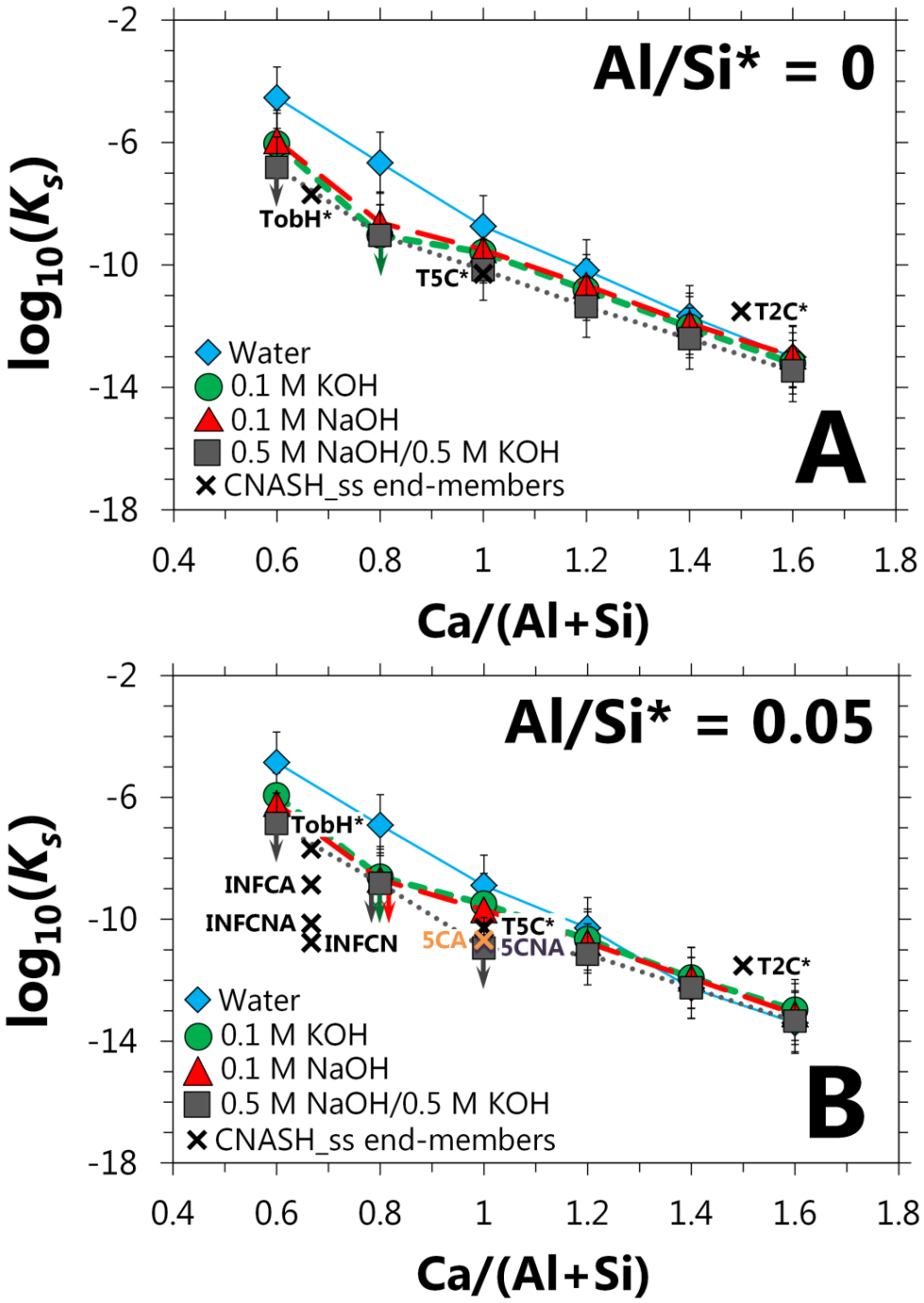


Figure 9.12. Solubility products ($K_s$) for hypothetical C-(N-)A-S-H phases with chemical compositions of A) Al/Si = 0 or B) Al/Si = 0.05, Na/(Al+Si) = 0.2 for the Na-containing systems, K/(Al+Si) = 0.2 for the K-containing systems, $H_2O$/Si = 1.2, and normalised to 1 mol Al + Si at 50°C. The estimated uncertainty depicted as error bars is ±1 unit in the $\log_{10}(K_s)$ values, except for the points with downward-pointing arrows, which additionally represent maximum solubility product values as described in the text. The small crosses are solubility products for end-members of the CNASH_ss thermodynamic model (Myers et al., 2014) at 50°C. Al/Si* = bulk Al/Si. Lines are for eye-guides only.

Figure 9.12 shows similar values and trends in the solubility products for both the Al-free and Al-containing C-(N-)A-S-H end-members, i.e., the results of this study indicate that this phase is not greatly stabilised by the incorporation of Al. This is consistent with recently published results for C-(A-)S-H synthesised with Ca/Si* = 1 and cured at 7-80°C (Myers et al., 2015b), where the measured solubility of this phase did not change greatly between Al/Si* ratios of 0 and 0.15. The downward-pointing arrows in Figure 9.12 for the Ca/Si* = 0.6 and 1 C-(N-)A-S-H samples synthesised with 0.5 M NaOH/0.5 M KOH, and the Ca/Si* = 0.8 samples synthesised with alkali hydroxide solutions, indicate that the calculated solubility products are considered to be upper bounds; supernatant Ca concentrations were below the detection limit for these samples, so an upper limit of [Ca] = 0.004 mmol/L was chosen. Dissolved Al concentrations were also below the detection limit for some samples (e.g. the Ca/Si* = 1.2, Al/Si* = 0.05 sample synthesised with water, Figure 9.9), so [Al] = 0.003 mmol/L was chosen for these samples. The low Al content of the C-(N-)A-S-H products (Al/Si ~ 0.05) means that the associated level of uncertainty in the calculated solubility products for samples with [Al] below the detection limit is lower than for the samples with [Ca] below the detection limit; downward pointing arrows are only shown for the latter case in Figure 9.12.

The lower solubility products calculated for C-(N-)A-S-H with higher Ca/(Al+Si) ratios in Figure 9.12 shows that this phase is stabilised at higher Ca content within the composition range analysed here, but also partly reflect the increased amounts of Ca included in the stoichiometric formulae for C-(N-)A-S-H in these calculations at higher Ca/(Al+Si) ratios (Figure 9.12 shows solubility products for C-(N-)A-S-H with chemical compositions normalised to one mole Al + Si). The solubility products of the C-(N-)A-S-H synthesised using 0.1 M solutions are similar irrespective of the alkali element used, indicating that both Na- and K-bearing C-(N-)A-S-H can be expected to form in hydrated cements with non-zero concentrations of these alkali elements. Figure 9.12 also shows that C-(N-)A-S-H solubility generally decreases slightly as the bulk alkali hydroxide concentration is increased, but this finding is only significant for some C-(N-)A-S-H phases with Ca/Si $\leq$ 1. Similar trends of

decreasing solubility with increasing alkali content are also identified in solubility product calculations for hypothetical C-(N-)A-S-H phases with (Na+K)/(Al+Si) = 0 and Ca/Si ≤ 1, which suggests that the structure of this phase is stabilised slightly as the bulk alkali concentration is increased. This will be discussed further in section 9.3.7.

The end-members of the CNASH_ss thermodynamic model (Figure 9.12) (Myers et al., 2014) show the same trends in C-(N-)A-S-H solubility as identified experimentally here. The reduced solubilities of the Na-bearing end-members in the CNASH_ss model compared to the experimental results are also consistent with their much higher Na content (0.4 ≤ Na/(Al+Si) ≤ 0.46). The solubility product of the T2C* model end-member is consistent with the experimental results, although the lower solubilities of the model T5C*, TobH* and INFCA end-members relative to the experimental data indicates that their thermodynamic properties should be adjusted slightly for simulations at 50°C to improve the temperature-dependent behaviour of CNASH_ss.

### 9.3.6 $^{29}$Si MAS NMR

The $^{29}$Si MAS NMR spectra of the C-(N-)S-H samples (Al/Si* = 0) contain three resonances that are assigned to chain-end sites ($Q^1$), bridging sites ($Q^2_b$) and paired sites ($Q^2_p$) (Figure 9.13A). In the spectra of the water-synthesised samples, these resonances are described by peaks located at isotropic chemical shifts ($\delta_{iso}$) of -79.3 ppm, -83.1 ppm and -85.1 ppm respectively. Similar $\delta_{iso}$ values have been reported for alkali- and Al-free C-S-H aged at 40°C (Brunet et al., 2004; Cong and Kirkpatrick, 1996a). The spectrum for the Al-free sample synthesised with 0.5 M NaOH contains the same peaks but shifted by +1 to +2 ppm, which indicates that silanol groups in the 0.5 M NaOH sample are on average charge-balanced by less positively-charged species (i.e. $Na^+$ and/or $H^+$ rather than $Ca^{2+}$) relative to the alkali-free specimen (Rejmak et al., 2012). Comparable $\delta_{iso}$ differences have also been

reported for $Q^1$, $Q^2_b$ and $Q^2_p$ sites in C-(N-)A-S-H synthesised at different alkali concentrations (L'Hôpital et al.; Lognot et al., 1998).

The deconvoluted spectra and quantified site environments for each of the Al-free C-(N-)S-H samples and C-(N-)A-S-H samples (Al/Si* = 0.1) are shown in Figures 9.14 and 9.15 respectively, with the results tabulated in Table 9.9.

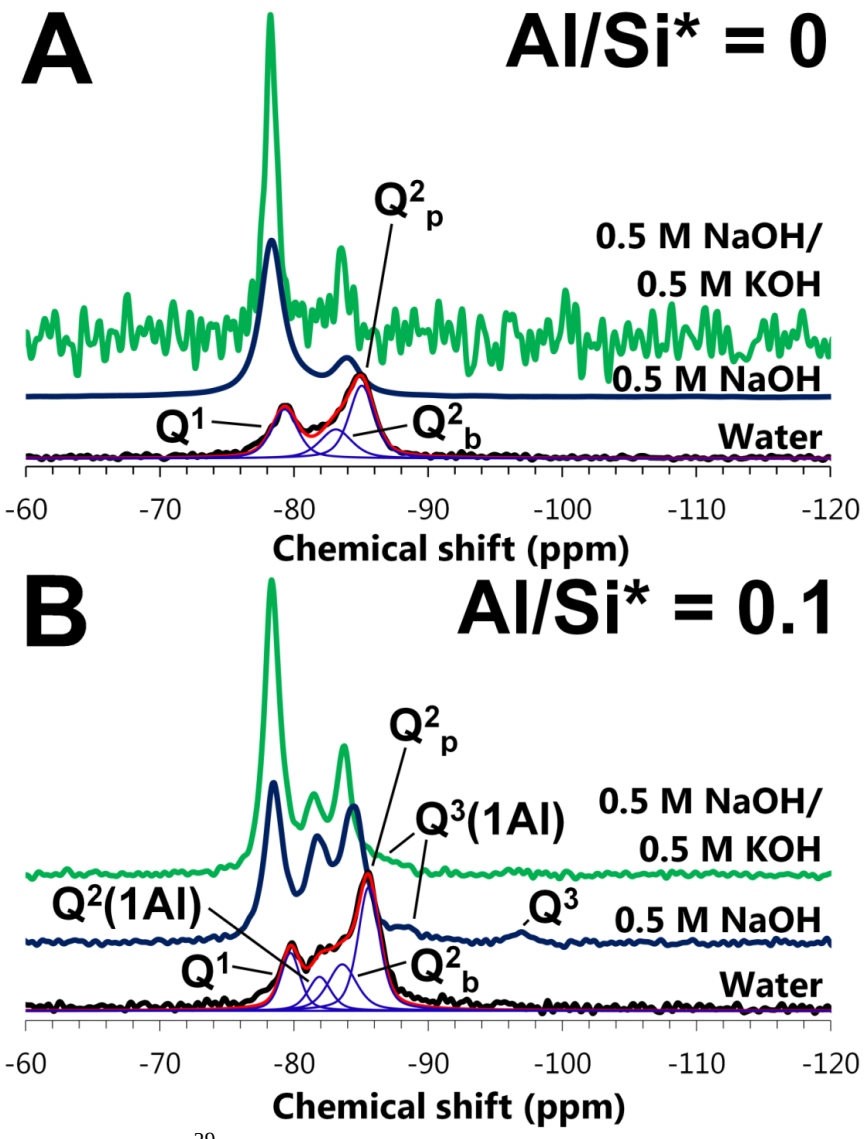


Figure 9.13. Solid-state $^{29}$Si MAS NMR spectra of A) C-(N-)S-H (Al/Si* = 0) and B) C-(N-)A-S-H (Al/Si* = 0.1) samples, synthesised with Ca/Si* = 1 and equilibrated at 50°C. The fits and deconvoluted peaks for the spectra of the water-synthesised samples are shown as red and blue lines respectively. Deconvolutions for each spectrum are shown in Figures 9.14-9.15. The relatively high level of noise in the spectrum of the Al/Si* = 0 sample synthesised with 0.5 M NaOH/0.5 M KOH is caused by the very rapid relaxation of this sample. Al/Si* = bulk Al/Si.

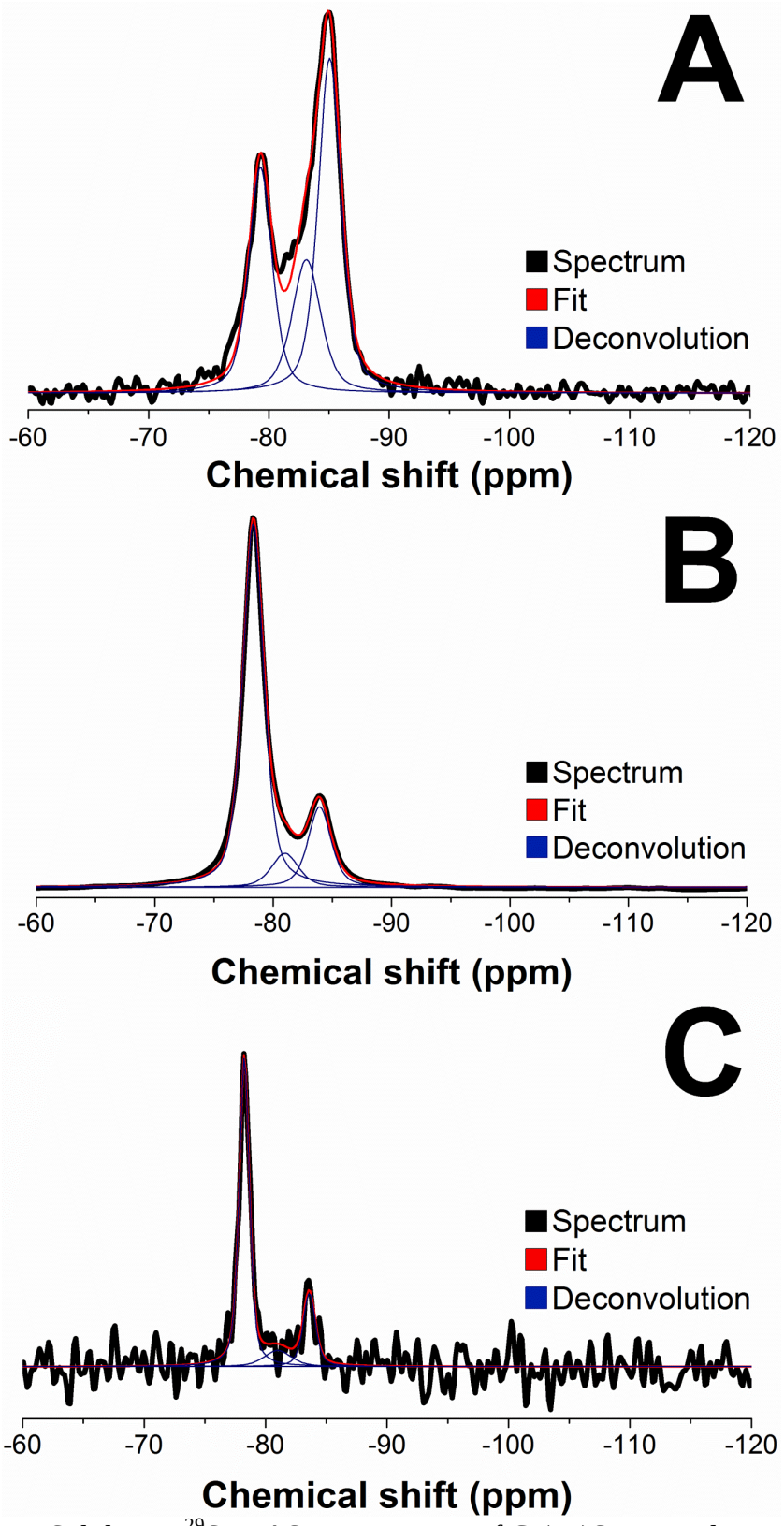


Figure 9.14: Solid-state $^{29}$Si MAS NMR spectra of C-(N-)S-H samples synthesised with Al/Si* = 0, Ca/Si* = 1 and A) water, B) 0.5 M NaOH, and C) 0.5 M NaOH/0.5 M KOH, and equilibrated at 50°C.

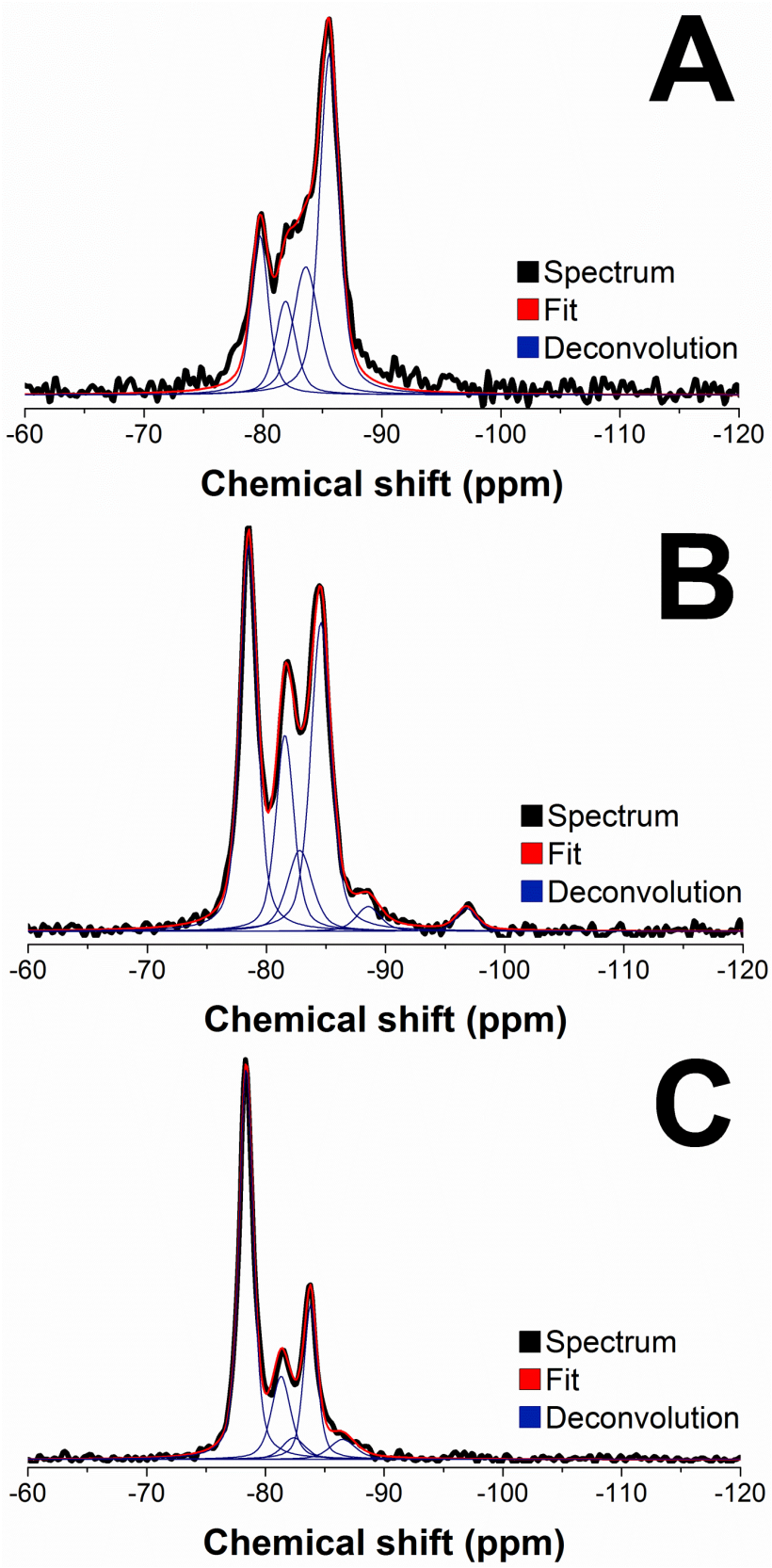


Figure 9.15. Solid-state $^{29}$Si MAS NMR spectra of C-(N-)S-H samples synthesised with Al/Si* = 0.1, Ca/Si* = 1 and A) water, B) 0.5 M NaOH, and C) 0.5 M NaOH/0.5 M KOH, and equilibrated at 50°C.

Table 9.9. Deconvolution results for the $^{29}$Si MAS NMR spectra of C-(N-)A-S-H samples synthesised with Ca/Si* = 1 and equilibrated at 50°C. The estimated error in absolute site percentages is ±0.02. Al/Si* = bulk Al/Si.

| **Al/Si*** | **Alkali solution type** | **$Q^1$ -79.0 ±0.7 ppm** | **$Q^2$(1Al) -81.7 ±0.4 ppm** | **$Q^2_b$ -82.4 ±1.3 ppm** | **$Q^2_p$ -84.4 ±0.8 ppm** | **$Q^3$(1Al) -87.6 ±1.1 ppm** | **$Q^3$ -96.8 ppm** |
|---|---|---|---|---|---|---|---|
| 0 | Water | 0.32 | 0 | 0.23 | 0.46 | 0 | 0 |
| 0 | 0.5 M NaOH | 0.74 | 0 | 0.09 | 0.18 | 0 | 0 |
| 0 | 0.5M NaOH/ 0.5 M KOH | 0.70 | 0 | 0.10 | 0.20 | 0 | 0 |
| 0.1 | Water | 0.20 | 0.16 | 0.21 | 0.43 | 0 | 0 |
| 0.1 | 0.5 M NaOH | 0.34 | 0.18 | 0.10 | 0.32 | 0.031 | 0.024 |
| 0.1 | 0.5M NaOH/ 0.5 M KOH | 0.54 | 0.16 | 0.05 | 0.20 | 0.052 | 0 |

$^{29}$Si resonances assigned to $Q^1$, $Q^2_b$ and $Q^2_p$ sites are also identified in the spectra of the C-(N-)A-S-H (Al/Si* = 0.1) samples (Figure 9.13B). These spectra also contain an additional resonance assigned to structurally-incorporated Al in non-cross-linked bridging sites ($Q^2$(1Al)), located at $\delta_{iso}$ = -82 ppm in the spectrum for the alkali-free sample. $Q^2$(1Al) sites identified in laboratory-synthesised C-A-S-H samples equilibrated at 23°C are located at similar $\delta_{iso}$ values (Pardal et al., 2012).

Peaks assigned to $Q^1$, $Q^2_b$, $Q^2_p$ and $Q^2$(1Al) are shifted by +0.4 to +1 ppm in the spectrum for the Al-containing sample synthesised with 0.5 M NaOH relative to the alkali-free C-A-S-H sample (Figure 9.13B), which is consistent with $^{29}$Si MAS NMR spectra of laboratory-synthesised C-(N-)A-S-H produced at 20-25°C (L'Hôpital et al.; Lognot et al., 1998). Additional $Q^3$(1Al) and $Q^3$ resonances at -88.6 and -96.8 ppm are observed in the spectrum of the 0.5 M NaOH sample, indicating the formation of a cross-linked C-(N-)A-S-H product. The $\delta_{iso}$ value of the $Q^3$ site is equivalent to the chemical shift of this site in laboratory-synthesised C-A-S-H equilibrated at 80°C (Myers et al., 2015b) and in Al-tobermorite formed in 2000-year old Roman seawater concrete (Jackson et al., 2013), and is similar to the chemical shift of this site in (Al-)tobermorites synthesised at 150°C (Houston et al., 2009) and 175°C (Cong and Kirkpatrick, 1996b; Tsuji et al., 1991). However, the $\delta_{iso}$ value of the $Q^3$(1Al) site is shifted by approximately +3 ppm relative to the chemical shift of this site in the aforementioned literature; this is again attributed to the association of a greater proportion of less positively-charged dissolved species (e.g. $Na^+$ rather than $Ca^{2+}$) with Si atoms in $Q^3$(1Al) sites, resulting from the much higher alkali concentrations used here.

Each component peak is shifted to a slightly more positive $\delta_{iso}$ value by further increasing the alkali hydroxide concentrations of the synthesis solutions to 1 M (Figure 9.13B, sample 0.5 M NaOH/0.5 M KOH), suggesting additional uptake of $Na^+/K^+/H^+$ in C-(N-)A-S-H interlayers, while the $Q^3$ site is no longer identified. The disappearance of the $Q^3$ site at a bulk alkali concentration of 1 M, and the presence of $Q^3$(1Al) resonances at -87 to -89 ppm in the Al and alkali-containing samples, are

consistent with the features of $^{29}$Si MAS NMR spectra of $Na_2CO_3$ and $Na_2SiO_3$-activated slag cement pastes cured under ambient conditions (Bernal et al., 2015; Myers et al., 2015a), where $Q^3$(1Al)-containing cross-linked C-(N-)A-S-H products are sometimes present in this chemical shift range. The identification of $Q^3$-type sites in the C-(N-)A-S-H samples equilibrated at 50°C here, rather than the higher temperatures needed to form these structures in C-A-S-H specimens synthesised with Al but without alkali (Myers et al., 2015b), shows that the formation of =Al-O-Si= cross-links in C-(N-)A-S-H products is greatly promoted at higher alkali content.

### 9.3.7 Structural Models and Implications

Mean chain lengths (MCLs), Al/Si ratios and cross-linked phase fractions for the C-(N-)A-S-H products (Figure 9.16) are calculated using the $^{29}$Si MAS NMR spectral deconvolution results (Table 9.9) and the 'Cross-linked Substituted Tobermorite Model' (CSTM) (Myers et al., 2013), by representing this phase as a mixture of cross-linked and non-cross-linked tobermorite-like components.

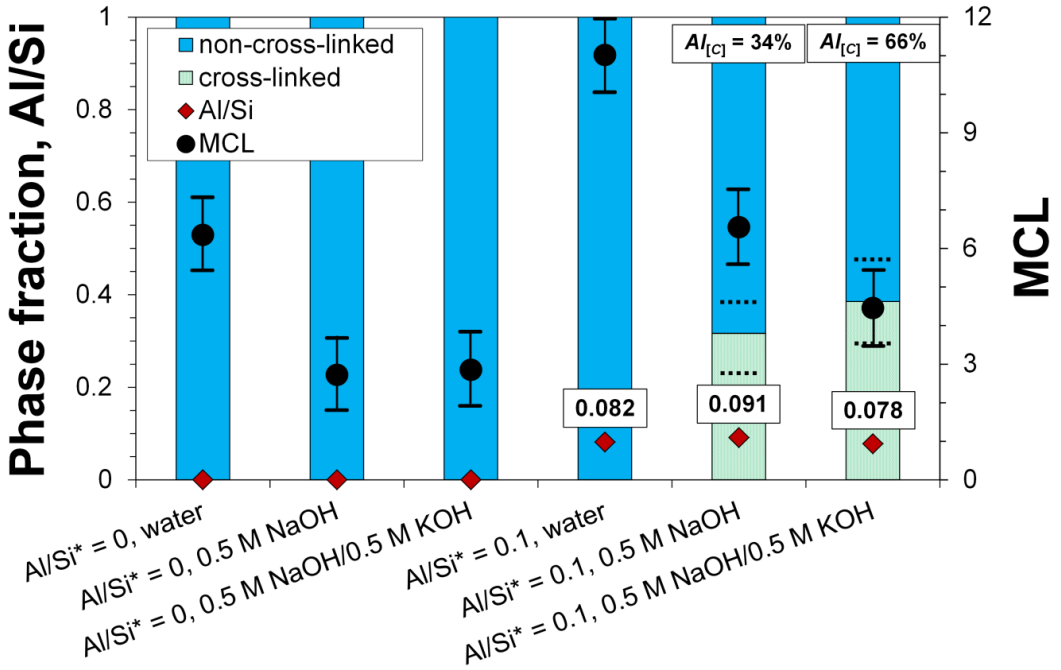


Figure 9.16. C-(N-)S-H and C-(N-)A-S-H structural parameters calculated from deconvolution analysis of the $^{29}$Si MAS NMR spectra (Figures 9.13-9.15), determined using the CSTM (Myers et al., 2013) for mixed cross-linked/non-cross-linked tobermorite-like phases. The expected error bounds of the deconvolution results are represented by symbol size for the Al/Si ratios, by dotted black lines for the cross-linked phase fractions and by error bars for the MCL values. $Al_{[C]}$ = percentage of Al in cross-linked C-(N-)A-S-H (eq.(5.1)). Al/Si* = bulk Al/Si.

The results obtained by applying the CSTM (Myers et al., 2013) to the $^{29}$Si MAS NMR spectral deconvolutions show that the MCLs of the C-(N-)A-S-H products decrease with increasing alkali concentration, and with decreasing bulk Al content. The calculated Al/Si ratios are similar to the Al/Si* ratios used in synthesis (Al/Si* = 0.1); the small differences are explained by the formation of small amounts of $C_3AH_6$/$Al(OH)_3$ in the alkali-free and 0.5 M NaOH/0.5 M KOH samples, and $C_4AcH_{11}$/$C_3AH_6$/$Al(OH)_3$ in the 0.5 M NaOH sample (Myers et al., 2015b) (Appendix D). The alkali and Al-containing C-(N-)A-S-H products show similar levels of cross-linking, although the percentage of Al in the cross-linked components ($Al_{[C]}$) of this phase is higher in the sample synthesised using 0.5 M NaOH/0.5 M KOH (66%) relative to the sample synthesised with 0.5 M NaOH (34%). This parameter is calculated using the CSTM representation of C-(N-)A-S-H chemistry (Myers et al., 2013), eq.(5.1) and the $^{29}$Si MAS NMR spectral deconvolution results (Table 9.9).

The calculated $Al_{[C]}$ values (Figure 9.16) show that the uptake of Al into cross-linked C-(N-)A-S-H components is enhanced as the bulk alkali hydroxide concentration is increased, but also that there is not an extremely strong preference for partitioning of Al into either one of the two structural types. This view is supported by recent work on the role of Al in cross-linking of C-(N-)A-S-H in $Na_2SiO_3$-activated slag cements cured for 1-180 days at room temperature, which reported $Al_{[C]}$ values of 40-60% (Myers et al., 2015a).

A comparison of the key alkali-dependent structural changes identified here (at Ca/Si* = 1) with the slightly reduced C-(N-)A-S-H solubilities determined at higher alkali concentration and Ca/(Al+Si) ratios $\leq$ 1 (section 9.3.5) suggests that the solubility and MCL of this phase may be directly related in this range of Ca/(Al+Si) ratios. The influence of Ca composition on C-(N-)A-S-H solubility dominates at higher Ca/(Al+Si) ratios, i.e. at low MCL values, demonstrated by large reductions in the solubility of this phase as a function of increasing Ca/(Al+Si) ratio at the limit MCL $\rightarrow$ 2 (region A in Figure 9.17).

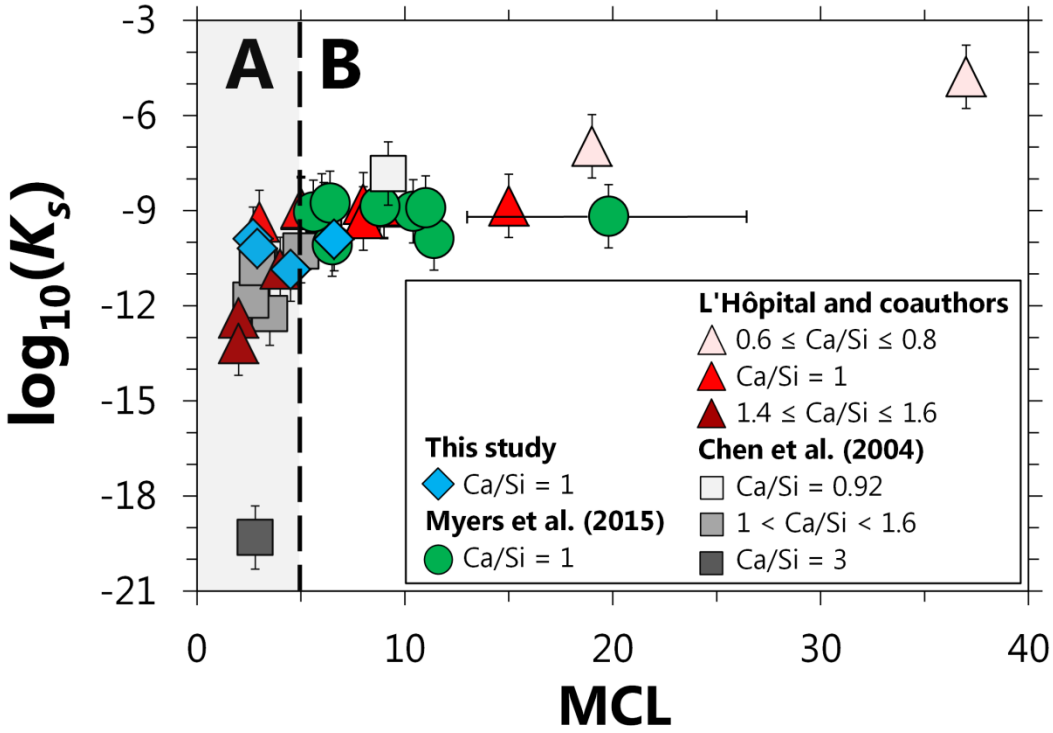


Figure 9.17. Solubility products for C-(N-)A-S-H plotted as a function of MCL, calculated using the dissolution reaction shown in eq.(3.8) with regions: A) describing C-(N-)A-S-H with highly variable Ca/(Al+Si) ratios and slightly variable MCLs; and B) describing C-(N-)A-S-H with variable Ca/(Al+Si) and MCL. The references for the symbols used are: blue diamonds, this study; green circles, C-(A-)S-H equilibrated at 7-80°C in (Myers et al., 2015b); red triangles, C-(N,K-)A-S-H equilibrated at 20°C in (L'Hôpital, 2014; L'Hôpital et al.); and grey squares, C-S-H equilibrated at 22°C in (Chen et al., 2004). Solubility products are calculated using $H_2O$/Si = 1.2 and Ca/Si ratios taken directly from the literature for the data in (Chen et al., 2004), or specified to have a total of 1 mole Si + Al with Ca/Si and Al/Si ratios equivalent to the bulk Ca-Al-Si compositions used, Na/Si ratios = 0.1 for the Na-containing phases, K/Si ratios = 0.1 for the K-containing phases and $H_2O$/Si ratios = 1.2 for the data in (L'Hôpital, 2014; L'Hôpital et al.; Myers et al., 2015b) and in this study. The expected experimental uncertainty is represented by error bars, or by the size of the symbols used in the absence of horizontal error bars for MCL values.

The effects of MCL and Ca composition on C-(N-)A-S-H solubility cannot be distinguished from one another in region B of Figure 9.17 because C-(N-)A-S-H can contain many different Ca/(Al+Si) ratios at a fixed MCL value, for MCL > 5 (Richardson, 2014). Therefore, selected solubility data for C-(N-)A-S-H with Ca/(Al+Si) = 1 were plotted as a function of MCL in Figure 9.18.

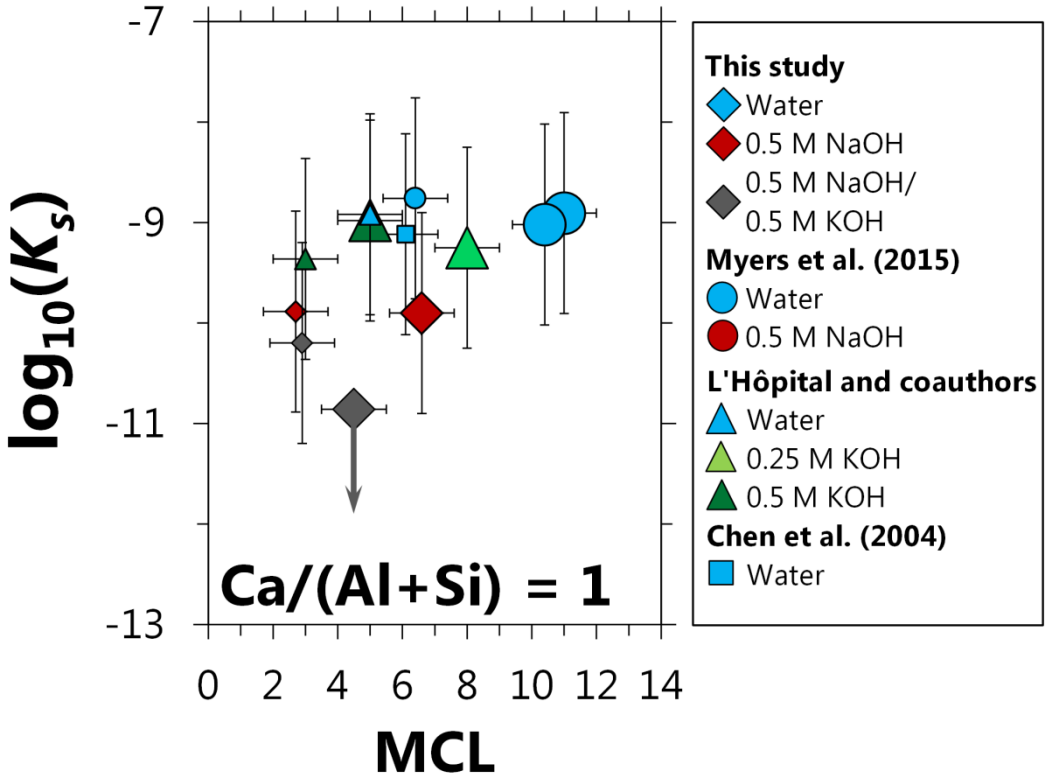


Figure 9.18. Solubility products for C-(N,K-)A-S-H plotted as a function of the MCL, calculated using the dissolution reaction shown in eq.(3.8) at a Ca/(Al+Si) ratio = 1. The references for the symbols used are: diamonds, this study (Ca/Si* = 1); circles, C-(A-)S-H synthesised with Ca/Si* = 1 and equilibrated at 20-50°C in (Myers et al., 2015b); triangles, C-(N,K-)A-S-H synthesised with Ca/Si* = 1 and equilibrated at 20°C in (L'Hôpital, 2014; L'Hôpital et al.); and square, C-S-H equilibrated at 22°C with Ca/Si = 1.03 in (Chen et al., 2004). Large symbols are data at Al/Si* = 0.1 and small symbols are data at Al/Si* = 0. C-(N,K-)A-S-H solubility products are calculated using $H_2O$/Si = 1.2 and Ca/Si ratios taken directly from the literature for the datum in (Chen et al., 2004), or specified to have a total of 1 mole Si + Al with Ca/Si and Al/Si ratios equivalent to the bulk Ca-Al-Si compositions used, Na/Si ratios = 0.2 for the Na-containing phases, K/Si ratios = 0.2 for the K-containing phases and $H_2O$/Si ratios = 1.2 for the data in (L'Hôpital, 2014; L'Hôpital et al.; Myers et al., 2015b) and in this study. Error bars represent the expected experimental uncertainty except for the point with a downward-pointing arrow, which additionally represents a maximum solubility product value, as described in the text for Figure 9.12.

Figure 9.18 shows an inverse correlation between MCL and the bulk alkali hydroxide concentration, in good agreement with the $^{29}$Si MAS NMR results presented in Figure 9.16, and also slightly reduced C-(N-)A-S-H solubility products in samples synthesised with more highly concentrated alkali solutions, consistent with the trends in C-(N-)A-S-H solubility shown in Figure 9.12 at Ca/(Al+Si) = 1. However, Figure

9.18 does not show a significant difference in C-(N-)A-S-H solubility as a function of Al content, despite the longer chain lengths of the Al-containing C-(N-)A-S-H phases compared to their Al-free counterparts; therefore, these results indicate that the MCL structural parameter does not play a key role in influencing the solubility of C-(N-)A-S-H at a Ca/(Al+Si) ratio = 1. This analysis is consistent with recently reported results for C-(A-)S-H that showed comparable solubility products for this phase independent of the Al content (Myers et al., 2015b).

Alternative factors that could account for the slightly stabilised C-(N-)A-S-H structures identified here at increased bulk alkali hydroxide concentrations and Ca/(Al+Si) ratios ≤ 1 (Figure 9.12) would then need to be proposed: increased cross-linking (Figure 9.16) or changes to the bulk layered structure of this phase (Figure 9.2 and as described by Richardson (2014)) could be potential candidates. However, the large uncertainty (±1 $\log_{10}$ unit) of the solubility products calculated here (Figure 9.12) and the limited availability of solubility data for C-(N-)A-S-H at Ca/(Al+Si) ratios < 1 means that the structure-solubility relationships proposed here cannot be considered fully conclusive. Further work clarifying the role of structure on the solubility of C-(N-)A-S-H would be greatly beneficial in further enabling the design of chemically-stable and durable cementitious binders based on engineering controls such as the mix design and curing temperature.

## 9.4 Conclusions

The effect of alkali, Al and Ca on the structure and solubility of C-(N-)A-S-H equilibrated at 50°C was investigated in this paper. The long-range order of the alkali-containing C-(N-)A-S-H products was much greater than in those synthesised in the absence of alkalis. C-(N-)A-S-H basal spacings were generally greater at lower Ca content and at higher alkali concentrations in the samples synthesised using alkaline hydroxide solutions; this latter factor was attributed to the uptake of additional $Na^+/K^+$ species in C-(N-)A-S-H interlayers. No clear trend in C-(N-)A-S-H basal spacing as a function of Al content was identified.

The concentrations of Ca decreased and the concentrations of Si and Al increased in the supernatants as functions of increasing alkali hydroxide concentration. More alkali was incorporated in C-(N-)A-S-H synthesised with lower Ca and higher alkali hydroxide concentrations, although alkali uptake in this phase was found to be independent, within the experimental uncertainty, of the alkali type (Na or K) and Al/Si ratio at the relatively low amounts of Al added to each sample (Al/Si* $\leq$ 0.05).

Shorter mean chain lengths, increased cross-linking, and incorporation of more Al into cross-linked C-(N-)A-S-H components were identified upon increasing the bulk alkali and Al content; mixed cross-linked/non-cross-linked C-(N-)A-S-H was only formed in the presence of both alkali and Al. More stable C-(N-)A-S-H was formed at higher bulk Ca and alkali concentrations, with significant changes in C-(N-)A-S-H solubility due to the latter factor only identified at Ca/Si ratios $\leq$ 1, but the stability of this phase did not vary greatly as a function of the Al/Si ratio. The reduced C-(N-)A-S-H solubility calculated at higher alkali and Ca content was discussed to be partly related to structural changes, and it was tentatively proposed that the MCL of this phase does not play a key role in these structural modifications. Therefore, these results provide insight into the composition-structure-solubility relationships in C-(N-)A-S-H, which will improve how hydrated alkali and Al-containing cements, i.e. the majority of cement-based materials used worldwide, are understood to perform in service.

# 10
# Conclusions

This thesis presented an analysis of C-(N-)A-S-H and AAS-based cement chemistry using structural and thermodynamic models developed here. This analysis is also relevant for some hybrid alkali-activated cements and hydrated PC/SCM blends. These models advance the detail in which C-(N-)A-S-H chemistry can be described, and the utility of thermodynamic modelling in predicting the chemistry of C-(N-)A-S-H-based cement materials. Therefore, this thesis presents key advancements needed to develop a broadly-applicable framework for understanding the chemistry, and therefore durability, of C-(N-)A-S-H-based cements.

The literature review presented in Chapter 2 showed that the lack of a flexible C-(N-)A-S-H structural model containing descriptions of mixed cross-linked/non-cross-linked tobermorite-like structures, and the lack of a C-(N-)A-S-H thermodynamic model with explicit description of Al and alkali uptake in this phase, were key limitations in the cement chemistry literature.

The structural model formulated in Chapter 4, the CSTM, contains the first flexible description of C-(N-)A-S-H as a mixture of cross-linked/non-cross-linked tobermorite-like structures explicitly in terms of $Q^n(m\text{Al})$ sites. This greatly advances the accuracy in which the chemistry of C-(N-)A-S-H-based cements can be described, by correctly accounting for cross-linked type C-(N-)A-S-H in structural analysis of these materials. The application of the CSTM to deconvoluted $^{29}$Si MAS NMR spectra of a $Na_2SiO_3$-activated slag cement showed the key advancement that a $Q^4$-containing reaction product must have formed to satisfy the structural constraints of mixed cross-linked/non-cross-linked tobermorite-like C-(N-)A-S-H. Complementary SEM-EDS analysis suggested that this $Q^4$-containing phase has an

Al/Si ratio ≈ 1 and is long-range disordered. It was hypothesised that this phase may be a disordered nanoparticulate zeolite-like product with similarities to the N-A-S(-H) ('geopolymer') gels formed in alkali-activated cements derived from MK and FA.

Additional structural analysis of C-(N-)A-S-H in $Na_2SiO_3$-activated slag cement was presented in Chapter 5, which showed that the MCL, cross-linked phase fraction and Al/Si ratio of this phase decreased slightly as a function of increasing curing time. A clear trend between the proportion of Al in the cross-linked C-(N-)A-S-H component and curing time was not found. A long-range disordered $Q^4$-containing activation product was found at 180 days of curing in addition to the identification of this phase at 56 days in Chapter 4. These results indicate that the chemical compositions of the fundamental structural units in mixed cross-linked/non-cross-linked C-(N-)A-S-H vary in a way that is not immediately apparent from the bulk chemistry of this phase.

The first thermodynamic model for C-(N-)A-S-H that explicitly describes Al and alkali uptake in this phase, CNASH_ss, was developed in Chapter 6. The CNASH_ss thermodynamic model was formulated in terms of tobermorite-like phases such as those described by the CSTM. This thermodynamic model was validated against a large set of solubility data in the CaO-($Na_2O$,$Al_2O_3$)-$SiO_2$-$H_2O$ and AAS cement systems, and chemical composition data for C-A-S-H, showing that it can reproduce experimental solubility results in AAS cements to ≤±1 order of magnitude and is applicable for C-(N-)A-S-H with Ca/Si ratios < 1.3. The CNASH_ss thermodynamic model described the volumetric properties of C-(N-)A-S-H in AAS cements, meaning that it can be used to simulate chemical shrinkage in these materials. This model greatly advances the utility of thermodynamic modelling to alkali-activated cements, and potentially hybrid alkali-activated cements and hydrated PC/SCM blends.

In Chapter 7, the CNASH_ss thermodynamic model and an ideal solid solution model for MgAl-OH-LDH, developed in this chapter, were applied to describe the chemistry of AAS-based cements. A good description of $Na_2SiO_3$ and $Na_2CO_3$-

activated slag cement chemistry was found. Phase diagrams for AAS-based cements were simulated, which showed the high stability of zeolites in these materials, and particularly calcite in $Na_2CO_3$-activated slag-based cement. The composition envelope where zeolites and C-(N-)A-S-H are both stable was found to be dependent on the bulk $CaO/(Al_2O_3 + SiO_2)$ ratio. Therefore, the results from this study can be used to guide the design of high-performance AAS-based materials, using the bulk chemical composition of the cement formulation.

The solubility, chemical composition and nanostructural analysis of C-(A-)S-H discussed in Chapter 8 shows that this phase increases in long-range order and polymerisation degree at higher temperatures, and that cross-linking is promoted significantly by Al at 80°C. The solubility products determined for C-(A-)S-H vary within the experimental uncertainty as a function of Al/Si ratio and temperature. These results are important for further development of C-(A-)S-H thermodynamic models and for understanding the stability of C-(A-)S-H under the majority of temperatures experienced by construction materials in service worldwide.

Chapter 9 expanded on the solubility analysis presented in Chapter 8 by additionally considering the influence of alkali; this analysis showed that C-(N-)A-S-H solubility and the uptake of alkali in this phase decreases significantly as a function of increasing Ca content. It was also found that this phase contains more alkali, lower MCL and is generally stabilised slightly in the presence of higher alkali concentrations at Ca/Si ratios $\leq 1$. Cross-linking was found to be greatly promoted by Al and alkali in the samples studied. More crystalline C-(N-)A-S-H was formed in the presence of alkali, and basal spacings in this phase were typically higher at lower Ca/Si ratios. These results are important to advance the accuracy with which the chemistry of C-(N-)A-S-H-based materials can be predicted by thermodynamic modelling, i.e. the majority of cementitious materials used worldwide.

Therefore, Chapter 10 has summarised the progress made in this thesis towards understanding the chemistry of C-(N-)A-S-H and C-(N-)A-S-H-based cementitious materials.

# 11
# Recommendations for Future Work

Improvement to the C-(N-)A-S-H structural model presented in this thesis (the CSTM) can be found in the description of adsorbed interlayer and surface species used. These species were located in two sublattice sites – one for species associated with bridging tetrahedra and one for species associated with the rest of the structure – but selective mixing in the sublattice sites was not specified. However, the different adsorbed species in C-(N-)A-S-H structures (e.g. $H^+$, $Ca^{2+}$, $Na^+$) may be non-randomly substituted into these sites in real systems. Development of more structurally-consistent C-(N-)A-S-H structural models using this information would enable the chemistry of C-(N-)A-S-H gels to be more accurately modelled from experimental results such as $^{29}$Si MAS NMR (e.g. by reducing the uncertainty in Ca/Si ratios output by the structural model).

The $^{29}$Si and $^{27}$Al MAS NMR analysis presented in this thesis is limited by the assumption of congruent slag dissolution that was applied to the spectral deconvolutions, which may not be fully attained. Further work clarifying the dissolution behavior of slags in cementitious systems, in particular the less basic $Na_2CO_3$-activated systems studied in Chapter 7, is necessary to improve the accuracy to which deconvoluted $^{29}$Si and 27Al MAS NMR spectra of slag-based cements can be analysed.

An improved understanding of the chemistry of the additional $Q^4$-containing aluminosilicate product identified in Chapters 4-5, discussed here in terms of a N-A-S(-H)-type gel, is necessary to obtain a more complete understanding of the chemistry of $Na_2SiO_3$-activated slag cements. Future research on this topic should

clarify whether this phase is a product from the reaction between the slag and alkali activator or whether it is a degradation product of carbonated C-(N-)A-S-H gel.

Each of the three recommendations presented above could be used to improve the utility of thermodynamic modelling of C-(N-)A-S-H-based cements, by: i) enabling the development of more structurally-consistent thermodynamic models for C-(N-)A-S-H gel; ii) more accurately defining slag reaction extents used in thermodynamic modelling simulations; and iii) informing the development of thermodynamic models for N-A-S(-H) gels, which are currently missing in thermodynamic databases for cement. The development and utilisation of reliable thermodynamic data for zeolites that tend to form in cementitious systems (e.g. gismondine) is also needed to improve the utility of thermodynamic modelling of C-(N-)A-S-H-based cements. Future work that clarifies and/or accounts for the influence of adsorbed species in the aqueous elemental concentrations output from thermodynamic modelling analysis of cements, which is not currently distinguished, seems to be an essential 'next step' in predicting the chemistry of these materials using this technique. Thermodynamic modelling of C-(N-)A-S-H-based cements under aggressive environmental conditions (e.g. in the presence of atmospheric $CO_2$) is also needed to assess the durability of these materials in service.

Finally, a complete understanding of the interplay between the stability, chemical composition and structure of C-(N-)A-S-H gel, and the influence of these factors on mechanical properties, is currently missing. Future work on this topic, with a view towards linking these factors to properties such as the mix design and temperature of curing, could lead to the design of C-(N-)A-S-H-based cements with improved performance.

# 12

# References


Abdolhosseini Qomi, M.J., Ulm, F.J. and Pellenq, R.J.M., Evidence on the dual nature of aluminum in the calcium-silicate-hydrates based on atomistic simulations, J. Am. Ceram. Soc., 2012, **95**, 1128-1137.

Abdolhosseini Qomi, M.J., Krakowiak, K.J., Bauchy, M., Stewart, K.L., Shahsavari, R., Jagannathan, D., Brommer, D.B., Baronnet, A., Buehler, M.J., Yip, S., Ulm, F.J., Van Vliet, K.J. and Pellenq, R.J.M., Combinatorial molecular optimization of cement hydrates, Nat. Commun., 2014, **5**, 4960.

Aïtcin, P.-C., Cements of yesterday and today: Concrete of tomorrow, Cem. Concr. Res., 2000, **30**, 1349-1359.

Allada, R., Navrotsky, A. and Boerio-Goates, J., Thermochemistry of hydrotalcite-like phases in the $MgO$-$Al_2O_3$-$CO_2$-$H_2O$ system: a determination of enthalpy, entropy, and free energy, Am. Mineral., 2005a, **90**, 329-335.

Allada, R.K., Pless, J.D., Nenoff, T.M. and Navrotsky, A., Thermochemistry of hydrotalcite-like phases intercalated with $CO_3^{2-}$, $NO_3^-$, $Cl^-$, $I^-$, and $ReO_4^-$, Chem. Mater., 2005b, **17**, 2455-2459.

Allen, A.J. and Thomas, J.J., Analysis of C-S-H gel and cement paste by small-angle neutron scattering, Cem. Concr. Res., 2007, **37**, 319-324.

Allen, A.J., Thomas, J.J. and Jennings, H.M., Composition and density of nanoscale calcium-silicate-hydrate in cement, Nat. Mater., 2007, **6**, 311-316.

Andersen, M.D., Jakobsen, H.J. and Skibsted, J., A new aluminium-hydrate species in hydrated Portland cements characterized by $^{27}Al$ and $^{29}Si$ MAS NMR spectroscopy, Cem. Concr. Res., 2006, **36**, 3-17.

Anderson, G.M. and Crerar, D.A., Thermodynamics in geochemistry: the equilibrium model, 1993, Oxford University Press, Oxford.

Andersson, J.O., Guillermet, A.F., Hillert, M., Jansson, B. and Sundman, B., A compound-energy model of ordering in a phase with sites of different coordination numbers, Acta Metall. Mater., 1986, **34**, 437-445.

Arthur, R., Sasamoto, H., Walker, C. and Yui, M., Polymer model of zeolite thermochemical stability, Clays Clay Miner., 2011, **59**, 626-639.

Atkins, M., Bennett, D.G., Dawes, A.C., Glasser, F.P., Kindness, A. and Read, D., A thermodynamic model for blended cements, Cem. Concr. Res., 1992a, **22**, 497-502.

Atkins, M. and Glasser, F.P., Application of portland cement-based materials to radioactive waste immobilization, Waste Manage., 1992, **12**, 105-131.

Atkins, M., Glasser, F.P. and Kindness, A., Cement hydrate phase: solubility at 25°C, Cem. Concr. Res., 1992b, **22**, 241-246.

Atkins, M., Glasser, F., Moroni, L.P. and Jack, J.J., Thermodynamic modelling of blended cements at elevated temperature (50-90°C), 1994, Aberdeen University, United Kingdom.

Atkinson, A., Hearne, J.A. and Knights, C.F., Aqueous chemistry and thermodynamic modelling of $CaO$-$SiO_2$-$H_2O$ gels, J. Chem. Soc., Dalton Trans., 1989, 2371-2379.

Bach, T.T.H., Cau-dit-Coumes, C., Pochard, I., Mercier, C., Revel, B. and Nonat, A., Influence of temperature on the hydration products of low pH cements, Cem. Concr. Res., 2012, **42**, 805-817.

Bach, T.T.H., Chabas, E., Pochard, I., Cau-dit-Coumes, C., Haas, J., Frizon, F. and Nonat, A., Retention of alkali ions by hydrated low-pH cements: mechanism and $Na^+/K^+$ selectivity, Cem. Concr. Res., 2013, **51**, 14-21.

Baerlocher, C., McCusker, L.B. and Olson, D.H., Atlas of zeolite framework types, 2007, Elsevier, Netherlands.

Bai, Y., Collier, N.C., Milestone, N.B. and Yang, C.H., The potential for using slags activated with near neutral salts as immobilisation matrices for nuclear wastes containing reactive metals, J. Nucl. Mater., 2011, **413**, 183-192.

Barbarulo, R., Comportement des matériaux cimentaires: actions des sulfates et de la température, 2003, Université Laval, Québec.

Beaudoin, J.J., Ramachandran, V.S. and Feldman, R.F., Interaction of chloride and C-S-H, Cem. Concr. Res., 1990, **20**, 875-883.

Bell, J.L., Sarin, P., Provis, J.L., Haggerty, R.P., Driemeyer, P.E., Chupas, P.J., van Deventer, J.S.J. and Kriven, W.M., Atomic structure of a cesium aluminosilicate geopolymer: a pair distribution function study, Chem. Mater., 2008, **20**, 4768-4776.

Ben Haha, M., Le Saoût, G., Winnefeld, F. and Lothenbach, B., Influence of activator type on hydration kinetics, hydrate assemblage and microstructural development of alkali activated blast-furnace slags, Cem. Concr. Res., 2011a, **41**, 301-310.

Ben Haha, M., Lothenbach, B., Le Saoût, G. and Winnefeld, F., Influence of slag chemistry on the hydration of alkali-activated blast-furnace slag - part I: effect of MgO, Cem. Concr. Res., 2011b, **41**, 955-963.

Ben Haha, M., Lothenbach, B., Le Saoût, G. and Winnefeld, F., Influence of slag chemistry on the hydration of alkali-activated blast-furnace slag - part II: effect of $Al_2O_3$, Cem. Concr. Res., 2012, **42**, 74-83.

Bennett, D.G., Read, D., Atkins, M. and Glasser, F.P., A thermodynamic model for blended cements. II: cement hydrate phases; thermodynamic values and modelling studies, J. Nucl. Mater., 1992, **190**, 315-325.

Bernal, J.D., Jeffery, J.W. and Taylor, H.F.W., Crystallographic research on the hydration of Portland cement. A first report on investigations in progress, Mag. Concr. Res., 1952, **4**, 49-54.

Bernal, S.A., Provis, J.L., Mejía de Gutierrez, R. and Rose, V., Evolution of binder structure in sodium silicate-activated slag-metakaolin blends, Cem. Concr. Compos., 2011a, **33**, 46-54.

Bernal, S.A., Provis, J.L., Rose, V. and Mejía De Gutierrez, R., Evolution of binder structure in sodium silicate-activated slag-metakaolin blends, Cem. Concr. Compos., 2011b, **33**, 46-54.

Bernal, S.A., Provis, J.L., Brice, D.G., Kilcullen, A., Duxson, P. and van Deventer, J.S.J., Accelerated carbonation testing of alkali-activated binders significantly underestimates service life: the pore solution chemistry, Cem. Concr. Res., 2012a, **42**, 1317-1326.

Bernal, S.A., Provis, J.L., Brice, D.G., Kilcullen, A., Duxson, P. and van Deventer, J.S.J., Accelerated carbonation testing of alkali-activated binders significantly underestimates service life: the role of pore solution chemistry, Cem. Concr. Res., 2012b, **42**, 1317-1326.

Bernal, S.A., Provis, J.L., Rose, V. and Mejía de Gutiérrez, R., High-resolution X-ray diffraction and fluorescence microscopy characterization of alkali-activated slag-metakaolin binders, J. Am. Ceram. Soc., 2013a, **96**, 1951-1957.

Bernal, S.A., Provis, J.L., Rose, V. and Mejía de Gutiérrez, R., High-resolution X-ray diffraction and fluorescence microscopy characterization of alkali-activated slag-metakaolin binders, J. Am. Ceram. Soc., 2013b, 1-7.

Bernal, S.A., Provis, J.L., Walkley, B., San Nicolas, R., Gehman, J.G., Brice, D.G., Kilcullen, A., Duxson, P. and van Deventer, J.S.J., Gel nanostructure in akali-activated binders based on slag and fly ash, and effects of accelerated carbonation, Cem. Concr. Res., 2013c, **53**, 127-144.

Bernal, S.A. and Provis, J.L., Durability of alkali-activated materials: progress and perspectives, J. Am. Ceram. Soc., 2014, **97**, 997-1008.

Bernal, S.A., Rose, V. and Provis, J.L., The fate of iron in blast furnace slag particles during alkali-activation, Mater. Chem. Phys., 2014a, **146**, 1-5.

Bernal, S.A., San Nicolas, R., Myers, R.J., Mejía de Gutiérrez, R., Puertas, F., van Deventer, J.S.J. and Provis, J.L., MgO content of slag controls phase evolution and structural changes induced by accelerated carbonation in alkali-activated binders, Cem. Concr. Res., 2014b, **57**, 33-43.

Bernal, S.A., Provis, J.L., Myers, R.J., San Nicolas, R. and van Deventer, J.S.J., Role of carbonates in the chemical evolution of sodium carbonate-activated slag binders, Mater. Struct., 2015, **48**, 517-529.

Berner, U.R., Evolution of pore water chemistry during degradation of cement in a radioactive waste repository environment, Waste Manage., 1992, **12**, 201-219.

Bernstein, L., Roy, J., Delhotal, K.C., Harnisch, J., Matsuhashi, R., Price, L., Tanaka, K., Worrell, E., Yamba, F. and Fengqi, Z., Industry, in: Climate change 2007: mitigation. Contribution of working group III to the fourth assessment report of the Intergovernmental Panel on Climate Change, Metz, B., Davidson, O.R., Bosch, P.R., Dave, R. and Meyer, L.A. (Eds.), 2007, Cambridge University Press, Cambridge, United Kingdom.

Bhattacharjee, U. and Kandpal, T.C., Potential of fly ash utilisation in India, Energy, 2002, **27**, 151-166.

Biagioni, C., Bonaccorsi, E., Merlino, S. and Bersani, D., New data on the thermal behavior of 14 Å tobermorite, Cem. Concr. Res., 2013, **49**, 48-54.

Blanc, P., Bourbon, X., Lassin, A. and Gaucher, E.C., Chemical model for cement-based materials: temperature dependence of thermodynamic functions for nanocrystalline and crystalline C-S-H phases, Cem. Concr. Res., 2010a, **40**, 851-866.

Blanc, P., Bourbon, X., Lassin, A. and Gaucher, E.C., Chemical model for cement-based materials: thermodynamic data assessment for phases other than C–S–H, Cem. Concr. Res., 2010b, **40**, 1360-1374.

Bonaccorsi, E., Merlino, S. and Taylor, H.F.W., The crystal structure of jennite, $Ca_9Si_6O_{18}(OH)_6 \cdot 8H_2O$, Cem. Concr. Res., 2004, **34**, 1481-1488.

Bonaccorsi, E., Merlino, S. and Kampf, A.R., The crystal structure of tobermorite 14 Å (plombierite), a C-S-H phase, J. Am. Ceram. Soc., 2005, **88**, 505-512.

Bonk, F., Schneider, J., Cincotto, M.A. and Panepucci, H., Characterization by multinuclear high-resolution NMR of hydration products in activated blast-furnace slag pastes, J. Am. Ceram. Soc., 2003, **86**, 1712-1719.

Brough, A.R. and Atkinson, A., Sodium silicate-based, alkali-activated slag mortars - part I. Strength, hydration and microstructure, Cem. Concr. Res., 2002, **32**, 865-879.

Brunet, F., Bertani, P., Charpentier, T., Nonat, A. and Virlet, J., Application of $^{29}Si$ homonuclear and $^{1}H–^{29}Si$ heteronuclear NMR correlation to structural studies of calcium silicate hydrates, J. Phys. Chem. B, 2004, **108**, 15494-15502.

Burciaga-Díaz, O. and Escalante-García, J.I., Structure, mechanisms of reaction, and strength of an alkali-activated blast-furnace slag, J. Am. Ceram. Soc., 2013, **96**, 3939-3948.

Bury, C.R. and Redd, R., The system sodium carbonate-calcium carbonate-water, J. Chem. Soc., 1933, 1160-1162.

Chappex, T. and Scrivener, K., Alkali fixation of C-S-H in blended cement pastes and its relation to alkali silica reaction, Cem. Concr. Res., 2012, **42**, 1049-1054.

Chase, M.W., Jr., NIST-JANAF thermochemical tables, fourth edition, 1998, J. Phys. Chem. Ref. Data.

Chen, J.J., Thomas, J.J., Taylor, H.F.W. and Jennings, H.M., Solubility and structure of calcium silicate hydrate, Cem. Concr. Res., 2004, **34**, 1499-1519.

Chen, W. and Brouwers, H.J.H., The hydration of slag, part 1: reaction models for alkali-activated slag, J. Mater. Sci., 2007, **42**, 428-443.

Choy, C.F., Revisiting the 'Bon curve', Constr. Manage. Econ., 2011, **29**, 695-712.

Cong, X. and Kirkpatrick, R.J., $^{29}$Si MAS NMR study of the structure of calcium silicate hydrate, Adv. Cem. Based Mater., 1996a, **3**, 144-156.

Cong, X. and Kirkpatrick, R.J., $^{29}$Si and $^{17}$O NMR investigation of the structure of some crystalline calcium silicate hydrates, Adv. Cem. Based Mater., 1996b, **3**, 133-143.

Conway, B.E., Ionic hydration in chemistry and biophysics, 1981, Elsevier Scientific, Amsterdam.

Courault, A.C., Simulation expérimentale des C-S-H dans les bétons modernes: étude de la composition et des propriétés à l'équilibre dans des milieux complexes, 2000, Université de Bourgogne, Dijon.

d'Espinose de Lacaillerie, J.-B., Fretigny, C. and Massiot, D., MAS NMR spectra of quadrupolar nuclei in disordered solids: the Czjzek model, J. Magn. Reson., 2008, **192**, 244-251.

Dai, Z., Tran, T.T. and Skibsted, J., Aluminum incorporation in the C–S–H phase of white Portland cement–metakaolin blends studied by $^{27}$Al and $^{29}$Si MAS NMR spectroscopy, J. Am. Ceram. Soc., 2014, **97**, 2662-2671.

Davidovits, J., Geopolymers - inorganic polymeric new materials, J. Therm. Anal., 1991, **37**, 1633-1656.

Davies, R.H., Gisby, J.A., Dinsdale, A., Tyrer, M., Walker, C.S. and Glasser, F.P., Thermodynamic modelling of phase equilibria in cement systems: multiple sublattice model for solids in equilibrium with non-ideal aqueous phase, Adv. Appl. Ceram., 2014, **113**, 509-516.

de Wolff, P.M., The crystal structure of artinite, $Mg_2(OH)_2CO_3 \cdot 3H_2O$, Acta Crystallogr., 1952, **5**, 286-287.

Dickens, B. and Brown, W.E., Crystal structures of $CaNa_2(CO_3)_2 \cdot 5H_2O$, synthetic gaylussite, and $CaNa_2(CO_3)_2 \cdot 2H_2O$, synthetic pirssonite, Inorg. Chem., 1969, **8**, 2093-2103.

Dickson, C.L., Brew, D.R.M. and Glasser, F.P., Solubilities of $CaO\text{-}SiO_2\text{-}H_2O$ phases at 25°, 55° and 85°C, Adv. Cem. Res., 2004, **16**, 35-43.

Dilnesa, B.Z., Lothenbach, B., Renaudin, G., Wichser, A. and Kulik, D., Synthesis and characterization of hydrogarnet $Ca_3(Al_xFe_{1-x})_2(SiO_4)_y(OH)_{4(3-y)}$, Cem. Concr. Res., 2014, **59**, 96-111.

Duchesne, J. and Reardon, E.J., Measurement and prediction of portlandite solubility in alkali solutions, Cem. Concr. Res., 1995, **25**, 1043-1053.

Duxson, P., Provis, J.L., Lukey, G.C., Separovic, F. and van Deventer, J.S.J., $^{29}Si$ NMR study of structural ordering in aluminosilicate geopolymer gels, Langmuir, 2005, **21**, 3028-3036.

Duxson, P., Fernandez-Jimenez, A., Provis, J.L., Lukey, G.C., Palomo, A. and van Deventer, J.S.J., Geopolymer technology: the current state of the art, J. Mater. Sci., 2007, **42**, 2917-2933.

Dyson, H.M., Richardson, I.G. and Brough, A.R., A combined $^{29}Si$ MAS NMR and selective dissolution technique for the quantitative evaluation of hydrated blast furnace slag cement blends, J. Am. Ceram. Soc., 2007, **90**, 598-602.

Engelhardt, G. and Michel, D., High-resolution solid-state NMR of silicates and zeolites, 1st ed., 1987, John Wiley & Sons, Chichester.

Engelhardt, G. and Koller, H., A simple procedure for the determination of the quadrupole interaction parameters and isotropic chemical shifts from magic angle spinning NMR spectra of half-integer spin nuclei in solids, Magn. Reson. Chem., 1991, **29**, 941-945.

Escalante-García, J.I. and Sharp, J.H., Effect of temperature on the hydration of the main clinker phases in portland cements: part I, neat cements, Cem. Concr. Res., 1998, **28**, 1245-1257.

Faucon, P., Delagrave, A., Petit, J.C., Richet, C., Marchand, J.M. and Zanni, H., Aluminum incorporation in calcium silicate hydrates (C-S-H) depending on their Ca/Si ratio, J. Phys. Chem. B, 1999a, **103**, 7796-7802.

Faucon, P., Petit, J.C., Charpentier, T., Jacquinot, J.F. and Adenot, F., Silicon substitution for aluminum in calcium silicate hydrates, J. Am. Ceram. Soc., 1999b, **82**, 1307-1312.

Fernández-Jiménez, A. and Palomo, A., Characterisation of fly ashes. Potential reactivity as alkaline cements, Fuel, 2003, **82**, 2259-2265.

Fernández-Jiménez, A. and Puertas, F., Effect of activator mix on the hydration and strength behaviour of alkali-activated slag cements, Adv. Cem. Res., 2003, **15**, 129-136.

Fernández-Jiménez, A., Puertas, F., Sobrados, I. and Sanz, J., Structure of calcium silicate hydrates formed in alkaline-activated slag: Influence of the type of alkaline activator, J. Am. Ceram. Soc., 2003, **86**, 1389-1394.

Flint, E.P. and Wells, L.S., Study of the system $CaO-SiO_2-H_2O$ at 30°C and of the reaction of water on the anhydrous calcium silicates, J. Res. Natl. Bur. Stand., 1934, **12**, 751-783.

Fujii, K. and Kondo, W., Heterogeneous equilibrium of calcium silicate hydrate in water at 30°C, J. Chem. Soc., Dalton Trans., 1981, 645-651.

Fyfe, C.A., Gobbi, G.C., Hartman, J.S., Klinowski, J. and Thomas, J.M., Solid-state magic-angle spinning. Aluminum-27 nuclear magnetic resonance studies of zeolites using a 400-MHz high-resolution spectrometer, J. Phys. Chem., 1982, **86**, 1247-1250.

Gallucci, E., Zhang, X. and Scrivener, K.L., Effect of temperature on the microstructure of calcium silicate hydrate (C-S-H), Cem. Concr. Res., 2013, **53**, 185-195.

Gao, W. and Li, Z., Solubility and $K_{SP}$ of $Mg_4Al_2(OH)_{14}\cdot 3H_2O$ at the various ionic strengths, Hydrometallurgy, 2012, **117–118**, 36-46.

García-Lodeiro, I., Palomo, A., Fernández-Jiménez, A. and MacPhee, D.E., Compatibility studies between N-A-S-H and C-A-S-H gels. Study in the ternary diagram $Na_2O$-CaO-$Al_2O_3$-$SiO_2$-$H_2O$, Cem. Concr. Res., 2011, **41**, 923-931.

Gisby, J.A., Davies, R.H., Dinsdale, A.T., Tyrer, M., Glasser, F.P., Hill, J., Livesey, P. and Walker, C., C-S-H solubility modeling at different temperatures, in: Proceedings of the 12th International Congress on the Chemistry of Cement, 2007, Cement Association of Canada, Montreal.

Glasser, F.P., Lachowski, E.E. and Macphee, D.E., Compositional model for calcium silicate hydrate (C-S-H) gels, their solubilities, and free energies of formation, J. Am. Ceram. Soc., 1987, **70**, 481-485.

Glasser, F.P. and Atkins, M., Cements in radioactive waste disposal, MRS Bull., 1994, **19**, 33-38.

Glasser, F.P., Tyrer, M., Quillin, K., Ross, D., Pedersen, J., Goldthorpe, K., Bennett, D. and Atkins, M., The chemistry of blended cements and backfills intended for use in radioactive waste disposal: R&D technical report P98, 1999, Environment Agency, Bristol.

Glasser, F.P., Pedersen, J., Goldthorpe, K. and Atkins, M., Solubility reactions of cement components with NaCl solutions: I. $Ca(OH)_2$ and C-S-H, Adv. Cem. Res., 2005, **17**, 57-64.

Glynn, P.D. and Reardon, E.J., Solid-solution aqueous-solution equilibria: thermodynamic theory and representation, Am. J. Sci., 1990, **290**, 164-201.

Glynn, P.D., MBSSAS: a code for the computation of Margules parameters and equilibrium relations in binary solid-solution aqueous-solution systems, Computat. Geosci., 1991, **17**, 907-966.

Gmira, A., Pellenq, R.J.M., Rannou, I., Duclaux, L., Clinard, C., Cacciaguerra, T., Lequeux, N. and Damme, H.V., A structural study of dehydration/rehydration of tobermorite, a model cement compound, in: Characterization of porous solids VI: proceedings of the 6$^{th}$ international symposium on the characterization of porous solids (COPS-VI), Rodriguez-Reinoso, F., McEnaney, B., Rouquerol, J. and Unger, K. (Eds.), 2002, Elsevier, Alicante, pp. 601-608.

Graf, D.L. and Bradley, W.F., The crystal structure of huntite, $Mg_3Ca(CO_3)_4$, Acta Crystallogr., 1962, **15**, 238-242.

Grangeon, S., Claret, F., Linard, Y. and Chiaberge, C., X-ray diffraction: a powerful tool to probe and understand the structure of nanocrystalline calcium silicate hydrates, Acta Crystallogr. B, 2013, **69**, 465-473.

Greenberg, S.A. and Chang, T.N., Investigation of the colloidal hydrated calcium silicates. II. Solubility relationships in the calcium oxide-silica-water system at 25°C, J. Phys. Chem., 1965, **69**, 182-188.

Gruskovnjak, A., Lothenbach, B., Holzer, L., Figi, R. and Winnefeld, F., Hydration of alkali-activated slag: comparison with ordinary Portland cement, Adv. Cem. Res., 2006, **18**, 119-128.

Grutzeck, M., Benesi, A. and Fanning, B., Silicon-29 magic angle spinning nuclear magnetic resonance study of calcium silicate hydrates, J. Am. Ceram. Soc., 1989, **72**, 665-668.

Haas, J., Pochard, I. and Nonat, A., Model for equilibrium, surface chemistry and interface properties of hydrates in the $CaO\text{-}SiO_2\text{-}Al_2O_3\text{-}H_2O$ system, in: Proceedings of the 13th International Congress on the Chemistry of Cement, 2011, Madrid.

Haas, J., Pochard, I. and Nonat, A., C-A-S-H synthesis and thermodynamics modelling in $CaO\text{-}Al_2O_3\text{-}SiO_2\text{-}H_2O$ system, in: Proceedings of the 32nd Cement and Concrete Science Conference, 2012, Belfast.

Haas, J. and Nonat, A., From C–S–H to C–A–S–H: Experimental study and thermodynamic modelling, 2015, **68**, 124-138.

Habert, G., Billard, C., Rossi, P., Chen, C. and Roussel, N., Cement production technology improvement compared to factor 4 objectives, Cem. Concr. Res., 2010, **40**, 820-826.

Hamid, S.A., The crystal structure of the 11 Å natural tobermorite $Ca_{2.25}[Si_3O_{7.5}(OH)_{1.5}]\cdot 1H_2O$, Z. Kristallogr., 1981, **154**, 189-198.

Harris, A.W., Manning, M.C., Tearle, W.M. and Tweed, C.J., Testing of models of the dissolution of cements—leaching of synthetic CSH gels, Cem. Concr. Res., 2002, **32**, 731-746.

Harris, R.K., Samadi-Maybodi, A. and Smith, W., The incorporation of aluminum into silicate ions in alkaline aqueous solutions, studied by $^{27}Al$ NMR, Zeolites, 1997, **19**, 147-155.

Helgeson, H.C., Delany, J.M. and Nesbitt, H.W., Summary and critique of the thermodynamic properties of rock-forming minerals, Am. J. Sci., 1978, **278-A**, 1-229.

Helgeson, H.C., Kirkham, D.H. and Flowers, G.C., Theoretical prediction of the thermodynamic behavior of aqueous electrolytes at high pressures and temperatures: IV. Calculation of activity coefficients, osmotic coefficients, and apparent molal and standard and relative partial molal properties to 600$^{o}$C and 5 kb, Am. J. Sci., 1981, **281**, 1249-1516.

Hemingway, B.S. and Robie, R.A., The heat capacities at low temperatures and entropies at 298.15K of huntite, $CaMg_3(CO_3)_4$, and artinite, $Mg_2(OH)_2CO_3 \cdot 3H_2O$, Am. Mineral., 1972, **57**, 1754-1767.

Hill, R.J., Canterford, J.H. and Moyle, F.J., New data for lansfordite, Mineral. Mag., 1982, **46**, 453-457.

Hillert, M. and Staffansson, L.-I., The regular solution model for stoichiometric phases and ionic melts, Acta Chem. Scand., 1970, **24**, 3618-3626.

Hillert, M., Phase equilibria, phase diagrams and phase transformations: their thermodynamic basis, 1998, Cambridge University Press, Cambridge.

Hong, S.Y. and Glasser, F.P., Alkali binding in cement pastes: part I. The C-S-H phase, Cem. Concr. Res., 1999, **29**, 1893-1903.

Hong, S.Y. and Glasser, F.P., Alkali sorption by C-S-H and C-A-S-H gels: part II. Role of alumina, Cem. Concr. Res., 2002, **32**, 1101-1111.

Houston, J., Maxwell, R. and Carroll, S., Transformation of meta-stable calcium silicate hydrates to tobermorite: reaction kinetics and molecular structure from XRD and NMR spectroscopy, Geochem. Trans., 2009, **10**, 1-14.

Hu, X., Provis, J.L., Van Deventer, J.S.J. and Krivenko, P.V., Characterization of aged slag concretes, ACI Mater. J., 2008, **105**, 131-139.

Hummel, W., Berner, U., Curti, E., Pearson, F.J. and Thoenen, T., Nagra/PSI Chemical Thermodynamic Database 01/01, 2002, Universal Publishers, Parkland, Florida.

Ismail, I., Bernal, S.A., Provis, J.L., San Nicolas, R., Hamdan, S. and van Deventer, J.S.J., Modification of phase evolution in alkali-activated blast furnace slag by the incorporation of fly ash, Cem. Concr. Compos., 2014, **45**, 125-135.

Jackson, M.D., Chae, S.R., Mulcahy, S.R., Meral, C., Taylor, R., Li, P., Emwas, A.-H., Moon, J., Yoon, S., Vola, G., Wenk, H.-R. and Monteiro, P.J.M., Unlocking the secrets of Al-tobermorite in Roman seawater concrete, Am. Mineral., 2013, **98**, 1669-1687.

Jennings, H.M., Aqueous solubility relationships for two types of calcium silicate hydrate, J. Am. Ceram. Soc., 1986, **69**, 614-618.

Jennings, H.M., Refinements to colloid model of C-S-H in cement: CM-II, Cem. Concr. Res., 2008, **38**, 275-289.

Jennings, H.M. and Bullard, J.W., From electrons to infrastructure: engineering concrete from the bottom up, Cem. Concr. Res., 2011, **41**, 727-735.

Johnson, C.A. and Glasser, F.P., Hydrotalcite-like minerals ($M_2Al(OH)_6(CO_3)_{0.5}\cdot XH_2O$, where M = Mg, Zn, Co, Ni) in the environment: synthesis, characterization and thermodynamic stability, Clays Clay Miner., 2003, **51**, 1-8.

Johnson, G.K., Flotow, H.E. and O'Hare, P.A.G., Thermodynamic studies of zeolites; analcime and dehydrated analcime, Am. Mineral., 1982, **67**, 736-748.

Johnson, G.K., Flotow, H.E., O'Hare, P.A.G. and Wise, W.S., Thermodynamic studies of zeolites; natrolite, mesolite and scolecite, Am. Mineral., 1983, **68**, 1134-1145.

Johnson, J.W., Oelkers, E.H. and Helgeson, H.C., SUPCRT92: A software package for calculating the standard molal thermodynamic properties of minerals, gases, aqueous species, and reactions from 1 to 5000 bar and 0 to 1000°C, Comput. Geosci., 1992, **18**, 899-947.

Juenger, M.C.G., Winnefeld, F., Provis, J.L. and Ideker, J.H., Advances in alternative cementitious binders, Cem. Concr. Res., 2011, **41**, 1232-1243.

Kalousek, G.L., Studies of portions of the quaternary system soda-lime-silica-water at 25°C, J. Res. Natl. Bur. Stand., 1944, **32**, 285-302.

Kalousek, G.L., Application of differential thermal analysis in a study of the system lime-silica-water, in: Proceedings of the Third International Symposium on the Chemistry of Cement, 1952, Cement and Concrete Association, London, pp. 296-311.

Kalousek, G.L., Crystal chemistry of hydrous calcium silicates: I, substitution of aluminum in lattice of tobermorite, J. Am. Ceram. Soc., 1957, **40**, 74-80.

Kirkpatrick, R.J., MAS NMR-spectroscopy of minerals and glasses, Rev. Mineral., 1988, **18**, 341-403.

Kirkpatrick, R.J., Kalinichev, A.G., Hou, X. and Struble, L., Experimental and molecular dynamics modeling studies of interlayer swelling: water incorporation in kanemite and ASR gel, Mater. Struct., 2005, **38**, 449-458.

Kiseleva, I., Navrotsky, A., Belitsky, I. and Fursenko, B., Thermochemical study of calcium zeolites—heulandite and stilbite, Am. Mineral., 2001, **86**, 448-455.

Klinowski, J., Nuclear magnetic resonance studies of zeolites, Prog. Nucl. Magn. Reson. Spectr., 1984, **16**, 237-309.

Kocaba, V., Gallucci, E. and Scrivener, K.L., Methods for determination of degree of reaction of slag in blended cement pastes, Cem. Concr. Res., 2012, **42**, 511-525.

Königsberger, E., Königsberger, L.-C. and Gamsjäger, H., Low-temperature thermodynamic model for the system $Na_2CO_3$−$MgCO_3$−$CaCO_3$−$H_2O$, Geochim. Cosmochim. Acta, 1999, **63**, 3105-3119.

Kulik, D.A. and Kersten, M., Aqueous solubility diagrams for cementitious waste stabilization systems: II. End-member stoichiometries of ideal calcium silicate hydrate solid solutions, J. Am. Ceram. Soc., 2001, **84**, 3017-3026.

Kulik, D.A. and Kersten, M., Aqueous solubility diagrams for cementitious waste stabilization systems. 4. A carbonation model for Zn-doped calcium silicate hydrate by Gibbs energy minimization, Environ. Sci. Technol., 2002, **36**, 2926-2931.

Kulik, D.A., Improving the structural consistency of C-S-H solid solution thermodynamic models, Cem. Concr. Res., 2011, **41**, 477-495.

Kulik, D.A., Wagner, T., Dmytrieva, S.V., Kosakowski, G., Hingerl, F.F., Chudnenko, K.V. and Berner, U., GEM-Selektor geochemical modeling package: revised algorithm and GEMS3K numerical kernel for coupled simulation codes, Comput. Geosci., 2013, **17**, 1-24.

Kuzel, H.J., Crystallographic data and thermal decomposition of synthetic gehlenite hydrate $2CaO.Al_2O_3.SiO_2.8H_2O$, Nueus. Jb. Miner. Monat., 1976, **148**, 319-325.

Kwan, S., LaRosa, J. and Grutzeck, M.W., $^{29}Si$ and $^{27}Al$ MAS NMR study of strätlingite, J. Am. Ceram. Soc., 1995, **78**, 1921-1926.

L'Hôpital, E., Lothenbach, B., Le Saoût, G., Kulik, D.A. and Scrivener, K., Incorporation of aluminium in calcium silicate hydrates, Cem. Concr. Res., submitted.

L'Hôpital, E., Aluminium and alkali uptake in calcium silicate hydrate (C-S-H), 2014, Ph.D. Thesis, École Polytechnique Fédérale de Lausanne, Lausanne.

Labbez, C., Pochard, I., Jönsson, B. and Nonat, A., C-S-H/solution interface: experimental and Monte Carlo studies, Cem. Concr. Res., 2011, **41**, 161-168.

Lager, G.A., Armbruster, T. and Faber, J., Neutron and X-ray diffraction study of hydrogarnet $Ca_3Al_2(O_4H_4)_3$, Am. Mineral., 1987, **72**, 756-765.

Langner, R., Fechtelkord, M., García, A., Palin, E.J. and López-Solano, J., Aluminum ordering and clustering in Al-rich synthetic phlogopite: $\{^{1}H\} \rightarrow {}^{29}Si$ CPMAS HETCOR spectroscopy and atomistic calculations, Am. Mineral., 2012, **97**, 341-352.

Le Saoût, G., Ben Haha, M., Winnefeld, F. and Lothenbach, B., Hydration degree of alkali-activated slags: a $^{29}Si$ NMR study, J. Am. Ceram. Soc., 2011, **94**, 4541-4547.

Lee, Y., Lee, Y. and Seoung, D., Natrolite may not be a "soda-stone" anymore: structural study of fully K-, Rb-, and Cs-exchanged natrolite, Am. Mineral., 2010, **95**, 1636-1641.

Leemann, A., Le Saout, G., Winnefeld, F., Rentsch, D. and Lothenbach, B., Alkali-silica reaction: the Influence of calcium on silica dissolution and the formation of reaction products, J. Am. Ceram. Soc., 2011, **94**, 1243-1249.

Lloyd, R.R., Provis, J.L. and van Deventer, J.S.J., Pore solution composition and alkali diffusion in inorganic polymer cement, Cem. Concr. Res., 2010, **40**, 1386-1392.

Locock, A.J., An Excel spreadsheet to recast analyses of garnet into end-member components, and a synopsis of the crystal chemistry of natural silicate garnets, Comput. Geosci., 2008, **34**, 1769-1780.

Loewenstein, W., The distribution of aluminum in the tetrahedra of silicates and aluminates, Am. Mineral., 1954, **39**, 92-96.

Lognot, I., Klur, I. and Nonat, A., NMR and infrared spectroscopies of C-S-H and Al-substituted C-S-H synthesised in alkaline solutions, in: Nuclear magnetic resonance spectroscopy of cement-based materials, Colombet, P., Zanni, H., Grimmer, A.-R. and Sozzani, P. (Eds.), 1998, Springer, Berlin, pp. 189-196.

Lothenbach, B. and Winnefeld, F., Thermodynamic modelling of the hydration of Portland cement, Cem. Concr. Res., 2006, **36**, 209-226.

Lothenbach, B. and Gruskovnjak, A., Hydration of alkali-activated slag: thermodynamic modelling, Adv. Cem. Res., 2007, **19**, 81-92.

Lothenbach, B., Winnefeld, F., Alder, C., Wieland, E. and Lunk, P., Effect of temperature on the pore solution, microstructure and hydration products of Portland cement pastes, Cem. Concr. Res., 2007, **37**, 483-491.

Lothenbach, B., Le Saout, G., Gallucci, E. and Scrivener, K., Influence of limestone on the hydration of Portland cements, Cem. Concr. Res., 2008a, **38**, 848-860.

Lothenbach, B., Matschei, T., Möschner, G. and Glasser, F.P., Thermodynamic modelling of the effect of temperature on the hydration and porosity of Portland cement, Cem. Concr. Res., 2008b, **38**, 1-18.

Lothenbach, B., Thermodynamic equilibrium calculations in cementitious systems, Mater. Struct., 2010, **43**, 1413-1433.

Lothenbach, B., Scrivener, K. and Hooton, R.D., Supplementary cementitious materials, Cem. Concr. Res., 2011, **41**, 1244-1256.

Lothenbach, B., Le Saout, G., Ben Haha, M., Figi, R. and Wieland, E., Hydration of a low-alkali CEM III/B–$SiO_2$ cement (LAC), Cem. Concr. Res., 2012a, **42**, 410-423.

Lothenbach, B., Pelletier-Chaignat, L. and Winnefeld, F., Stability in the system $CaO–Al_2O_3–H_2O$, Cem. Concr. Res., 2012b, **42**, 1621-1634.

Lothenbach, B., Rentsch, D. and Wieland, E., Hydration of a silica fume blended low-alkali shotcrete cement, Phys. Chem. Earth, 2014, **70–71**, 3-16.

Love, C.A., Richardson, I.G. and Brough, A.R., Composition and structure of C–S–H in white Portland cement–20% metakaolin pastes hydrated at 25 °C, Cem. Concr. Res., 2007, **37**, 109-117.

MacKenzie, K.J.D., Meinhold, R.H., Sherrif, B.L. and Xu, Z., $^{27}$Al and $^{25}$Mg solid-state magic-angle spinning nuclear magnetic resonance study of hydrotalcite and its thermal decomposition sequence, J. Mater. Chem., 1993, **3**, 1263-1269.

Macphee, D.E., Luke, K., Glasser, F.P. and Lachowski, E.E., Solubility and aging of calcium silicate hydrates in alkaline solutions at 25°C, J. Am. Ceram. Soc., 1989, **72**, 646-654.

Manz, O.E., Worldwide production of coal ash and utilization in concrete and other products, Fuel, 1997, **76**, 691-696.

Manzano, H., Dolado, J.S., Griebel, M. and Hamaekers, J., A molecular dynamics study of the aluminosilicate chains structure in Al-rich calcium silicate hydrate (C-S-H) gels, Phys. Status Solidi A, 2008, **205**, 1324-1329.

Manzano, H., Dolado, J.S. and Ayuela, A., Elastic properties of the main species present in Portland cement pastes, Acta Mater., 2009a, **57**, 1666-1674.

Manzano, H., Dolado, J.S. and Ayuela, A., Aluminum incorporation to dreierketten silicate chains, J. Phys. Chem. B, 2009b, **113**, 2832-2839.

Masse, S., Zanni, H., Lecourtier, J., Roussel, J.C. and Rivereau, A., $^{29}$Si solid state NMR study of tricalcium silicate and cement hydration at high temperature, Cem. Concr. Res., 1993, **23**, 1169-1177.

Massiot, D., Fayon, F., Capron, M., King, I., Le Calvé, S., Alonso, B., Durand, J.-O., Bujoli, B., Gan, Z. and Hoatson, G., Modelling one- and two-dimensional solid-state NMR spectra, Magn. Reson. Chem., 2002, **40**, 70-76.

Matschei, T., Lothenbach, B. and Glasser, F.P., The AFm phase in Portland cement, Cem. Concr. Res., 2007a, **37**, 118-130.

Matschei, T., Lothenbach, B. and Glasser, F.P., Thermodynamic properties of Portland cement hydrates in the system $CaO$-$Al_2O_3$-$SiO_2$-$CaSO_4$-$CaCO_3$-$H_2O$, Cem. Concr. Res., 2007b, **37**, 1379-1410.

Matschei, T. and Glasser, F.P., Temperature dependence, 0 to 40 °C, of the mineralogy of Portland cement paste in the presence of calcium carbonate, Cem. Concr. Res., 2010, **40**, 763-777.

McConnell, J.D.C., The hydrated calcium silicates riversideite, tobermorite, and plombierite, Mineral. Mag., 1954, **30**, 293-305.

McLellan, B.C., Williams, R.P., Lay, J., van Riessen, A. and Corder, G.D., Costs and carbon emissions for geopolymer pastes in comparison to ordinary portland cement, J. Cleaner Prod., 2011, **19**, 1080-1090.

Merlino, S., Bonaccorsi, E. and Armbruster, T., Tobermorites: their real structure and order-disorder (OD) character, Am. Mineral., 1999, **84**, 1613-1621.

Merlino, S., Bonaccorsi, E. and Armbruster, T., The real structures of clinotobermorite and tobermorite 9Å: OD character, polytypes, and structural relationships, Eur. J. Mineral., 2000, **12**, 411-429.

Merlino, S., Bonaccorsi, E. and Armbruster, T., The real structure of tobermorite 11Å: normal and anomalous forms, OD character and polytypic modifications, Eur. J. Mineral., 2001, **13**, 577-590.

Mitsuda, T. and Taylor, H.F.W., Normal and anomalous tobermorites, Mineral. Mag., 1978, **42**, 229-235.

Moir, G., Cements, in: Advanced Concrete Technology: Constituent Materials, Newman, J. and Choo, B.S. (Eds.), 2003, Butterworth-Heinemann, Oxford, pp. 1-45.

Moloy, E.C., Liu, Q. and Navrotsky, A., Formation and hydration enthalpies of the hydrosodalite family of materials, Micropor. Mesopor. Mat., 2006, **88**, 283-292.

Monnin, C. and Schott, J., Determination of the solubility products of sodium carbonate minerals and an application to trona deposition in Lake Magadi (Kenya), Geochim. Cosmochim. Acta, 1984, **48**, 571-581.

Morimoto, K., Anraku, S., Hoshino, J., Yoneda, T. and Sato, T., Surface complexation reactions of inorganic anions on hydrotalcite-like compounds, J. Colloid Interf. Sci., 2012, **384**, 99-104.

Möschner, G., Lothenbach, B., Rose, J., Ulrich, A., Figi, R. and Kretzschmar, R., Solubility of Fe–ettringite ($Ca_6[Fe(OH)_6]_2(SO_4)_3 \cdot 26H_2O$), Geochim. Cosmochim. Acta, 2008, **72**, 1-18.

Möschner, G., Lothenbach, B., Winnefeld, F., Ulrich, A., Figi, R. and Kretzschmar, R., Solid solution between Al-ettringite and Fe-ettringite ($Ca_6[Al_{1-x}Fe_x(OH)_6]_2(SO_4)_3 \cdot 26H_2O$), Cem. Concr. Res., 2009, **39**, 482-489.

Muller, A.C.A., Scrivener, K.L., Gajewicz, A.M. and McDonald, P.J., Densification of C–S–H Measured by $^1$H NMR Relaxometry, J. Phys. Chem. C, 2013a, **117**, 403-412.

Muller, A.C.A., Scrivener, K.L., Gajewicz, A.M. and McDonald, P.J., Use of bench-top NMR to measure the density, composition and desorption isotherm of C–S–H in cement paste, Micropor. Mesopor. Mat., 2013b, **178**, 99-103.

Myers, R.J., L'Hôpital, E., Provis, J.L. and Lothenbach, B., Composition-solubility-structure relationships in calcium (alkali) aluminosilicate hydrate (C-(N,K-)A-S-H), in preparation.

Myers, R.J., Bernal, S.A., San Nicolas, R. and Provis, J.L., Generalized structural description of calcium-sodium aluminosilicate hydrate gels: the cross-linked substituted tobermorite model, Langmuir, 2013, **29**, 5294-5306.

Myers, R.J., Bernal, S.A. and Provis, J.L., A thermodynamic model for C-(N-)A-S-H gel: CNASH_ss. Derivation and application, Cem. Concr. Res., 2014, **66**, 27-47.

Myers, R.J., Bernal, S.A., Provis, J.L., Gehman, J.D. and van Deventer, J.S.J., The role of Al in cross-linking of alkali-activated slag cements, J. Am. Ceram. Soc., 2015a, **98**, 996-1004.

Myers, R.J., L'Hôpital, E., Provis, J.L. and Lothenbach, B., Effect of temperature and aluminium on calcium aluminosilicate hydrate chemistry under equilibrium conditions, Cem. Concr. Res., 2015b, **68**, 83-93.

Neuville, D.R., Cormier, L. and Massiot, D., Al environment in tectosilicate and peraluminous glasses: a $^{27}$Al MQ-MAS NMR, Raman, and XANES investigation, Geochim. Cosmochim. Acta, 2004, **68**, 5071-5079.

Ng, S.T., Fan, R.Y.C., Wong, J.M.W., Chan, A.P.C., Chiang, Y.H., Lam, P.T.I. and Kumaraswamy, M., Coping with structural change in construction: experiences gained from advanced economies, 2009, **27**, 165-180.

Nieto, P. and Zanni, H., Polymerization of alkaline-calcium-silicate hydrates obtained by interaction between alkali–silica solutions and calcium compounds. A $^{29}$Si nuclear magnetic resonance study, J. Mater. Sci., 1997, **32**, 3419-3425.

O'Connor, B.H. and Raven, M.D., Application of the Rietveld refinement procedure in assaying powdered mixtures, Powder Diffr., 1988, **3**, 2-6.

Oh, J.E., Clark, S.M., Wenk, H.R. and Monteiro, P.J.M., Experimental determination of bulk modulus of 14Å tobermorite using high pressure synchrotron X-ray diffraction, Cem. Concr. Res., 2012, **42**, 397-403.

Olivier, J.G.J., Janssens-Maenhout, G. and Peters, J.A.H.W., Trends in global $CO_2$ emissions; 2012 report, 2012, PBL Netherlands Environmental Assessment Agency, The Hague.

Palacios, M. and Puertas, F., Effect of carbonation on alkali-activated slag paste, J. Am. Ceram. Soc., 2006, **89**, 3211-3221.

Pardal, X., Pochard, I. and Nonat, A., Experimental study of Si-Al substitution in calcium-silicate-hydrate (C-S-H) prepared under equilibrium conditions, Cem. Concr. Res., 2009, **39**, 637-643.

Pardal, X., Brunet, F., Charpentier, T., Pochard, I. and Nonat, A., $^{27}$Al and $^{29}$Si solid-state NMR characterization of calcium-aluminosilicate-hydrate, Inorg. Chem., 2012, **51**, 1827-1836.

Passaglia, E. and Rinaldi, R., Katoite, a new member of the $Ca_3Al_2(SiO_4)_3$-$Ca_3Al_2(OH)_{12}$ series and a new nomenclature for the hydrogrossular group of minerals, Bull. Minéral., 1984, **107**, 605-618.

Pegado, L., Labbez, C. and Churakov, S.V., Mechanism of aluminium incorporation into C-S-H from ab initio calculations, J. Mater. Chem. A, 2014, **2**, 3477-3483.

Pellenq, R.J.M., Kushima, A., Shahsavari, R., Van Vliet, K.J., Buehler, M.J., Yip, S. and Ulm, F.J., A realistic molecular model of cement hydrates, P. Natl. Acad. Sci. USA, 2009, **106**, 16102-16107.

Pitzer, K.S., Ion interaction approach: theory and data correlation, in: Activity Coefficients in Electrolyte Solutions, 1991, CRC Press, Boca Raton, pp. 75-153.

Provis, J.L., Duxson, P., Lukey, G.C. and Van Deventer, J.S.J., Statistical thermodynamic model for Si/Al ordering in amorphous aluminosilicates, Chem. Mater., 2005a, **17**, 2976-2986.

Provis, J.L., Lukey, G.C. and van Deventer, J.S.J., Do geopolymers actually contain nanocrystalline zeolites? A reexamination of existing results, Chem. Mater., 2005b, **17**, 3075-3085.

Provis, J.L., Myers, R.J., White, C.E., Rose, V. and van Deventer, J.S.J., X-ray microtomography shows pore structure and tortuosity in alkali-activated binders, Cem. Concr. Res., 2012, **42**, 855-864.

Provis, J.L., Geopolymers and other alkali activated materials: why, how, and what?, Mater. Struct., 2014, **47**, 11-25.

Provis, J.L. and Bernal, S.A., Geopolymers and related alkali-activated materials, Annu. Rev. Mater. Res., 2014, **44**, 299-327.

Puertas, F., Fernández-Jiménez, A. and Blanco-Varela, M.T., Pore solution in alkali-activated slag cement pastes. Relation to the composition and structure of calcium silicate hydrate, Cem. Concr. Res., 2004, **34**, 139-148.

Puertas, F., Palacios, M., Manzano, H., Dolado, J.S., Rico, A. and Rodríguez, J., A model for the C-A-S-H gel formed in alkali-activated slag cements, J. Eur. Ceram. Soc., 2011, **31**, 2043-2056.

Purdon, A.O., The action of alkalis on blast-furnace slag, J. Soc. Chem. Ind.-Trans. Commun., 1940, **59**, 191-202.

Purnell, P., Material nature versus structural nurture: The embodied carbon of fundamental structural elements, Environ. Sci. Technol., 2012, **46**, 454-461.

Rashad, A.M., Bai, Y., Basheer, P.A.M., Milestone, N.B. and Collier, N.C., Hydration and properties of sodium sulfate activated slag, Cem. Concr. Compos., 2013, **37**, 20-29.

Rawal, A., Smith, B.J., Athens, G.L., Edwards, C.L., Roberts, L., Gupta, V. and Chmelka, B.F., Molecular silicate and aluminate species in anhydrous and hydrated cements, J. Am. Ceram. Soc., 2010, **132**, 7321-7337.

Reardon, E.J., An ion interaction model for the determination of chemical equilibria in cement/water systems, Cem. Concr. Res., 1990, **20**, 175-192.

Rejmak, P., Dolado, J.S., Stott, M.J. and Ayuela, A., $^{29}$Si NMR in cement: a theoretical study on calcium silicate hydrates, J. Phys. Chem. C, 2012, **116**, 9755-9761.

Renaudin, G., Russias, J., Leroux, F., Cau dit Coumes, C. and Frizon, F., Structural characterization of C-S-H and C-A-S-H samples - part II: local

environment investigated by spectroscopic analyses, J. Solid State Chem., 2009a, **182**, 3320-3329.

Renaudin, G., Russias, J., Leroux, F., Frizon, F. and Cau dit Coumes, C., Structural characterization of C-S-H and C-A-S-H samples - part I: long-range order investigated by Rietveld analyses, J. Solid State Chem., 2009b, **182**, 3312-3319.

Richardson, I., Model structures for C-(A)-S-H(I), Acta Crystallogr. B., 2014, **70**, 903-923.

Richardson, I.G. and Groves, G.W., Microstructure and microanalysis of hardened cement pastes involving ground granulated blast-furnace slag, J Mater Sci, 1992a, **27**, 6204-6212.

Richardson, I.G. and Groves, G.W., Models for the composition and structure of calcium silicate hydrate (CSH) gel in hardened tricalcium silicate pastes, Cem. Concr. Res., 1992b, **22**, 1001-1010.

Richardson, I.G., Brough, A.R., Brydson, R., Groves, G.W. and Dobson, C.M., Location of aluminum in substituted calcium silicate hydrate (C-S-H) gels as determined by $^{29}$Si and $^{27}$Al NMR and EELS, J. Am. Ceram. Soc., 1993, **76**, 2285-2288.

Richardson, I.G. and Groves, G.W., Microstructure and microanalysis of hardened ordinary Portland cement pastes, J. Mater. Sci., 1993a, **28**, 265-277.

Richardson, I.G. and Groves, G.W., The incorporation of minor and trace elements into calcium silicate hydrate (C-S-H) gel in hardened cement pastes, Cem. Concr. Res., 1993b, **23**, 131-138.

Richardson, I.G. and Groves, G.W., A reply to discussions by H.F.W. Taylor of the papers "Models for the composition and structure of calcium silicate hydrate (CSH) gel in hardened tricalcium silicate pastes" and "the incorporation of minor and trace elements into calcium silicate hydrate (CSH) gel in hardened cement pastes", Cem. Concr. Res., 1993c, **23**, 999-1000.

Richardson, I.G., Brough, A.R., Groves, G.W. and Dobson, C.M., The characterization of hardened alkali-activated blast-furnace slag pastes and the nature of the calcium silicate hydrate (C-S-H) phase, Cem. Concr. Res., 1994, **24**, 813-829.

Richardson, I.G., Nature of C-S-H in hardened cements, Cem. Concr. Res., 1999, **29**, 1131-1147.

Richardson, I.G., Tobermorite/jennite- and tobermorite/calcium hydroxide-based models for the structure of C-S-H: applicability to hardened pastes of tricalcium silicate, β-dicalcium silicate, Portland cement, and blends of Portland cement with blast-furnace slag, metakaolin, or silica fume, Cem. Concr. Res., 2004, **34**, 1733-1777.

Richardson, I.G., The calcium silicate hydrates, Cem. Concr. Res., 2008, **38**, 137-158.

Richardson, I.G., The importance of proper crystal-chemical and geometrical reasoning demonstrated using layered single and double hydroxides, Acta Crystallogr. B, 2013a, **69**, 150-162.

Richardson, I.G., Clarification of possible ordered distributions of trivalent cations in layered double hydroxides and an explanation for the observed variation in the lower solid-solution limit, Acta Crystallogr. B., 2013b, **69**, 629-633.

Rinaldi, R., Sacerdoti, M. and Passaglia, E., Strätlingite: crystal structure, chemistry, and a reexamination of its polytype vertumnite, Eur. J. Mineral., 1990, **2**, 841-849.

Robie, R.A. and Hemingway, B.S., Thermodynamic properties of minerals and related substances at 298.15 K and 1 bar ($10^5$ Pascals) pressure and at higher temperatures, 1995, United States Government Printing Office, Washington D.C.

Roller, P.S. and Ervin, G., The system calcium oxide-silica-water at 30°C. The association of silicate ion in dilute alkaline solution, J. Am. Chem. Soc., 1940, **62**, 461-471.

Roy, A., Sulfur speciation in granulated blast furnace slag: an X-ray absorption spectroscopic investigation, Cem. Concr. Res., 2009, **39**, 659-663.

Roy, D.M., Alkali-activated cements: opportunities and challenges, Cem. Concr. Res., 1999, **29**, 249-254.

Rozov, K., Stability and solubility of hydrotalcite-pyroaurite solid solutions: synthesis, characterization and thermodynamic modelling, 2010, Ph.D. Thesis, The University of Bern, Bern.

Rozov, K.B., Berner, U., Kulik, D.A. and Diamond, L.W., Solubility and thermodynamic properties of carbonate-bearing hydrotalcite-pyroaurite solid solutions with a 3:1 Mg/(Al+Fe) mole ratio, Clays Clay Miner., 2011, **59**, 215-232.

Runčevski, T., Dinnebier, R.E., Magdysyuk, O.V. and Pöllmann, H., Crystal structures of calcium hemicarboaluminate and carbonated calcium hemicarboaluminate from synchrotron powder diffraction data, Acta Crystallogr. B, 2012, **68**, 493-500.

Sakulich, A.R., Anderson, E., Schauer, C. and Barsoum, M.W., Mechanical and microstructural characterization of an alkali-activated slag/limestone fine aggregate concrete, Constr. Build. Mater., 2009, **23**, 2951-2957.

Sakulich, A.R., Miller, S. and Barsoum, M.W., Chemical and microstructural characterization of 20-month-old alkali-activated slag cements, J. Am. Ceram. Soc., 2010, **93**, 1741-1748.

Savage, D., Soler, J.M., Yamaguchi, K., Walker, C., Honda, A., Inagaki, M., Watson, C., Wilson, J., Benbow, S., Gaus, I. and Rueedi, J., A comparative study of the modelling of cement hydration and cement–rock laboratory experiments, Appl. Geochem., 2011, **26**, 1138-1152.

Schilling, P.J., Butler, L.G., Roy, A. and Eaton, H.C., $^{29}$Si and $^{27}$Al MAS-NMR of NaOH-activated blast-furnace slag, J. Am. Ceram. Soc., 1994a, **77**, 2363-2368.

Schilling, P.J., Roy, A., Eaton, H.C., Malone, P.G. and Brabston, W.N., Microstructure, strength, and reaction products of ground granulated blast-furnace slag activated by highly concentrated NaOH solution, J. Mater. Res., 1994b, **9**, 188-197.

Schmidt, T., Lothenbach, B., Romer, M., Scrivener, K., Rentsch, D. and Figi, R., A thermodynamic and experimental study of the conditions of thaumasite formation, Cem. Conc. Res., 2008, **38**, 337-349.

Schneider, J., Cincotto, M.A. and Panepucci, H., $^{29}$Si and $^{27}$Al high-resolution NMR characterization of calcium silicate hydrate phases in activated blast-furnace slag pastes, Cem. Concr. Res., 2001, **31**, 993-1001.

Schneider, M., Romer, M., Tschudin, M. and Bolio, H., Sustainable cement production—present and future, Cem. Concr. Res., 2011, **41**, 642-650.

Scrivener, K.L. and Kirkpatrick, R.J., Innovation in use and research on cementitious material, Cem. Concr. Res., 2008, **38**, 128-136.

Shi, C. and Qian, J., High performance cementing materials from industrial slags - a review, Resour. Conserv. Recy., 2000, **29**, 195-207.

Shi, C., Krivenko, P.V. and Roy, D., Alkali-Activated Cements and Concretes, 1$^{st}$ ed., 2006, Taylor & Francis, New York.

Shock, E.L., Helgeson, H.C. and Sverjensky, D.A., Calculation of the thermodynamic and transport properties of aqueous species at high pressures and temperatures: standard partial molal properties of inorganic neutral species, Geochim. Cosmochim. Acta, 1989, **53**, 2157-2183.

Shock, E.L., Sassani, D.C., Willis, M. and Sverjensky, D.A., Inorganic species in geologic fluids: correlations among standard molal thermodynamic properties of aqueous ions and hydroxide complexes, Geochim. Cosmochim. Acta, 1997, **61**, 907-950.

Sideris, P.J., Blanc, F., Gan, Z. and Grey, C.P., Identification of cation clustering in Mg–Al layered double hydroxides using multinuclear solid state nuclear magnetic resonance spectroscopy, Chem. Mater., 2012, **24**, 2449-2461.

Skibsted, J., Nielsen, N.C., Bildsøe, H. and Jakobsen, H.J., Satellite transitions in MAS NMR spectra of quadrupolar nuclei, J. Magn. Reson., 1991, **95**, 88-117.

Skibsted, J. and Andersen, M.D., The effect of alkali ions on the incorporation of aluminum in the calcium silicate hydrate (C–S–H) phase resulting from Portland cement hydration studied by $^{29}$Si MAS NMR, J. Am. Ceram. Soc., 2013, **96**, 651-656.

Skinner, L.B., Chae, S.R., Benmore, C.J., Wenk, H.R. and Monteiro, P.J.M., Nanostructure of calcium silicate hydrates in cements, Phys. Rev. Lett., 2010, **104**, 1-4.

Snellings, R., Mertens, G. and Elsen, J., Supplementary cementitious materials, Rev. Mineral. Geochem., 2012, **74**, 211-278.

Snellings, R., Solution-controlled dissolution of supplementary cementitious material glasses at pH 13: the effect of solution composition on glass dissolution rates, J. Am. Ceram. Soc., 2013, **96**, 2467-2475.

Song, S. and Jennings, H.M., Pore solution chemistry of alkali-activated ground granulated blast-furnace slag, Cem. Concr. Res., 1999, **29**, 159-170.

Stade, H. and Wieker, W., Zum Aufbau schlecht geordneter Calciumhydrogensilicate. I. Bildung und Eigenschaften einer schlecht geordneten Calciumhydrogendisilicatphase, Z. Anorg. Allg. Chem., 1980, **466**, 55-70.

Stade, H. and Müller, D., On the coordination of Al in ill-crystallized C-S-H phases formed by hydration of tricalcium silicate and by precipitation reactions at ambient temperature, Cem. Concr. Res., 1987, **17**, 553-561.

Stade, H., On the reaction of C-S-H(di, poly) with alkali hydroxides, Cem. Concr. Res., 1989, **19**, 802-810.

Sun, G.K., Young, J.F. and Kirkpatrick, R.J., The role of Al in C-S-H: NMR, XRD, and compositional results for precipitated samples, Cem. Concr. Res., 2006, **36**, 18-29.

Suzuki, K., Nishikawa, T. and Ito, S., Formation and carbonation of C-S-H in water, Cem. Concr. Res., 1985, **15**, 213-224.

Sverjensky, D.A., Shock, E.L. and Helgeson, H.C., Prediction of the thermodynamic properties of aqueous metal complexes to 1000°C and 5 kb, Geochim. Cosmochim. Acta, 1997, **61**, 1359-1412.

Taga, T., Crystal structure of $Na_2CO_3 \cdot 10H_2O$, Acta Crystallogr. B, 1969, **25**, 2656-2658.

Talling, B. and Krivenko, P.V., Blast furnace slag - the ultimate binder, in: Waste Materials Used in Concrete Manufacturing, Chandra, S. (Ed.), 1997, Noyes Publications, Park Ridge, NJ, pp. 235-289.

Taylor, H.F.W., Hydrated calcium silicates. Part I. Compound formation at ordinary temperatures, J. Chem. Soc., 1950, 3682-3690.

Taylor, H.F.W., Proposed structure for calcium silicate hydrate gel, J. Am. Ceram. Soc., 1986, **69**, 464-467.

Taylor, H.F.W., A discussion of the papers "Models for the composition and structure of calcium silicate hydrate (C-S-H) gel in hardened tricalcium silicate pastes" and "The incorporation of minor and trace elements into calcium silicate hydrate (C-S-H) gel in hardened cement pastes", Cem. Concr. Res., 1993, **23**, 995-998.

Taylor, H.F.W., Cement Chemistry, 2$^{nd}$ ed., 1997, Thomas Telford Publishing, London.

Taylor, M., Tam, C. and Gielen, D., Energy efficiency and $CO_2$ emissions from the global cement industry, 2006, International Energy Agency, Paris.

Taylor, R., Richardson, I.G. and Brydson, R.M.D., Composition and microstructure of 20-year-old ordinary Portland cement-ground granulated blast-furnace slag blends containing 0 to 100% slag, Cem. Concr. Res., 2010, **40**, 971-983.

Thoenen, T., Hummel, W. and Berner, U., The PSI/Nagra Chemical Thermodynamic Database 12/07: present status and future developments, Mineral. Mag., 2013, **77**, 2327.

Thomas, J.J. and Jennings, H.M., Free-energy-based model of chemical equilibria in the CaO–$SiO_2$-$H_2O$ system, J. Am. Ceram. Soc., 1998, **81**, 606-612.

Thomas, J.J., Rothstein, D., Jennings, H.M. and Christensen, B.J., Effect of hydration temperature on the solubility behavior of Ca-, S-, Al-, and Si-bearing solid phases in Portland cement pastes, Cem. Concr. Res., 2003, **33**, 2037-2047.

Thomas, J.J., Allen, A.J. and Jennings, H.M., Density and water content of nanoscale solid C-S-H formed in alkali-activated slag (AAS) paste and implications for chemical shrinkage, Cem. Concr. Res., 2012, **42**, 377-383.

Tilley, C.E., Megaw, H.D. and Hey, M.H., Hydrocalumite ($4CaO{\cdot}Al_2O_3{\cdot}12H_2O$), a new mineral from Scawt Hill, Co. Antrim, Mineral. Mag., 1934, **23**, 607-615.

Trojer, F.J., The crystal structure of parawollastonite, Z. Kristallogr., 1968, **127**, 291-308.

Tsuji, M., Komarneni, S. and Malla, P., Substituted tobermorites: $^{27}$Al and $^{29}$Si MAS NMR, cation exchange, and water sorption studies, J. Am. Ceram. Soc., 1991, **74**, 274-279.

U.S. Geological Survey, Mineral commodity summaries: cement, http://minerals.usgs.gov/minerals/pubs/commodity/cement/index.html, accessed on 1 April 2014.

van Deventer, J.S.J., Provis, J.L. and Duxson, P., Technical and commercial progress in the adoption of geopolymer cement, Miner. Eng., 2012, **29**, 89-104.

Viallis, H., Faucon, P., Petit, J.C. and Nonat, A., Interaction between salts (NaCl, CsCl) and calcium silicate hydrates (C−S−H), J. Phys. Chem. B, 1999, **103**, 5212-5219.

Vyalikh, A., Massiot, D. and Scheler, U., Structural characterisation of aluminium layered double hydroxides by $^{27}$Al solid-state NMR, Solid State Nucl. Magn. Reson., 2009, **36**, 19-23.

Wagman, D.D., Evans, W.H., Parker, V.B., Schumm, R.H. and Halow, I., The NBS tables of chemical thermodynamic properties: selected values for inorganic and $C_1$ and $C_2$ organic substances in SI units, 1982, American Chemical Society and the American Institute of Physics for the National Bureau of Standards, New York.

Wagner, T., Kulik, D.A., Hingerl, F.F. and Dmytrieva, S.V., GEM-Selektor geochemical modeling package: TSolMod library and data interface for multicomponent phase models, Can. Mineral., 2012, **50**, 1173-1195.

Walker, C.S., Savage, D., Tyrer, M. and Ragnarsdottir, K.V., Non-ideal solid solution aqueous solution modeling of synthetic calcium silicate hydrate, Cem. Concr. Res., 2007, **37**, 502-511.

Wang, S.D. and Scrivener, K.L., Hydration products of alkali activated slag cement, Cem. Concr. Res., 1995, **25**, 561-571.

Wang, S.D. and Scrivener, K.L., $^{29}$Si and $^{27}$Al NMR study of alkali-activated slag, Cem. Concr. Res., 2003, **33**, 769-774.

Way, S.J. and Shayan, A., Study of some synthetically prepared hydrous alkali calcium silicates, Cem. Concr. Res., 1992, **22**, 915-926.

World Business Council for Sustainable Development: Cement Sustainability Initiative, Getting the numbers right (GNR),

http://www.wbcsdcement.org/index.php/key-issues/climate-protection/gnr-database, accessed on 28 July 2014.

Worrell, E., Price, L., Martin, N., Hendriks, C. and Meida, L.O., Carbon dioxide emissions from the global cement industry, Annu. Rev. Energ. Env., 2001, **26**, 303-329.

Xu, H., Provis, J.L., van Deventer, J.S.J. and Krivenko, P.V., Characterization of aged slag concretes, ACI Mater. J., 2008, **105**, 131-139.

# Publications from the Thesis

*Peer-Reviewed Journal Publications*

1. Myers, R.J.; L'Hopital, E.; Provis, J.L.; Lothenbach, B. "The effect of temperature and aluminium on calcium aluminosilicate hydrate chemistry under equilibrium conditions", *Cement and Concrete Research*, **2015**, 68, 83-93.

2. Myers, R.J.; Bernal, S.A.; Provis, J.L.; Gehman, J.D.; van Deventer, J.S.J., "The role of Al in cross-linking of alkali-activated slag binders", *Journal of the American Ceramic Society*, **2015**, DOI: 10.1111/jace.13360.

3. Myers, R.J.; Bernal, S.A.; Provis, J.L., "A thermodynamic model for C-(N-)A-S-H gel: CNASH_ss. Derivation and validation", *Cement and Concrete Research*, **2014**, 66, 27-47.

4. Bernal, S.A.; San Nicolas, R.; Myers, R.J.; de Gutiérrez, R.B.; Puertas, P.; van Deventer, J.S.J.; Provis, J.L., "MgO content of slag controls phase evolution and structural changes induced by accelerated carbonation in alkali-activated binders", *Cement and Concrete Research*, **2014**, 57, 33-43.

5. Myers, R.J.; Bernal, S.A.; San Nicolas, R.; Provis, J.L., "Generalized structural description of calcium-sodium aluminosilicate hydrate gels: the cross-linked substituted tobermorite model", *Langmuir*, **2013**, 29, 5294-5306.

*In Preparation*

1. Myers, R.J.; Bernal, S.A.; Provis, J.L., "Thermodynamic modelling of alkali-activated slag-based binders".

2. Myers, R.J.; L'Hopital, E.; Provis, J.L.; Lothenbach, B. "Composition-solubility-structure relationships in calcium (alkali) aluminosilicate hydrate (C-(N,K-)A-S-H)".

*Conference Presentations*

1. Provis, J.L.; Bernal, S.A.; Myers, R.J. "Alkali-activated binders – linking chemistry, structure and performance", The International Symposium on Cementitious Materials: XIII Encontro da SBPMat, João Pessoa, Brazil, 28 September – 2 October 2014.

2. Myers, R.J.; Bernal, S.; Barbara, L.; Provis, J.L. "The CNASH_ss thermodynamic model: formulation and validation", 34$^{th}$ Cement and Concrete Science Conference, Sheffield, United Kingdom, 14-16 September 2014.

3. Myers, R.J.; Bernal, S.; Barbara, L.; Provis, J.L. "The CNASH_ss thermodynamic model: formulation and validation", Workshop on Waste Cementation, 17 September 2014.

4. Myers, R.J.; Bernal, S.A.; Provis, J.L. "Thermodynamic modelling of Al and alkali-rich cements", The University of Sheffield Engineering Symposium (USES), Sheffield, United Kingdom, 24 June 2014.

5. Myers, R.J.; L'Hopital, E.; Provis, J.L.; Barbara, L. "The effect of temperature, alkali and aluminium on calcium aluminosilicate hydrate chemistry under equilibrium conditions", The Second International Conference on Advances in Chemically-Activated Materials, Changsa, China, 1-3 June 2014.

6. Myers, R.J.; L'Hopital, E.; Provis, J.L.; Barbara, L. "The effect of temperature and aluminium on calcium aluminosilicate hydrate chemistry under equilibrium conditions", EMPA C-A-S-H Workshop, Dübendorf, Switzerland, 5-6 May 2014. [invited presentation]

7. Myers, R.J.; Bernal, S.A.; Provis, J.L. "Development of a sublattice thermodynamic model for C-(N)-A-S-H gel in alkali-activated cements", Born to be Wise: EMPA PhD Students' Symposium, Dübendorf, Switzerland, 23 October 2013.

8. Myers, R.J.; Bernal, S.A.; Provis, J.L. "Sublattice thermodynamic model for C-(N)-A-S-H gel: solid phase assemblages and gel chemistry in alkali-activated slag cements", 1st International Conference on the Chemistry of Construction Materials, Berlin, Germany, 7-9 October 2013.

9. Myers, R.J.; Bernal, S.A.; Provis, J.L. "Crosslinked substituted tobermorite model (CSTM): sodium silicate-activated slag cement chemistry", 33rd Cement and Concrete Science Conference, Portsmouth, United Kingdom, 2-3 September 2013.

10. Myers, R.J. and Provis, J.L. "A sublattice thermodynamic model for C-(N)-A-S-H gel", Research Frontiers in Radioactivate Waste Management, Sheffield, United Kingdom, 10 October 2012.

11. Myers, R.J. and Provis, J.L. "A sublattice thermodynamic model for C-(N)-A-S-H gel", 32nd Cement and Concrete Science Conference, Belfast, United Kingdom, 17-18 September 2012.

# Appendix A

Additional XRD data were measured to support the differential mass loss peak assignments described in Chapters 8 and 9. These data were obtained by heating C-(A-)S-H samples (synthesised under the procedure described in Chapter 3) in a Carbolite HTF 1700 furnace at a rate of 300°C/hour to upper and lower temperatures with respect to the differential mass loss peaks analysed here (Table A.1). The samples were held at the specified temperatures for 1 hour, then cooled at a rate of ~30°C/minute to room temperature under laboratory atmosphere, and subsequently stored in a desiccator (for up to 6 hours in the presence of $SiO_2$ gel) until analysis.

Table A.1. Lower and upper temperatures to which C-(A-)S-H samples were heated for analysis of differential mass loss peaks. Ca/Si* = bulk Ca/Si. Al/Si* = bulk Al/Si.

| Ca/Si* | Al/Si* | Equilibration temperature (°C) | Differential mass loss peak temperature (°C) | Lower temperature (°C) | Upper temperature (°C) |
|---|---|---|---|---|---|
| 1 | 0.1 | 80 | ~500 | 320 | 600 |
| 1 | 0.05 | 50 | ~380 | 250 | 520 |
| 1 | 0 | 50 | ~810 | 550-650 | 950 |
| 1 | 0.1 | 50 | ~810 | 550-650 | 950 |

Figure A.1 shows that heating the C-A-S-H samples equilibrated at 80°C with bulk Al/Si = 0.1 to 600°C, and heating the 50°C C-A-S-H samples with Al/Si* = 0.05 to 520°C, results in the decomposition of C-A-S-H only. Heating these samples to 250°C (Figure A.1B) or 320°C (Figure A.1A) transforms C-A-S-H to a phase with similar long-range order to 9 Å tobermorite (represented by $C_3$ in Figure A.1, $Ca_5Si_6O_{16}(OH)_2$, PDF# 04-012-1761) (Merlino et al., 2000). The C-A-S-H phase loses some structural similarity to 9 Å tobermorite on further heating to 520°C (Figure A.1B) or 600°C (Figure A.1A), which can be identified by the shift of the major 9 Å tobermorite reflections (~29.5° 2θ) to higher angles.

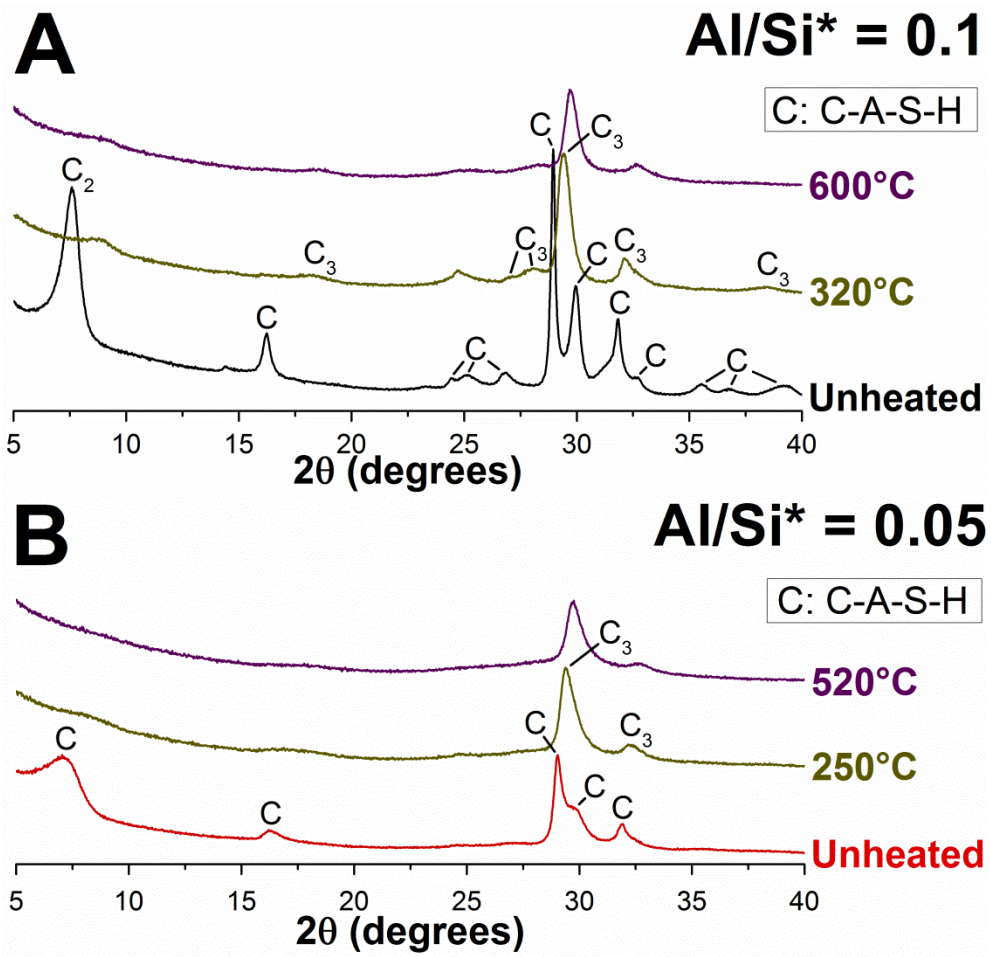


Figure A.1. Cu Kα diffractograms of C-A-S-H samples with A) Al/Si* = 0.1 and equilibrated at 80°C, and B) Al/Si* = 0.05 and equilibrated at 50°C, heated to the temperatures shown in the plots. Al/Si* = bulk Al/Si.

Figure A.2 shows Cu Kα diffractograms for C-(A-)S-H samples equilibrated at 50°C and heated to 550-650°C and 950°C (Al/Si* = 0 and 0.1). Decomposition of C-(A-)S-H occurs up to 550-650°C, which is shown by the loss of the $d_{(002)}$ basal spacing peaks and shifting of the major reflections at ~29° 2θ to higher angles. Formation of a small amount of mayenite ($C_{12}A_7$, PDF# 00-009-0413) is observed in the bulk Al/Si = 0.1 sample during heating to/at 550-650°C (Figure A.2B). Wollastonite ($CaSiO_3$, PDF# 01-076-0925) is formed and decomposition of C-(A-)S-H occurs during heating between 550-650°C and 950°C; complete decomposition of C-(A-)S-H is attained after heating at 950°C for 1 hour. Mayenite is also formed in the C-A-S-H sample during heating at 950°C (Figure A.2B).

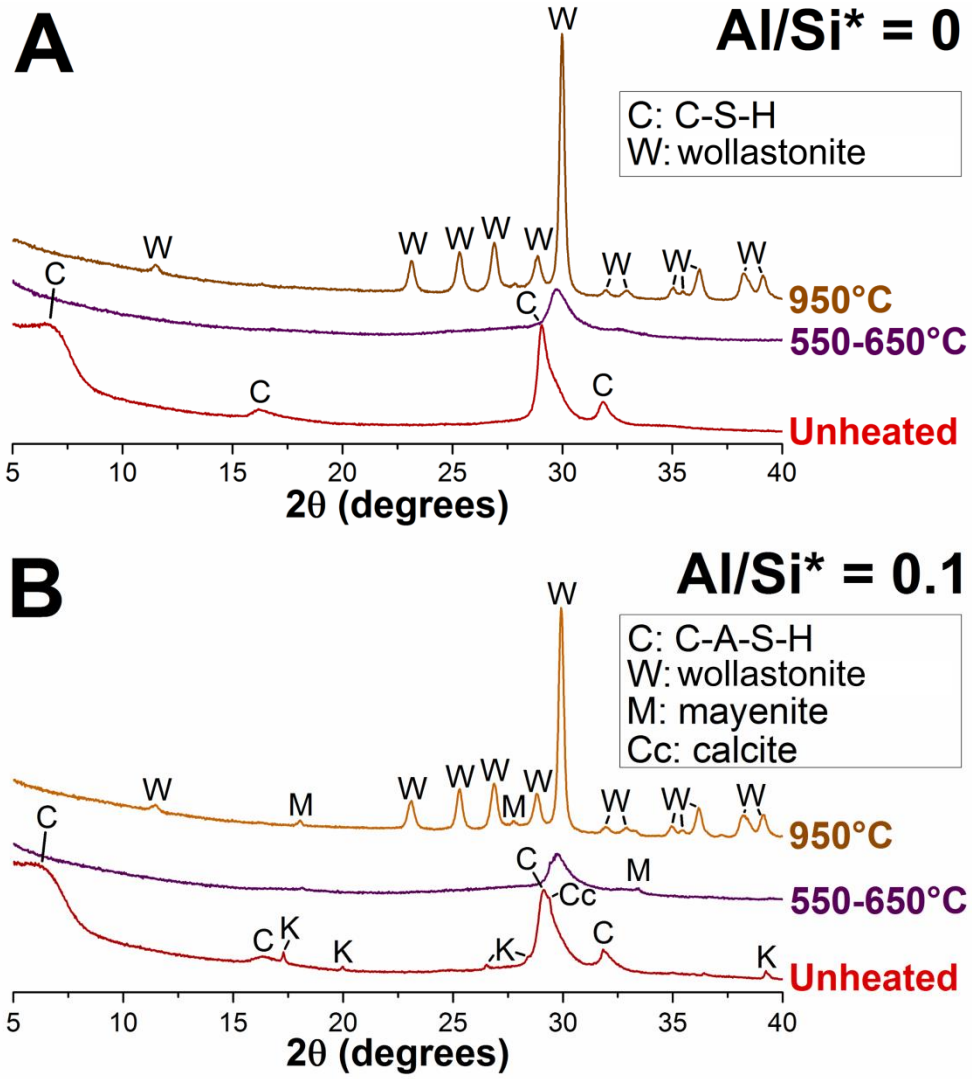


Figure A.2. Cu Kα diffractograms of C-(A-)S-H samples equilibrated at 50°C with A) Al/Si* = 0 and B) Al/Si* = 0.05, heated to the elevated temperatures shown in the plots.

These results confirm the assignment of the differential mass loss peaks at ~380°C and ~500°C in Chapters 8 and 9 to thermal decomposition of C-(A-)S-H, and assignment of the differential mass loss peaks at ~810°C in Chapters 8 and 9 to the decomposition of C-(A-)S-H to wollastonite. These data also show that the thermal behaviour of the C-(A-)S-H products synthesised here is relatively similar to that of 14Å tobermorite (Biagioni et al., 2013), which highlights the high level of structural and chemical similarity between these solid phases.

# Appendix B

Aqueous phase compositions and pH results for the C-(A-)S-H samples investigated in Chapter 8 are shown in Table B.1, and $\log_{10}(K_{so})$ values calculated for the C-(A-)S-H products (using the chemical compositions determined by mass balance and reported in Table 8.5) are shown in Table B.2.

Table B.1. Aqueous phase compositions and pH results for the C-S-H and C-A-S-H systems. Al/Si* = bulk Al/Si.

| **Temperature (°C)** | **[Si] (mmol/L)** | **[Ca] (mmol/L)** | **[Al] (mmol/L)** | **[$OH^-$] (mmol/L)** | **pH †** |
|---|---|---|---|---|---|
| | | **Al/Si* = 0** | | | |
| 7 | 0.025 | 2.0 | 0 | 2.6 | 11.4 |
| 20 | 0.083 | 3.2 | 0 | 3.9 | 11.7 |
| 50 | 0.091 | 2.8 | 0 | 5.9 | 11.7 |
| 80 | 0.11 | 1.7 | 0 | 4.4 | 11.6 |
| | | **Al/Si* = 0.05** | | | |
| 7 | 0.046 | 2.0 | 0.020 | 2.9 | 11.5 |
| 20 | 0.15 | 2.1 | 0.020 | 5.2 | 11.8 |
| 50 | 0.10 | 2.4 | 0.003 | 5.3 | 11.6 |
| 80 | 0.073 | 1.9 | b.d.l. ‡ | 4.2 | 11.6 |
| | | **Al/Si* = 0.1** | | | |
| 7 | 0.053 | 1.7 | 0.036 | 2.5 | 11.4 |
| 20 | 0.11 | 2.9 | 0.031 | 4.2 | 11.7 |
| 50 | 0.17 | 1.5 | 0.028 | 3.5 | 11.5 |
| 80 | 0.074 | 1.7 | 0.005 | 4.2 | 11.6 |
| | | **Al/Si* = 0.15** | | | |
| 7 | 0.069 | 1.3 | 0.043 | 1.9 | 11.3 |
| 20 | 0.34 | 1.3 | 0.023 | 3.0 | 11.5 |
| 50 | 0.32 | 1.2 | 0.043 | 2.1 | 11.3 |
| 80 | 0.094 | 1.1 | 0.039 | 3.0 | 11.4 |

† pH measured at 23°C

‡ b.d.l. = below detection limit for Al (~0.003 mmol/L)

Table B.2. Solubility products for the C-(A-)S-H products with chemical compositions given in Table 8.5, which refer to the dissolution reaction given by eq.(3.8) and $Ca^{2+}_{(aq)}$, $SiO_3^{2-}{}_{(aq)}$, $AlO_2^-{}_{(aq)}$, $OH^-{}_{(aq)}$ and $H_2O_{(l)}$. Al/Si* = bulk Al/Si.

| **Temperature (°C)** | **$\log_{10}(K_{so})$** |
|---|---|
| **Al/Si* = 0** | |
| 7 | -9.98 |
| 20 | -8.91 |
| 50 | -8.66 |
| 80 | -8.80 |
| **Al/Si* = 0.05** | |
| 7 | -9.65 |
| 20 | -8.83 |
| 50 | -8.82 |
| 80 | -9.08 † |
| **Al/Si* = 0.1** | |
| 7 | -9.69 |
| 20 | -8.68 |
| 50 | -8.64 |
| 80 | -9.21 |
| **Al/Si* = 0.15** | |
| 7 | -9.47 |
| 20 | -8.52 |
| 50 | -8.73 |
| 80 | -9.35 |

† Solubility product calculated with [Al] = 0.001 mmol/L because the measured Al concentration was below the detection limit.

# Appendix C

Aqueous phase compositions and pH results for the C-(N-)S-H (Al/Si* = 0) and C-(N-)A-S-H (Al/Si* = 0.05) samples investigated in Chapter 9 are shown in Tables C.1 and C.2 respectively. Solubility products ($K_s$) for the C-(N-)A-S-H products, calculated using the chemical compositions determined by mass balance and reported in Tables 9.7-9.8 (Chapter 9), are shown in Table C.3.

*Appendix C*

Table C.1. Aqueous phase compositions and pH results for the C-(N-)S-H samples (Al/Si* = 0, Ca/Si* = 1) equilibrated at 50°C.

| Synthesis solution | [Si] (mmol/L) | [Ca] (mmol/L) | [Al] (mmol/L) | [K] (mmol/L) | [Na] (mmol/L) | [$OH^-$] (mmol/L) | pH [a] |
|---|---|---|---|---|---|---|---|
| **Ca/Si* = 0.6** | | | | | | | |
| Water | 4.72 | 1.50 | 0 | 0 | 0 | 0.0471 | 9.70 |
| 0.1 M NaOH | 35.3 | 0.008 | 0 | 0 | 54.8 | 14.1 | 12.1 |
| 0.1 M KOH | 30.8 | 0.006 | 0 | 45.4 | 0.291 [c] | 18.4 | 12.2 |
| 0.5 M NaOH/0.5 M KOH | 43.6 | b.d.l. [b] | 0 | 462 | 470 | 576 | 13.7 |
| **Ca/Si* = 0.8** | | | | | | | |
| Water | 2.75 | 1.22 | 0 | 0 | 0 | 0.113 | 10.1 |
| 0.1 M NaOH | 2.65 | 0.004 | 0 | 0 | 61.8 | 50.3 | 12.6 |
| 0.1 M KOH | 2.13 | b.d.l. [b] | 0 | 57.0 | 0.430 [c] | 57.0 | 12.7 |
| 0.5 M NaOH/0.5 M KOH | 0.386 | 0.074 | 0 | 485 | 486 | 639 | 13.7 |
| **Ca/Si* = 1** | | | | | | | |
| Water | 0.091 | 2.77 | 0 | 0 | 0 | 5.93 | 11.7 |
| 0.1 M NaOH | 0.336 | 0.147 | 0 | 0 | 77.2 | 72.5 | 12.8 |
| 0.1 M KOH | 0.079 | 0.540 | 0 | 75.3 | 0.489 [c] | 79.1 | 12.8 |
| 0.5 M NaOH | 0.560 | 0.039 | 0 | 0 | 444 | 390 | 13.5 |
| 0.5 M KOH | 0.288 | 0.132 | 0 | 432 | 0 | 431 | 13.5 |
| 0.5 M NaOH/0.5 M KOH | 1.23 | 0.031 | 0 | 460 | 453 | 639 | 13.7 |
| **Ca/Si* = 1.2** | | | | | | | |
| Water | 0.038 | 6.29 | 0 | 0 | 0 | 11.3 | 12.0 |
| 0.1 M NaOH | 0.124 | 0.533 | 0 | 0 | 91.7 | 87.0 | 12.9 |
| 0.1 M KOH | 0.090 | 0.517 | 0 | 90.4 | 0.493 [c] | 97.0 | 12.9 |
| 0.5 M NaOH/0.5 M KOH | 0.69 | 0.058 | 0 | 465 | 460 | 639 | 13.7 |

Table C.1. Continued.

| Synthesis solution | [Si] (mmol/L) | [Ca] (mmol/L) | [Al] (mmol/L) | [K] (mmol/L) | [Na] (mmol/L) | [$OH^-$] (mmol/L) | pH [a] |
|---|---|---|---|---|---|---|---|
| **Ca/Si* = 1.4** | | | | | | | |
| Water | 0.013 | 9.91 | 0 | 0 | 0 | 17.5 | 12.2 |
| 0.1 M NaOH | 0.040 | 1.37 | 0 | 0 | 100 | 99.9 | 12.9 |
| 0.1 M KOH | 0.032 | 1.34 | 0 | 95.5 | 0.515 [c] | 105 | 12.9 |
| 0.5 M NaOH/0.5 M KOH | 0.491 | 0.103 | 0 | 467 | 464 | 639 | 13.7 |
| **Ca/Si* = 1.6** | | | | | | | |
| Water | 0.006 | 13.1 | 0 | 0 | 0 | 24.1 | 12.4 |
| 0.1 M NaOH | 0.023 | 2.69 | 0 | 0 | 102 | 105 | 12.9 |
| 0.1 M KOH | 0.016 | 2.40 | 0 | 97.3 | 0.544 [c] | 110 | 12.9 |
| 0.5 M NaOH/0.5 M KOH | 0.433 | 0.125 | 0 | 592 | 577 | 639 | 13.7 |

[a] pH measured at ~24°C

[b] b.d.l. = below detection limit (~0.004 mmol/L for Ca)

[c] A small amount of Na is present as an impurity in the 0.1 M KOH synthesis solution

Table C.2. Aqueous phase compositions and pH results for the C-(N-)A-S-H samples (Al/Si* = 0.05, Ca/Si* = 1) equilibrated at 50°C.

| Synthesis solution | [Si] (mmol/L) | [Ca] (mmol/L) | [Al] (mmol/L) | [K] (mmol/L) | [Na] (mmol/L) | [$OH^-$] (mmol/L) | pH [a] |
|---|---|---|---|---|---|---|---|
| **Ca/Si* = 0.6** | | | | | | | |
| Water | 4.25 | 1.27 | b.d.l. [b] | 0 | 0 | 0.060 | 9.80 |
| 0.1 M NaOH | 23.2 | 0.008 | 0.086 | 0 | 45.8 | 22.7 | 12.4 |
| 0.1 M KOH | 18.6 | 0.004 | 0.036 | 46.0 | 0.303 [d] | 23.4 | 12.3 |
| 0.5 M NaOH/0.5 M KOH | 48.9 | b.d.l. [b] | 1.38 | 447 | 447 | 613 | 13.7 |
| **Ca/Si* = 0.8** | | | | | | | |
| Water | 2.13 | 1.19 | b.d.l. [b] | 0 | 0 | 0.158 | 10.2 |
| 0.1 M NaOH | 2.89 | b.d.l. [b] | 0.235 | 0 | 55.0 | 61.5 | 12.8 |
| 0.1 M KOH | 2.04 | b.d.l. [b] | 0.104 | 60.2 | 0.392 [d] | 51.9 | 12.7 |
| 0.5 M NaOH/0.5 M KOH | 10.0 | b.d.l. [b] | 0.708 | 425 | 422 | 635 | 13.7 |
| **Ca/Si* = 1** | | | | | | | |
| Water | 0.104 | 2.36 | 0.003 | 0 | 0 | 5.29 | 11.6 |
| 0.1 M NaOH | 0.417 | 0.092 | 0.026 | 0 | 77.4 | 88.5 | 12.9 |
| 0.1 M KOH | 0.162 | 0.227 | 0.031 | 78.7 | 0.51 [d] | 71.6 | 12.8 |
| 0.5 M NaOH | 0.780 | 0.036 | 0.194 | 0 | 448 | 408 | 13.5 |
| 0.5 M KOH | 0.537 | 0.074 | 0.082 | 441 | 3.28 [d] | 448 | 13.5 |
| 0.5 M NaOH/0.5 M KOH [c] | 1.48 | b.d.l. [b] | 0.121 | 453 | 446 | 645 | 13.7 |

Table C.2. Continued.

| Synthesis solution | [Si] (mmol/L) | [Ca] (mmol/L) | [Al] (mmol/L) | [K] (mmol/L) | [Na] (mmol/L) | [$OH^-$] (mmol/L) | pH [a] |
|---|---|---|---|---|---|---|---|
| **Ca/Si* = 1.2** | | | | | | | |
| Water | 0.057 | 4.16 | b.d.l. [b] | 0 | 0 | 8.11 | 11.9 |
| 0.1 M NaOH | 0.159 | 0.414 | 0.008 | 0 | 86.9 | 97.0 | 12.9 |
| 0.1 M KOH | 0.125 | 0.488 | 0.005 | 93.7 | 0.518 [c] | 84.1 | 12.9 |
| 0.5 M NaOH/0.5 M KOH | 0.744 | 0.087 | 0.085 | 457 | 445 | 658 | 13.8 |
| **Ca/Si* = 1.4** | | | | | | | |
| Water | 0.016 | 3.84 | b.d.l. [b] | 0 | 0 | 17.0 | 12.2 |
| 0.1 M NaOH | 0.025 | 2.53 | b.d.l. [b] | 0 | 93.0 | 116 | 13.0 |
| 0.1 M KOH | 0.022 | 2.38 | b.d.l. [b] | 103 | 0.558 [c] | 94.9 | 12.9 |
| 0.5 M NaOH/0.5 M KOH | 0.563 | 0.128 | 0.062 | 461 | 452 | 682 | 13.8 |
| **Ca/Si* = 1.6** | | | | | | | |
| Water | 0.005 | 8.89 | b.d.l. [b] | 0 | 0 | 29.5 | 12.4 |
| 0.1 M NaOH | 0.018 | 2.90 | b.d.l. [b] | 0 | 95.4 | 122 | 13.0 |
| 0.1 M KOH | 0.018 | 2.85 | b.d.l. [b] | 103 | 0.553 [c] | 98.8 | 12.9 |
| 0.5 M NaOH/0.5 M KOH | 0.520 | 0.152 | 0.059 | 458 | 448 | 682 | 13.8 |

[a] pH measured at ~24°C

[b] b.d.l. = below detection limit (~0.004 mmol/L for Ca and ~0.003 mmol/L for Al)

[c] A small amount of Na is present as an impurity in the 0.1 M KOH synthesis solution

Table C.3. Solubility products ($K_s$) for the C-(N-)A-S-H products synthesised at 50°C, with chemical compositions (Tables 9.7-9.8) determined by TGA, IC and pH measurements (italic font), and TGA, XRD, Rietveld analysis, IC and pH measurements (normal font), which refer to the reaction given by eq.(3.8) and $Ca^{2+}$, $SiO_3^{2-}$, $AlO_2^-$, $Na^+$, $K^+$, $OH^-$ and $H_2O$.

| **Synthesis solution** | **$\log_{10}(K_s)$** | |
|---|---|---|
| | **Ca/Si* = 0.6** | |
| | **Al/Si* = 0** | **Al/Si* = 0.05** |
| Water | -4.6 | ≤-5.1 [a,b] |
| 0.1 M NaOH | -8.9 | -9.7 |
| 0.1 M KOH | -9.6 | -9.8 |
| 0.5 M NaOH/0.5 M KOH | ≤-8.3 [a,c] | ≤-10.0 [a,c] |
| | **Ca/Si* = 0.8** | |
| | **Al/Si* = 0** | **Al/Si* = 0.05** |
| Water | *-6.7* | *≤-7.5* [a,b] |
| 0.1 M NaOH | *-10.1* | *≤-11.1* [a,c] |
| 0.1 M KOH | *≤-10.8* [a,c] | *≤-10.9* [a,c] |
| 0.5 M NaOH/0.5 M KOH | - [d] | *≤-11.8* [a,c] |
| | **Ca/Si* = 1** | |
| | **Al/Si* = 0** | **Al/Si* = 0.05** |
| Water | -8.6 | -9.2 |
| 0.1 M NaOH | -10.2 | -10.8 |
| 0.1 M KOH | -10.3 | -10.9 |
| 0.5 M NaOH/0.5 M KOH | -10.9 | ≤-12.4 [a,c] |
| | **Ca/Si* = 1.2** | |
| | **Al/Si* = 0** | **Al/Si* = 0.05** |
| Water | *-9.9* | *≤-10.7* [a,b] |
| 0.1 M NaOH | *-10.6* | *-11.7* |
| 0.1 M KOH | *-10.9* | *-11.4* |
| 0.5 M NaOH/0.5 M KOH | *-11.1* | *-12.2* |
| | **Ca/Si* = 1.4** | |
| | **Al/Si* = 0** | **Al/Si* = 0.05** |
| Water | -11.3 | ≤-12.6 [a,b] |
| 0.1 M NaOH | -11.4 | ≤-12.6 [a,b] |
| 0.1 M KOH | -11.8 | ≤-12.0 [a,b] |
| 0.5 M NaOH/0.5 M KOH | -11.0 | -13.0 |
| | **Ca/Si* = 1.6** | |
| | **Al/Si* = 0** | **Al/Si* = 0.05** |
| Water | *-12.5* | *≤-13.7* [a,b] |
| 0.1 M NaOH | *-11.3* | *≤-12.4* [a,b] |
| 0.1 M KOH | *-11.6* | *≤-11.8* [a,b] |
| 0.5 M NaOH/0.5 M KOH | *-11.5* | *-13.4* |

[a] Maximum values. Activities of $Ca^{2+}$, $SiO_3^{2-}$, $AlO_2^-$, $Na^+$, $K^+$, $OH^-$ and $H_2O$ were calculated using [b] [Al] = 0.003 mmol/L or [c] [Ca] = 0.004 mmol/L, as the measured concentrations of these elements in the supernatants were below the detection limit.
[d] Solid phase assemblage not measured.

# Appendix D

The TGA results shown in Figure D.1 support the slight discrepancies between the Al/Si ratios determined through the deconvolution analysis presented in Chapter 9 and the Al/Si* ratios used during synthesis, via the identification of $C_3AH_6$, $Al(OH)_3$ ,and $C_4AcH_{11}$ secondary products.

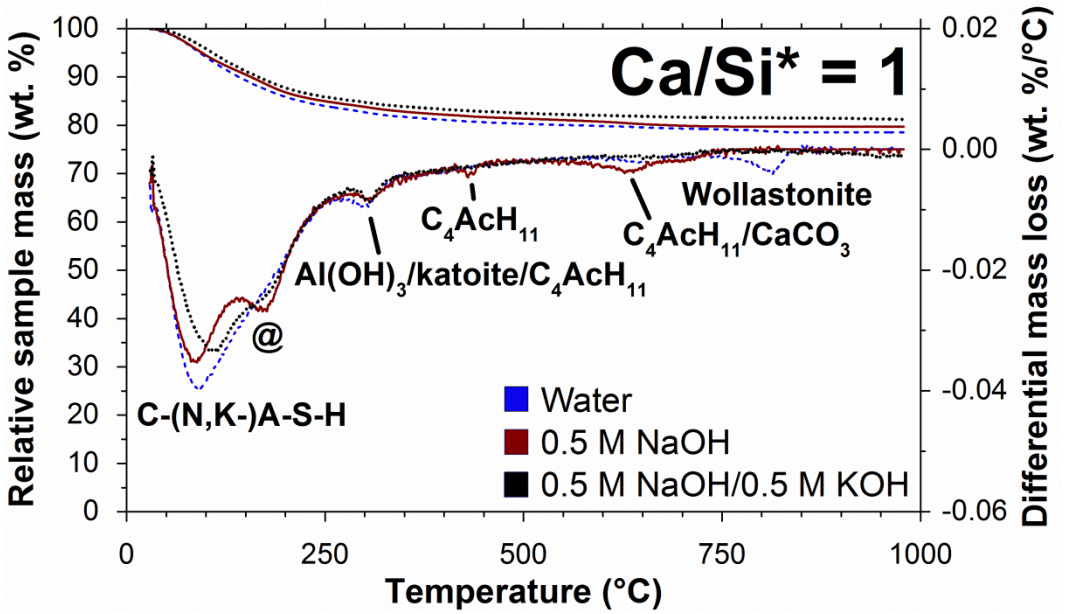


Figure D.1. TGA results for C-(N-)A-S-H samples equilibrated at 50°C with Ca/Si* = 1 and Al/Si* = 0.1. The peak marked by @ is tentatively assigned to decomposition of C-(N-)A-S-H and $C_4AcH_{11}$. Ca/Si* = bulk Ca/Si. Al/Si* = bulk Al/Si.

# Appendix E

Additional solubility data for the alkali and Al-containing C-(N-)A-S-H products studied by $^{29}$Si MAS NMR (Figures 9.13-9.15), investigated in Chapter 9, are shown in Table E.1.

*Appendix E*

Table E.1. Aqueous phase compositions and pH results for C-(N-)A-S-H samples (Al/Si* = 0.1, Ca/Si* = 1) equilibrated at 50°C studied in the structural component of this work.

| **Synthesis solution** | **[Si] (mmol/L)** | **[Ca] (mmol/L)** | **[Al] (mmol/L)** | **[K] (mmol/L)** | **[Na] (mmol/L)** | **[$OH^-$] (mmol/L)** | **pH [a]** |
|---|---|---|---|---|---|---|---|
| 0.5 M NaOH | 0.792 | 0.031 | 0.122 | 0 | 436 | 408 | 13.5 |
| 0.5 M NaOH/0.5 M KOH | 1.38 | b.d.l. [b] | 0.250 | 449 | 445 | 668 | 13.7 |

[a] pH measured at ~24°C

[b] b.d.l. = below detection limit (~0.004 mmol/L for Ca)